

Electrical Geophysics of Carbonate Mound Spring Complexes of the South-Western Great Artesian Basin

Kent Inverarity

Discipline of Geology and Geophysics

School of Earth and Environmental Science

The University of Adelaide

Sunday 13th July, 2014



THE UNIVERSITY
of ADELAIDE

To Pip

The northern vent at Warburton Spring.

“... the party discovered a very beautiful and copious spring of excellent water between [Beresford and Warburton] hills. It rises to a rocky ledge over which it is then heard to fall underground with a sound most pleasant in that arid part of the world, whilst ere long emerging to the light it flows amongst reeds...”

— *South Australian Register*, 30 December 1859, p. 3.

Contents

List of Figures	ix
List of Tables	xvii
Abstract	xxiii
Declaration	xxv
Acknowledgements	xxvii
1 Introduction	1
1.1 Organisation	2
1.2 Conventions	3
2 Geology	5
2.1 Mound springs	6
2.1.1 Hydrochemistry	7
2.2 Great Artesian Basin	8
2.2.1 Stratigraphy of the Lake Eyre region	12
2.2.2 Hydrostratigraphy	14
2.3 Beresford and Warburton Springs	16
2.3.1 Beresford Spring	21
2.3.2 Warburton Spring	22
2.4 The Bubbler Spring complex	23
2.5 Freeling Springs	27
3 Methods	31
3.1 Magnetotellurics	31
3.1.1 Physics	31
3.1.2 The impedance tensor	32
3.1.3 Phase tensor	36

3.1.4	Modelling	38
3.1.5	Instrumentation	41
3.2	Self potential	43
3.2.1	Physics	43
3.2.2	Instrumentation and field procedure	47
3.2.3	Analytical techniques	47
3.3	Time-domain electromagnetics (TEM)	51
3.3.1	Physics	51
3.3.2	Application and modelling	52
3.3.3	Induced polarization effects	52
4	Beresford Spring	55
4.1	SP	59
4.1.1	Data reduction	59
4.1.2	Median potential maps	59
4.1.3	Profile A	60
4.1.4	Profiles B and C	63
4.1.5	Profiles D and E	66
4.1.6	Profile F	66
4.2	TEM	71
4.3	MT data	74
4.3.1	Broad survey line	74
4.3.2	Detailed survey line	79
4.4	Anisotropic 1D MT modelling	82
4.4.1	Type A	83
4.4.2	Type B	87
4.5	2D MT inversion	91
4.5.1	Broad survey	91
4.5.2	Detailed survey line	93
5	Warburton Spring	95
5.1	SP	97
5.2	Magnetotelluric data	99
5.2.1	AMT data	99
5.2.2	MT data	104
5.3	2D MT modelling	109
5.3.1	High-frequency AMT sites	109
5.3.2	Low-frequency MT sites	111

6	Area surrounding Beresford and Warburton Springs	115
6.1	MT data	117
6.1.1	Line A	117
6.1.2	Line C	117
6.2	2D MT modelling	123
6.2.1	Line A	123
6.2.2	Line C	123
7	The Bubbler Spring complex	125
7.1	SP	128
7.1.1	Data processing	128
7.1.2	Line A	128
7.1.3	Line B	130
7.1.4	Line C	133
7.2	TEM	139
7.3	MT data	141
7.3.1	Line A	141
7.3.2	Line C	146
7.4	Anisotropic 1D MT modelling	151
7.5	2D MT inversion	155
7.5.1	Line A	155
7.5.2	Line C	156
8	Freeling Springs	163
8.1	SP	166
8.1.1	Data quality	166
8.1.2	Data processing	168
8.1.3	Line N1	168
8.1.4	Lines N2 and N3	171
8.1.5	Line S1	176
8.2	TEM	180
8.3	MT data	183
8.3.1	Southern line	183
8.3.2	Northern line	187
8.4	2D MT modelling	189
8.4.1	Southern line	190
8.4.2	Northern line	195

9 Interpretation	197
9.1 Beresford/Warburton Spring complex	197
9.1.1 Beresford Spring	197
9.1.2 Beresford Hill	201
9.1.3 Vertical flow in aquifer west of the mound	202
9.1.4 Downward infiltration in playa	202
9.1.5 Warburton Spring	203
9.2 The Bubbler Spring complex	205
9.2.1 Vertical flow beneath mounds	205
9.2.2 Fault-controlled thinning of aquitard	205
9.2.3 Flow variation parallel to strike	208
9.2.4 Little Bubbler mound	209
9.3 Freeling Springs	210
9.3.1 Subsurface lithology	210
9.3.2 Vertical flow paths	213
10 Conclusions	215
10.1 Hydrogeology	215
10.1.1 Flow paths	215
10.1.2 Fault structures	216
10.2 Geophysical techniques	217
10.2.1 Self potential	217
10.2.2 Magnetotellurics and TEM	218
10.3 Future work	219
Appendix A Magnetotelluric data	221
A.1 Beresford Spring	221
A.1.1 Broad-scale survey	221
A.1.2 Detailed survey over spring	228
A.2 Warburton Spring	233
A.2.1 AMT survey	233
A.2.2 MT survey	238
A.3 Area surrounding Beresford and Warburton Springs	245
A.3.1 Line C	245
A.4 The Bubbler Spring complex	253
A.4.1 Line A	253
A.4.2 Line C	260
A.5 Freeling Springs	265

A.5.1	Line S1	265
A.5.2	Line N1	270
Appendix B	Self-potential	273
B.1	Data tables	273
B.1.1	Beresford Spring	274
B.1.2	Warburton Spring	290
B.1.3	The Bubbler spring complex	292
B.1.4	Freeling Springs	298
References		303

List of Figures

2.1	Map of the central and south-western GAB.	10
2.2	Map of the Lake Eyre region of the south-western GAB.	11
2.3	Geological cross-section through the western GAB.	12
2.4	Overview geological map of the Beresford and Warburton Springs complex.	17
2.5	Detailed geological maps of (A) Beresford Spring and (B) Warburton Spring.	19
2.6	Panoramic photographs of the Beresford/Warburton playa with the locations of AMT and MT sites shown.	20
2.7	Overview geological map of the Bubbler Spring complex.	24
2.8	Geological map of the Bubbler Spring complex.	26
2.9	Overview geological map of the Freeling Spring complex.	28
2.10	Geological cross-section through the Freeling Springs complex.	28
2.11	Panoramic photographs of the Freeling Springs complex.	30
3.1	Structural anisotropy as a scale effect of averaged fields across isotropic conductors.	34
3.2	The MT phase tensor.	39
3.3	Photographic mosaic of a typical MT site near Warburton Hill.	42
3.4	The diffuse layer of charges (electrical double layer) formed on the interface between silicate grain boundaries and pore fluids.	44
3.5	Field technique for measuring self-potential.	47
3.6	Sensitivity of forward-modelled SP profiles to variations in a source area's geometry and location.	50
3.7	Instrument setup used in the field to measure time-domain electromagnetic responses.	52
4.1	Location of MT sites near Beresford Spring.	57

4.2	Location of SP observations and composite profiles over Beresford Spring.	58
4.3	(A) Corrected self-potential data across Beresford Spring. The spring vent is at station 0. Each SP measurement is shown as a point. Field traverses are shown as coloured lines. Note that station numbers are different to the composite profile figures which follow.	60
4.4	Self-potential data around Beresford Spring on a 60 x 60 m grid.	61
4.5	Self-potential data around Beresford Spring on a 30 x 30 m grid.	61
4.6	Self-potential data from Profile A.	62
4.7	Self-potential data from Profile B.	64
4.8	Self-potential data from Profile C.	65
4.9	Self-potential data from Profile D.	67
4.10	Self-potential data from Profile E.	68
4.11	Self-potential data from Profile F.	70
4.12	Location of TEM stations over Beresford Spring.	72
4.13	TEM responses for all decay times between 1 μ s and 2.5 ms. . .	72
4.14	Resistivity model obtained by 1D inversion of TEM data. . . .	73
4.15	Fit of resistivity model to TEM data for selected sites.	73
4.16	Pseudosection of phase tensors from the broad survey line. . .	76
4.17	Pseudosection of phase tensor azimuths along the broad survey line.	77
4.18	Cross-section of apparent resistivity and phase from the broad survey at Beresford Spring.	78
4.19	Pseudosection of phase tensors from the detailed survey. . . .	80
4.20	Pseudosection of phase tensor azimuths along the detailed survey line.	81
4.21	Cross-section of apparent resistivity and phase from the detailed survey at Beresford Spring.	81
4.22	Magnetotelluric sites used to create the composite responses. .	83
4.23	Type A composite MT response averaged from sites at Beresford Spring.	84
4.24	Anisotropic 1D resistivity models from $k=5$ that best fit the Type A composite response.	85
4.25	Anisotropic 1D resistivity models from $k=7$ that best fit the Type A composite response.	86

4.26	Type B composite MT response averaged from sites at Beresford Spring.	87
4.27	Anisotropic 1D resistivity models from $k=1$ that best fit the Type B composite response.	89
4.28	Anisotropic 1D resistivity models from $k=10$ that best fit the Type B composite response.	90
4.29	Resistivity model from 2D inversion fitting to within 20% of apparent resistivities and 5% of phases along the broad survey line.	92
4.30	Fit of 2D MT model (Figure 4.29) forward responses to observations.	92
4.31	Resistivity model from 2D inversion fitting to within 20% of apparent resistivities (excluding BSPR) and 5% of phases along the detailed survey line.	93
4.32	Fit of 2D MT model (Figure 4.31) forward responses to observations.	94
5.1	Location of SP and MT observations near Warburton Spring.	96
5.2	Self-potential and potential gradient ΔV at Warburton Spring.	98
5.3	Self-potential data (A) and image reconstruction (B) over Warburton Spring.	98
5.4	Configuration of an AMT spread recorded at Warburton Spring, containing three sites.	100
5.5	Cross-section of apparent resistivity and phase from the western spread of the AMT survey.	101
5.6	Pseudosection of phase tensors from the AMT survey.	102
5.7	Pseudosection of phase tensor azimuths for the AMT survey.	103
5.8	Cross-section of apparent resistivity and phase from AMT sites at Warburton Spring.	103
5.9	Pseudosection of phase tensors from the MT survey.	106
5.10	Pseudosection of phase tensor azimuths for the MT survey.	107
5.11	Cross-section of apparent resistivity and phase from MT sites at Warburton Spring.	108
5.12	Cross-section of approximate maximum penetration depths for 20 Hz responses at WW1, WWB, WS, WE0, and WE1.	109
5.13	Resistivity model from 2D inversion fitting to within 40% of apparent resistivities and 10% of phases for AMT data.	110

5.14	Fit of 2D AMT model (Figure 5.13) forward responses to observations.	110
5.15	Resistivity model from 2D inversion fitting to within 20% of apparent resistivities and 5% of phases for MT sites.	112
5.16	Fit of 2D MT model (Figure 5.15) forward responses to observations.	113
6.1	Location of MT sites near the Beresford Hill playa.	116
6.2	Pseudosection of phase tensors from Line A.	118
6.3	Cross-section of apparent resistivity and phase from MT sites along Line A in the Beresford/Warburton area.	119
6.4	Pseudosection of phase tensors from Line C.	121
6.5	Cross-section of apparent resistivity and phase from MT sites along Line C in the Beresford/Warburton area.	122
6.6	2D resistivity model for MT data on Line A near the Beresford Hill playa, fitting to 5% of phase data and 20% of apparent resistivity data.	124
6.7	2D resistivity model for MT data on Line C near the Beresford Hill playa, fitting to 5% of phase data and 20% of apparent resistivity data.	124
7.1	Map of SP observations at the Bubbler Spring complex	127
7.2	Self-potential and potential gradient ΔV along Line A.	129
7.3	Self-potentials (A) and image reconstruction (B) over Line A.	131
7.4	Self-potential and potential gradient ΔV along Line B at the Bubbler Spring complex.	132
7.5	Self-potential data (A) and image reconstruction (B) over Line B.	133
7.6	Self-potential and potential gradient ΔV along Line C.	134
7.7	Map of potentials near the intersection of Line A and Line C.	136
7.8	SP data (A) and image reconstruction (B) over Line C at the Bubbler Spring complex.	136
7.9	Image reconstructions calculated for subsets of the Line C data between stations 1150 and 1500 which are left after removal of different sets of measured potentials.	138
7.10	TEM responses along Line A for all decay times between 1 μs and 2.5 ms.	140
7.11	Resistivity model obtained by 1D inversion of TEM data.	140
7.12	Fit of resistivity model to TEM data for selected sites.	141

7.13 Pseudosection of phase tensors from Line A.	143
7.14 Pseudosection of phase tensor azimuths along Line A.	144
7.15 Cross-section of apparent resistivity and phase from MT sites on Line A.	145
7.16 Pseudosection of phase tensors from Line C.	148
7.17 Pseudosection of phase tensor azimuths along Line C.	149
7.18 Cross-section of apparent resistivity and phase from MT sites on Line C.	150
7.19 MT sites used to create the composite response used for anisotropic modelling.	151
7.20 Composite MT response averaged from sites at the Bubbler Spring complex.	152
7.21 Anisotropic 1D resistivity models from $k=5$ that best fit the composite site.	152
7.22 Anisotropic 1D resistivity models from $k=4$ that best fit the composite site.	153
7.23 Anisotropic 1D resistivity models from $k=6$ that best fit the composite site.	154
7.24 Resistivity model from 2D inversion fitting to within 50% of apparent resistivities and 2% of phases along Line A.	156
7.25 Fit of 2D MT model (Figure 7.24) forward responses to obser- vations.	157
7.26 Resistivity model from 2D inversion fitting to within 20% of apparent resistivities and 4% of phases along Line C, with a strike of 090°	158
7.27 Fit of 2D MT model (Figure 7.26) forward responses to obser- vations.	158
7.28 Resistivity model from 2D inversion fitting to within 20% of apparent resistivities and 3% of phases along Line C, with a strike of 020°	160
7.29 Fit of 2D MT model (Figure 7.28) forward responses to obser- vations.	160
8.1 Location of SP, TEM, and MT observations at Freeling Springs	165
8.2 Range of contact resistances and potentials encountered on dif- ferent surveys.	167
8.3 Self-potential and potential gradient ΔV along Line N1 at Freel- ing Springs.	169

8.4	SP data (A) and image reconstruction (B) over Line N1.	170
8.5	Image reconstructions calculated for Line N1 data after the removal of different subsets of anomalously negative potentials near station 1050.	170
8.6	Self-potential and potential gradient ΔV along Line N1, showing only those measurements with contact resistances below 1 M Ω	171
8.7	Contact resistance and SP for observations along Line N1. . . .	172
8.8	Location of SP observations along Lines N1, N2, and N3.	172
8.9	Self-potential and potential gradient ΔV along Lines N1 and N2.	173
8.10	SP data (A) and image reconstruction (B) over Line N2.	174
8.11	Self-potential and potential gradient ΔV along Line N3.	175
8.12	Image reconstructions calculated for Line N3 data before (A) and after (B) removal of two outlier potential measurements at stations 45 and 75.	175
8.13	Self-potential and potential gradient ΔV along Line S1 including high-resistance measurements in the highlands.	176
8.14	Contact resistance and SP for observations along Line S1. . . .	177
8.15	Self-potential and potential gradient ΔV along Line S1 excluding measurements with contact resistances greater than 1 M Ω	177
8.16	Self-potential data (A) and image reconstruction (B) over Line S1.	178
8.17	Image reconstructions calculated for subsets of the Line S1 data left after removal of different portions of data collected in the highlands.	179
8.18	Resistivity model obtained by 1D inversion of TEM data.	181
8.19	Fit of resistivity model to TEM data for selected sites.	181
8.20	TEM responses along Line N1 for all decay times between 1 μ s and 2.5 ms.	183
8.21	Pseudosection of phase tensors from Line S1.	185
8.22	Apparent resistivity and phase along Line S1.	186
8.23	Pseudosection of phase tensors from Line N1.	188
8.24	Apparent resistivity and phase along Line N1.	189
8.25	Resistivity model from 2D inversion fitting to within 20% of apparent resistivities and 5% of phases along Line S1. Sites FW2 and FW1 were not included in the inversion.	191

8.26	Fit of 2D MT model (Figure 8.25) forward responses to observations.	191
8.27	Resistivity model from 2D inversion fitting to within 30% of apparent resistivities and 5% of phases along Line S1. FW2 was not included in the inversion.	192
8.28	Fit of 2D MT model (Figure 8.27) forward responses to observations.	193
8.29	Resistivity model from 2D inversion fitting to within 20% of apparent resistivities and 10% of phases along Line S1, with only the TM mode fitted at FW2 and FW1.	194
8.30	Fit of 2D MT model (Figure 8.29) forward responses to observations.	194
8.31	Resistivity model from 2D inversion fitting to within 30% of apparent resistivities and 10% of phases along Line N1.	195
8.32	Fit of 2D MT model (Figure 8.32) forward responses to observations.	196
9.1	Hydrogeology of Beresford Spring, showing the (A) SP data along Profile A, and (B) TEM and (C) broad-survey MT 2D resistivity models.	198
9.2	Hydrogeology of Warburton Spring, showing the (A) SP data, and (B) AMT and (C) MT 2D models.	204
9.3	Hydrogeology of the Bubbler Spring complex along Line C. . .	206
9.4	Hydrogeology of the Little Bubbler, showing (A) SP data from Line A, and (B) the TEM resistivity model.	209
9.5	Hydrogeology of the Freeling Springs complex, showing (A) SP data and (B) the TEM resistivity model from Line N1, and (C) the SP data and (D) 2D MT resistivity model from an inversion for all sites on Line S1.	211
B.1	Uncertainty in field potential measurements due to voltmeter polarity.	273
B.2	Corrections applied to potential data from 21 April 2012.	275
B.3	No corrections were applied to potential data from 22 April 2012.	276
B.4	Corrections applied to potential data from 23 April 2012.	276
B.5	Corrections applied to potential data from 24 April 2012.	277
B.6	Corrections applied to potential data from 25 April 2012.	277
B.7	Spatial corrections for potentials measured along Line MAIN. . .	278

B.8	Spatial corrections for potentials measured along Line SE. . . .	279
B.9	Spatial corrections for potentials measured along Line A. . . .	294
B.10	Spatial corrections for potentials measured along Line B. . . .	294

List of Tables

2.1	Ages of structures at the Beresford/Warburton Spring complex estimated from U-series thermoluminescence dating.	18
2.2	Electrical resistivity of aquifer water at the Beresford/Warburton Spring complex.	18
2.3	Electrical resistivity of water in the Beresford Spring vent. . . .	22
2.4	Electrical resistivity of spring water at the Warburton Spring vent.	23
2.5	Spring discharge flow rates at the Bubbler Spring complex. . . .	24
2.6	Ages of structures at the Bubbler Spring complex estimated from U-series thermoluminescence dating.	25
7.1	Elevated SP features associated with spring mounds on Line A.	130
7.2	Elevated SP features associated with spring mounds on Line B.	132
7.3	Elevated SP features associated with spring mounds on Line C.	135
A.1	Impedance tensor estimates made at BWA1000.	221
A.1	Impedance tensor estimates made at BWA1000 (continued). . . .	222
A.2	Impedance tensor estimates made at BWA1335.	222
A.2	Impedance tensor estimates made at BWA1335 (continued). . . .	223
A.3	Impedance tensor estimates made at BWA1930.	223
A.4	Impedance tensor estimates made at BWA2350.	224
A.5	Impedance tensor estimates made at BWA2890.	224
A.5	Impedance tensor estimates made at BWA2890 (continued). . . .	225
A.6	Impedance tensor estimates made at BWA3140.	225
A.6	Impedance tensor estimates made at BWA3140 (continued). . . .	226
A.7	Impedance tensor estimates made at BWA3700.	226
A.7	Impedance tensor estimates made at BWA3700 (continued). . . .	227
A.8	Impedance tensor estimates made at BWA4200.	227
A.9	Impedance tensor estimates made at BSPRW1.	228
A.9	Impedance tensor estimates made at BSPRW1 (continued). . . .	229

A.10 Impedance tensor estimates made at BSPRW2.	229
A.10 Impedance tensor estimates made at BSPRW2 (continued). . . .	230
A.11 Impedance tensor estimates made at BSPR.	230
A.11 Impedance tensor estimates made at BSPR (continued).	231
A.12 Impedance tensor estimates made at BSPRE1.	231
A.12 Impedance tensor estimates made at BSPRE1 (continued). . . .	232
A.13 Impedance tensor estimates made at BSPRE2.	232
A.13 Impedance tensor estimates made at BSPRE2 (continued). . . .	233
A.14 Impedance tensor estimates made at WZW3.	233
A.14 Impedance tensor estimates made at WZW3 (continued).	234
A.15 Impedance tensor estimates made at WZW2.	234
A.15 Impedance tensor estimates made at WZW2 (continued).	235
A.16 Impedance tensor estimates made at WZW1.	235
A.17 Impedance tensor estimates made at WZS.	235
A.17 Impedance tensor estimates made at WZS (continued).	236
A.18 Impedance tensor estimates made at WZE1.	236
A.18 Impedance tensor estimates made at WZE1 (continued).	237
A.19 Impedance tensor estimates made at WZE2.	237
A.19 Impedance tensor estimates made at WZE2 (continued).	238
A.20 Impedance tensor estimates made at WW2.	238
A.20 Impedance tensor estimates made at WW2 (continued).	239
A.21 Impedance tensor estimates made at WW1.	239
A.21 Impedance tensor estimates made at WW1 (continued).	240
A.22 Impedance tensor estimates made at WWB.	240
A.22 Impedance tensor estimates made at WWB (continued).	241
A.23 Impedance tensor estimates made at WWA.	241
A.24 Impedance tensor estimates made at WS.	242
A.25 Impedance tensor estimates made at WE0.	242
A.25 Impedance tensor estimates made at WE0 (continued).	243
A.26 Impedance tensor estimates made at WE1.	243
A.26 Impedance tensor estimates made at WE1 (continued).	244
A.27 Impedance tensor estimates made at WE2.	244
A.27 Impedance tensor estimates made at WE2 (continued).	245
A.28 Impedance tensor estimates made at BWR1.	245
A.28 Impedance tensor estimates made at BWR1 (continued).	246
A.29 Impedance tensor estimates made at BWC1000.	246
A.30 Impedance tensor estimates made at BWC1500.	247

A.31 Impedance tensor estimates made at BWC2000.	247
A.31 Impedance tensor estimates made at BWC2000 (continued). . .	248
A.32 Impedance tensor estimates made at BWC2500.	248
A.32 Impedance tensor estimates made at BWC2500 (continued). . .	249
A.33 Impedance tensor estimates made at BWC3000.	249
A.34 Impedance tensor estimates made at BWC3580.	250
A.35 Impedance tensor estimates made at BWC4050.	250
A.35 Impedance tensor estimates made at BWC4050 (continued). . .	251
A.36 Impedance tensor estimates made at BWC4700.	251
A.36 Impedance tensor estimates made at BWC4700 (continued). . .	252
A.37 Impedance tensor estimates made at BWC5150.	252
A.37 Impedance tensor estimates made at BWC5150 (continued). . .	253
A.38 Impedance tensor estimates made at WKA5750.	253
A.38 Impedance tensor estimates made at WKA5750 (continued). . .	254
A.39 Impedance tensor estimates made at WKA5625.	254
A.40 Impedance tensor estimates made at WKA5475.	255
A.41 Impedance tensor estimates made at WKA5360.	255
A.41 Impedance tensor estimates made at WKA5360 (continued). . .	256
A.42 Impedance tensor estimates made at WKA5250.	256
A.42 Impedance tensor estimates made at WKA5250 (continued). . .	257
A.43 Impedance tensor estimates made at WKA5125.	257
A.43 Impedance tensor estimates made at WKA5125 (continued). . .	258
A.44 Impedance tensor estimates made at WKA5050.	258
A.44 Impedance tensor estimates made at WKA5050 (continued). . .	259
A.45 Impedance tensor estimates made at WKA4930.	259
A.46 Impedance tensor estimates made at WKA4645.	260
A.47 Impedance tensor estimates made at WKC2350.	260
A.47 Impedance tensor estimates made at WKC2350 (continued). . .	261
A.48 Impedance tensor estimates made at WKC2200.	261
A.48 Impedance tensor estimates made at WKC2200 (continued). . .	262
A.49 Impedance tensor estimates made at WKC2100.	262
A.49 Impedance tensor estimates made at WKC2100 (continued). . .	263
A.50 Impedance tensor estimates made at WKC1850.	263
A.50 Impedance tensor estimates made at WKC1850 (continued). . .	264
A.51 Impedance tensor estimates made at WKC1330.	264
A.52 Impedance tensor estimates made at WKC1100.	265
A.53 Impedance tensor estimates made at FW2.	265

A.53 Impedance tensor estimates made at FW2 (continued).	266
A.54 Impedance tensor estimates made at FW1.	266
A.54 Impedance tensor estimates made at FW1 (continued).	267
A.55 Impedance tensor estimates made at FS.	267
A.56 Impedance tensor estimates made at FE1.	268
A.57 Impedance tensor estimates made at FE2.	268
A.57 Impedance tensor estimates made at FE2 (continued).	269
A.58 Impedance tensor estimates made at FE3.	269
A.58 Impedance tensor estimates made at FE3 (continued).	270
A.59 Impedance tensor estimates made at FN1.	270
A.59 Impedance tensor estimates made at FN1 (continued).	271
A.60 Impedance tensor estimates made at FN2.	271
A.61 Impedance tensor estimates made at FN3.	272
B.1 Self-potential data along Line 21_E.	280
B.2 Self-potential data along Line 21_MAIN.	280
B.2 Self-potential data along Line 21_MAIN (continued).	281
B.2 Self-potential data along Line 21_MAIN (continued).	282
B.3 Self-potential data along Line 21_SE.	282
B.4 Self-potential data along Line 22_MAINEXT.	283
B.5 Self-potential data along Line 22_SE.	283
B.6 Self-potential data along Line 22B_MAINEXT.	284
B.7 Self-potential data along Line 23_ENE.	284
B.8 Self-potential data along Line 23_NW.	284
B.8 Self-potential data along Line 23_NW (continued).	285
B.9 Self-potential data along Line 23_SSW.	285
B.9 Self-potential data along Line 23_SSW (continued).	286
B.10 Self-potential data along Line 24_ENE.	286
B.11 Self-potential data along Line 24_MAIN.	286
B.11 Self-potential data along Line 24_MAIN (continued).	287
B.12 Self-potential data along Line 24_N.	287
B.12 Self-potential data along Line 24_N (continued).	288
B.13 Self-potential data along Line 24_W.	288
B.14 Self-potential data along Line 24_WSW.	289
B.15 Self-potential data along Line 25_NE.	289
B.16 Self-potential data along Line 25_S.	289
B.16 Self-potential data along Line 25_S (continued).	290
B.17 Self-potential data from Warburton Spring.	290

B.17 Self-potential data from Warburton Spring (continued).	291
B.17 Self-potential data from Warburton Spring (continued).	292
B.18 Self-potential data along Line A.	292
B.18 Self-potential data along Line A (continued).	293
B.19 Self-potential data along Line B.	295
B.19 Self-potential data along Line B (continued).	296
B.20 Self-potential data along Line C.	296
B.20 Self-potential data along Line C (continued).	297
B.21 Static corrections applied to SP data from the Bubbler spring complex.	298
B.20 Self-potential data along Line C (continued).	298
B.22 Self-potential data along Line N1.	299
B.22 Self-potential data along Line N1 (continued).	300
B.23 Self-potential data along Line N2.	300
B.24 Self-potential data along Line N3.	300
B.24 Self-potential data along Line N3 (continued).	301
B.25 Self-potential data along Line S1.	301
B.25 Self-potential data along Line S1 (continued).	302

Abstract

Artesian mound springs occur along the south-western edge of the Great Artesian Basin, in northern South Australia, but their underground structure and relationship to faulting is not well understood. This work aims to address this shortcoming with geophysical surveys over three mound spring systems (Beresford and Warburton Springs, the Bubbler Spring complex, and Freeling Springs), using a range of techniques: self-potential, magnetotellurics, and time-domain electromagnetics.

The self-potential data contain elevated local responses to spring vents and seeps. Spatial correlation suggests that these responses are caused by flow related to springs. Similar responses also occur underneath 'extinct' springs, suggesting shallow subsurface discharge of aquifer water is still occurring. Little evidence was found for significant downward infiltration from spring tails.

Modelling of time-domain electromagnetic and magnetotelluric data show that the confining Bulldog Shale, which is generally very conductive, contains slightly more resistive areas underneath springs and spring complexes, which may be related to a combination of carbonate buildup in the subsurface and more resistive aquifer water flowing to the surface. Magnetotelluric data and anisotropic 1D modelling suggests that fault zones exist under many of the mound springs, particularly at Beresford and Warburton Springs and the Bubbler Spring complex, with data consistent with models containing parallel vertical fault planes striking NW/SE. The models contain fault zones in the aquifer and the immediately underlying basement, suggesting that fluids may be sourced from the aquifer and deeper layers, and that faults may be acting as conduits through the aquitard. However, neither the faults nor the conduits to specific springs have been successfully imaged using the techniques employed here, suggesting that the conduits are narrow and present only a slight contrast in fluid resistivities.

Declaration

I certify that this work contains no material which has been accepted for the award of any other degree or diploma in my name, in any university or other tertiary institution and, to the best of my knowledge and belief, contains no material previously published or written by another person, except where due reference has been made in the text. In addition, I certify that no part of this work will, in the future, be used in a submission in my name, for any other degree or diploma in any university or other tertiary institution without the prior approval of the University of Adelaide and where applicable, any partner institution responsible for the joint-award of this degree.

I give consent to this copy of my thesis, when deposited in the University Library, being made available for loan and photocopying, subject to the provisions of the Copyright Act 1968.

I also give permission for the digital version of my thesis to be made available on the web, via the University's digital research repository, the Library Search and also through web search engines, unless permission has been granted by the University to restrict access for a period of time.

Kent Inverarity

Acknowledgements

I would like to thank my supervisors Graham Heinson, Michael Hatch, and Stephan Thiel, from the University of Adelaide, for all their help, advice, support, and patience! Thanks also to Volmer Berens, Adrian Costar, and Dan Wohling, from the South Australian Department for Environment, Water, and Natural Resources, and Andrew Love, from Flinders University, for advice and logistical support. I would also like to thank those people who helped me in the field: Hamish Adam, Goran Boren, Anastasia Costopoulos, Robert Lampe, Alison Langsford, David Pedler-Jones, Aixa Rivera-Rios, Jonathan Ross, Sebastian Schnaidt, Katherine Stoate, and James Wilson. Thanks also to Jared Peacock and Lars Krieger for their help with computing.

I would also like to thank the programs and organisations which funded my work:

- the “Allocating Water and Maintaining Springs of the Great Artesian Basin” project of the National Water Commission
- the Geoscientists *Without* Borders initiative of the Society of Exploration Geophysicists’ Foundation
- the University of Adelaide.

Thanks also to the AuScope facility at the University of Adelaide, and Zonge Engineering & Research Organization (Aust) for providing geophysical instruments used in the field.

Chapter 1

Introduction

Artesian mound springs occur all over the world. Those which occur in the south-western edge of the Great Artesian Basin, in the arid part of central-eastern Australia (Habermehl, 2006), are valuable natural and cultural resources because of their rich cultural history (Florek, 1987; Harris, 1992) and the unique surface water systems which they support (Ponder, 1986). They act as an 'archipelago of aquatic islands in an arid sea' (Morton et al., 1995, pp. 57–63), and play a central role in the life of Aboriginal people (Ah Chee, 1995).

The way in which these springs are connected to the underlying artesian aquifers is poorly understood. Ecological and cultural sensitivities prevent the extensive use of boreholes to investigate the hydrogeological system. In addition, observation wells would disturb the flow regime significantly. Therefore non-intrusive methods are preferred, such as remote sensing (White and Lewis, 2011; Lewis et al., 2013).

Electrical geophysics is another non-invasive method which is frequently used for hydrogeological investigations (Nobes, 1996; Pellerin, 2002; Rubin and Hubbard, 2005). Measurements of electromagnetic (EM) fields at the surface can provide information on underground structures, in terms of how electrical resistivity varies spatially (e.g. magnetotellurics and EM induction surveys) (Pous et al., 2002; Unsworth et al., 2007; Danielsen et al., 2003). Similar measurements can utilise the electrokinetic effect to provide information on the way in which water is flowing (e.g. self-potential surveys) (Jardani et al., 2006a; Ball et al., 2010).

This work describes electrical geophysical surveys which we performed at

three different mound spring complexes, and interprets the data with a view to establishing how water is flowing between aquifers and springs, whether it is possible to sense that flow with geophysical methods, and how the flow is related to geological structures which may have also contributed to the development of the complexes in which spring vents are generally found.

Three geophysical techniques were used: magnetotellurics, time-domain surface electromagnetic induction, and self-potential. The former two methods measure the variation and geometry of electrical resistivity in the subsurface, which has a relationship to both lithology and hydrochemistry. The latter method measures the presence of naturally-occurring electrical signals which are partly caused by groundwater flow.

We specifically wanted to investigate:

1. whether self-potential surveys would be able to sense the vertical flow from aquifers to springs; and
2. whether magnetotelluric surveys would be able to identify resistivity structures related to the mounds and/or spring conduits.

The three spring complexes which were studied are Beresford and Warburton Springs, the Bubbler Spring complex, and Freeling Springs.

Beresford and Warburton Springs are modern springs located in a playa between two mesas with extinct spring vents on their summits. Both the modern and extinct spring vents are aligned NW/SE in a way that strongly suggests they lie on a fault zone. The Bubbler Spring complex lies in a similar geological setting, but with little surface evidence of faulting. Freeling Springs occurs where the aquifer abuts a basement inlier at a prominent regional fault scarp.

1.1 Organisation

Chapter 1 contains a brief introduction to this thesis.

Chapter 2 contains a review of mound springs and the Great Artesian Basin. The first part reviews the hydrogeology and chemistry of carbonate mound springs, which occur in a variety of forms. The second part reviews the geology of the Great Artesian Basin and also contains detailed descriptions of each of the spring systems studied in this work.

Chapter 3 reviews the theoretical basis of each of the geophysical methods

used in this work: magnetotellurics, self-potential, and electromagnetics.

Chapters 4 through 8 present the results of the geophysical surveys performed over each of the spring systems: Beresford Spring in Chapter 4, Warburton Spring in Chapter 5, the area surrounding the Beresford/Warburton playa in Chapter 6, the Bubbler Spring complex in Chapter 7, and the Freeling Springs complex in Chapter 8. These chapters contain figures showing all the data, and a discussion of modelling results, although detailed hydrogeological interpretation is left for later chapters.

Chapter 9 contains hydrogeological interpretations of the geophysical results for each of the spring systems. It contains synthesis figures which bring together self-potential data, magnetotelluric and TEM models, and the hydrogeological interpretations.

Chapter 10 presents the main conclusions of the work.

Data tables and correction procedures are presented and described fully in Appendices A (magnetotellurics) and B (self-potential).

1.2 Conventions

The Universal Transverse Mercator (UTM) zone 53J coordinate system and the Geocentric Datum of Australia 1994 (GDA94) are used for all maps and geographic coordinates. Directions are given as azimuths with respect to grid north. Tensor magnetotelluric data is presented in various rotated coordinate systems (see Section 3.1.1). If it is not made explicit, x refers to geographic north and y to geographic east.

Chapter 2

Geology

Mound springs are carbonate deposits precipitated from discharging groundwater (Roberts and Mitchell, 1987; Nelson et al., 2001; Linares et al., 2010). Dome and shield-shaped mounds such as these are located where groundwater discharges from the Great Artesian Basin (GAB) in the Lake Eyre region of northern South Australia (Williams and Holmes, 1978; Ponder, 1986; Miles et al., 2012). These springs occur in a variety of forms and are present throughout the GAB; this work focuses on those occurring in the south-western GAB, in the modern Lake Eyre Basin. The mounds consist of tufa deposited from GAB groundwater discharging from spring vents (Keppel et al., 2011, 2013b).

Section 2.1 reviews the morphology and chemistry of carbonate mound springs (also known as spring mounds).

Section 2.2 describes the overall geology of the GAB, and the following sections describe the three spring systems studied in this work. These systems occur in the Lake Eyre region between Maree and Oodnadatta, and are:

- Beresford Spring and Warburton Spring, which occur within 1.4 km of one another, about 40 km south-east of William Creek (Section 2.3).
- The Bubbler Spring complex, which is named after a large spring from which bubbles of gas emerge at regular intervals. It is surrounded by a number of smaller springs and is located about halfway between Maree and William Creek (Section 2.4), to the south-west of the Beresford/Warburton Spring complex.
- Freeling Springs, which are a set of springs occurring along the north-eastern edge of the Denison Range, about 100 km NNW of William

Creek (Section 2.5).

2.1 Mound springs

Calcium carbonate deposits occur at springs all over the world, precipitated from groundwater containing dissolved CO_2 and Ca^{2+} ions. These deposits have been divided into two types by Ford and Pedley (1996): travertines and tufas. Travertines are carbonates which form from warm spring water (e.g. hydrothermal springs), while tufas are carbonates which precipitate from spring water at ambient temperatures. The artesian springs of the GAB are tufas.

Quaternary tufa and travertine deposits at active springs are very common, with several reviews discussing their existence and the difficulty of classifying them (Ford and Pedley, 1996; Pentecost, 2005; Jones and Renaut, 2010). The scheme of Ford and Pedley (1996) is used here, which divides tufa occurrences into:

1. Fluvial deposits, which occur in streams and often form a series of bar-rages.
2. Perched springline deposits, which occur where spring waters discharge along a slope and deposit tufa downslope (e.g. Özkul et al., 2010; Sanders et al., 2011).
3. Lacustrine deposits, where carbonate reefs are deposited underwater. One example are the exposed carbonate pinnacles and towers at Mono Lake in the USA, which developed in a lake which is now dry (Scholl, 1960; Scholl and Taft, 1964).
4. Paludal deposits, which develop in poorly drained parts of the landscape.

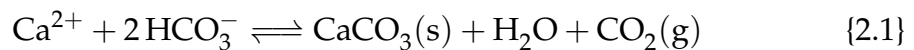
The artesian mound springs of the Lake Eyre region of the GAB are most closely related to perched springline tufas, although there are some important differences. The artesian mound springs do not generally occur on slopes and do not usually share the same terraced morphology. Most springs in the region are located on flat plains and form roughly circular mounds or shields of carbonate, with up to 5 m of local relief. The mounds have very low topographic slope ratios; they are often 50 m to 300 m in diameter. Similar features occur elsewhere in the world. Examples include indurated tufa ledges and

mounds collocated with range-front faulting at Lake Tecopa in south-eastern California (Nelson et al., 2001), lacustrine and spring mound carbonates in arid parts of Egypt (Crombie et al., 1997; Adelsberger and Smith, 2010) and Tunisia (Roberts and Mitchell, 1987), and artesian mounds in karst terrain in north-east Spain (Linares et al., 2010).

Hancock et al. (1999) emphasise the close relationship that many tufa deposits have with structural features like faults, classifying tufa deposits into terraced mounds (similar to perched springlines), vertical fissure ridges, range-front deposits formed in the immediate footwall of faults, and cones, towers, and pinnacles (lacustrine deposits), along with eroded remnants of these forms. Although some of the springs in the Lake Eyre region do fit into this classification, for example range-front deposits at Freeling Springs (Section 2.5), typically the only indications of a relationship to faulting are either an alignment along lineaments with regional significance (e.g. the NW/SE alignment of vents at the Beresford/Warburton complex, see Section 2.3) or a predominant orientation of veins and fracture-filled ridges. The latter occurs at Warburton Spring (Keppel, 2012, Appendix 1).

2.1.1 Hydrochemistry

The main cause of CaCO_3 precipitation is the degassing of dissolved CO_2 from groundwater containing Ca^{2+} ions, via



When the concentration of CO_2 in groundwater is higher than that in the atmosphere, the emerging spring water will lose CO_2 from solution (degassing), and the equilibrium shifts to the right side of Equation 2.1. This results in precipitation of calcium carbonate (Pentecost, 2005, p. 11). There are other barriers to precipitation, such as the extra energy required for nucleation of calcite crystals. Conditions like an increase in turbulent flow can be important as they increase the rate of degassing and therefore the shift in equilibrium: this is why tufa deposits often form at waterfalls or rapids (Herman and Lorah, 1988).

Keppel et al. (2011) have shown that in the case of the GAB mound springs, carbonate precipitation is microbially-mediated and occurs only after waters have degassed in the vent and upper tail, with most precipitation occurring

in spring tails.

2.2 Great Artesian Basin

The Great Artesian Basin (GAB) is a spatially extensive system of mostly artesian interconnected aquifers and aquitards underlying much of eastern Australia. It stretches for over 1100 km from central and northern South Australia to the Great Dividing Range in northern and central Queensland and New South Wales, and consists of a series of alluvial, fluvial, and marine Mesozoic sediments (Ransley et al., 2012a). Repeated marine transgressions resulted in the deposition of a series of sedimentary layers which vary in lithology from sandstones to mudstones. These layers form a laterally extensive hydrogeological system with multiple aquifers and aquitards that are partially connected over hundreds of kilometres.

The central and south-western parts of the GAB are shown on Figure 2.1.

The GAB was originally believed to form a continuous artesian system stretching from central South Australia to the Great Dividing Range (Habermehl, 1980). However, the basin is now understood to be more complex, consisting of partly-connected sub-basins (Ransley et al., 2012a). This work is focused on the south-western GAB, particularly the area to the southwest of Lake Eyre (Keppel et al., 2013c).

An geological map of the GAB sequences in the Lake Eyre region is shown in Figure 2.2. The main geographical features in the area are the large playa of Lake Eyre in the west, Proterozoic basement outcrops in the northern Flinders Ranges and Willouran Ranges in the south-west, and Palaeoproterozoic basement outcrops in the Denison and Davenport Ranges in the north-east. Mesozoic Eromanga Basin rocks outcrop mainly in the east and dip gently to the west, where they are overlain by Cenozoic sediments of the Lake Eyre Basin. A geological cross-section through this area running from south-west to north-east is shown in Figure 2.3.

The major tectonic feature in the area is the Torrens Hinge Zone, which separates a thick Neoproterozoic sequence of deformed sedimentary and intrusive rocks of the Adelaide Geosyncline in the west from the relatively undeformed sedimentary rocks deposited during the same period on the Stuart Shelf to the east. Deformation occurred during the late Cambrian and early Ordovician in the Delamerian Orogeny. The area was a plate boundary during the Cam-

brian, along what is now the eastern margin of the Palaeoproterozoic Gawler Craton (Forbes, 1988).

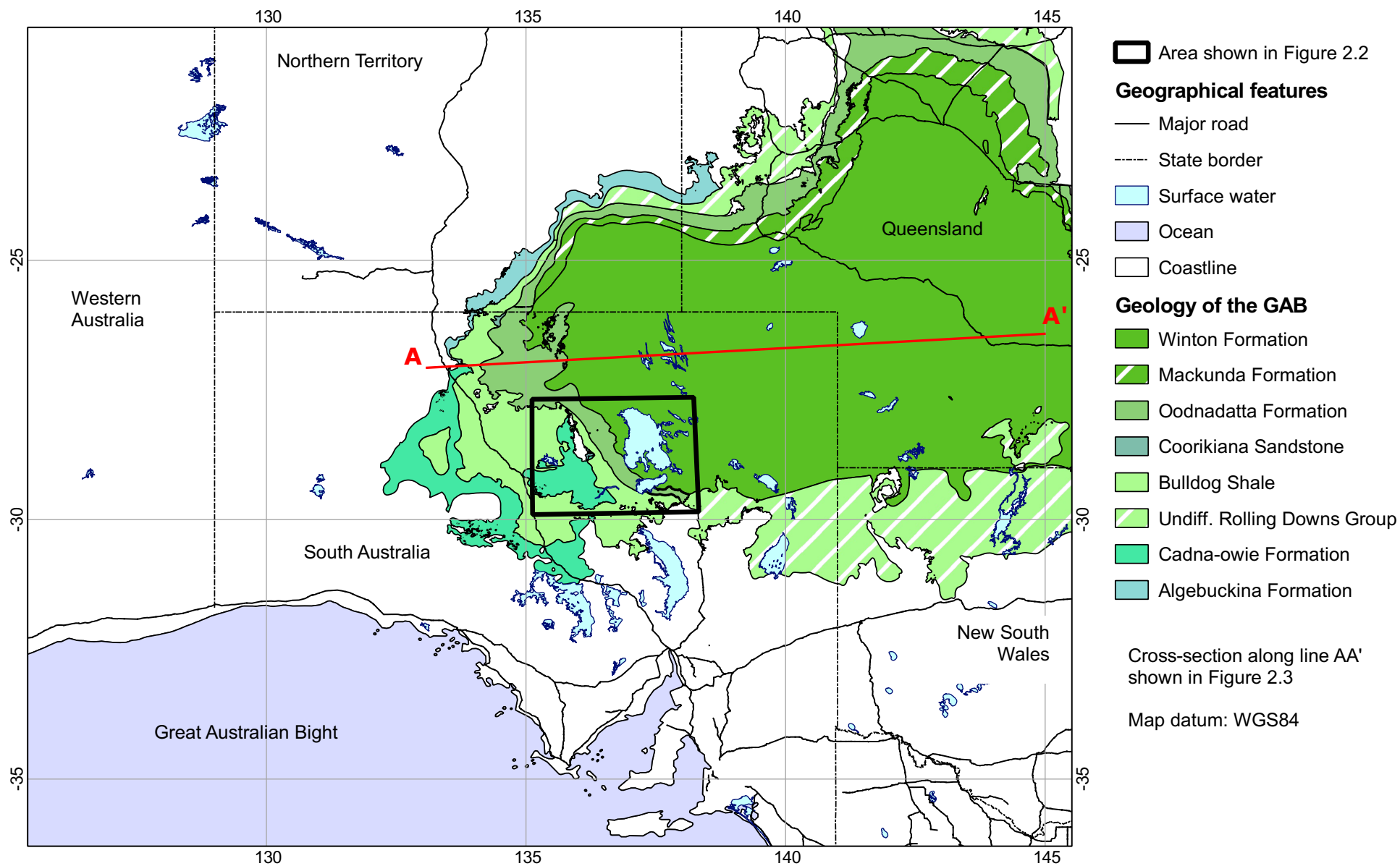


Figure 2.1: The central and south-western GAB. Formation boundaries from Habermehl (2011).

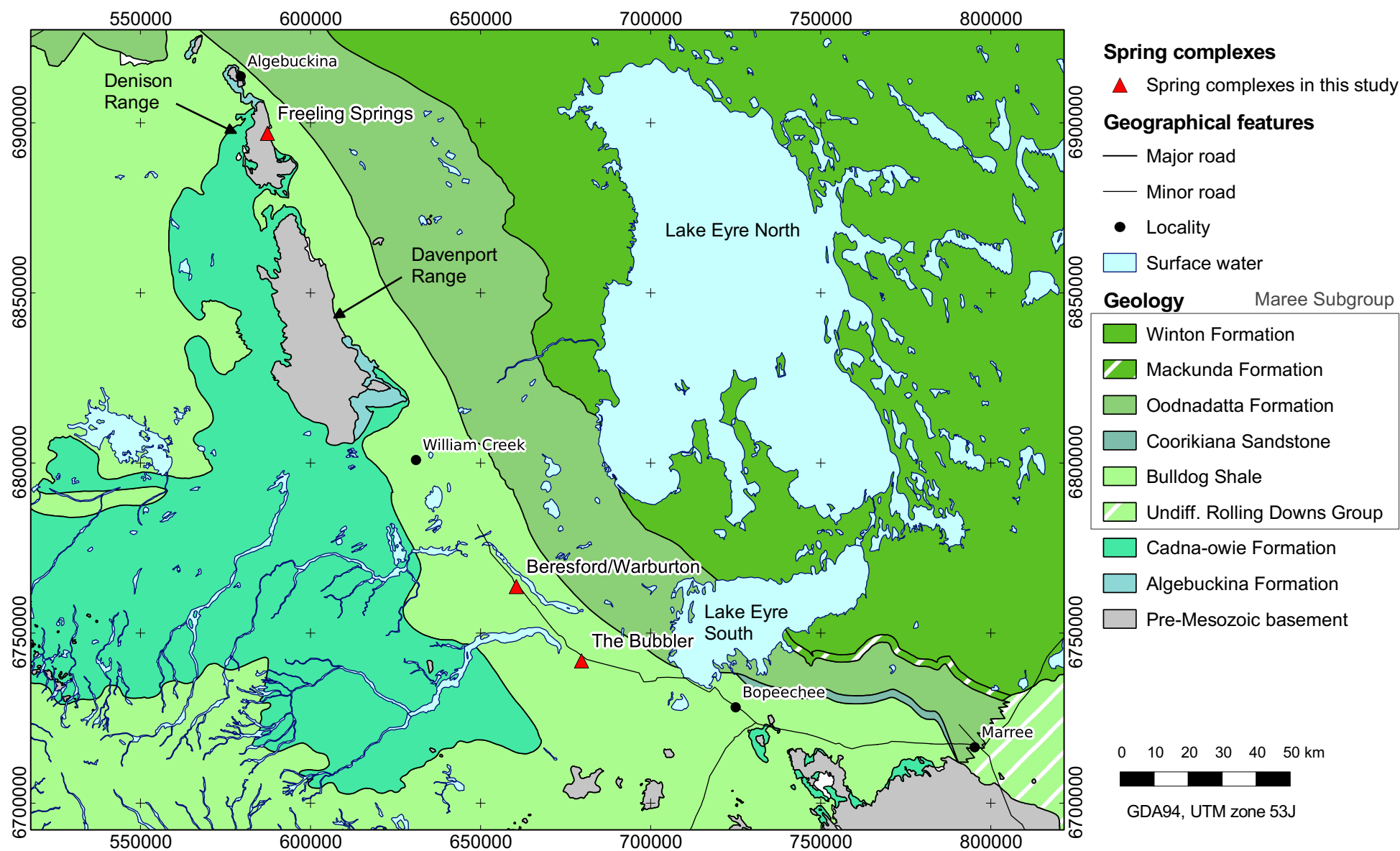


Figure 2.2: The Lake Eyre region of the south-western GAB. Formation boundaries from Habermehl (2011). Cenozoic units at the surface have been omitted to show the underlying geology.

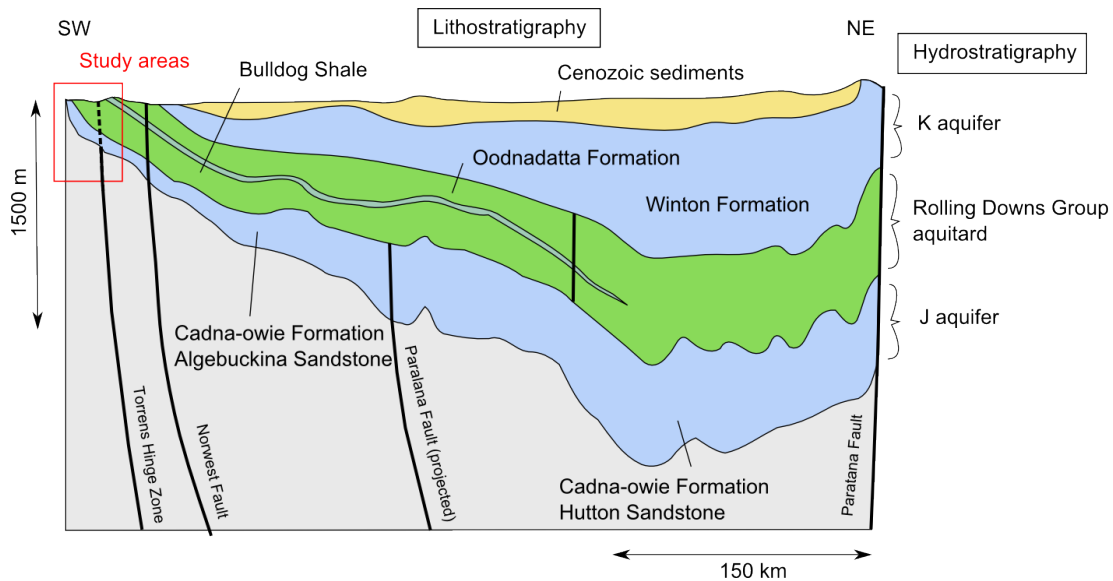


Figure 2.3: Geological cross-section through the western GAB after Keppel et al. (2013a, Fig. 3.1). The red area shows the area of the mound spring complexes, and the dashed line is an interpreted continuation of Torrens Hinge Zone faults to the surface.

2.2.1 Stratigraphy of the Lake Eyre region

The following descriptions are based on government geological mapping of the southern (Krieg et al., 1991; Forbes, 1988) and northern (Rogers and Freeman, 1996b) parts of the Lake Eyre region.

2.2.1.1 Palaeoproterozoic (Denison Range)

The oldest rocks in the region are the Palaeoproterozoic igneous and metamorphic rocks of the Peake and Denison Inlier. These cratonic igneous and metamorphic rocks outcrop in the Denison and Davenport Ranges, and are encountered in this study at the Freeling Springs complex (see Section 2.5 for more detail).

2.2.1.2 Neoproterozoic (Adelaidean basement)

The basement rocks which unconformably underlie most of the region were deposited during the Neoproterozoic and early Cambrian in the Adelaide Geosyncline (Preiss, 1987). The sequence consists of a wide variety of igneous, sedimentary, and metasedimentary rocks, which were later deformed during the Delamerian Orogeny in the Cambrian and Ordovician. Deformation events included thrust faulting and recumbent folding, and these were accompanied by regional metamorphism and the emplacement of granites

and mafic rocks (Preiss, 2000). The principal compressive stress throughout the deformation was from the west or WNW, which produced structures generally striking north-south (Jensen-Schmidt et al., 2006). Karlstrom et al. (2013) suggests that major crustal features developed during this time may have subsequently been reactivated during more recent tectonic events.

2.2.1.3 Mesozoic (Eromanga Basin)

After tectonic activity throughout the Palaeozoic and the deposition of sediments in the Cooper, Warburton, and Perdirka Basins further east, regional tilting and uplift of the western part of these basins resulted in widespread erosion in the Middle Triassic (Jensen-Schmidt et al., 2006; Radke, 2009). Subsequently the area experienced subsidence and transgressive eustatic conditions throughout the late Mesozoic leading to the deposition of the sediments of the Eromanga Basin, which onlaps and overlies the Palaeozoic basins mentioned above, and also extends further east (Alexander et al., 2006; Ransley and Smerdon, 2012).

The Eromanga Basin contains both the aquifer and aquitard units which are relevant to the spring systems studied in this work, and therefore the sedimentary sequence is described in detail below. The sequence consists of sandstone, siltstone and shale deposited in facies ranging from terrestrial and braided fluvial in the Jurassic through to marine facies in the Early Cretaceous. The following descriptions are specific to the area immediately west and south-west of Lake Eyre.

Algebuckina Formation

This is a terrestrial fluvial sandstone rich in quartz and kaolin. It was likely deposited by large river systems flowing to the east, and lies unconformably on underlying Adelaidean (Neoproterozoic) rocks. The basal unconformity is also marked by weathered horizons (e.g. Bopeechee Regolith to the south and the Mount Margaret Surface further north), which range from Permian to late Jurassic in age.

Cadna-owie Formation

This unit is a transgressive sequence of predominantly siltstone with minor shale and some sandstone lenses, reflecting generally rising sea levels. The

upper layer is a calcite-cemented sandstone, with the amount of calcareous material in general increasing in the upper parts of the unit. The upper parts of the Hooray Sandstone are the equivalent correlative beds in the eastern GAB.

Maree Subgroup

The Maree Subgroup consists of marine to paralic shale, siltstone and minor sandstone units deposited during a period of relatively high eustatic sea levels.

The basal unit is the Bulldog Shale, which consists of marine mudstone with thin layers of clayey sandstone. Shell and plant fragments, pyrite, and carbonate concretions are also common. A basal conglomerate layer commonly occurs, with suggested interpretations including fluvial transport and deposition on local basement highs (e.g. Morgan, 1980, p. 26), ice-rafting (Rogers and Freeman, 1996b, p. 25), or transport in the roots of floating trees (Krieg et al., 1991, p. 24). The equivalent unit in the eastern GAB is the Wallumbilla Formation.

The Bulldog Shale is conformably overlain by the Coorikiana Sandstone, deposited during a regressive event, and the Oodnadatta, Mackunda, and Winton Formations (Krieg et al., 1991; Ransley et al., 2012c). These units outcrop to the east of the region studied here and are not discussed further.

2.2.1.4 Cenozoic

A complex series of sedimentary deposits cover much of the Eromanga Basin. There are remnants of Palaeogene–Neogene lacustrine sediments from Lake Eyre (Magee et al., 2004) and sandstones and silcretes (Krieg et al., 1991) which are partly eroded and overlain by Quaternary alluvium, colluvium, and aeolian dunes and sheetwash deposits.

2.2.2 Hydrostratigraphy

The Mesozoic sediments of the Eromanga Basin form part of the Great Artesian Basin. In hydrostratigraphic terms the basin is divided into a lower confined aquifer, known as the Jurassic aquifer or ‘J-aquifer’, overlain by a confining aquitard and an unconfined aquifer in shallower sediments (Keppel et al., 2013a).

2.2.2.1 Lower artesian J-aquifer

The Algebuckina Formation and parts of the Cadna-owie Formation – particularly the upper calcareous unit – form an aquifer sequence referred to as either the J-aquifer (Jurassic) or Cadna-owie–Hooray Aquifer (Keppel et al., 2013a; Ransley et al., 2012b). Although lateral heterogeneities mean that the aquifers are not necessarily fully connected and continuous, the equivalent aquifer units further east in Queensland and New South Wales are the Namur Sandstone, Hooray Sandstone, Pilliga Sandstone, and Gilbert River Formation (Ransley and Smerdon, 2012), and the De Souza Sandstone in the Northern Territory (Keppel et al., 2013a).

The potentiometric surface for the J-aquifer is generally above the topographic surface, except in the westernmost part of the GAB, where the Cadna-owie Formation and Algebuckina Sandstone outcrop. This is where recharge has been assumed to occur (Habermehl, 1980), although recent work has demonstrated that modern recharge is small and greater amounts must have occurred in previous, wetter climatic regimes (Love et al., 2013).

2.2.2.2 Aquitard

The Bulldog Shale is part of a GAB-wide sequence of aquitards which were deposited during the mid-Cretaceous marine incursion (Keppel et al., 2013a). Collectively these formations are referred to as the Rolling Downs Group aquitard (Ransley et al., 2012b). Studies of hydraulic pressure variations over long periods at two bores drilled into the Bulldog Shale (but not penetrating through to the underlying aquifer) found that while the porosity is high ($> 35\%$), the hydraulic conductivity is very low ($1 \times 10^{-14} \text{ m s}^{-1}$) and the unit is therefore an effective aquitard (Harrington et al., 2013).

The basal layer of the Rolling Downs Group (i.e. Bulldog Shale or Wallumbilla Formation) has long been recognised to be a low-velocity layer which causes a regionally recognisable seismic reflection horizon at the top of the Cadna-owie Formation (Watterson et al., 2000). This stratigraphic layer is associated with high pore fluid pressures found in drillholes, which may be caused by upward movement of groundwater from the underlying J-aquifer into the shale aquitard (Ransley et al., 2012a, p. 22), or rapid sedimentation and burial of marine sediment which prevented de-watering and compaction (Watterson et al., 2000, p. 157). The same low-velocity layer may also play a role in the

development of polygonal fault systems (Cartwright, 1994, 2011), which are laterally extensive intraformational extensional faults that have been identified across much of the Rolling Downs Group in the western GAB, but not yet in the east, although they may exist (Ransley et al., 2012b, section 5.6.1). Such systems are probably responsible for most diffuse discharge from the J-aquifer (Harrington et al., 2013). Diffuse discharge is defined as any discharge from structures other than springs (Harrington et al., 2013).

2.2.2.3 Upper non-artesian aquifer

The Winton Formation forms the upper aquifer which is generally not artesian (Keppel et al., 2013b). It is not discussed in this work as it outcrops to the east of Lake Eyre, and is therefore not important to the hydraulics of the spring systems studied here. The only GAB units in the immediate region of the spring complexes are the J-aquifer and overlying aquitard.

2.3 Beresford and Warburton Springs

Beresford and Warburton Springs are actively flowing carbonate mound springs located 50 km south-east of William Creek (Figure 2.2). Adjacent to these springs are two mesas, Beresford Hill and Warburton Hill, standing 40 m above the surrounding plains. The springs lie near the margin between regionally outcropping Bulldog Shale to the west and a thin regional cover of Quaternary aeolian and alluvial deposits to the east. The geology of the area is shown in Figure 2.4 and Figure 2.5, while Figure 2.6 shows the area in panoramic photographs taken from the summit of each hill. Both the hills and springs lie in or on the edges of a topographically depressed playa (e.g. flooding in Figure 2.6b) which is underlain by Bulldog Shale.

The hills are approximately elliptical in plan view and are capped by 5 m to 10 m of spring carbonate which was deposited from vents which are now extinct (Prescott and Habermehl, 2008, pp. 169-70). Each hill's carbonate cap is underlain by 25 m to 40 m of Bulldog Shale, which has been protected from the general denudation of the land surface by the cap. There is another similar deposit of spring carbonates from an extinct vent 1 km west of Beresford Hill which is less topographically pronounced.

Carbonates from both the spring platforms and hills have been dated using U-series thermoluminescence (Prescott and Habermehl, 2008; Priestley et al.,

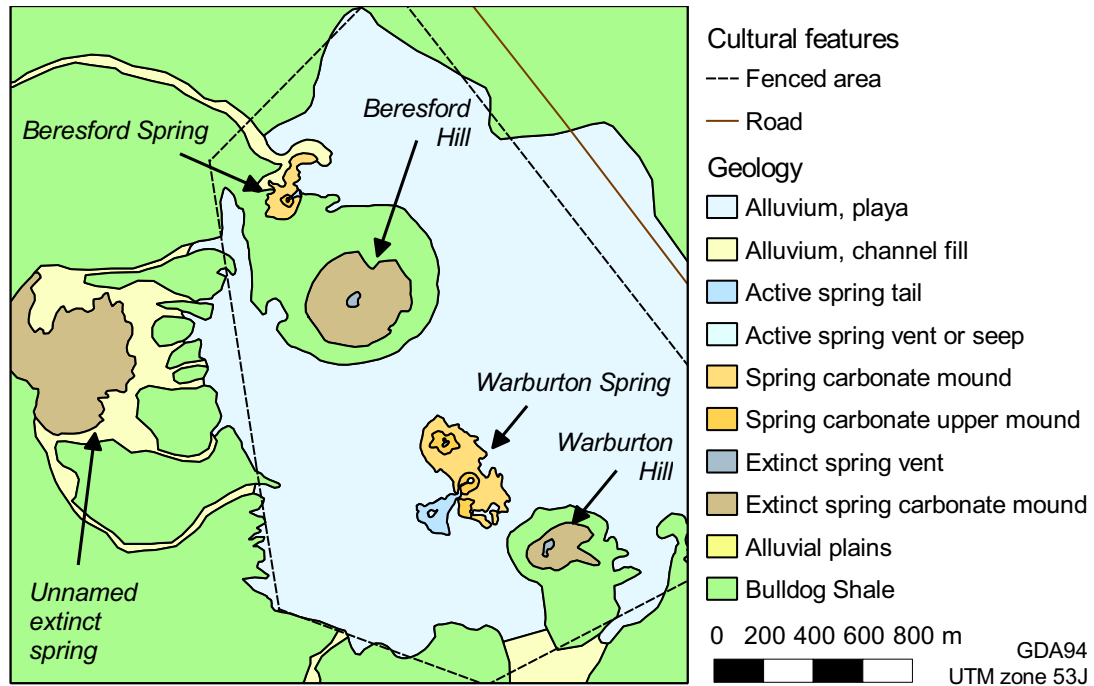


Figure 2.4: Overview geological map of the Beresford and Warburton Springs complex. More detailed maps are shown in Figure 2.5.

2013) (Table 2.1). Beresford Hill is the oldest spring structure, with ages between 250 ka and 372 ka. Warburton Hill and the Beresford Spring mound are slightly younger, with ages between 104 ka and 187 ka, and Warburton Spring is the youngest structure at 30 ka to 38 ka.

The conductivity of the underlying aquifer water is approximately $1.6 \Omega \text{ m}$, which is estimated from measurements made from the Beresford Railway Station Bore (6239-4), 3 km north of the complex, and the Angas Bores (6239-6 and 6239-44), 6 km east of the complex (Table 2.2).

The springs and hills are aligned in a north-west to south-east direction, on a bearing of approximately 315° .

Table 2.1: Ages of structures at the Beresford/Warburton Spring complex estimated from U-series thermoluminescence dating. P indicates Priestley et al. (2013) and PH indicates Prescott and Habermehl (2008). Note that the $104 \text{ ka} \pm 5 \text{ ka}$ age is from tufa at the base of Beresford Hill, and is not directly related to the present-day Beresford Spring platform.

Site	Location	Age/ka	Reference
Warburton Spring	Along SW edge of present mound	30.2 ± 3.2	P
		33.9 ± 5.2	P
		37.9 ± 7.5	P
Warburton Hill	Base of carbonates atop hill	100 ± 4	P
	Top of carbonates atop hill	187.0 ± 2.7	P
Beresford Spring	Friable carbonate base of platform	13.9 ± 1.0	PH
	Hard carbonate cap on platform	219 ± 35	PH
Beresford Spring/Hill	At SE base of hill	104 ± 5	P
Beresford Hill	North edge of cap atop hill	128 ± 33	PH
		250 ± 5	P
	SE edge of cap atop hill	372 ± 15	P

Table 2.2: Electrical resistivity of aquifer waters at the Beresford/Warburton Spring complex (Department of Environment, Water and Natural Resources, South Australia, 2013).

Date	Resistivity / $\Omega \text{ m}$	Location
27 Sep 2008	1.46	Beresford Railway Bore (6239-4)
10 Nov 2004	1.45	
20 Nov 1986	1.62	
03 Nov 1961	1.58	Angas Bore (6239-6)
27 Sep 2008	1.57	Angas Bore 2 (6239-44)
10 Nov 2004	1.57	
31 Aug 2002	1.66	

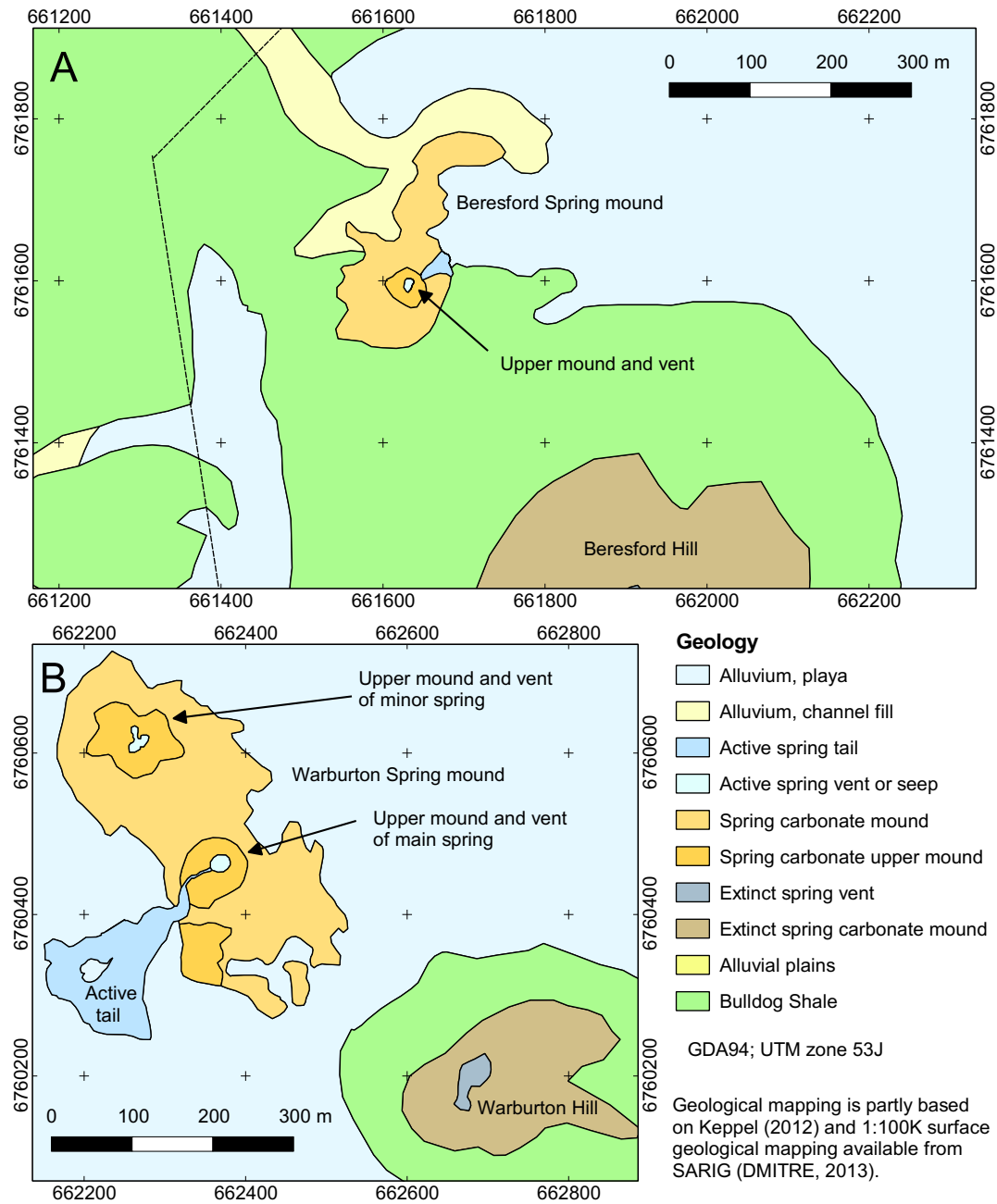
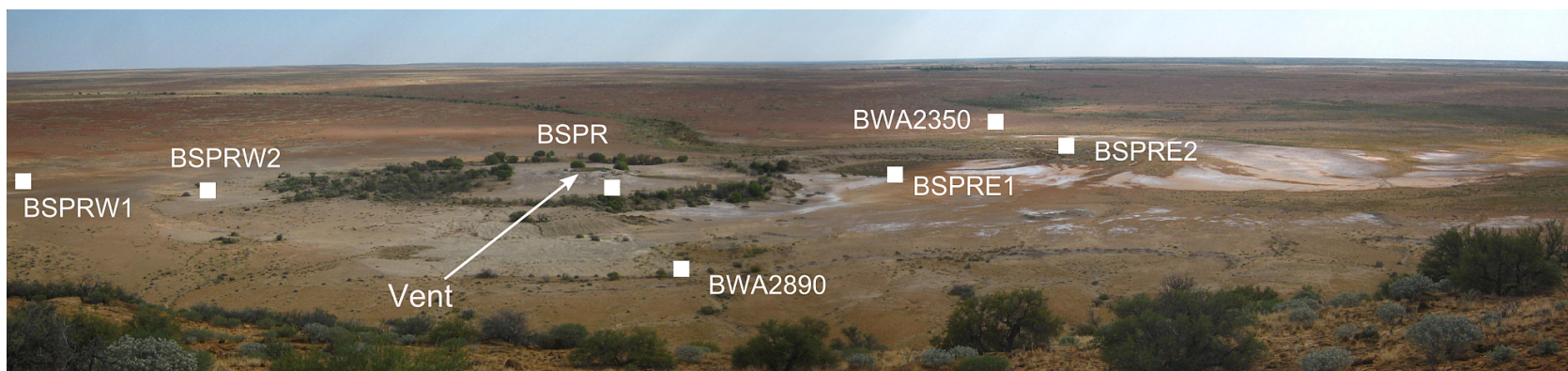
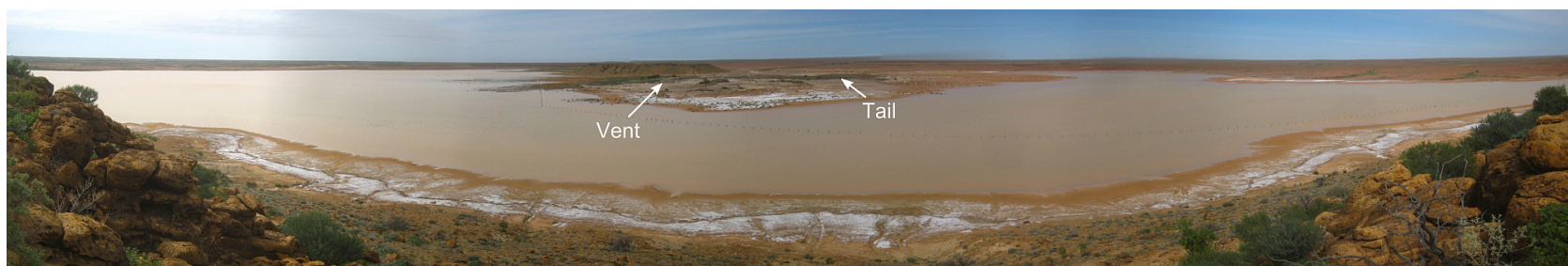


Figure 2.5: Geological map of (A) Beresford Spring and (B) Warburton Spring. See Figure 2.4 for an overview of the whole area.



(a) Looking north-west from Beresford Hill towards Beresford Spring (2 August 2011).



(b) Looking south-east from Beresford Hill towards Warburton Spring after heavy rain (21 April 2012).



(c) Looking north-west from Warburton Hill towards Warburton Spring (21 November 2012).

Figure 2.6: Panoramic photographs of the Beresford/Warburton plays with the locations of AMT and MT sites shown.

2.3.1 Beresford Spring

Beresford Spring is a shield-shaped carbonate mound. The upper mound is approximately 3 m to 5 m high and 60 m in diameter and is located on a larger flat-topped platform of carbonate which is approximately 200 m across (see map in Figure 2.5A). The pool at the spring vent is about 4 m wide and is full of sand and mud rich in organic material. The vent does not have free-standing water, but the sediment within it is saturated. Water discharges at a rate of less than 0.1 L s^{-1} (Keppel et al., 2011) and flows to the north-east through a shallow break in the upper mound carbonates that act as a barrage. Water discharges onto the flank of the upper mound and underlying platform in a stream about 4 m wide and 1 cm to 2 cm deep. A geological map of the mound is shown in Figure 2.5A.

The platform is surrounded by outcropping Bulldog Shale and alluvial playa sediments. The western side is gently sloping and a significant amount of colluvial and alluvial carbonate is present on the surface. The eastern side of the platform ends in a 1 m to 2 m high scarp. The playa is exposed at the surface adjacent to the eastern side of the platform, near the area where the discharging water flows out. This water flows around the north-eastern corner and flows as a stream to the north-west.

Indurated carbonate from the northern edge of the platform has been dated at $219 \text{ ka} \pm 35 \text{ ka}$, while a friable sample retrieved by auger at the same spot was dated at $13.9 \text{ ka} \pm 1.0 \text{ ka}$ (Prescott and Habermehl, 2008, pp. 174, 179). A date of $104 \text{ ka} \pm 5 \text{ ka}$ was obtained from carbonate exposed at the base of Beresford Hill, on the opposite side from the present-day spring vent, by the same method (Priestley et al., 2013). It is not clear how the last sample relates to the present-day platform but it is likely that the spring has been intermittently or continuously active throughout the history indicated by these dates, and has deposited a substantial amount of carbonate across the region between the present-day vent and the extinct hill.

Measurements of the conductivity of water in the spring vent range from $1.13 \Omega \text{ m}$ to $1.80 \Omega \text{ m}$ (Table 2.3); these are close to the value of $1.6 \Omega \text{ m}$ obtained from bore measurements nearby of water from the aquifer at 100 m depth (Table 2.2) (Cobb, 1975; Keppel et al., 2011). The bore is about 2 km north of the playa.

Table 2.3: Electrical resistivity of water in the Beresford Spring vent.

Reference	Date	Resistivity / Ω m
This work	2 Aug 2011	1.13
Keppel et al., 2011	Oct 2008	1.52
Cobb, 1975	12 Aug 1974	1.80

2.3.2 Warburton Spring

Warburton Spring is a shield-shaped carbonate mound spring located approximately in the centre of the playa surrounding both springs in the Beresford/Warburton complex (Figures 2.4 and 2.5B). There are at least two currently active springs on a broad platform of carbonate which is approximately 480 m long, 150 m wide, 4 m to 5 m high, and oriented in a north-west/south-east direction. The main spring has a vent 25 m in diameter in the centre of a slightly elevated upper mound which is approximately 80 m in diameter. The vent consists of saturated sediment filled with shrubs. There is a shallow pool of water in spring and early summer following periods of relatively low evapotranspiration. Water discharges from the pool at a rate of 3 L s^{-1} (Keppel et al., 2011) through a break in the carbonate upper mound on the south-western side of the vent and flows through a narrow channel (the tail) for 60 m before exiting the mound platform and discharging in a broad deltaic fan covered with vegetation. The tail fan is broadly triangular in shape, about 170 m long and 170 m broad at the base. It is a site of active carbonate precipitation, which is described and modelled in detail by Keppel et al. (2011). The precipitated tufa forms a thin mat across the tail. The base of the tail is marked by a small (sub-metre scale) dune of sediment and the platform and tail are surrounded by heavy clay playa sediments. There is another spring vent at the northern end of the platform marked by a growth of *Phragmites* reeds and a much smaller discharge stream flowing to the ESE, with no significant tail. Only the main vent was examined in this work. A geological map of the mound is shown in Figure 2.5B.

Warburton Hill stands approximately 400 m south-east of the modern spring platform. It is an extinct spring mesa, with a carbonate deposit several metres thick atop a 20 m to 30 m-high mesa of Bulldog Shale. The mesa is an erosional remnant presumed to have formed after the carbonate cap protected the underlying shale from the general lowering of the land surface through erosion over the past 500 kyr, as likely also occurred to Beresford Hill and

Table 2.4: Electrical resistivity of spring water at the Warburton Spring vent.

Reference	Date	Resistivity/ Ω m
This work	2 Aug 2011	1.61
		1.52
Keppel et al., 2011	Oct 2008 to Mar 2009	1.56
	Mar 2009 to May 2009	1.65
	Jul 2009 to Jul 2010	1.92
Cobb, 1975	12 Aug 1974	1.51

Hamilton Hill (Section 2.4).

A number of U-series thermoluminescence dates have been obtained for carbonate from both the modern spring and the extinct hill (Priestley et al., 2013). The deposits on Warburton Hill have been dated at $100 \text{ ka} \pm 4 \text{ ka}$ at the top and $187.0 \text{ ka} \pm 2.7 \text{ ka}$ at the base, while samples taken from the base of deposits at the modern spring mound near the tail range between 30 ka and 40 ka (Table 2.1).

Measurements of the conductivity of water in the spring vent and tail range from $1.51 \Omega \text{ m}$ to $1.92 \Omega \text{ m}$ (Table 2.4), which is very close to the $1.6 \Omega \text{ m}$ aquifer water from the nearby Beresford Railway Bore (Table 2.2), which is about 2 km north of the playa (Cobb, 1975; Keppel et al., 2011).

Halihan et al. (2013) have conducted electrical resistivity surveys over the Warburton Spring platform in several orientations and concluded from a ‘connectivity analysis’ that more connections between the aquifer and surface were found along a survey line parallel to the long axis of the carbonate mound (NW to SE), which crosses the two active springs, compared to a line surveyed perpendicular (i.e. SW to NE), which crosses only the main spring.

2.4 The Bubbler Spring complex

The Bubbler Spring complex is a group of springs located near the extinct spring mesa of Hamilton Hill, about 75 km south-east of William Creek. There are at least seven active springs in the complex, with at least another five apparently inactive springs in a 1 km^2 area (Figure 2.7). The springs are generally surrounded by sand dunes, which have been interpreted as reworked Mesozoic sediments from the aquifer deposited by spring waters (Krieg et al., 1991, p. 66 and Prescott and Habermehl, 2008, p. 176), but are more likely to be Quaternary aeolian deposits which contain calcareous material precipi-

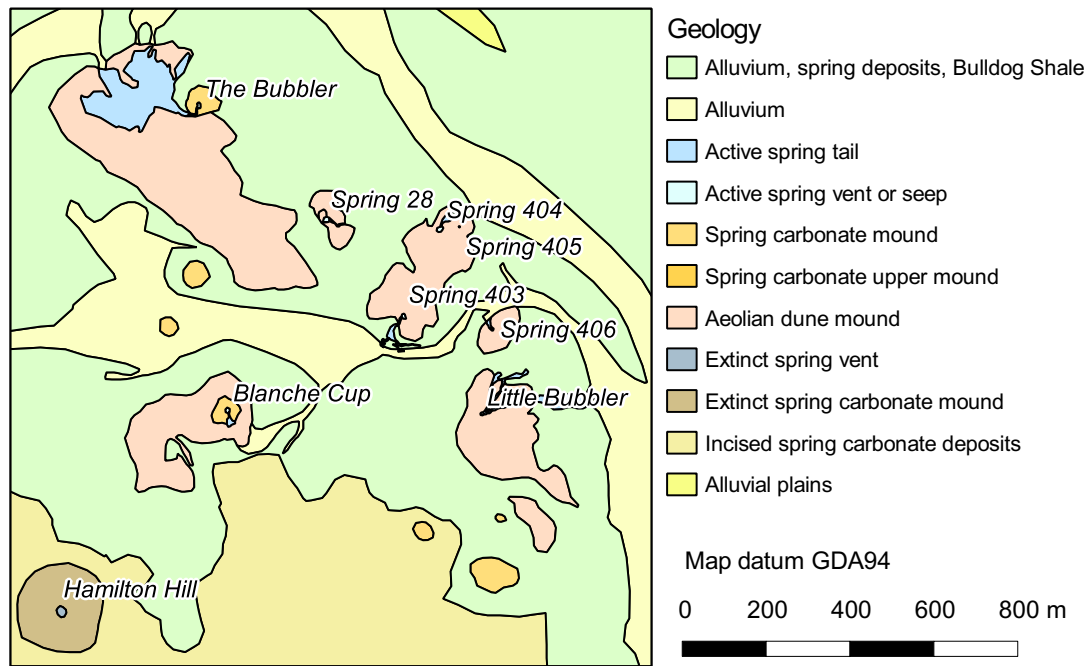


Figure 2.7: Overview geological map of the Bubbler Spring complex. A more detailed map is shown in Figure 2.8.

Table 2.5: Spring discharge flow rates at the Bubbler Spring complex (V. Berens, pers. comm., 2011).

Spring	Date	Discharge rate L min^{-1}
The Bubbler	May 2009	558
	May 2011	540
		576
Blanche Cup	May 2009	15.2
Little Bubbler	May 2009	51.2
Spring 403	May 2009	7.8

tated from spring waters (L. Crossey and K. Karlstrom, pers. comm., 2011).

The main spring is known as the Bubbler; it is a shield-shaped mound approximately 350 m wide and 3 m to 5 m high, with an upper carbonate mound about 70 m in diameter. The vent contains a pool of water approximately 0.5 m to 1 m deep with a base of sand. Bubbles of gas can be seen emerging from the sandy base. Water discharges from the vent pool through a break in the upper mound and forms a discharge tail over a broad part of the northern flank of the mound, an area in which carbonate precipitation is currently occurring (Keppel et al., 2012). The discharge has been measured at the break in the upper mound at 558 L min^{-1} (Table 2.5). The Bubbler has the highest discharge of any mound spring in the Lake Eyre South region.

Table 2.6: Ages of structures at the Bubbler Spring complex estimated from U-series thermoluminescence dating. P indicates Priestley et al. (2013) and PH indicates Prescott and Habermehl (2008).

Site	Location	Age/ka	Reference
The Bubbler		15.3 ± 0.5	PH
		29 ± 4	PH
Blanche Cup		21.3 ± 2.1	PH
		23 ± 12	P
Hamilton Hill		106 ± 2	P
		238.0 ± 3.1	P

Blanche Cup is a dome-shaped carbonate mound around 10 m high and 70 m wide, with a 10 m-wide vent at the summit. Water discharges over the southern flank of the mound at a rate of 15.2 L min^{-1} (Table 2.5).

The Little Bubbler spring is located in calcareous dunes on the eastern edge of the complex. The vent is partly filled with *Phragmites* plants and bubbles of gas emerge from the vent pool periodically, leading to its name. Water discharges at approximately 51 L min^{-1} to the east and north-east (Table 2.5).

Other springs in the area have vents filled with *Phragmites* plants and are referred to with numbers (Springs 403 through 406); their locations can be seen on Figure 2.8. Spring 403 is the largest of this latter group of springs, with a discharge of 7.8 L min^{-1} (Table 2.5). There are also a number of dome-shaped mounds, which are most likely associated with inactive springs. Some of these mounds have clumps of *Phragmites* reeds at their apex suggesting there may still be vertical subsurface flow but the high rate of annual evapotranspiration results in no surface discharge.

Hamilton Hill stands slightly apart from the active springs, about 630 m south-west of Blanche Cup. It is a mesa about 35 m high and 200 m in diameter, capped by carbonates deposited from an extinct spring, the vent of which is in the centre of the mesa.

The springs in this area are surrounded by Quaternary sediments which are generally less than 5 m thick and consist of alluvial mud and sand, carbonate precipitated from spring water, and colluvial and alluvial calcareous sand and gravel derived from the adjacent spring platforms. Underlying these sediments is the Bulldog Shale, which is exposed in several areas. At the southern edge of the complex is an area which has been mapped as an ‘incised’ spring platform believed to be associated with past spring activity (Figure 2.8).

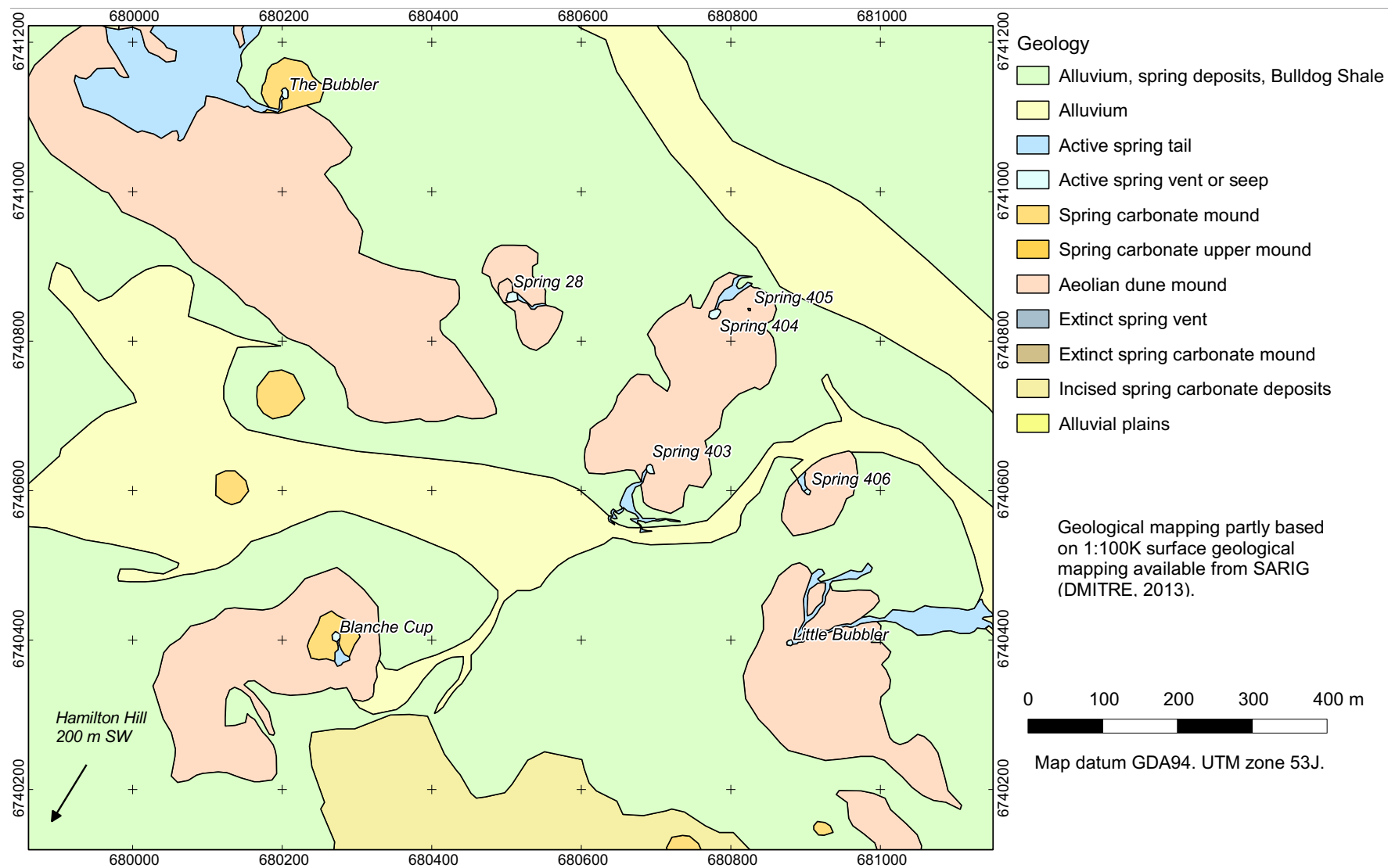


Figure 2.8: Geological map of the Bubbler Spring complex.

2.5 Freeling Springs

Freeling Springs is a complex of springs located about 70 km south-east of Oodnadatta. Numerous spring vents lie along the base of a fault scarp associated with the Kingston Fault, which offsets Mesozoic Eromanga Basin sediments and Quaternary sediments of the Lake Eyre Basin against highlands consisting of Palaeoproterozoic basement to the west (the Denison Range). The spring complex lies in a wedge-shaped valley, bounded on the western side by the Kingston Fault (bearing NNW), and on the eastern side by an alluvial terrace overlying Bulldog Shale (boundary bearing NNE). The valley is filled with spring carbonate deposits and alluvial outwash from the highlands (Keppel et al., 2013b, Appendix A, pp. 9-10), with Cadna-owie Formation interpreted to be near the surface (Keppel et al., 2013b, p. 41, Aldam and Kuang, 1988, p. 10). A geological map is shown in Figure 2.9 and a cross-section in Figure 2.10. Figure 2.11 shows two panoramic photographs of the northern part of the wedge-shaped valley.

The southernmost spring vent (Freeling Spring, or FS1) is located at the southern apex of the wedge, with discharge from this seep joining other streams flowing down from the highlands and flowing NNE. The total outflow from FS1 was estimated at 18.65 L min^{-1} by Green and Berens (2013).

Numerous smaller springs are located on the western side of the wedge, with the springs marked by thickly vegetated seeps. Immediately to the north of FS1 there are a number of seeps along the base of the fault scarp, while further north the seeps occur across carbonate terraces which lie 25 m to 150 m east of the fault scarp (springs FS13 through 19), with the distance from the scarp increasing to the north. The outflow for these springs varies, with many seeps having discharges of less than 1.7 L min^{-1} . Other seeps and vents with large discharges are FS16 (in the group noted on Figure 2.9) at 63 L min^{-1} and FS20 at 17.9 L min^{-1} (Green and Berens, 2013). The springs and associated carbonate terraces extend for about 2 km from south to north, filling the western and central part of the wedge-shaped valley (Keppel, 2012, Appendix A, p. 12).

The highlands are primarily composed of Palaeoproterozoic igneous and metamorphic rocks (the Wirriecurie Granite and Tidnamurkana Volcanics), and Mesoproterozoic intrusives (Rogers and Freeman, 1996b, pp. 8-10). Early Cretaceous and Tertiary sediments on the eastern side of the Kingston and

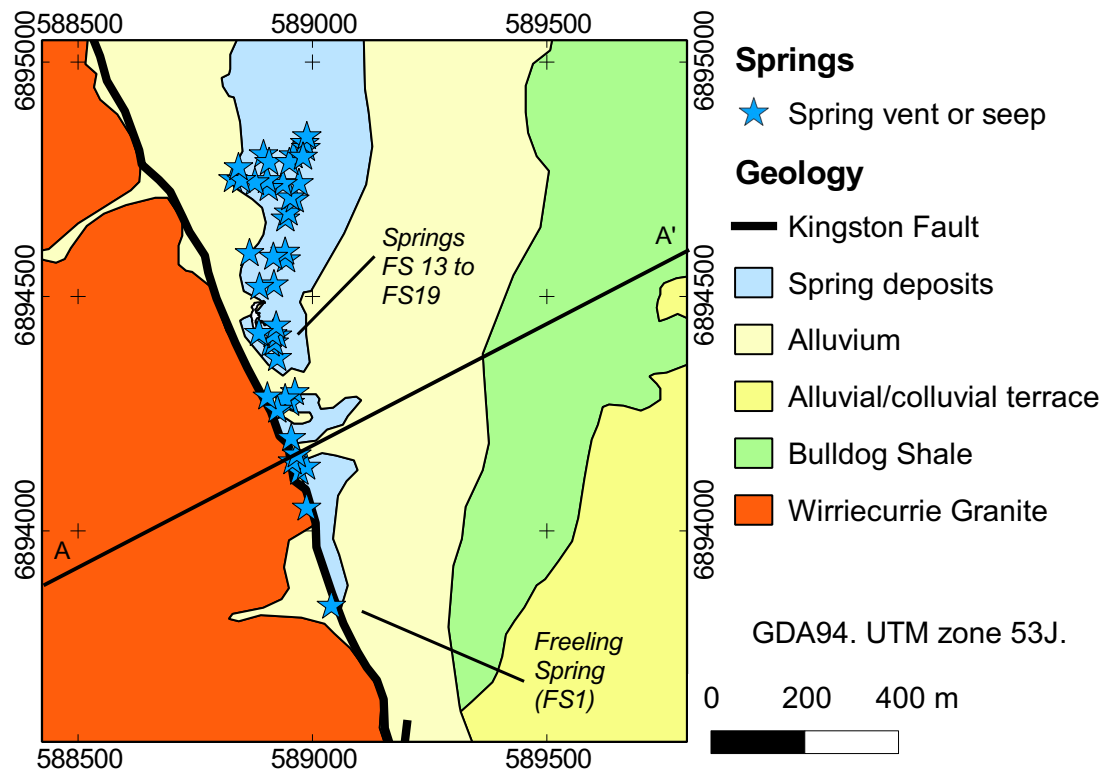


Figure 2.9: Overview geological map of the Freeling Spring complex.

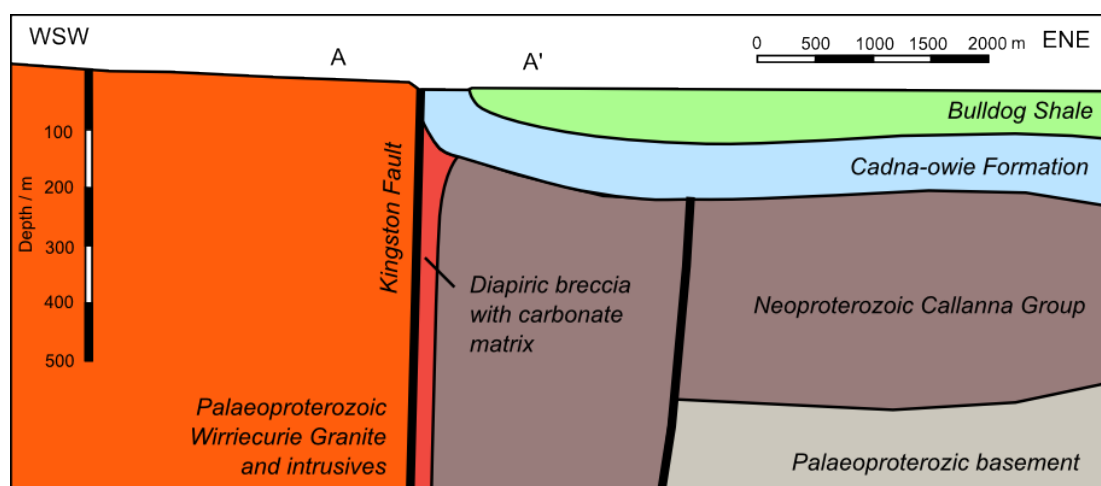
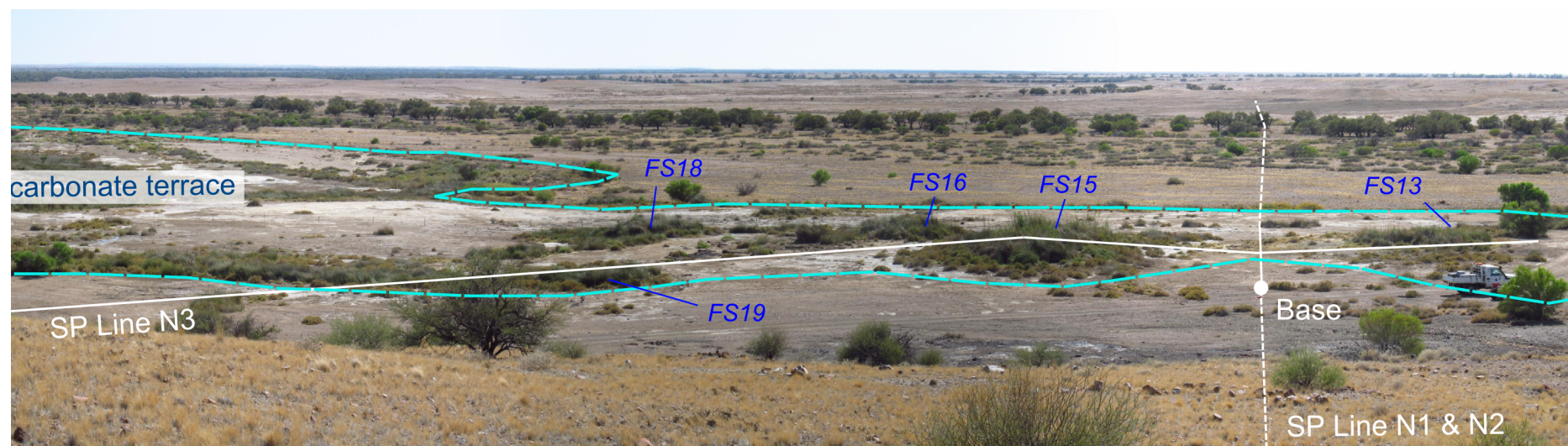


Figure 2.10: Geological cross-section through the Freeling Springs complex, based on seismic and drillhole data (Rogers and Freeman, 1996a).

Levi Faults dip to the east, with steep dips recorded close to the faults. These features have been interpreted as being caused by movement on the faults during and after deposition (Rogers and Freeman, 1996b, p. 33 and Aldam and Kuang, 1988, p. 10). Diapiric breccia with a carbonate matrix occurs about 500 m south of FS1 along the fault zone at the edge of the highlands; these diapirs were probably formed at the same time as deformation and activity on the Kingston Fault during the Cambrian and Ordovician (Rogers and Freeman, 1996b, pp. 15-16).



(a) Northern part of the Freeling Springs complex, looking ENE from the highlands.



(b) Detail of area containing seeps FS13 to FS19. White lines show the locations of the SP survey Lines N2 and N3.

Figure 2.11: Panoramic photographs of the Freeling Springs complex.

Chapter 3

Methods

3.1 Magnetotellurics

3.1.1 Physics

Magnetotellurics (MT) is an electromagnetic (EM) induction method that utilises natural variations in the EM field of the Earth as a source of signal. Magnetotelluric surveys measure the Earth's surface wave impedance Z , which is defined as the ratio of the electric field E to the orthogonal magnetic field H (Stratton, 1941). The impedance is measured for different frequencies. A brief outline of the method follows below; for further detail see the publications by Simpson and Bahr (2005), Berdichevsky and Dmitriev (2008), and Chave and Jones (2012).

The EM signals used as a source in the magnetotelluric method are generated through two different mechanisms:

1. Interactions between the solar wind and the ionosphere cause natural EM signals which have frequencies mainly below 0.1 Hz.
2. Electromagnetic energy from lightning strikes disperses to signals with frequencies between 1 Hz and 1000 Hz due to propagation between the Earth's surface and the ionosphere (Garcia and Jones, 2002a; Sternberg, 2010).

Most of the energy in these EM waves is reflected from the Earth's surface, but a small part diffuses into the ground and induces currents to flow. The electric field associated with these currents can be measured together with

the source magnetic field as the surface wave impedance. When measured across a range of frequencies, these impedances relate to a volume of the subsurface, because, under a quasistatic approximation where the fields do not change significantly with time, the electric and magnetic fields driving the currents decay in amplitude with depth at a rate that partly depends on their frequency:

$$A_z = A_0 e^{-ikz}, \quad (3.1)$$

where A_0 is the magnitude of either field at the surface, A_z is its magnitude at z metres depth, and $k = \sqrt{\sigma\mu_0\omega/2} - i\sqrt{\sigma\mu_0\omega/2}$, where σ is the ground's conductivity in S m^{-1} , μ_0 is the magnetic constant ($4 \times 10^{-7} \text{ N A}^{-2}$), and ω is the angular frequency in rad s^{-1} (Keller and Frischknecht, 1966). For a wave of a given frequency, the skin depth δ is given by

$$\delta \approx 500 \sqrt{1/\sigma f}, \quad (3.2)$$

This is the depth at which the field magnitudes have dropped by about 63% in electrically homogeneous ground (Keller and Frischknecht, 1966).

3.1.2 The impedance tensor

When the electric and magnetic fields are measured in orthogonal horizontal directions, the impedance which relates them is defined as a tensor $Z = E/H$:

$$\begin{pmatrix} E_x \\ E_y \end{pmatrix} = \begin{pmatrix} Z_{xx} & Z_{xy} \\ Z_{yx} & Z_{yy} \end{pmatrix} \cdot \begin{pmatrix} H_x \\ H_y \end{pmatrix} \quad (3.3)$$

where x and y are the orthogonal horizontal directions, and $Z_{ij} = E_i/H_j$. The first subscript denotes the direction of the electric field, and the second subscript the direction of the magnetic field (Swift, 1962, p. 57).

There are a number of constraints on the form that the impedance tensor can take, depending on the dimensionality, which refers to the distribution of resistivity variations in the Earth (Berdichevsky and Dmitriev, 2008, pp. 16–25) and whether conduction is isotropic or anisotropic (Martí, 2013).

3.1.2.1 Effects of dimensionality

When the ground is isotropic, so that the direction of current flow is irrelevant, the ground can be classed as 1D, 2D, or 3D (Martí et al., 2009):

- 1D: The subsurface consists of horizontally flat layers with different resistivities. The diagonal terms Z_{xx} and Z_{yy} will be zero, and the off-diagonal terms Z_{xy} and Z_{yx} will differ only in sign.
- 2D: There are lateral variations in resistivity in one direction (e.g. the y direction) but not in the orthogonal direction (x), which is the geoelectric strike. When an impedance tensor is measured in the x and y directions, the diagonal terms are zero and the off-diagonal terms measure two field polarisations: Z_{xy} measures the transverse electric (TE) mode, with currents running along geoelectric strike, and Z_{yx} measures the transverse magnetic (TM) mode, with currents running across resistivity contrasts. When the impedance tensor's coordinate axes are not parallel to x and y the two modes will mix into all the components and the diagonal terms of the impedance tensor will not be zero.
- In a 3D model, where resistivity varies laterally in both directions, all the tensor terms may be non-zero and different in magnitude and sign.

In 2D environments the coordinate system in which the impedance tensor is measured may not necessarily be aligned with the geoelectric coordinates (Fischer and Masero, 1994). In this case the measured tensor can be rotated to give impedances in different directions by:

$$\begin{pmatrix} Z_{x'x'} & Z_{x'y'} \\ Z_{y'x'} & Z_{y'y'} \end{pmatrix} = R^T \cdot Z \cdot R \quad (3.4)$$

where R is the rotation matrix

$$R = \begin{pmatrix} \cos \theta & -\sin \theta \\ \sin \theta & \cos \theta \end{pmatrix} \quad (3.5)$$

and the rotated directions are $x' = x + \theta$ and $y' = x + \theta + 90^\circ$. The impedances Z'_{xy} and Z'_{yx} are referred to in following chapters as the orthogonal or off-diagonal modes, and Z'_{xx} and Z'_{yy} as the parallel or diagonal modes.

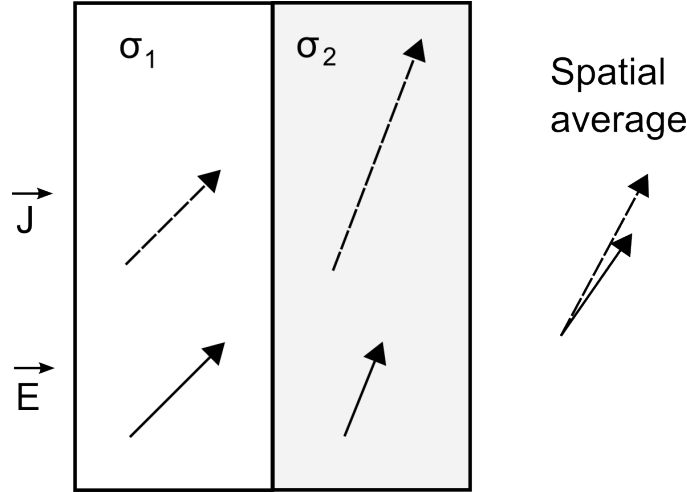


Figure 3.1: Structural anisotropy as a scale effect of averaged fields across isotropic conductors where $\sigma_2 \simeq 2.2\sigma_1$. Note boundary conditions at the interface between σ_1 and σ_2 , where the components of E parallel to the interface are equal, as are the components of J normal to the interface (Jones and Price, 1970). From Figure 2 of Weidelt (1999).

3.1.2.2 Effects of anisotropy

The ground can also be anisotropic, such that the resistivity/conductivity depends on the direction of current flow. This also affects the form that the impedance tensor takes, in a similar way to the effect of dimensionality. In a fully anisotropic medium the conductivity tensor is defined as:

$$\hat{\sigma}(x, y, z) = \begin{bmatrix} \sigma_{xx} & \sigma_{xy} & \sigma_{xz} \\ \sigma_{yx} & \sigma_{yy} & \sigma_{yz} \\ \sigma_{zx} & \sigma_{zy} & \sigma_{zz} \end{bmatrix} \quad (3.6)$$

where x, y, z are orthogonal coordinate axes with x, y are horizontal and z is downward. Where off-diagonal components of $\hat{\sigma}$ are non-zero, the current density vector \vec{J} may be deflected from the electric field vector \vec{E} , as described by the full version of Ohm's Law:

$$\vec{J} = \hat{\sigma} \cdot \vec{E} \quad (3.7)$$

In a diffusive geophysical technique like MT, anisotropic conductivity can be either a microscopic property of the material (intrinsic anisotropy) or a scale effect of oriented structures present within the averaging volume of the fields (structural anisotropy; see Figure 3.1) (Weidelt, 1999).

The conductivity tensor is symmetric (Dekker and Hastie, 1980, p. 20) and can be decomposed into three primary conductivities and three rotation angles: strike (α_S) as a rotation around the z -axis, dip (α_D) around the once-rotated x' axis, and slant (α_L) around the twice-rotated z'' -axis (Martí, 2013, Fig. 1):

$$\hat{\sigma}'(x, y, z) = R \cdot \hat{\sigma} \cdot R^T = \begin{bmatrix} \sigma_x & 0 & 0 \\ 0 & \sigma_y & 0 \\ 0 & 0 & \sigma_z \end{bmatrix} \quad (3.8)$$

where R is the rotation matrix resulting from the rotations defined by α_S , α_D , and α_L .

In the case of vertical planar conductors within an averaging volume, the structural anisotropy conductivity tensor can be represented with only three parameters:

1. The conductivity parallel to the conductive planes ($\sigma_x = \sigma_z$)
2. The conductivity normal to the conductive planes (σ_y)
3. The anisotropy strike (α_S).

In isotropic 1D models with only one layer which contains a vertical planar anisotropy, the impedance tensor takes the form of a 2D tensor with a strike equal to the anisotropy strike; Z appears to be 3D when there are multiple anisotropic layers with different α_S angles (Martí et al., 2010, pp. 143–144). The main criteria by which isotropic 2D responses can be distinguished from 1D anisotropic responses is by examining the response at nearby locations. If the response is the same, then it is likely to be caused by 1D anisotropy. Responses due to isotropic 2D structures will vary gradually with increasing lateral offset (Martí et al., 2010; Martí, 2013).

The phase tensor (see Section 3.1.3) has also been shown by Heise et al. (2006) to discriminate between vertical changes in anisotropy strike. Heise et al. (2006) showed that phase splits can be produced by vertical gradients in conductivity: current-parallel phase tensor ellipses are perpendicular to the strike of conductive sheets when the anisotropic layer overlies an isotropic one, and parallel when the isotropic layer overlies the anisotropic one. Both orientations of phase tensor ellipses are found where an anisotropic layer is sandwiched between isotropic layers (Heise et al., 2006, Fig. 5).

3.1.2.3 Galvanic distortion

The effect of conductivity variations on the impedance tensor can be divided into two forms: galvanic distortions which occur due to ‘excess’ charges built up on conductivity boundaries in the Earth, and inductive effects which occur due to modifications of current flow by conductivity structures (Berdichevsky and Dmitriev, 2008, p. xix). Galvanic distortions develop due to the horizontal flow of current across conductivity variations which result in the development of secondary electric or magnetic fields (Price, 1973; Kaufman, 1988). They can be distinguished from inductive effects because they do not cause any change in the phase relationships between the fields (Jiracek, 1990, p. 166). Thus they can be described by a real galvanic distortion tensor C acting on a ‘regional’ impedance tensor Z_r to produce the distorted and observed impedance tensor Z_{obs} (Bahr, 1988; Groom and Bailey, 1989):

$$Z_{obs} = \begin{pmatrix} C_{xx} & C_{xy} \\ C_{yx} & C_{yy} \end{pmatrix} \cdot Z_r \quad (3.9)$$

Z_r contains the inductive effects of conductivity variations in the Earth (described above for 1D, 2D, and 3D structures). The problem of decomposing Z_{obs} in order to remove C and retrieve Z_r for interpretation is a difficult one which many studies have addressed (Bahr, 1988; Groom and Bailey, 1989; Groom and Bahr, 1992; Garcia and Jones, 2002b).

3.1.3 Phase tensor

Caldwell et al. (2004) demonstrated that a phase tensor Φ can be calculated from the observed impedance tensor Z_{obs} in such a way as to avoid the effects of the real galvanic distortion tensor D , but retain important information about the impedance phases and dimensionality. Assuming that the galvanic effects are limited to the electric field, which is usually but not always the case (e.g. Kaufman 1988, p. 152 and Jiracek 1990, p. 346), then we have:

$$E_{obs} = E_r + E_s \quad (3.10)$$

where E_{obs} is the observed electric field, E_r is the inductive or regional field, and E_s is the secondary field due to the galvanic charges developed over local conductivity variations. A galvanic distortion tensor D can then be defined

as:

$$E_{obs} = \begin{pmatrix} D_{xx} & D_{xy} \\ D_{yx} & D_{yy} \end{pmatrix} \cdot E_r \quad (3.11)$$

where all the components of D are real (i.e. they cause no shift in phase). The calculation of the phase tensor requires that D does not effect the magnetic field, i.e. that:

$$H_{obs} = H_r \quad (3.12)$$

Note that D is therefore not strictly to C . E_r and H_r are related to each other by the fundamental magnetotelluric relationship:

$$E_r = Z_r \cdot H_r \quad (3.13)$$

Combining Equations 3.11, 3.12, and 3.13 gives:

$$E_{obs} = D \cdot (Z_r \cdot H_r) \quad (3.14)$$

$$= (D \cdot Z_r) \cdot H_{obs} \quad (3.15)$$

If the impedance tensors are separated into two real tensors containing their real and imaginary components of the two impedance tensors:

$$Z_{obs} = X_{obs} + iY_{obs} \quad (3.16)$$

$$Z_r = X_r + iY_r \quad (3.17)$$

and noticing that

$$X_{obs} = DX_r \quad (3.18)$$

$$Y_{obs} = DY_r \quad (3.19)$$

then a phase tensor Φ can be calculated through:

$$\Phi = X^{-1} \cdot Y \quad (3.20)$$

Note that Φ is independent from D and therefore contains only information

about the regional or inductive response:

$$\Phi = X^{-1} \cdot Y \quad (3.21)$$

$$= (D \cdot X_r)^{-1} \cdot (D \cdot Y_r) \quad (3.22)$$

$$= X_r^{-1} \cdot D^{-1} \cdot D \cdot Y_r \quad (3.23)$$

$$= X_r^{-1} \cdot Y_r \quad (3.24)$$

$$= \Phi_r \quad (3.25)$$

The phase tensor's components measure the difference in phase between the electric and magnetic fields (i.e. the undistorted impedance phase) for 1D and 2D impedance tensors.

Singular value decompositions of the phase tensor have proven to be particularly useful for diagnosing the dimensionality of an impedance response. This has been shown both through the analysis of 3D forward models (Caldwell et al., 2004, pp. 463-4) and analytical calculations (Booker, 2013, section 2.2.3). The decomposition is defined by Equation 20 of Caldwell et al. (2004):

$$\Phi = R^T(\alpha - \beta) \cdot \begin{pmatrix} \phi_{max} & 0 \\ 0 & \phi_{min} \end{pmatrix} \cdot R(\alpha + \beta) \quad (3.26)$$

where the orientation of the coordinate system in which $\arctan(\phi_{max})$ and $\arctan(\phi_{min})$ give the phases of the TM and TE mode impedances is given by $\alpha - \beta$. Furthermore β measures the extent to which 3D inductive effects are present.

Booker (2013) gives an alternative decomposition of the phase tensor and suggests plotting the phase tensor as an ellipse oriented towards $\theta = 90^\circ + (\alpha - \beta)$ which is the azimuth of the TE electric field (i.e. the geoelectric strike) for 2D conductivity structures (Figure 3.2). The size of the ellipse indicates the phase: circular ellipses have no difference in phase between modes. Booker (2013) also shows that the normalised phase tensor skew $\psi = 2\beta$ must meet the condition $|\psi| < 6^\circ$ in order for 3D effects to be considered negligible.

3.1.4 Modelling

There are an infinite number of resistivity models which produce responses that fit any finite set of observed MT data (Parker, 1983). The inversion pro-

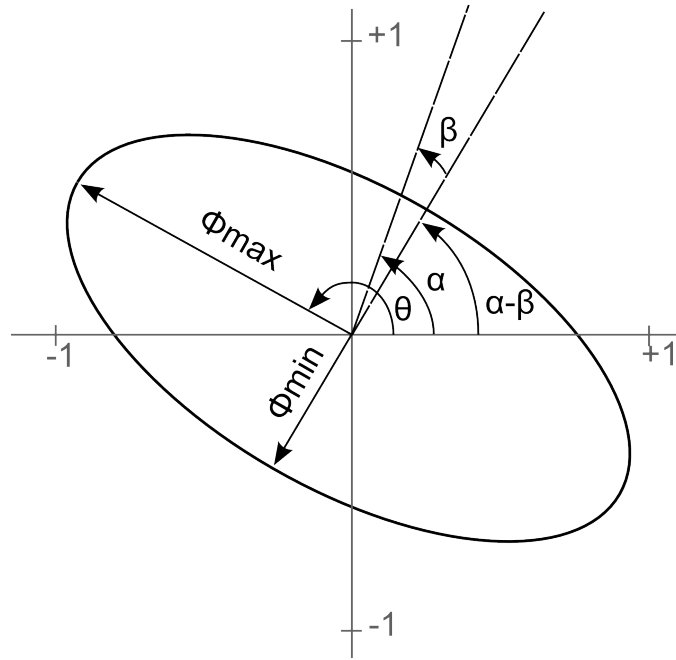


Figure 3.2: The phase tensor plotted as an ellipse following the convention of Booker (2013), with ϕ_{max} plotted at an azimuth of $90^\circ + (\alpha - \beta)$. This tensor has $\phi_{max} = 1$ and $\phi_{min} = 0.5$, indicating the TE phase is 45° and the TM phase is 26° , with a geoelectric strike of approximately 300° . The 2D interpretation is only valid because β is negligible.

cess through which a preferred model for interpretation is found uses a misfit criterion to measure how well the model's forward responses fit the observed responses. This criterion is minimised in order to find a *possible* model, but there are usually many such models, and the range of their parameters depends on the observational errors (Weidelt, 1972). Sometimes an additional constraint is added to narrow the range of resulting models, such as a smoothness or 'simplicity' criterion (Constable et al., 1987; Smith and Booker, 1988). The results of inversions are therefore to a certain extent subjective and approximate.

3.1.4.1 1D anisotropic inversion

One-dimensional resistivity models consist of horizontal layers with different resistivities overlying a halfspace. Although a 1D model can generally be found to fit a single set of impedance data for a given bandwidth, where there are differences in phase or apparent resistivity (i.e. different components in the impedance tensor), a more complicated model is required. Rather than assuming that such differences require a 2D model, with lateral changes in resistivity, this work uses anisotropic 1D modelling to test whether an anisotropic

response in one of the horizontal layers is sufficient to explain the difference in phase or apparent resistivity (see Sections 4.4 and 7.4). The algorithm used to perform this modelling is described in the following.

The algorithm used to perform anisotropic 1D modelling in this work used a Monte Carlo method. For each inversion run the algorithm began with a 1D resistivity model containing m layers, obtained by an Occam 1D (Constable et al., 1987) inversion of one of the observed modes. Usually m was between 5 and 10. A log-normal distribution of resistivities was then generated for each of the m layers, centred on the layer's resistivity in the starting model. For each inversion at least one layer (the k -th layer) was designated as anisotropic. This layer was given two separate resistivity distributions, one for the resistivity $\rho_1 = \rho_3$ along the first and third coordinate axes (i.e. horizontally and vertically), and another for the resistivity ρ_2 along the second coordinate axis (horizontally), with an additional condition that $\rho_1 < \rho_2$. A uniform distribution between 0 and 180 degrees was also generated for the strike α of the anisotropic layer. Because the slant and dip of the anisotropy were kept constant and only the strike varied, the anisotropic layer can be visualised as consisting of vertical sheets which are more conductive along their surface than across it. In addition to this, a log-normal distribution of layer thicknesses was also generated, centred on the thicknesses of the starting model layers. The number of models used in each inversion run (i.e. the length of the distributions N) ranged from 10^5 to 10^6 .

A total of m inversions were then run, with each layer in turn being permitted to be anisotropic (i.e. $k = 0, 1, 2, \dots, m$). The Z1ADR code was used to generate forward responses for each of the N models (Pek and Santos, 2002). Successful models were then selected from the forward results by choosing a measure of fit ($\text{NRMS}(\phi_{xy}) + \text{NRMS}(\phi_{yx})$) and finding a threshold below which the goodness of fit between the forward data and the observed data was considered reasonable. Because each inversion contains only one anisotropic layer and therefore only one anisotropy strike, the misfit measure chosen relies only on the off-diagonal impedances, as the diagonal impedances are insignificant in this case (Martí, 2013, p. 10). Only one anisotropic layer was used in the inversion process because the skew of the impedance tensors (e.g. the phase tensor skew β) was sufficiently close to zero in all sites measured; if there were more than one anisotropic layer with significantly varying strike, the skew would be significantly different from zero.

The threshold was selected by looking at the level of misfit for the best 1000 models and selecting the portion with the lowest misfits, which was usually between 10 for $N=10^5$ and 50 for $N=10^6$, or less for runs which did not contain good fits at all. The figure of $N=10^5$ was chosen as a good trade-off between obtaining a measure of confidence regarding how well the models fitted and a practical computational time.

3.1.4.2 2D smooth inversion

The process of narrowing an inversion to find the ‘best’ model is significantly more difficult with 2D models, as the gridded resistivity models generally have far more parameters which can be varied than the number of observed data points. The problem is under-determined. Therefore additional constraints on the model are necessary to guide the inversion process. The most commonly used constraint is a smoothness criterion, where spatial variations in resistivity are minimised (de Groot-Hedlin and Constable, 1990; Rodi and Mackie, 2001). Although this process does not usually find the true resistivity structure in the subsurface, it means that resistivity features will only be introduced where it is necessary for the model to depart from a homogeneous halfspace in order to fit the data.

The inversion package used here is Occam2D (de Groot-Hedlin and Constable, 1990), and inversions were run with increasingly strict requirements on fitting the data in order to identify the most important resistivity model features. Note that in all cases standard errors of 5% were applied to the MT data being inverted, because the effect of measurement uncertainties (e.g. orientation and length of dipoles and magnetometers) are likely to be of this order, and were much greater than the statistical errors calculated during the robust response function estimation process (Chave and Thomson, 2004). This process of testing increasingly strict misfit criteria was followed for all the 2D modelling performed and presented in the following chapters; generally at least 10 to 20 inversion setups were investigated for each profile being modelled.

3.1.5 Instrumentation

Magnetotelluric responses were calculated from time series of the electric and magnetic fields collected in the field using a robust bounded influence estimator to calculate the response tensor Z (Chave and Thomson, 2004). Another

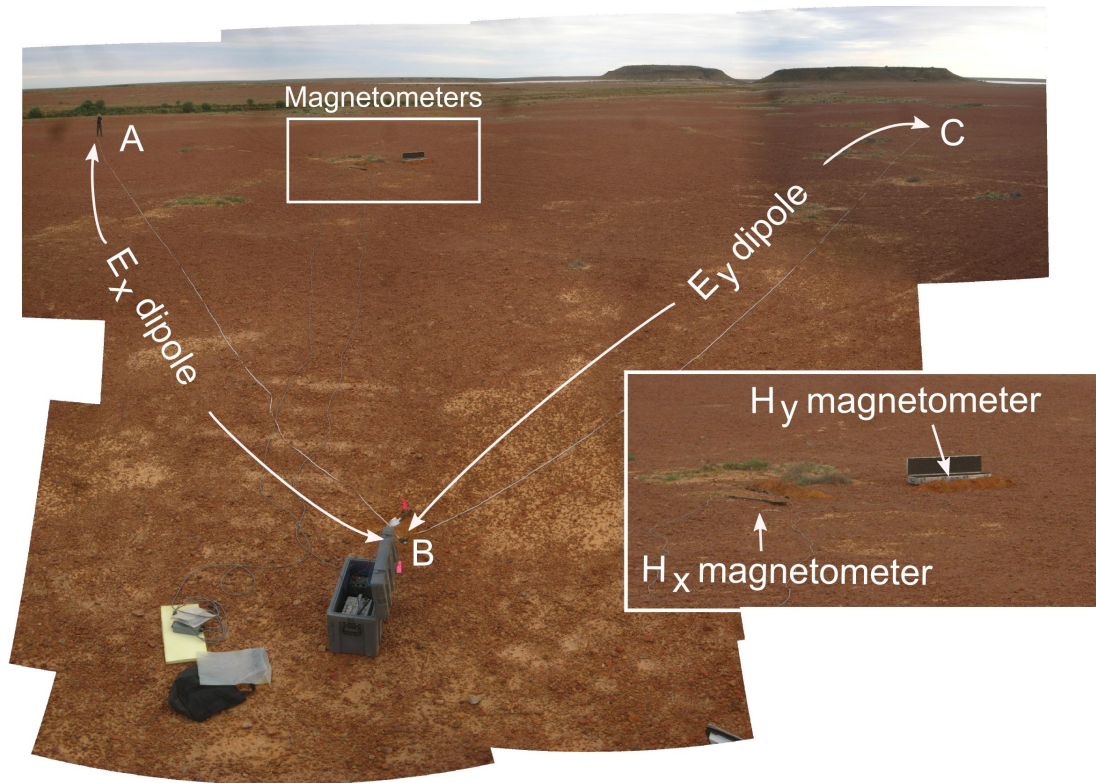


Figure 3.3: Photographic mosaic of a typical MT site near Warburton Hill. Electrodes are buried a few inches deep in the soil at A, B, and C to make two 50 m-long orthogonal dipoles. The magnetometers are placed parallel to the dipoles, levelled, and buried a few inches deep.

magnetotelluric site recorded simultaneously (either from another part of the survey line, or a special-purpose reference site) was used as a remote reference for the processing (Gamble et al., 1979). The layout of a typical site is shown in Figure 3.3. Both orthogonal components of the electric field were measured with three electrodes arranged in an L-shape with each dipole being approximately 50 m long; the electrodes used were Cu-CuSO₄ and Pb-PbCl₂ porous pots (Petiau, 2000).

The magnetic field was measured with pairs of horizontally levelled and shallowly buried induction coil magnetometers laid in orthogonal directions, parallel to the electric dipoles. KMS Technologies LEMI-120 coils were used for MT sites; these coils have a sensitivity of $> 100 \text{ mV nT}^{-1}$ between 0.5 Hz and 1000 Hz, with noise levels of $< 1 \times 10^{-3} \text{ nT}/\sqrt{\text{Hz}}$ in the same frequency range. For the Warburton AMT survey (Section 5.2.1) Schlumberger EMI BF-10 coils were used; these have a sensitivity of $> 200 \text{ mV nT}^{-1}$ between 1 Hz and 10 000 Hz, with noise levels of $< 1 \times 10^{-4} \text{ nT}/\sqrt{\text{Hz}}$ in the same frequency range.

The electric and magnetic field data at MT sites were recorded with AuScope instruments from the University of Adelaide. Data was recorded at a rate of 1000 Hz for all but the broad survey at Beresford Spring (Section 4.3.1) which was recorded at 500 Hz. The AMT survey at Warburton Spring (Section 5.2.1) was recorded on a Zonge Engineering GDP-32II receiver, producing estimates of responses at frequencies between 3 Hz and 8 kHz.

3.2 Self potential

The existence of static electrical potentials in the Earth (self-potentials, or SP) is one of the oldest known geophysical phenomena (Fox, 1830; Barus, 1882). It has been used to explore for sulfides and graphite for much of the twentieth century (Corry, 1985). There are several mechanisms by which self-potentials are generated. The largest potentials are believed to be caused by electrochemical effects associated with redox gradients (Sato and Mooney, 1960), while smaller potentials are generated by water flowing through porous material (the electrokinetic effect) (Revil et al., 2012, p. 622). While smaller, the electrokinetic effect has been found to be the dominant source of field self-potentials in this work.

3.2.1 Physics

3.2.1.1 Electrokinetic potentials

The electrokinetic effect is caused by the flow of fluid through a porous medium. It was first identified experimentally in the nineteenth century (Burbank 1905, p. 38, Rust 1938). Electrical charges exist on the surface of mineral grains; for silicate minerals these are usually negative charges (Fitterman, 1978; Revil et al., 1999). Pore fluid ions with the opposite polarity (e.g. cations) are attracted to and adsorbed on the mineral surface, while ions with the same charge are repulsed, creating a diffuse layer of differing electrical charge (often referred to as an electrical double layer). In this layer there is an excess of ions with the opposite polarity in the vicinity of the charged mineral surface. Outside the layer the pore fluid is unaffected and neutral. If the pore fluid flows, part of the diffuse layer containing the excess of opposite-polarity ions moves in the direction of fluid flow. The separation of charges created by the flow constitutes an electric potential which is called a streaming potential (Fitterman, 1978; Jackson, 2010), and the flow itself constitutes

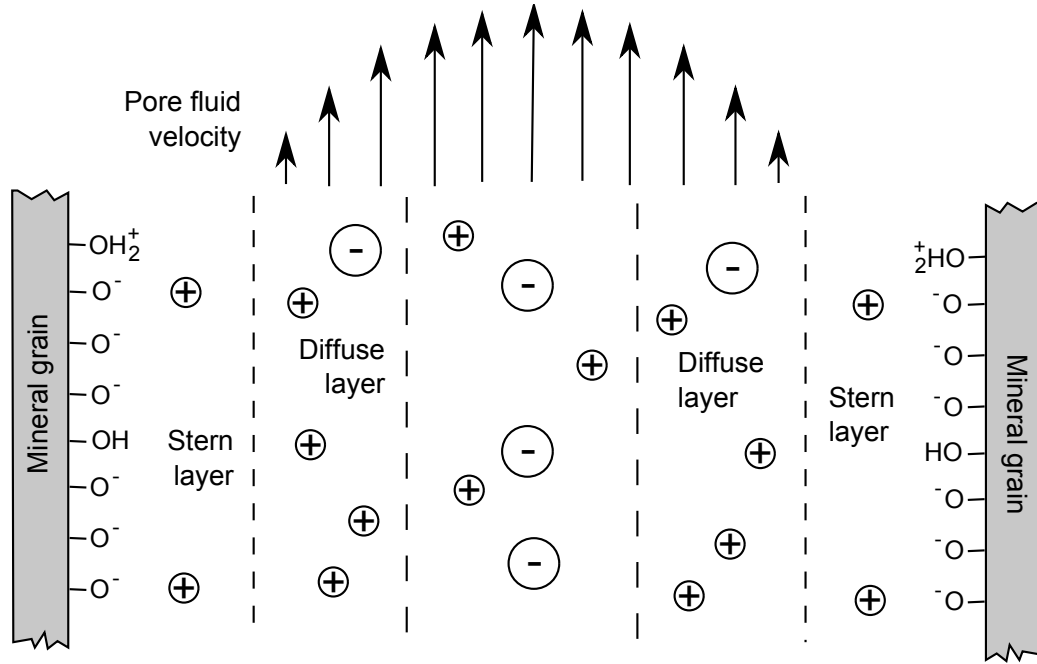


Figure 3.4: The diffuse layer of charges (electrical double layer) formed on the interface between silicate grain boundaries and pore fluids, from Figure 2 of Revil (2003a).

an advective electrical current. Figure 3.4 illustrates the process at the grain boundary scale.

The magnitude and polarity of the streaming potential developed by the pore fluid flow depends on how charges are distributed in the diffuse layer (the zeta potential), which is determined by the potential at the mineral surface (the Stern potential) and the salinity, pH, and temperature of the pore fluid (Revil et al., 1999; Kosmulski and Dahlsen, 2006; Morgan, 1989).

The empirical relationship between fluid flow and electrical streaming potentials is defined by the following cross-coupling equation (Nourbehecht, 1963; Fitterman, 1978; Sill, 1983):

$$\begin{bmatrix} J \\ Q \end{bmatrix} = \begin{bmatrix} L_{11} & L_{12} \\ L_{21} & L_{22} \end{bmatrix} \begin{bmatrix} \nabla V \\ \nabla P \end{bmatrix} \quad (3.27)$$

where L_{11} and L_{22} are the primary conductivities present in the two fundamental constitutive equations. The first is Ohm's Law:

$$J = \sigma \nabla V \quad (3.28)$$

where J is the electric current, $\sigma = L_{11}$ is the electrical conductivity, and V is

the electric potential. The second is Darcy's Law:

$$Q = K \nabla P \quad (3.29)$$

where Q is the fluid flux, $K = L_{22}$ is the hydraulic conductivity, and ∇P is the hydraulic pressure gradient. The electric current flow is then dependent on both primary fields:

$$J_{EK} = L_{12} \nabla P \quad (3.30)$$

$$J_{cond} = \sigma \nabla V \quad (3.31)$$

where J_{EK} is the advective source current and J_{cond} is the conduction current, and

$$J_{total} = L_{12} \nabla P + \sigma \nabla V \quad (3.32)$$

If we assume there are no external sources of current then:

$$\nabla \cdot J_{total} = 0 \quad (3.33)$$

and combining Equations 3.32, 3.33, and 3.31 gives:

$$\nabla \cdot J_{cond} = - \nabla L_{12} \cdot \nabla P \quad (3.34)$$

$$- \frac{L_{12}}{K} \nabla \cdot Q \quad (3.35)$$

$$+ L_{12} \frac{Q}{K^2} \nabla K \quad (3.36)$$

Therefore SP sources can be found either where there are sources or sinks of fluid flow (Equation 3.35), parallel gradients in coupling coefficient and pressure (Equation 3.34), or in hydraulic conductivity (Equation 3.36), or any combination of these effects (Hammann et al., 1997).

In general the streaming current coupling coefficient L_{12} is higher in sand than in clay because of the higher surface conductivity in clays and higher zeta potentials on sand grains (Revil and Leroy, 2001).

The return current J_{cond} usually flows by electrolytic conduction in the pore fluid. The geometry and magnitude of the observed potential field therefore

not only depends on the SP sources, but also the conductivity structure of the medium, which will control the paths which this return current will take (Boleve et al., 2007, p. 1664). For example a highly conductive clay-rich overburden will 'short out' the return current, making the potential anomaly due to the same electrokinetic source (J_{EK}) broader than in the absence of such an overburden.

3.2.1.2 Electrochemical potentials

There are at least two different forms of electrochemical potentials commonly developed in the subsurface. Where there are gradients in the concentration of particular ions in subsurface pore fluids, the diffusion of the ions along the gradient may cause an electric potential to develop (Jouniaux et al., 2009, pp. 930–931).

Much larger potentials of up to 1 V are both theoretically possible (Sato and Mooney, 1960) and have been observed and modelled (Burr, 1986; Stoll et al., 1995) in relation to reduction-oxidation electrochemical cells which may involve a number of different chemical species. These redox cells usually involve an electric conductor to connect the different parts of the cell (i.e. a non-electrolytic conduction path), and graphite or sulfide deposits often provide this conduction path, making the large SP anomaly a valuable indicator of possible mineralisation (Corry, 1985). Redox-related SP anomalies have also been identified under certain groundwater conditions (Hamilton and Hattori, 2008) and in the presence of microbial activity (Williams et al., 2007; Revil et al., 2010).

A wide variety of potential-field analytical techniques have been developed to identify the geometry and depth of the mineralised conductor which is part of redox SP anomalies (de Witte, 1948; Paul, 1965; Abdelrahman et al., 2003, and many others). These techniques are not generally pursued in this work because electrokinetic SP is generated by the flow of groundwater, which is always occurring at some scale throughout the subsurface, whereas mineral SP current densities are usually highly concentrated in the graphite/sulfide zone. Therefore the analytical techniques referenced above are not well-suited to the investigation of electrokinetic potentials.

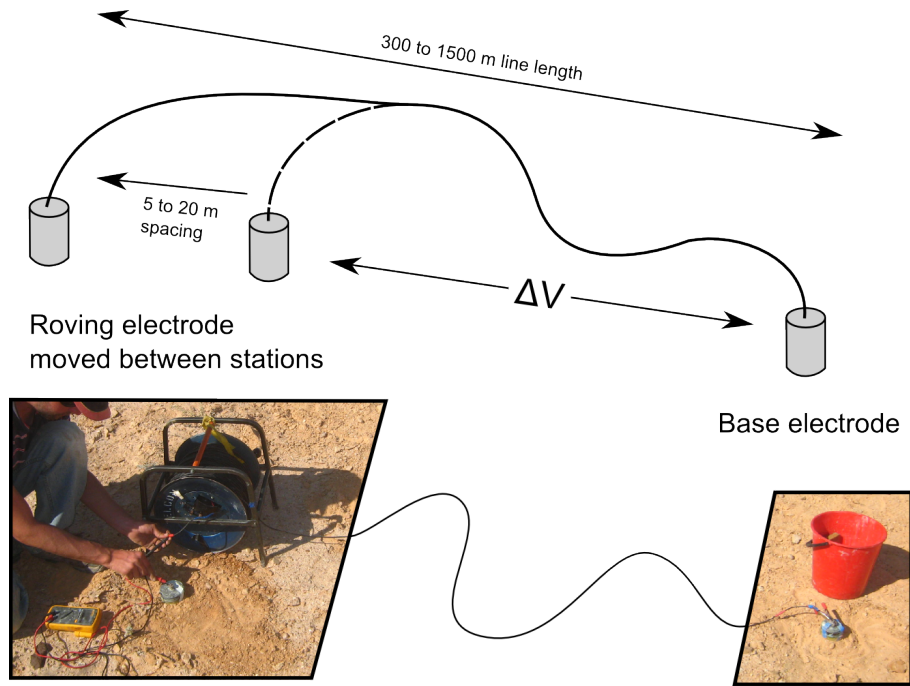


Figure 3.5: Method used to measure self-potential. The base electrode is left stationary and at a distance such that the measurement ΔV is of a total potential with regard to the fixed reference electrode.

3.2.2 Instrumentation and field procedure

Self-potential can be measured in the field either using the gradient method, where a pair of electrodes separated by a fixed distance are used to leapfrog across an area and measure the potential field gradient ΔV , or the total potential method, where the base electrode is left stationary and a roving electrode is used to sample the potential field V at different locations (Corry et al., 1983). The total potential method was used for all the surveys in this study. The field set-up is shown in Figure 3.5. Cu-CuSO₄ and Pb-PbCl₂ porous pot electrodes were used (Petiau, 2000).

3.2.3 Analytical techniques

Because electrochemical and electrokinetic processes both contribute to a single potential measurement at the surface, it is difficult to separate each of their contributions without further information (such as water samples to constrain the chemistry, or hydraulic head measurements to determine groundwater flow patterns). Furthermore, because the electrokinetic coupling coefficient depends on a large number of hydrogeological properties, modelling SP measurements quantitatively in terms of those properties is a difficult task and

is the subject of active research and discussion (Revil et al., 2008; Jouniaux et al., 2010). Inversion of SP measurements for groundwater flow regimes is also a new endeavour (Boleve et al., 2007; Jardani et al., 2006a, 2008; Minsley et al., 2007). However, simple qualitative interpretations are still used. One of the most useful is to simply interpret the geometry of flow from the shape of the SP anomaly. Another is an image reconstruction technique developed by Hammann et al. (1997) that is described in the next section.

Where the coupling coefficient is positive, upward flow generates a positive SP anomaly and downward flow a negative anomaly (Ishido and Pritchett, 1999; Hammann et al., 1997, p. 15,251). Lateral flow also generates a positive anomaly in the direction of flow. Studies have demonstrated that vertical flow results in significant SP anomalies: for example, downward leakage through dams results in negative SP anomalies (Ogilvy et al., 1969; Al-Saigh et al., 1994), while others show an association between positive anomalies and upward flow on volcanoes (Zlotnicki and Nishida, 2003) and at natural groundwater springs (Schiavone and Quarto, 1984). Factors which can be difficult to measure, like coupling coefficient, resistivity structure, and temperature variations, can alter the SP field in more complex ways (Schiavone and Quarto, 1984; Aizawa et al., 2008; Byrdina et al., 2009), making interpretation more difficult.

3.2.3.1 Image reconstruction

A relatively simple method of reconstructing images of the most likely location for SP sources is outlined by Hammann et al. (1997); similar techniques have also been developed by others (Patella, 1997; Sailhac and Marquis, 2001; Gibert and Pessel, 2001; Revil, 2003b; Jardani et al., 2006b; Alaia et al., 2009). The method involves finding the extent to which a potential source at some given location correlates to the measured response. The correlation coefficients for all locations on a 2D profile are all calculated and presented as an ‘image reconstruction’ of the most likely locations.

The horizontal electric field gradient ΔV (i.e. what is measured at the surface with the SP method) for a source with horizontal location $x = x_k$ and depth z (with the surface $z = 0$) is

$$\Delta V(x_k) \propto \frac{x}{x^2 + z^2} \quad (3.37)$$

The calculated potential gradient ΔV_{calc} at a location $x = x_k, z = 0$ on the surface due to a source at a given location $x = x_i, z = z_j$ is then:

$$\Delta V_{calc}(x_k, x_i, z_j) \propto \frac{x_k - x_i}{(x_k - x_i)^2 + (-z_j)^2} \quad (3.38)$$

Then for a set of n measured potential gradients ΔV_{obs} at $x = x_k, z = 0$ the correlation coefficient \hat{C} for a source at location $x = x_i, z = z_j$ is calculated:

$$\hat{C}(x_i, z_j) = \sum_{k=1}^n \Delta V_{calc}(x_k, x_i, z_j) \Delta V_{obs}(x_k) \quad (3.39)$$

and then normalised:

$$C(x_i, z_j) = \frac{\hat{C}(x_j, z_j)}{\left[\sum_{k=1}^n \Delta V_{calc}(x_k, x_i, z_j) \sum_{k=1}^n \Delta V_{obs}(x_k) \right]^{1/2}} \quad (3.40)$$

The function C then represents a depth-section of correlation coefficients, where values near zero are associated with locations in the subsurface with little correlation to any sources, and values near $+1$ or -1 are associated with near-perfect correlation with positive and negative streaming potential sources. These are the theoretical limits. Actual field data may contain a number of sources together with the short-wavelength ‘noise’ typical of field SP data (Ernstson and Scherer, 1986).

3.2.3.2 Sensitivity

Self-potential data is highly sensitive to near-surface sources. Because the magnitude of the response is inversely proportional to the square of the distance, the most sensitive parameter is always the distance to the shallowest SP source. Birch (1993) uses this fact together with a hydrogeological assumption about the nature of groundwater flow in the area to measure variation in the depth of the water table. A natural consequence of this is that little information can be gained about the existence or non-existence of SP sources *underlying* shallower sources of potential. Figure 3.6 shows an example of this, where one aspect of the geometry of an area on a 2D section that is filled with positive SP sources is varied in order to see the effect on the forward modelled SP response:

- In Figure 3.6A there are SP sources filling a rectangular area 20 m wide

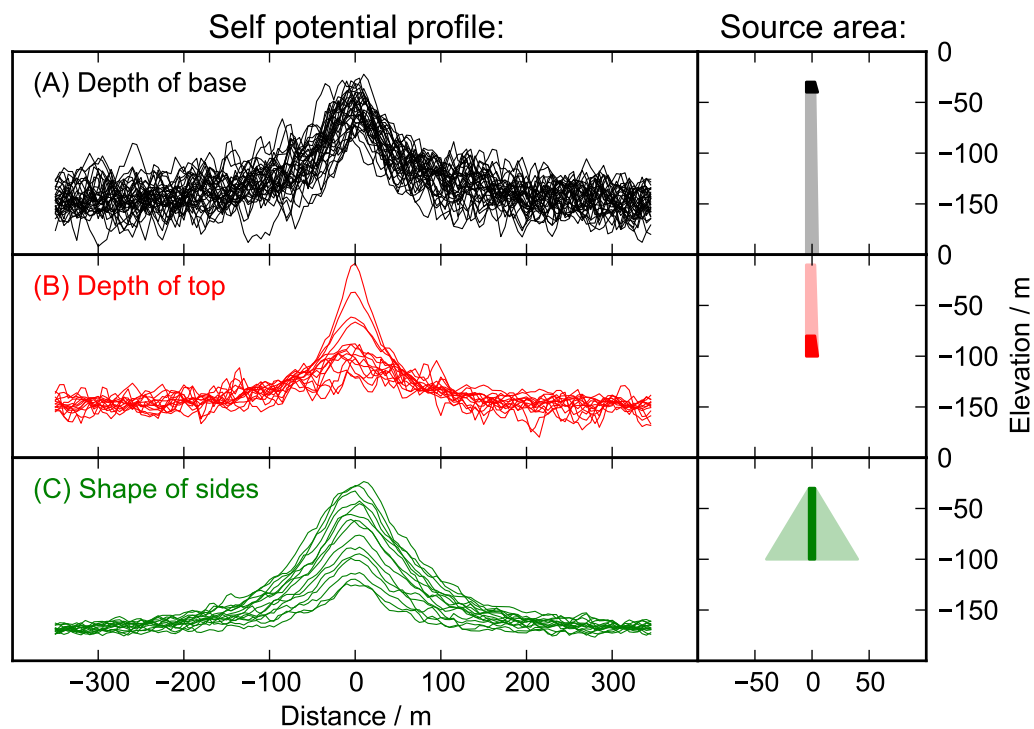


Figure 3.6: Sensitivity of forward-modelled SP profiles to variations in (A) the depth to the base of a source area, (B) the depth to the top of a source area, and (C) the dip of a source area's sides. In each experiment only one aspect of the geometry of the area containing positive sources is modified; this is shown in the depth-sections in the right-hand column by a partly transparent area. Gaussian noise of 2% has been added to all the SP measurements; the uncertainty of real field measurements is at least this large.

and 30 m below the surface, with the depth to the bottom of the area filled with sources varying from 40 m to 200 m. The forward modelled SP profiles are all similar, despite the significant variation in the size and depth of the SP source area, showing that there is no ability to resolve variation in the depth to the bottom of a given source feature.

- In Figure 3.6B there are SP sources filling a rectangular area 20 m wide, with the depth to the source area varying from 10 m to 80 m. The base of the source area is fixed at a depth of 100 m. The forward modelled SP profiles vary significantly in shape and magnitude, showing the strong dependence of SP profiles on the depth to the shallowest sources.
- In Figure 3.6C there are SP sources filling an area between fixed depths of 20 m and 100 m, with the width at the top fixed at 20 m and the width at the base varying from 10 m to 100 m. The forward modelled SP profiles vary significantly in magnitude, and less significantly in shape, showing moderate dependence of SP profiles on the shape of source features.

3.3 Time-domain electromagnetics (TEM)

3.3.1 Physics

Time-domain electromagnetic induction techniques (TEM) use an artificial signal to induce currents in the subsurface and measure the ground's resistivity. An electric current is passed through a transmitting loop of wire laid on the ground, and the current is then abruptly switched off. The large change in this primary EM field causes loops of electric current to flow in the subsurface. These loops decay in magnitude as the primary field diffuses and dissipates into the ground, generating a secondary field which induces currents to flow in a receiving loop of wire which is also laid out on the surface. In discrete transient EM, these currents are sampled at closely-spaced intervals of time after the transmitter current is shut off, and the decay of the secondary magnetic field is reconstructed. The rate of decay is related to the resistivity: in resistive ground the secondary field dissipates more rapidly than in conductive ground (McNeill, 1980). For more details on the physics of the technique see Nabighian and Macnae (1991)

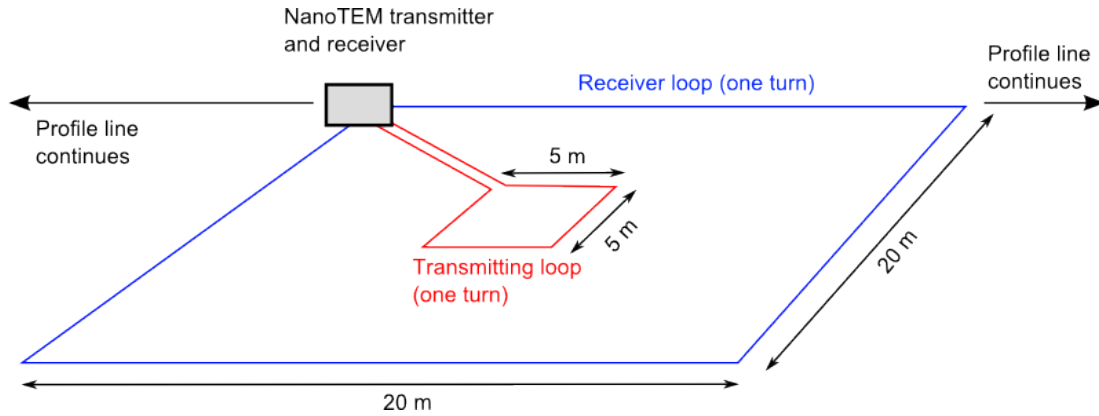


Figure 3.7: Instrument setup used in the field to measure time-domain electromagnetic responses. A large electric current passed through the transmitting loop is shut off and the induced currents described in the text are measured in the receiving loop.

3.3.2 Application and modelling

When used for hydrogeological investigations, TEM is often used to characterise the subsurface down to depths of 50 m to 80 m (Nobes, 1996; Danielsen et al., 2003; Auken et al., 2006). Zonge Engineering’s NanoTEM system was used for the surveys in this work, with the instrument layout shown in Figure 3.7.

A number of individual responses are stacked, averaged, and then checked for consistency and smooth decays with time. The transient responses are then inverted for a best-fitting 1D resistivity model using Zonge Engineering’s STEMINV routine (MacInnes, 2010). These 1D models for each site are then presented alongside each other as a 2D section; note that the results are 1D inversions, and do not take the effect of lateral variations in resistivity on the geophysical response into account.

3.3.3 Induced polarization effects

For ground with real resistivity (i.e. frequency-independent conduction), TEM responses are always positive (Weidelt, 1982). However negative transients are sometimes observed at late decay times, and studies have demonstrated that these transients are likely to be caused by polarizable layers (Flis et al., 1989; Hohmann and Newman, 1990). This is the same effect measured by the induced polarization (IP) method (see Vacquier et al., 1957; Sumner, 1984), but the current generated from the decay of the electrical polarization is masked by the primary current induced by the TEM system, and only ap-

pears as a small negative response at late decay times (Smith and West, 1988). A large primary current is required to charge the polarizable material. Such a current occurs only if the chargeable material is also highly conductive. The polarizable material may be sulfides or a layer of clay-coated sand or gravel (Bodmer et al., 1968; Slater and Lesmes, 2002). Both are highly conductive and can be chargeable, and are therefore able to cause negative transients in TEM data. It should be noted that where the conductive and polarizable layer is too thick, the time required for the primary currents to decay is too long, and the negative transients are not observed at all (Smith and West, 1988). The data may still be affected, but it is not as easy to infer the presence of polarizable material.

Chapter 4

Beresford Spring

Summary

Beresford Spring is a shield-shaped carbonate mound spring located on the edge of a playa. Water flows from the 10 m-wide spring vent over the carbonate edifice of the upper mound into playa alluvial deposits on the eastern side of the mound, which is 250 m long and 100 m wide. An extinct spring vent lies on top of a 40 m-high mesa in the centre of the playa (Beresford Hill) 400 m south-east of the currently active spring. See Section 2.3.1 for more detail.

Self-potential, TEM, and MT data were collected over the Beresford Spring mound. See Figures 4.1 and 4.2 for the locations of SP and MT sites collected.

SP data were collected on lines which run over the modern mound and the extinct hill (Figure 4.2). A narrow 150 m-wide zone of elevated potential exists at the spring vent and another zone of elevated potential is present over the extinct spring.

Inversion of TEM data collected across the mound shows a resistive zone underneath the upper spring mound at a depth of 40 m. Anisotropic 1D and isotropic 2D inversion of MT data collected across the mound and surrounding playa suggests that conductive planar structures at depths of 150 m to 500 m are aligned towards the northwest and are associated with the platform of spring carbonates at the surface. Resistive areas in 2D inversions of MT data

(striking north-west) appear to be associated with both the modern spring mound and the extinct mounds.

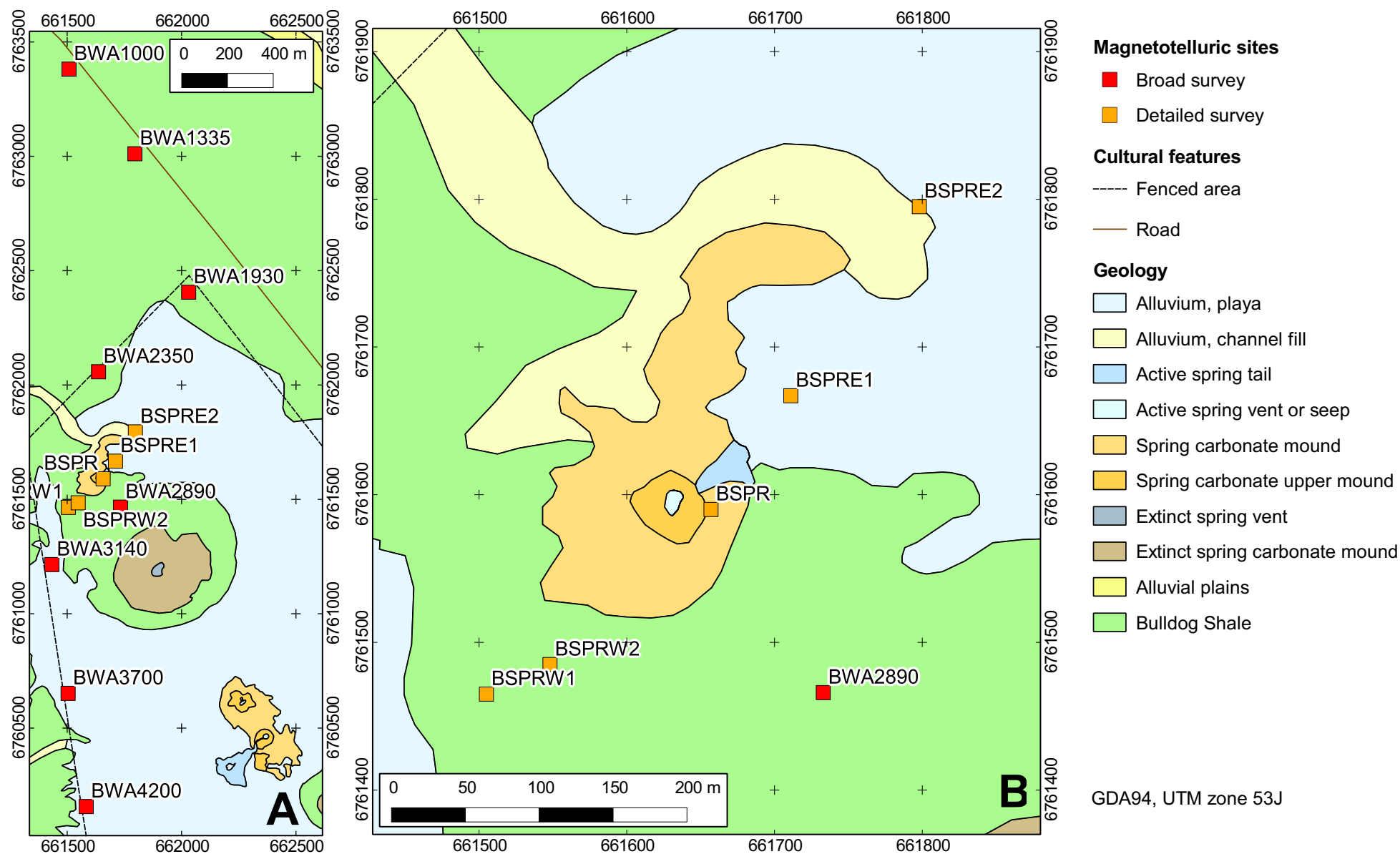


Figure 4.1: Location of MT sites near Beresford Spring. (A) Broad survey, (B) detailed survey.

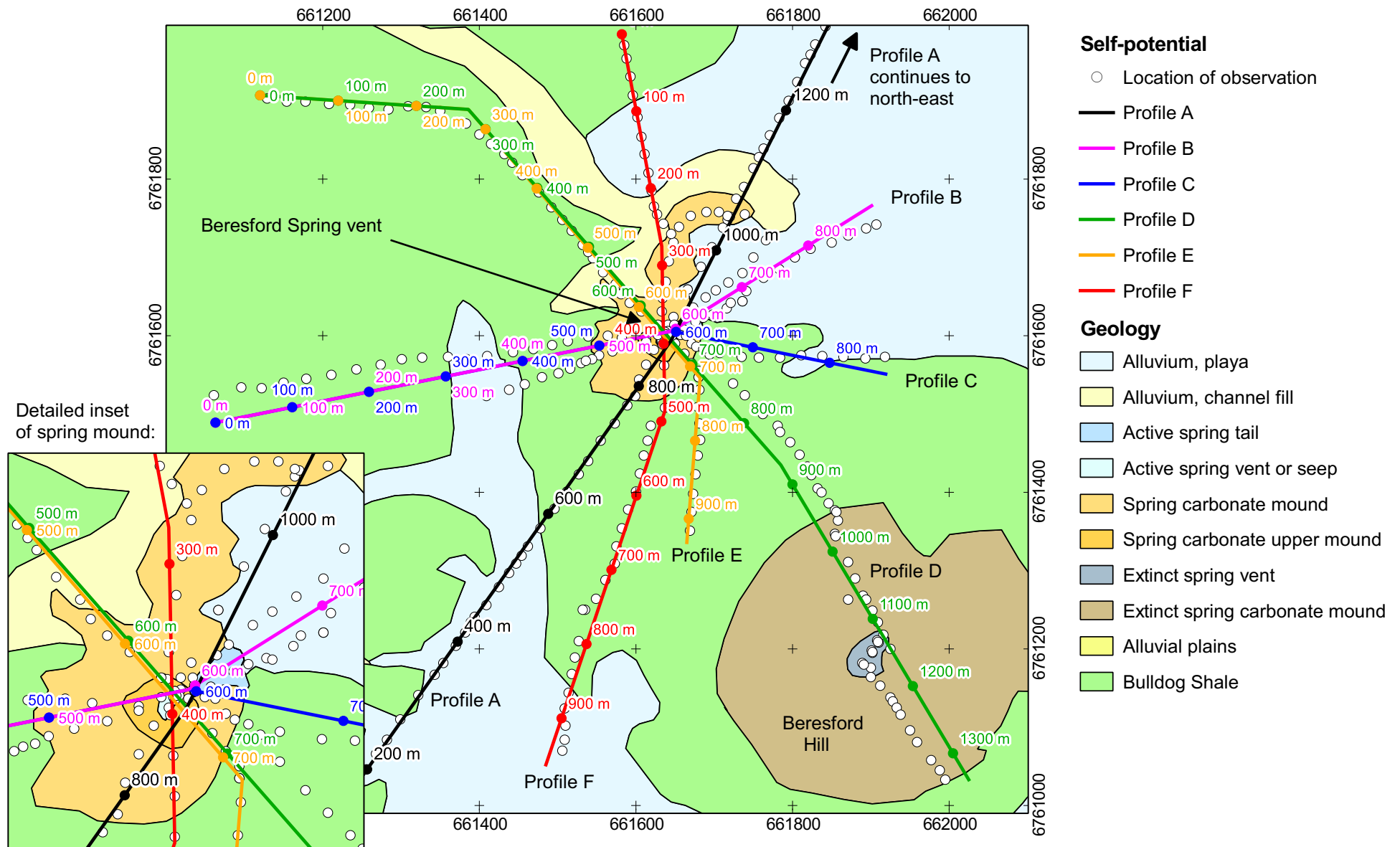


Figure 4.2: Location of SP observations and composite profiles over Beresford Spring.

4.1 SP

Self-potential data were collected at Beresford Spring between 21 April 2012 and 25 April 2012. Twelve lines of data were collected on different azimuths from the Beresford Spring vent, with measurements made at a nominal spacing of 25 m. A total of sixteen datasets were collected along these lines, with some overlapping areas. All datasets used the same base electrode, which was located 1020 m away from the Beresford Spring vent, on a bearing of 032° .

4.1.1 Data reduction

The data were corrected for electrode potentials and spatial consistency (see Section B.1.1). The electrode potentials were estimated using a reference electrode, and then subtracted from the measured potential to retrieve the true self-potential.

Self-potential observations were made along a number of field traverses across the spring vent (Figure 4.3). In order to simplify the presentation of data, several composite profiles (Profiles A through F) were constructed from all the data points by taking lines at various orientations through the spring vent. The location of these profiles and all the SP data points are shown on Figure 4.2. At a nominal spacing of 40 m along each profile a data point was constructed for that location by using the median SP from the measurements that fell within a circular area (nominal radius of 40 m) centred on that location. Note that the radius is greater than half the nominal station spacing, meaning that the median data has been smoothed in this process.

4.1.2 Median potential maps

To show the general variation in potential across the area, a map of median potentials calculated for 60×60 m squares is shown in Figure 4.4A. High potentials are found at the spring vent (40 mV to 60 mV) and at Beresford Hill in the southeast (50 mV to 65 mV). An area of low potentials (-35 mV to -25 mV) exists at the northern edge of the playa, approximately 1000 m north-east of the vent. The two highs are approximately 30 mV to 40 mV above surrounding potentials, and about 75 mV to 85 mV higher than the low potentials in the playa. There are also small areas of isolated high potentials in the northwest and southwest, which are not obviously related to any surface features.

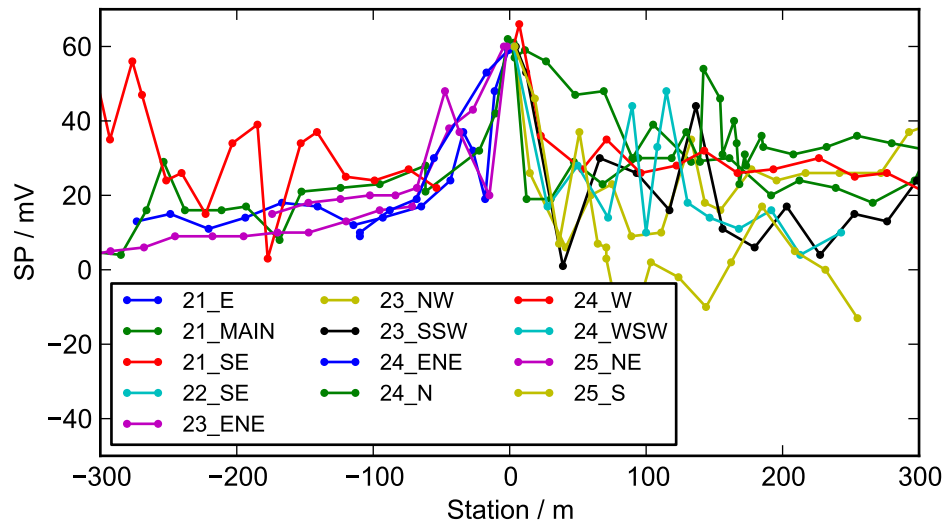


Figure 4.3: (A) Corrected self-potential data across Beresford Spring. The spring vent is at station 0. Each SP measurement is shown as a point. Field traverses are shown as coloured lines. Note that station numbers are different to the composite profile figures which follow.

Figure 4.5 shows median potentials on smaller 30 x 30 m squares in the vicinity of the spring vent. The highest potentials (60 mV) occur at the vent and are limited to a small area (one 30 x 30 m square). Moderately high potentials adjoin to the east and west, while low potentials exist to the northwest and southeast.

4.1.3 Profile A

Profile A is 2384 m long with a bearing of approximately 030°. Self-potential observations and the median SP and potential gradient along it are shown in Figure 4.6A. There is a strongly elevated SP response between stations 720 and 900, with the peak potential at station 880 approximately 35 mV higher than surrounding measurements at stations 650 and 950. This peak is closely correlated with the location of the Beresford Spring vent, and the overall elevated response with the spring mound. Potential gradients are generally between -0.2 mV m^{-1} and 0.2 mV m^{-1} , with the potential generally dropping along the profile towards the north-northeast.

The image reconstruction (Figure 4.6C) contains an area of positively-correlated sources (coefficient 0.1 to 0.15) between stations 760 and 900, extending to a depth of at least 200 m, associated with the Beresford Spring vent anomaly. This area correlates closely to the extent of the spring carbonate platform. The absolute potential gradient on the eastern side of the mound (around station

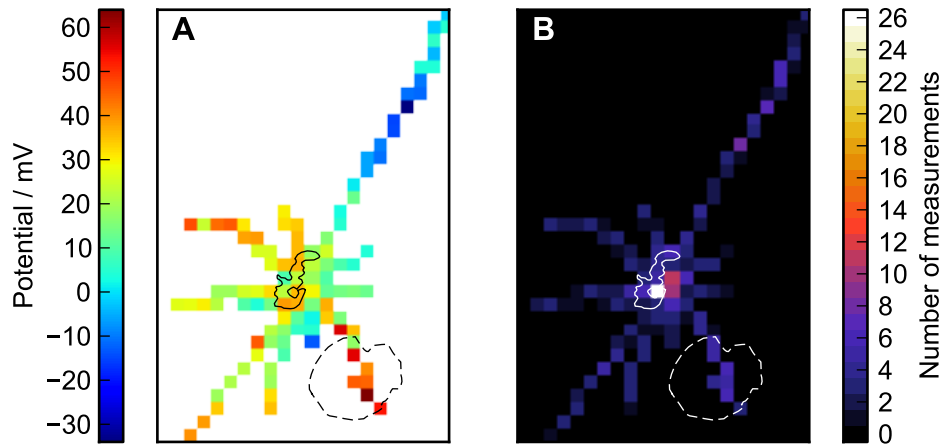


Figure 4.4: Self-potential data around Beresford Spring. Median potentials for each square on a 60 x 60 m grid are shown in (A) and the number of measurements in each square in (B). The spring mound's carbonate platform is shown outlined with a solid gray line, and Beresford Hill with a dashed gray line. Low potentials are found north-east of the spring, while high potentials are found at the spring, over Beresford Hill, and to the north-west of the spring.

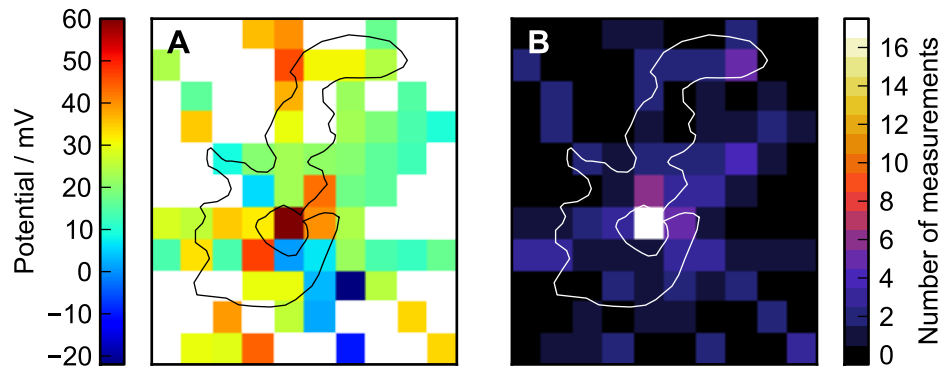


Figure 4.5: Self-potential data around Beresford Spring. Median potentials for each square on a 30 x 30 m grid are shown in (A) and the number of measurements in each square in (B). The spring mound's carbonate platform is shown outlined in gray. High potentials are consistently observed at the spring vent.

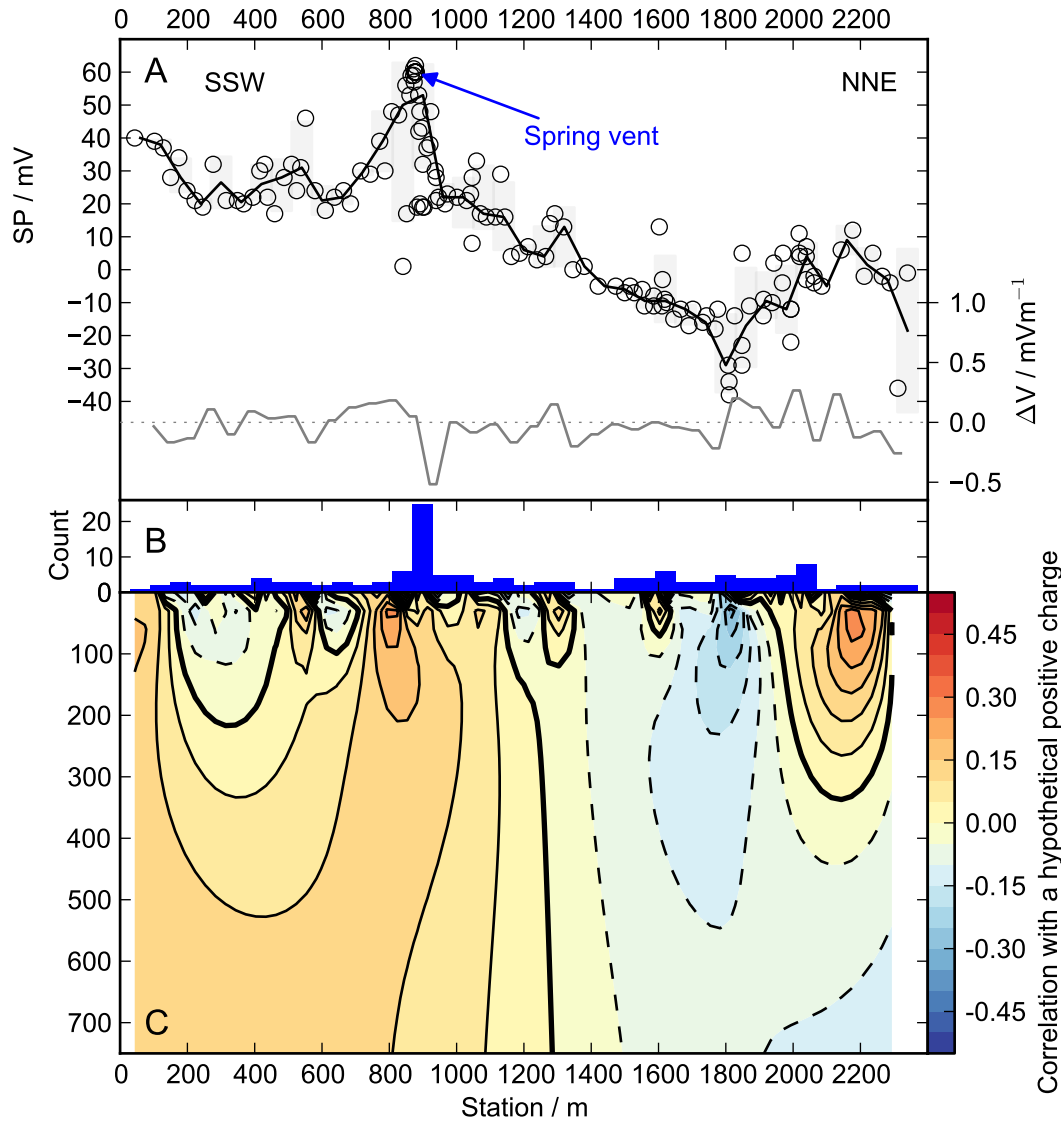


Figure 4.6: (A) Self-potential data (circles) from Profile A. The median of SP measurements falling in circular bins (radius 30 m, spacing 60 m) is shown as a black line, and the gradient of the median SP is shown as a gray line. (B) The number of SP measurements in each circular bin. (C) Image reconstruction for all the SP data on this profile. The wide variability in potential at the spring vent is due to the bins capturing measurements away from the spring vent (see Figure 4.5).

900) is 0.5 mV m^{-1} , greater than the more gradual drop in potential on the south-western side at station 880 (0.2 mV m^{-1}).

There is a horizontally-oriented dipole source represented in the image reconstruction, with the negative end underneath station 1800 and the positive end underneath station 2200, at a depth of approximately 50 m. This area is 400 m northeast of the edge of the playa, and 1000 m north-northeast of the Beresford Spring vent and Beresford Hill.

The area between stations 200 and 650, south-southwest of the spring mound, is generally weakly-correlated to negative sources down to a depth of 90 m to 200 m. This is caused by the increase in potential between stations 0 and 200 and may be related to another negatively-correlated area on Profile F (see below).

4.1.4 Profiles B and C

Profile B is 896 m long with a bearing of approximately 072° , and Profile C is 873 m long with a bearing of approximately 086° . The two profiles share the same location to the west of the spring vent, but diverge to the east, with Profile B extending 300 m at 058° , and Profile C extending 278 m at 101° .

Self-potential observations and the median SP and potential gradient along Profile B are shown in Figure 4.7A and Profile C in Figure 4.8A. There is a significant rise in potential between stations 500 and 630 on both profiles, with the peak potentials about 30 mV higher than potentials to the west, and 35 mV to 50 mV higher than to the east. Potential gradients along both profiles are generally very low, with the exception of gradients of $\pm 0.7 \text{ mV m}^{-1}$ on either side of the positive anomaly mentioned above.

The image reconstructions (Figures 4.7C and 4.8C) both contain an area strongly-correlated to positive sources underneath the positive anomaly, at station 600, which is the location of the spring vent on this profile. The area has a correlation coefficient greater than 0.2 between stations 500 and 640, down to a depth of 180 m. This correlates to the extent of the spring mound, suggesting that on this profile the area strongly correlated to positive sources and therefore upward flow is limited to the area underneath the mound.

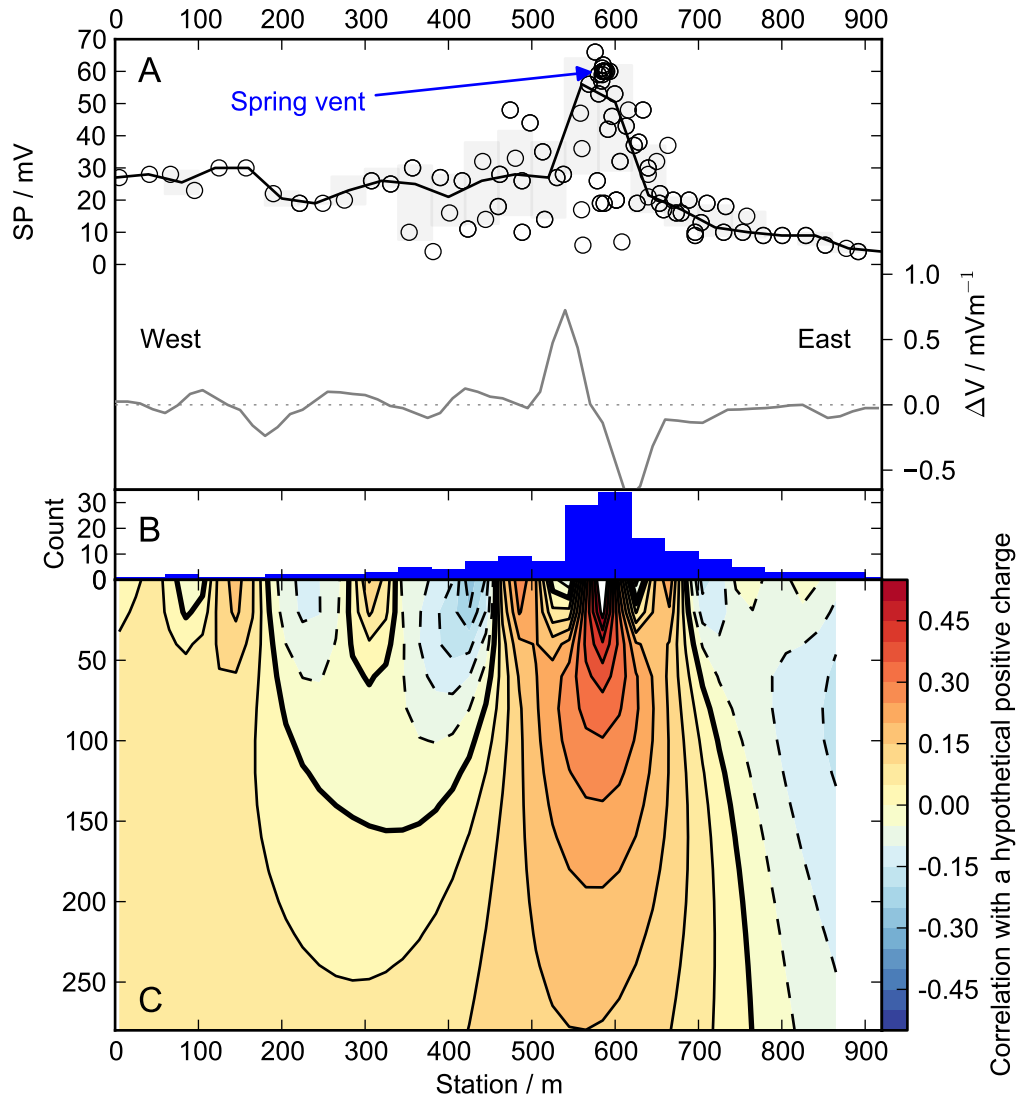


Figure 4.7: (A) Self-potential data (circles) from Profile B. The median of SP measurements falling in circular bins (radius 40 m, spacing 40 m) is shown as a black line, and the gradient of the median SP is shown as a gray line. (B) The number of SP measurements in each circular bin. (C) Image reconstruction for all the SP data on this profile. The wide variability in potential at the spring vent is due to the bins capturing measurements away from the spring vent (see Figure 4.5).

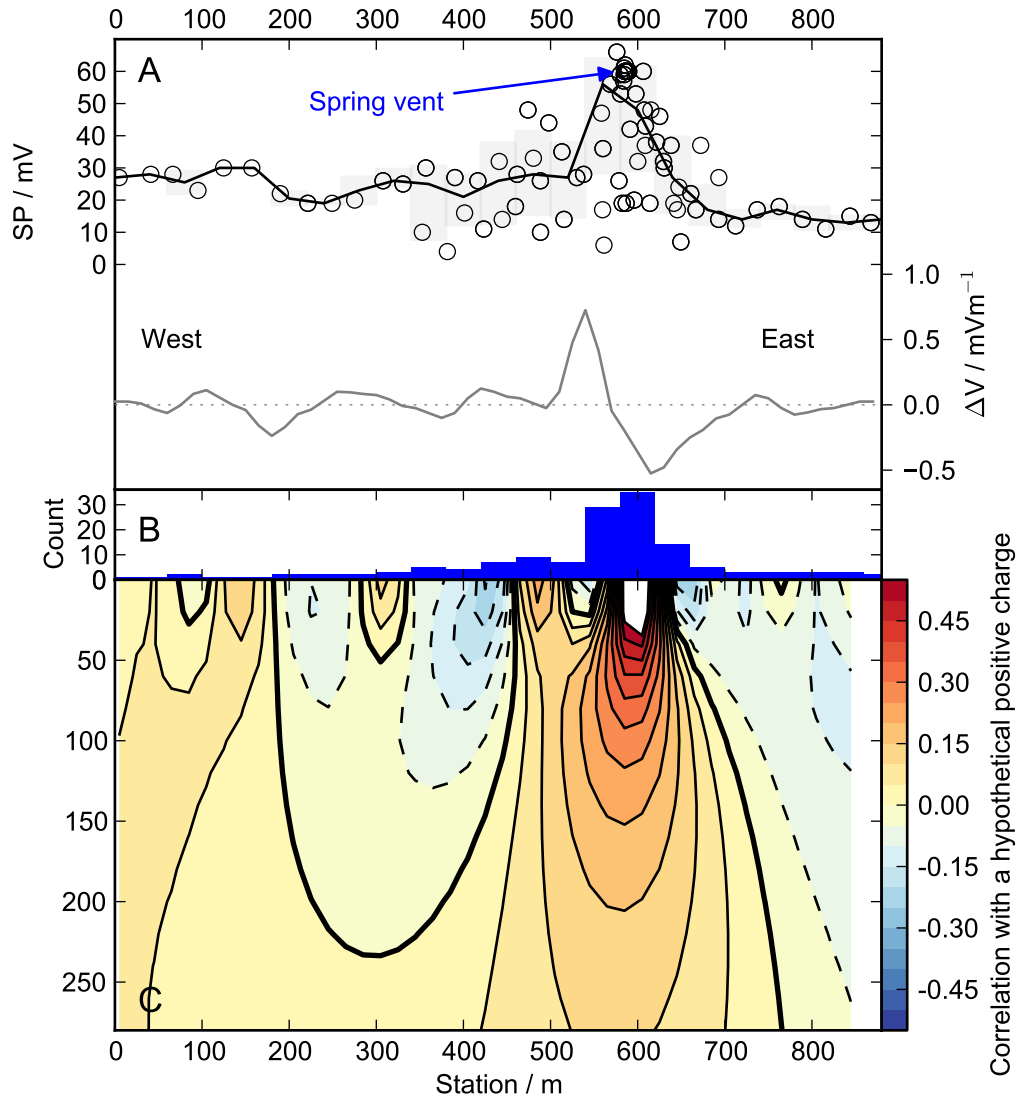


Figure 4.8: (A) Self-potential data (circles) from Profile C. The median of SP measurements falling in circular bins (radius 40 m, spacing 40 m) is shown as a black line, and the gradient of the median SP is shown as a gray line. (B) The number of SP measurements in each circular bin. (C) Image reconstruction for all the SP data on this profile. The wide variability in potential at the sprint vent is due to the bins capturing measurements away from the spring vent (see Figure 4.5).

4.1.5 Profiles D and E

Profile D is 1339 m long with a bearing of approximately 134° , and Profile E is 930 m long with a bearing of approximately 136° . The two profiles share the same location to the north of the spring vent, but diverge to the south, with Profile D extending for 1072 m at 144° , ascending and crossing Beresford Hill, while Profile E extends 311 m at 185° , remaining on the edge of the playa.

Self-potential observations and the median SP and potential gradient along Profile D are shown in Figure 4.9A and Profile E in Figure 4.10A. There is a significant rise in potential between stations 620 and 700, with peak potentials approximately 40 mV higher than those adjacent to this area. The elevated potential anomaly is narrow and the absolute potential gradients on its edges are high, ranging from 0.9 mV m^{-1} to 1.0 mV m^{-1} .

The potential generally increases to the north, at an absolute gradient of approximately 0.05 mV m^{-1} ; the median potential 600 m north of the spring vent is approximately 48 mV, a rise of 30 mV compared to the low potentials adjacent to the spring mound.

To the south of the mound the trend in potential varies significantly. Potentials along Profile D increase, rising to median values atop Beresford Hill ranging from 35 mV to 60 mV, while those along Profile E, which does not ascend the hill, remain low (approximately 0 mV).

The image reconstructions (Figures 4.9C and 4.10C) both contain areas with correlations greater than 0.1 to positive sources between stations 600 and 680, which corresponds closely to the location and extent of the spring mound on these profiles. The correlation on Profile D underneath the Beresford Spring vent is weaker and smaller (no deeper than 100 m) than that on Profile E, which has a correlation coefficient of at least 0.1 down to depths of 150 m. On Profile D, Beresford Hill (between stations 950 and 1350) is underlain by a positively-correlated area (correlation coefficient approximately 0.05) extending to depths greater than 200 m.

4.1.6 Profile F

Profile F is 963 m long with a bearing of approximately 186° . Self-potential observations and the median SP and potential gradient along it are shown in Figure 4.11A. There is an elevated SP response between stations 360 and

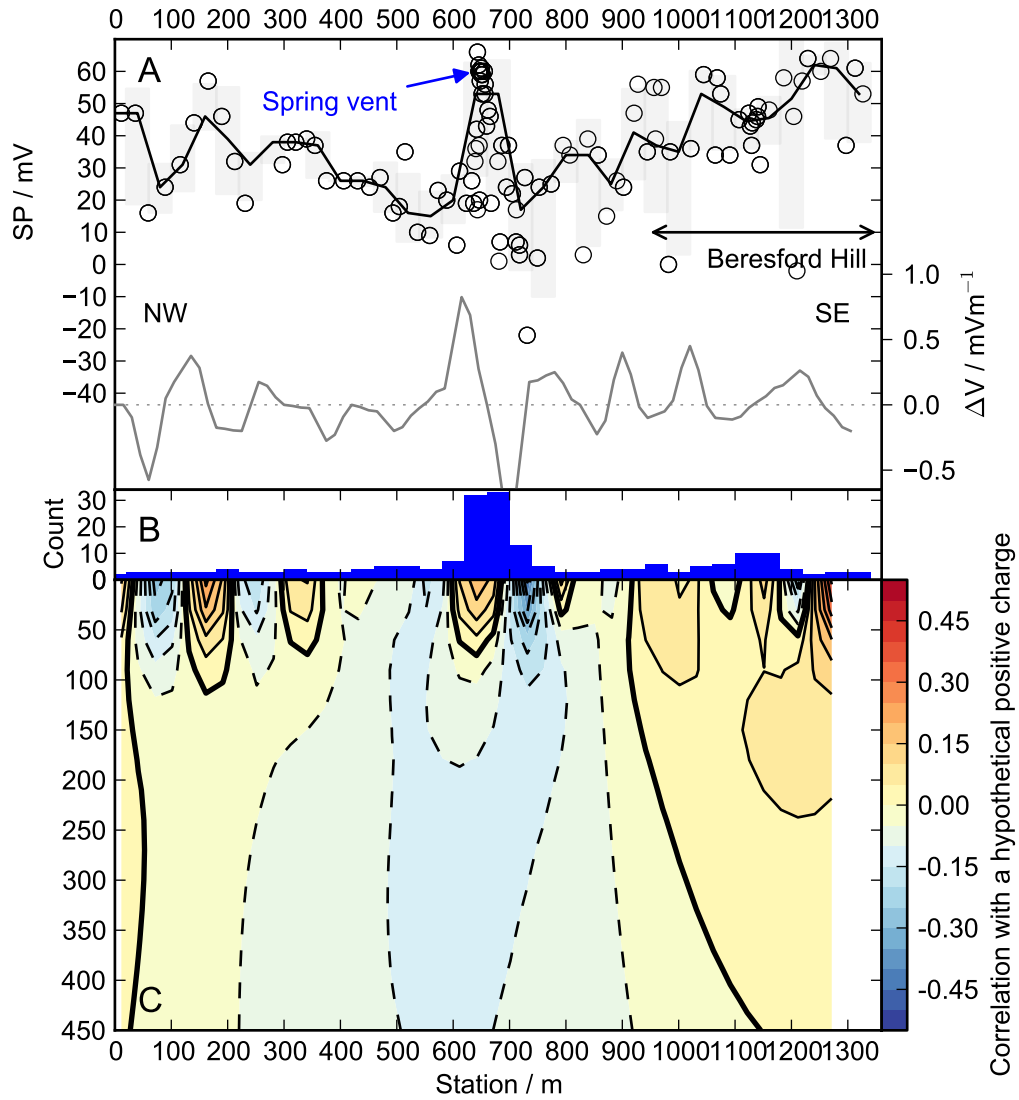


Figure 4.9: (A) Self-potential data (circles) from Profile D. The median of SP measurements falling in circular bins (radius 40 m, spacing 40 m) is shown as a black line, and the gradient of the median SP is shown as a gray line. (B) The number of SP measurements in each circular bin. (C) Image reconstruction for all the SP data on this profile. The wide variability in potential at the spring vent is due to the bins capturing measurements away from the spring vent (see Figure 4.5).

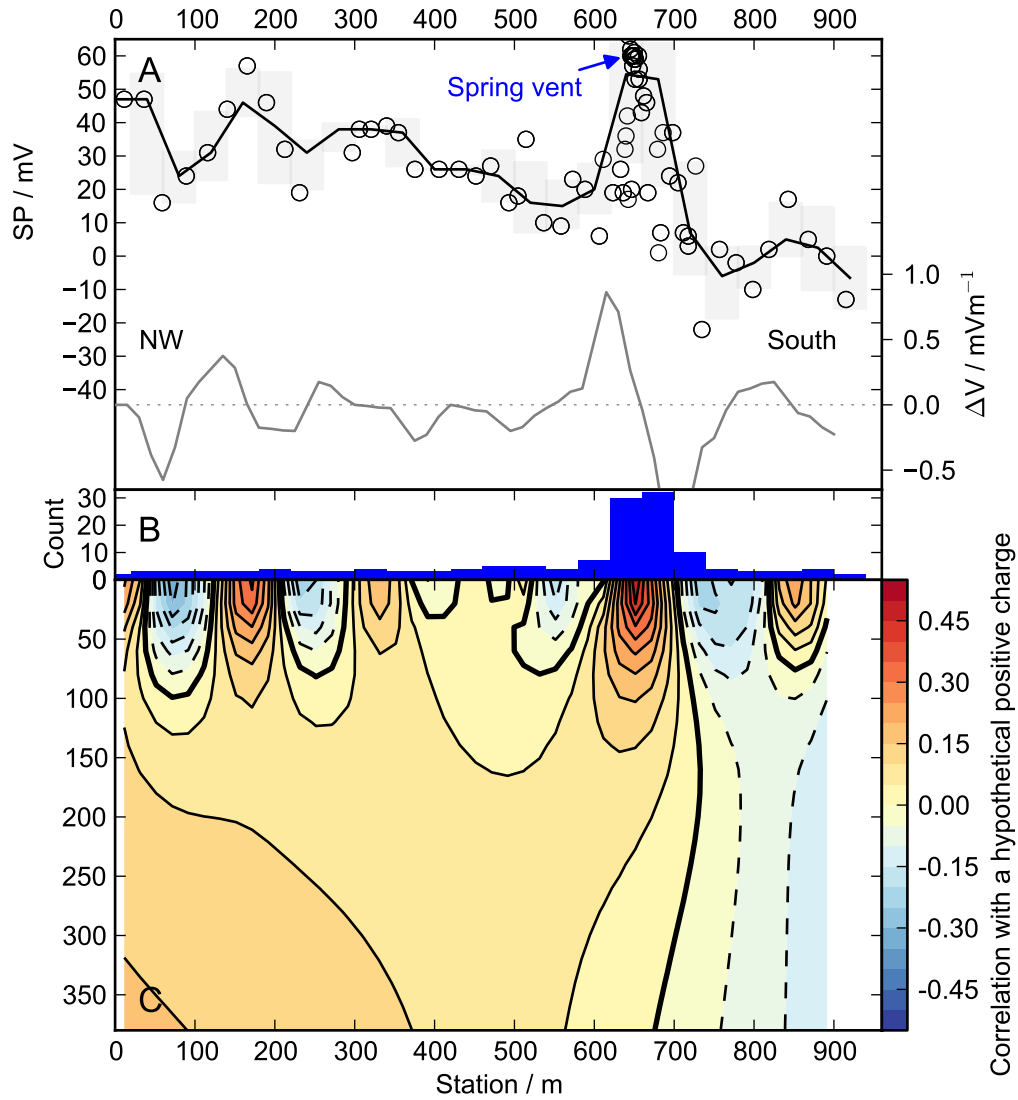


Figure 4.10: (A) Self-potential data (circles) from Profile E. The median of SP measurements falling in circular bins (radius 40 m, spacing 40 m) is shown as a black line, and the gradient of the median SP is shown as a gray line. (B) The number of SP measurements in each circular bin. (C) Image reconstruction for all the SP data on this profile. The wide variability in potential at the spring vent is due to the bins capturing measurements away from the spring vent (see Figure 4.5).

420, with peak potentials approximately 30 mV higher at the spring vent than at adjacent sites. The peak occurs at station 390, which is the location of the Beresford Spring vent, and the absolute potential gradients on the edges of the elevated response are approximately 0.7 mV m^{-1} .

Potentials to the north are 25 mV less than the spring vent peak voltage and do not vary significantly, except for a small peak of 15 mV at station 230, which is at a distance of 160 m from the modern spring vent, and is where the tail passes along the northern edge of the carbonate mound. Potentials to the south drop to values almost 50 mV below the spring vent peak voltage, and then rise gradually by 30 mV over 350 m to values similar to those on the northern side of the spring.

The image reconstruction (Figure 4.11C) shows positively-correlated areas underneath the spring vent and the lesser peak at station 230, with the correlation generally quite weak (less than 0.05) below depths of 50 m. There is a strong correlation to negative sources (coefficients less than -0.15) between stations 580 and 850, suggesting downward vertical flow in this area.

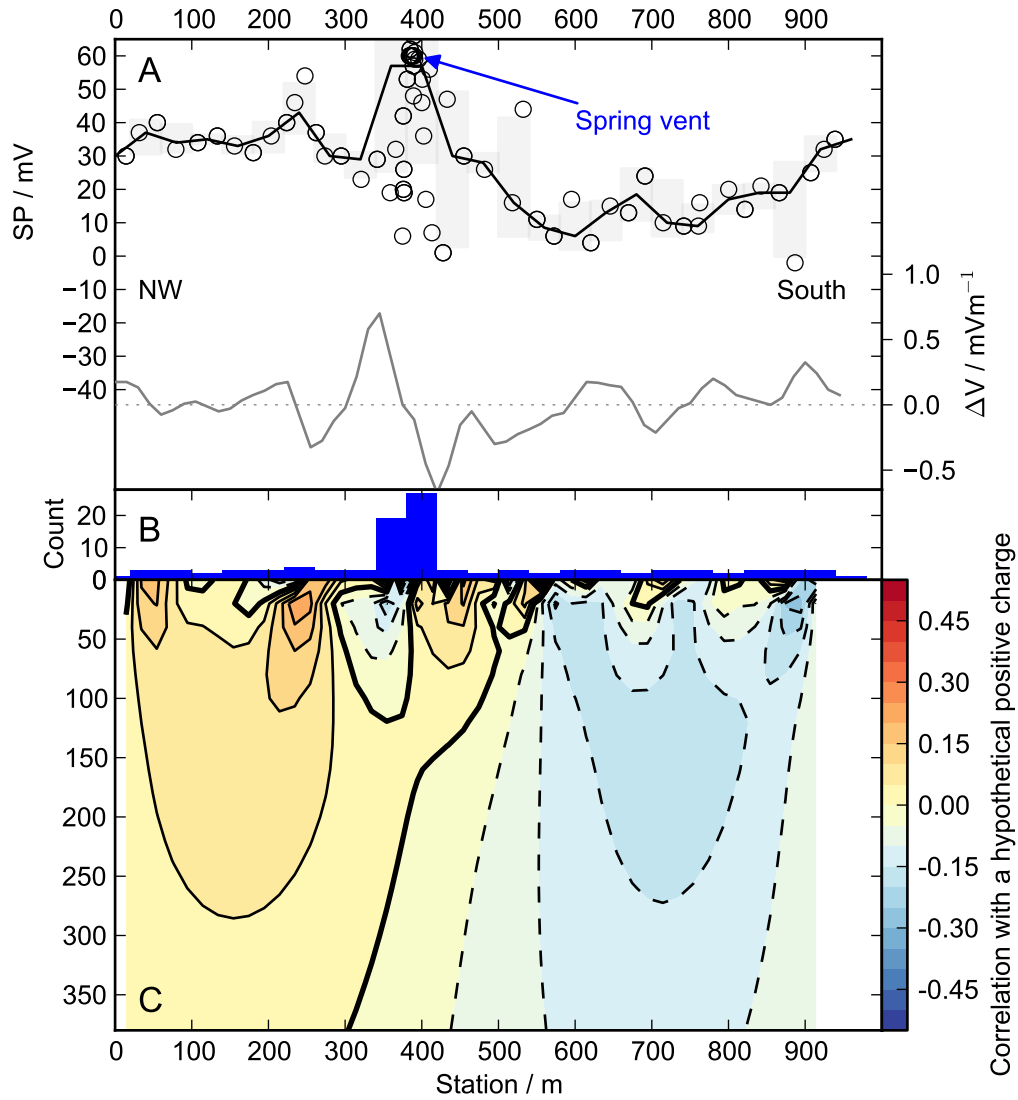


Figure 4.11: (A) Self-potential data (circles) from Profile F. The median of SP measurements falling in circular bins (radius 30 m, spacing 40 m) is shown as a black line, and the gradient of the median SP is shown as a gray line. (B) The number of SP measurements in each circular bin. (C) Image reconstruction for all the SP data on this profile. The wide variability in potential at the spring vent is due to the bins capturing measurements away from the spring vent (see Figure 4.5).

4.2 TEM

Time-domain electromagnetic data were collected over a 383 m-long line on a bearing of 050° , running over the Beresford Spring mound platform and vent (Figure 4.12). The survey used the central in-loop configuration, with a 20 m square transmitter loop and a 5 m square receiver loop.

The observations (Figure 4.13) were inverted for a resistivity model using Zonge Engineering's STEMINV routine. The model is shown in Figure 4.14, and the fits between model responses and observations are shown for three stations in Figure 4.15. Note that some noisy and negative late-time responses were removed from the inversion.

At the surface in the resistivity model (Figure 4.14) the carbonate mound platform is significantly more resistive than the surrounding playa, with surface resistivities increasing from approximately $1\ \Omega\text{ m}$ in the playa to $3.5\ \Omega\text{ m}$ on the mound platform and $5.5\ \Omega\text{ m}$ on the upper mound.

Near the surface the model contains a highly conductive layer which becomes more resistive underneath the mound platform, and most resistive underneath the upper mound around the spring vent. Away from the mound this conductor has a resistivity of $0.4\ \Omega\text{ m}$ at an elevation of -5 m ($1.2\ \Omega\text{ m}$ at an elevation of -13 m), while over the mound platform it is approximately $1.8\ \Omega\text{ m}$ down to an elevation of -10 m .

The deepest layer of the model is also more resistive underneath the mound, with a sharp lateral increase in model resistivity (from $2\ \Omega\text{ m}$ to $4\ \Omega\text{ m}$) occurring underneath stations 200 and 400, which are close to the edges of the mound platform (stations 200 to 220 and station 380). Underneath the mound it is approximately $3.5\ \Omega\text{ m}$ at an elevation of -25 m , while off the mound at the same depth it is from $1.8\ \Omega\text{ m}$ to $2.2\ \Omega\text{ m}$.

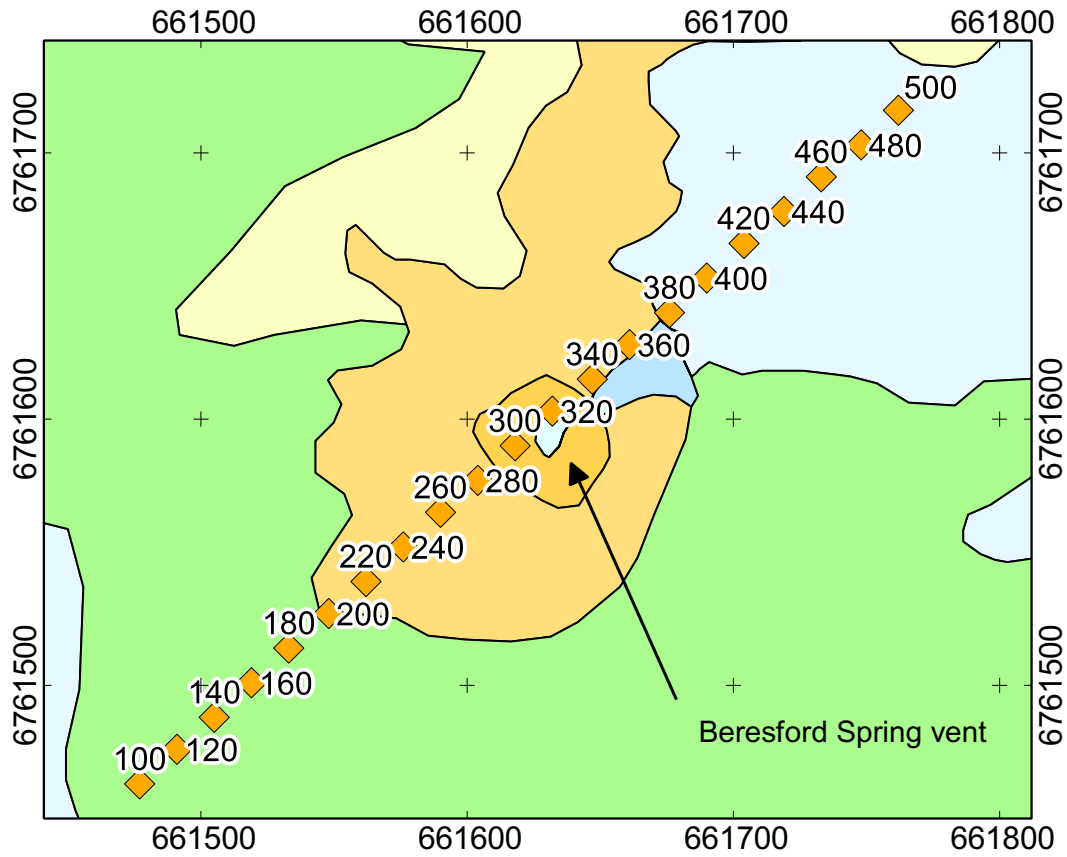


Figure 4.12: Location of TEM stations over Beresford Spring.

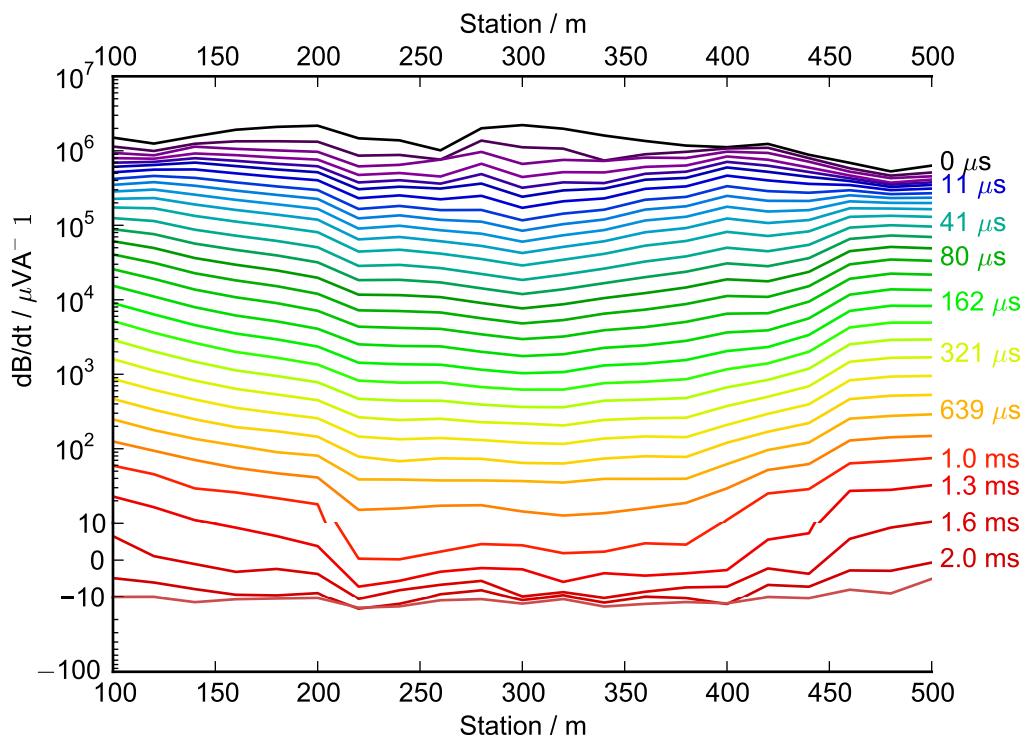


Figure 4.13: TEM responses for all decay times between 1 μs and 2.5 ms. The decay times for selected curves are shown on the right hand side.

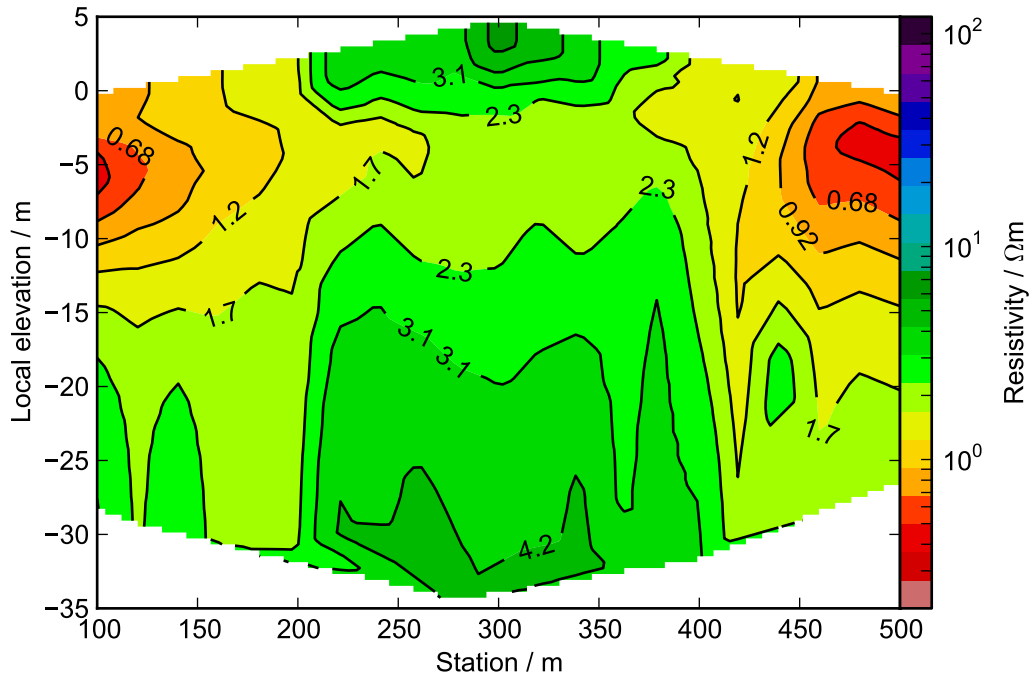


Figure 4.14: Resistivity model obtained by 1D inversion of TEM data.

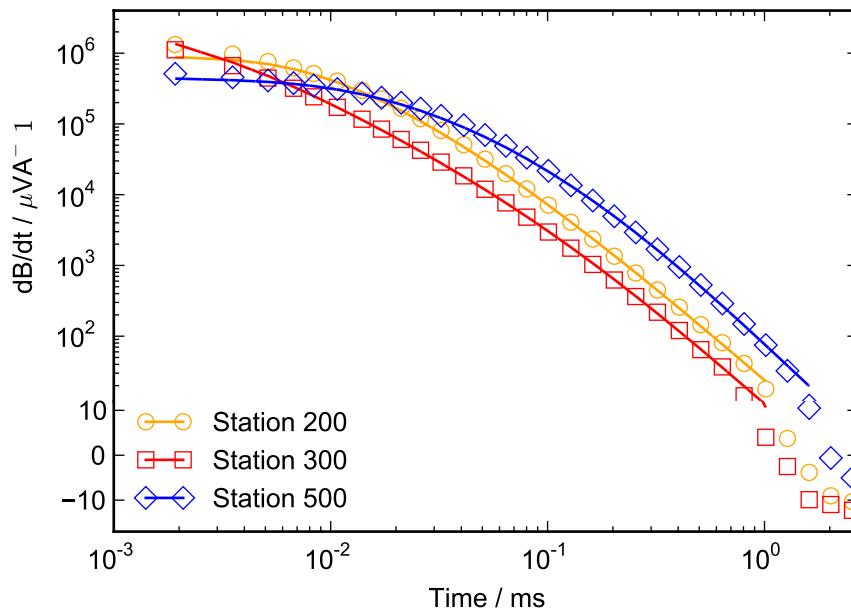


Figure 4.15: Fit of resistivity model (Figure 4.14) to TEM data for selected sites. Shapes show the observed data, and lines show the modelled data, with different stations shown in different colours.

4.3 MT data

Magnetotelluric data were collected at Beresford Spring in June 2010 and April 2012. Eight sites were located along a broad survey line oriented approximately north-south which passes over the Beresford Spring mound, and five sites along a detailed survey line oriented NW-SE. The latter includes a site recorded on the vent of the currently active spring. The locations of these sites are shown on Figure 4.1.

4.3.1 Broad survey line

Data were collected from eight sites located along a 3.3 km-long line which is oriented approximately north-south (Figure 4.1A).

Responses were estimated between 0.03 Hz and 125 Hz, from 5.5 h windows of time series recorded overnight at a sampling rate of 500 Hz. Electrode dipoles were oriented north/south and east/west, and a pair of LEMI-120 induction coil magnetometers were laid parallel to the electrode dipoles at each site and used to record the magnetic field.

The MT sites are described below in order from north to south:

1. BWA1000 and BWA1335 were 1780 m and 1425 m north of the spring mound, on the thin but regionally extensive alluvial and colluvial Quaternary sediments overlying Bulldog Shale.
2. BWA1930 was 930 m north-east and BWA2350 was 470 m north of the spring mound, on the northern edge of the playa.
3. BWA2890 was 150 m south-east of the spring vent, halfway between the actively flowing Beresford Spring and the extinct spring mound of Beresford Hill.
4. BWA3140, BWA3700, and BWA4200 were south of the spring vent and are located on the western edge of the playa at distances of 400 m, 900 m, and 1400 m.

Phase tensor ellipses are shown in Figure 4.16. All such ellipses shown in this thesis have been rotated by 90° such that the major axis is parallel to the TE mode under a ‘quasi-2D’ assumption (see Section 3.1.3 for more discussion). Most sites are 1D at high frequencies with the prominent exception of BWA2890, which is 2D throughout the recorded bandwidth (approximately

0.1 Hz to 90 Hz). No 3D effects are seen until a quasi-2D response occurs below 0.1 Hz, which is shared by all sites (Figure 4.16B).

Figure 4.17 shows the orientation of the responses. The 2D response at BWA2890 is oriented strongly towards approximately 315° , as is the low-frequency quasi-2D response at all sites.

Apparent resistivity and phase curves in the coordinate system corresponding to the phase tensor preferred orientation at BWA2890 are shown in Figure 4.18. The curves for all sites are similar, with apparent resistivities rising from approximately $1 \Omega \text{ m}$ at 100 Hz to $40 \Omega \text{ m}$ to $100 \Omega \text{ m}$ at 0.1 Hz. There are two significant features:

1. The 2D response at BWA2890 is made up of a comparatively high Zyx mode phase, with a phase split of 10° at 10 Hz. The high phase is associated with currents flowing towards an azimuth of 045° (i.e. the TM mode).
2. Sites to the south of the Beresford Spring mound (BWA3140, BWA3700, and BWA4200) exhibit a smaller phase split at frequencies between 1 Hz and 10 Hz, with the Zyx phase rising by 2° to 5° in that bandwidth compared to a flat Zxy phase curve. The higher phase is again associated with currents flowing towards 045° (potentially the TM mode).

A similar feature, although smaller in magnitude, occurs at BWA2350, which is north of the spring mound.

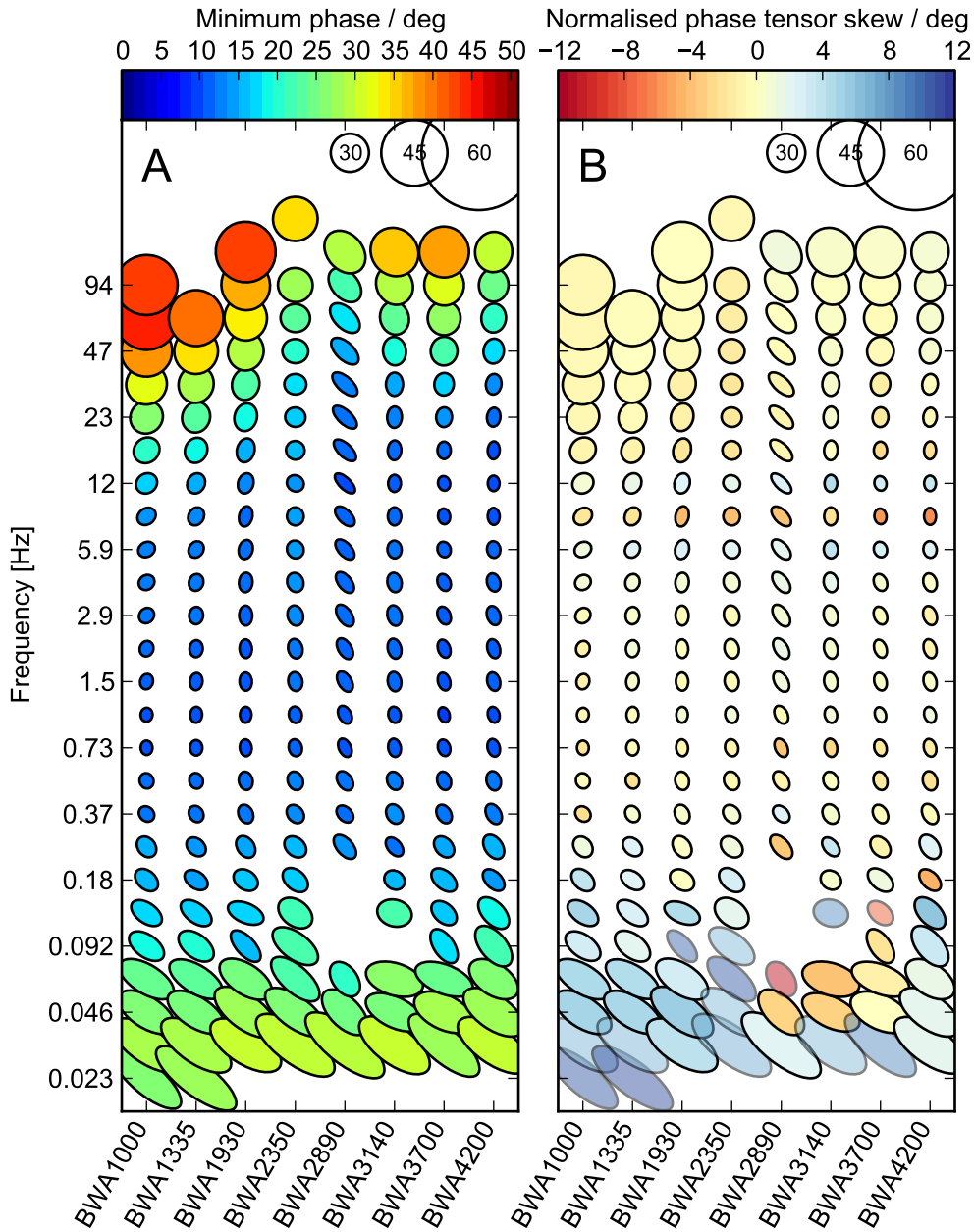


Figure 4.16: Pseudosection of phase tensors from the broad survey line, filled with (A) minimum phase and (B) the normalised skew ψ (faint coloured ellipses have $|\psi| > 6^\circ$ and faint gray ellipses $|\psi| > 12^\circ$, both representing tensors significantly affected by 3D induction). Phase tensors have been rotated by 90° so that the major axis is parallel to the TE mode under a quasi-2D assumption (Booker, 2013) and ellipses with phases of 30° , 45° , and 60° are shown in the upper left for comparison.

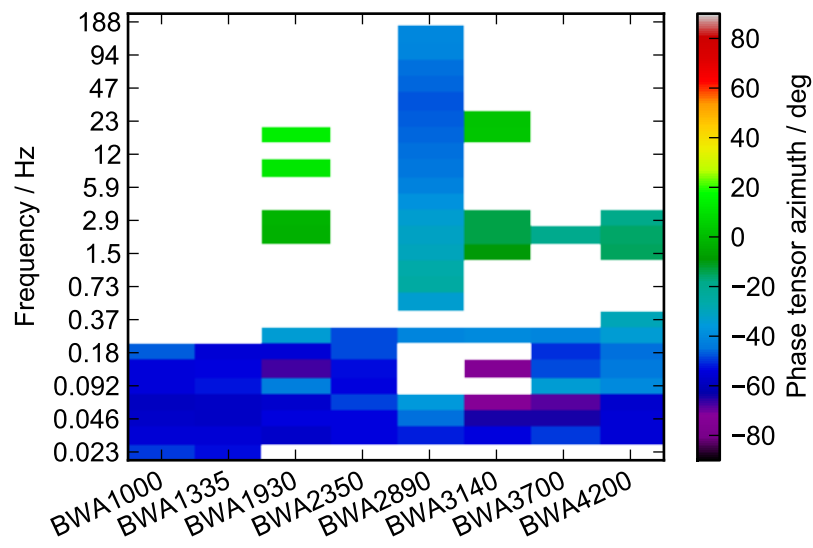


Figure 4.17: Pseudosection of phase tensor azimuths (θ_{ellipse}) along the broad survey line. Azimuths are only shown for tensors with a split in the principal phases greater than 5° .

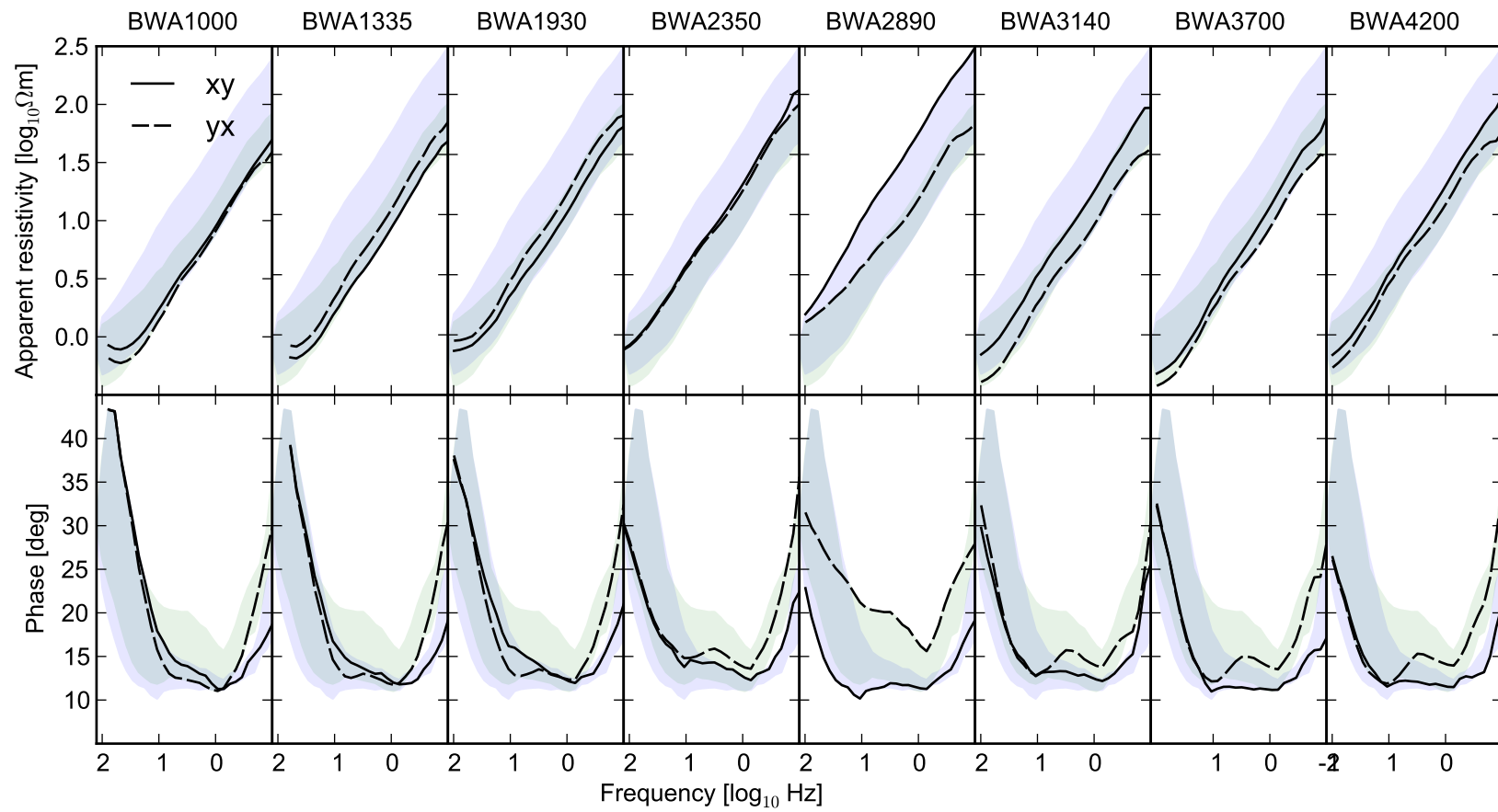


Figure 4.18: Cross-section of apparent resistivity and phase from the broad survey at Beresford Spring. The shaded areas are to help with comparison between sites and show the range of data for each mode across all sites on the line. Coordinate system x 225° , y 135° .

4.3.2 Detailed survey line

Five MT sites were collected along a 500 m-long line which is oriented towards an azimuth of 037° (Figure 4.1B). The sites are listed in order from south-west to north-east:

1. BSPRW1 and BSPRW2 are 180 m and 140 m southwest of the spring vent respectively, on alluvial gravels overlying playa sediments and/or Bulldog Shale. Note that the station numbering here is reversed; BSPRW2 is closer to the spring.
2. BSPR is located on the spring vent, on the upper carbonate mound.
3. BSPRE1 is 110 m north-east of the spring vent, located where spring discharge passes between clay-rich playa sediments and the eastern edge of the carbonate mound platform.
4. BSPRE2 is located at the easternmost edge of the spring tail, 265 m north-east of the spring vent.

Most sites are 2D to varying degrees, with the most elliptical phase tensor ellipses at BSPR and BSPRE1 (Figure 4.19). These two sites are also quasi-2D for most responses, although BSPR appears to be subject to 3D effects, with absolute normalized skews of up to 7° from 0.1 Hz to 40 Hz. Figure 4.20 shows the orientation of 2D phase tensors across the profile. The orientation of the response varies, with tensors at BSPR and BSPRE1 oriented toward 280° between 8 Hz and 70 Hz, and those at BSPRW2 and oriented towards 050° , the same approximate direction indicated by the broader survey (see previous section). The low-frequency quasi-2D response is also oriented towards an azimuth of approximately 050° .

Data from all sites were rotated into the coordinate system aligned with the responses at BSPR and BSPRE1. Apparent resistivity and phase curves in this coordinate system are shown in Figure 4.21.

All sites exhibit similar behaviour in the Zxy phase, associated with currents flowing towards an azimuth of 280° . The phase drops to the first of two minima at a frequency around 12 Hz, and then rises by approximately 3° before dropping to the second minimum at 0.9 Hz. Both phases rise steeply at lower frequencies.

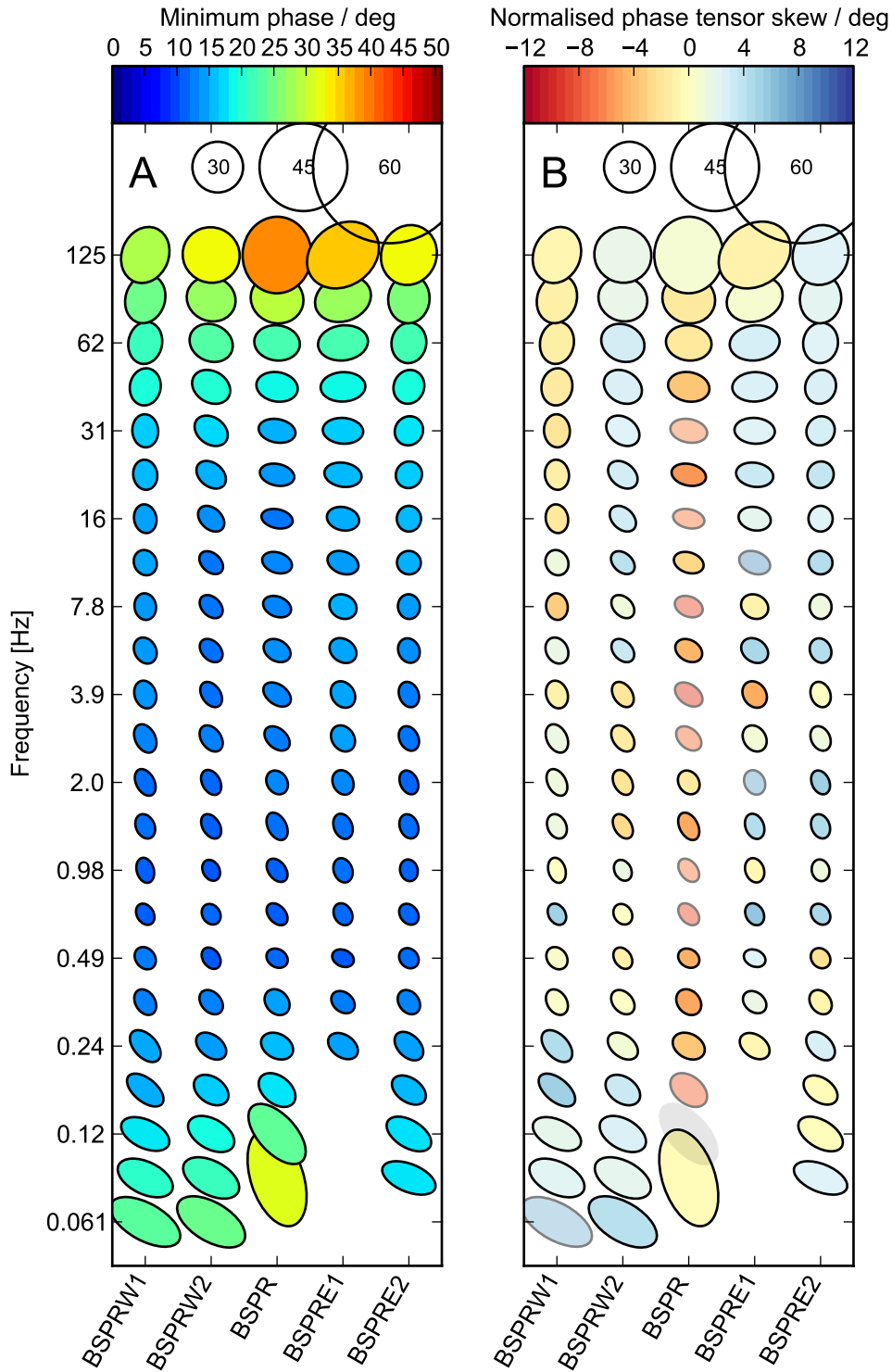


Figure 4.19: Pseudosection of phase tensors from the detailed survey, filled with (A) minimum phase and (B) the normalised skew ψ (faint coloured ellipses have $|\psi| > 6^\circ$ and faint gray ellipses $|\psi| > 12^\circ$, both representing tensors significantly affected by 3D induction). Phase tensors have been rotated by 90° so that the major axis is parallel to the TE mode under a quasi-2D assumption (Booker, 2013) and ellipses with phases of 30° , 45° , and 60° are shown in the upper left for comparison.

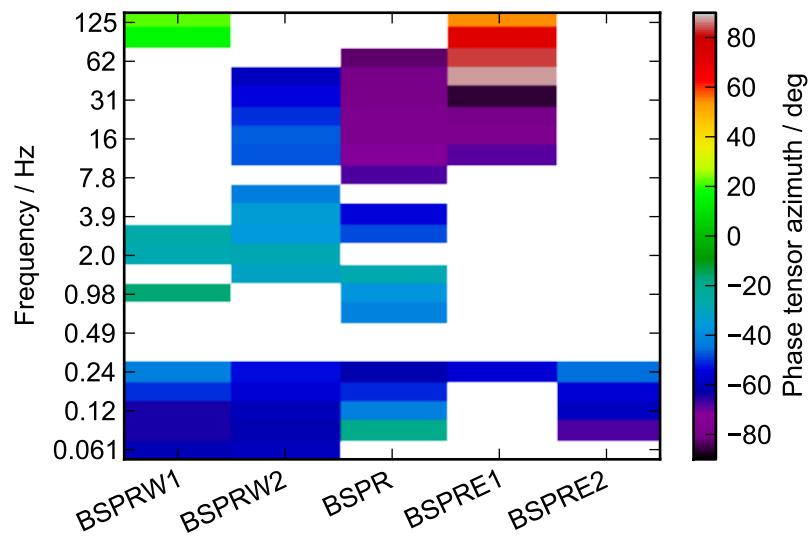


Figure 4.20: Pseudosection of phase tensor azimuths (θ_{ellipse}) along the detailed survey line. Azimuths are only shown for tensors with a split in the principal phases greater than 5° .

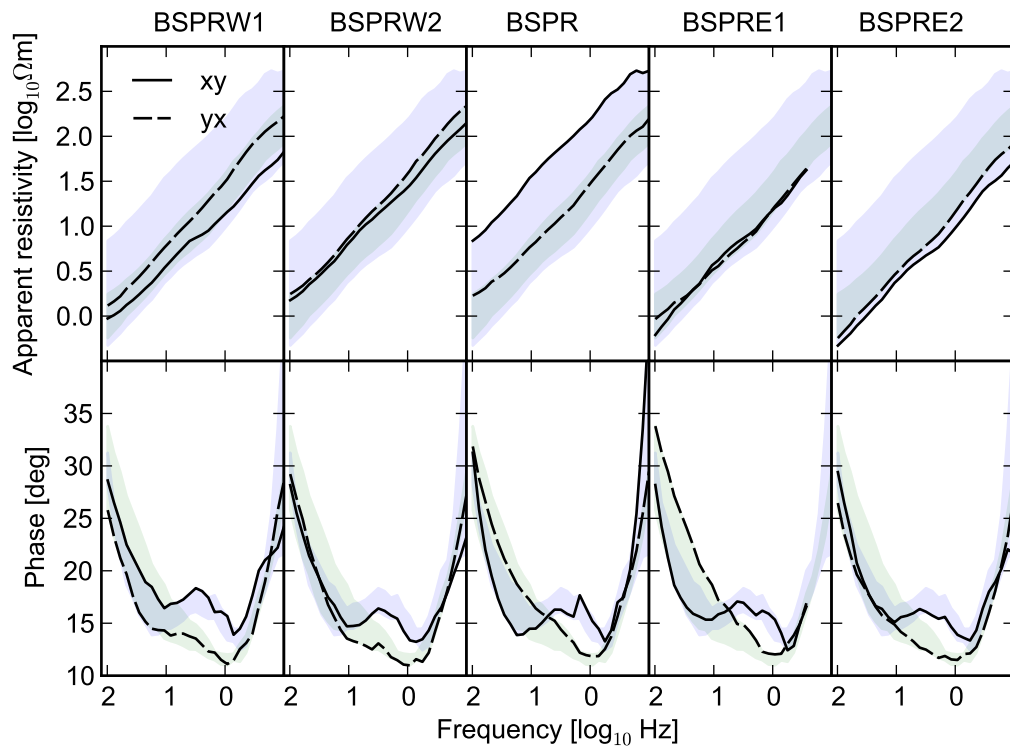


Figure 4.21: Cross-section of apparent resistivity and phase from the detailed survey at Beresford Spring. The shaded areas are to help with comparison between sites and show the range of data for each mode across all sites on the line. Coordinate system x 280° , y 010° .

The shape of the Zyx phase curve is similar at all sites: it drops steadily to a minimum at approximately 1 Hz before rising steeply. However, the Zyx phase is in general higher at BSPR and BSPRE1, with the two modes' phase curves crossing at those sites at 5 Hz. At the other sites more distant from the spring the Zyx phase is the lowest phase at all frequencies.

4.4 Anisotropic 1D MT modelling

There are two features in the MT responses that appear at multiple sites, where the sites are separated laterally by a distance at least as great as the skin depth for the relevant bandwidth. The features change only slightly for sites with increasing lateral separation, suggesting that they may be caused by a bulk property of the subsurface within the skin depth, such as anisotropic resistivity, rather than lateral distance from a resistivity boundary (2D induction).

The two features are (1) elevated phases at high frequencies, which is most obvious at BSPR and BSPRE1, and has been labelled a Type A feature, and (2) an elevated 'bump' in phase at low frequencies, which is labelled a Type B feature, and appears at all sites from the detailed survey and at least three from the broader survey. The Type A feature only appears in sites close to the Beresford Spring mound, while the Type B feature appears only in sites in or near the western side of the playa (Figure 4.22). In order to test what kind of anisotropic resistivity structures might explain these two kinds of features, two composite responses were created. The sites used to create these responses are shown in Figure 4.22.

These composite responses have then been inverted for anisotropic 1D resistivity structures using a Monte Carlo procedure in which 10^5 1D models were generated where some layers contained vertically-dipping sheets which are more conductive along their surface than across it. All layer depths and resistivities were given values from probability distributions based on the best-fitting isotropic model. A uniform probability distribution was also used to set the strike of the conductive sheets. Forward responses were then calculated for each model using the code of Pek and Santos (2002), and the best-fitting models were selected for interpretation. A more detailed description of the methodology is provided in Section 3.1.4.1.

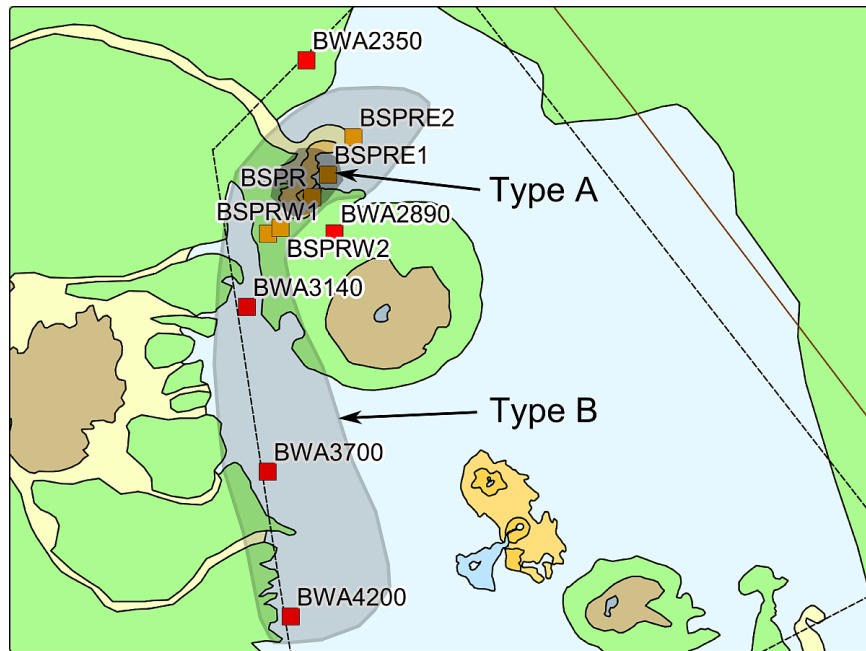


Figure 4.22: Magnetotelluric sites used to create the composite responses.

4.4.1 Type A

4.4.1.1 Composite response

The MT sites BSPR and BSPRE1 are located on or near the spring vent and have elevated Z_{yx} phases compared to sites located further southwest or northeast. The yx mode relates to currents induced in a WNW direction. The Z_{xy} phase at these two sites is similar to the same mode at all the sites from the detailed survey. These responses for BSPR and BSPRE1 were therefore averaged to create the Type A composite response shown in Figure 4.23, which is spatially associated with the Beresford Spring vent and upper tail.

The phase is particularly elevated between 10 Hz and 100 Hz, which corresponds to skin depths between 50 m and 300 m. Although BSPR and BSPRE1 are less than 100 m apart, the distance between the nearest adjacent sites at which the elevated phases are not seen is more than 300 m, which is a similar scale to the maximum skin depth. This means that any bulk resistivity anisotropy in an area 200 m wide, centred on the spring mound and extending no deeper than 200 m, may affect the Type A composite response but is not likely to affect the adjacent sites BSPRW2 and BSPRE2.

Although BWA2890 (located further southeast of the vent) contains elevated phases for currents induced in a northwest/southeast direction, it was not

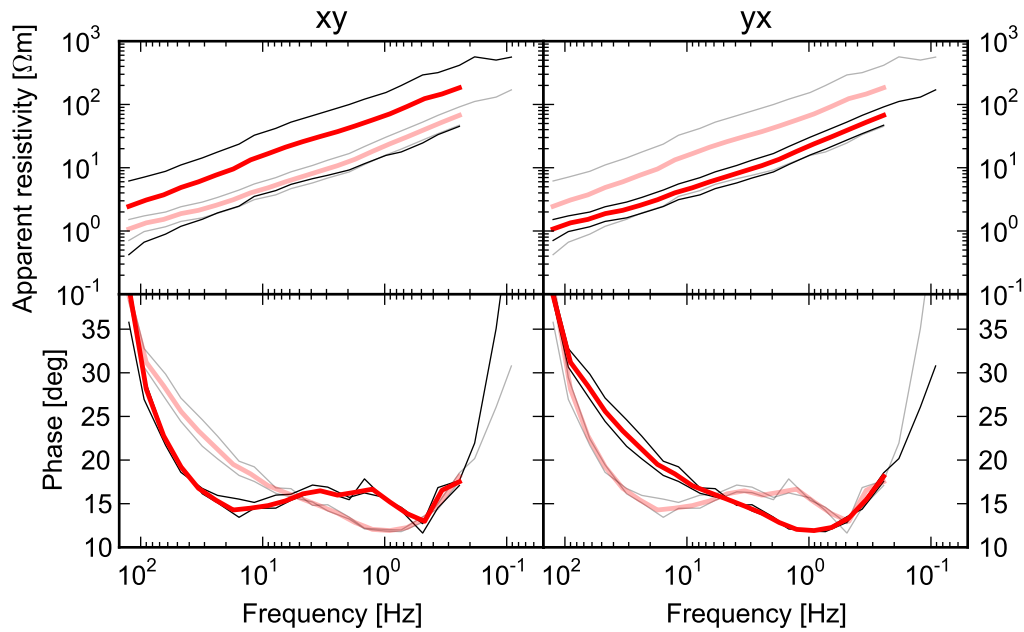


Figure 4.23: Type A composite MT response averaged from sites shown in Figure 4.22. The original responses are shown in black, the average in red, and the opposite mode in gray. Coordinate system x 280° , y 010° .

included in the Type A composite because the phase is significantly more elevated and it may be affected by the proximity of the Beresford Hill complex. There are too few sites in this direction to make a proper evaluation of the dimensionality and possible resistivity features.

4.4.1.2 Best-fitting models

Eleven inversions were conducted, where each inversion run involved modelling a set of 10^5 11-layer 1D models with the k -th layer allowed to contain a vertical planar anisotropy, with k varying from 1 to 11. Models with the anisotropic layer ranging between depths of 100 m and 650 m fit part of the Type A phase split, with the best fits overall achieved in the $k=5$ and $k=7$ inversions. It is not clear why the $k=6$ inversion did not yield models which fit the composite response well.

The $k=5$ inversion produced two models which fit the higher-frequency part of the phase split reasonably well (Figure 4.24). The fit is poorest between 6 Hz and 20 Hz, where the models fail to reproduce the full phase split, with the Z_{yx} phase too low around 12 Hz. However the shape of the Z_{xy} phase curve at the same bandwidth is well-reproduced.

The anisotropic layer in the $k=5$ models is between depths of 130 m and 180 m

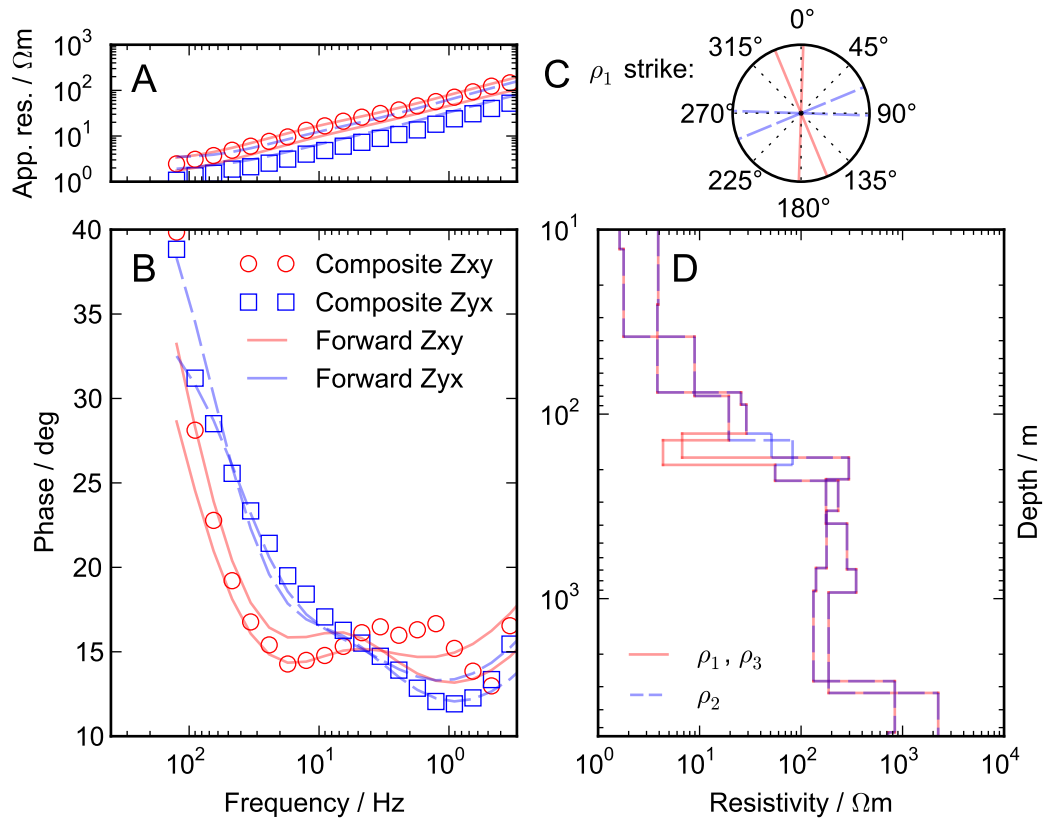


Figure 4.24: Anisotropic 1D resistivity models from $k=5$ that best fit the Type A composite response. Coordinate system: x 280° , y 010° . (A) Fit to apparent resistivity data; (B) fit to phase data; (C) anisotropy strike for models; (D) resistivity models. Symbols show composite response data and lines show forward model responses.

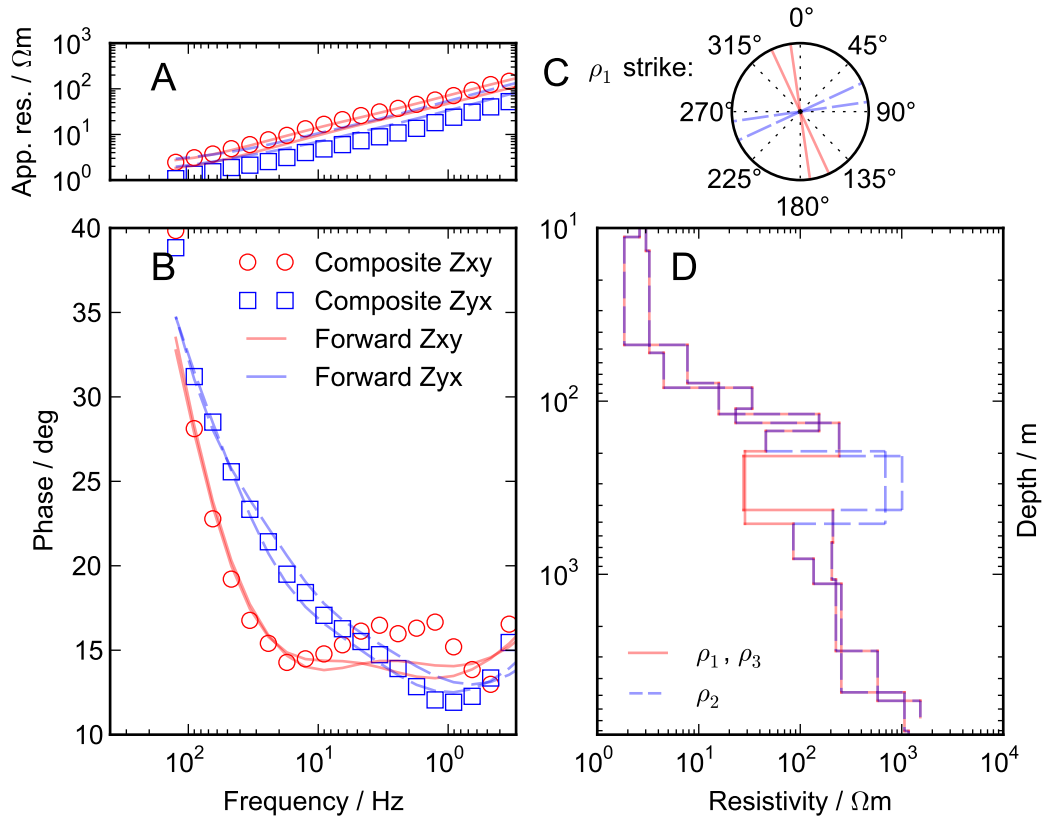


Figure 4.25: Anisotropic 1D resistivity models from $k=7$ that best fit the Type A composite response. Coordinate system: x 280° , y 010 . (A) Fit to apparent resistivity data; (B) fit to phase data; (C) anisotropy strike for models; (D) resistivity models. Symbols show composite response data and lines show forward model responses.

and contains conductive sheets striking either north or NNW with a strong resistivity contrast: $4\,\Omega\text{m}$ to $6\,\Omega\text{m}$ along the surface of the sheets and $50\,\Omega\text{m}$ to $80\,\Omega\text{m}$ across the sheet. Note that the surface resistivity is similar to the isotropic resistivity from depths of 40 m to 70 m, while the across-sheet resistivity is intermediate between the isotropic layers immediately above ($20\,\Omega\text{m}$ to $30\,\Omega\text{m}$ from 90 m to 130 m depth) and below ($120\,\Omega\text{m}$ to $300\,\Omega\text{m}$ down to 3000 m depth).

The other inversion which partly reproduced the Type A phase split was where $k=7$ (Figure 4.25). These models produced an excellent fit to the Zyx phase, but reproduced only the higher-frequency part of the Zxy phase, with the modelled phase remaining at 14° at frequencies below 20 Hz, compared to the observed phase which rises in that bandwidth to 17 Hz.

The anisotropic layer for the $k=7$ models lies between depths of 200 m to be-

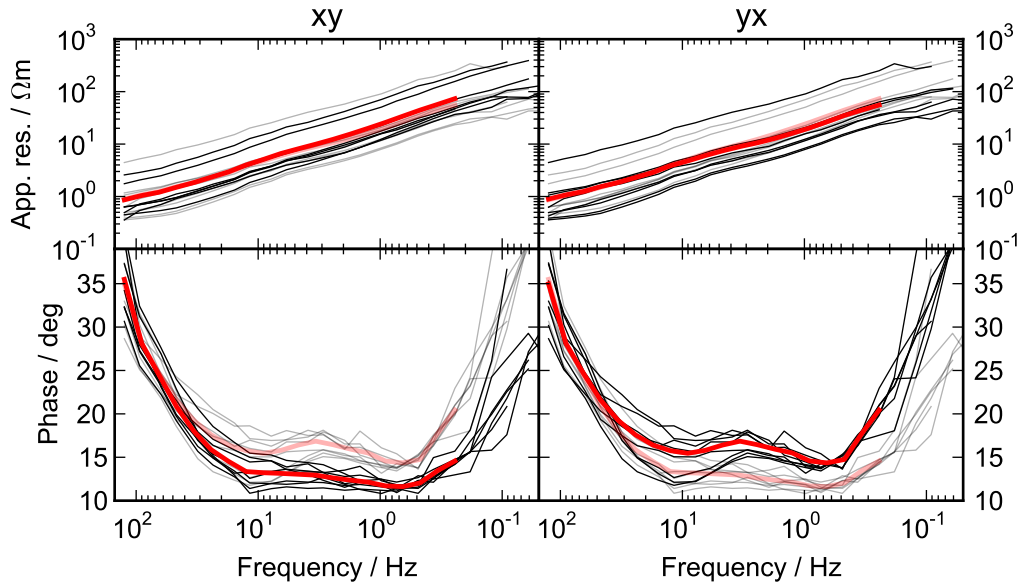


Figure 4.26: Type B composite MT response averaged from sites shown in Figure 4.22. The original responses are shown in black, the average in red, and the opposite mode in gray. Coordinate system x 045° , y 135° .

tween 450 m and 500 m. The conductive sheets again strike approximately NNW and have a resistivity contrast from $20 \Omega \text{ m}$ along the surface of the sheet to $800 \Omega \text{ m}$ to $1000 \Omega \text{ m}$ across it. Unlike the $k=5$ models above, the across-sheet resistivity is anomalously high compared to the isotropic layers both above it ($40 \Omega \text{ m}$ to $200 \Omega \text{ m}$ between 120 m and 200 m) and below it (consistently from $100 \Omega \text{ m}$ to $210 \Omega \text{ m}$ down to 3000 m to 5000 m depth).

4.4.2 Type B

4.4.2.1 Composite response

Elevated phases at lower frequencies are also present at all sites from the detailed survey, and BWA3140, BWA3700, and BWA4200 from the broad survey. The phase split is caused by an elevated 'bump' between 0.7 Hz and 10 Hz for the impedance phase related to currents flowing in a northwest direction. The phase split is approximately 4° in the composite response, which was created by averaging all the relevant sites' responses (Figure 4.26). The sites range across a distance of nearly 2000 m, while the range of skin depths for the bandwidth in which the phase split occurs is approximately 180 m to 2500 m.

4.4.2.2 Best-fitting models

Eleven inversions were conducted, where each inversion run involved modelling a set of 10^5 11-layer 1D models with the k -th layer allowed to contain a vertical planar anisotropy, with k ranging from 1 to 11. Note that the starting model and resulting distributions from which the set of models was generated was not the same as that for the Type A modelling above. This was because a focus on slightly deeper layers was required for modelling the lower-frequency Type B feature. Successful fits to the composite response were achieved only when the surface layer was anisotropic ($k=1$) or a much deeper layer at a depth of approximately 3 km was anisotropic ($k=10$).

The $k=1$ inversion produced a set of models which fit the phase split reasonably well (Figure 4.27). The surface layer is anisotropic in these models, with conductive sheets striking towards either 280° or 315° and extending to a depth of around 20 m. The sheets' surface resistivity is $0.2 \Omega \text{ m}$ to $0.7 \Omega \text{ m}$, and the perpendicular resistivity is $0.8 \Omega \text{ m}$ to $1.2 \Omega \text{ m}$.

The other inversion which fits the composite response phase split is $k=10$ (Figure 4.28), where the anisotropic layer is at a depth of approximately 3 km. The isotropic resistivity in these models rises with depth to a maximum of $200 \Omega \text{ m}$ to $400 \Omega \text{ m}$ at 200 m to 300 m depth, with a thin, more conductive layer of $20 \Omega \text{ m}$ at approximately 700 m depth. Underlying this is the anisotropic layer, which extends from a depth of 1000 m to somewhere from 2600 m to 4000 m; the modelling is sensitive mainly to the conductance, with the models containing thicker anisotropic layers having lower contrasts in resistivity. The conductive sheets consistently strike towards an azimuth of 020° , with the sheets' surface resistivity ranging from $40 \Omega \text{ m}$ to $80 \Omega \text{ m}$ (the perpendicular resistivity is around $200 \Omega \text{ m}$).

Although the fit for $k=1$ is better at high frequencies, whereas the $k=10$ phase split only begins at 12 Hz, it should be noted that the sites from which the composite response was created had a wide range of phase values at this bandwidth (Figure 4.26, particularly for the Zyx mode) and that the most relevant part of the phase split bandwidth (i.e. the part shared between sites) is from 0.8 Hz to 8 Hz. Given the way in which the observed phase curves for the modes cross over at high frequencies at BSPRW2 and BWA3140 in particular, the $k=1$ models are not considered to be particularly realistic.

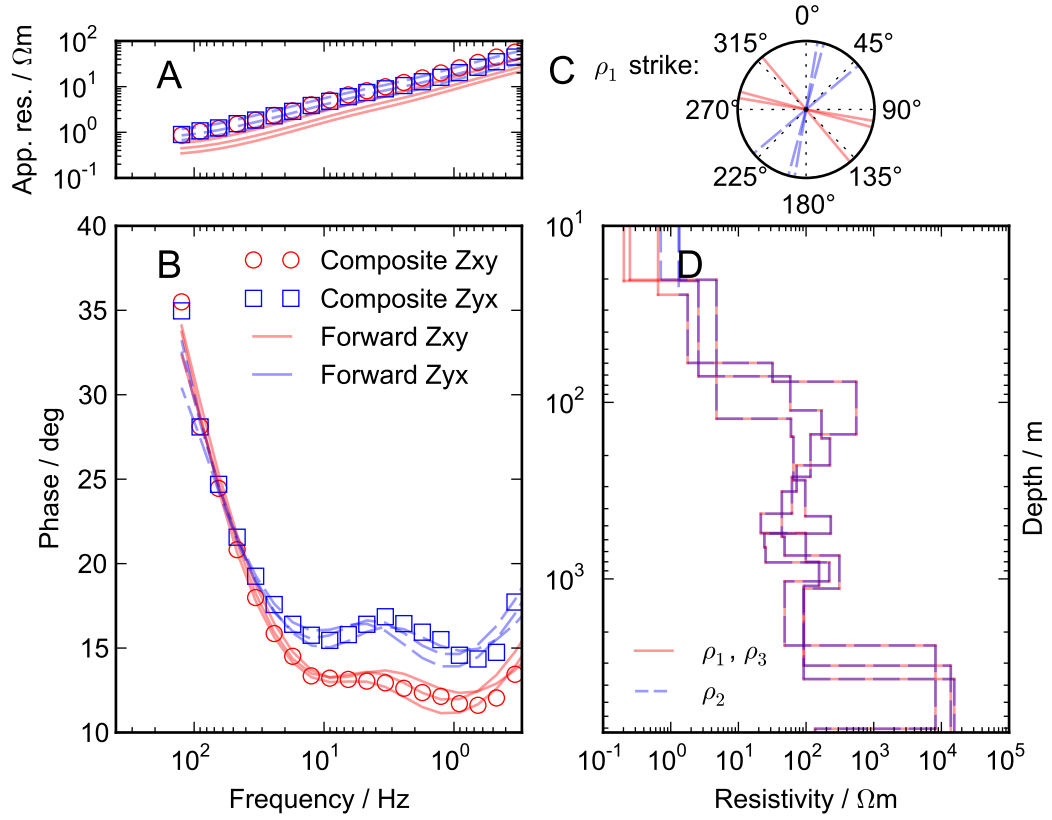


Figure 4.27: Anisotropic 1D resistivity models from $k=1$ that best fit the Type B composite response. Coordinate system: x 045° , y 135° . (A) Fit to apparent resistivity data; (B) fit to phase data; (C) anisotropy strike for models; (D) resistivity models.

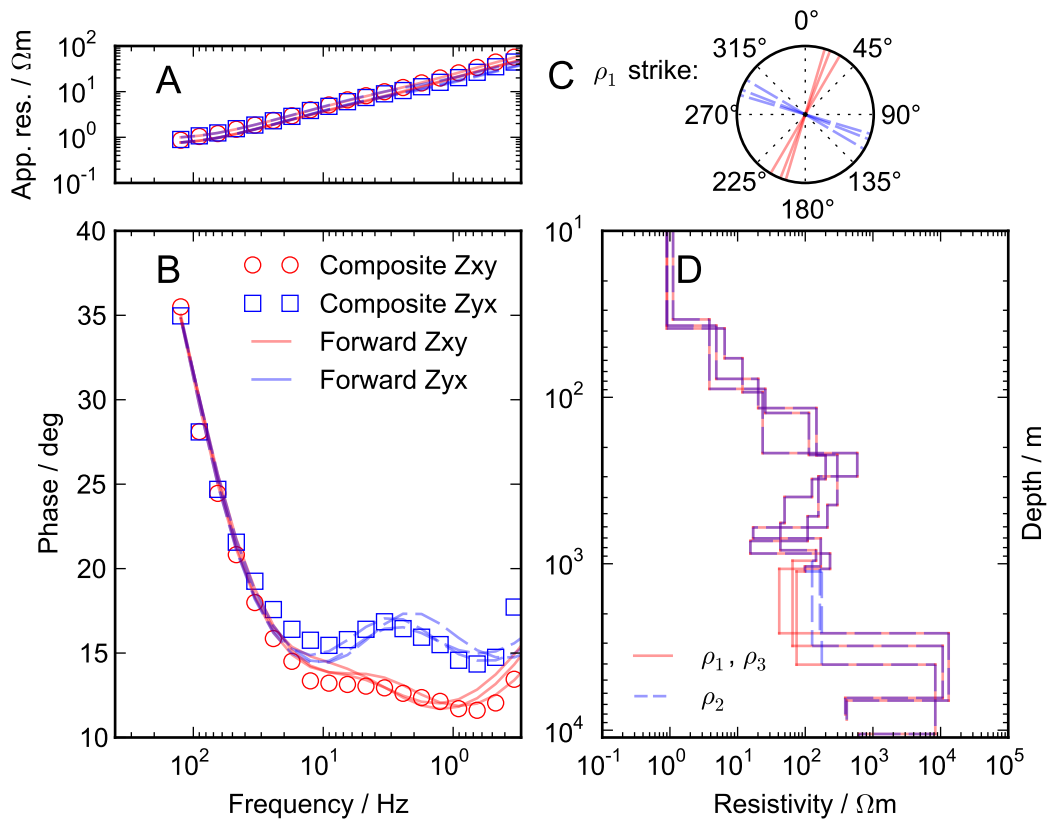


Figure 4.28: Anisotropic 1D resistivity models from $k=10$ that best fit the Type B composite response. $N=10^5$. Coordinate system: x 045° , y 135° . (A) Fit to apparent resistivity data; (B) fit to phase data; (C) anisotropy strike for models; (D) resistivity models.

4.5 2D MT inversion

Two-dimensional isotropic inversions were run using the Occam2D inversion software (de Groot-Hedlin and Constable, 1990).

4.5.1 Broad survey

Although the sites recorded for the broad survey are distributed approximately from north to south, the most suitable coordinate system for a 2D interpretation strikes north-west, as discussed in Section 4.3.1 above. Therefore the coordinate system where x is 225° and y is 135° was used for 2D modelling, where the geoelectric strike is to the northwest and Z_{xy} is the TM mode and Z_{yx} the TE mode. Inversions for both modes in these coordinates converge to a model of the basic form shown in Figure 4.29 (fits in Figure 4.30).

The model has a surface layer which is highly conductive (less than $2\ \Omega\text{m}$ down to a depth of 60 m), underlain by increasingly more resistive ground. The resistivity varies significantly laterally between depths of 90 m and 500 m, with resistive zones between BWA2890 and BWA3140, and between BWA3700 and BWA4200. These zones are most resistive at depths from 200 m to 400 m, with resistivities up to $150\ \Omega\text{m}$. There is a conductive area between the two zones (between BWA3700 and BWA3140), and another much broader conductive region underneath the eastern part of the model (east of BWA2890). The fit to the data (Figure 4.30) is generally excellent, with the poorest part of the fit being slight underestimation of the TE mode phase at the westernmost sites.

The resistive zones match up closely with the strike continuations of the two extinct spring structures in the area: Beresford Hill is aligned with the gap between BWA2890 and BWA3140, and the other extinct spring structure west of the playa is aligned with the gap between BWA3700 and BWA4200. Beresford Spring itself is on the strike continuation of BWA2890, which is underlain by the vertical boundary of the resistive zone described above.

Note that sites BWA1000 and BWA1335 were not included in the inversion because they have similar data to BWA1930 and are along strike from the latter site.

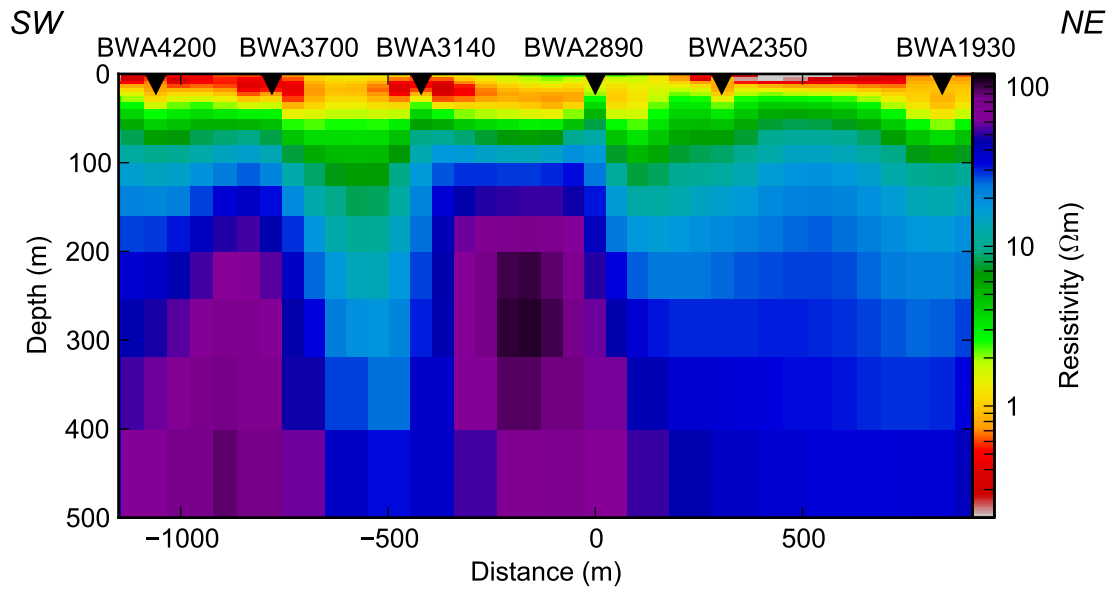


Figure 4.29: Resistivity model from 2D inversion fitting to within 20% of apparent resistivities and 5% of phases along the broad survey line (see fits in Figure 4.30)

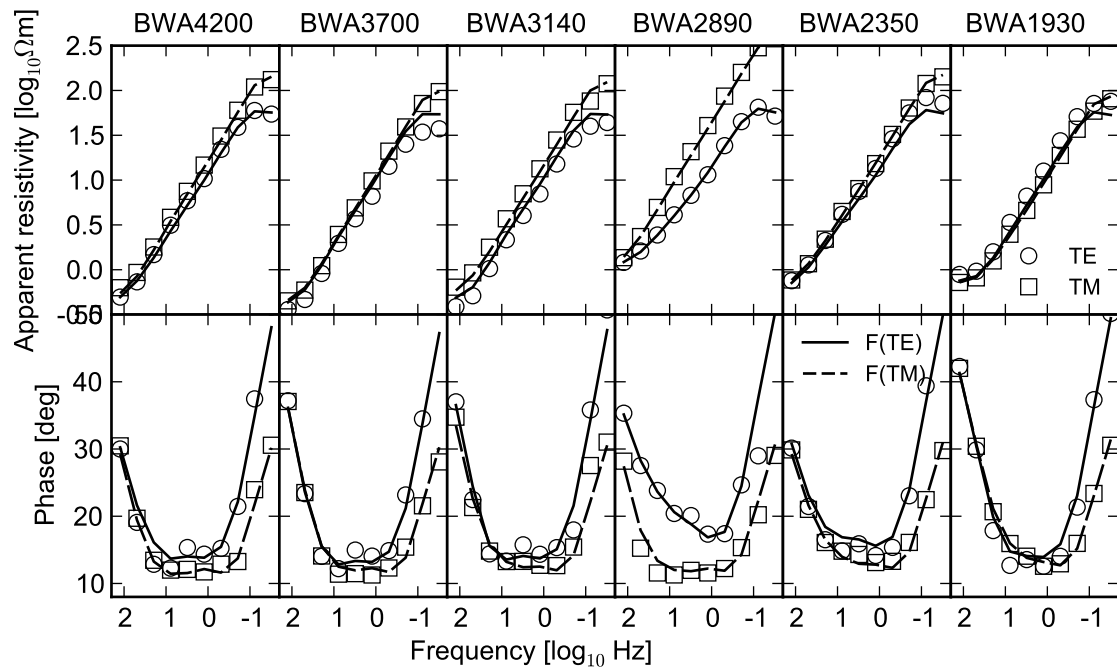


Figure 4.30: Fit of 2D MT model (Figure 4.29) forward responses to observations.

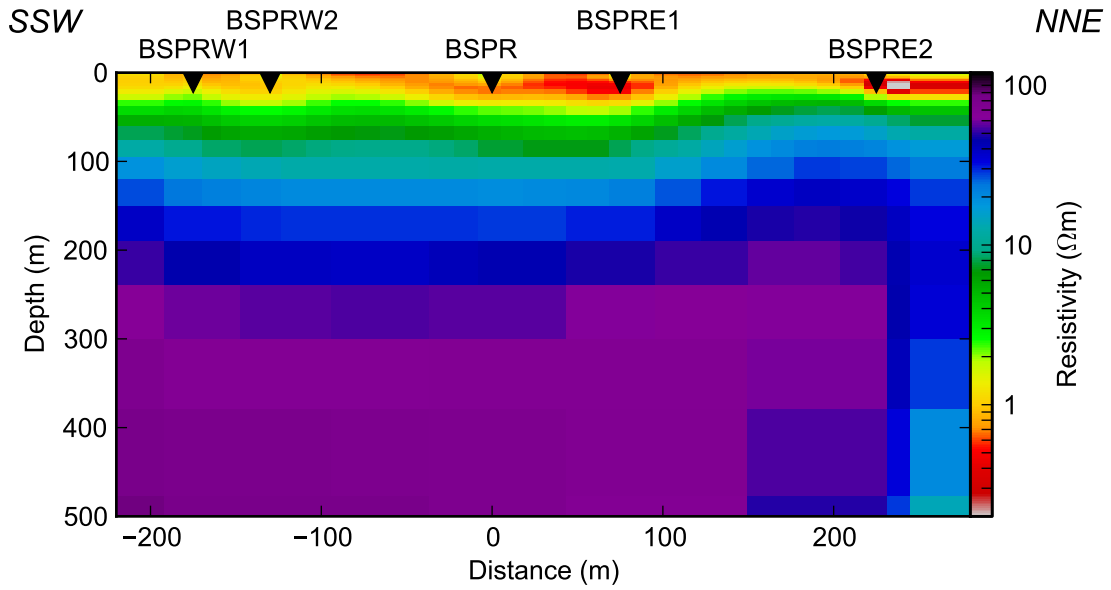


Figure 4.31: Resistivity model from 2D inversion fitting to within 20% of apparent resistivities (excluding BSPR) and 5% of phases along the detailed survey line (see fits in Figure 4.32)

4.5.2 Detailed survey line

Separate inversions were performed for the sites along the detailed survey line near the Beresford Spring vent. Of the sites along this line, BSPR and BSPRE1 in particular have a preferred orientation towards 280° . For modelling the sites were rotated into this coordinate system ($x\ 280^\circ$, $y\ 010^\circ$), and the Zxy mode was used as the TE mode, such that the 2D geoelectric strike is towards 280° , which is 35° to the east of the strike used for modelling the broad survey data above.

Inversions converged to a resistivity model with the features seen in Figure 4.31 (fits in Figure 4.32). The model has a highly conductive surface layer, which has a resistivity of less than $2\ \Omega\text{m}$ down to a depth of 60 m, thinning between BSPRE1 and BSPRE2 to only 20 m, although note there are no data to constrain the exact location or extent of thinning.

The major lateral features in the model are a conductive zone at a depth of approximately 500 m underneath BSPRE2, and a slightly resistive zone dipping to the southwest between BSPRE1 and BSPRE2. These two features appear to suffice to explain the small phase splits that are explored in the anisotropy modelling above. However, requiring closer fits than those in Figure 4.32 introduces significant and unrealistic artifacts into the model, such as strongly

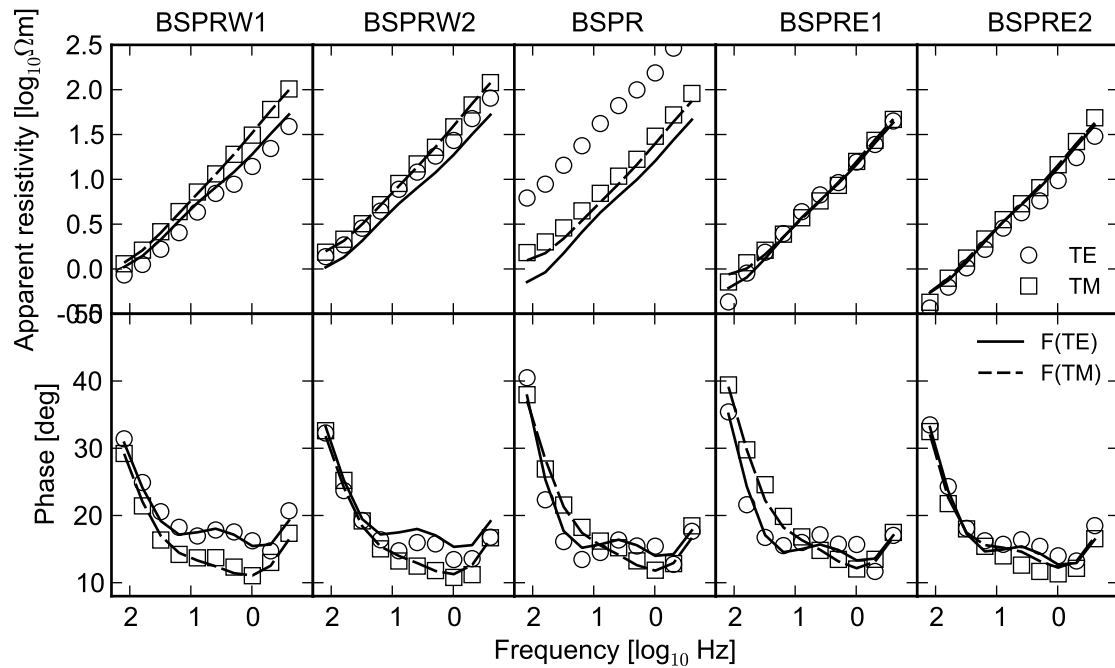


Figure 4.32: Fit of 2D MT model (Figure 4.31) forward responses to observations.

conductive horizontal areas at depths of more than 500 m and a vertical conductor between BSPRW2 and BSPR (model not shown). The most persistent feature in all the 2D modelling is the southwest-dipping resistive zone mentioned above, which tends to occur at a depth of approximately 200 m underneath BSPRE1 and BSPR, and is nearest the surface at BSPRE2.

Chapter 5

Warburton Spring

Summary

Warburton Spring is a shield-shaped carbonate mound spring located in a playa. Water flows from the 30 m-wide spring vent through a gutter in the carbonate edifice of the upper mound and discharges to a thickly vegetated fan-shaped delta on the southwestern side of the mound, which varies in width from 280 m to 400 m (see Figure 5.1 and Section 2.3.2 for more details).

SP data were collected over the mound along a 1200 m-long line on a bearing of 046° . There is an elevated SP feature centred on the spring mound and vegetated fan. Voltages are elevated by 50 mV over 150 m. The feature does not have a narrow voltage peak, but does have an unusually high voltage gradient on the spring vent's north-eastern side.

AMT and MT data were collected on the same line as SP data. At each site the resistivity rises with depth, from $1\ \Omega\text{ m}$ near the surface to more than $100\ \Omega\text{ m}$ at 200 m. Some sites have data that are consistent with 2D models striking toward 325° . Two-dimensional inversions of AMT data require a 30 m-thick surface resistive layer to the east of the mound, underlain by a 30 m-thick conductor. Two-dimensional models inverted for lower-frequency MT data contain laterally alternating conductive/resistive/conductive zones overlain on 1D resistivity structures, with the central resistive zone underlying the spring vent.

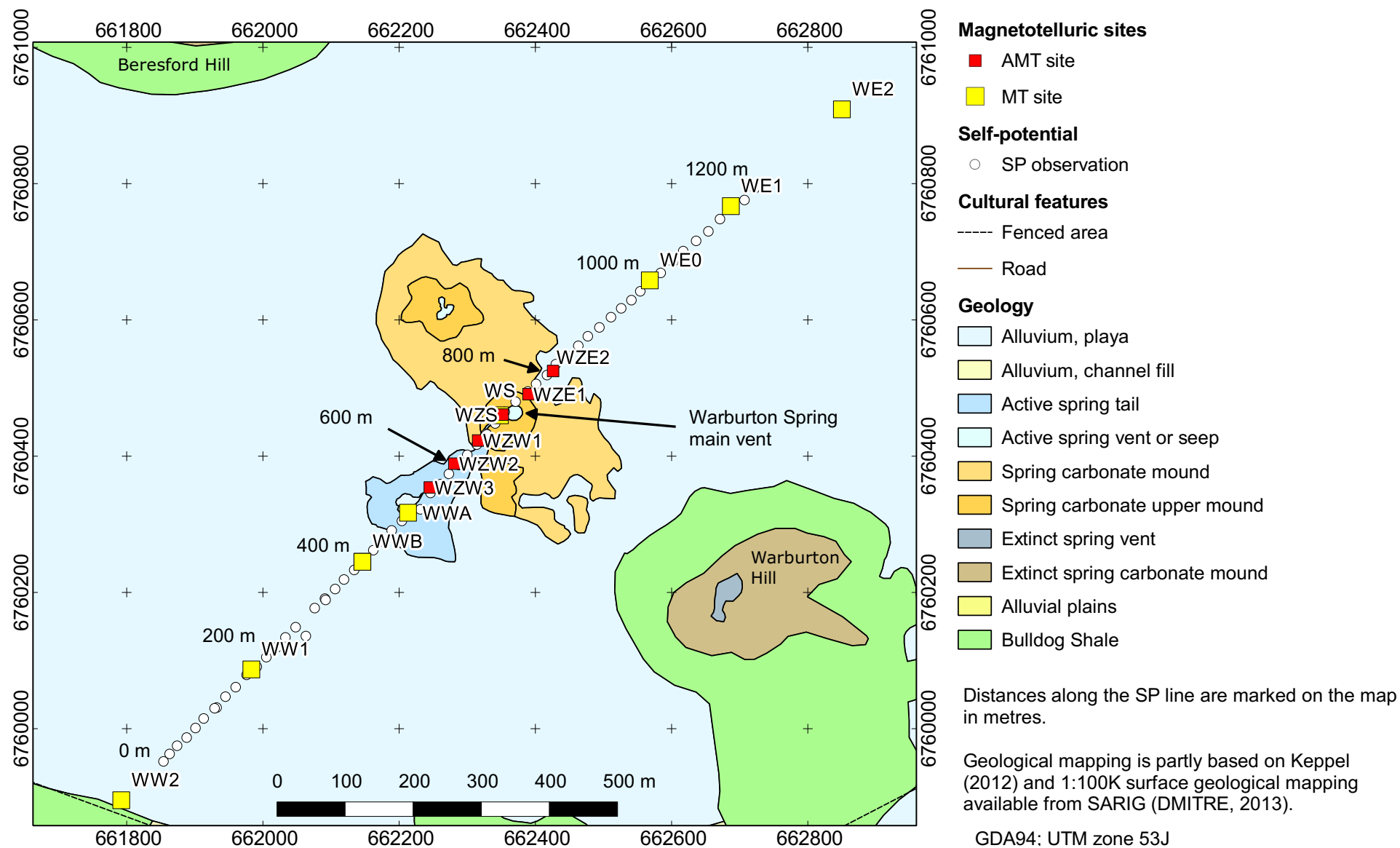


Figure 5.1: Location of SP and MT observations near Warburton Spring.

5.1 SP

Self-potential data were collected at Warburton Spring in November 2012. The potential was measured between a stationary base electrode and a roving electrode, which was moved along a profile in 20 m steps. The base electrode was located in the playa 720 m south-west of the Warburton Spring vent, and measurements were taken along the bearing 046° , directly over the vent and for a further 500 m into the playa. The profile was 1200 m long; the location of observations are shown on Figure 5.1. Observed potentials are shown in Figure 5.2.

There is a large rise in potential between stations 540 and 800, with peak potentials around station 600 of 62 mV. The area of elevated potentials is approximately 170 m wide, with a 45 mV drop in potential occurring on the north-eastern side near station 800 (potential gradient of -0.3 mV m^{-1}). The drop in potential on the south-western side occurs in two areas: around station 580 at a gradient of 0.24 mV m^{-1} , and at the lower or distal edge of the vegetated fan surrounding the spring discharge tail at station 440, where the potential gradient is 0.22 mV m^{-1} . The elevated potentials are generally coincident with the location of the carbonate mound and tail fan.

There are also two elevated responses to the south-west of the spring mound, each about 50 m to 100 m wide with an increase in potential from 12 mV to 20 mV, centred on stations 180 and 310. These occur in the playa and are not associated with any surface features. Their significance is unclear.

The image reconstruction (Figure 5.3B) contains an area strongly correlated with positive sources (correlation coefficient greater than 0.2) between station 760 on the north-eastern side and station 540 on the south-western side. The positively-correlated area is sloped on the south-western side, extending between stations 440 and 760 at a depth of 300 m. Areas to the north-east of station 800 are correlated strongly to negative sources (coefficient < -0.15) down to a depth of 150 m, compared to generally positive correlations on the other side of the spring mound (stations 100 to 500), suggesting that any downward seepage in the playa is occurring on the eastern side of Warburton Spring rather than the western side.

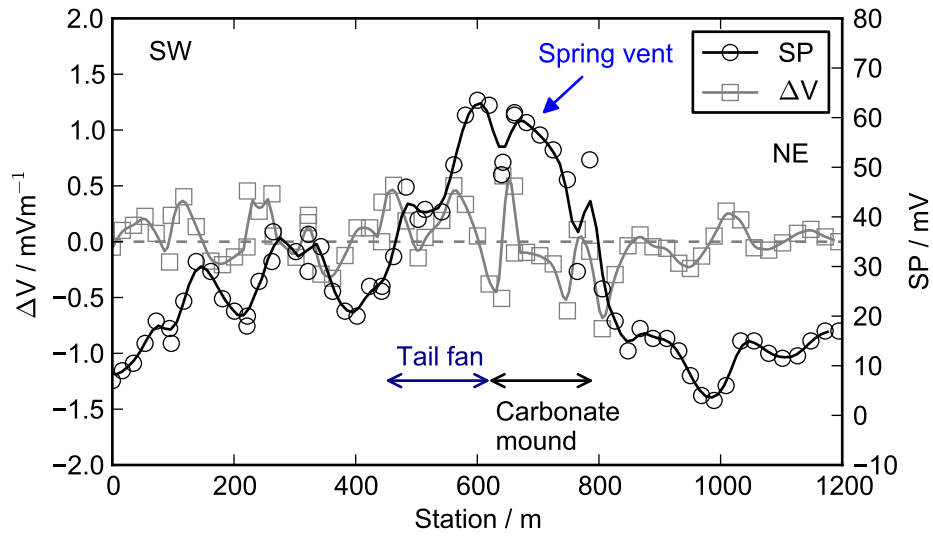


Figure 5.2: Self-potential and potential gradient ΔV at Warburton Spring. The black and grey lines are moving averages.

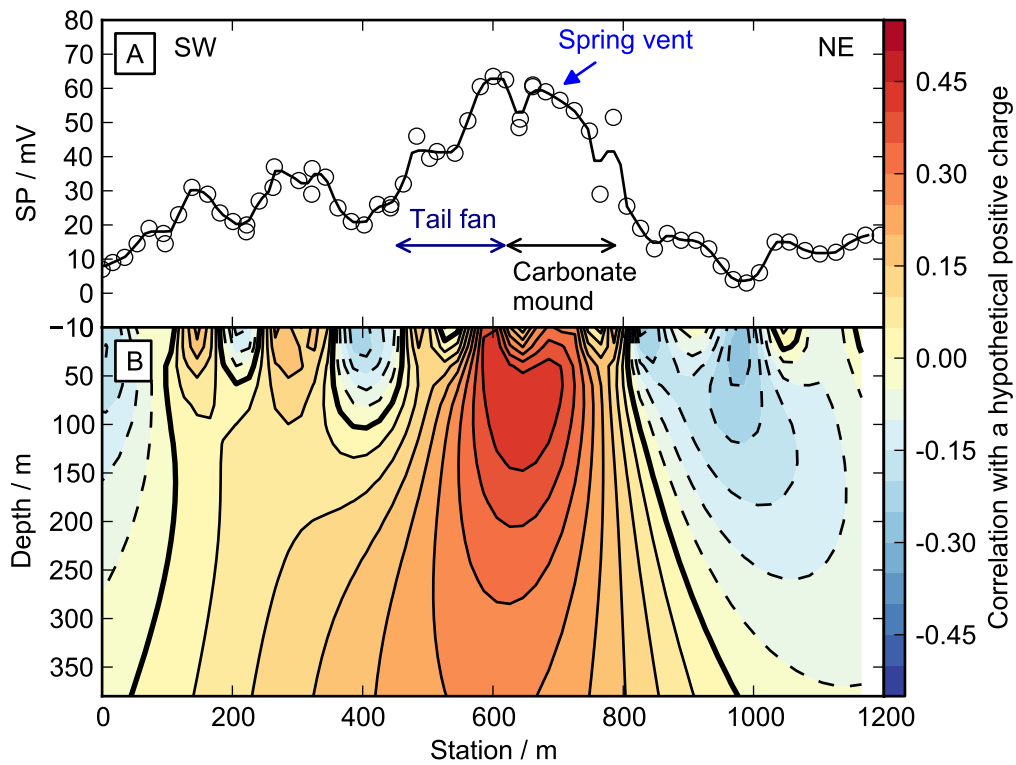


Figure 5.3: Self-potential data (A) and image reconstruction (B) over Warburton Spring. The black line in (A) is a moving average. The grey dashed horizontal line indicates $\Delta V = 0$.

5.2 Magnetotelluric data

Magnetotelluric data were collected at Warburton Spring in November 2012 along a 1465 m-long line which ran from south-west to north-east across the playa and over the Warburton Spring tail, upper mound, and vent. High-frequency AMT data were collected at five sites located over the mound, and lower-frequency MT data were collected at eight sites located in the playa and on the mound.

5.2.1 AMT data

The AMT sites were collected with a Zonge Engineering GDP-32II receiver, and two EMI BF-10 coil magnetometers. Impedance responses were calculated for windows ranging from 3 Hz to 8192 Hz, stacked over 25 min to 60 min of total recording time.

Electrode dipoles and coils were arranged in 'spreads', each consisting of three sites at 50 m spacing (Figure 5.4). Each spread covered 150 m of distance along the surveyed line.

Two spreads were recorded. The first extended from the spring vent to the north-east. The second extended to the south-west. Electric and magnetic fields were recorded in the coordinate system x 315° and y 045° , i.e. Zyx corresponds to currents flowing along the survey line, and Zxy to currents flowing perpendicular. The locations of the AMT sites are shown on Figure 5.1 and are described below in order from south-west to north-east:

1. WZW3 and WZW2. These are located 150 m and 100 m respectively from the spring, and are in the upper part of the thickly vegetated tail.
2. WZW1 is located 50 m from the spring, adjacent to the uppermost and steepest part of the tail, where it incises a narrow channel into older spring carbonate deposits.
3. WZS is located at the spring vent on top of the mound. The y dipole is coincident with the same dipole for the MT site WS.
4. WZW1 and WZW2 are located 50 m and 150 m respectively from the spring, on the drier northeastern flank of the mound.

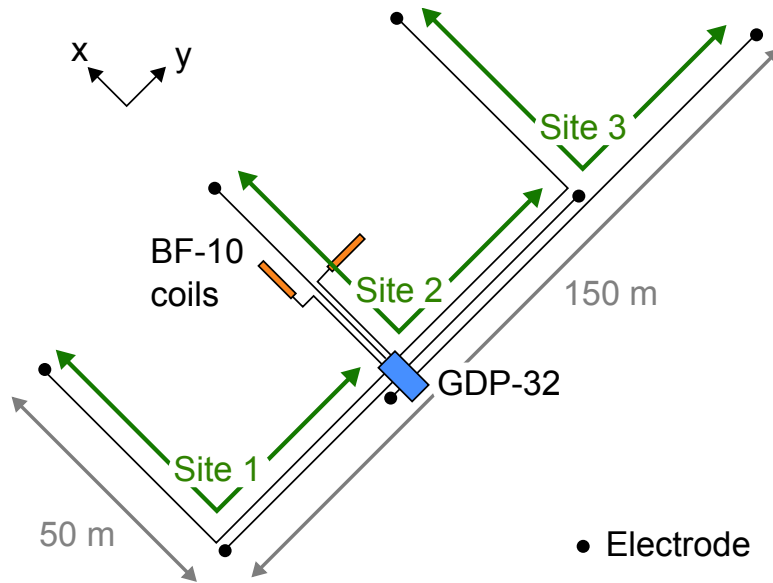


Figure 5.4: Configuration of an AMT spread recorded at Warburton Spring, containing three sites.

5.2.1.1 Data quality

The western spread of sites (WZW1, WZW2, and WZW3) are affected by noise in the measured magnetic field. Apparent resistivity and phase curves for WZW1 in particular are inconsistent, with the change in apparent resistivity at 200 Hz not reflected in the phase as it should be (Figure 5.5). On the day the south-western spread was recorded (20 November 2012) there was a strong breeze from the north-east, buffeting the Hx induction coil magnetometer, which was aligned perpendicular to the wind direction. Both coils were stabilised by weights rather than buried because the site was located on exposed carbonate. The data is partly consistent and possibly unaffected in the Ex/Hy mode, so the Ey/Hx mode alone has been omitted from the 2D interpretation and modelling.

5.2.1.2 Data analysis

Phase tensor ellipses are shown in Figure 5.6. The high-phase high-frequency ellipses at WZS are very elongated, while other sites' ellipses are circular, with phases relatively close to 45° at high frequencies.

Frequencies between 10 kHz and 50 Hz are mostly quasi-2D (i.e. normalised phase tensor skew $|\psi| < 10$), with the exception of the three western sites WZW1, WZW2, and WZW3.

The phase tensor ellipse orientations vary between azimuths of 000° and 300°

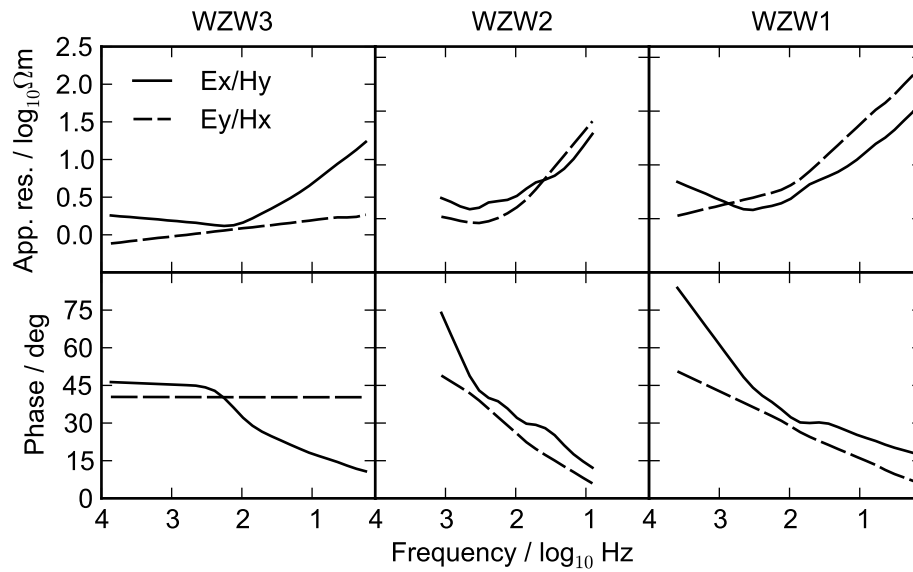


Figure 5.5: Cross-section of apparent resistivity and phase from the western spread of the AMT survey. Coordinate system x 315° , y 045° .

(Figure 5.7), with the most common orientation in the eastern spread being 315° at WZS and 305° at WZE1. The orientation at WZE1 rotates around towards north at frequencies around 200 Hz. An orientation of 315° was chosen for 2D interpretation.

Apparent resistivity and phase data are shown in Figure 5.8. Below 100 Hz the data from WZS and WZE1 closely resembles the Type A feature at Beresford Spring (e.g. Figure 4.23), with apparent resistivity rising steeply and phases dropping, with an elevated Zxy phase. Note that the conventions used for coordinate systems are reversed, such that the Zxy mode here has roughly the same orientation as the Zyx mode in the Beresford Spring data.

The main high-frequency feature near the spring and eastern sites is a drop in apparent resistivity and associated rise in phase around 200 Hz, caused by a conductive layer. This feature is present to varying degrees at WZS, WZE1, and WZE2, but is absent from the western sites. At WZE1 it is accompanied by particularly low Zyx phases and apparent resistivities at frequencies above 1000 Hz.

Also note that in these AMT data the two modes' phase curves meet at a common phase of 35° to 45° at approximately 200 Hz; this is the highest frequency reliably estimated in the MT data here (see Section 5.2.2 below) and in other surveys, and suggests that the conclusions drawn below from modelling this high-frequency AMT data may apply to other spring systems over

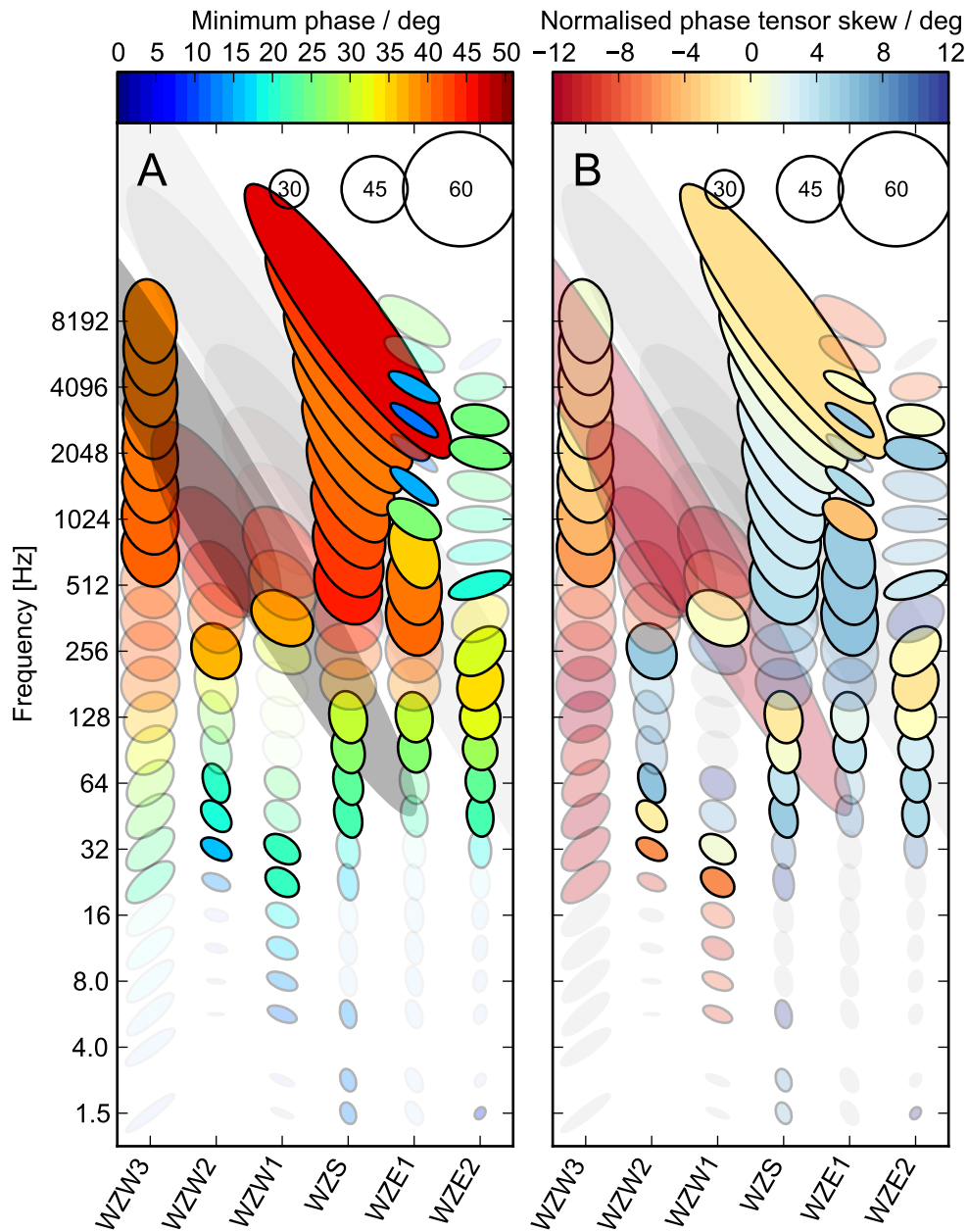


Figure 5.6: Pseudosection of phase tensors from the AMT survey, filled with (A) minimum phase and (B) the normalised skew ψ . Faint coloured ellipses have $|\psi| > 6^\circ$ and faint gray ellipses $|\psi| > 12^\circ$, both representing tensors significantly affected by 3D induction. Phase tensors have been rotated by 90° so that the major axis is parallel to the TE mode under a quasi-2D assumption (Booker, 2013) and ellipses with phases of 30° , 45° , and 60° are shown in the upper left for comparison.

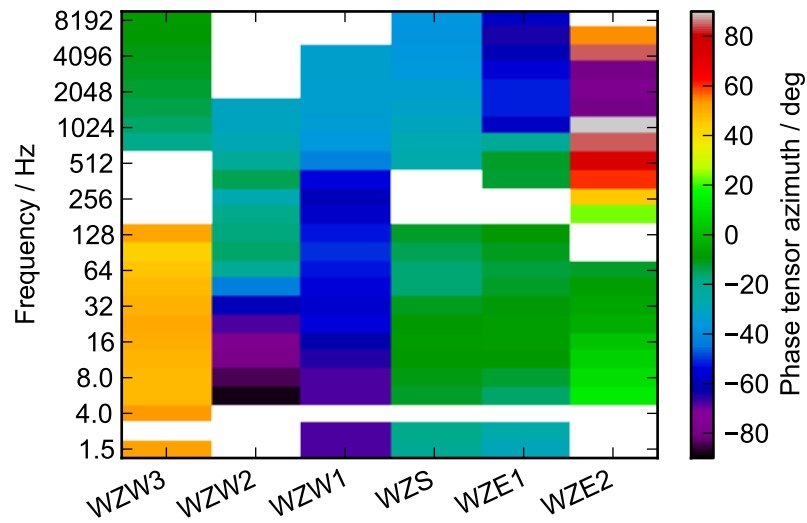


Figure 5.7: Pseudosection of phase tensor azimuths (θ_{ellipse}) for the AMT survey. Azimuths are only shown for tensors with a split in the principal phases greater than 5° .

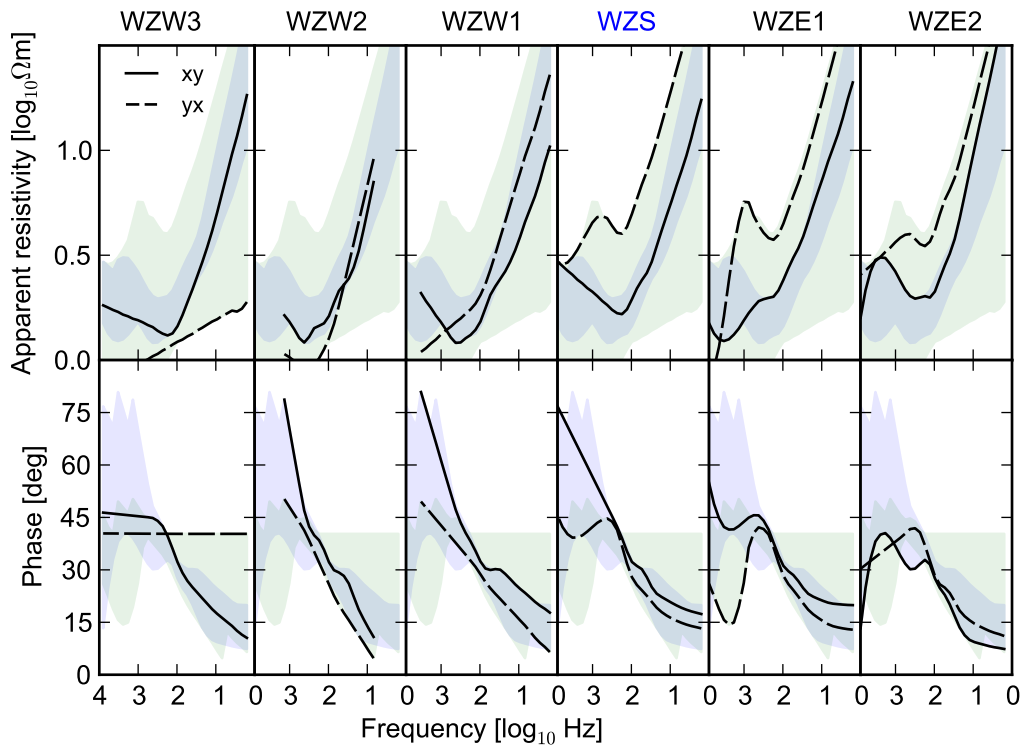


Figure 5.8: Cross-section of apparent resistivity and phase from AMT sites at Warburton Spring. The shaded area is to help with comparison between sites and shows the range of data from all the sites on the section. Coordinate system: x 315° , y 045° .

which AMT data were not collected. Further discussion can be found in Section 10.2.2.

5.2.2 MT data

Lower-frequency MT data were collected at eight sites along a 1480 m-long line oriented towards an azimuth of 045° . This line runs over the Warburton Spring mound and tail. The locations of the sites are shown on Figure 5.1.

Responses were estimated between 375 Hz and 0.05 Hz, from 2.7 h windows of time series recorded overnight at a sampling rate of 1000 Hz. Electrode dipoles were oriented towards an azimuth of 315° for x and 045° for y , the latter being parallel to the survey line; an exception is noted below for WS. Pairs of LEMI-120 induction coil magnetometers were located parallel to the dipoles, with two exceptions being WWA and WWB, which shared the same pair of coils.

The MT sites and their distances from the spring vent are, in order from south-west to north-east:

1. WW2 was located near the south-western edge of the playa, 800 m from the spring vent.
2. WW1 was located on the playa, 520 m from the spring.
3. WWB was located on the playa immediately adjacent to the edge of the thickly vegetated fan formed by discharge from the spring, 300 m from the vent.
4. WWA was located 200 m from the vent, in the thickly vegetated fan.
5. WS was located at the spring vent on top of the mound. The x electrode was set up on the south-eastern side of the line (towards an azimuth of 135°), opposite to that of all the other sites. The y electrode dipole straddled the edge of the vent pool and was coincident with the same dipole for the AMT site WZS.
6. WE0, WE1, and WE2 were located in the playa to the northeast of the mound, at distances from the vent of 300 m, 450 m, and 675 m respectively.

Phase tensor ellipses are shown in Figure 5.9. Most responses are either 1D or quasi-2D, except for frequencies below 8 Hz at WE1, which have a large

diagonal component, the cause of which is not clear.

Figure 5.10 shows the orientation of phase tensor ellipses for those responses which have principal phase splits of more than 4° . The only sites which have such a split at frequencies above 0.5 Hz are WS and WE0. The former (WS), located at the spring vent, is oriented towards an azimuth of approximately 325° throughout the bandwidth from 100 Hz to less than 0.1 Hz, while the latter (WE0), located more than 200 m northeast of the mound, is oriented towards an azimuth of 025° in the same bandwidth. The strike for WE0 also rotates around to the north at lower frequencies.

Apparent resistivity and phase curves are shown in the coordinate system defined by the orientation of WS at high frequencies in Figure 5.11. The response at WS is similar to the Type A response from Beresford Spring, although the Zxy mode for which the phase is elevated at frequencies above 10 Hz remains elevated down to a frequency of 1 Hz. There is little indication of a Type B response with an elevated bump in phase at low frequencies, except for WW2. This suggests that the Type B response may be limited to the western edge of the playa.

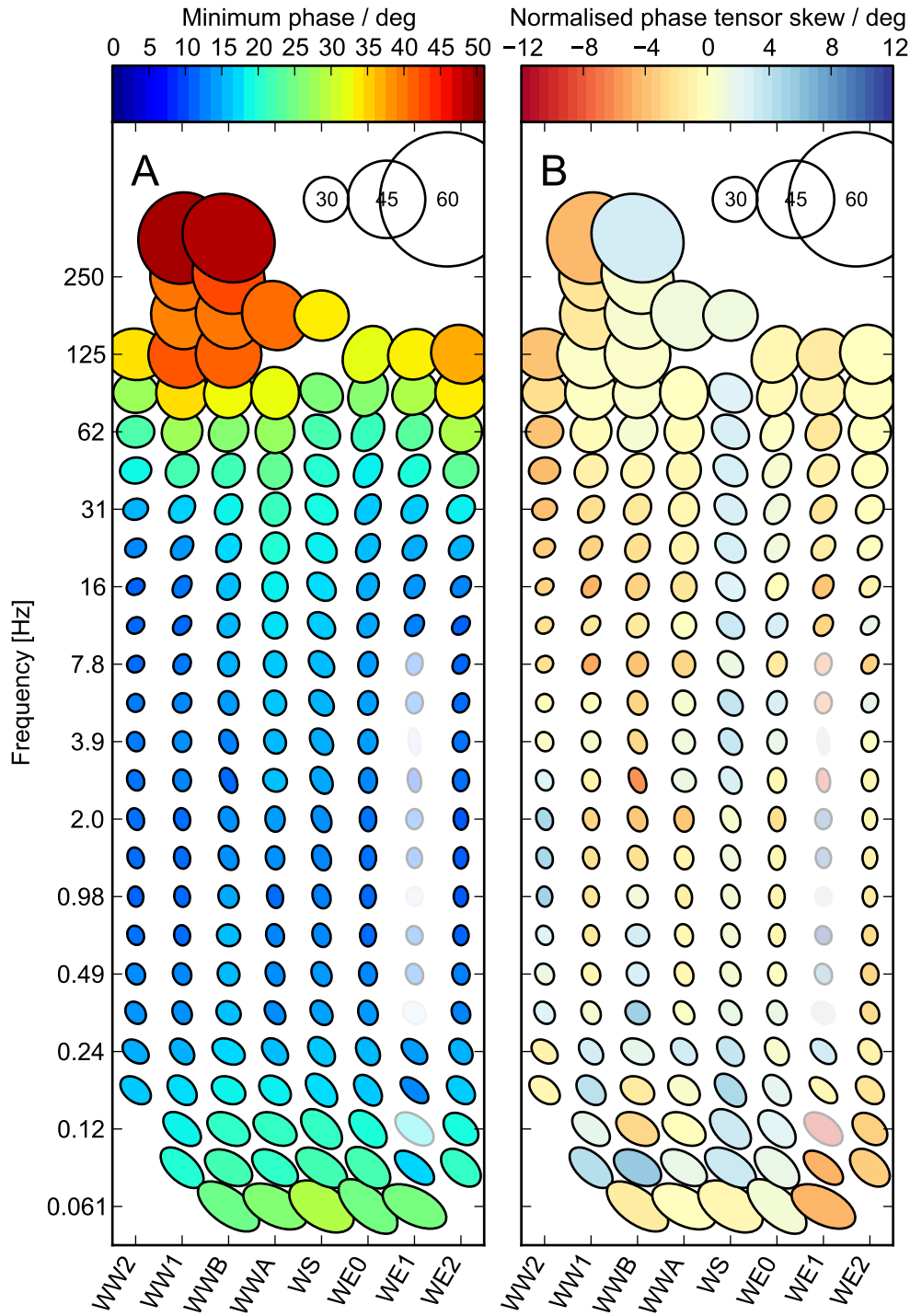


Figure 5.9: Pseudosection of phase tensors from the MT survey, filled with (A) minimum phase and (B) the normalised skew ψ . Faint coloured ellipses have $|\psi| > 6^\circ$ and faint gray ellipses $|\psi| > 12^\circ$, both representing tensors significantly affected by 3D induction. Phase tensors have been rotated by 90° so that the major axis is parallel to the TE mode under a quasi-2D assumption (Booker, 2013) and ellipses with phases of 30° , 45° , and 60° are shown in the upper left for comparison.

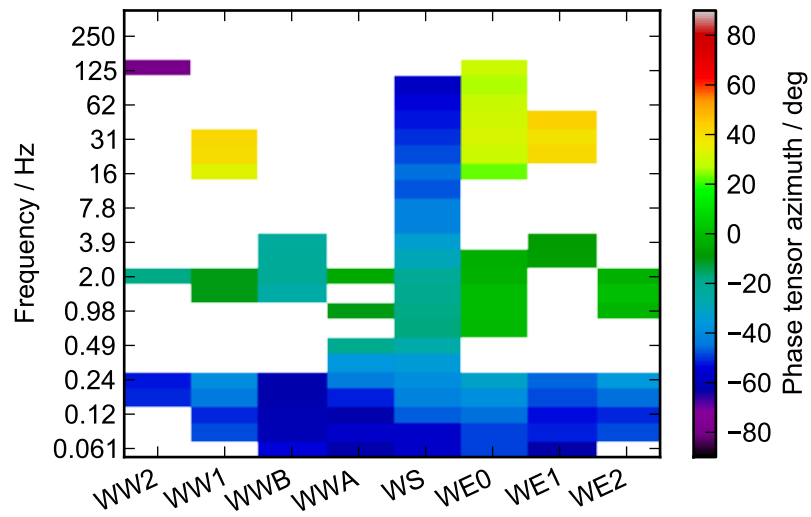


Figure 5.10: Pseudosection of phase tensor azimuths (θ_{ellipse}) for the MT survey. Azimuths are only shown for tensors with a split in the principal phases greater than 4° .

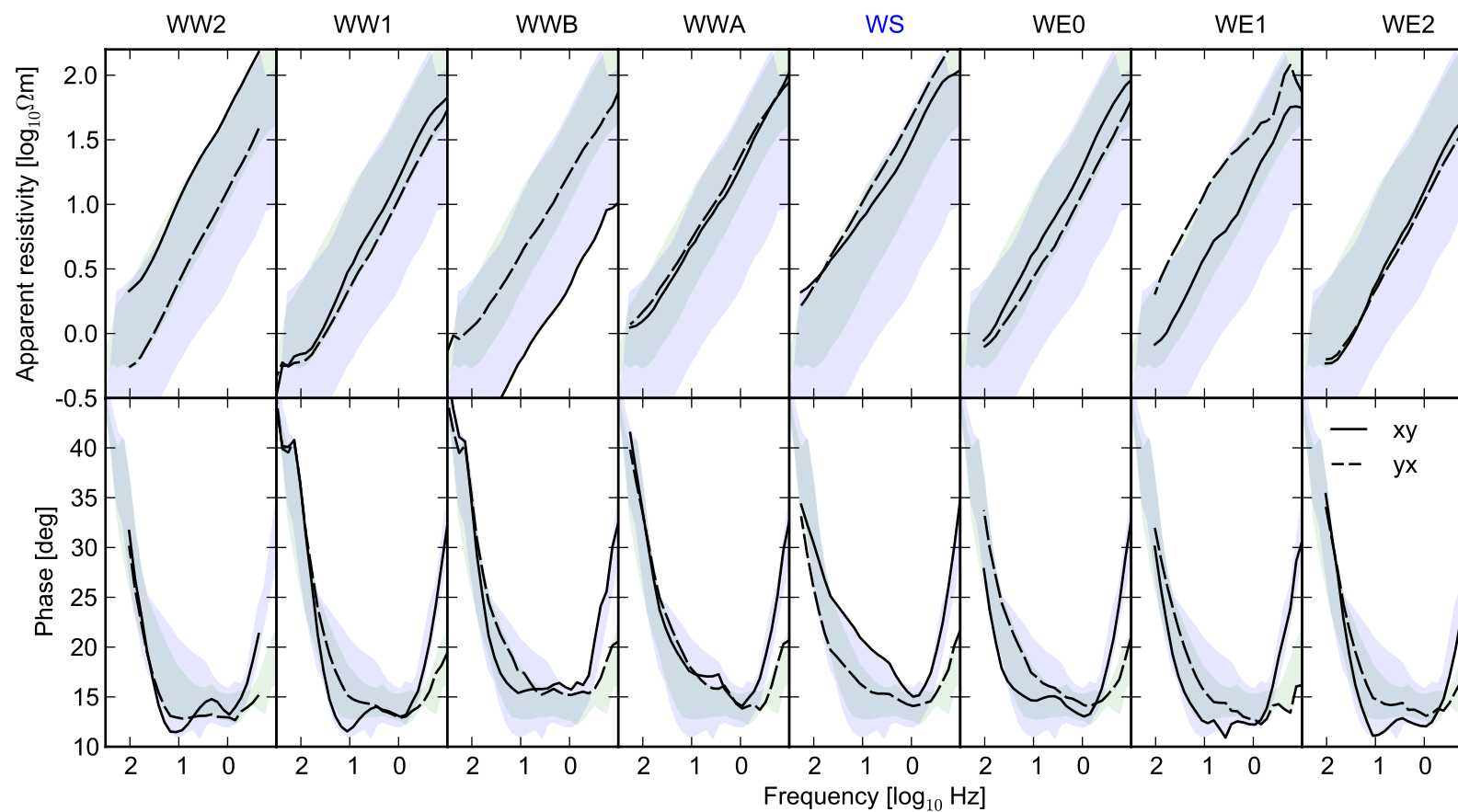


Figure 5.11: Cross-section of apparent resistivity and phase from MT sites at Warburton Spring. The shaded area is to help with comparison between sites and shows the range of data from all the sites on the section. Coordinate system: x 325° , y 55° .

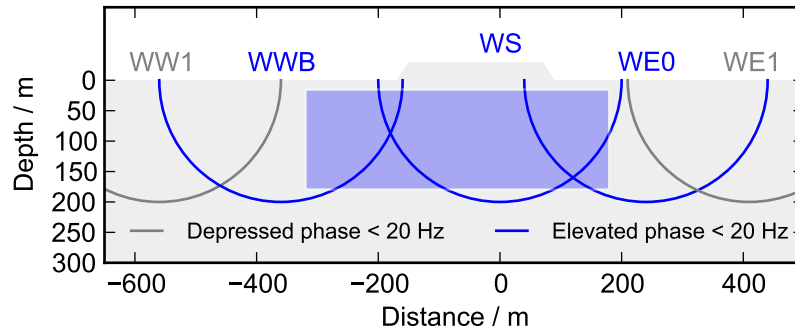


Figure 5.12: Cross-section of approximate maximum penetration depths for 20 Hz responses at WW1, WWB, WS, WE0, and WE1. Gray area shows the spring platform with an exaggerated elevation, and blue area shows the extent of structures likely responsible for the elevated phase (see text).

The phase curves drop to values less than 15° at the western (WW2 and WW1) and eastern (WE1 and WE2) ends of the line, while the sites closer to the mound (WWB, WWA, WS, and WE0) do not drop so low; they have minimum phases greater than 15° . Minimum phases at WE0 lie in between (note that WE0 is close but not adjacent to the mound). Because the drop in phase is caused by the increase in resistivity with depth, this alone suggests that a resistive zone lies underneath the mound and tail (Figure 5.12).

5.3 2D MT modelling

Two-dimensional isotropic inversions were run using the Occam2D inversion software (de Groot-Hedlin and Constable, 1990).

5.3.1 High-frequency AMT sites

The AMT sites were modelled in a coordinate system with TE mode currents running along the azimuth of 315° , as discussed above in Section 5.2.1. The result of an inversion constrained to fit within 40% of apparent resistivity and 10% of phase data for both TM and TE modes at WZS and the eastern sites and only the TE mode for the western sites is shown in Figure 5.13 (fits in Figure 5.14). The TM mode was excluded from the western sites because of data quality problems with the TE mode magnetic field measurements (Section 5.2.1.1).

The resistivity model (Figure 5.13) contains a shallow conductor which accounts for the rise in phase at 200 Hz in the TM mode. The conductor has a

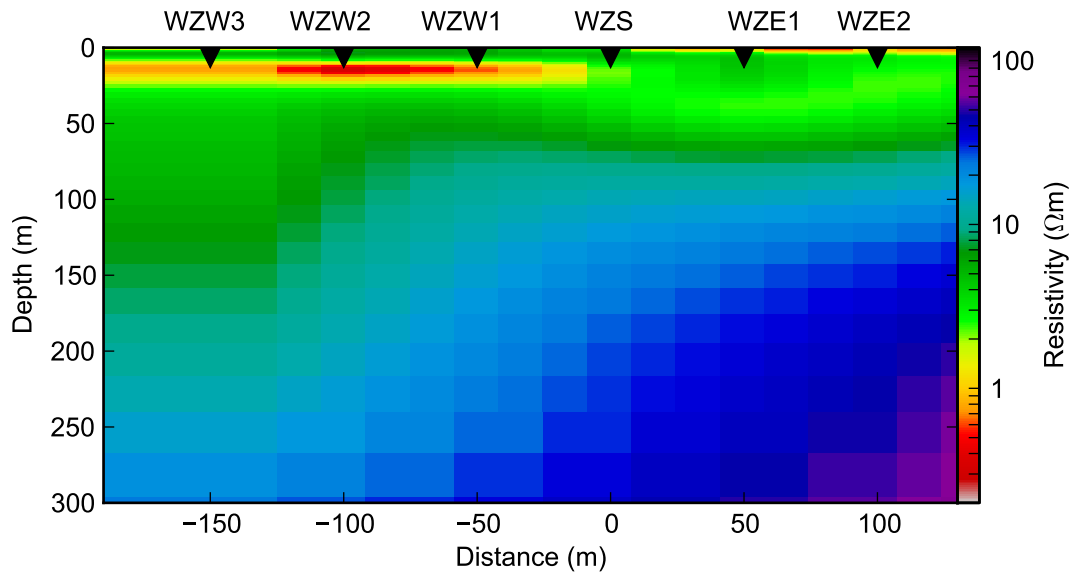


Figure 5.13: Resistivity model from 2D inversion fitting to within 40% of apparent resistivities and 10% of phases for AMT data (see fits in Figure 5.14 and note there was no requirement to fit the TM mode at WZW1, WZW2, and WZW3).

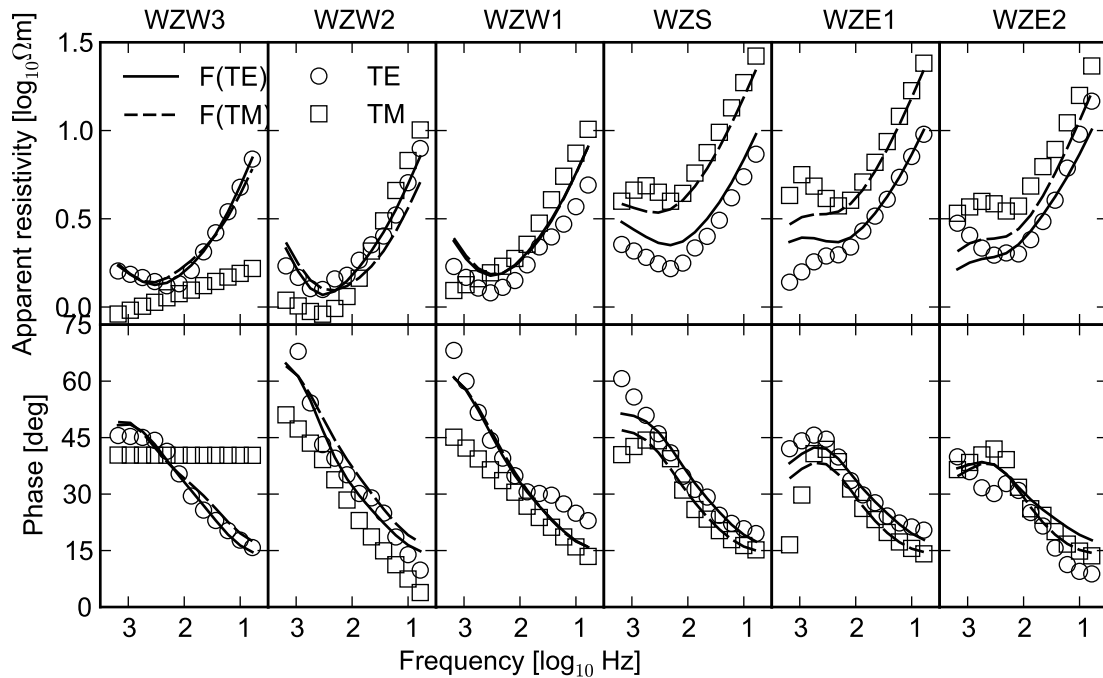


Figure 5.14: Fit of 2D AMT model (Figure 5.13) forward responses to observations. Note that there was no requirement to fit the TM mode at WZW3, WZW2, and WZW1.

resistivity of between $2\ \Omega\text{m}$ and $5\ \Omega\text{m}$ from the surface to a depth of 60 m under the eastern stations and to a depth of almost 140 m underneath the western sites. The transition in depth occurs underneath WZW2. There is also a thin and highly conductive layer near the surface underneath the western sites.

Model fits are moderately good, with the general trends of the apparent resistivity and phase reproduced at all sites. Inversions which required a closer fit generated inconsistent and geologically unrealistic structures with very high conductivities. It should be noted there are features in the data, especially in the eastern sites, which are not reproduced, such as a drop in the TE mode phase at WZW3.

5.3.2 Low-frequency MT sites

The MT sites were modelled in a coordinate system with TE mode currents running along the azimuth of 325° , which corresponds to the orientation of WS at high frequencies (see Figure 5.10). Initial attempts at modelling all data on the line failed to reproduce the very low TE apparent resistivities at WWB together with the TE phase. To remove this effect of galvanic distortion on the modelling, inversions were not required to fit any data from WWB. A model from an inversion constrained to fit within 5% of phases and 20% of apparent resistivities is shown in Figure 5.15 (fits in Figure 5.16).

The model in Figure 5.15 contains a surface conductor beneath which the resistivity steadily rises. In the shallowest part of the model the surface conductor is slightly more resistive underneath WS compared to the rest of the model by a factor of 2.5 ($1.5\ \Omega\text{m}$ to $0.6\ \Omega\text{m}$). This resistive zone exists down to a depth of approximately 100 m.

Between 100 m and 250 m the model alternates laterally between being more conductive and more resistive: a conductor underneath WWA, a resistor underneath WS, and a less obvious conductor underneath the eastern sites WE0 and WE1. These 'conductors' and 'resistors' are not homogeneously conductive or resistive but are overlain on a 1D resistivity structure that is seen clearly beneath WW2 and WW1 on the western side, and WE1 and WE2 on the eastern side. The lateral variations extend to depths no greater than about 600 m and are similar to those noted on the broad survey at Beresford Spring in Figure 4.29.

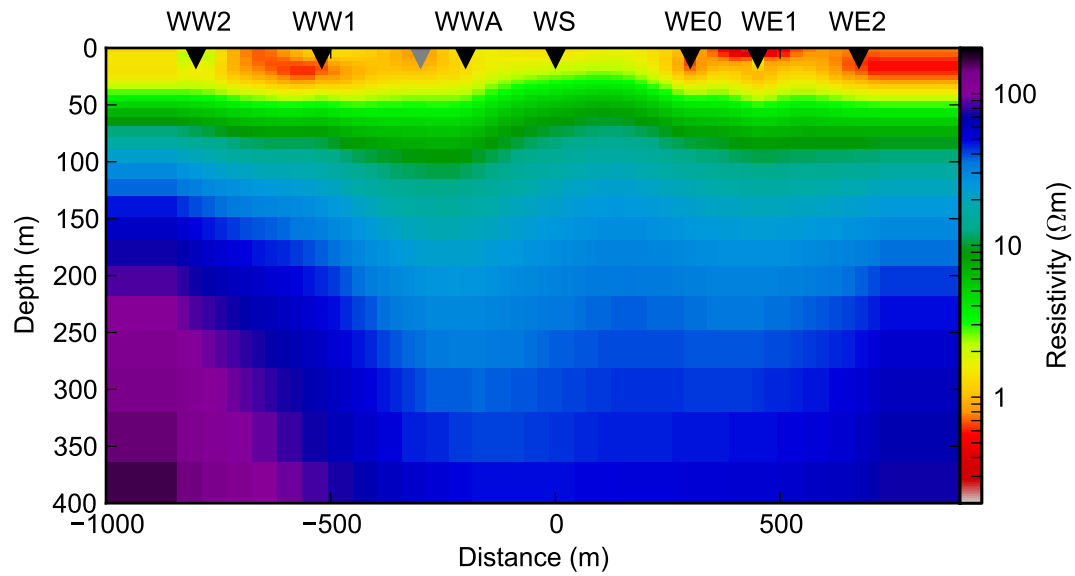


Figure 5.15: Resistivity model from 2D inversion fitting to within 20% of apparent resistivities and 5% of phases for MT sites (see fits in Figure 5.16).

Figure 5.16 shows that all major features of the phase data are fitted well, and despite the looser constraint on the apparent resistivities (the TM mode in particular), these are reproduced closely from the phase for most sites, except for WE1, which is subject to 3D effects as noted above, and WW2, which may also be subject to galvanic distortion.

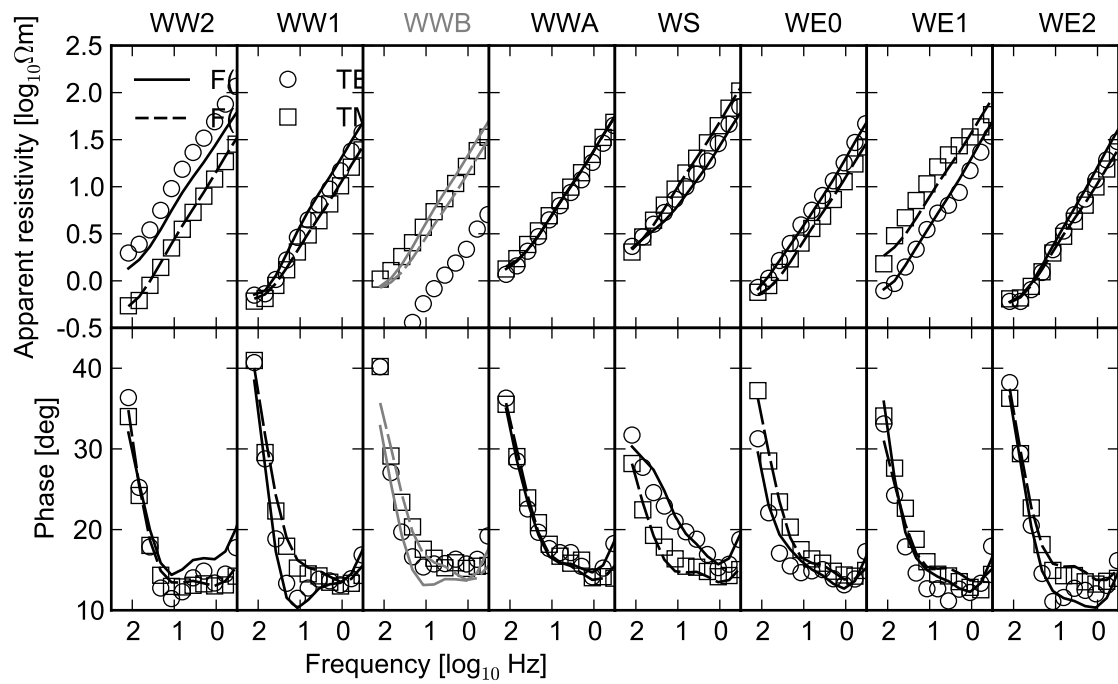


Figure 5.16: Fit of 2D MT model (Figure 5.15) forward responses to observations. Note that forward model responses were calculated at WWB, but that site was not part of the inversion.

Chapter 6

Area surrounding Beresford and Warburton Springs

Summary

Beresford and Warburton Springs (Chapters 4 and 5) are located in a playa which is 1570 m wide and 2200 m long. This playa lies on the southwestern edge of a thin, regionally extensive cover of Quaternary aeolian and alluvial sediments. These Quaternary sediments overlie the Bulldog Shale, which outcrops around the playa and to the southwest (Figure 6.1).

MT sites were collected to the north and the east of the playa at approximately 500 m intervals (Figure 6.1). The northern sites (1150 m-long Line A) are underlain by uniformly 1D ground which becomes more resistive at depth, while the eastern sites (4650 m-long Line C) are similar but contain a surface conductor which thickens to the east. At the base of the Bulldog Shale, a depth of approximately 100 m, the dip to the east is 0.6° , while at the base of the GAB aquifer sequences the dip is 1.4° .

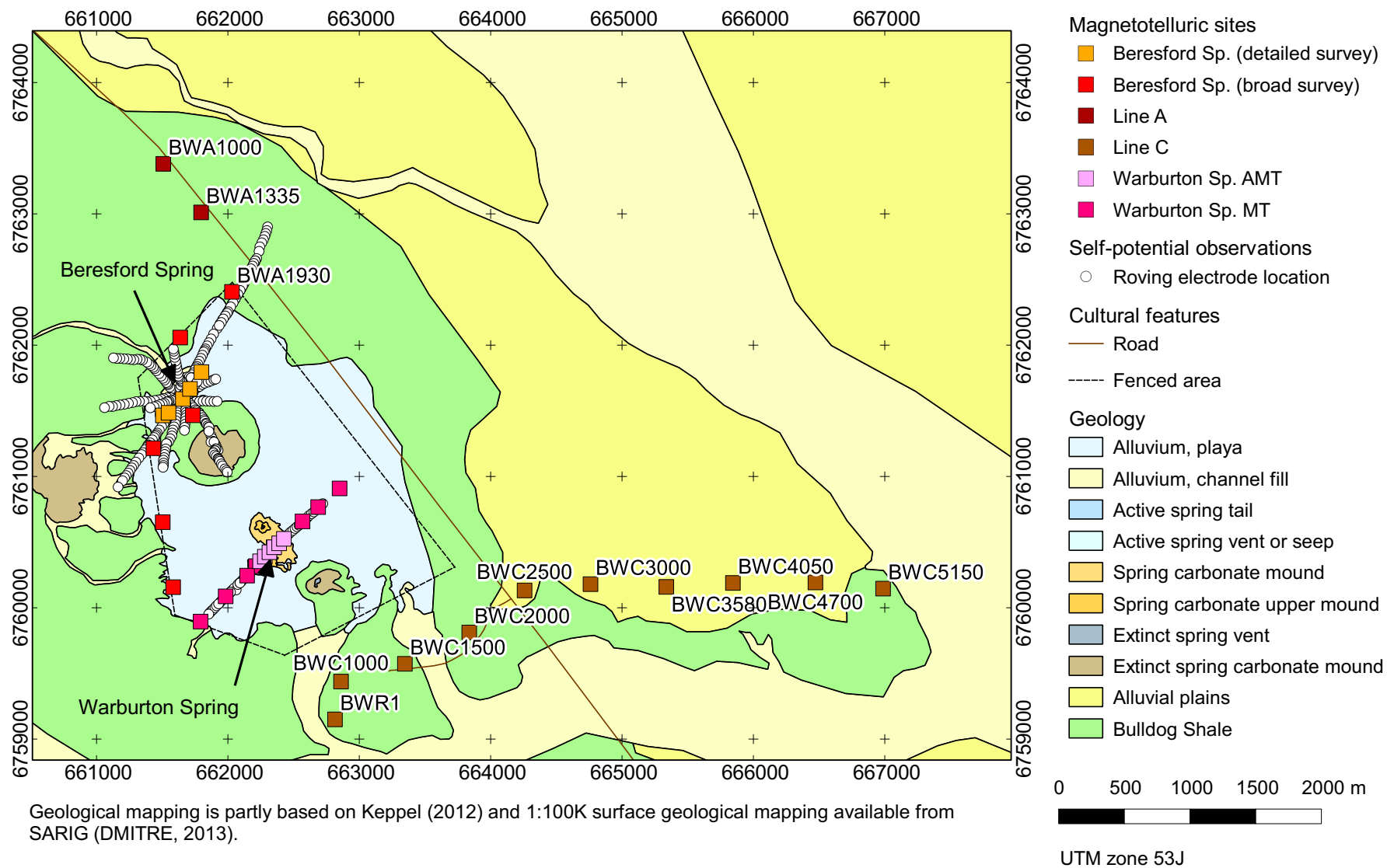


Figure 6.1: Location of MT sites near the Beresford Hill playa.

6.1 MT data

Magnetotelluric data were collected in the area around Beresford and Warburton Spring in June 2010. Sites were located along Line A, which extended to the north of the complex, and Line C, which ran east-west immediately south of the complex. The locations of these sites are shown on Figure 6.1.

6.1.1 Line A

Data were collected at three sites located at ≈ 500 m intervals to the north of the playa. These sites are aligned along Line A, which is 1150 m long and has a bearing of 150° . The sites are BWA1000, BWA1335, and BWA1930. All are located on outcropping Bulldog Shale, with BWA1930 immediately adjacent to the edge of the playa.

Responses were estimated between 125 Hz and 0.03 Hz, from 5.5 h windows of time series recorded overnight at a sampling rate of 500 Hz. Electrode dipoles were oriented north/south and east/west, and a pair of LEMI-120 induction coil magnetometers were used parallel to the electrode dipoles at each site to record the magnetic field.

Phase tensor ellipses are shown in Figure 6.2. The responses from all sites are close to 1D, with BWA1930 the most 2D site, with ellipses oriented approximately north/south at frequencies between 1 Hz and 16 Hz.

For comparison with the surveys at Beresford Spring and Warburton Spring, the data were rotated into the coordinate system x 315° , y 045° . Apparent resistivity and phase curves are shown in Figure 6.3. The main features of the data are:

1. Apparent resistivity increases as the frequency drops, changing from approximately $0.8 \Omega \text{ m}$ at 100 Hz to approximately $40 \Omega \text{ m}$ at 0.1 Hz.
2. There is a small split between phases at frequencies from 1 Hz to 30 Hz, where the Zy x phase is 2° to 3° higher than the Zxy phase. The split in phase is greatest at BWA1930.

6.1.2 Line C

Data were collected at ten sites, located at 500 m intervals over the area immediately to the south and east of the playa. The sites are located along Line C,

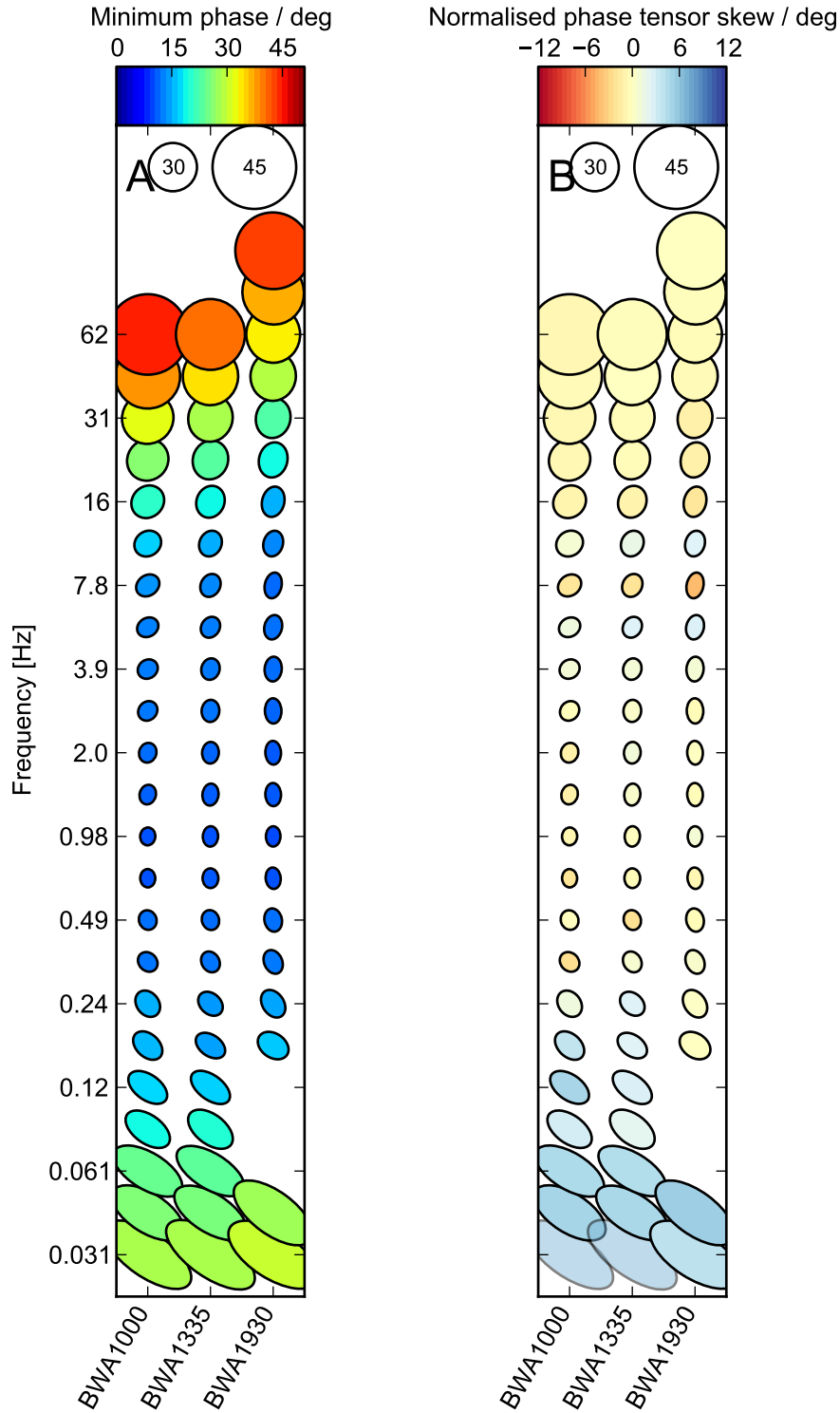


Figure 6.2: Pseudosection of phase tensors from Line A, filled with (A) minimum phase and (B) the normalised skew ψ (faint coloured ellipses have $|\psi| > 6^\circ$ and faint gray ellipses $|\psi| > 12^\circ$, both representing tensors significantly affected by 3D induction). Phase tensors have been rotated by 90° so that the major axis is parallel to the TE mode under a quasi-2D assumption (Booker, 2013) and ellipses with phases of 30° and 45° are shown in the upper left for comparison.

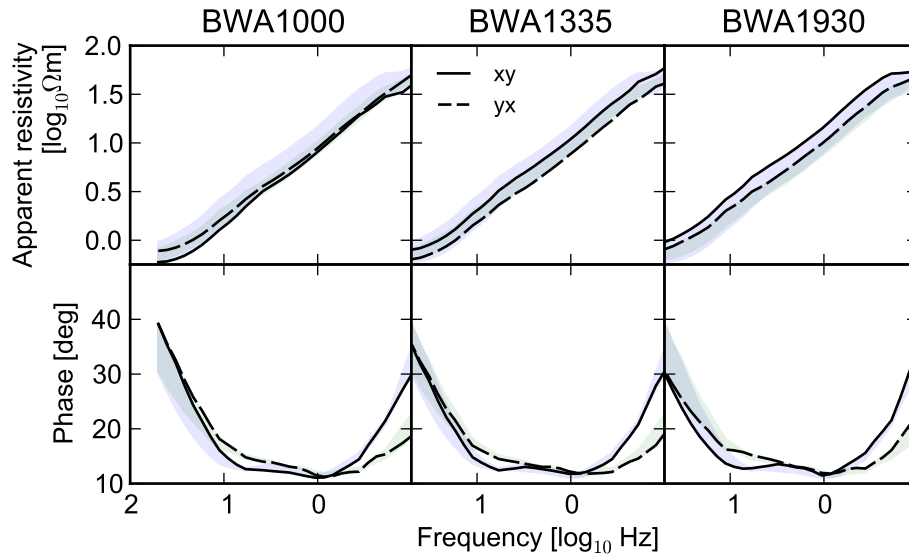


Figure 6.3: Cross-section of apparent resistivity and phase from MT sites along Line A in the Beresford/Warburton area. The shaded area is to help with comparison between sites and shows the range of data from all the sites on the section. Coordinate system: x 315° , y 45° .

which is 4650 m long and has a bearing of 052° for 1650 m at its western end and then extends for 3000 m at a bearing of 088° . The location of these sites are shown on Figure 6.1.

Responses at each site were estimated between 125 Hz and 0.03 Hz, from 5.5 h windows of time series recorded overnight at a sampling rate of 500 Hz. Electrode dipoles were oriented north/south and east/west, and a pair of LEMI-120 induction coil magnetometers were used parallel to the electrode dipoles at each site to record the magnetic field.

The MT sites are listed below in order from west to east, with their position on Line C indicated in parentheses:

1. BWR1 (780 m). Located 860 m south of Warburton Hill.
2. BWC1000 (1000 m). Located 760 m south of Warburton Hill.
3. BWC1500 (1500 m). Located 860 m south-east of Warburton Hill, this site lies on the western side of a swamp which drains the playa.
4. BWC2000 (2000 m). Located 500 m south-east of the south-eastern corner of the playa, this site lies on the eastern side of the swamp described above.
5. BWC2500 (2500 m). Located 780 m east of the south-eastern corner of

the playa. Line C changes bearing at this site to 088° .

6. BWC3000 (3000 m). Located 1285 m east of the playa.
7. BWC3580 (3580 m). Located 1855 m east of the playa.
8. BWC4050 (4050 m). Located 2350 m east of the playa.
9. BWC4700 (4700 m). Located 2975 m east of the playa.
10. BWC5150 (5150 m). Located 3500 m east of the playa. The new Angas Bore (borehole unit number 6239-44) is 230 m southeast from this site.

Phase tensor ellipses are shown in Figure 6.4. Almost all responses are 1D.

For comparison with the surveys at Beresford Spring and Warburton Spring, the data were rotated into the coordinate system x 315° , y 045° . Apparent resistivity and phase curves are shown in Figure 6.5. The main features of the data are:

1. All data are 1D at frequencies greater than 10 Hz.
2. There is a small split between phases at frequencies below 10 Hz, similar to the Type B anomaly described in Chapters 4 and 5, where the xy phase is elevated. This split occurs only for sites at the western end of the line (BWR1 and BWC1000).

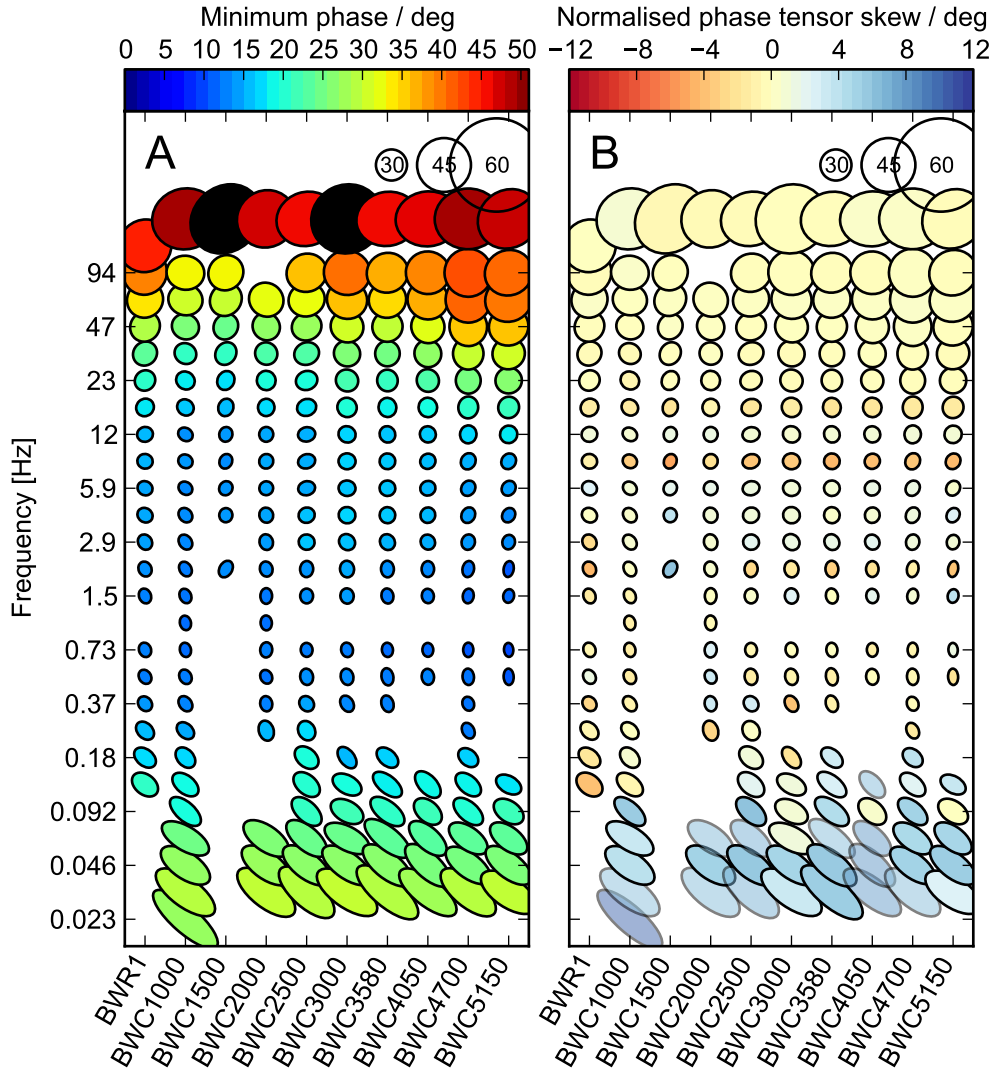


Figure 6.4: Pseudosection of phase tensors from Line C, filled with (A) minimum phase and (B) the normalised skew ψ (faint coloured ellipses have $|\psi| > 6^\circ$ and faint gray ellipses $|\psi| > 12^\circ$, both representing tensors significantly affected by 3D induction). Phase tensors have been rotated by 90° so that the major axis is parallel to the TE mode under a quasi-2D assumption (Booker, 2013) and ellipses with phases of 30° , 45° , and 60° are shown in the upper left for comparison.

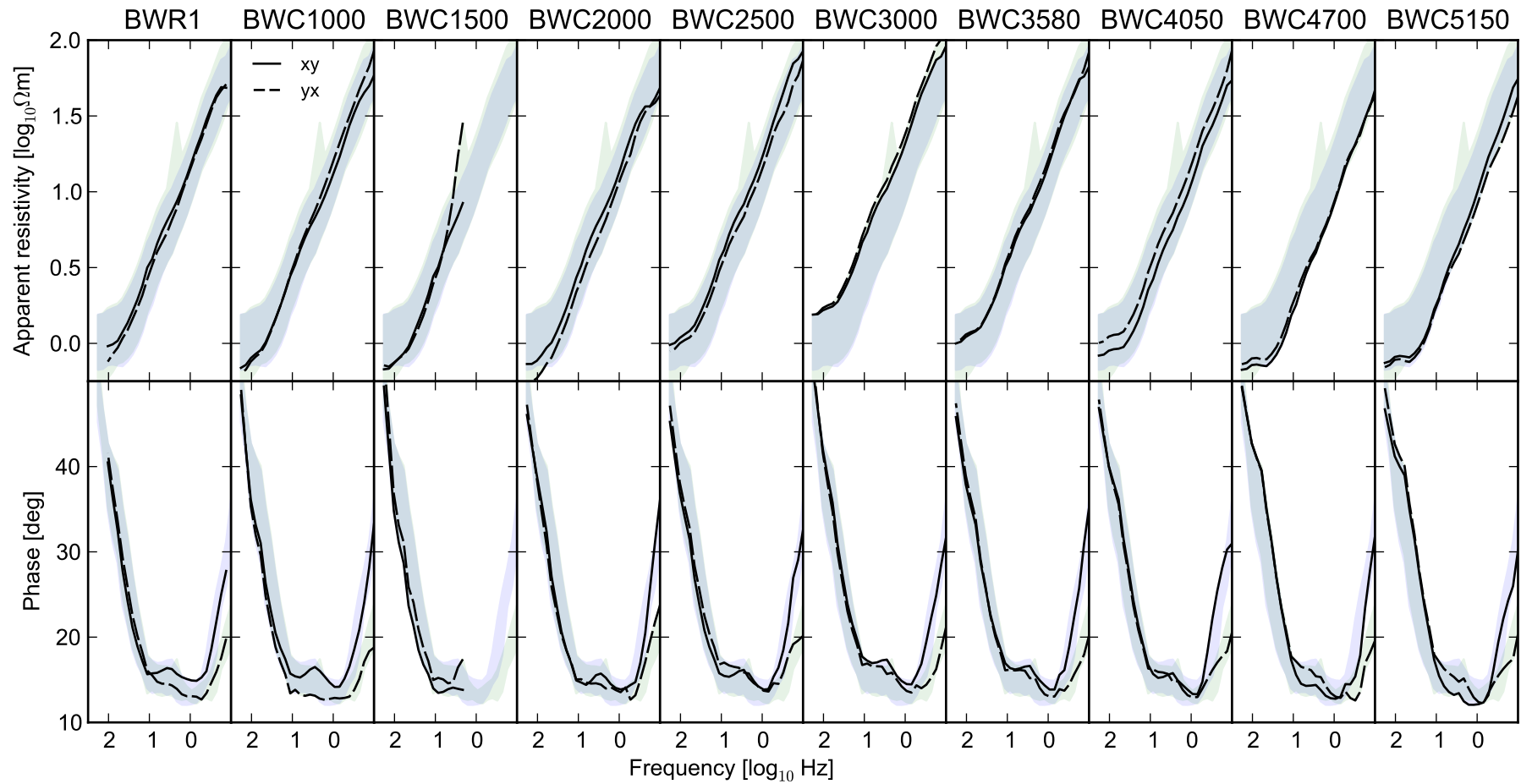


Figure 6.5: Cross-section of apparent resistivity and phase from MT sites along Line C in the Beresford/Warburton area. The shaded area is to help with comparison between sites and shows the range of data from all the sites on the section. Coordinate system: x 315° , y 45° .

6.2 2D MT modelling

The MT data along both lines were inverted for 2D resistivity models using Occam2D (de Groot-Hedlin and Constable, 1990).

6.2.1 Line A

The data were rotated to the coordinate system x 315° , y 045° , and Z_{xy} was used for the TE mode, Z_{yx} for TM. The result of an inversion constrained to fit within 20% of apparent resistivity and 5% of phase data is shown in Figure 6.6. The forward responses fit all the data quite well, and the model has almost no lateral resistivity variations, becoming uniformly more resistive with depth.

6.2.2 Line C

The data were rotated to the coordinate system x 315° , y 045° , and Z_{xy} was used for the TE mode, Z_{yx} for TM. The result of an inversion constrained to fit within 20% of apparent resistivity and 5% of phase data is shown in Figure 6.7. The forward responses fit all the data quite well.

The model is generally 1D, with resistivity increasing with depth. Sites to the east (right-hand side of Figure 6.7) tend to be more conductive at all depths down to more than 500 m, suggesting that a surface conductor is thickening to the east. The thickening can be measured with approximate contour lines showing the depths of different resistivities within the model: these are shown on Figure 6.7. Resistivities of $9\ \Omega\text{ m}$ are reached at a depth of $\approx 100\text{ m}$, and this depth increases to the east with a dip angle of 0.6° . Resistivities of $30\ \Omega\text{ m}$ occur at a depth of $\approx 250\text{ m}$, and this depth increases to the east at a dip angle of 1.4° .

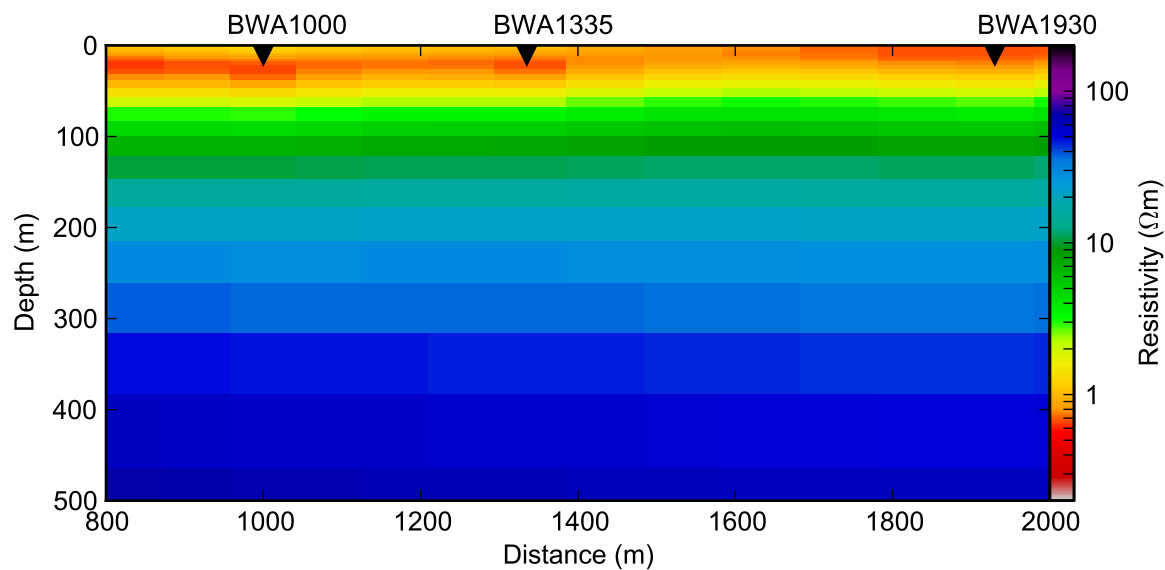


Figure 6.6: 2D resistivity model for MT data on Line A near the Beresford Hill playa, fitting to 5% of phase data and 20% of apparent resistivity data.

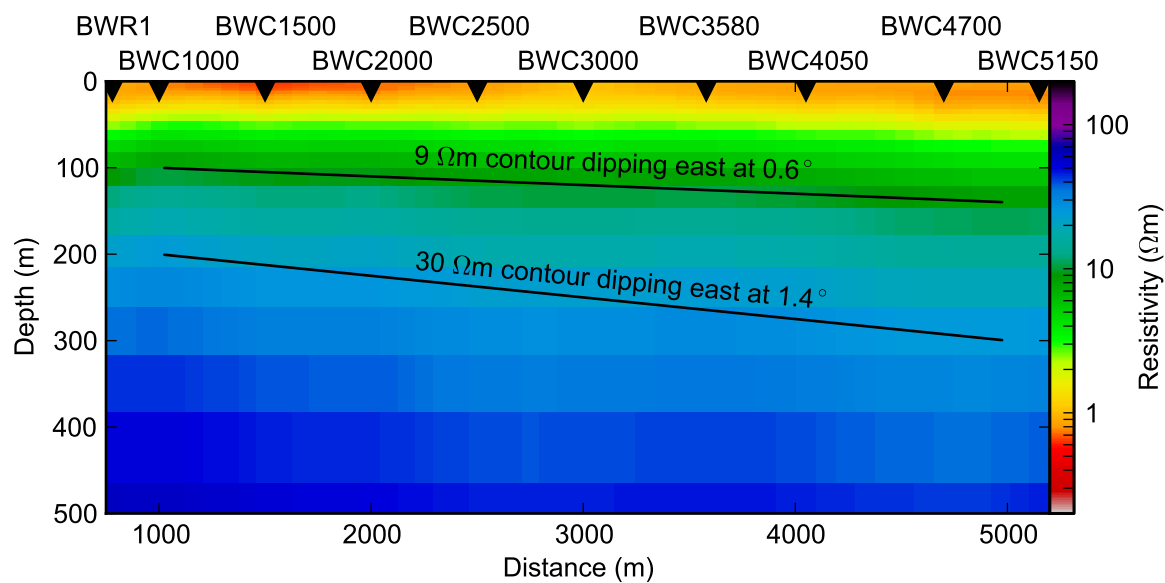


Figure 6.7: 2D resistivity model for MT data on Line C near the Beresford Hill playa, fitting to 5% of phase data and 20% of apparent resistivity data. 2D model strike is 315° .

Chapter 7

The Bubbler Spring complex

Summary

The Bubbler Spring complex is a group of springs located near Hamilton Hill, which is a mesa capped by extinct spring carbonates (see Figure 2.2 for location). The Bubbler is the largest of a group of at least seven active springs and at least five apparently inactive springs in a small area (Figure 7.1). These springs range in form between elevated tufa mounds (e.g. Blanche Cup) to spring vents surrounded by aeolian dunes ranging from 10^3 m^2 to 10^5 m^2 in area. The mounds are surrounded by modern alluvial sediments and extensive spring carbonate deposits, both of which are about 5 m thick and overlie Bulldog Shale (see Section 2.4 for further details).

Self-potential data were collected along three profiles, passing over at least five active springs. There are elevated SP features centred on almost all springs, with a laterally broad area of elevated potentials in the western part of the complex, between Blanche Cup and the Spring 403/Little Bubbler group of springs. There is also an unusually high potential gradient along the eastern side of these springs.

Time-domain electromagnetic and MT data were collected on two of the SP profiles, passing over the Little Bubbler, Blanche Cup, and Spring 403. The TEM data and resistivity inversions contain conductive responses along the edges of the aeolian dune surrounding the Little Bubbler and a resistive area underneath the mound,

possibly related to faulting. Two-dimensional MT inversions show that a shallow and slightly more resistive area exists beneath the western part of the complex, associated with elevated SP, suggesting structural thinning of the aquitard, and a dipping conductive feature near the eastern side edge of the group which may be a fault zone. Anisotropic 1D Monte Carlo modelling of MT sites from the central part of the spring complex shows that a layer containing conductive sheets oriented approximately north/south lies between depths of 300 m and 1000 m.

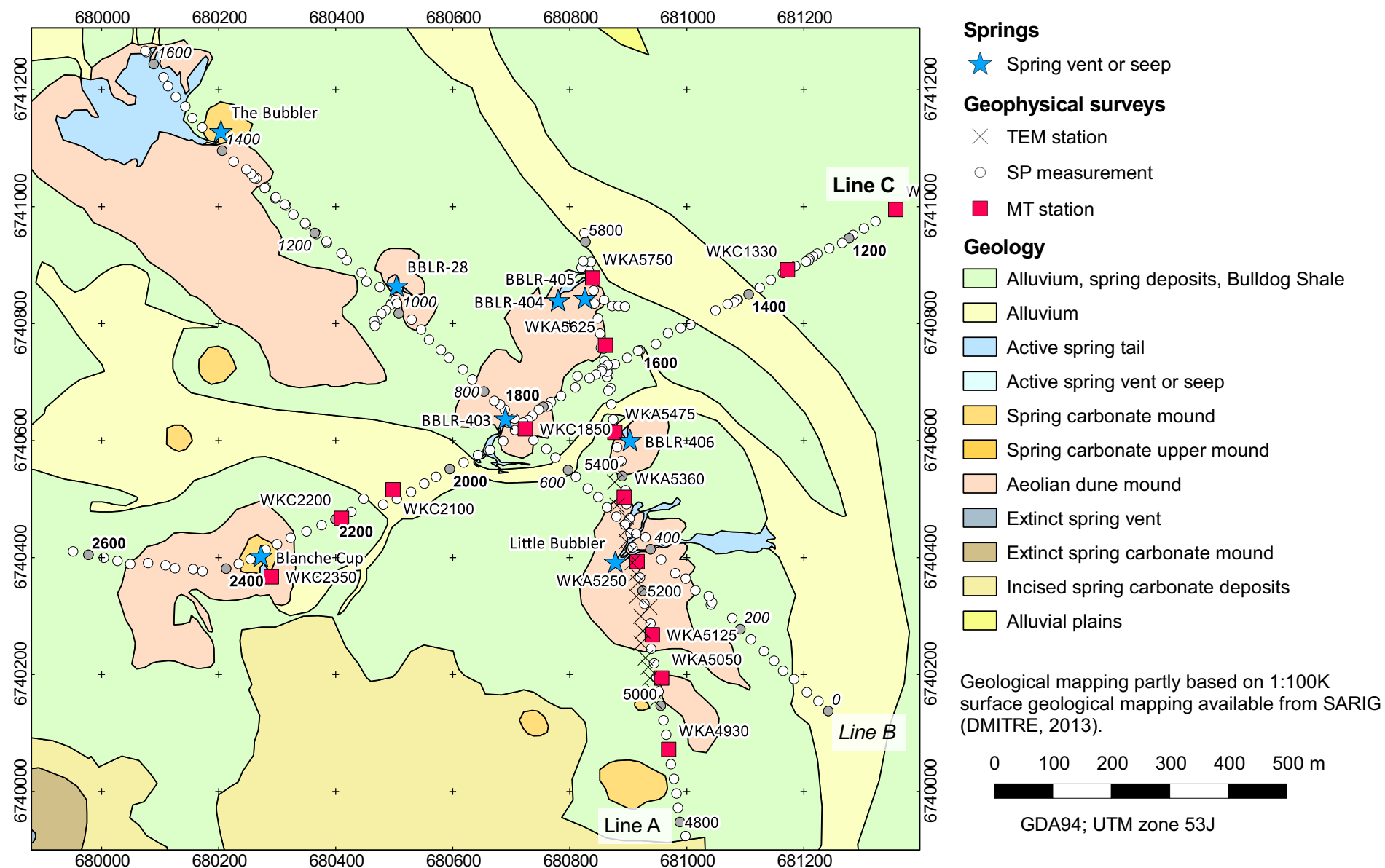


Figure 7.1: Location of SP, MT, and TEM observations at the Bubbler Spring complex, with distances on each line marked in metres.

7.1 SP

Self-potential data were collected at the Bubbler complex in April 2011 along three lines which pass over different spring vents in the complex. Line A is 1045 m long, bearing 350° , and runs over the Little Bubbler. Line B is 1624 m long, bearing 314° , and runs over Spring 403 and the Bubbler. Line C is 1483 m long, bearing 202° , and runs over Spring 403 and Blanche Cup. The location of these lines and the stations where observations were made are shown in Figure 7.1. The potential along each line was measured between a stationary base electrode and a roving electrode, which was moved along the line in 25 m steps. Lines A and B shared the same base electrode, which was located at station 4775 on Line A, while Line C used a different base electrode, located at station 1150 on Line C.

7.1.1 Data processing

Two corrections were applied to the potential data:

1. Forward and reverse potential measurements made in the field were averaged (see Section B.1).
2. Data north of station 5551 on Line A, and north-west of station 1020 on Line B had a correction potential added to the observed values. This was done so that data collected on different days at the same locations had similar absolute values. The difference is believed to be due to electrode potentials and soil conditions varying with time. The corrections are described further in Section B.1.3.1.

The graphs in the following sections show the observed (corrected) potentials and potential gradients calculated from each pair of observations as symbols, with lines showing a 60 m-wide moving average of the potential. Potential gradients are positive in the direction of increasing station numbers. Image reconstructions are calculated from the observed (corrected) potentials.

7.1.2 Line A

Self-potential observations from Line A are shown in Figure 7.2. Potentials range from 0 mV to 40 mV along the southern part of the line, with peaks at stations 5000 and 5200. Potential gradients are low, mostly in the range of -0.2 mV m^{-1} to 0.2 mV m^{-1} , with the exception of those bounding an area of

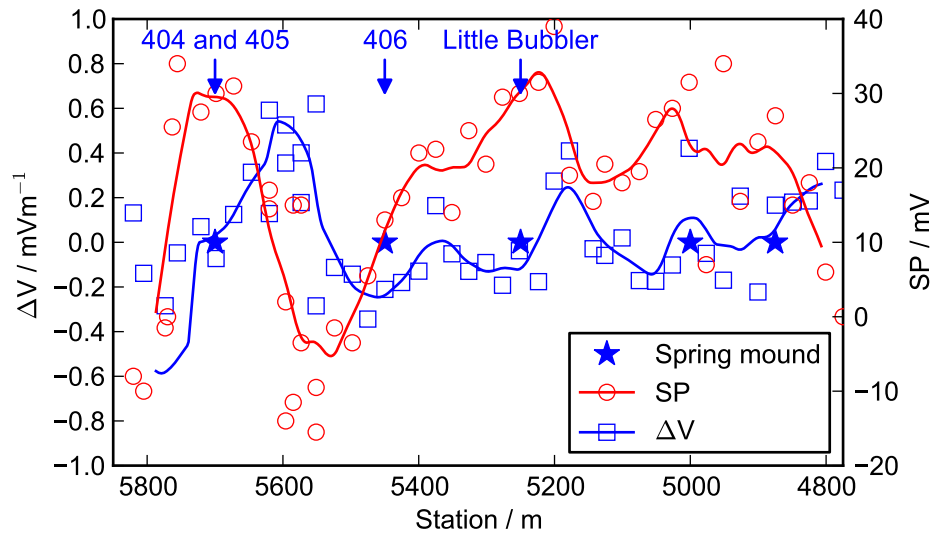


Figure 7.2: Self-potential and potential gradient ΔV along Line A. The solid lines are 3-point moving averages.

high potential at the northern end of the line, where the potential gradients are 0.6 mV m^{-1} and -1.2 mV m^{-1} at stations 5600 and 5775.

At least three of five spring mounds on the line (stars on Figure 7.2) are associated with elevated SP responses, where there are high absolute potential gradients on either side of the mound (positive ΔV when measured towards the centre of the mound) and anomalously high potential at the vent (Table 7.1). The mounds which are associated with this SP response are:

- the pair of Spring 404 and Spring 405, which have large growths of *Phragmites* reeds but no visible discharge at the surface
- the Little Bubbler, which is the only spring on Line A with present-day surface discharge
- the unnamed carbonate mound adjacent to station 4875, which has no evidence of surface discharge.

The mounds which are not associated directly with elevated SP responses are Spring 406, and the mound near station 5000 (which has a growth of *Phragmites* plants at the apex, but is apparently dry). The latter mound is adjacent to what would be an elevated response if not for an anomalously low potential measurement at station 4975, which is 35 mV less than adjacent measurements 25 m away.

Spring 406 is located in an area where the potential is dropping to the north; the potential gradient is approximately -0.2 mV m^{-1} over 125 m. This spring

Table 7.1: Elevated SP features associated with spring mounds on Line A. The absolute potential gradient ($|\Delta V|$) is noted where it is at its maximum, defining the edges of the elevated SP feature associated with the spring.

Spring	Station	$ \Delta V /\text{mV m}^{-1}$	Peak/mV	Magnitude/mV
Springs 404 and 405	5775	1.2		
	5700		30	35
	5580	0.7		
Little Bubbler	5300	0.15		
	5250		30	11
	5200	0.1		
Unnamed	4925	0.05		
	4900		24	5 to 10
	4825	0.2		

appears to lack a significant SP response, despite abundant *Phragmites* growth suggestive of activity. It is not clear why this is the case. It is possible that the response is affected by downward infiltration in the alluvial channel immediately north of Spring 406.

The image reconstruction (Figure 7.3B) shows that a dipole source may be present at the northern end of the line, with positive sources between stations 5600 and 5750 having very high correlation coefficients (0.2 to 0.5), and negative sources between stations 5575 and 5540 having coefficients from -0.1 to -0.3 . The positively-correlated end of the dipole is the area covered by the dunes surrounding springs 404 and 405, while the negatively-correlated end is a drainage area containing Holocene alluvium and spring carbonate deposits, immediately to the north of Spring 406.

There are much weaker correlations with positive sources in the southern part of the line, with the most positively-correlated areas having a correlation coefficient of 0.1 from the surface down to a depth of 70 m at stations 5225, 5025, and 4875. These areas are close to the location of springs on this part of the line (the Little Bubbler and two unnamed mounds).

7.1.3 Line B

Self-potential observations from Line B are shown in Figure 7.4. The potential is highest at the north-western end of the line (48 mV to 66 mV), dropping to lower values at the south-eastern end (20 mV to 30 mV). Three very low potentials (-5 mV to 5 mV) were recorded in the large present-day drainage

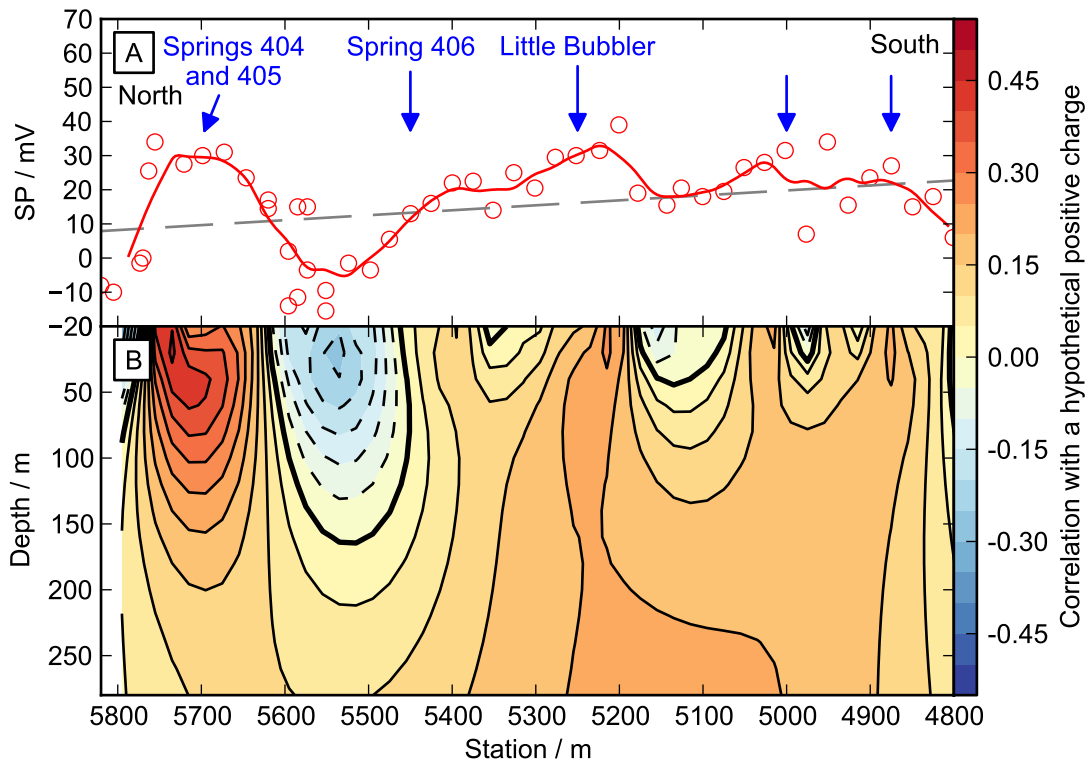


Figure 7.3: Self-potentials (A) and image reconstruction (B) over Line A. The grey dashed line is a least-squares linear fit to the SP. The solid line is a 3-point moving average.

channel to the east of the spring complex. The potential gradient is generally between -0.3 mV m^{-1} and 0.3 mV m^{-1} .

The line passes directly over three spring mounds (the Bubbler, Spring 28, and Spring 403), all of which are strongly associated with elevated SP features. The line also passes within 60 m of the Little Bubbler, where it is partly associated with an elevated feature in the SP. The elevated features range in magnitude from 10 mV to 28 mV and in width from 90 m to 225 m and are described in Table 7.2.

The image reconstruction (Figure 7.5) contains a number of areas which correlate to positive sources, with correlation coefficients from 0.1 to 0.25. All the areas are closely correlated to the location of springs except for station 120. The areas which retain significant positive correlations at depths greater than 150 m are those under the Bubbler, Spring 403, and the Little Bubbler.

The regional potential gradient is 0.013 mV m^{-1} (a potential difference of 20 mV over the length of the line). Although the peak potentials are similar for the three vents intersected on the line (56 mV to 58 mV), the 'inter-spring'

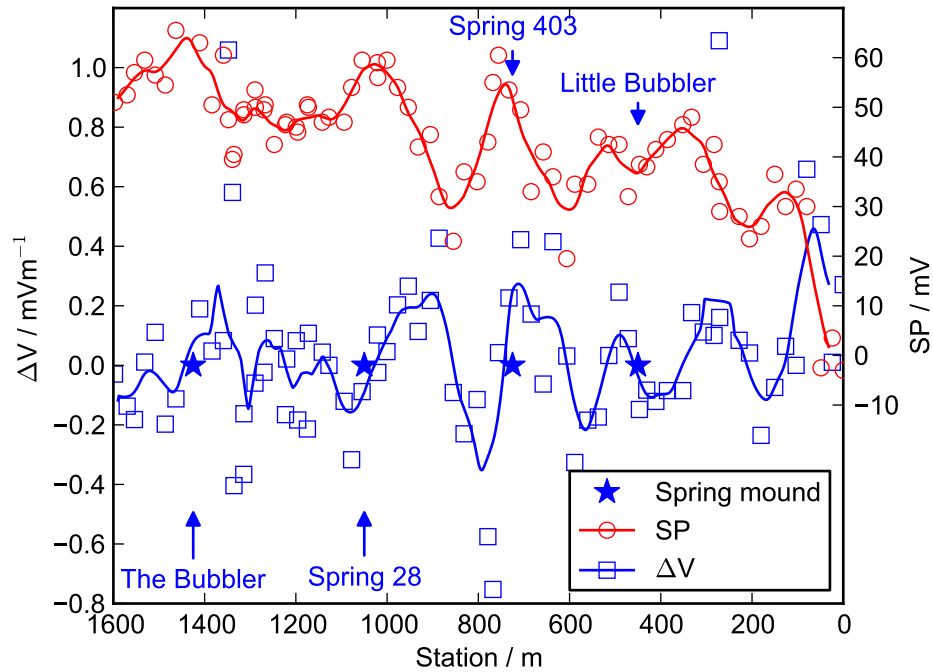


Figure 7.4: Self-potential and potential gradient ΔV along Line B at the Bubbler Spring complex. The solid lines are 3-point moving averages.

Table 7.2: Elevated SP features associated with spring mounds on Line B. The absolute potential gradient ($|\Delta V|$) is noted where it is at its maximum, defining the edges of the elevated SP feature associated with the spring. See text for discussion of the Little Bubbler feature, which has two peaks.

Spring	Station	$ \Delta V /\text{mV m}^{-1}$	Peak/mV	Magnitude/mV
The Bubbler	1575	0.10		
	1450		65	10 to 20
	1350	0.35		
Spring 28	1075	0.18		
	1025		58	15 to 28
	900	0.25		
Spring 403	790	0.48		
	750		56	26
	700	0.28		
Little Bubbler	450	0.12		
	375		46	16
	275	0.45		

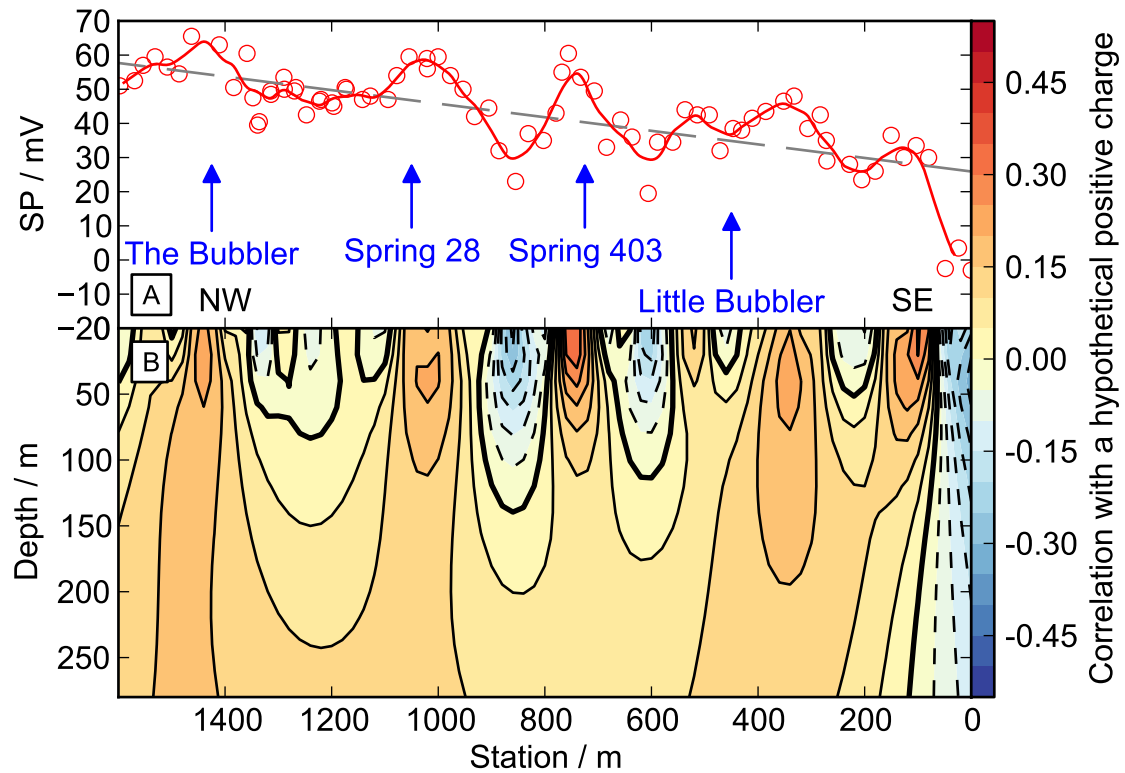


Figure 7.5: Self-potential data (A) and image reconstruction (B) over Line B. The grey line is a least-squares fit. The solid line is a 3-point moving average.

potential observed at the northwestern end of the line is approximately 15 mV to 25 mV higher than potentials in similar settings from the south-eastern end of the line. This may reflect generally greater upward flow at the northern end of the line.

7.1.4 Line C

Self-potential observations from Line C are shown in Figure 7.6. There is a significant difference in potential from west to east across the line. Between stations 1800 and 2425, the potential ranges from 24 mV to 50 mV, whereas potentials to the east of station 1800 are much lower, ranging from -20 mV to 20 mV. The potential gradient varies throughout the line. There are a number of sharp transitions in potential where the gradient is as high as $\pm 0.5 \text{ mV m}^{-1}$, and also an area where it remains between $\pm 0.1 \text{ mV m}^{-1}$.

The line passes over two spring mounds: Blanche Cup at station 2350 and Spring 403 at station 1875. Both mounds are presently active, discharging water at the surface, and both are correlated with elevated SP features (Table 7.3). These features have a magnitude of 50 mV compared to adjacent potentials (to

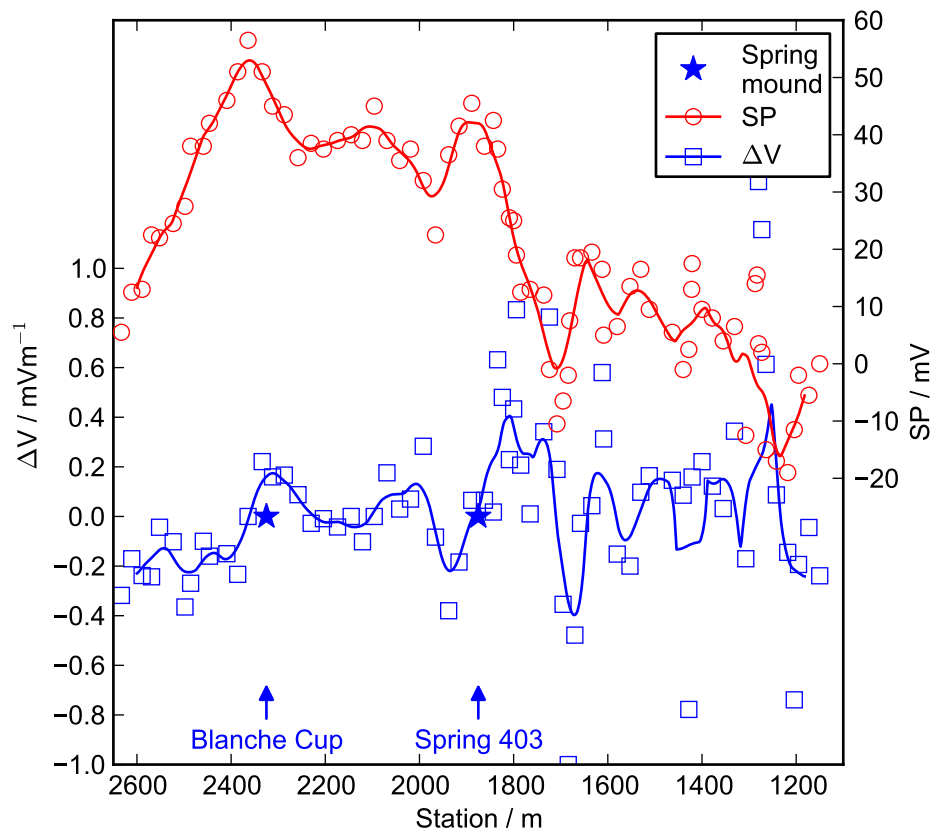


Figure 7.6: Self-potential and potential gradient ΔV along Line C. The solid lines are 3-point moving averages.

Table 7.3: Elevated SP features associated with spring mounds on Line C. The absolute potential gradient ($|\Delta V|$) is noted where it is at its maximum, defining the edges of the elevated SP feature associated with the spring. See text for discussion of the unnamed feature at station 1650.

Spring	Station	$ \Delta V /\text{mV m}^{-1}$	Peak/mV	Magnitude/mV
Blanche Cup	2600	0.22		
	2350		45	7 to 35
	2300	0.08		
Spring 403	1925	0.22		
	1875		43	13 to 50
	1775	0.35		
Springs 404 and 405	1675	1.0		
	1650		18	8 to 25
	1600	0.3		

the southwest at Blanche Cup, and to the northeast at spring 403). There is a plateau of moderately high potential between these features (between stations 1800 and 2600), and compared to this plateau the magnitude of the features associated with these springs is smaller (14 mV). Note that there is also a single isolated elevated potential at station 2100 that is not associated with any surface spring or mound, but it is surrounded by a gradual increase in potential indicated by the moving average.

There is also an elevated SP feature centred on station 1650. There is no spring at this location; it is 120 m from the pair of Springs 404 and 405 to the north, and the same distance from Spring 406 to the south. It is also very close to the intersection with measurements along Line A: all the potentials from this area are shown in Figure 7.7. The elevated potentials from Line C are clearly part of the area of elevated SP extending further north along Line A.

The image reconstruction (Figure 7.8) contains two large zones that correlate to positive sources to depths of several hundred metres. The first of these is the area of high potential between Blanche Cup and Spring 403 (between stations 2600 and 1900). It is quite likely that positive sources are distributed relatively evenly underneath the western part of the line (the plateau of elevated potential), especially at depths greater than 100 m.

The second positively-correlated area is at the eastern end of the line between stations 1450 and 1250, where the correlation coefficient is 0.2 near the surface and above 0.05 slightly to the west, down to 250 m depth. This feature is

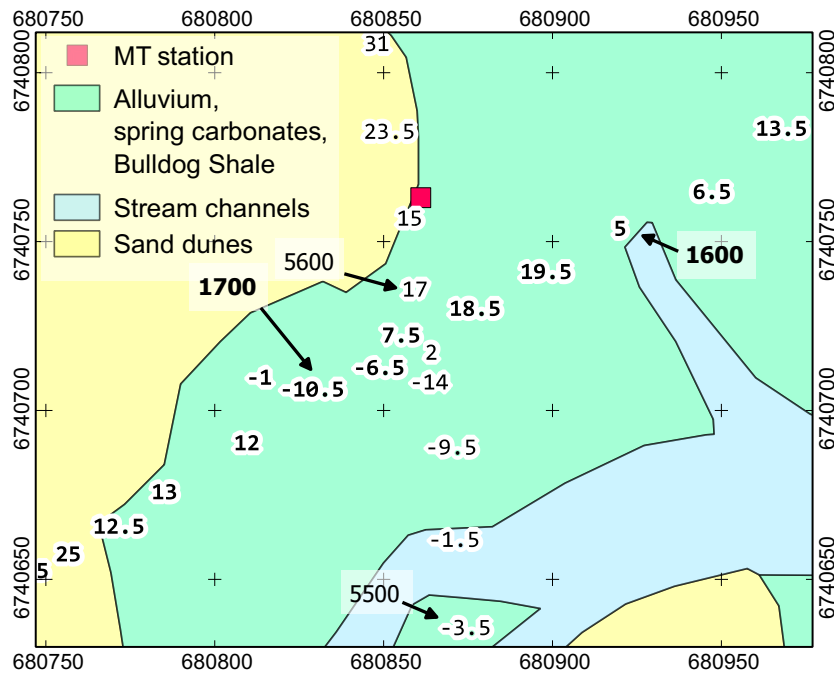


Figure 7.7: Map of potentials near the intersection of Line A (normal typeface) and Line C (bold typeface). Note that the potentials on these two lines are not directly comparable, as they are measured against different base electrodes. North is up and axes coordinates are eastings and northings in metres (GDA94, UTM zone 53J).

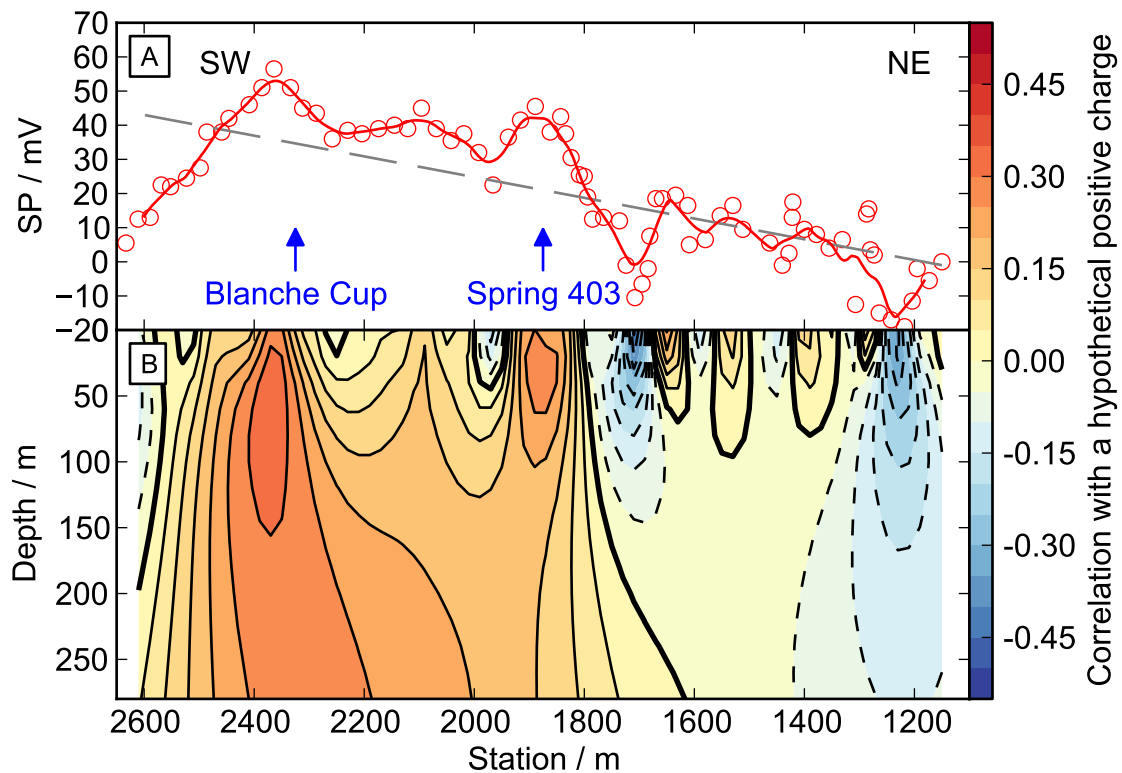


Figure 7.8: SP data (A) and image reconstruction (B) over Line C at the Bubbler Spring complex. The grey line is a least-squares fit. The solid line is a 3-point moving average.

caused by the high potential gradient at station 1275 of more than 1 mV m^{-1} , which causes a dipole to occur in the image reconstructions. The positive end of the dipole is the positively-correlated area as noted above, and the negative end is further east, underneath station 1225 in Figure 7.8.

In order to investigate how important various data points are to the interpreted dipole source, various groups of data were removed from the dataset and image reconstructions were recalculated for the remaining data points. These are shown in Figure 7.9. The positive end of the dipole disappears only when the particularly high gradient at station 1275 is removed, as in Figure 7.9H, although it should be noted that the significance of the correlation to positive sources can be reduced through removal of anomalously high potentials in the area, as in Figure 7.9D. Station 1275 is located about 50 m east of the eastern edge of the spring carbonate platform deposits that exist extensively across the whole complex. Further east are primarily outcrops of Bulldog Shale.

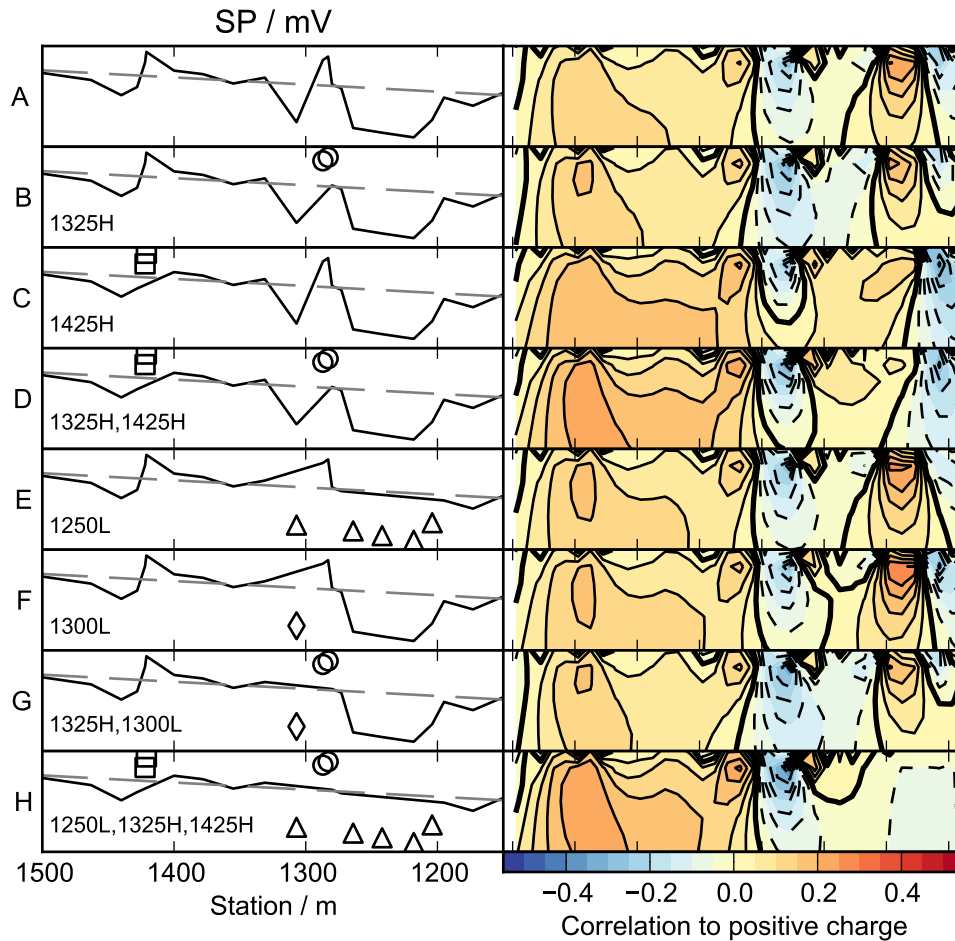


Figure 7.9: Image reconstructions calculated for subsets of the Line C data between stations 1150 and 1500 which are left after removal of different sets of measured potentials. The symbols show the removed data points, and the solid line shows the remaining data (stations further west than station 1500 are unchanged and not shown). The right panel contains the image reconstruction for the remaining data. The grey dashed line is the least-square fit to the original data, in all panels.

7.2 TEM

Time-domain electromagnetic data were collected over a 400 m-long section of Line A, which has a bearing of 350° , and runs north across the spring mound associated with the Little Bubbler. The latter's spring mound extends between TEM stations 5110 and 5350. The TEM measurements did not extend further north to the vicinity of springs S04, 405, or 406. The survey used Zonge Engineering's NanoTEM system in a central in-loop configuration, with a 20 m square transmitter loop and 5 m square receiver loop.

The decay profile varied little with position along the line, with the response dropping to nearly zero at > 2 ms. The most significant lateral variation in the decay profiles is an elevated response at early to middle times between stations 5070 and 5130, which is most pronounced at station 5110 (Figure 7.10).

The transient responses were inverted for a resistivity model using Zonge Engineering's STEMINV routine. The resulting model is shown in Figure 7.11, and the fit to the data for selected stations is shown in Figure 7.12. The fit is excellent for middle and late decay times, but in general the forward model responses underestimated the magnitude of the early time response at all stations.

The model consists of a surface conductor approximately 15 m thick, with the most conductive part of $1.2 \Omega \text{ m}$ occurring 7 m below the surface. Underlying this conductor is a slightly more resistive layer ($2 \Omega \text{ m}$ to $3 \Omega \text{ m}$) extending down to a depth of at least 50 m. The overall variation in resistivities in the model is approximately half an order of magnitude.

There is some lateral variation in the model around station 5350, on the northern margin of the Little Bubbler spring mound. Here the surface conductor is thinner and nearer the surface, with a resistivity of $2 \Omega \text{ m}$ at a depth 10 m compared to resistivities of about $1.4 \Omega \text{ m}$ elsewhere on the line at the same depth. The model in this area is also more resistive in the underlying layer, with a resistivity of $5 \Omega \text{ m}$ to $6 \Omega \text{ m}$ at a depth of 35 m. There is another resistive section in the lower layer at station 5210 (the centre of the spring mound), with a resistivity of $4 \Omega \text{ m}$ at a depth of 35 m.

The southern margin of the spring mound is between stations 5090 and 5110, which is the location of elevated transient responses in the raw data, and also a more conductive area in the model. The model resistivity underneath

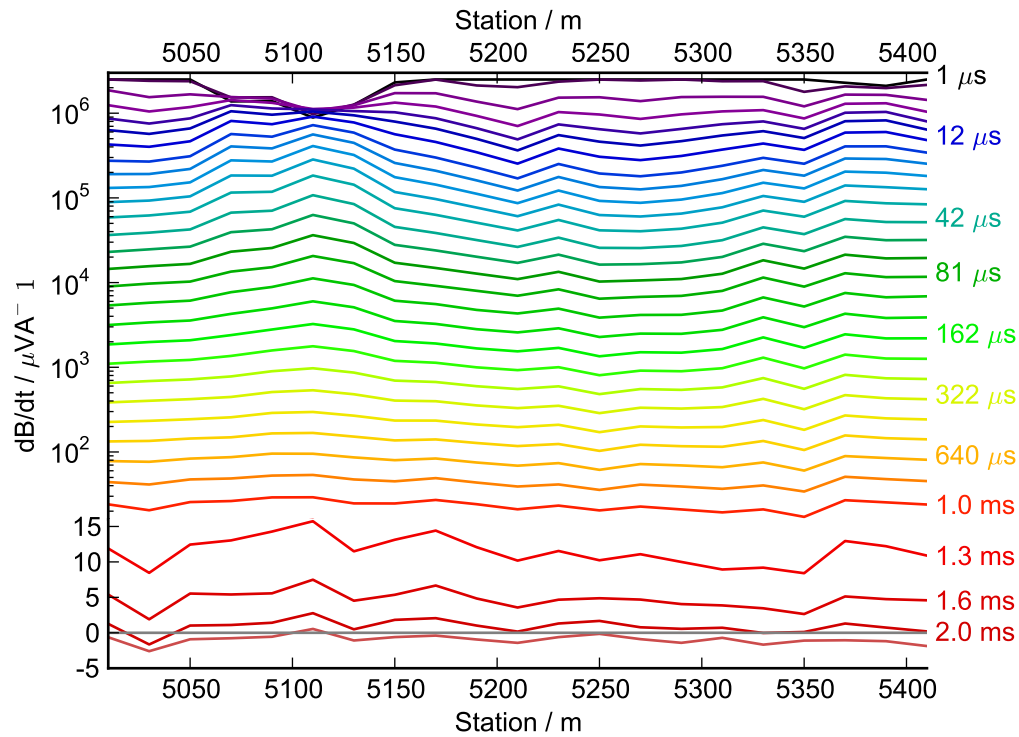


Figure 7.10: TEM responses along Line A for all decay times between $1 \mu\text{s}$ and 2.5 ms. The decay times for selected curves are shown on the right hand side.

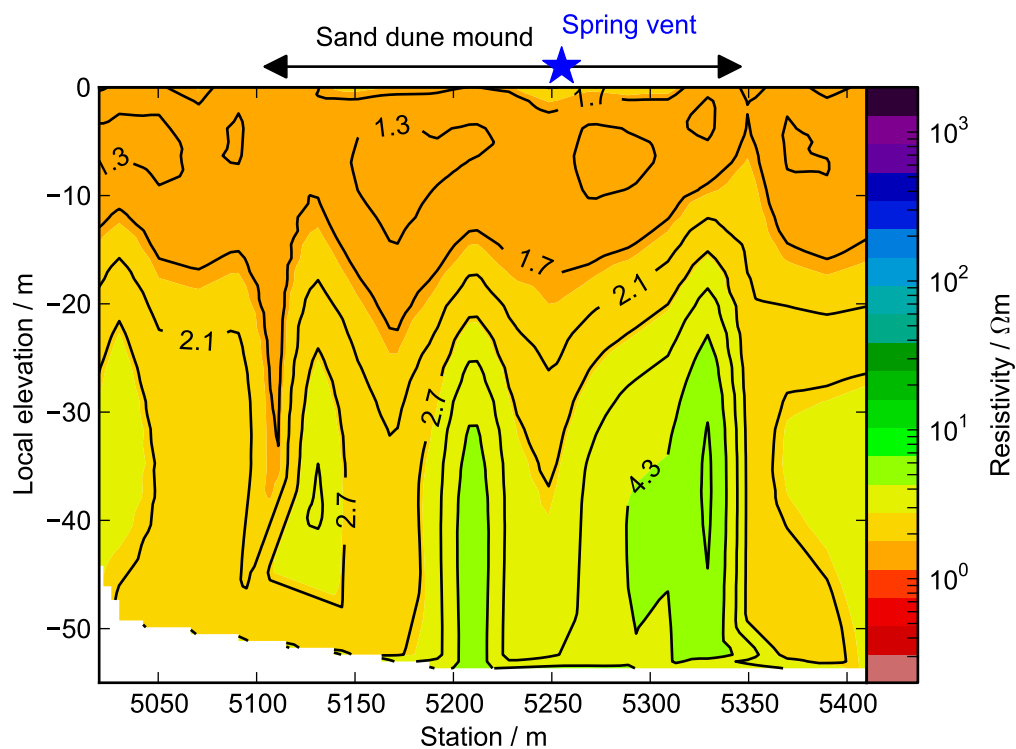


Figure 7.11: Resistivity model obtained by 1D inversion of TEM data.

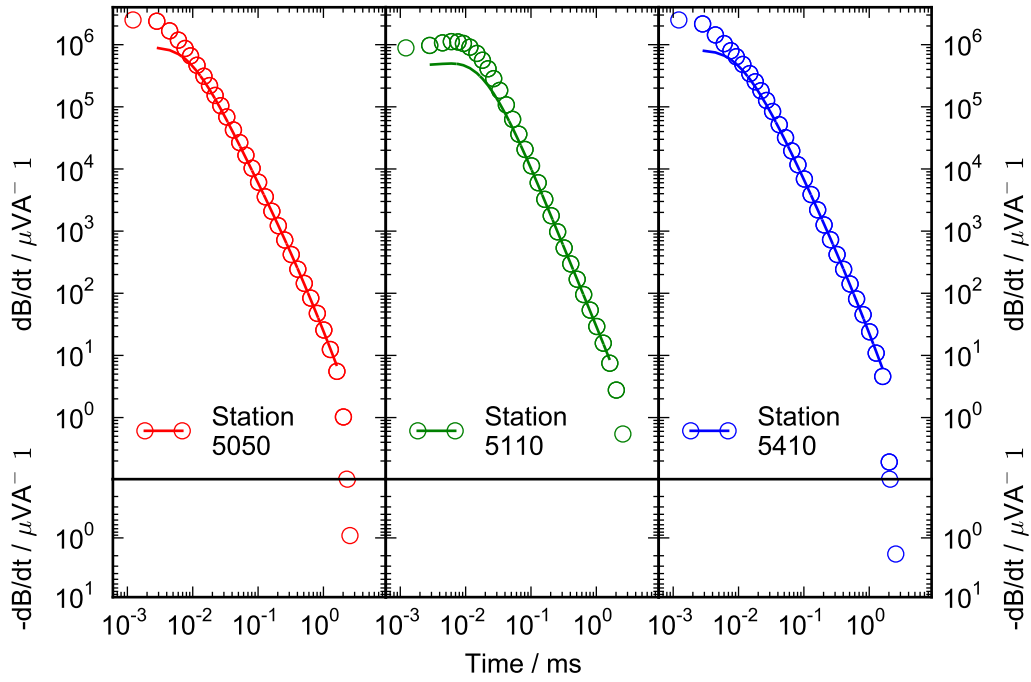


Figure 7.12: Fit of resistivity model (Figure 7.11) to TEM data for selected sites. Circles show the observed data, and lines show the modelled data.

station 5110 is between $1 \Omega \text{ m}$ to $2 \Omega \text{ m}$ down to a depth of 40 m. The existence of a small topographical scarp (about 3 m high) suggests that a fault may be present along the southern edge of the spring mound. See Section 9.2.4 for further discussion.

7.3 MT data

Magnetotelluric data were collected at the Bubbler Spring complex in April 2011. Sixteen sites were located along two profiles: Line A runs approximately north–south across the Little Bubbler spring mound and the mound surrounding Springs 404 and 405; Line C runs from south-west to north-east, crossing directly over Blanche Cup and away from the complex to the east (Figure 7.1).

7.3.1 Line A

Data were collected at nine sites located at approximately 120 m spacings along Line A, which is 820 m long on a bearing of 345° (Figure 7.1).

Responses were estimated between 375 Hz and 0.06 Hz, from 4 h windows of time series recorded overnight at a sampling rate of 1000 Hz. Electrode

dipoles were oriented north/south for x and east/west for y . Pairs of LEMI-120 induction coil magnetometers were located parallel to the dipoles at each site.

In order from north to south along this line, the sites collected are listed below (the distance along the line is incorporated into the site name):

1. WKA5750 is on the northern edge of the sand dune surrounding Springs 404 and 405. The *Phragmites* reeds marking the spring vents are 60 m distant from the site.
2. WKA5625 is on the southern edge of the same dune, approximately 100 m away from the vents of Springs 404 and 405.
3. WKA5475 is on carbonate deposits at the northern edge of the Spring 406 mound, the vent for which is approximately 50 m distant.
4. WKA5360 is on the northern edge of the Little Bubbler dune system, 112 m north of the vent.
5. WKA5250 is in the centre of the Little Bubbler dune system. The vent is 35 m from the site.
6. WKA5125 is on the southern edge of the Little Bubbler dunes, 145 m south of the vent.
7. WKA5050 is on modern alluvial clay and silt deposits 100 m south of the Little Bubbler dunes.
8. WKA4930 and WKA4645 are on eroded spring carbonate deposits, which are extensive across the south-western part of the spring complex.

Phase tensor ellipses are shown in Figure 7.13, with the orientation of the major axis shown in Figure 7.14. Most sites are 1D at high frequencies, especially at the northern end of the line. There is a slight ellipticity to responses in the bandwidth from 2 Hz to 60 Hz, with TE mode currents oriented toward approximately 070° (Figure 7.14). The ellipticity is more pronounced at WKA4645, where ellipses are aligned towards an azimuth of 290° between 20 Hz and 200 Hz. There is no directionality to the phase tensor response at frequencies below 2 Hz in the north, and 16 Hz in the south, although below 0.5 Hz a regional quasi-2D/3D response aligned towards an azimuth of 310° occurs.

At the highest frequencies there is a 3D response at sites WKA5250, WKA5125,

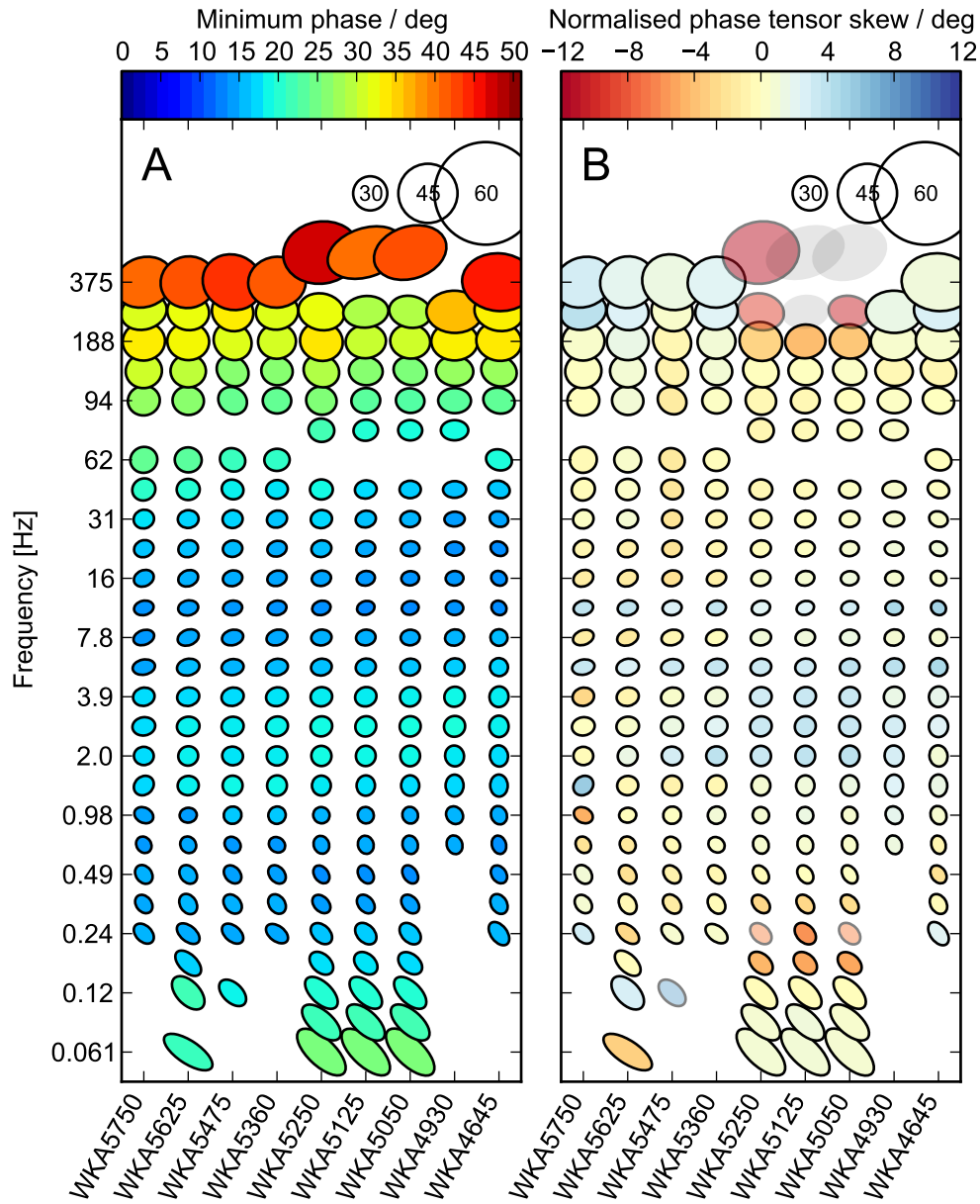


Figure 7.13: Pseudosection of phase tensors from Line A, filled with (A) minimum phase and (B) the normalised skew ψ (faint coloured ellipses have $|\psi| > 6^\circ$ and faint gray ellipses $|\psi| > 12^\circ$, both representing tensors significantly affected by 3D induction). Phase tensors have been rotated by 90° so that the major axis is parallel to the TE mode under a quasi-2D assumption (Booker, 2013) and ellipses with phases of 30° , 45° , and 60° are shown in the upper left for comparison.

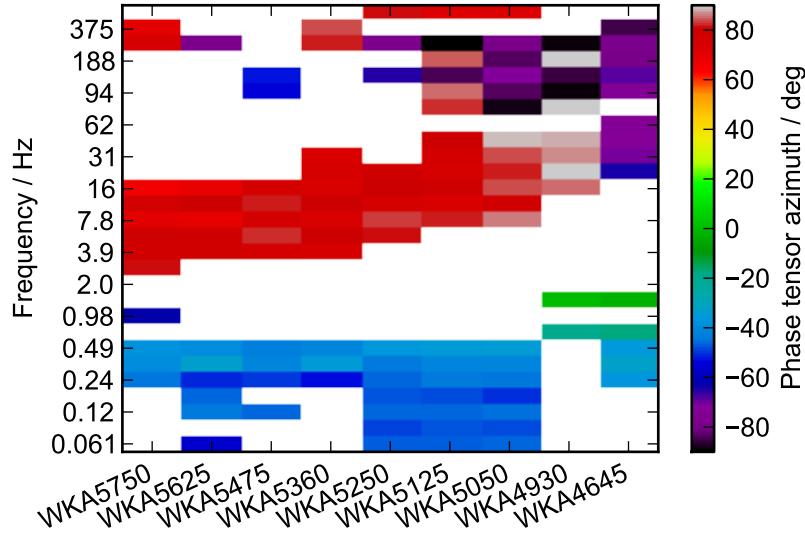


Figure 7.14: Pseudosection of phase tensor azimuths (θ_{ellipse}) along Line A. Azimuths are only shown for tensors with a split in the principal phases greater than 3° .

and WKA5050, oriented towards an azimuth of 080° . The effect is strongest at WKA5125, which suggests it may be related to either the southern edge of the dunes surrounding the Little Bubbler, or the narrow drainage depression which runs in the same direction between these dunes. See Section 9.2.4 for further discussion. The effect is only present for frequencies at these stations above 200 Hz, which implies it must be due to features within the maximum penetration depth of 50 m for this frequency (Spies, 1989).

Apparent resistivity and phase soundings are shown in grid coordinates (x 000° , y 090°) in Figure 7.15. There is a split in the phase curves of 3.5° for all sites at frequencies around 10 Hz. There is little variation in apparent resistivity between sites. The phase curves both drop to minima centred around 10 Hz to 20 Hz, with the Zxy minimum phase around 18° compared to 15° in the Zyx phase. The phases then rise by 2° to 5° before dropping to a common minimum at 0.9 Hz. At lower frequencies both phases rise steeply together.

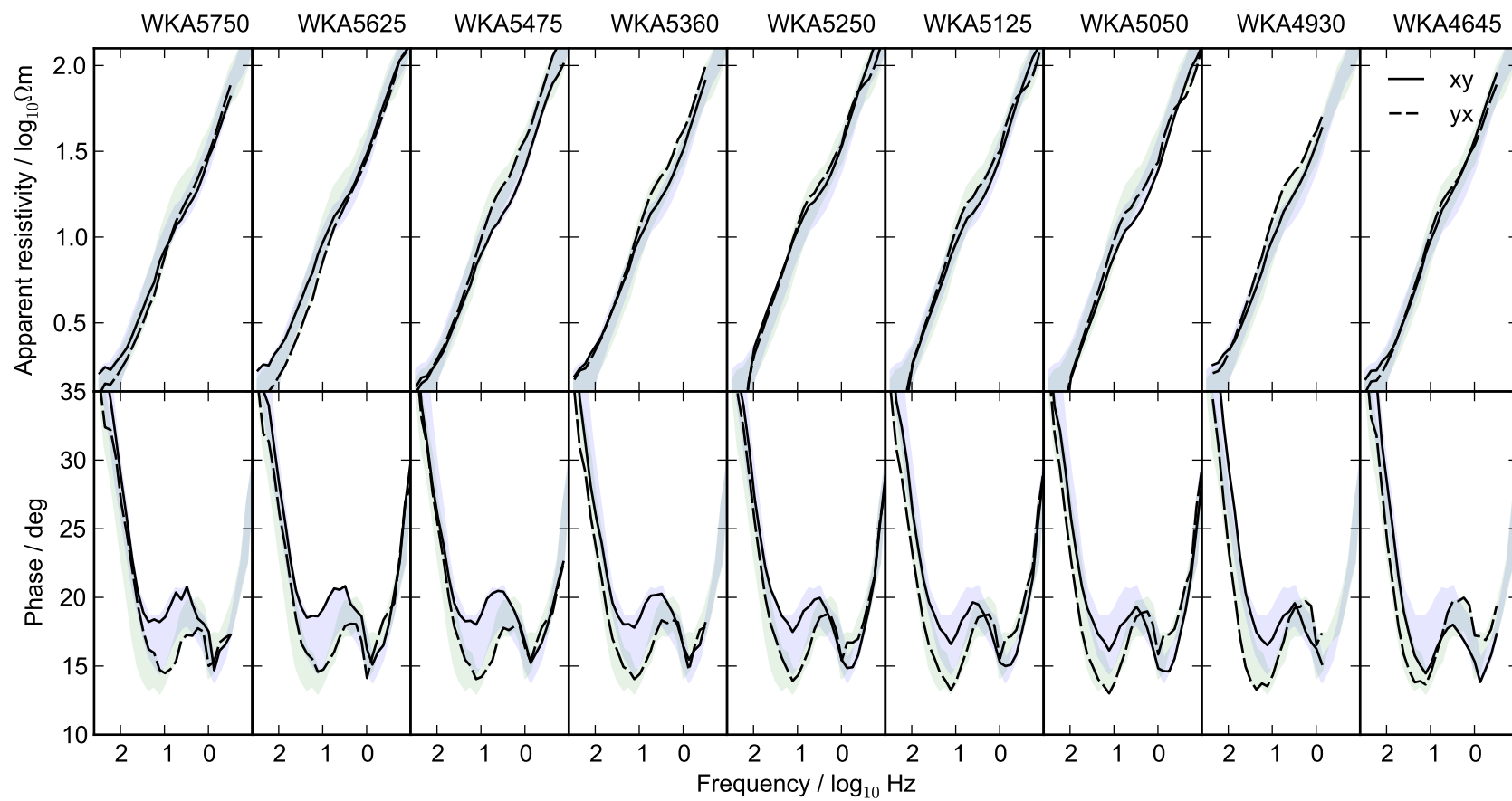


Figure 7.15: Cross-section of apparent resistivity and phase from MT sites on Line A. The shaded area shows the range of data from all the sites on the section and is to help with comparison between sites. Coordinate system: x 000°, y 090.

The phase split is similar at WKA5750, WKA5625, and WKA5475. The southernmost site (WKA4645) is different, with similar higher-frequency minimum phases in both modes. The sites in the middle of the line, near the Little Bubbler spring mound, are transitional between the two kinds of phase splits, with smaller phase splits than sites to the north. Although the gradual variation in the shape of the phase curves along the centre and southern end of the line supports a 2D interpretation (see Section 7.5 below), the northern phase split is very similar to those seen on the central and western parts of Line C (Section 7.3.2), and to the Type A feature seen at Beresford Spring, suggesting that anisotropic conductivity is a possible cause (see Section 7.4).

7.3.2 Line C

Data were collected at seven sites located at approximately 200 m spacing along Line C, which is 1250 m long with a bearing of 240° (Figure 7.1).

Responses were estimated between 375 Hz and 0.06 Hz, from 4 h windows of time series recorded overnight at a sampling rate of 1000 Hz. Electrode dipoles were oriented north/south for x and east/west for y. Pairs of LEMI-120 induction coil magnetometers were located parallel to the dipoles at each site.

In order from southwest to northeast along this line, the sites collected are listed below:

1. WKC2350 is on the Blanche Cup carbonate mound. The dipoles straddle the upper mound.
2. WKC2200 and WKC2100 are on modern alluvial deposits. WKC2100 is approximately midway between Blanche Cup and the Spring 403 mound (220 m to 260 m from both).
3. WKC1850 is on aeolian dune deposits on the south-eastern side of the Spring 403 vent, which is 40 m away.
4. WKA5625, which lies on the intersection of Lines A and C, is on the southern edge of the dunes surrounding Springs 404 and 405, approximately 100 m south of these springs' vents.
5. WKC1330 and WKC1100 are on Quaternary alluvium underlain by Bulldog Shale, more than 400 m east of the nearest spring vent (Spring 405).

Phase tensor ellipses are shown in Figure 7.16, and the orientation of the major axis in Figure 7.17. Most sites are close to 1D at high frequencies (circular ellipses). There are three areas in which phase tensor ellipses become elongated:

1. At a frequency of 70 Hz TE mode currents at the two easternmost sites WKC1100 and WKC1330 are oriented towards an azimuth of approximately 020° , with the orientation gradually rotating to the east at lower frequencies (070° at 2.5 Hz) (Figure 7.17).
2. In a similar bandwidth (3 Hz to 40 Hz) the westernmost sites WKC2350, WKC2200, and WKC2100 are oriented towards an azimuth of 080° to 090° (Figure 7.17). This is a similar orientation to that seen at the northern end of Line A, although the bandwidth here is a little higher. The bandwidth may be higher due to slightly higher resistivity in this part of the Bubbler complex. Note that station WKC1850 has responses oriented similarly in this bandwidth to those at WKA5625, which is located at the intersection of Lines A and C.
3. Almost all sites are oriented toward an azimuth of approximately 310° below a frequency of 0.5 Hz; this is the regional 2D response mentioned previously (Figure 7.17).

Apparent resistivity and phase curves in grid coordinates (x 000° , y 090°) are shown in Figure 7.18. The phase split seen at the northern end of Line A is also present at WKC1850. A larger phase split is seen further west on Line C at stations WKC2350, WKC2200, and WKC2100, with the higher-frequency phase minima of the two modes occurring as 21° at 15 Hz in Zxy, and 14° at 11 Hz in Zyx at WKC2350. The phase split is similar to the Type A split described at Beresford Spring (Section 4.4.1), although at a slightly higher frequency.

Slight variation in the phase curves is seen with distance along the line (reduction in the size of the split with distance to the east), but a significant change occurs between WKC2100 and WKC1850, and another change between WKA5625 and WKC1330. The two easternmost sites have similar behaviour for the phase in both modes, with the Zxy mode dropping to slightly lower phases (13°) at the higher-frequency minimum (12 Hz) compared to the Zyx mode. Note that the Zyx phase curves vary only gradually across the line. This is evidence that the Zxy mode should be interpreted as the TM

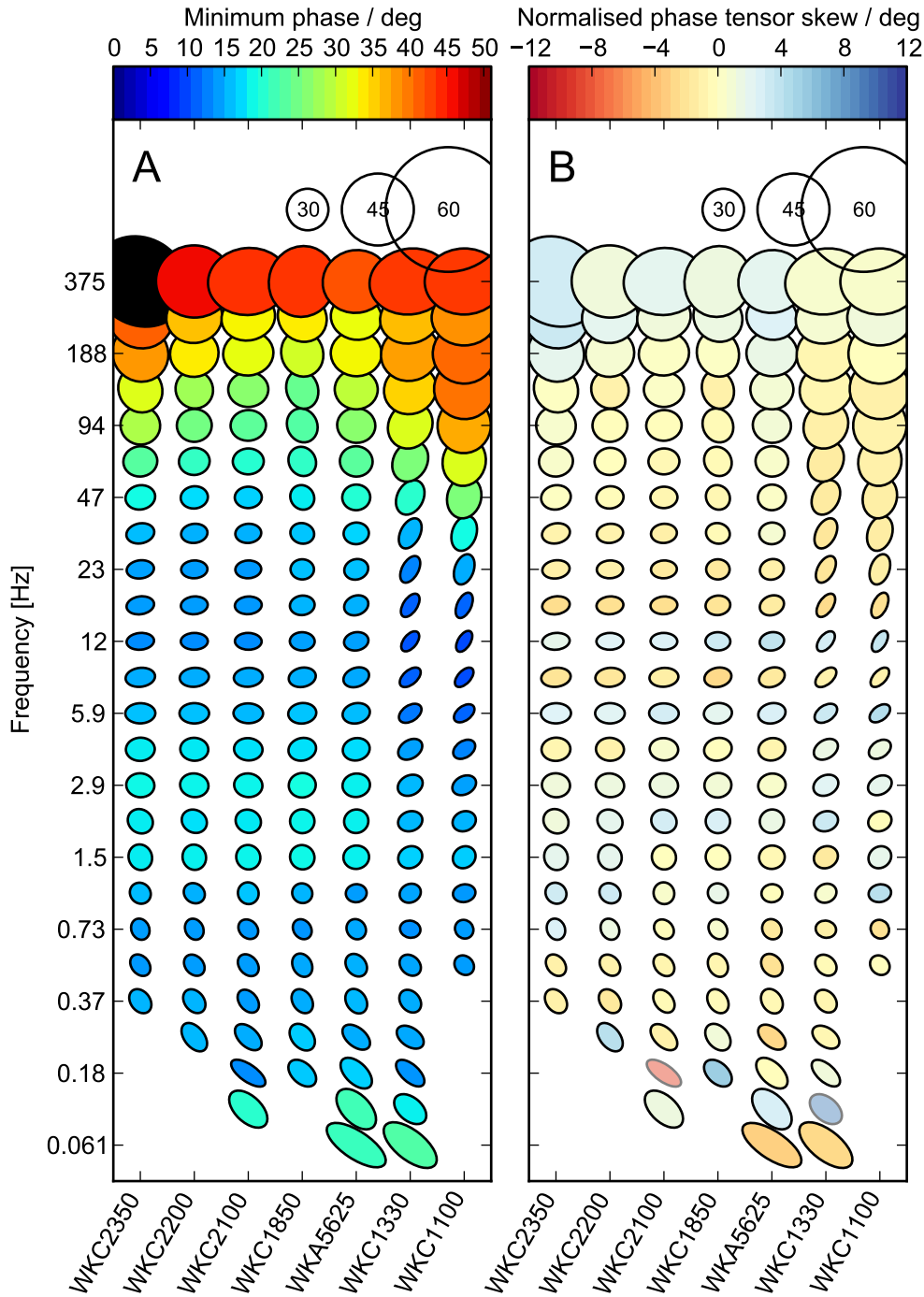


Figure 7.16: Pseudosection of phase tensors from Line C, filled with (A) minimum phase and (B) the normalised skew ψ (faint coloured ellipses have $|\psi| > 6^\circ$ and faint gray ellipses $|\psi| > 12^\circ$, both representing tensors significantly affected by 3D induction). Phase tensors have been rotated by 90° so that the major axis is parallel to the TE mode under a quasi-2D assumption (Booker, 2013) and ellipses with phases of 30° , 45° , and 60° are shown in the upper left for comparison.

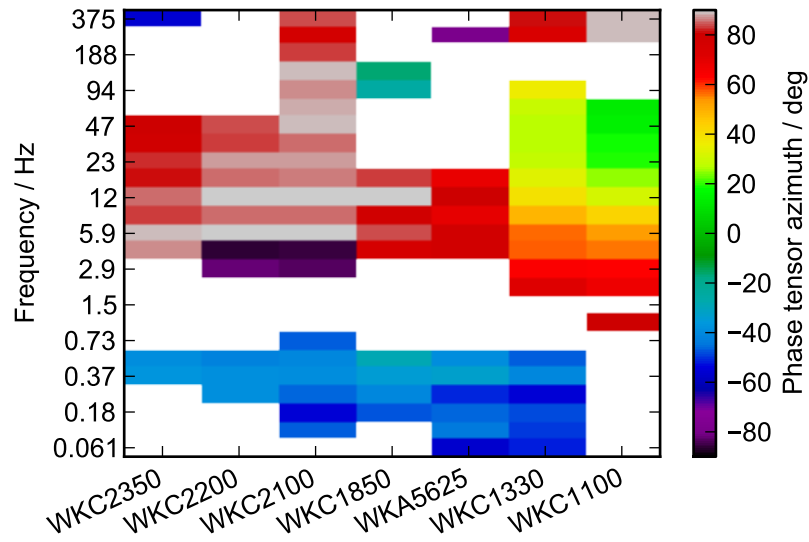


Figure 7.17: Pseudosection of phase tensor azimuths (θ_{ellipse}) along Line C. Azimuths are only shown for tensors with a split in the principal phases greater than 5° .

mode for a 2D model striking east/west with lateral conductivity contrasts at the points where the Zxy phase is spatially discontinuous: primarily between WKA5625 and WKC1330, but also between WKC2100 and WKC1850 (Simpson and Bahr, 2005, p. 30).

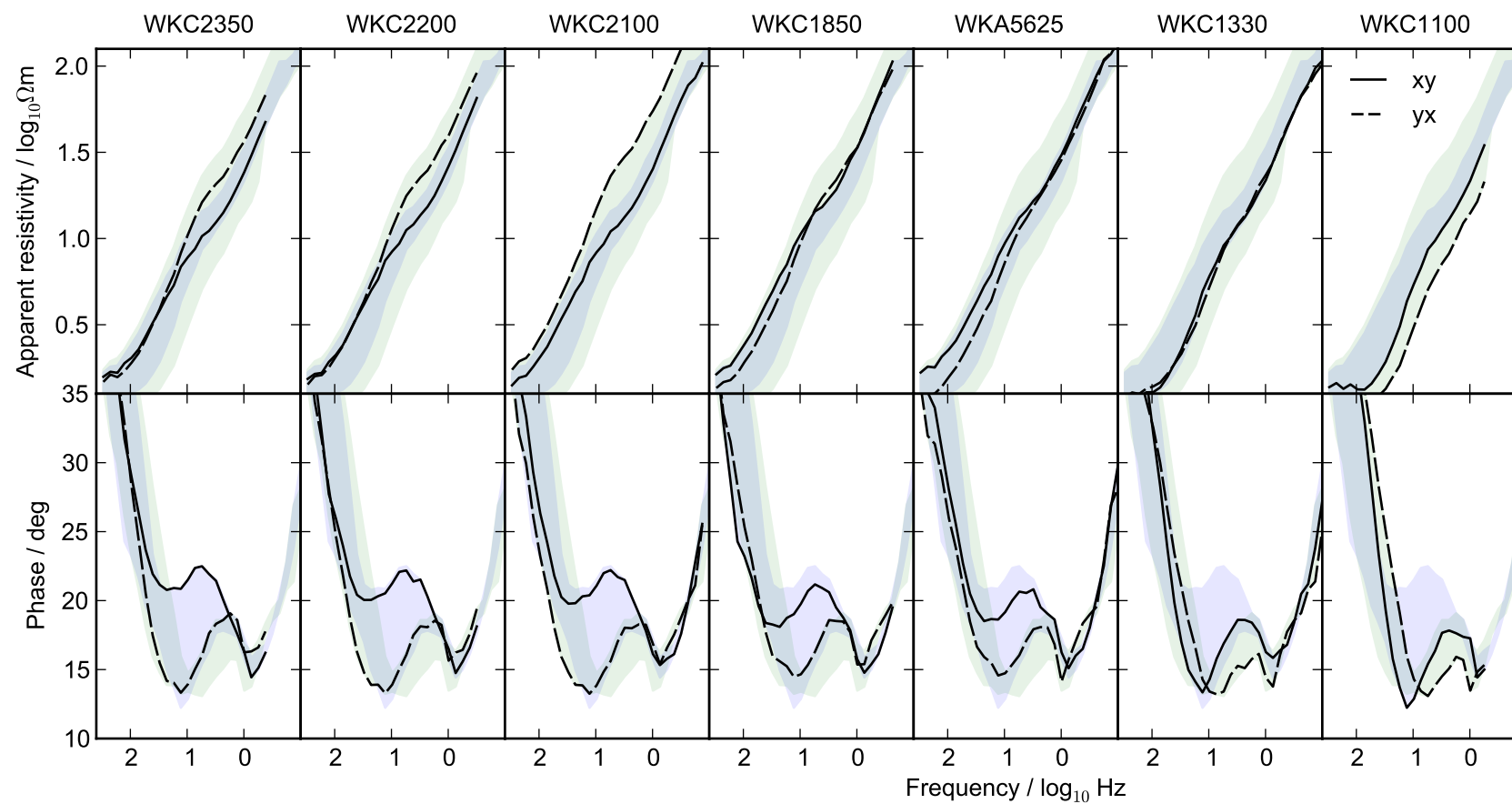


Figure 7.18: Cross-section of apparent resistivity and phase from MT sites on Line C. The shaded area shows the range of data from all the sites on the section and is to help with comparison between sites. Coordinate system: x 000°, y 090.

7.4 Anisotropic 1D MT modelling

Magnetotelluric sites located on the northern end of Line A and the western end of Line C all contain a phase split in the bandwidth 3 Hz to 60 Hz which varies little despite the sites being separated by more than 750 m. A composite response was created from these sites (WKA5475, WKA5625, WKA5750, WKC1850, WKC2100, WKC2200, WKC2350) (Figure 7.20) by using the average of each component of the impedance tensor for each frequency. The phase split was then inverted for using the anisotropic 1D Monte Carlo procedure described in Section 3.1.4.1.

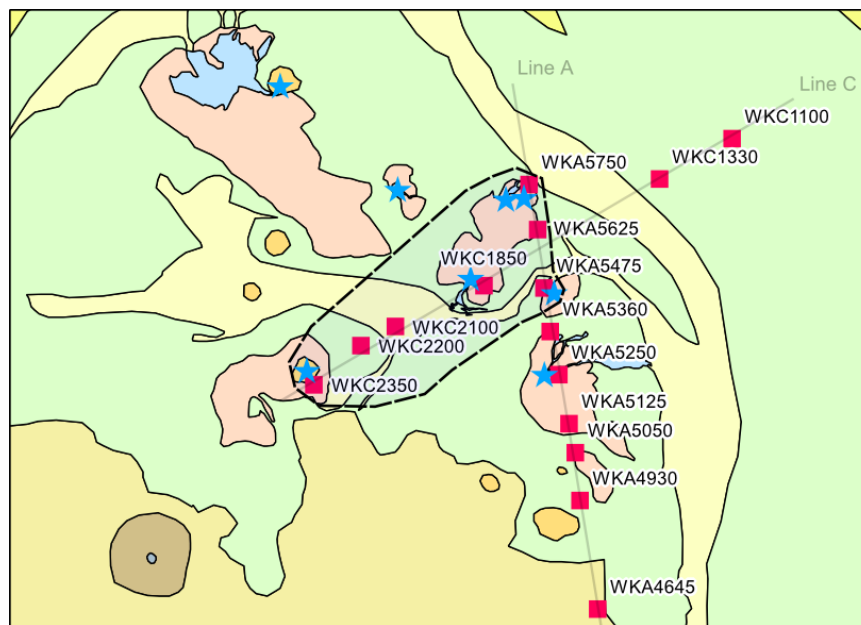


Figure 7.19: MT sites used to create the composite response (Figure 7.20) used for anisotropic modelling.

A set of 1D inversion runs was set up using a 10-layer starting model with layers of increasing thickness ranging between a 50 m-thick surface layer to a 4000 m-thick layer overlying a halfspace beginning at a depth of 10 km.

The phase split between 3 Hz to 60 Hz was best fit by the inversion run for which the fifth layer was allowed to be anisotropic. Partial fits were achieved on the runs with the fourth and sixth layer respectively allowed to be anisotropic. The best-fitting sets of models from these inversions are shown in Figure 7.21 ($k=5$), Figure 7.22 ($k=4$), and Figure 7.23 ($k=6$).

The best-fitting models all contain a conductive ($1 \Omega \text{ m}$ to $3 \Omega \text{ m}$) near-surface layer approximately 60 m thick, underlain by a resistive layer of $500 \Omega \text{ m}$ to $2000 \Omega \text{ m}$ with its base at 130 m to 300 m. Below this resistive layer is the

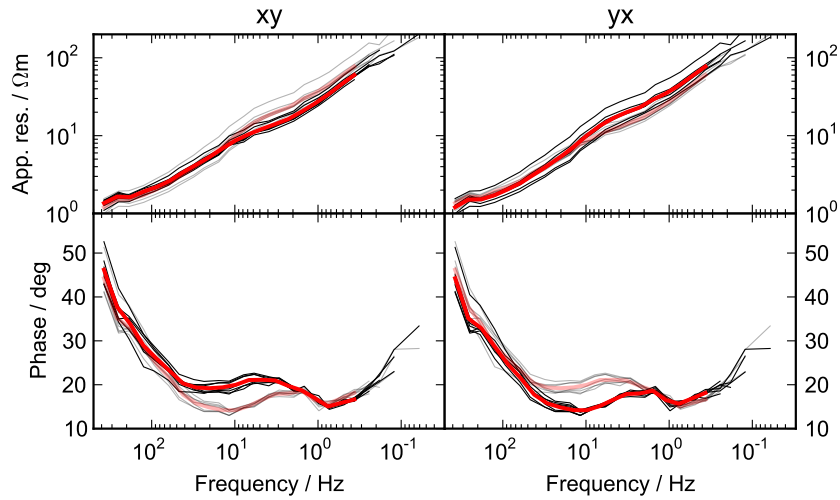


Figure 7.20: Composite MT response averaged from sites shown in Figure 7.19. The original responses are shown in black, the average in red, and the opposite mode in gray. Coordinate system: x 000° , y 090° .

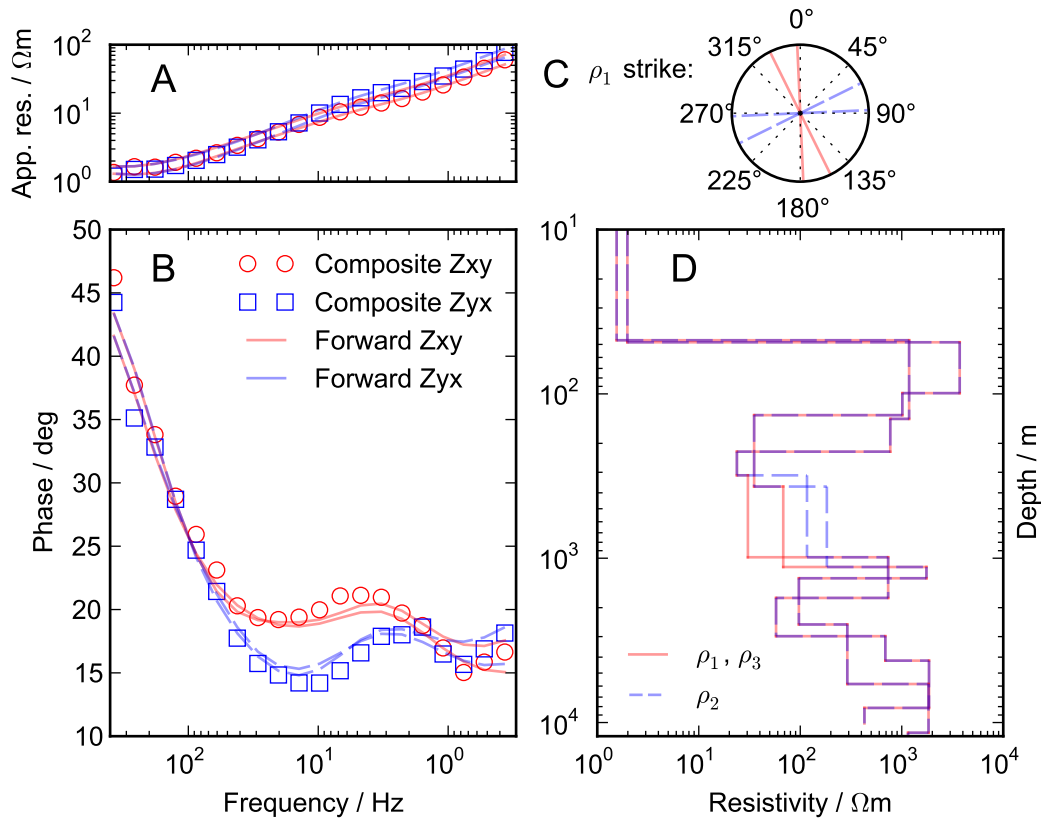


Figure 7.21: Anisotropic 1D resistivity models from $k=5$ that best fit the composite site. Coordinate system: x 000° , y 090° . (A) Fit to apparent resistivity data; (B) fit to phase data; (C) anisotropy strike for models; (D) resistivity models. Symbols show composite response data and lines show forward model responses.

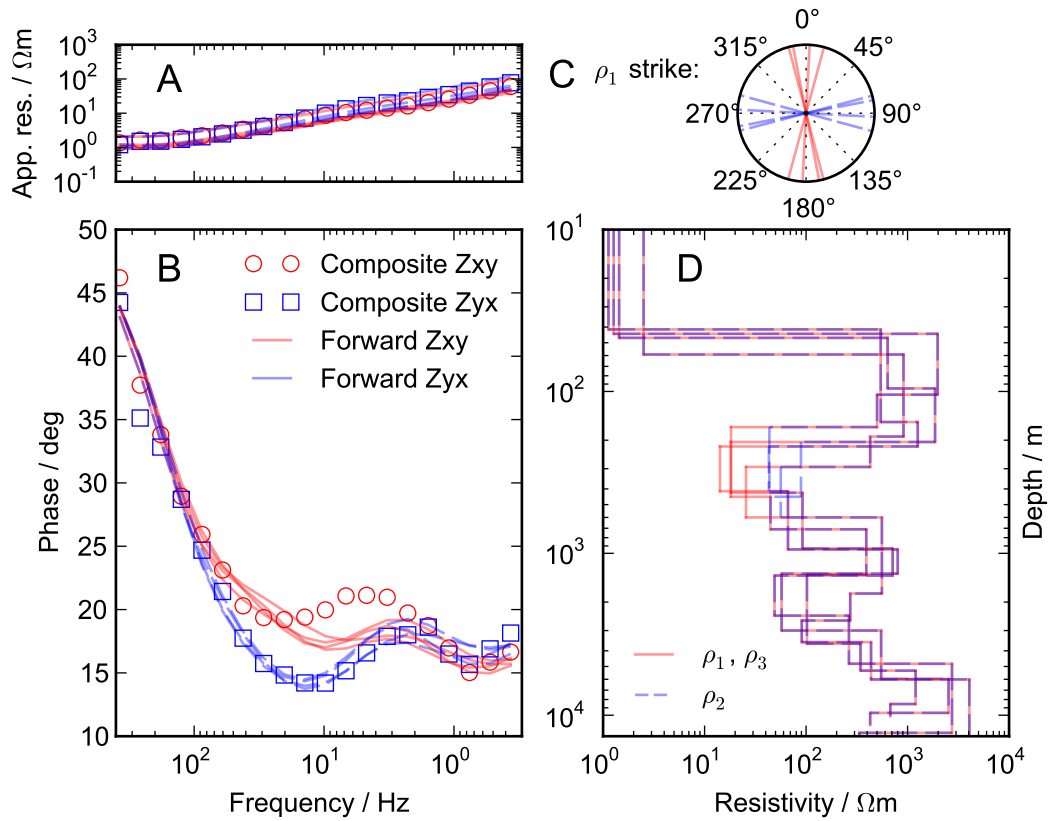


Figure 7.22: Anisotropic 1D resistivity models from $k=4$ that best fit the composite site. Coordinate system: x 000° , y 090° . (A) Fit to apparent resistivity data; (B) fit to phase data; (C) anisotropy strike for models; (D) resistivity models. Symbols show composite response data and lines show forward model responses.

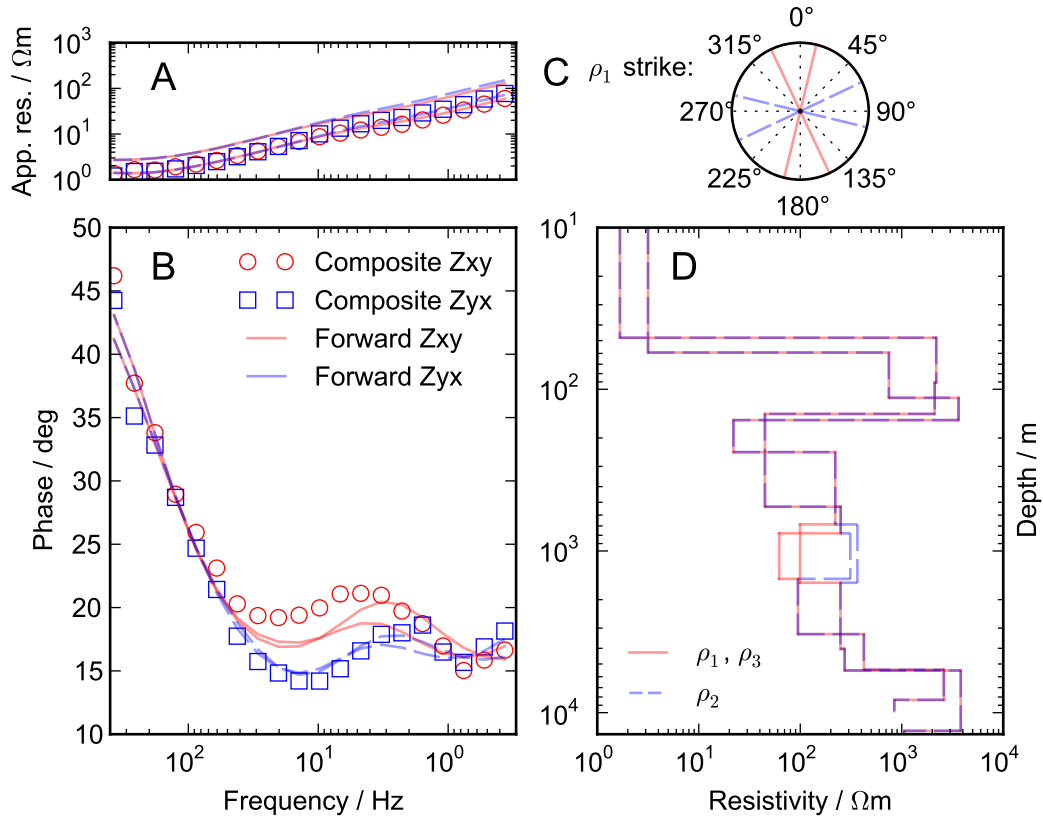


Figure 7.23: Anisotropic 1D resistivity models from $k=6$ that best fit the composite site. Coordinate system: x 000° , y 090° . (A) Fit to apparent resistivity data; (B) fit to phase data; (C) anisotropy strike for models; (D) resistivity models. Symbols show composite response data and lines show forward model responses.

anisotropic layer, which extends between depths of 300 m and 1000 m in the set of best-fitting models (Figure 7.21). In the models which reproduce the higher-frequency end of the phase split well (Figure 7.22) the top of the anisotropic layer ranges between depths of 150 m to 300 m, while the results in Figure 7.23 suggest the base of the layer is likely to be no deeper than 1300 m.

In all the models the anisotropic layer was preferentially conductive in a direction which ranges between azimuths of 330° and 020° . The conductivity contrast depends on the layer thickness, but generally the along-sheet resistivity (ρ_1 and ρ_3 ; see Section 3.1.4.1) was between $30 \Omega \text{ m}$ and $70 \Omega \text{ m}$, with the shallower models ranging between $15 \Omega \text{ m}$ and $30 \Omega \text{ m}$. The across-sheet resistivity ρ_2 ranged from $90 \Omega \text{ m}$ to $200 \Omega \text{ m}$.

There is a difference of approximately 90° between the preferred orientation of current-parallel phase tensor ellipses at the lower-frequency end of the phase split (e.g. Figure 7.16), and the direction in which the anisotropic sheets are most conductive. Ellipses at the higher-frequency end of the split are generally circular, with a phase of 45° . Note that according to Heise et al. (2006, Fig. 5), current-parallel phase tensor ellipses will be perpendicular to the strike of conductive sheets when the anisotropic layer overlies an isotropic layer, and parallel when the isotropic layer overlies the anisotropic one, with both orientations found when the anisotropic layer is sandwiched in an otherwise isotropic 1D model. In this case only the lower-frequency end of the phase split is reproduced in the phase tensor ellipses, suggesting that the anisotropy may extend closer to the surface than represented in the modelling here where only one layer is permitted to be anisotropic, and therefore there is, in effect, relatively little upper constraint on the anisotropic layer's thickness.

7.5 2D MT inversion

Two-dimensional isotropic inversions were run using the Occam2D inversion software (de Groot-Hedlin and Constable, 1990).

7.5.1 Line A

Line A runs from north to south, and as the data at a number of sites on the line had a preferred orientation toward 070° , the data were rotated by 70° for 2D inversions, such that x is toward 070° and y toward 160° , and Z_{xy} is the TE mode and Z_{yx} is the TM mode. Inversions run in this coordinate system con-

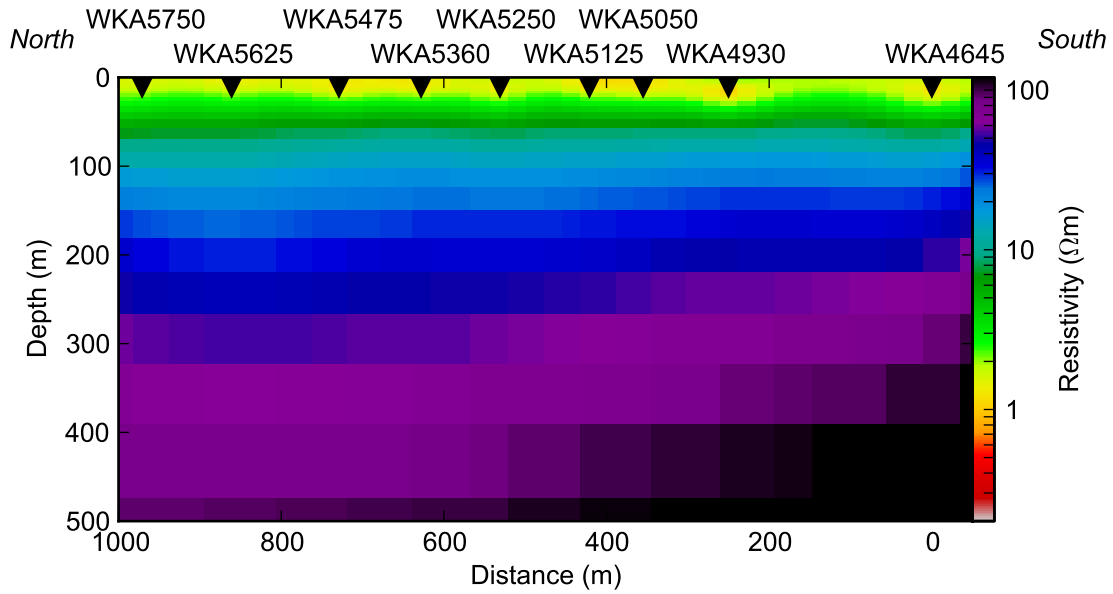


Figure 7.24: Resistivity model from 2D inversion fitting to within 50% of apparent resistivities and 2% of phases along Line A (see fits in Figure 7.25)

verge quickly to smooth and homogeneous models where resistivity increases with depth, for example the model shown in Figure 7.24 (fits in Figure 7.25).

The model is quite conductive in the top 20 m, transitioning to greater resistivities at depth: $20 \Omega\text{m}$ occurs at a depth of 100 m across the model. A slightly more resistive area at depths greater than 300 m underneath WKA4645 accounts for the reduced phase split at that site, which is adequately fit by the forward responses.

7.5.2 Line C

Although Line C runs approximately from south-west to north-east, there are indications in the data (discussed above) that the MT responses are aligned with a geoelectric strike of either 090° or 020° . Modelling was done in both of these strike directions.

7.5.2.1 Strike towards 090°

For these inversions the data were rotated such that x is towards 090° and y is towards 180° . Z_{xy} is then the TE mode and Z_{yx} the TM mode. Note that distances between stations under this modelling assumption are reduced to their projected distance from Line C onto a hypothetical model profile oriented perpendicular to the strike. The strike of 090° is based on the orientation of the

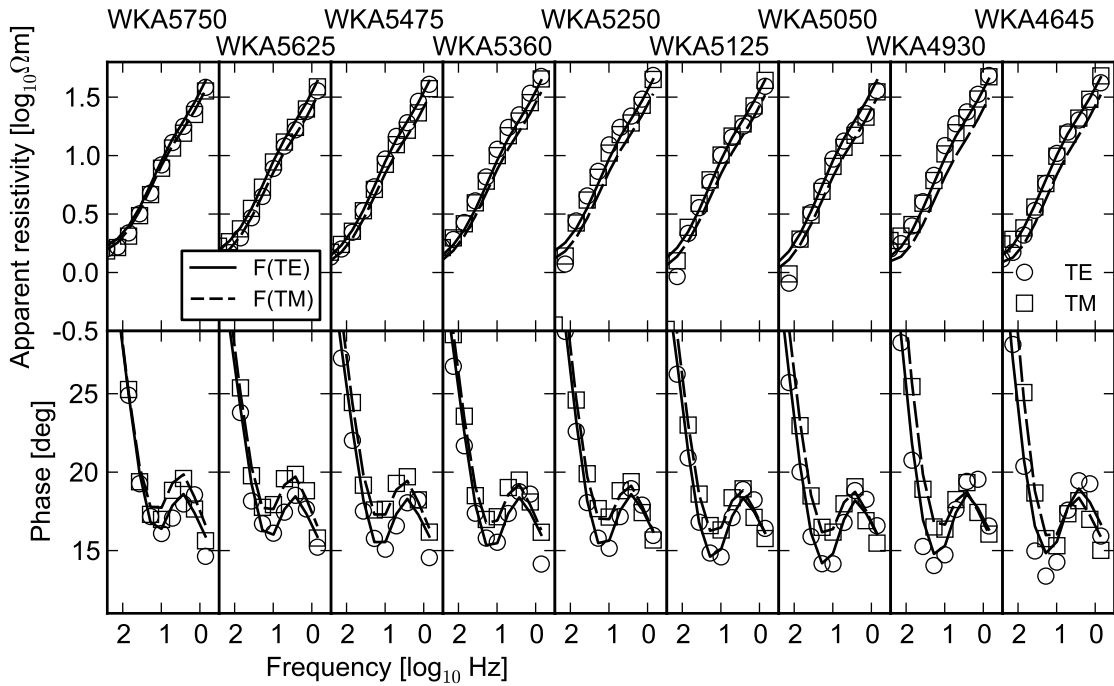


Figure 7.25: Fit of 2D MT model (Figure 7.24) forward responses to observations.

impedance tensor for which the phase split present at WKC2350, WKC2200, and WKC2100 is largest.

Inversions run for these data successfully converged for a variety of misfit criteria, with the models retaining basic features that became increasingly pronounced as the fit was improved. A strict misfit criteria was applied to the phase in particular in order to reproduce the subtle variations of $< 6^\circ$. A model fitting to within 20% of apparent resistivities and 4% of phases is shown in Figure 7.26 (fits in Figure 7.27).

The model contains a conductive surface layer underlain by increasingly resistive ground, with two significant features:

1. The surface conductor is significantly thicker at WKC1100 ($< 2 \Omega\text{m}$ down to a depth of 100 m, compared to the same resistivity down to depths of about 30 m to 40 m along the rest of the model).
2. A conductive zone underlying WKA5625. This zone is $15 \Omega\text{m}$ at a depth of 110 m, underlain by a region about 200 m wide with a resistivity of $15 \Omega\text{m}$ to $30 \Omega\text{m}$ extending down to a depth of 500 m, dipping at 65° to the south in the model space. This compares to more resistive regions on either side: for example underneath WKC1100, the model has

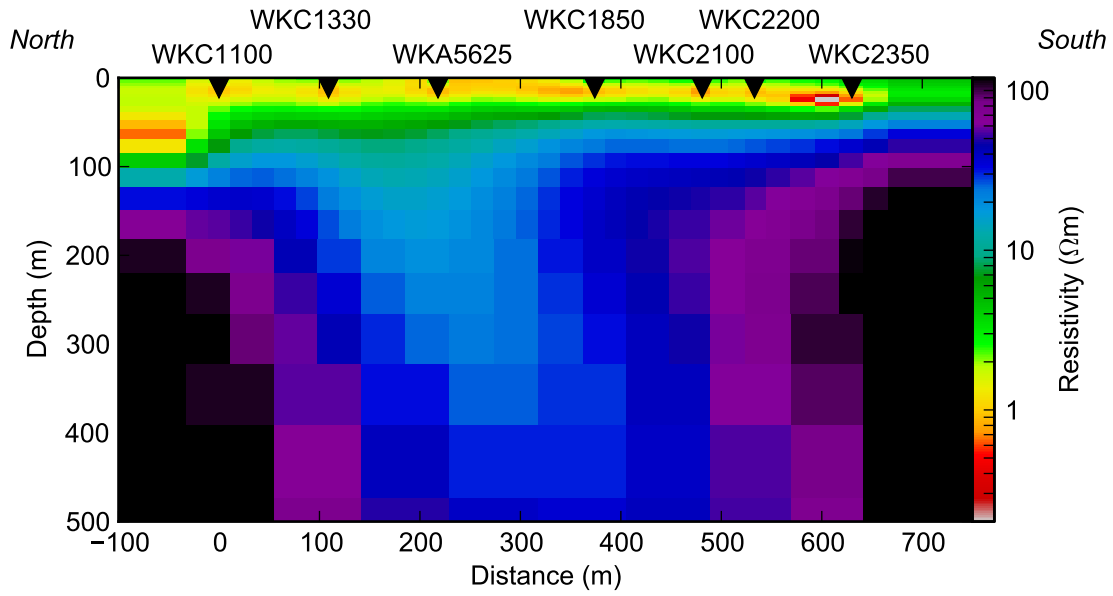


Figure 7.26: Resistivity model from 2D inversion fitting to within 20% of apparent resistivities and 4% of phases along Line C, with a strike of 090° (see fits in Figure 7.27)

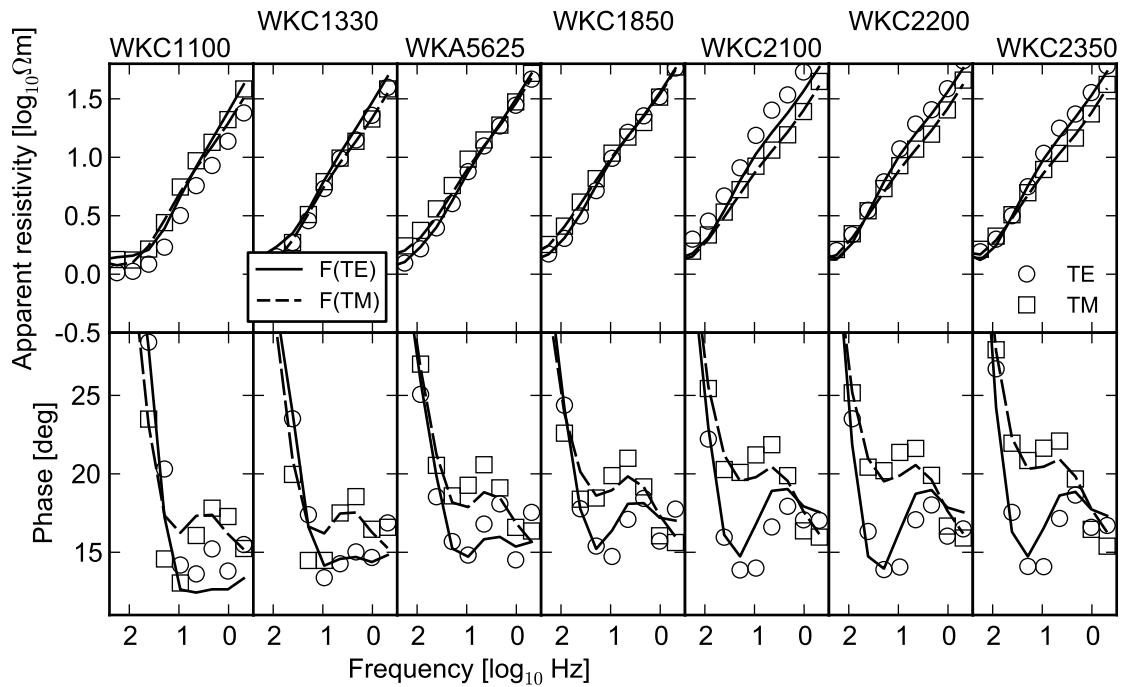


Figure 7.27: Fit of 2D MT model (Figure 7.26) forward responses to observations.

a resistivity of $60\ \Omega\text{ m}$ at a depth of 200 m, while underneath WKC2100 and WKC2350 the model resistivity is $90\ \Omega\text{ m}$ and $200\ \Omega\text{ m}$ at the same depth, respectively.

The fits of the model's forward responses to the data are generally good (Figure 7.27), with the large and consistent phase split at WKC2100, WKC2200, and WKC2350 well reproduced. The smaller phase splits at WKA5625 and WKC1850 are also well fitted. An exception is the low minimum phase in both modes at WKC1100, which is not reproduced at all compared to the other sites along the line. Given that phase tensors in this bandwidth at WKC1100 are oriented towards 020° rather than the strike in the 2D model used here, the poor fit is expected.

7.5.2.2 Strike towards 020°

For these inversions the data were rotated such that x is towards 020° and y is towards 110° . Z_{xy} is then the TE mode and Z_{yx} the TM mode. The strike of 020° is based on the orientation of the phase tensor at WKC1100 and WKC1330.

Inversions run for these data successfully converged on similar resistivity features for those obtained in the previous section, suggesting that these features are primarily variations in the 1D resistivity structure underneath each site, and that lateral effects play only a minor role in the modelling. A model fitting to within 20% of apparent resistivities and 3% of phases is shown in Figure 7.28 (fits in Figure 7.29).

Despite the similarity of the model features, the model fit is improved when compared to the previous section, with the trend of increasingly lower phase minima at WKC1100 present in the forward responses (Figure 7.29), although WKC1100 is still not closely fitted.

The model in Figure 7.28 contains the same conductive surface layer underlain by increasingly resistive ground, and contains the same features as Figure 7.26. The thickened surface conductor at WKC1100 ($2\ \Omega\text{ m}$ to $9\ \Omega\text{ m}$ down to 110 m) now extends westward to WKA5625, although at the western end the lower part is slightly more resistive ($6\ \Omega\text{ m}$ to $10\ \Omega\text{ m}$ between 25 m and 110 m depth). This can be contrasted to further west along the line, underneath the active springs (e.g. WKC1850 to WKC2350), where the resistivity is from $20\ \Omega\text{ m}$ to $40\ \Omega\text{ m}$ between depths of 65 m to 110 m. The dipping conduc-

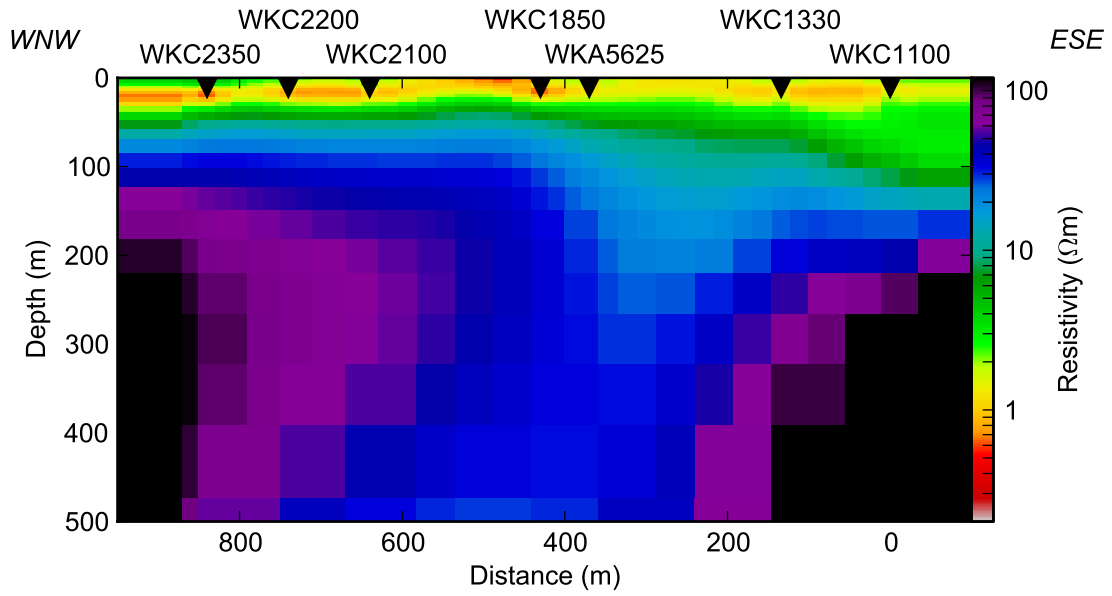


Figure 7.28: Resistivity model from 2D inversion fitting to within 20% of apparent resistivities and 3% of phases along Line C, with a strike of 020° (see fits in Figure 7.29)

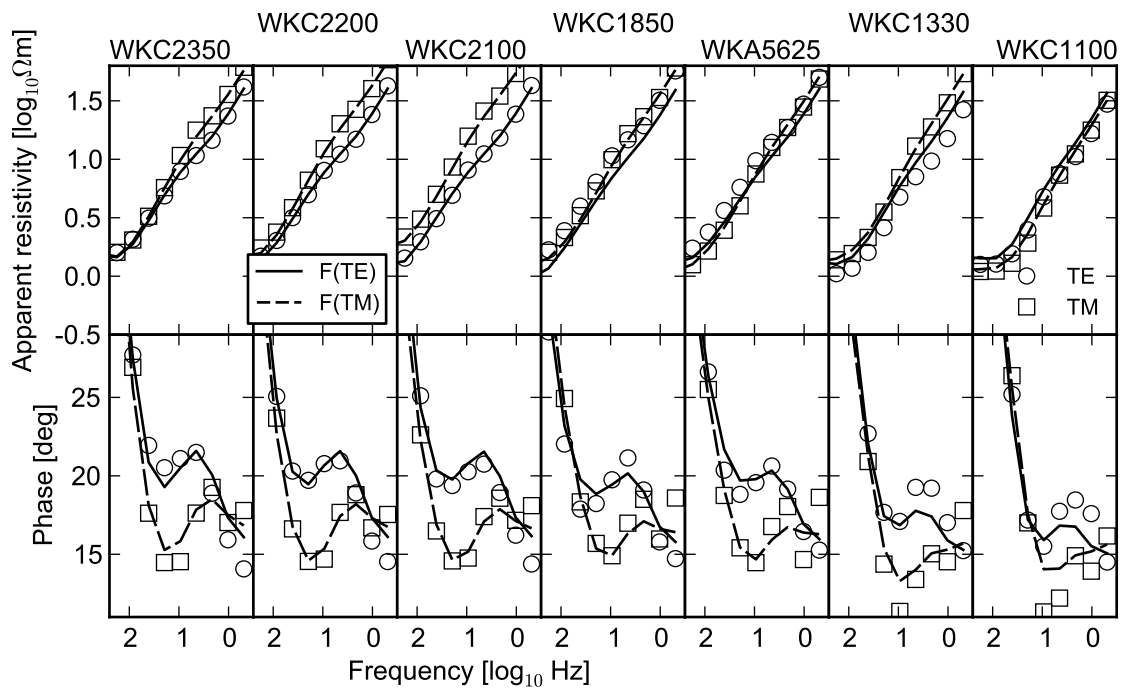


Figure 7.29: Fit of 2D MT model (Figure 7.28) forward responses to observations.

tor at greater depths is less prominent but retains the same shape and is dipping to the WNW along the profile; given the results for the two differently-oriented inversions, the conductor dips approximately to the south-west. It is interpreted that this conductor may be related to a faulted zone, and that the resistive area between depths of 50 m to 110 m along the western part of the line is related to structural thinning of the surface conductive layer.

Chapter 8

Freeling Springs

Summary

Freeling Springs is a complex of springs located 70 km south-east of Oodnadatta (see Figure 2.2). Ninety-eight spring vents and seeps lie along the base of a fault scarp associated with the Kingston Fault, which offsets Mesozoic GAB sediments to the east against highlands consisting of outcropping Palaeoproterozoic basement to the west (Rogers and Freeman, 1996b). The spring complex lies in a wedge-shaped valley, oriented north–south, bounded on the western side by the Kingston Fault and on the eastern side by an incised exposure of Bulldog Shale. The valley is filled with spring carbonate deposits and alluvial outwash from the highlands, with Cadna-owie Formation interpreted to be near the surface (Section 2.5 and Figure 8.1).

The largest single spring (FS1) is located at the southern apex of the wedge, with spring run-off joining other streams from the highlands and flowing north-northeast. Smaller springs are located on the western side of the wedge, along the Kingston Fault scarp. A terrace of spring carbonates and spring vents lies against this scarp.

Self-potential and magnetotelluric data were recorded along two west-east profiles: a southern line (570 m to 790 m long) running eastwards from the highlands over the main spring (FS1) and across alluvial deposits onto Bulldog Shale; and an 800 m-long northern line, running eastwards from the base of the hills over a spring

carbonate terrace which contains a number of small spring vents, and then over alluvium onto the Bulldog Shale. TEM data were also recorded over the northern line.

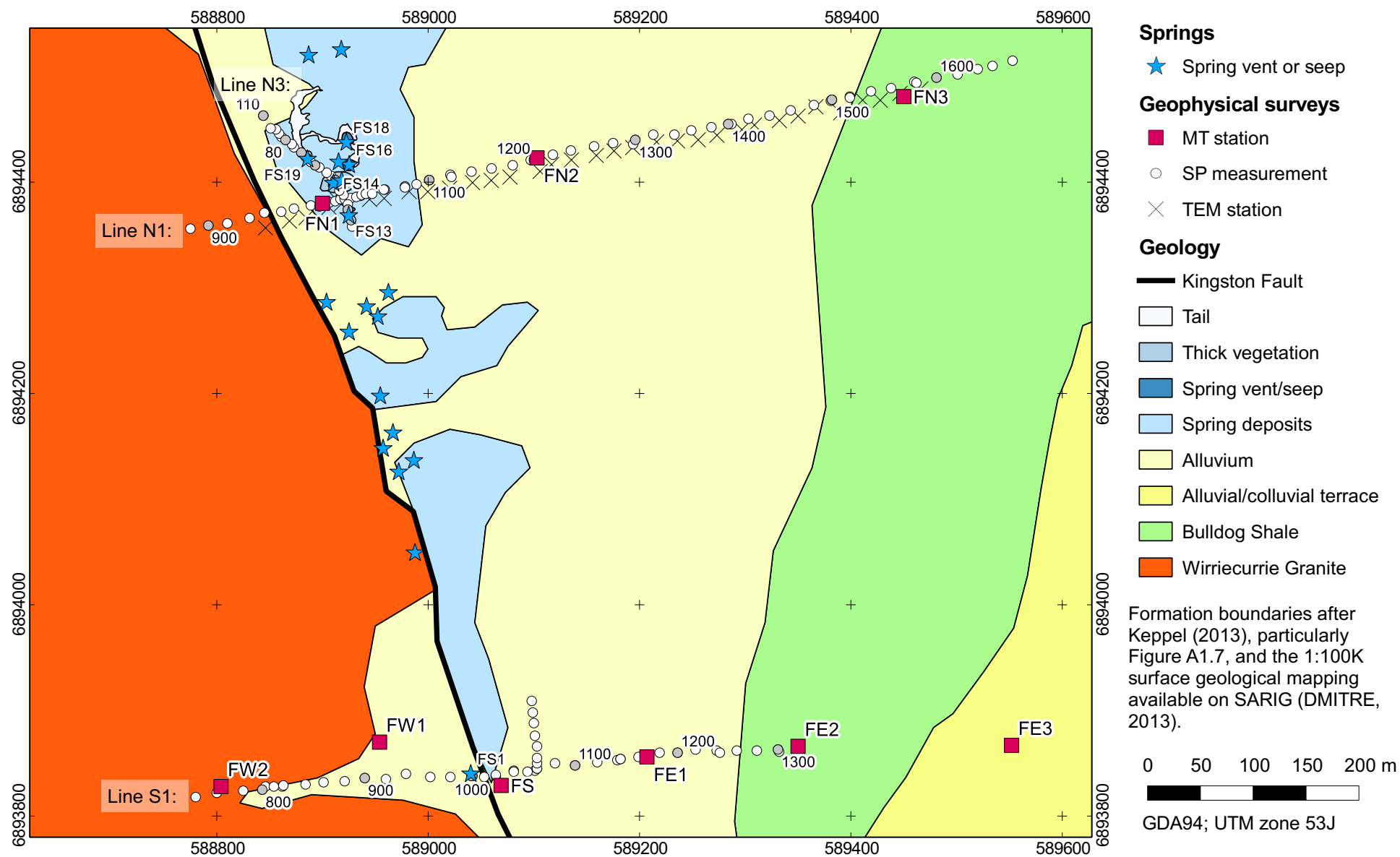


Figure 8.1: Location of SP, TEM, and MT observations at Freeling Springs, with distances on each line marked in metres.

8.1 SP

Self-potential data were collected at Freeling Springs in November 2012 along four lines. Line N1 is 797 m long with bearing 078° and runs across a complex of small springs on a carbonate terrace in the central part of the Freeling Springs complex. The spacing between roving electrode locations on this line was nominally 20 m. Lines N2 and N3 are 50 m and 150 m long respectively, aligned orthogonally on the same carbonate terrace, with potential measurements made at nominal 5 m spacing. Line S1 is 567 m long with bearing 085° and is further south, running across Spring FS1; measurements along this line were made at nominal 20 m spacing. The location of these lines and the stations where observations were made are shown in Figure 8.1. The potential along each line was measured between a stationary base electrode and a roving electrode, which was moved along the line in 20 m steps. Lines N1, N2, and N3 share the same base electrode location, and absolute potentials are directly comparable between these lines. Line S1 uses a different base electrode.

8.1.1 Data quality

The data are much noisier than the data collected at Beresford, Warburton, and the Bubbler, with the potential between sites 20 m apart often varying by more than 30 mV. The range of potentials observed is from -59 mV to 125 mV, which is greater than the other surveys by a factor of nearly 2. The greater variability in potentials is probably due to high contact resistances, which range from $1\text{ k}\Omega$ to $> 10\text{ M}\Omega$. Figure 8.2 shows the values for all the surveys. The high resistances at Freeling Springs were due to very low levels of soil moisture at the time of the survey, in late spring (November), with the daytime shade temperature approaching 40°C . Contact resistances were much lower ($0.3\text{ }\Omega$ to $1\text{ k}\Omega$) on surveys at sites with soils rich in clay such as the Beresford playa and the Bubbler complex. The latter surveys were also undertaken during the coldest part of the year (late April to early August). Slightly higher resistances ($1\text{ k}\Omega$ to $3\text{ k}\Omega$) were found in the clay-rich environment at Warburton Spring in late spring (November). Importantly the range of potentials (i.e. 2 standard deviations) encountered on the surveys where the contact resistance was below $0.1\text{ M}\Omega$ was 80 mV, compared to a range of 140 mV for more resistive measurements.

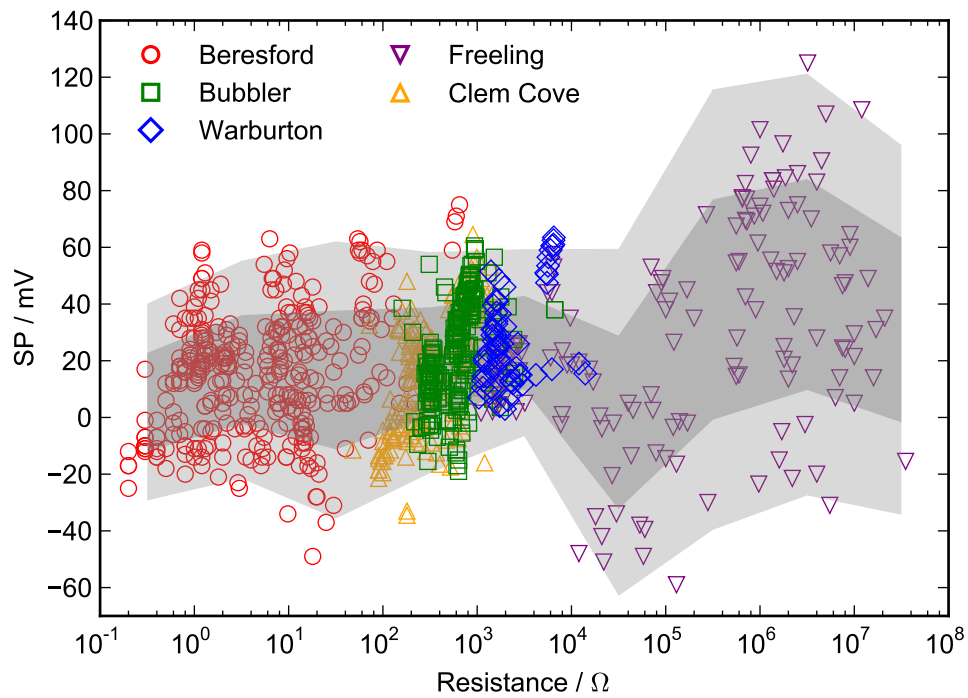


Figure 8.2: Range of contact resistances and potentials encountered on different surveys. The potentials are before any spatial corrections were applied. The dark and light gray panels show the mean ± 1 and ± 2 standard deviations for each decade of resistances. The Clem Cove survey data are unpublished and are from a survey on the lower Eyre Peninsula unrelated to groundwater.

Contact resistances greater than $1\text{ M}\Omega$ exceed the limit suggested by Revil et al. (2012) of restricting measurements to resistances of less than one-tenth of the input impedance of the voltmeter being used, which was in this case nominally $10\text{ M}\Omega$. Contact resistances close to the input impedance cause leakage currents in the voltmeter that degrade the accuracy of the potential measurement (Revil et al., 2012, p. 618). Thirty-four percent of SP measurements at Freeling Springs had contact resistances above the $1\text{ M}\Omega$ limit, compared to zero measurements on any other survey. Nonetheless, clear trends can be observed in some of the data; see below for further discussion of variations in quality.

8.1.2 Data processing

No corrections were applied to the potentials measured in the field beyond the standard polarity checks and averaging described in Section B.1.

Figures 8.3, 8.9, 8.11, and 8.13 show the observed potentials and potential gradients calculated from each pair of observations, with symbols showing the raw data and lines showing a moving average of the potential. The moving average filter is 5 m wide for data on Lines N2 and N3, and 75 m wide for the other lines. Potential gradients are positive in the direction of increasing station numbers. Image reconstructions are calculated from the observed potentials.

8.1.3 Line N1

Self-potential observations from Line N1 are shown in Figure 8.3. There is a large rise in potential centred around stations 1220 and 1280, with potentials at the peak (105 mV) around 85 mV to 120 mV higher than potentials to the west, and up to 140 mV higher than potentials in the east. The magnitude of this feature (approximately 110 mV) is much larger compared to those at Beresford (35 mV), Warburton (45 mV), and the Bubbler (50 mV)

The central rise in potential is not correlated with any springs. The only spring vents near the line are within 15 m of station 1020. This part of the line corresponds to scattered potential measurements between 5 mV to 30 mV , with three outliers below this range (down to -60 mV).

The image reconstruction (Figure 8.4) shows an area strongly correlated to positive sources underneath the central rise in potential, between stations 1120

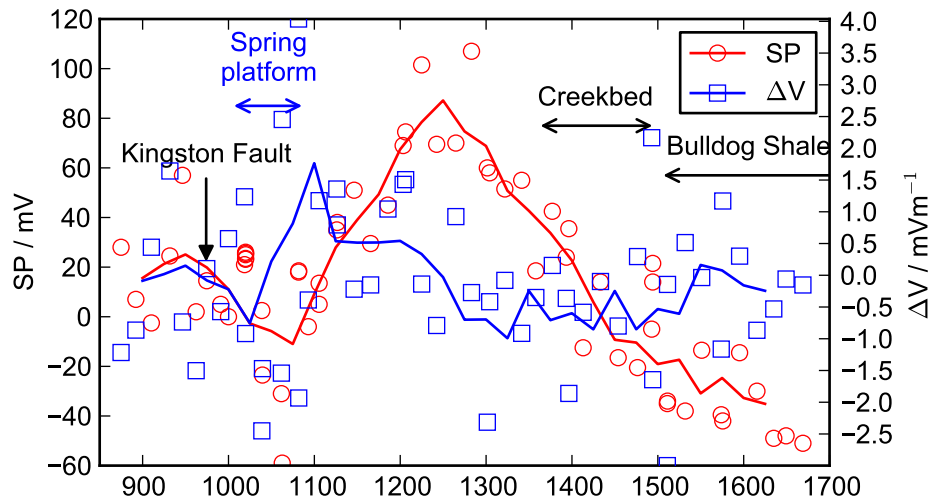


Figure 8.3: Self-potential and potential gradient ΔV along Line N1 at Freeling Springs. The solid lines are moving averages.

and 1400. The correlation coefficient in this area is 0.25 at depths down to 100 m and drops off to 0.1 at depths greater than 250 m.

Unusually, the carbonate terrace containing active small springs is underlain by an area correlated to negative sources. The correlation coefficients range from -0.2 directly underneath the anomalous -60 mV mentioned above, to a coefficient of 0 at a depth of 200 m. Note that the magnitude of this negatively-correlated area may be exaggerated by its proximity to the strongly correlated positive sources to the east. This low response can be modified by removing some of the “noisy” responses in this area (the three potentials less than -5 mV) (Figure 8.5). Nevertheless, the area remains negatively correlated despite this and therefore there is little evidence for significant positive sources (upward movement of water) underneath the terrace in general. This implies that water is more likely to be flowing laterally to this area rather than vertically.

8.1.3.1 Data quality

The potential along each line was measured between a stationary base electrode and a roving electrode, which was moved along the line in 20 m steps. The observations are quite noisy, but even after removal of measurements with contact resistances above $1\text{ M}\Omega$ there remains a clear trend to high potentials in the centre of the line, and lower potentials at the eastern end (Figure 8.6).

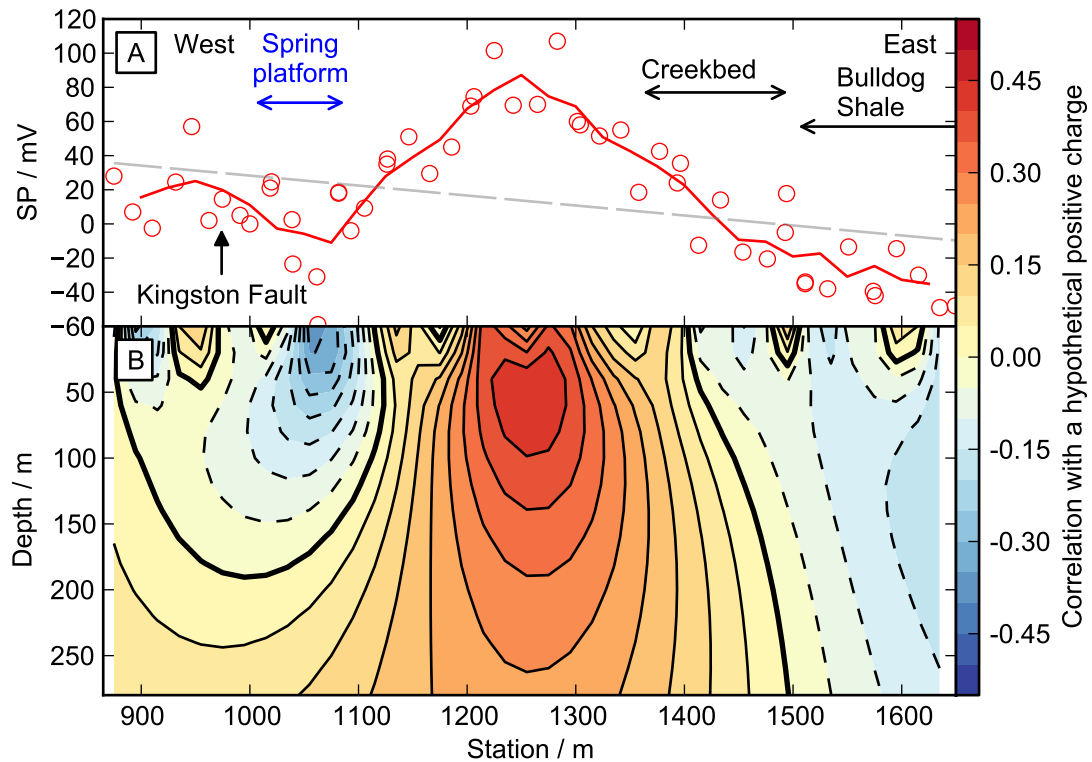


Figure 8.4: SP data (A) and image reconstruction (B) over Line N1. The grey line is a least-squares fit. The solid line is a moving average.

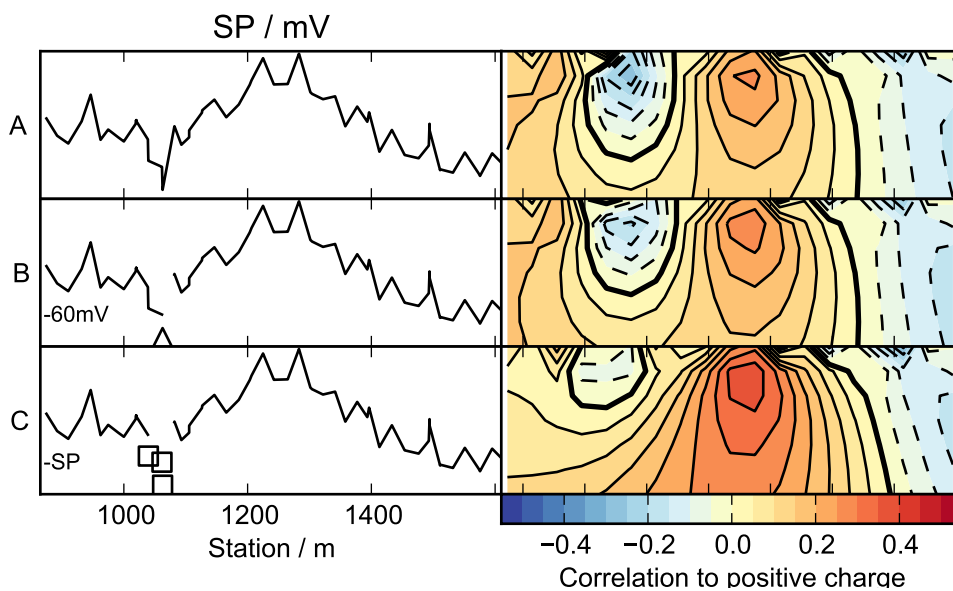


Figure 8.5: Image reconstructions calculated for Line N1 data after the removal of different subsets of anomalously negative potentials near station 1050: in (B) a single anomalously low potential of -60 mV was removed, and in (C) three potentials less than -5 mV were removed. The symbols show the removed data points, and the solid line shows the remaining data, which was used to calculate the image reconstruction in the right panel.

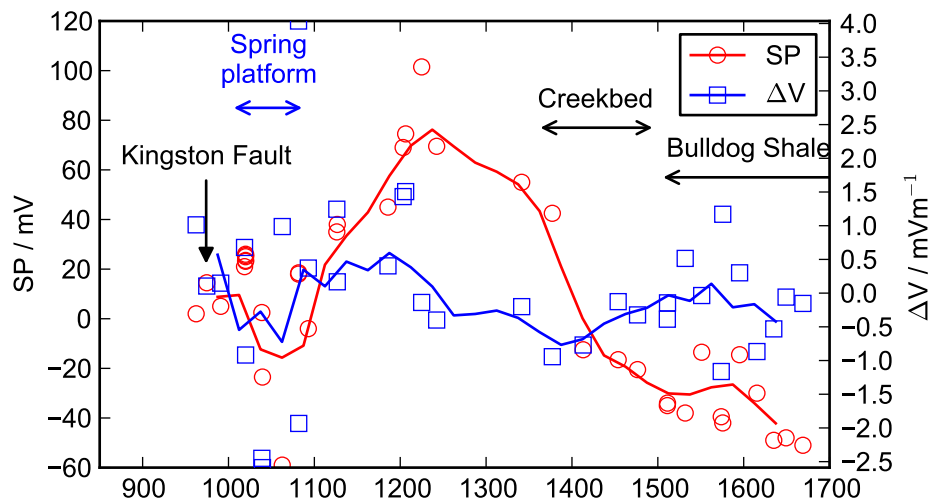


Figure 8.6: Self-potential and potential gradient ΔV along Line N1, showing only those measurements with contact resistances below $1\text{ M}\Omega$. The solid lines are moving averages.

Note that there is a strong lithological control on the contact resistance (Figure 8.7), with measurements in the spring terrace at the western end of the line being the least resistive (mostly $1\text{ k}\Omega$ to $3\text{ k}\Omega$), and those in the dry but clay-rich Bulldog Shale at the eastern end of the line slightly more resistive ($10\text{ k}\Omega$ to $100\text{ k}\Omega$). Note that the high-resistance measurements in the alluvium in the middle of the line contain a much greater level of scatter in the potential, suggesting that the high level of noise is due to very high contact resistance.

8.1.4 Lines N2 and N3

There was no significant peak in SP over the carbonate terrace springs, as noted above. A smaller scale SP survey was conducted on the terrace to further investigate, as peaks in potential were expected to be associated with the spring vents on the terrace. Lines N2 and N3 were collected as part of this small-scale survey, with the potential along each line measured between a stationary base electrode and a roving electrode, which was moved along the line in nominal 5 m steps. Line N2 is parallel and coincident with part of Line N1. The locations of these lines are shown on Figure 8.8.

8.1.4.1 Line N2

Potentials along Line N2 were between -60 mV and 24 mV . The potential drops from values around 10 mV at the base of the highlands (the Kingston

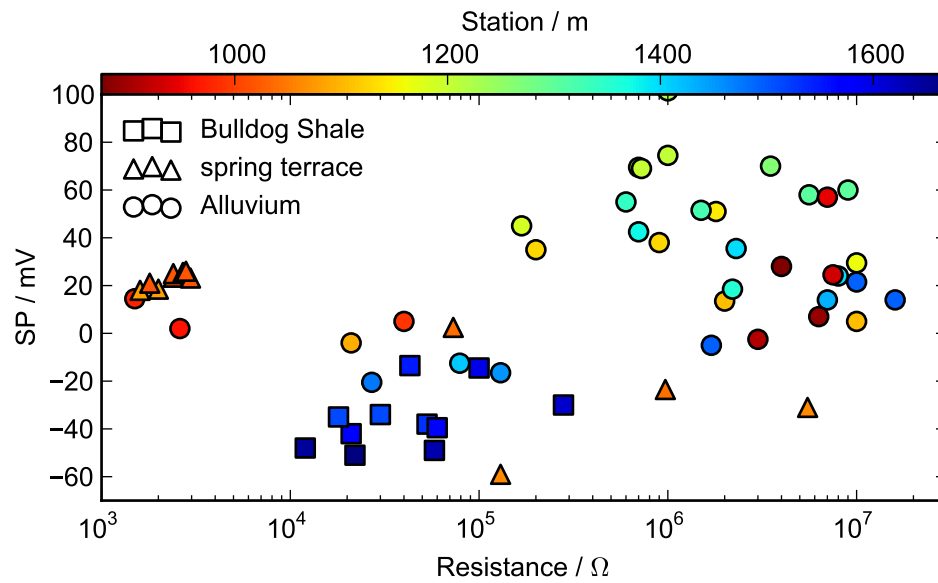


Figure 8.7: Contact resistance and SP for observations along Line N1, coloured by station number with symbols grouped by lithology.

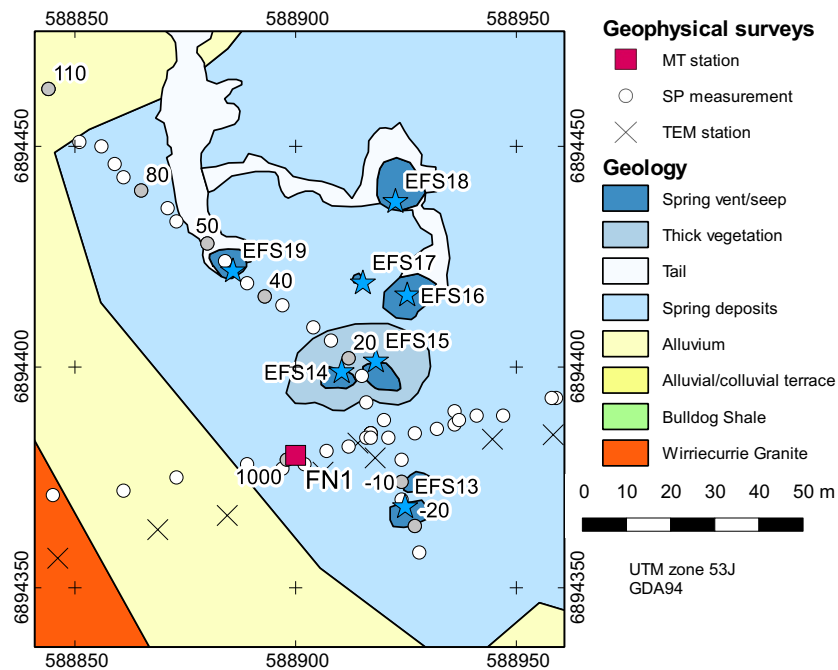


Figure 8.8: Location of SP observations along Lines N1, N2, and N3.

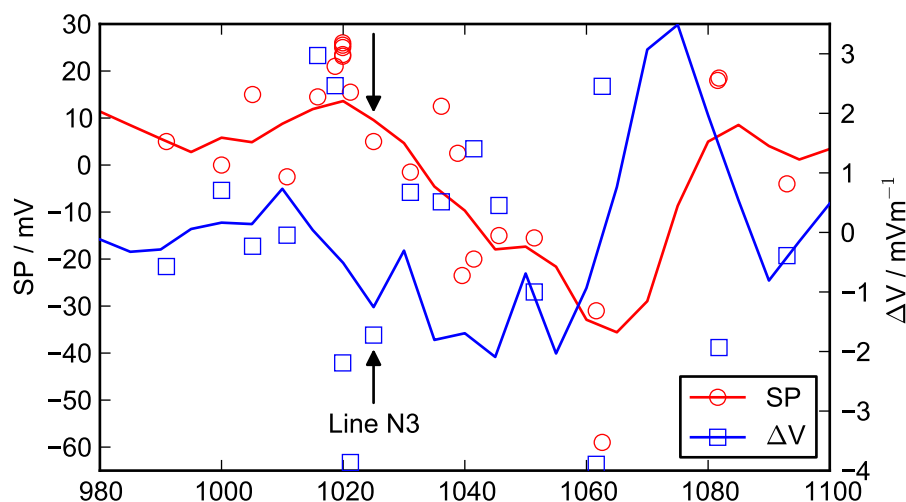


Figure 8.9: Self-potential and potential gradient ΔV along Lines N1 and N2. The location where Line N3 crosses the line is noted with black arrows. Solid lines are moving averages.

Fault at station 980) to -30 mV to -60 mV at station 1060, at a gradient of approximately -1.8 mV m^{-1} . Measurements beyond this point are sparsely spaced, but there is a peak in potential at the edge of the carbonate terrace at station 1080 (18 mV).

Line N2 does not cross any springs. It passes between two sets of spring seeps (identified by patches of *Phragmites* reeds) between stations 1015 and 1030: springs FS14 and FS15 are 14 m to the north, and FS13 is 17 m to the south. This point correlates to the location where the potential begins to drop to the east, as noted above. Potentials further west are scattered but there is a slight drop in the spatially smoothed potential; the gradient of this decline is 0.1 mV m^{-1} to 0.5 mV m^{-1} .

The large step decline in potential to the east is reflected in the image reconstruction (Figure 8.10), which contains a strongly negatively-correlated area between stations 1040 and 1070, with shallower positively-correlated areas to the west of station 1030. Figure 8.10 was calculated only for the potentials shown in Figure 8.10A rather than the full set of Line N1 data.

8.1.4.2 Line N3

Potentials along Line N3, which runs over the spring platform carbonates, parallel to and about 50 m east of the Kingston Fault, ranged between -5 mV to 30 mV , with two outliers at -20 mV and 48 mV . Potentials are generally between 0 mV to 10 mV in the southern part of the line, rising to scattered but

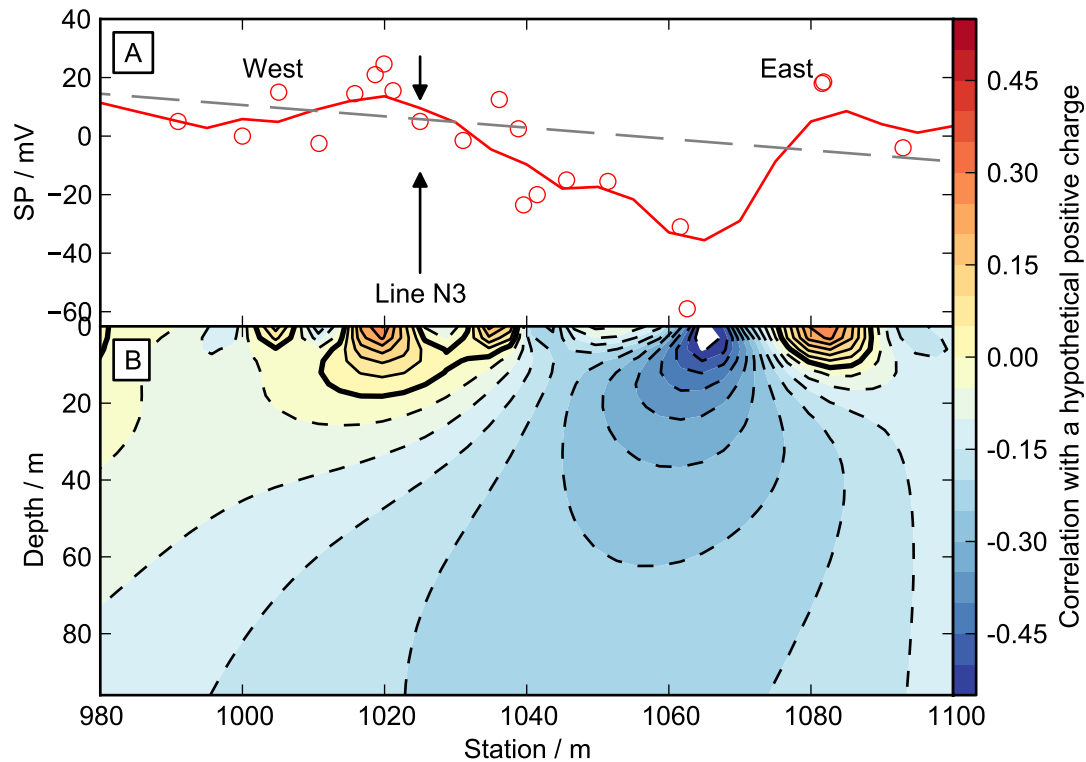


Figure 8.10: SP data (A) and image reconstruction (B) over Line N2. The grey line is a least-squares fit. The solid line is a moving average.

generally higher values (10 mV to 30 mV) between stations 42 and 80.

The line ran directly through the *Phragmites* growth at the FS13 seep, between *Phragmites* growths at FS14 and FS15, and through the saturated mud and sand of the FS19 seep. There was no apparent change in potential at FS13, FS14, or FS15 (stations -14, 15, and 20), but there was a 9 mV to 15 mV increase associated with FS19 (stations 55 and 60). The gradient on the southern side of this increase is approximately 1.5 mV m^{-1} . There were also several anomalous increases in potential not associated with surface features, at stations 75 and 95.

The image reconstruction (Figure 8.12A) is strongly affected by the potential outliers at stations 75 and 95. After removal of these outliers (Figure 8.12B) the image contains:

- a boundary between positive sources to the north of station 40 (i.e. underneath FS19) and negative sources further south
- correlations to positive sources in the shallow part of the image (surface to 20 m) underneath spring FS13 (between stations -10 and -20) and spring FS19 (station 50).

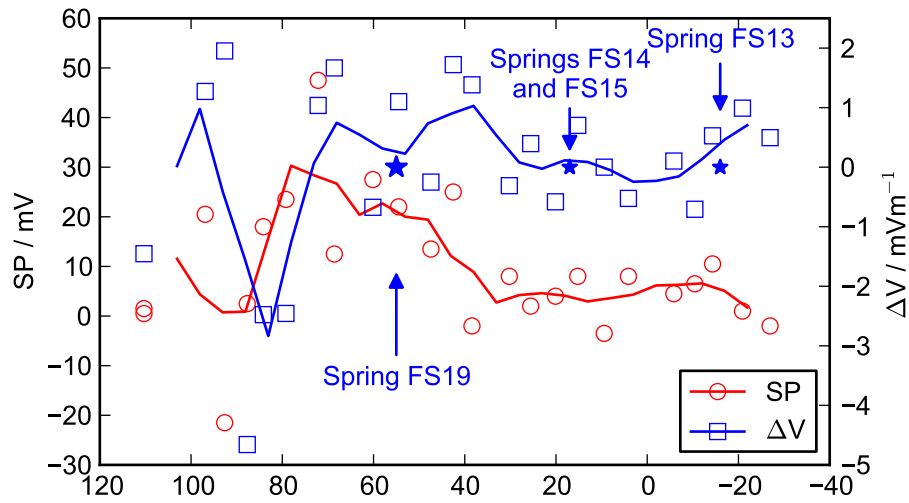


Figure 8.11: Self-potential and potential gradient ΔV along Line N3. Solid lines are moving averages.

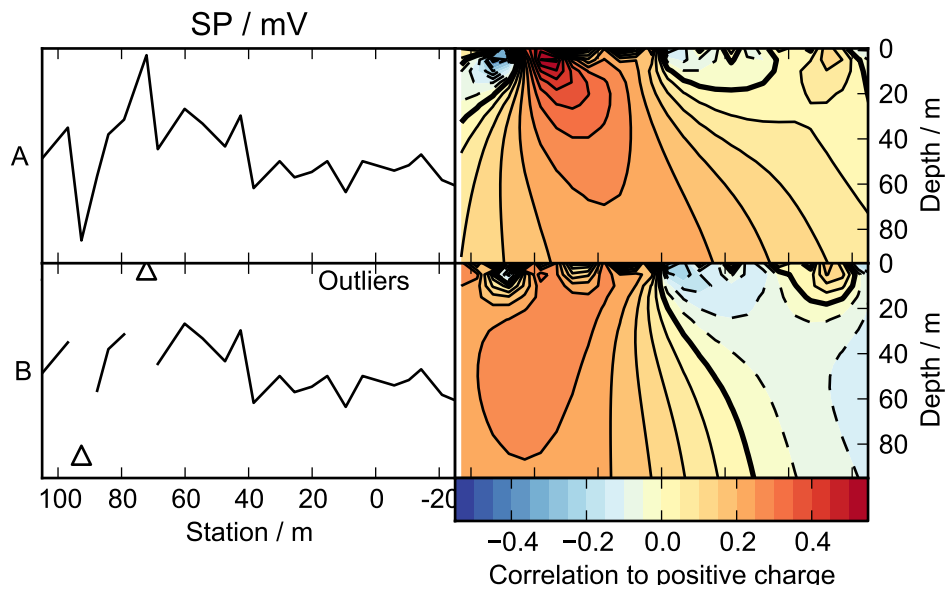


Figure 8.12: Image reconstructions calculated for Line N3 data before (A) and after (B) removal of two outlier potential measurements at stations 45 and 75. The triangles show the outliers when removed, and the solid line shows the remaining data. The right panel contains the image reconstruction for the remaining data.

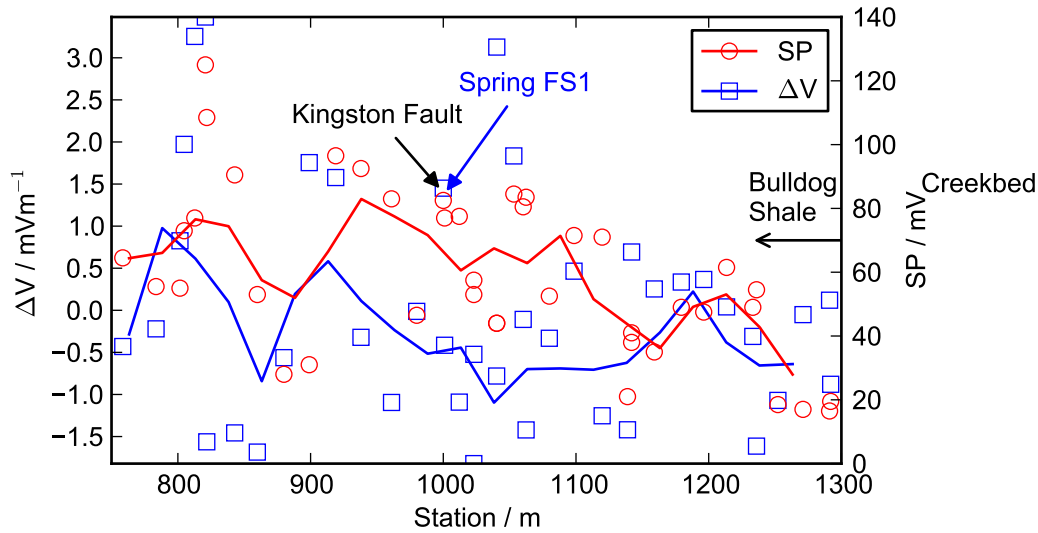


Figure 8.13: Self-potential and potential gradient ΔV along Line S1 including high-resistance measurements in the highlands. Solid lines are moving averages.

8.1.5 Line S1

Self-potential observations from Line S1 are shown in Figure 8.13. The potential was measured between a stationary base electrode and a roving electrode, which was moved along the line in 20 m steps. Potentials are widely distributed between 20 mV to 120 mV, with most high values occurring in the highlands. To the west of the Kingston Fault the potential generally drops, and the average gradient is approximately -0.75 mV m^{-1} .

The data are very noisy, with the potential gradient varying between extremes of -1.5 mV m^{-1} to 3 mV m^{-1} . Potential measurements made in the highlands (between stations 760 and 1000) are widely scattered. They are shown as triangles on Figure 8.14. Contact resistances were above $1 \text{ M}\Omega$ for 11 of 15 measurements in the highlands, compared to 8 of 26 measurements further east; in general these resistances approach the limit where leakage currents in the voltmeter may affect the accuracy of SP measurements (Revil et al., 2012, p. 618), as discussed in Section 8.1.1. Measurements along Line S1 with contact resistances below $1 \text{ M}\Omega$ are shown in Figure 8.15.

There are two main points with significantly elevated potentials that may be associated with springs. The vent of the main spring FS1 is at station 1000. Measurements between stations 1000 and 1020 are 25 mV to 30 mV higher than measurements further east, with another set of similarly elevated

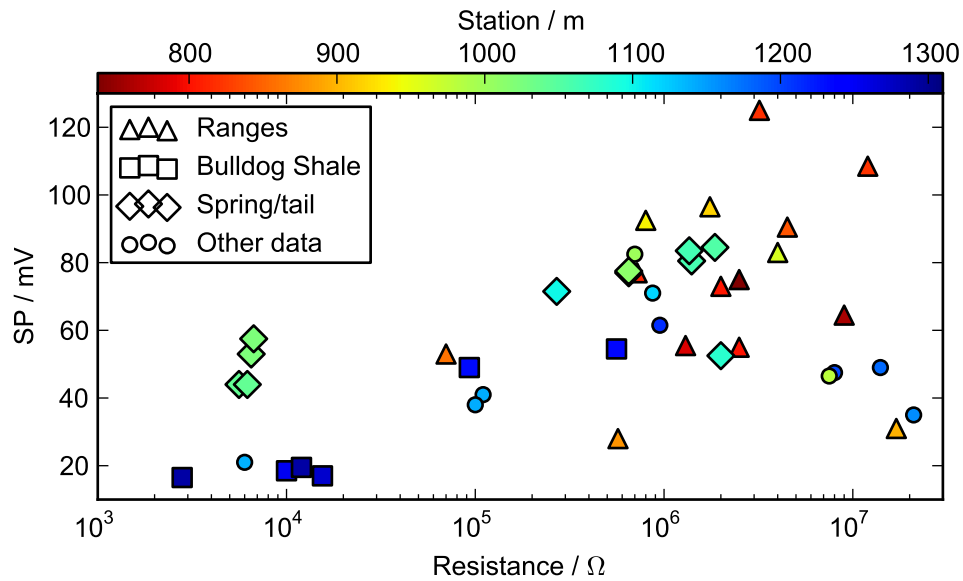


Figure 8.14: Contact resistance and SP for observations along Line S1, coloured by station number with symbols grouped by lithology.

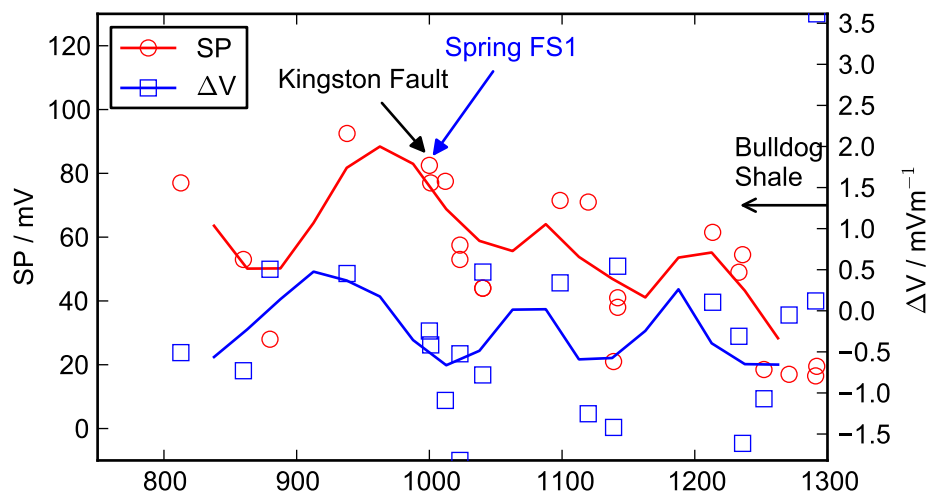


Figure 8.15: Self-potential and potential gradient ΔV along Line S1 excluding measurements with contact resistances greater than $1 \text{ M}\Omega$. Solid lines are moving averages.

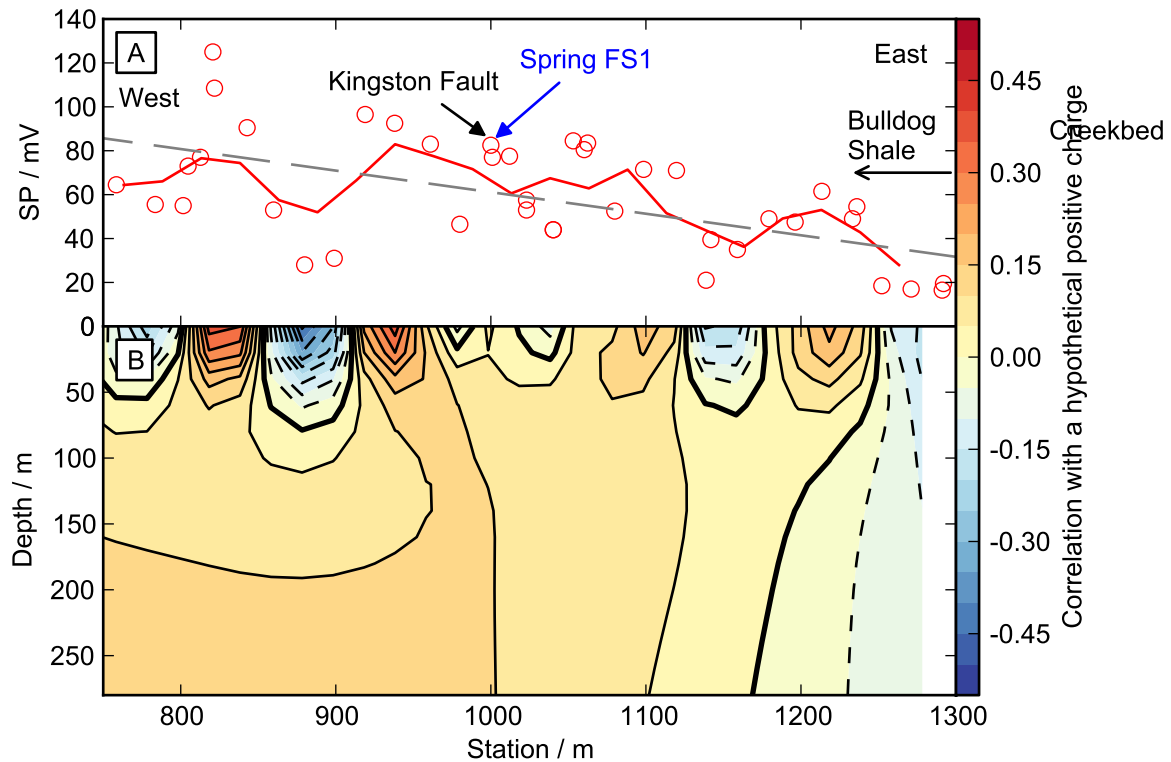


Figure 8.16: Self-potential data (A) and image reconstruction (B) over Line S1. The grey line is a least-squares fit.

potentials at station 1060, which is immediately adjacent to the FS1 discharge tail. Measurements near stations 1100 and 1120 are also slightly elevated by 10 mV to 15 mV. All these peaks are very narrow, with wavelengths no greater than 40 m, implying very shallow sources.

The image reconstruction (Figure 8.16) contains an area correlated to positive sources between stations 860 and 1180 at depths greater than 70 m (correlation coefficient 0.15); at greater depths of more than 130 m there is a stronger correlation of 0.2 between stations 920 and 1120. Although this area does underlie the main spring FS1, a comparison of images constructed to match different subsets of the data (Figure 8.17) shows the feature to be primarily caused by the presence of relatively low potentials measured at the western end of the line, more than 200 m west of the spring vent.

When measurements from the highlands which had contact resistances above 1 M Ω are removed from the image reconstruction (Figure 8.17D), almost all stations west of the Bulldog Shale contact are correlated to positive sources, with a strong correlation found near the surface between stations 920 and 1000, and at depths of 100 m between stations 920 and 1050, which corresponds to the vent at FS1 and the Kingston Fault. This correlation supports

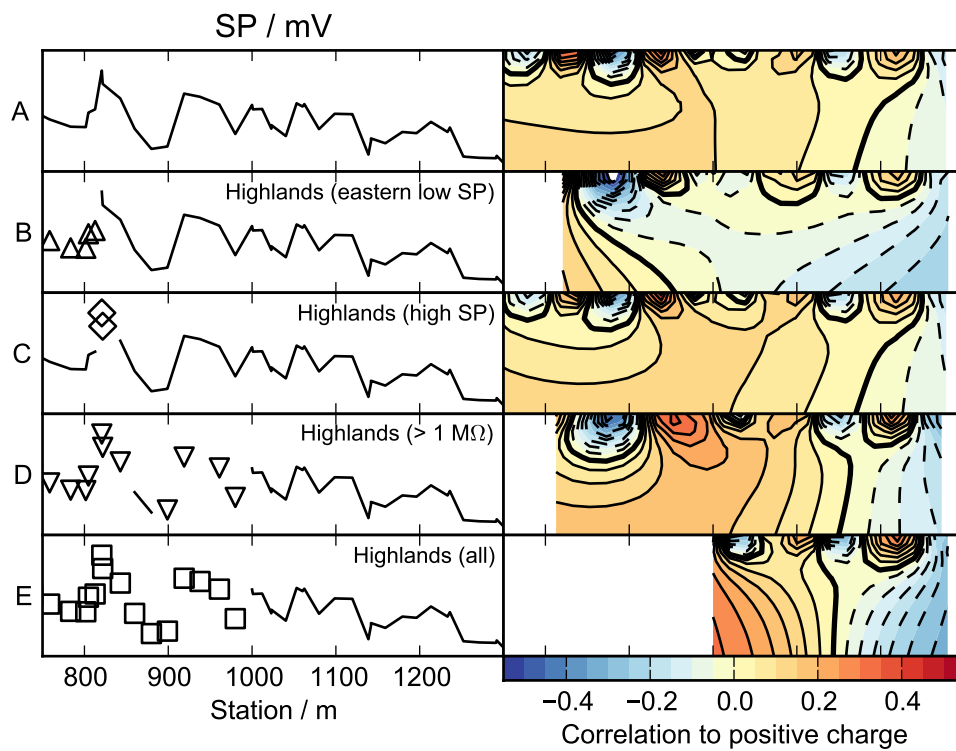


Figure 8.17: Image reconstructions calculated for subsets of the Line S1 data left after removal of different portions of data collected in the highlands. The symbols show the removed data points, and the solid line shows the remaining data. The right panel contains the image reconstruction for the remaining data.

the hypothesis that at least some of the water discharging from the FS1 vent comes from fractured rock aquifers in the highlands via the fault zone.

8.2 TEM

Time-domain electromagnetic data were collected over a 640 m-long section of Line N1, which has a bearing of 078° , running from the Kingston Fault at the base of the highlands (station 940) on to the Bulldog Shale (stations 1500 and beyond). The survey used the central in-loop configuration, with a 20 m square transmitter loop and a 5 m square receiver loop.

The observations were inverted for a resistivity model using Zonge Engineering's STEMINV routine. The model is shown in Figure 8.18. Fits to data were good for early and middle times, prior to rapid decay and the onset of negative responses (Figure 8.19).

The model contains a conductive layer at the surface which becomes more conductive and thicker to the east. The resistivity of this layer decreases from $60 \Omega \text{ m}$ at 10 m depth at station 940, to $0.9 \Omega \text{ m}$ at the same depth at stations between 1400 and 1580. The thickness of the surface conductor also increases, with the $10 \Omega \text{ m}$ contour at the surface at station 960 and at a depth of 30 m at station 1400.

There is a near-vertical feature at station 1100 in the surface conductor, shown with a dashed red line in Figure 8.18. This demarcates a resistive area 100 m wide and 10 m deep, extending at the surface from the Kingston Fault at stations 980 and 1000 to the edge of the carbonate terrace at station 1100. The resistive area is likely to be the spring carbonate terrace. The feature at station 1100 correlates closely with the edge of the spring terrace carbonates, which do not appear westward of station 1080 on this line. As the vertical feature is more than 100 m west of the Kingston Fault, it is interpreted to be a separate fault structure.

Below the surface conductor the model becomes resistive in two areas: between stations 940 and 1000 the resistivity increases to more than $1000 \Omega \text{ m}$ at 40 m depth, while between stations 1150 and 1350 there is a resistive layer that is most strongly resistive near station 1200 ($200 \Omega \text{ m}$). The main break in this mid-model resistor is a conductive area 60 m wide centred on station 1080 between depths of 25 m and 60 m, with a resistivity of $30 \Omega \text{ m}$, directly underneath the resistive area in the surface conductor noted above. There

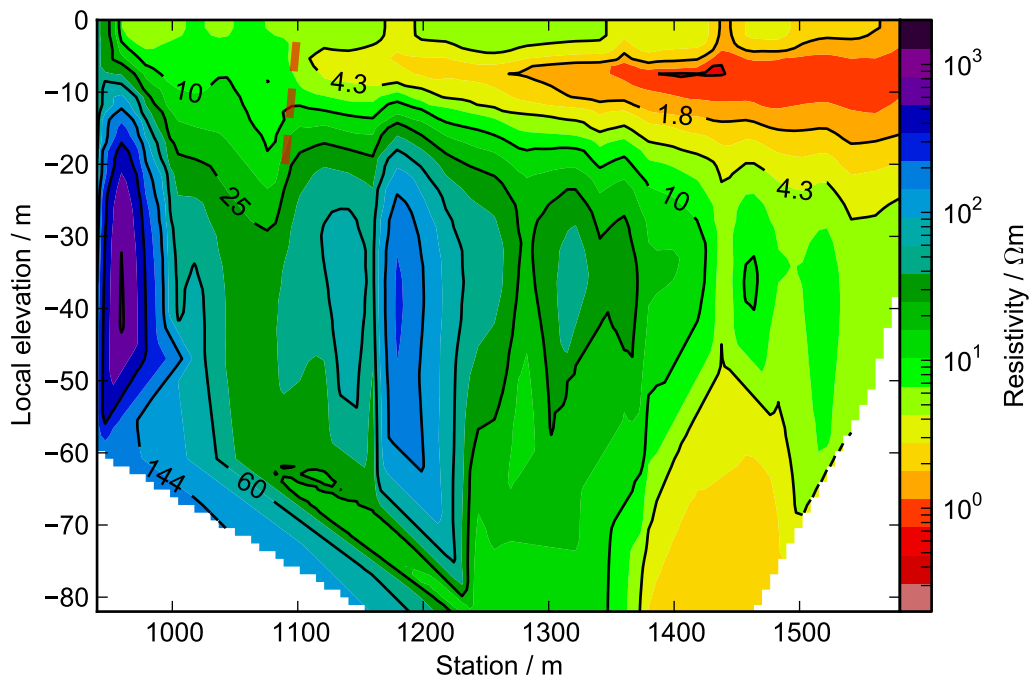


Figure 8.18: Resistivity model obtained by 1D inversion of TEM data. See text for a discussion of the dashed red line at station 1100.

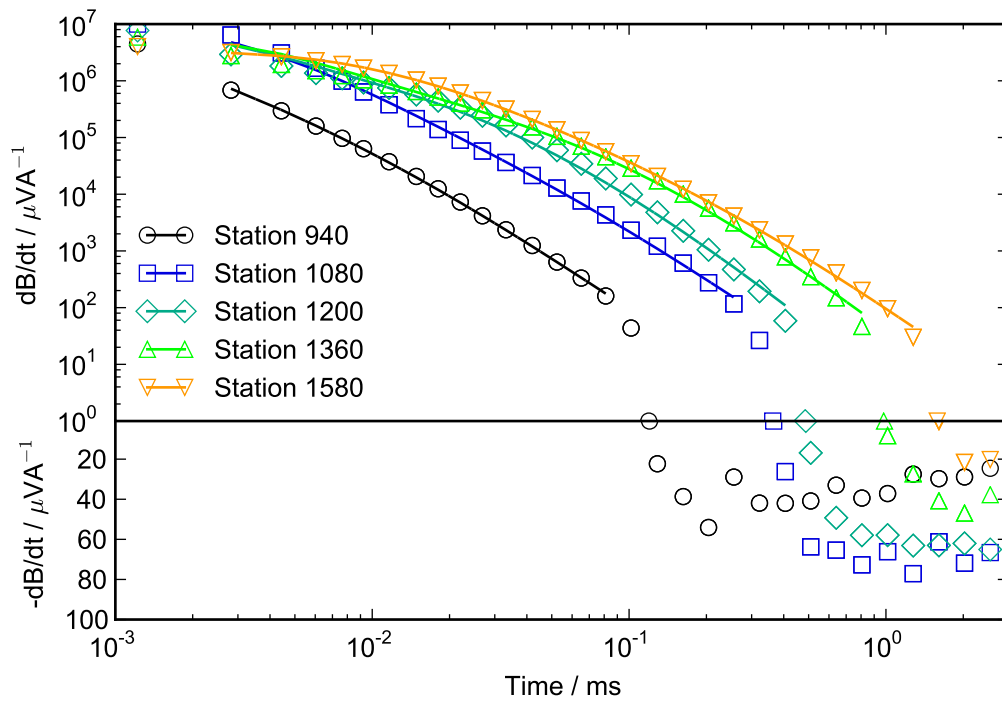


Figure 8.19: Fit of resistivity model (Figure 8.18) to TEM data for selected sites. Shapes show the observed data, and lines show the modelled data, with each station shown in a different colour.

is another similar, slightly more conductive ($20\ \Omega\text{ m}$) gap around 20 m wide found at station 1280.

At depths greater than 65 m the model fit was relatively unconstrained due to the onset of negative responses, but there is a generally conductive layer ($3\ \Omega\text{ m}$ to $25\ \Omega\text{ m}$) underlying stations between 1200 and 1500.

The inverted resistivity model was not required to fit the negative responses recorded at late decay times, nor the transition to these negative responses (Figure 8.19). The onset of the negative response varied along the line from 0.1 ms at the Kingston Fault to 1.2 ms east of station 1360 (Figure 8.20). The decay time at which the negative response became static with respect to time also increased along the line, from 0.2 ms at station 940 to 2 ms for stations east of 1360. The final response (within the measured time windows) varied between $-6\ \mu\text{V A}^{-1}$ to $-22\ \mu\text{V A}^{-1}$, with the most negative response between stations 1000 and 1060, and the final response at stations becoming gradually less negative to the east. The presence of these negative transients suggests that the surface conductor is polarizable (Flis et al., 1989; Smith and West, 1988), and that it becomes less polarizable with increasing distance from the Kingston Fault. See Section 9.3.1.2 for further discussion.

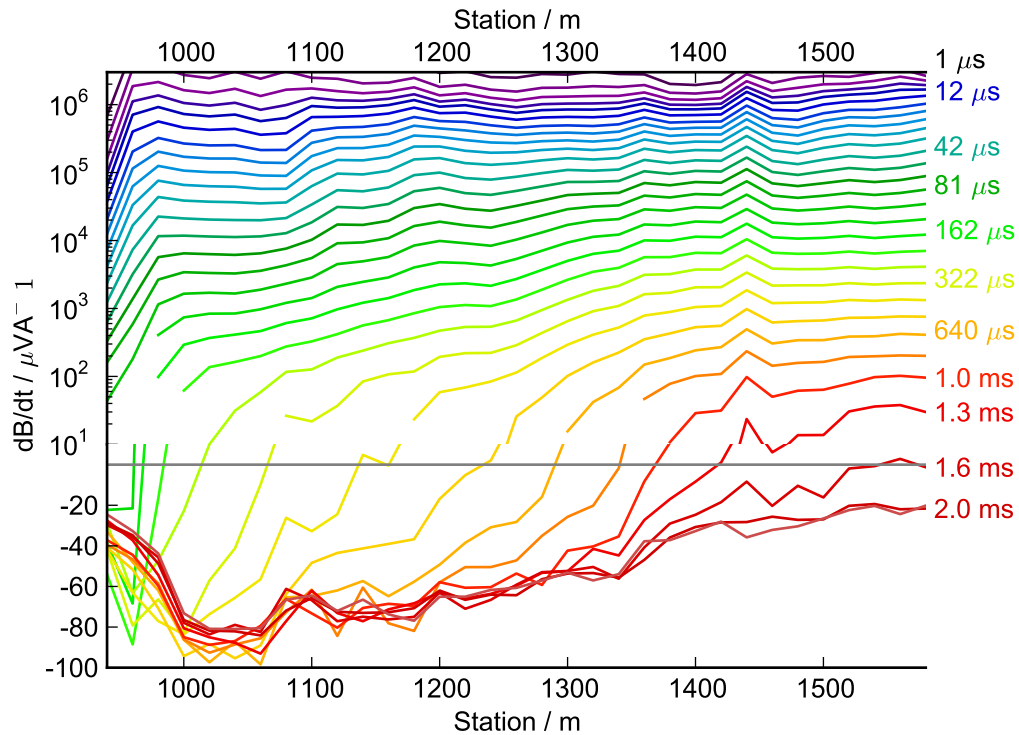


Figure 8.20: TEM responses along Line N1 for all decay times between 1 μ s and 2.5 ms. The decay times for selected curves are shown on the right hand side.

8.3 MT data

Magnetotelluric data were collected at Freeling Springs in November 2012. Data were collected at nine sites located along two lines: both run eastwards from the Kingston Fault. Six sites were located along the southern line, which is 770 m long and runs over Spring FS1. Three sites were located on the northern line, which is 570 m long and runs eastwards from an area containing the carbonate terrace Springs FS13 to FS19.

8.3.1 Southern line

Data were collected at six sites located along the southern line, which is 748 m long and has a bearing of 086°.

Responses were estimated between 250 Hz and 0.1 Hz from 2.7 h windows of time series recorded at a sampling rate of 1000 Hz. Electrode dipoles were oriented towards an azimuth of magnetic north for x and magnetic west for y, the exceptions being FW1 and FW2, where the local topography required different orientations to be used (noted below).

The sites are listed below in order from west to east:

1. FW2 was located in a rugged creek valley 270 m into the highlands. The steep local topography meant that one of the dipoles was laid out in the bed of the creek, bearing 229° , and the other was placed directly up the southern bank of the creek, bearing 139° , with a 30 m difference in elevation across the length of the 50 m-long dipole.
2. FW1 was placed 100 m west of the Kingston Fault, in the mouth of the creek valley on the edge of the highlands. The electrode dipoles were oriented towards an azimuth of 168° for x and 258° for y, also due to rugged terrain.
3. FS was laid over the Spring FS1 vent, at the approximate location of the Kingston Fault.
4. FE1 was located in alluvial outwash, approximately 140 m west of the Kingston Fault and outcropping Bulldog Shale to the east.
5. FE2 was placed on an exposure of Bulldog Shale approximately 280 m east of the Kingston Fault, near the edge of a regional terrace of alluvium 5 m thick which overlies the Bulldog Shale.
6. FE3 was on the alluvial terrace, approximately 480 m east of the Kingston Fault.

Figure 8.21 shows phase tensor ellipses from all sites. Almost all sites have non-zero normalised phase tensor skews (ψ) with most having $|\psi| > 6^\circ$ (Figure 8.21B), indicating that there are significant 3D effects in the area (Booker, 2013). FW2 and FE2 have quasi-2D skews at frequencies above 10 Hz and 60 Hz respectively, and at these stations the strike indicated by current-parallel ellipses is 005° . This is close to the strike of the Kingston Fault in the area of Line S1, which varies between 342° at FS and to the north, and 354° and 028° about 200 m and 400 m to the south. It should be noted that some responses on Figure 8.21B where $|\psi| < 6$ are not 2D, but may represent localised symmetries above 3D structures which appear 2D.

Given that the data are subject to 3D effects, and that no rotation will fully remove the diagonal impedances, a coordinate system parallel to the Kingston Fault was chosen for 2D modelling, as it is the most significant geological feature on the line. The data were rotated by 150° , such that x is parallel to the fault, making Zxy the TE mode and Zyx the TM mode. Apparent resistivity

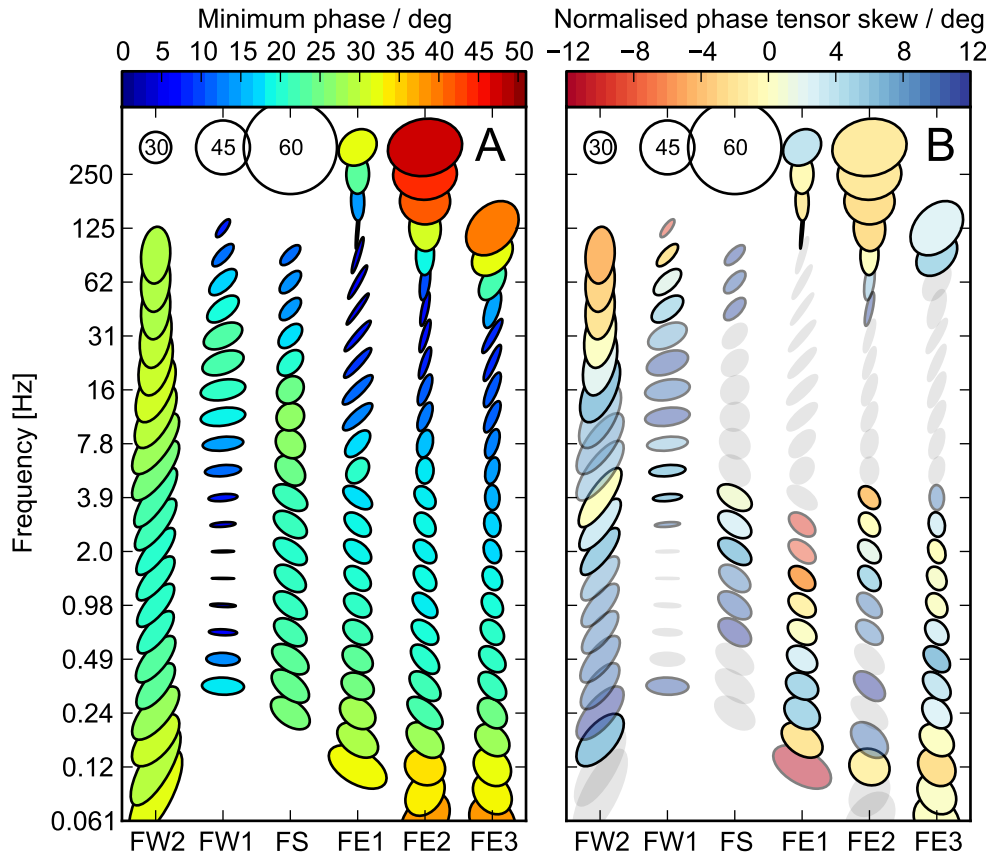


Figure 8.21: Pseudosection of phase tensors from Line S1, filled with (A) minimum phase and (B) the normalised skew ψ (faint coloured ellipses have $|\psi| > 6^\circ$ and faint gray ellipses $|\psi| > 12^\circ$, both representing tensors significantly affected by 3D induction). Phase tensors have been rotated by 90° so that the major axis is parallel to the TE mode under a quasi-2D assumption (Booker, 2013) and ellipses with phases of 30° , 45° , and 60° are shown in the upper left for comparison.

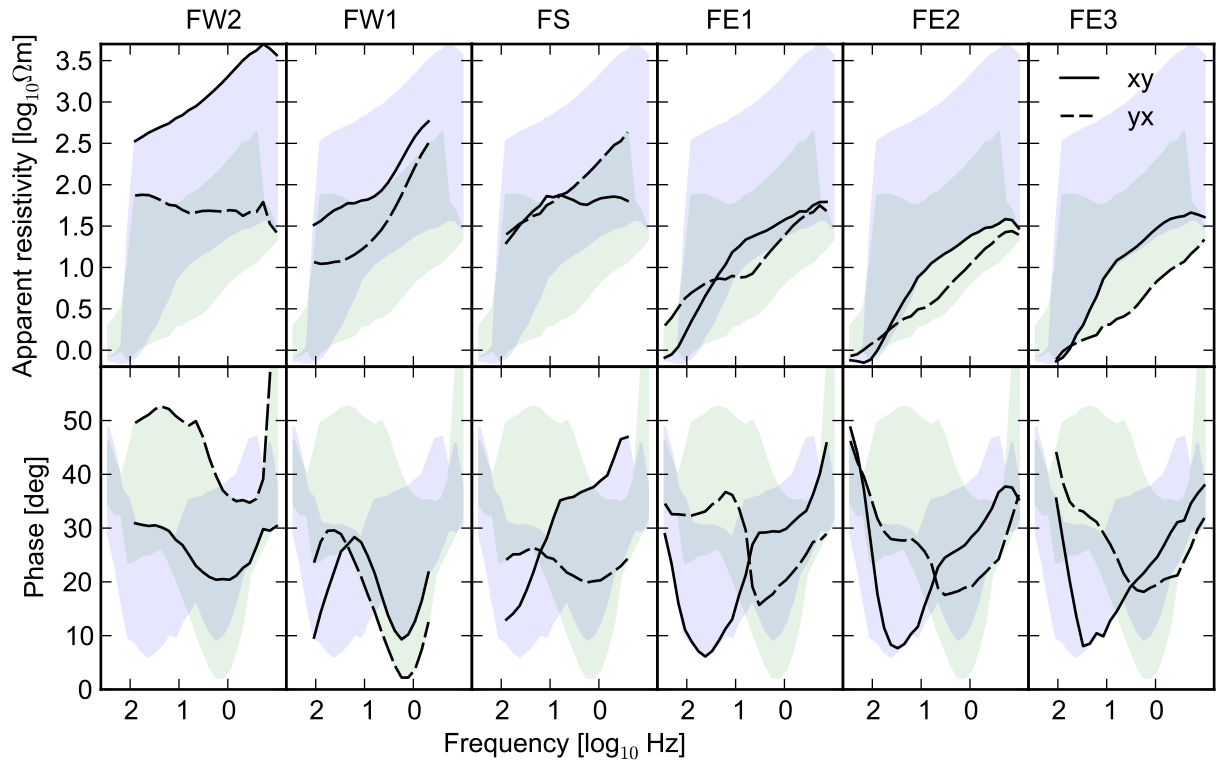


Figure 8.22: Apparent resistivity and phase along Line S1. Coordinate system: x 150°, y 240°.

and phase graphs in this coordinate system are shown in Figure 8.22.

Apparent resistivities drop from west to east, particularly at higher frequencies; FW2, FW1, and FS are between $10 \Omega \text{ m}$ to $300 \Omega \text{ m}$ at 100 Hz, while FE1, FE2, and FE3 are less than $3 \Omega \text{ m}$ at the same frequency. The resistivity generally rises with decreasing frequency.

In the eastern sites, a very low phase feature (10°) occurs in the Zxy mode, centred on 40 Hz with phases dropping steeply by 25° to 35° from 100 Hz. At the same frequency the Zyx phase, which is also dropping in response to a conductor, either flattens out (FE2 and FE3) or slightly rises (FS and FE1) in response to a resistive feature. The Zyx phase then also continues to drop to relatively low phases (20°) at 1 Hz.

The western sites have similar shapes but do not share the same features. The highest frequency phase responses at FW2 are 30° for the Zxy mode and 50° for the Zyx mode, and these do not change significantly for frequencies above 10 Hz, which suggests the top 1000 m contains little variation in resistivity from an initial value around $100 \Omega \text{ m}$.

8.3.2 Northern line

Data were collected at three sites located along the northern line, which is 600 m long and has a bearing of 078° .

Responses were estimated between 250 Hz and 0.1 Hz from 2.7 h windows of time series recorded at a sampling rate of 1000 Hz. Electrode dipoles were collected in line coordinates, with the x electrode oriented towards an azimuth of 348° and the y electrode towards 078° .

The sites are listed below in order from west to east.

1. FN1 was located on the spring carbonate terrace approximately 50 m east of the Kingston Fault. The MT time series collected here were relatively short and due to poor electrode conditions on the rocky ground it was only possible to estimate MT responses for a limited bandwidth (see below).
2. FN2 was located in alluvium about 260 m east of the Kingston Fault.
3. FN3 was located on Bulldog Shale exposure 620 m east of the Kingston Fault.

Figure 8.23 shows phase tensor ellipses for all responses. As with data collected along the southern line, most sites have non-zero normalised phase tensor skews and many have $|\psi| > 6$ (Figure 8.23B), indicating that 3D induction is occurring (Booker, 2013). An exception is that FN2 appears to be quasi-2D from 1 Hz to 60 Hz.

All the ellipses at higher frequencies are strongly oriented towards a strike of between 340° and 350° , which is the same as the Kingston Fault in this area. This suggests that although there are 3D effects, induced currents are flowing parallel to the fault and their geometry is at least approximately similar to those represented by a 2D interpretation in a coordinate system parallel to the fault. Therefore the data were rotated by 150° , making Zxy the TE mode and Zyx the TM mode. Apparent resistivity and phase graphs in this coordinate system are shown in Figure 8.24.

The apparent resistivity data for the off-diagonal components shown in Figure 8.24 are quite similar between sites, and drop from west to east (e.g. at 10 Hz, which represents a penetration depth between 400 m and 3000 m, the apparent resistivity is $320 \Omega \text{ m}$ at FN1, $40 \Omega \text{ m}$ at FN2 and $10 \Omega \text{ m}$ at FN3). A

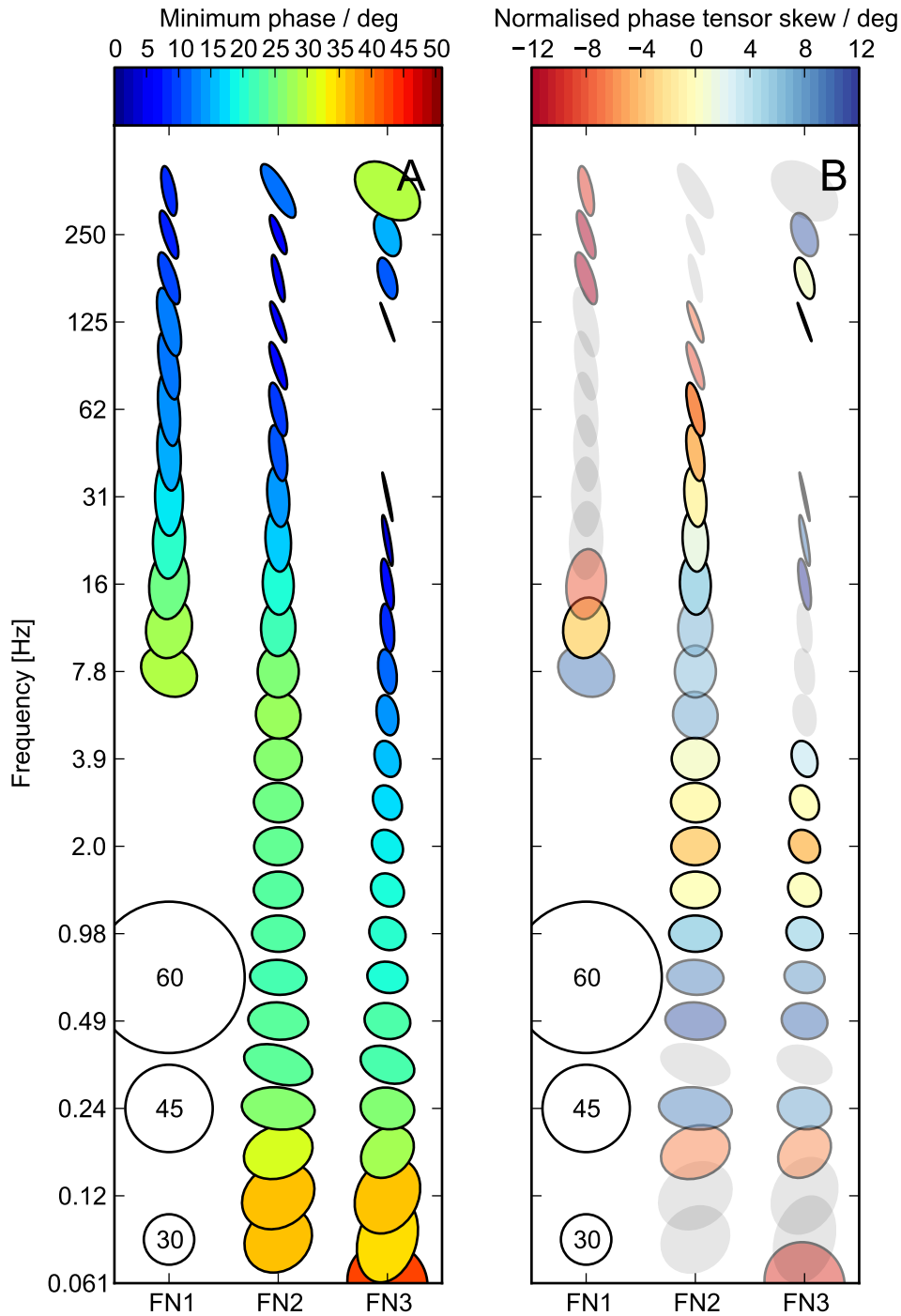


Figure 8.23: Pseudosection of phase tensors from Line N1, filled with (A) minimum phase and (B) the normalised skew ψ (faint coloured ellipses have $|\psi| > 6^\circ$ and faint gray ellipses $|\psi| > 12^\circ$, both representing tensors significantly affected by 3D induction). Phase tensors have been rotated by 90° so that the major axis is parallel to the TE mode under a quasi-2D assumption (Booker, 2013).

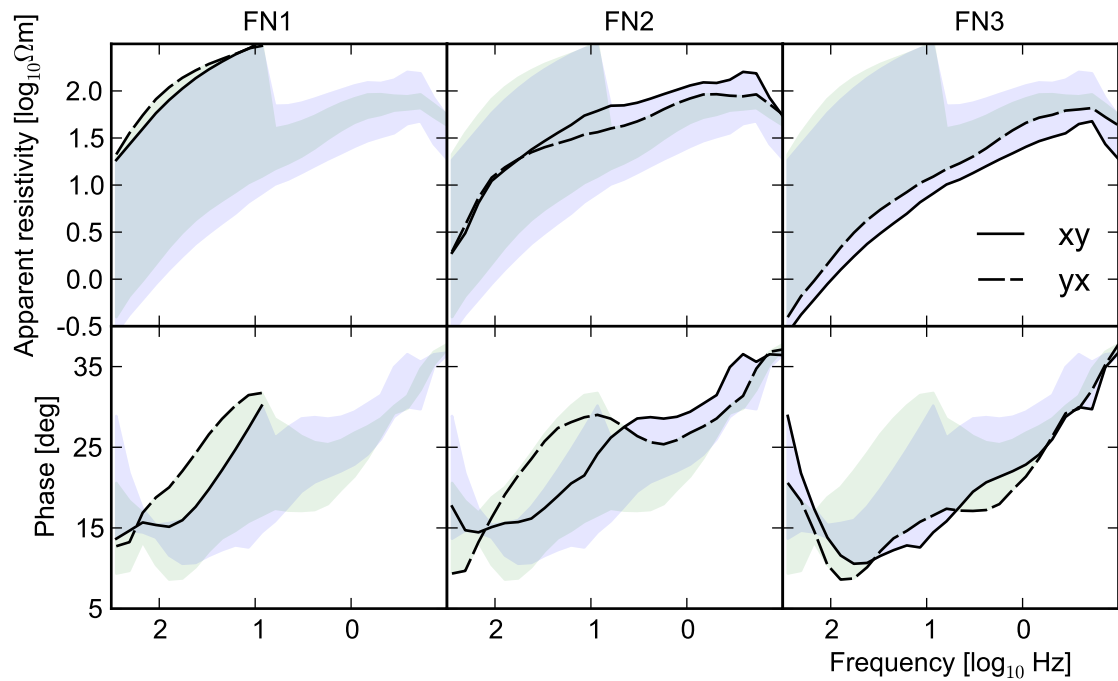


Figure 8.24: Apparent resistivity and phase along Line N1. Coordinate system: x 150° , y 240° .

near-surface conductor can be inferred from the drop in phase occurring at 100 Hz at FN3. This conductor appears at a higher frequency at FN2, where it is only apparent from a slight drop in the already low Z_{xy} phase at 120 Hz. Although this increase in frequency may be due to a general increase in conductivity at FN3 (which is on Bulldog Shale) changing the penetration depth, it may also be caused by a thickening of the surface conductor. The latter interpretation is supported by the eastward-thickening surface conductor found in TEM data (Figure 8.18).

There is a second deeper conductive feature causing phases to drop which occurs at 1.5 Hz and 25° at FN2 and more subtly at 2 Hz and 16° at FN3. It may occur at FN1 but the bandwidth does not extend far enough.

8.4 2D MT modelling

Anisotropic 1D modelling was not performed for the data here because the responses are clearly subject to 2D/3D effects, and there are significant lateral variations. Instead 2D modelling was done using the Occam2D inversion software (de Groot-Hedlin and Constable, 1990), with sites modelled in a coordinate system with TE mode currents parallel to the Kingston Fault. Although this omits some important information present in the observed di-

agonal impedances (see Figure 8.23B), it is a useful guide to the simplest kind of 2D resistivity structures that are sufficient for causing the observed off-diagonal impedances. However, it is important to note that the 2D modelling process presented in this section cannot fully constrain the kind of resistivity structures required by the data, as these must incorporate 3D features (i.e. resistivity variations off the profile).

8.4.1 Southern line

Inversions were conducted for several subsets of data along the line in order to identify where 3D structures had affected the data being inverted, and to avoid introducing unnecessary artefacts into the models. This was done by inverting the simplest data first, which was the eastern sites, and then progressively including data from additional sites to the west. The inversion results are presented in this order.

8.4.1.1 Inversions excluding FW1 and FW2

Inversions for FS and the eastern sites (FE1, FE2, and FE3) converged readily to a common resistivity model (Figure 8.25; fits in Figure 8.26) that is similar to that obtained on the TEM survey to the north (Figure 8.18). There is a highly conductive layer near the surface which is very thin or not present at FS, thickens between FE1 and FE2, thins between FE2 and FE3, and becomes more conductive and thicker again at FE3. The layer has a resistivity in a range from $0.4 \Omega \text{ m}$ to $4 \Omega \text{ m}$, with its base at a depth of approximately 100 m near FE1, 60 m between FE2 and FE3, and 150 m east of FE3.

Underlying the surface conductor is a transitional zone with resistivities from $20 \Omega \text{ m}$ to $200 \Omega \text{ m}$ and its base at a depth of 500 m, underlain by a resistive basement with resistivity $> 1000 \Omega \text{ m}$. This transitional zone comes to the surface at FS; note that points in the model further west of FS are unconstrained in this inversion. It also comes close to the surface between FE2 and FE3, where resistivities of $20 \Omega \text{ m}$ are present in the model at a depth of 80 m.

The surface conductor is inferred to be composed separately of alluvial deposits near FE1 and FE2 and Bulldog Shale near FE3, while the transitional zone is interpreted to be the Cadna-owie Formation (see Section 9.3.1.1 for further discussion).

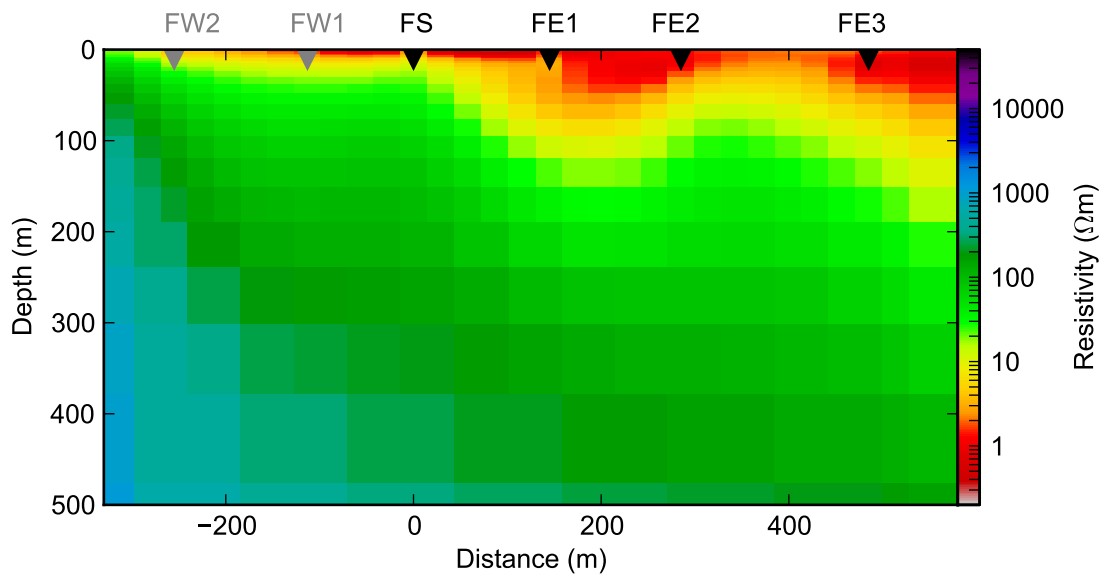


Figure 8.25: Resistivity model from 2D inversion fitting to within 20% of apparent resistivities and 5% of phases along Line S1 (see fits in Figure 8.26). Sites FW2 and FW1 are shown in gray because they were not included in the inversion.

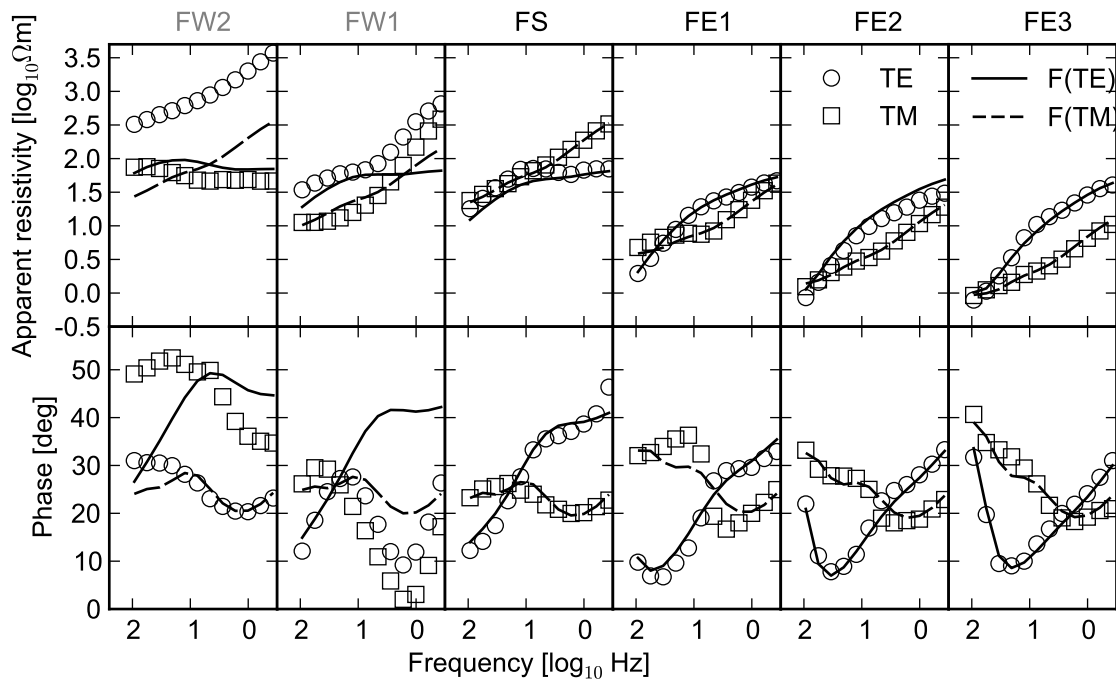


Figure 8.26: Fit of 2D MT model (Figure 8.25) forward responses to observations. Although forward responses were calculated and are shown at FW2 and FW1, these sites were not part of the inversion.

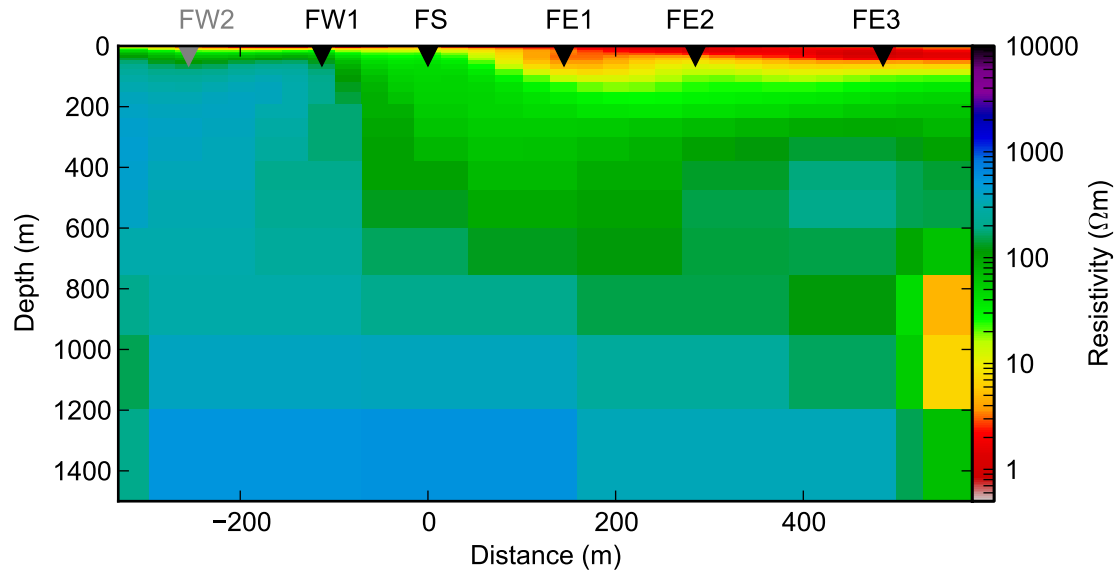


Figure 8.27: Resistivity model from 2D inversion fitting to within 30% of apparent resistivities and 5% of phases along Line S1 (see fits in Figure 8.28). FW2 is shown in gray because it was not included in the inversion.

8.4.1.2 Inversions including FW1

Figure 8.27 shows the model obtained through the most successful inversion including FW1, but still excluding FW2 (fits in Figure 8.28). The model introduces a resistive zone of $1000\ \Omega\text{m}$ at a depth of 100 m beneath FW2 and FW1, with a vertical boundary between FW1 and FS that separates the resistive zone and the transitional zone described in the previous section down to a depth of approximately 900 m. The same boundary then dips to the east at about 40° . The resistive zone is inferred to be the Palaeoproterozoic Wirriecurie Granite and associated intrusive units, and possible Neoproterozoic sediments underneath the transitional zone on the downthrown side of the Kingston Fault.

The TM mode phase at FW1 is fit reasonably well, although the TE mode phase forward response at frequencies below 10 Hz contradicts the data by continuing to rise, while the observed curve drops steeply together with the TM curve. Overall the TE curve at FW1 is following the same trend as the TE curves further east, suggesting that the Z_{xy} drop in phase at low frequencies at FW1 (and potentially also at FW2) is a 3D effect outside of the scope of the 2D modelling.

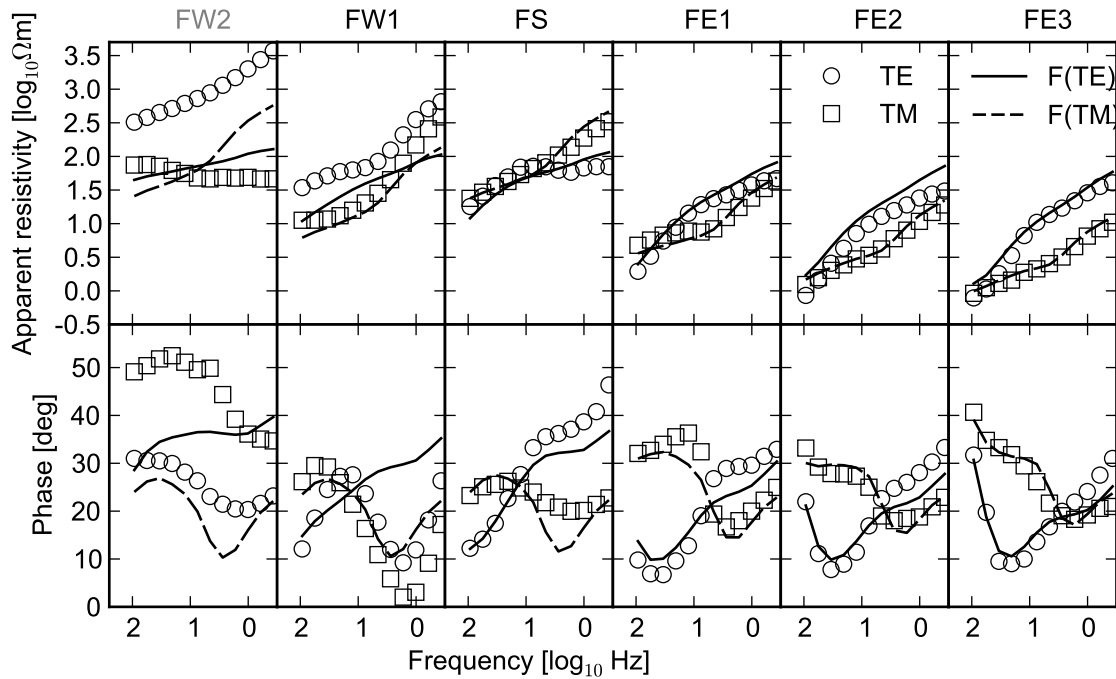


Figure 8.28: Fit of 2D MT model (Figure 8.27) forward responses to observations. Although forward responses were calculated and are shown at FW2, that site was not part of the inversion.

8.4.1.3 Inversions for all sites

Inversions including FW2 resulted in models with a vertical conductive zone between FW1 and FW2. One model is shown in Figure 8.29, and resulted from an inversion which was set to fit within 20% of apparent resistivities and 10% of phases, with only the TM mode used at FW2 and FW1, and both modes used at the remaining sites (Figure 8.30). The justification for this lies in the observation about the TE phase curve remaining unfitted at FW1 in the previous section, despite forming part of the inversion's misfit penalty. The same argument about the elevated TE phases applies to the elevated TE phase and apparent resistivity at FW2. Nonetheless, the vertical conductor also appears, albeit modified, in inversions which include misfit penalties on the TE data at the western sites (and therefore have poorer fits for the TM modes, and both modes east of FW1, and are not shown here).

The vertical conductor has a resistivity of $20 \Omega \text{ m}$ near the surface just to the west of FW1, increasing to $100 \Omega \text{ m}$ at a depth of 300 m. It is bounded to the west by an extremely resistive area ($> 10 \times 10^3 \Omega \text{ m}$, and to the east by a wedge of resistive material (light blue on Figure 8.29) with a resistivity of $400 \Omega \text{ m}$ to $1000 \Omega \text{ m}$. This wedge's western boundary is vertical and lies

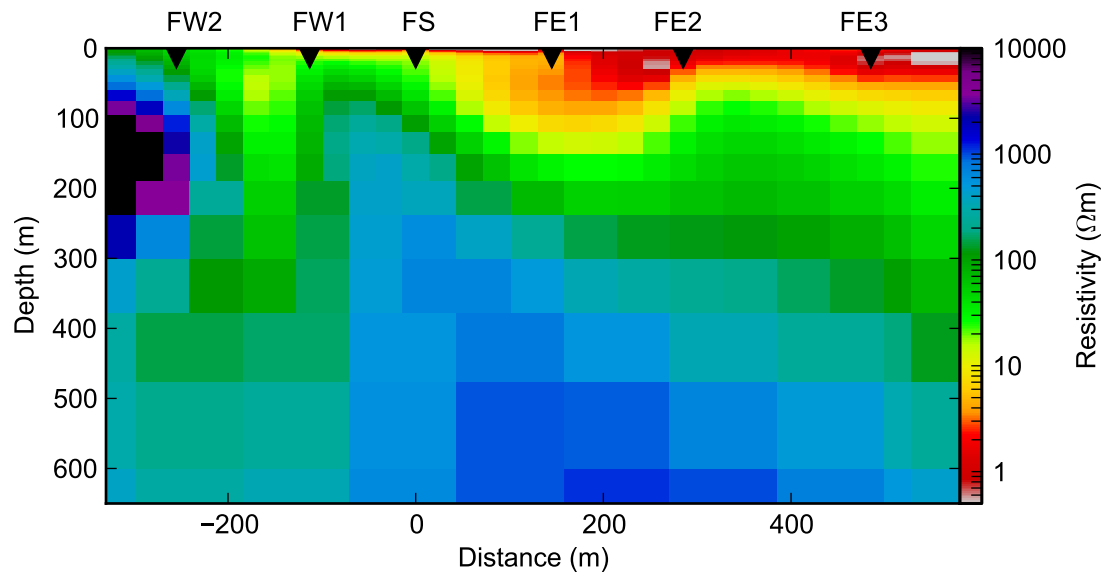


Figure 8.29: Resistivity model from 2D inversion fitting to within 20% of apparent resistivities and 10% of phases along Line S1, with only the TM mode fitted at FW2 and FW1; both modes were fitted at other sites (see fits in Figure 8.30).

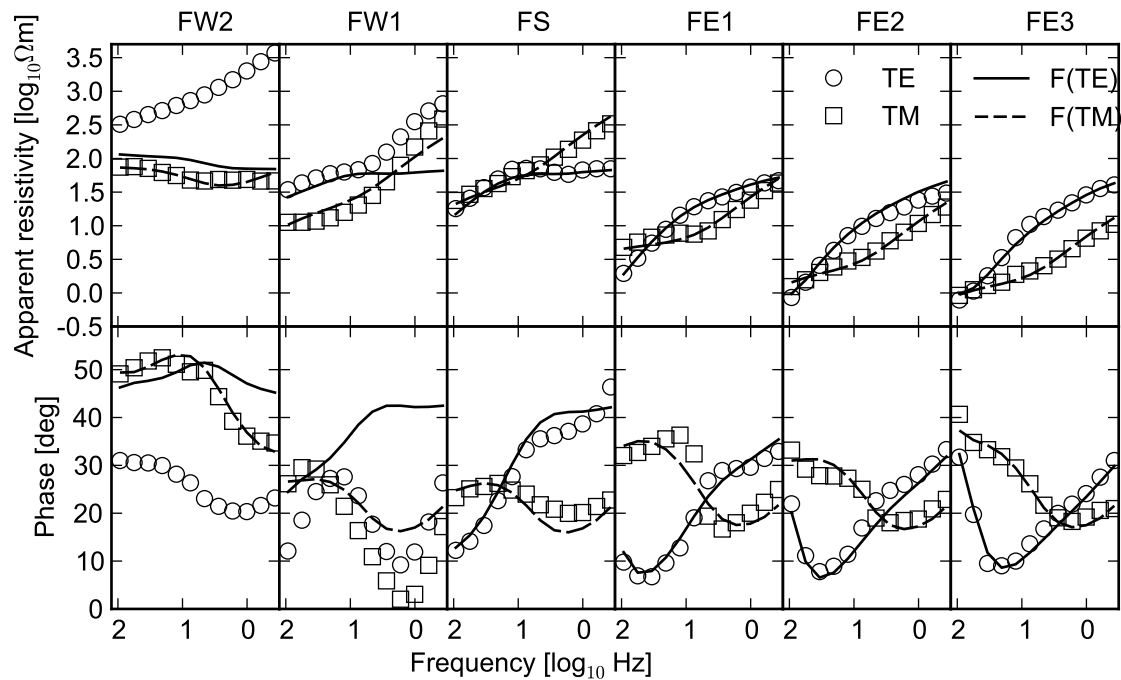


Figure 8.30: Fit of 2D MT model (Figure 8.29) forward responses to observations.

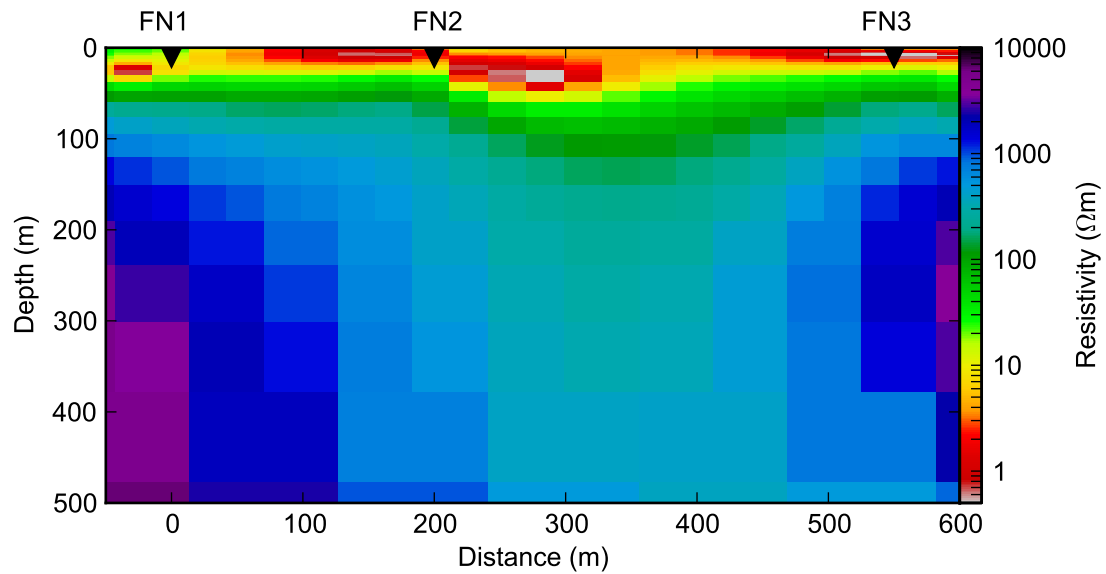


Figure 8.31: Resistivity model from 2D inversion fitting to within 30% of apparent resistivities and 10% of phases along Line N1 (see fits in Figure 8.31).

between FW1 and FS. It is inferred to be the location of the Kingston Fault. The wedge's tip is at a depth of 100 m halfway between FW1 and FS, and the eastern/upper surface of the wedge dips at 45° underneath the 'transitional' zone of Section 8.4.1.1.

The wedge is interpreted to be basement material (possibly Neoproterozoic Callanna Group) underlying the Mesozoic GAB sediments, with its vertical western boundary being the Kingston Fault. The vertical conductor may be a combination of several effects which are discussed further in Section 9.3.2.2.

8.4.2 Northern line

Inversions along the northern line generally resulted in a resistivity model such as that shown in Figure 8.31 (fits in Figure 8.32). This particular model is from an inversion required to fit both modes to within 30% of the apparent resistivities and 10% of the phases, which produced the best-fitting result of a number of inversions. The observations were too spatially sparse and narrow in bandwidth (particularly at FN1) for inversions which were fitted to only the phase, with the resulting models being unrealistically conductive. Results obtained when inverting for only the TM data were similar, suggesting that the general structures described below are required to successfully reproduce the data.

The model contains a highly conductive surface layer as in the model de-

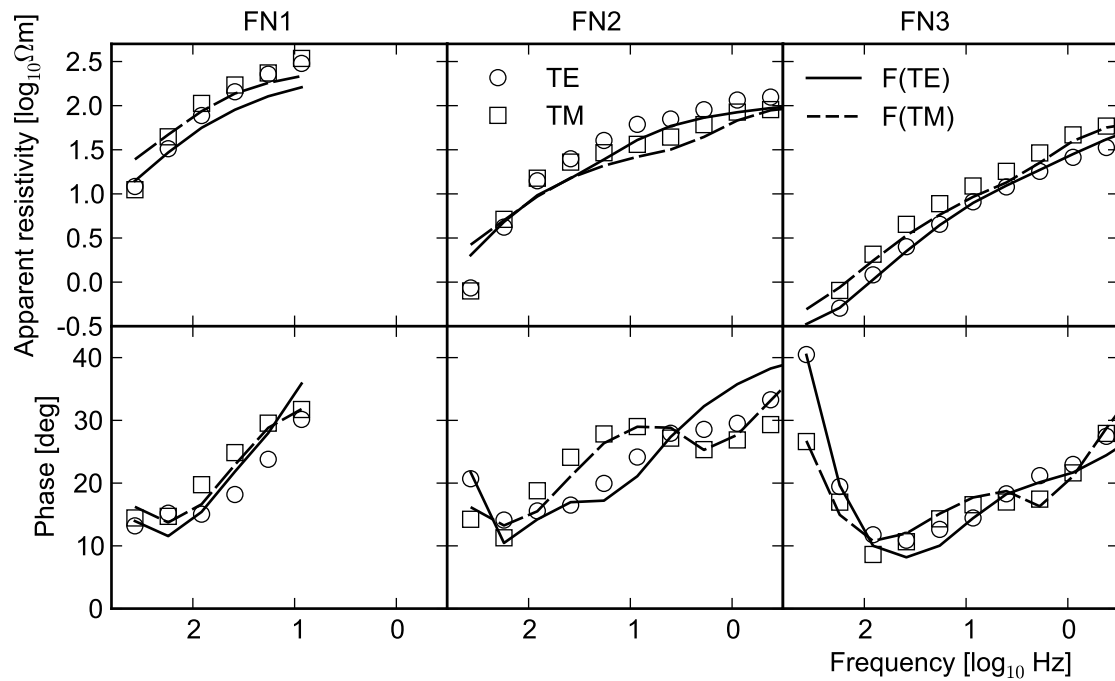


Figure 8.32: Fit of 2D MT model (Figure 8.32) forward responses to observations.

scribed on the southern line (Figure 8.25). Resistivities in this layer range from $0.2 \Omega m$ to $4 \Omega m$, and the layer varies in thickness, extending from the surface to a depth of about 20 m between FN1 and FN2, thickening to the east of FN2 to a depth of 50 m, before thinning again at FN3 with the base at a depth of 20 m. Note that the MT data in the bandwidth collected is sensitive mainly to the conductance – especially when there are few, distant sites such as here – meaning that a model with a slightly more resistive but slightly thicker surface layer would fit the observations equally well.

The surface conductor is interpreted to be the alluvial valley fill as on the southern line, thickening toward the centre of the valley. Note that the Bulldog Shale occurs at the surface to the east of FN3; it should be noted here that all inversions prefer that the surface conductor is thinner under FN3, contrary to expectations of a thicker conductor, given the Bulldog Shale's nature elsewhere on these surveys, and the TEM data collected at this point (station 1600 on Figure 8.18).

Chapter 9

Interpretation

9.1 Beresford/Warburton Spring complex

9.1.1 Beresford Spring

The hydrogeological interpretation for Beresford Spring is summarised in Figure 9.1, and discussed in detail in the following sections.

9.1.1.1 Fault-controlled vertical flow

Results from Beresford Spring suggest that water is flowing up to the mound along structures striking towards an azimuth of 315° . The evidence for this comes primarily from the anisotropic 1D MT modelling, and differences in the SP response measured along and across strike.

The anisotropic 1D MT modelling shows that layers with anomalously conductive vertical sheets striking approximately towards the north or NNW exist at depths between 120 m and 500 m. These layers produce the Type A MT response which is associated with the spring mound (Section 4.4.1). This is the primary evidence for the existence of a set of fault planes directly under the mound.

Elevated SP measurements were also made at the mound, suggesting vertical flow of water underneath the mound. Evidence for the linear distribution of vertical flow along a fault lies in how the positive jump in potential is only 200 m wide on SP profiles which cross the mound from south-west to north-east (Profiles A, B, and C), whereas lines which run parallel to the suggested strike of fault structures (north-west to south-east, Profiles D and E) have sev-

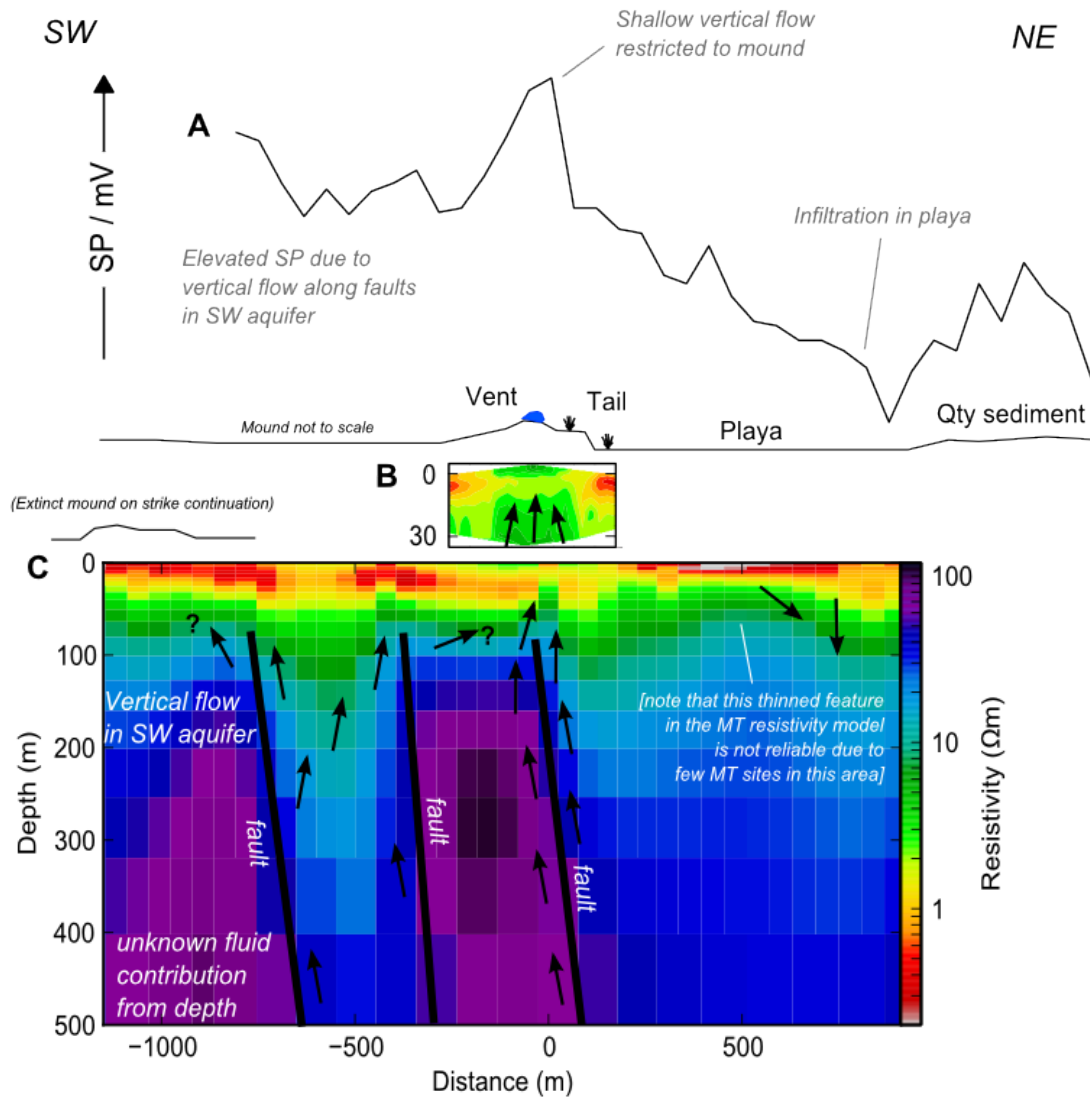


Figure 9.1: Hydrogeology of Beresford Spring, showing the (A) SP data along Profile A, and (B) TEM and (C) broad-survey MT 2D resistivity models. Small black arrows show interpreted groundwater flow directions. Resistivity colour scales are the same in both (B) and (C).

eral elevated jumps in potential (Section 4.1). Note also that there are few other significant positive peaks on the across-strike profiles, as expected if the vertical flow were primarily fault-controlled. The only elevated SP features on across-strike profiles are on Profile A (Figure 9.1), which appear to be aligned with the edges of resistive structures in the MT model. These resistive structures are interpreted to be the location of the other fault planes, responsible for the anisotropic response. Although the fault planes are drawn on Figure 9.1 dipping to the north-east to match the MT resistivity model, this feature of the model has not been rigorously tested against the requirements of the data and the fault geometry could be sub-vertical, as in the anisotropic 1D inversions.

There is little evidence for a significant amount of throw (> 10 m) in the uppermost conductive layer on any fault striking north-west at Beresford Spring. A throw greater than 10 m would appear as either a lateral (2D) effect in MT data at sites near the spring, or at least as a lateral variation in the thickness and/or conductivity of the uppermost conductive layer in 1D inversions of data from sites across the spring. Neither of these are seen: the Bulldog Shale (the shallow conductor) has a homogeneous conductance in the detailed MT survey (Figure 4.31). Nor does it appear closer to the surface in the TEM modelling, where the main effect seems to be an increase in resistivity related to the mound. Note that at the neighbouring Warburton Spring there is some evidence for an offset in the near-surface conductor (see Section 9.1.5).

The interpreted fault is likely to be a structure which was originally active during the initial deposition of Eromanga Basin sediments in the Mesozoic, and has recently become reactivated under the influence of an east-west compressive stress field throughout the Cenozoic (Karlstrom et al., 2013, p. 54). There is a marked difference in the strike of the anisotropic layer between models which reproduce the high-frequency Type A response (NNW to north) and models which reproduce the mid- to low-frequency Type B response (consistently NNE). The difference in strike suggests that different structures are responsible. However it should be noted that all sites have a common response at low frequencies (< 0.2 Hz) with phase tensor ellipses oriented towards an azimuth of 315° . There is a similar orientation for higher frequency responses from the two sites closest to the location of any likely NW-striking fault (BSPR and BWA2890). No attempt was made to model the low frequency response using 1D anisotropic or 2D isotropic inversions, because there were

no sites collected away from the complex, but the similarity of the phase tensor ellipses suggests that it may be related to the same fault structure in a mid-crustal environment with a stronger electrical contrast over the fault zone.

It is likely that the fault structures are channels for groundwater from the GAB aquifers with a fluid resistivity of approximately $1.6 \Omega \text{ m}$ (Table 2.2), at least in the area between the surface and a depth of 130 m (i.e. the upper J-aquifer); deeper aquifer water may have a different resistivity. The modelled resistivity of the aquifer ranges between $50 \Omega \text{ m}$ and $80 \Omega \text{ m}$ in the most geologically plausible anisotropic 1D MT models (Type A $k=5$) and $20 \Omega \text{ m}$ and $100 \Omega \text{ m}$ in the 2D models. In the anisotropic model, the along-fault resistivity is $4 \Omega \text{ m}$ to $6 \Omega \text{ m}$.

9.1.1.2 Resistive area beneath the mound

The Beresford Spring mound is underlain by a resistive zone in the inverted TEM resistivity model (Figures 4.14 and 9.1B). In the shallowest part of the model, no deeper than 15 m, the zone is more than 300 m to 400 m wide (similar to the width of the carbonate platform) and is therefore probably due to the subsurface presence of poorly conducting carbonate mixed with more conductive mixtures of sand, clay, and water. Below a depth of 20 m the width of the resistive zone is similar but the contrast is less ($4 \Omega \text{ m}$ to $5 \Omega \text{ m}$ underneath the mound compared to $2 \Omega \text{ m}$ off the mound). There are two potential hypotheses which explain the contrast in resistivity at depths of more than 20 m:

1. Carbonate precipitated in the subsurface by past or present spring activity is more electrically resistive than the clay-rich Bulldog Shale.
2. Upwelling aquifer water is more resistive than the pore fluids in the surrounding Bulldog Shale and the resistive zone reflects the presence of the spring conduit(s) carrying this more resistive fluid.

It is difficult to determine which of these is correct; it is possible that the resistive response is due to a combination of both. For example, any injection of aquifer sand along a fault zone, or precipitation of carbonate in or near the spring conduit, would result in an increase in resistivity, mainly because it would have displaced or removed highly conductive clays from the Bulldog Shale. Regarding the proposed difference in pore fluids, any infiltration of

surface water into the Bulldog Shale is likely to increase the conductivity of the aquitard, as the high evapotranspiration rate at the surface increases the salinity and therefore the conductivity of any surface water prior to infiltration. Therefore infiltration would accentuate the effect described by the second hypothesis above. It should be noted, however, that almost no infiltration was indicated by SP measurements made close to the mound. Because the observed resistivity of water from the aquifer at Beresford Railway Station Bore (see Table 2.2) is approximately $1.6 \Omega \text{ m}$, it is not likely that 'resistive aquifer water' is solely responsible for the presence of the resistive area underneath the mound.

Resistive zones also exist at greater depths (100 m to 300 m) below both the current mound and along strike from the extinct mound springs at Beresford Hill and the unnamed structure west of the playa. It is possible that these isotropic models are struggling to fit layering that is anisotropic, and are therefore generating alternating conductive/resistive zones laterally in the same depth range. These areas are below the Bulldog Shale, and may indicate lateral variation in fluid resistivity within the aquifer. Such variation could be caused by structural compartments formed by fault planes blocking horizontal flow but permitting vertical flow between the Cadna-owie and Algebuckina Formations, and possibly deeper sources of fluids (Bense and Person, 2006; Anderson and Bakker, 2008). Dual conduit/barrier fault zone systems such as this have been described in a number of other environments (e.g. Bense and Balen, 2004; Apaydin, 2010; Smith, 1980), and have also been proposed to occur for GAB aquifers across the Norwest Fault, which is south-east of the Beresford/Bubbler region (Mudd, 2000).

9.1.2 Beresford Hill

Elevated SP values were recorded over Beresford Hill on Profile D (Section 4.1.5), which runs from north-west to south-east, parallel to the strike of the faults discussed above. Although the ground was more resistive and drier owing to the increased elevation, and the SP measurements are more scattered, they clearly trend towards high levels similar to those recorded at the Beresford Spring vent. They are also elevated across a much broader region compared to the narrow anomaly at the modern spring vent. This suggests that vertical upward flow of water is still occurring but there is no discharge at the surface due to a general lowering of the hydraulic head, and that water rising

through the 'extinct' spring conduit is instead flowing into the unconfined aquifer. The water table is usually quite close to the playa surface (Green and Berens, 2013). This is consistent with the observations of Halihan et al. (2013) that springs which were not actively discharging still had resistive connections to the aquifer. Unfortunately no MT sites were located on or immediately to the south of Beresford Hill, which could provide further constraints on the kind of resistivity structure that exists under the hill.

9.1.3 Vertical flow in aquifer west of the mound

Figure 9.1 shows that vertical flow along fault planes to the south-west of the Beresford Spring mound may be responsible for the generally elevated potentials on the south-western end of Profile A (elevated compared to the north-eastern end). As there are no obvious discharge points on the surface in this area the possibility of lateral flow up the western side of the mound to the vent has been noted on Figure 9.1C. There are not enough data to the south-west (particularly SP measurements) to define flow paths in that area. However, given the interpretation made above for Beresford Hill, it follows that there may still be vertical flow occurring beneath the 'extinct' mound to the west of the Beresford Spring playa, as indicated on Figure 9.1C.

9.1.4 Downward infiltration in playa

Low SP measurements were consistently made in two areas: the north-eastern end of Profile A, which crosses over the north-eastern tip of the playa surrounding the mound, and in an area at the southern end of Profiles A and F which also crosses over a northern extension of playa sediments (see Sections 4.1.3 and 4.1.6). These results suggest either that downward vertical flow of water (i.e. infiltration) is occurring in the playa, or that the electrokinetic coupling coefficient is significantly lower underneath the playa than it is under the mound. The observation that the SP rises once off the playa at the far north-eastern end of Profile A suggests that downward infiltration is at least partly responsible, because the thin layer of Quaternary sediments that begin at the eastern edge of the playa should have little effect on the SP. The very low hydraulic conductivity of the Bulldog Shale (Harrington et al., 2013) suggests that any downward infiltration is only into the very shallow unconfined aquifer at the surface underlying the playa, and should be a seasonal effect which depends on the amount of surface water and evapotranspiration levels.

9.1.5 Warburton Spring

The hydrogeological interpretation for Warburton Spring is summarised in Figure 9.2, and discussed in detail in the following sections.

9.1.5.1 Vertical flow underneath mound and tail

Elevated SP data were observed across the Warburton Spring mound and tail, suggesting that vertical flow is occurring below both. The very high potential gradient on the north-eastern side of the mound compared to a lower, stepped reduction in potential on the south-western side (which contains the tail) also suggests that the depth of the positive potential sources (i.e. groundwater flowing upwards) is increasing to the south-west and/or the strength of these sources is decreasing. The image reconstruction in Figure 5.3 suggests that positive sources (i.e. vertical flow) occurring along a south-west-dipping fault zone would account for these observations. The angle of dip indicated in Figure 5.3B is between 60° and 82° to the west.

The SP response at Beresford Spring suggests that most upward flow is limited to a narrow zone directly under the upper mound, but at Warburton Spring the width of the elevated SP suggests that vertical flow is occurring beneath both the upper mound and at least the upper part of the tail. The most elevated potentials are along the upper tail, which is a narrow channel in the upper mound. The gradual variation in SP across the upper tail and vent indicates there may be multiple conduits in the mound and upper tail responsible for vertical flow.

9.1.5.2 Fault zone

Resistivity modelling of shallow AMT data shows the existence of a near-surface conductive layer, with a more resistive layer underneath; these layers are not seen in the MT models. On the north-eastern side of the mound, resistivities typical of the aquifer ($15\ \Omega\text{m}$) occur at a depth of 80 m, while underneath the tail on the south-western side they occur at a depth between 100 m and 150 m. There is a large change in the thickness of the surface conductor (i.e. the Bulldog Shale aquitard) at the junction between the tail and the upper mound, on the south-western side of the spring vent. This feature is evident in both the AMT and MT modelling. The change in thickness is difficult to estimate from the smoothed models produced by the kind of

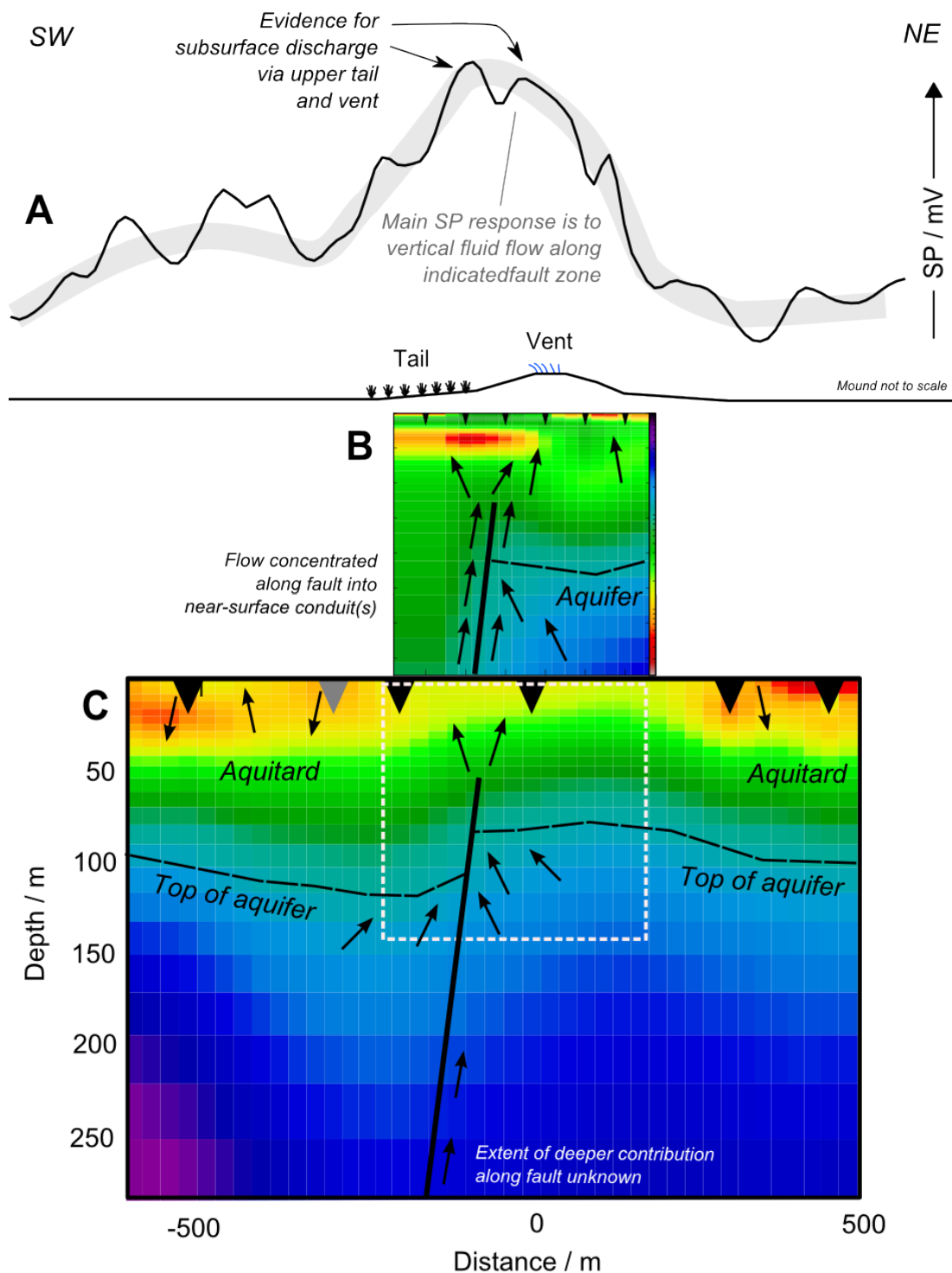


Figure 9.2: Hydrogeology of Warburton Spring, showing the (A) SP data, and (B) AMT and (C) MT 2D models. The white dotted rectangle in (C) shows the extent of the model shown in (B). The thick grey line in (A) shows the general trend of the SP data, while the thin black line shows a moving average. Small black arrows show interpreted groundwater flow directions. See Figure 9.1 for resistivity colour scale legend.

modelling performed here, but it is on the order of 30 m to 60 m, with the conductive layer on the south-western side thicker.

The difference in thickness supports the hypothesis of a fault zone underneath the south-western side of the mound (as seen in the SP), with the location of the lateral change in resistivity at the central location of the elevated SP. The interpreted location of the fault zone is shown in Figure 9.2B. Flow up to the mound is probably coming from the aquifer on both sides of the mound, focused via the fault zone at depths of 120 m and less. It is not clear whether there is any contribution from deeper fluid sources, although the fault is very likely a reactivated Mesozoic structure extending to depth, as the same feature is also found at greater depths in the MT modelling (Figure 9.2C).

9.2 The Bubbler Spring complex

The hydrogeological interpretation for the Bubbler Spring complex is summarised in Figure 9.3, and discussed in detail in the following sections.

9.2.1 Vertical flow beneath mounds

The SP results confirm that groundwater is flowing vertically upward underneath spring vents at the Bubbler. Measurements were made over nine mounds, and seven of those had elevated SP with high potential gradients tending to occur at the edge of the mounds. The only active spring which did not have a response (Spring 406) was located on the flank of a rise in potential associated with a nearby larger spring (the Little Bubbler).

However, there was little indication of any shallow resistivity structures associated with the vertical flow identified in the SP results. The best-fitting TEM resistivity model contained no obviously unique structures in the top 30 m underneath the Little Bubbler spring vent (Figure 7.11), and MT results were consistent with a laterally homogeneous conductive layer down to a depth of around 40 m (e.g. Figure 7.24).

9.2.2 Fault-controlled thinning of aquitard

Both the MT and SP results contain indications that the thickness of the Bulldog Shale aquitard is reduced across the western and south-western part of the spring complex. There are two separate pieces of evidence for this:

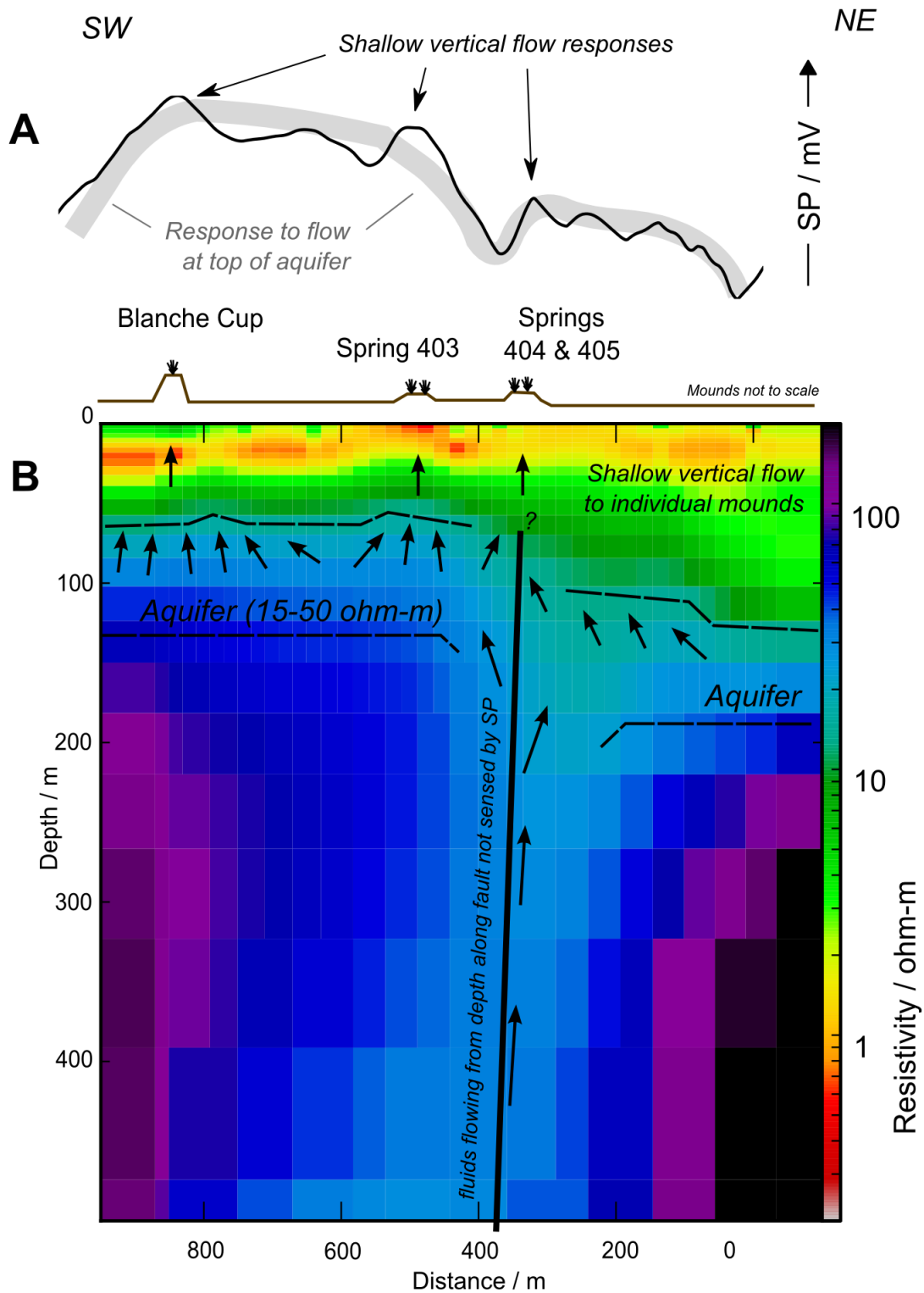


Figure 9.3: Hydrogeology of the Bubbler Spring complex along Line C (see Sections 7.1.4 and 7.3.2). (A) SP data and (B) 2D MT resistivity model. The thick grey line in (A) shows the general trend of the SP data, while the thin black line shows a moving average. Small black arrows show interpreted groundwater flow directions.

1. 2D MT inversion results show that the near-surface conductor is thinner to the west of station WKC1850 than further east. The point of transition appears to be between WKA5265 and WKC1330, which is along the eastern side of the spring complex. The models show that a resistivity of $20\ \Omega\text{m}$ occurs at a depth of 60 m in the western part of the complex, and 120 m at the eastern sites. Based on evidence from the surveys at Beresford and Warburton Springs, the resistivity of the aquifer is expected to be between $20\ \Omega\text{m}$ and $100\ \Omega\text{m}$ and therefore the aquifer is much closer to the surface in the western part of the complex than either the eastern edge (Springs 403, 404, and 405, and the Little Bubbler) or at sites several hundred metres east of the spring complex.
2. There is a broad region of elevated potential in the south-western half of Line C (Figures 7.6 and 9.3A). The potential between stations 2500 and 1800 is consistently higher than the potential further east between stations 1800 and 1200. The difference is at least as large as the magnitude of responses related to individual springs. The difference between the south-western and north-eastern SP responses may be related to either the strength of the underlying SP response (either the electrokinetic coupling coefficient or the hydraulic gradient) or the distance (i.e. depth) to the source. Given the evidence from the MT models, the preferred interpretation is that the SP sources are in the aquifer and that the distance to the uppermost sources in the aquifer is reduced in the west because the aquitard is thinner (Figure 9.3)

The reduction in thickness of the aquitard is interpreted to be due to offset on a steeply-dipping fault which has its surface trace along the eastern side of the complex. The inverted 2D MT models in Figure 7.26 and Figure 7.28 contain a laterally narrow conductive zone which dips WSW from this area and extends to depths greater than 500 m. This zone is interpreted to be a reactivated basin fault zone which is channelling upward flow of water from depth into the aquifer, and may have controlled the development of springs at the complex. The resistivity of the fault zone is similar to the aquifer ($15\ \Omega\text{m}$ to $30\ \Omega\text{m}$), although it should be noted that the width of the fault zone in the MT models (about 200 m) may be overestimated due to the relatively large dimensions of the discrete blocks used for the inversion (60 m to 100 m wide at a depth of 450 m), and if so the conductance estimated in the model would imply that the fault zone is more conductive than the aquifer. Such a situation

could be caused by the presence of hot fluids on the fault zone at depth. Any such flow is unlikely to affect SP measurements at the surface, which are dominated by the closest sources, such as those at the top of the aquifer.

The surface geology suggests two likely fault orientations: along the eastern side of the Little Bubbler and Spring 404 mounds (bearing 343°) and on an axis connecting the Bubbler, Spring 28, and Spring 406 (bearing 315°). The MT data and modelling done here support both orientations, as WKC1850 and WKA5625 both lie on the fault zone in the modelling and interpretation, and they are located at the intersection of the two suggested fault locations. The presence of four spring vents at this location, as well as a steep gradient in the SP, supports the conclusion of Halihan et al. (2013) that spring discharge tends to be focussed at the intersection of fault lines.

9.2.3 Flow variation parallel to strike

Self-potential measurements were made along the proposed fault linking the Bubbler, Spring 28, and Spring 406 (Line B). There were elevated SP responses corresponding to all the spring vents on this line, with magnitudes similar to those measured on Line C, which is perpendicular to the fault (10 mV to 25 mV on Line B compared to 7 mV to 15 mV on Line C). Self-potential anomalies of this magnitude and no more than 250 m wide are interpreted to be caused primarily by vertical flow through the aquitard in the top 30 m to 60 m of the subsurface—i.e. the shallow spring conduits which have not been detected in resistivity models. The broadly elevated potentials on Line C reflect vertical flow in the upper part of the aquifer, which is closer to the surface in the western area.

Thus there is no indication from the data along Line B that vertical flow is strongly enhanced throughout the plane of the fault zone. If it was, there would be broadly elevated potentials on Line B rather than the anomalies which exist. The fault zone probably controlled the initial development of conduits, and indeed the presence of aligned mounds is one of the pieces of evidence that the fault exists, but present-day vertical flow along the plane of the fault zone—in the aquitard—is focused only underneath active or inactive mounds. On the other hand there does appear to be vertical flow broadly distributed under the western half of the complex where the aquitard is thinner. The thinner aquitard may have facilitated the development of conduits and mounds away from the fault zone, although more detailed surveys at mounds

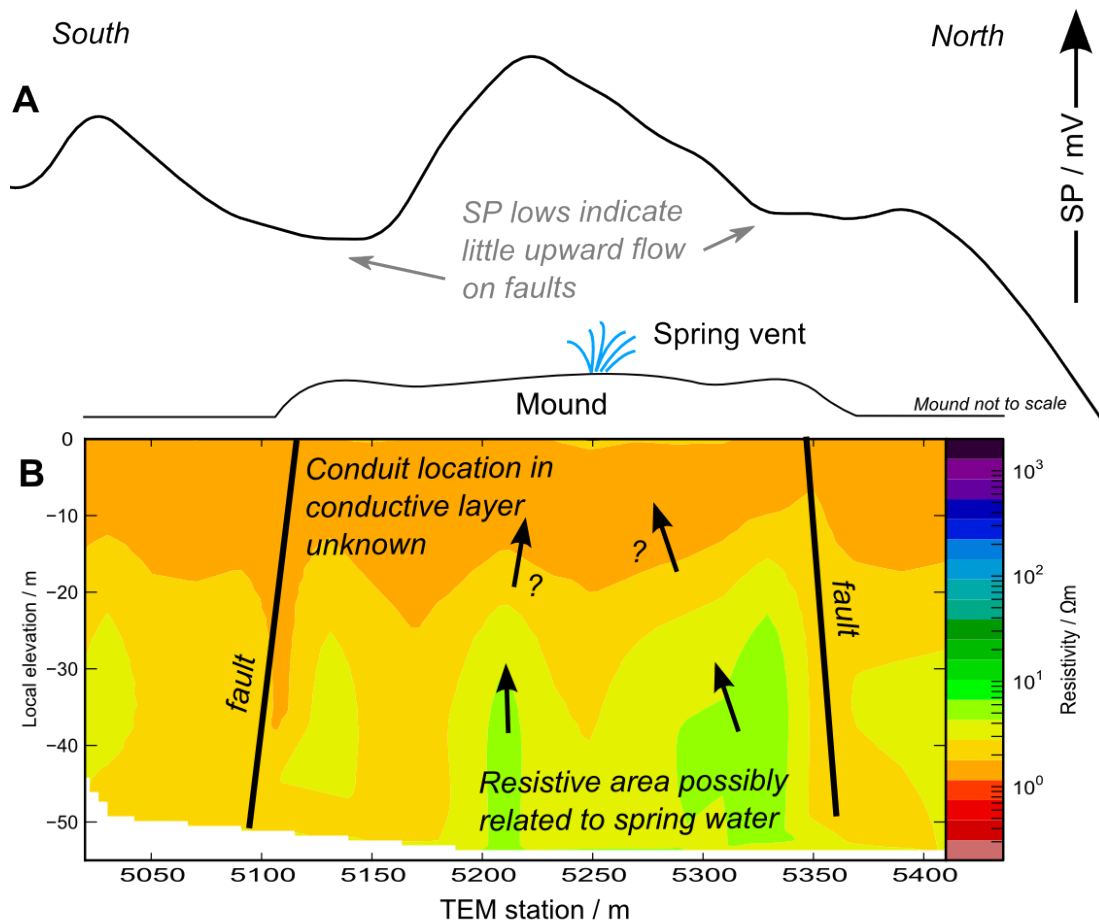


Figure 9.4: Hydrogeology of the Little Bubbler, showing (A) SP data from Line A, and (B) the TEM resistivity model. Small black arrows show the interpreted location of groundwater flow from the aquifer to the spring.

like Blanche Cup would be needed to confirm this hypothesis.

9.2.4 Little Bubbler mound

The TEM resistivity model over the dunes and mound surrounding the Little Bubbler spring vent (Section 7.2) contains narrow vertical conductive features at the southern edge of the mound, and at the northern edge (station 5390), which extend to depths of 40 m and 50 m respectively. These are interpreted to be faults which have partly controlled the extent of the dunes that surround the present-day vent (Figure 9.4).

The southern fault in particular may have a surface expression in the form of a 3 m-high scarp at TEM station 5110 which strikes approximately east/west. The conductive nature of the faults is likely due to clay smearing on the fault plane, which in turn probably also causes a reduction in permeability across

and possibly along the fault plane (Egholm et al., 2008). The interaction between these interpreted faults and the conduit responsible for the discharge of water at the spring vent at station 5270 is not clear, although the lack of an elevated SP response between stations 5250 and 5350 (i.e. the steady drop in SP to the north) indicates that the main component of vertical flow must lie further south, underneath the vent, and that shallow spring conduit(s) and any structures controlling flow at depths of approximately 50 m are not resolved by the TEM resistivity modelling.

9.3 Freeling Springs

The hydrogeological interpretation for the Freeling Springs complex is summarised in Figure 9.5, and discussed in detail in the following sections.

9.3.1 Subsurface lithology

9.3.1.1 Cadna-owie Formation

Previous tectonic and hydrogeological studies have noted steep dips in outcrops of Mesozoic and Cenozoic sedimentary rocks where they abut the boundary faults of the Denison and Davenport Ranges (Rogers and Freeman, 1996b, p. 33 and Aldam and Kuang, 1988, p. 10). Dipping structures are seen in 2D MT resistivity models. The layer indicated in Figure 9.5D by green colours is made up of sediments with resistivities in the expected range for GAB aquifers ($20\ \Omega\text{m}$ to $100\ \Omega\text{m}$) and is present at the surface at the FS1 vent and dips at approximately 50° to the east. This layer is interpreted to be the Cadna-owie Formation. Further east the thickness of the layer increases. The increase in thickness could be explained by movement on the fault (eastern block downthrown) during the deposition of the sediments, or structural alteration by unresolved faults or folding.

9.3.1.2 Surface alluvium

There are highly conductive layers at the surface which are interpreted to be a combination of modern alluvium deposited by runoff from the highlands, and Bulldog Shale which overlies the Cadna-owie Formation. Although the alluvium observed at the surface in the field is mostly sand and gravel, the measurement of significantly elevated potentials away from spring vents indicates that a confining layer (e.g. clay) is likely to exist in the alluvium (see Sec-

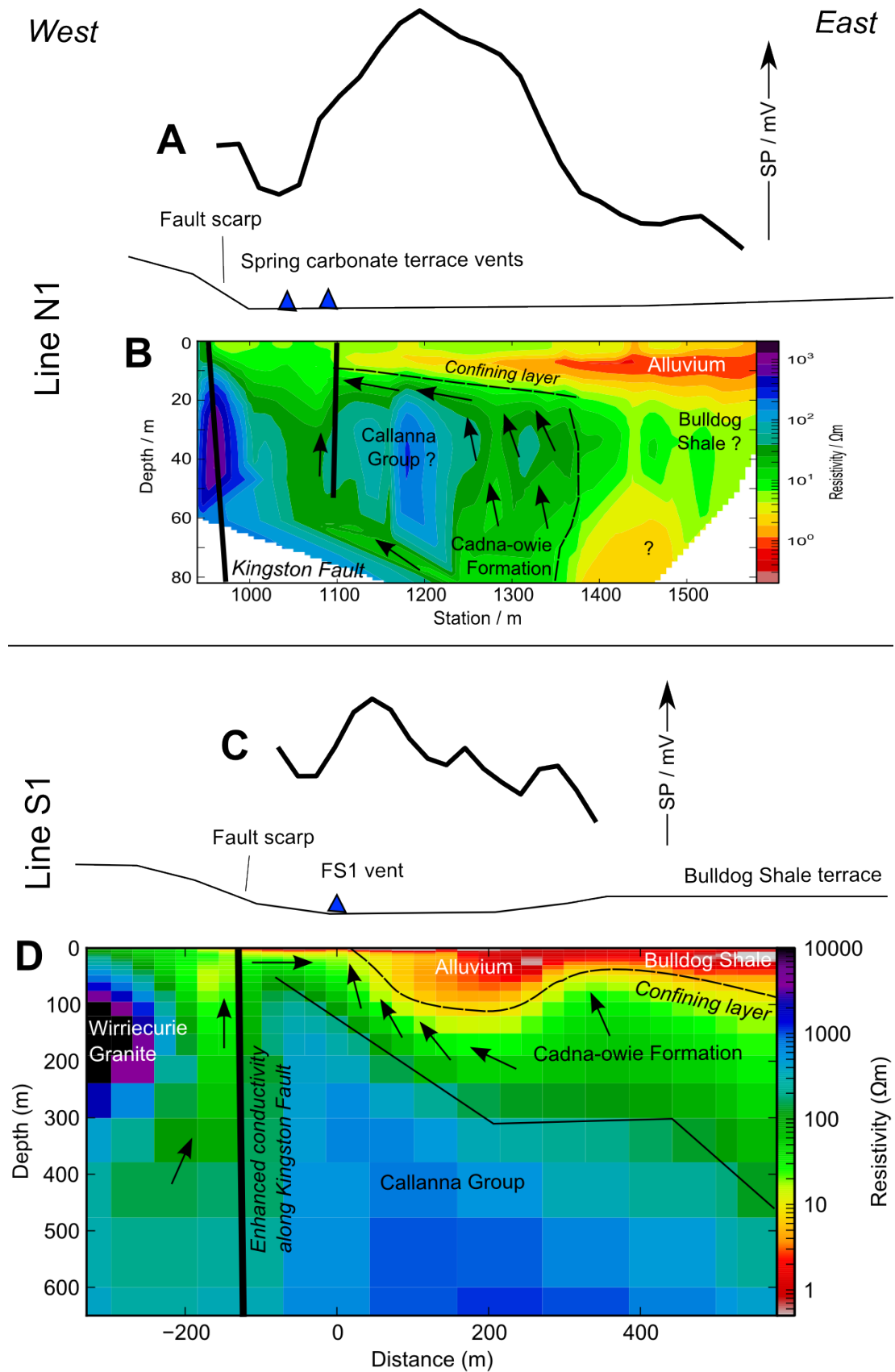


Figure 9.5: Hydrogeology of the Freeling Springs complex, showing (A) SP data and (B) the TEM resistivity model from Line N1, and (C) the SP data and (D) 2D MT resistivity model from an inversion for all sites on Line S1. Self-potential profiles include only those measurements with contact resistances less than $1\text{ M}\Omega$. Both SP profiles are shown with the same scale. Small black arrows show interpreted groundwater flow directions.

tion 9.3.2 below). This is further confirmed by the IP effects in the TEM data in the form of negative late-time transients (Section 8.2), which are probably due to a polarizable surface conductor (Smith and West, 1988). The observations that (1) the negative transients' onset time increases with increasing distance from the Kingston Fault and (2) the magnitude of the final negative response also drops steadily between stations 1100 and 1400 can be explained by either:

1. An increase in the conductance of the near-surface conductor (i.e. an increase in thickness or conductivity or both), masking the IP effect (Flis et al., 1989). Such an increase does occur (Section 8.2).
2. A drop in the total charge polarization occurring in the near-surface conductor with distance to the east, due to changes in the capacitive properties of the conductor.

Either or both of these reasons may be responsible for the changes across the profile. Notably, there is little change in the nature of the small negative response at stations to the east of station 1420, which is close to the surface contact between the alluvium and Bulldog Shale. This last observation leads to the conclusion that the polarizable response is related to the alluvium which fills the valley, rather than clays in the Bulldog Shale.

The cause of the IP itself is most likely the presence of clayey sand. Current flow builds up a high surface polarization of pore fluid ions on the charged surfaces of some clay minerals (Bodmer et al., 1968; Slater and Lesmes, 2002). In the case of detecting the polarization response in TEM measurements, high conductivity is necessary to induce enough current flow to polarize the material (Smith and West, 1988); this increased conductivity is provided by the contribution of the clays' surface conductivity to the electrolytic conduction in the pore fluid (Revil et al., 1998). Once the induced current decays and disperses to greater depths, the polarization discharges, creating a negative response in the receiver loop at late decay times. The polarizability of the alluvium at Freeling Springs is interpreted to be caused by high clay content.

9.3.1.3 Other lithologies

The MT and TEM models in Figure 9.5 contain blocks with resistivities between $200\ \Omega\text{m}$ and $1200\ \Omega\text{m}$. These areas are tentatively interpreted to be comparatively impermeable shale, siltstone, dolomite, and sandstone from

the Neoproterozoic Callanna Group (Rogers and Freeman, 1996a). The 2D MT inversion models also contain highly resistive areas on the western side of the Kingston Fault ($> 2000 \Omega \text{ m}$) which is interpreted to be weathered Wirriecurie Granite (Dailey, 2011; Rogers and Freeman, 1996b).

9.3.2 Vertical flow paths

9.3.2.1 Cadna-owie Formation

The SP profiles along Lines N1 and S1 contain elevated anomalies which are not located over the main points of discharge at spring vents and seeps. On Line N1 the potential peaks approximately 150 m east of the spring carbonate terrace. On Line S1 the peak is 50 m east of the FS1 vent. However, the peaks do correspond closely to the location where the Cadna-owie Formation is interpreted to be closest to the surface and is directly overlain by modern alluvium. It is likely that upward vertical flow is occurring within the aquifer but is then directed laterally along the base of the alluvium by a thin confining clay-rich layer until the flow reaches a point where it can penetrate to the surface. This point may be where the alluvium is thinner or more permeable (e.g. at the Kingston Fault scarp, or where another fault zone provides a permeable path, such as the feature at station 1100 on Line N1) (Figure 9.5B). This is consistent with the SP observations, in that westward lateral flow would result in an increase in potentials to the west. A similar lateral flow path underneath the valley alluvium was found in previous resistivity surveys by Dailey (2011).

The magnitude of the elevated SP feature is much greater on Line N1 than on Line S1. This is consistent with both the greater thickness of the interpreted aquifer in Figure 9.5B compared to Figure 9.5D, and the greater total discharge from springs in the north estimated by Green and Berens (2013): approximately 19 L min^{-1} on Line S1, against 70 L min^{-1} on Line N1.

9.3.2.2 Kingston Fault

There are some indications in the SP data along Line S1 (persistent positive correlations in Figure 8.17) that vertical upward flow may be occurring in the highlands. Dailey (2011) concluded that flow from fractured aquifers in the Wirriecurie Granite were contributing to discharge from the FS1 vent via a sub-vertical flow path along the Kingston Fault. This is also partly supported by

the results in Figure 9.5D, which shows a steeply dipping conductive zone on the highlands side of the Kingston Fault. This conductive zone may be caused by the presence of conductive fluids, smeared clay minerals from the long history of movement on the fault, or simply different lithologies (e.g. carbonate breccias associated with faulting and diapirism in the Cambrian, seen in outcrop 400 m south of FS1).

There are unfortunately few reliable SP measurements in the area to confirm the hypothesis of flow along the fault. It should also be noted that the electrokinetic coupling coefficient in the fractured rock aquifer of the Wirricurie Granite is certainly different and likely lower than that in the porous sediments and rocks further west, and at other locations studied in this work. Such complicating factors, combined with the high contact resistances, make it difficult to fully interpret the highland SP measurements, and the presence of deep or shallow-sourced fluid flow along the Kingston Fault is not fully demonstrated by this work.

Chapter 10

Conclusions

10.1 Hydrogeology

10.1.1 Flow paths

There is strong evidence from SP measurements that vertical upward flow of water is occurring underneath active spring vents and the upper part of spring tails in some cases. There are usually indications of flow underneath the entire mound, focussed at the vent.

Vertical flow indicated by SP surveys is not only occurring at spring vents which are visibly discharging water at the surface, but also at seeps harbouring vegetation growth, and even at mounds consisting of carbonate deposits which are apparently dormant or extinct. These observations were made mainly at the Bubbler Spring complex, which has a large number and variety of such mounds, but similar observations were also made at Beresford Hill, which has 'extinct' deposits dating back to 255 ka to 373 ka. The observations are strong evidence in favour of the hypothesis that near-surface but underground discharge of aquifer water may be occurring under mounds considered dormant or extinct.

The conduits for specific spring mounds have not been sensed in any of the techniques sensitive to resistivity structure used here (TEM, AMT, or MT). This may be because aquifer water has a similar fluid resistivity to the water which saturates the aquitard, particularly in the mid-to-lower parts of the aquitard (i.e. depths of 30 m to 90 m), but it may also be because the permeable structures which channel this water are quite narrow (e.g. < 5 m).

There is little to no evidence from SP observations that downward infiltration is occurring to a significant degree in spring tails, which was previously suspected to be the case. Measurements at Warburton Spring in particular show that vertical *upward* flow is occurring underneath the upper tail, and measurements at Freeling Spring show that no significant amount of downward infiltration is occurring in the spring discharge tail. The only measurements which are likely to be caused by downward vertical infiltration of water were made in low-lying parts of the Warburton/Beresford complex, where the process was more likely to be related to the presence of a topographically depressed playa rather than related to the spring mounds themselves.

10.1.2 Fault structures

Faults have been found to be present underneath spring mounds, vents, or seeps at all the sites surveyed, with only a few exceptions (e.g. Blanche Cup). The faults generally strike NW/SE, which suggests that they are related to the Torrens Hinge Zone, a basin-scale deformation zone striking in this direction and in the same location as the alignment of mound spring complexes in the Lake Eyre region (Krieg et al., 1991; Aldam and Kuang, 1988; Karlstrom et al., 2013).

Most of the faults were identified by anisotropic modelling of a typical feature in MT data labelled a Type A response. It has been shown that this response may be caused by parallel conductive fault planes contained in a fault zone in a depth range similar to that of the J aquifer (identified from regional geological interpretation and borehole logs). The anisotropic response also occurs in the underlying Adelaidean sedimentary rocks. Although the fault zone may be present in the shallow aquitard (e.g. Bulldog Shale), it does not present a resistivity contrast in these layers and is therefore not sensed by the MT and TEM surveys employed in this study. While the modelled resistivity of the J aquifer in general is between $15\ \Omega\text{ m}$ and $80\ \Omega\text{ m}$, the estimated resistivity along fault planes is approximately $4\ \Omega\text{ m}$ to $6\ \Omega\text{ m}$, which is close to the general resistivity of the clay-rich and saturated aquitard ($0.8\ \Omega\text{ m}$ to $5\ \Omega\text{ m}$).

Self-potential data shows that upward vertical flow of water is generally only occurring along faults underneath spring mounds, vents, and seeps. There are only weak indications of laterally-distributed upward flow along fault plane surfaces at Beresford/Warburton and the Bubbler Spring complex. Although most flow does occur on the fault planes, it is concentrated underneath dis-

charge points at the surface. Not enough SP data was collected at Freeling Springs to investigate fault-parallel upward flow.

Although there are laterally distributed SP sources (e.g. the western part of the Bubbler Spring complex), these are believed to be caused by flow in the upper part of the aquifer, rather than laterally widespread discharge. The locations of vertical flow indicated by narrow-wavelength SP responses are mostly limited to the locations of vents and seeps.

The J aquifer is generally resistive compared to the highly conductive Bulldog Shale aquitard, and all the modelling suggests that the resistivities of these layers are $15\ \Omega\text{ m}$ to $80\ \Omega\text{ m}$ and $0.8\ \Omega\text{ m}$ to $5\ \Omega\text{ m}$ respectively. Although the smooth modelling performed in this study is inherently unsuited to determining an exact depth to the top of the aquifer, sharp-boundary resistivity modelling techniques may be suited to determining the depth to the aquifer at other locations (de Groot-Hedlin and Constable, 2004).

10.2 Geophysical techniques

10.2.1 Self potential

Self-potential measurements were found to be useful for sensing the location of vertical groundwater flow paths. However, SP profiles also contained elevated and depressed potential anomalies with amplitudes of up to $\pm 15\text{ mV}$ which were not correlated with any surface geological features. Furthermore, repeated SP measurements at the same locations were not always the same. We recommend that, where possible, SP survey lines should be run more than once to help determine noise levels and repeatability.

We conclude, based on our experiences here (particularly at Freeling Springs), and consistent with other studies (Ernstson and Scherer, 1986; Revil et al., 2012), that unpredictable changes in SP are largely caused by high contact resistances, which are in turn typically caused by dry soil conditions and loss of soil moisture during the survey. In the extremely dry conditions which were typically encountered in the semi-arid to arid Lake Eyre region, soil moisture is rapidly lost by evaporation upon digging electrode pot holes. This leads to very high contact resistances ($> 1\text{ M}\Omega$), as found at Freeling Springs (Section 8.1.1). The effect of high contact resistance on potential variability is shown in Figure 8.2.

A particularly significant problem occurs when evaporation of soil moisture is occurring in the base electrode hole throughout a survey, as this affects every measurement. We suggest using a deep hole (> 20 cm) filled with bentonite clay for the base electrode, and that this hole should be dug and prepared before the survey is performed (i.e. the day before if possible). The extra time is to allow for moisture levels to equilibrate in the immediate surroundings. The base electrode hole should also be protected from the sun and wind as much as possible to minimise evaporation of moisture, as upward flow of water in the immediate surroundings due to increased evaporation at the surface will interfere with measurements. If bentonite is not available, use a location in the landscape with higher levels of clay. Very sandy locations should be avoided for base electrodes (and indeed any electrode for which repeatability is important) as it is impossible to prevent changes in soil moisture.

As recommended by Revil et al. (2012), electrode holes should never be watered, as this will cause variations in local flow, salinity, and coupling coefficient, causing changes in the SP with time as the water infiltrates and evaporates.

10.2.2 Magnetotellurics and TEM

Magnetotellurics is not often thought to be useful for relatively shallow hydrogeological studies like this performed here. Although normal processing of data (i.e. 2D inversions) was useful, it was found to be particularly effective to use MT data to investigate the dimensionality of resistivity structures through techniques such as anisotropic 1D modelling. This led to the identification and interpretation of faults underlying a number of sites. However, because most of the MT data collected for this thesis was ‘broadband’ MT (responses estimated between 0.1 Hz and 200 Hz), there was little resolution of structures and variations within the aquitard, particularly within the top 60 m. The high inter-site distance was also a limitation, as MT sites were generally placed at least 200 m apart, which is much wider than expected variations due to spring conduits (< 20 m) or mound structures themselves (50 m to 400 m).

The TEM surveys were effective in investigating resistivity structures in the near surface, although the sensitivity at depths greater than 30 m to 50 m is limited by the highly conductive near-surface layers which absorb most of the transmitted source signal.

Audio-magnetotelluric (AMT) surveys, with responses estimated between 5 Hz and 8 kHz, showed that there are important resistivity structures in the aquitard which are missed by areas only surveyed with MT sites. AMT should be considered for future work instead of lower frequency MT, as it can obtain responses across the entire depth range of interest (15 m to 1000 m), and still has the ability to provide information on dimensionality. Another priority should be to obtain continuous profiles of sites wherever possible (e.g. Torres-Verdin and Bostick, 1992).

10.3 Future work

One of the most significant strengths of this work lies in the fact that multiple techniques were used. The information gained from these different survey types (SP, MT, and TEM) complemented each other and allowed a full interpretation to be made.

A list of specific questions that I believe would be fruitful for further investigation are listed below:

- Is vertical flow occurring underneath spring deposits considered extinct, such as Beresford Hill? This question could be addressed with more extensive TEM and AMT sites, located over and near the hill, together with more robust SP measurements following the principles described above. A similar question of whether very shallow subsurface discharge is still occurring beneath small carbonate mounds which appear to be extinct could be further explored with SP surveys at sites like Strangways Springs.
- What are the resistivity structures in the aquitard that underlie spring vents and seeps at complexes with a variety of mound types, such as the Bubbler Spring complex? This question is primarily motivated by the interesting shallow fault structures found at the Little Bubbler Spring, and might be best addressed with an extensive TEM survey (potentially airborne TEM) in the Bubbler Spring complex area.
- Does the magnitude of SP measurements correlate to spring flow rates? This question could be answered with a more extensive SP survey at the Bubbler Spring complex, which contains the spring with the highest flow rate in the Lake Eyre region; in particular, an SP profile oriented SW/NE crossing the Bubbler Spring vent, with other survey lines to tie

in to the responses already measured on this survey, all with respect to a common base electrode.

- What are the resistivity structures at Freeling Springs? The initial results obtained here could be further investigated with 3D modelling and the collection of AMT sites in particular.

Appendix A

Magnetotelluric data

The impedance tensor estimates made at all sites are presented in the following Tables, and are also available for download at <http://dx.doi.org/10.6084/m9.figshare.828511>.

A.1 Beresford Spring

A.1.1 Broad-scale survey

Table A.1: Impedance tensor estimates made at BWA1000.

Freq / Hz	Z_{xx}	Z_{xy}	Z_{yx}	Z_{yy}
62.5	-1.040-0.888i	10.90+10.52i	-10.45-10.04i	0.332+0.424i
46.9	-0.971-0.709i	10.24+7.94i	-9.775-7.546i	0.363+0.344i
31.2	-0.890-0.563i	9.428+5.819i	-8.972-5.529i	0.298+0.305i
23.4	-0.835-0.498i	9.150+4.547i	-8.672-4.307i	0.266+0.295i
15.6	-0.737-0.421i	8.807+3.472i	-8.342-3.252i	0.191+0.298i
11.7	-0.706-0.423i	8.790+2.820i	-8.391-2.594i	0.156+0.171i
7.81	-0.592-0.296i	8.335+2.332i	-8.159-2.133i	0.183+0.327i
5.86	-0.554-0.339i	8.259+2.100i	-8.120-1.908i	0.087+0.143i
3.91	-0.421-0.241i	7.789+1.865i	-7.988-1.851i	0.000+0.084i
2.93	-0.379-0.192i	7.358+1.698i	-7.519-1.757i	-0.015+0.112i
1.95	-0.389-0.127i	6.996+1.470i	-6.863-1.613i	0.020+0.096i
1.46	-0.345-0.128i	6.810+1.351i	-6.505-1.520i	-0.019+0.094i
0.977	-0.339-0.072i	6.580+1.196i	-6.164-1.313i	-0.074+0.017i
0.732	-0.310-0.018i	6.489+1.168i	-5.967-1.307i	-0.032+0.032i

Table A.1: Impedance tensor estimates made at BWA1000 (continued).

Freq / Hz	Z_{xx}	Z_{xy}	Z_{yx}	Z_{yy}
0.488	-0.336-0.024i	6.256+1.331i	-5.678-1.326i	-0.093-0.067i
0.366	-0.362+0.095i	6.096+1.417i	-5.457-1.288i	-0.238-0.110i
0.244	-0.301+0.079i	5.721+1.670i	-5.032-1.566i	0.058-0.202i
0.183	-0.351+0.108i	5.409+1.847i	-4.838-1.592i	0.034-0.403i
0.122	-0.498+0.131i	4.688+2.089i	-4.228-1.531i	0.402-0.397i
0.0916	-0.609+0.171i	4.319+2.162i	-4.098-1.702i	0.288-0.458i
0.061	-0.679+0.089i	3.044+2.294i	-3.455-1.815i	0.624-0.399i
0.0458	-0.657+0.065i	2.925+2.296i	-3.308-1.876i	0.628-0.400i
0.0305	-0.627+0.016i	2.236+2.024i	-2.644-1.729i	0.720-0.345i

x is grid north, and y is grid east.

Table A.2: Impedance tensor estimates made at BWA1335.

Freq / Hz	Z_{xx}	Z_{xy}	Z_{yx}	Z_{yy}
62.5	0.667+0.589i	11.94+9.85i	-11.31-9.58i	-0.645-0.517i
46.9	0.646+0.411i	10.99+7.28i	-10.46-7.23i	-0.598-0.364i
31.2	0.635+0.267i	10.22+5.43i	-9.586-5.414i	-0.606-0.201i
23.4	0.640+0.174i	9.864+4.187i	-9.220-4.284i	-0.620-0.112i
15.6	0.680+0.121i	9.538+3.240i	-8.812-3.344i	-0.664-0.005i
11.7	0.689-0.054i	9.675+2.621i	-8.845-2.696i	-0.684-0.086i
7.81	0.761+0.097i	9.076+2.185i	-8.515-2.310i	-0.640+0.111i
5.86	0.816-0.063i	9.078+2.075i	-8.408-2.075i	-0.729-0.097i
3.91	0.808+0.077i	8.535+1.875i	-7.876-2.007i	-0.708-0.103i
2.93	0.759+0.150i	8.063+1.706i	-7.388-1.947i	-0.698-0.129i
1.95	0.699+0.119i	7.699+1.538i	-6.849-1.761i	-0.647-0.133i
1.46	0.657+0.100i	7.460+1.435i	-6.478-1.692i	-0.622-0.085i
0.977	0.551+0.111i	7.183+1.310i	-6.130-1.488i	-0.610-0.088i
0.732	0.557+0.143i	7.007+1.323i	-5.894-1.385i	-0.613-0.116i
0.488	0.465+0.240i	6.876+1.427i	-5.638-1.351i	-0.710-0.154i
0.366	0.465+0.237i	6.612+1.494i	-5.420-1.354i	-0.670-0.282i
0.244	0.191+0.238i	6.352+1.868i	-5.011-1.429i	-0.601-0.448i
0.183	0.491+0.452i	5.989+2.121i	-4.870-1.466i	-0.494-0.548i
0.122	0.032+0.517i	5.312+2.436i	-4.251-1.619i	-0.284-0.700i
0.0916	0.120+0.555i	4.648+2.453i	-4.042-1.839i	-0.318-0.738i

Table A.2: Impedance tensor estimates made at BWA1335 (continued).

Freq / Hz	Z_{xx}	Z_{xy}	Z_{yx}	Z_{yy}
0.061	-0.219+0.394i	3.293+2.561i	-3.312-1.750i	0.304-0.622i
0.0458	-0.210+0.369i	3.078+2.559i	-3.136-1.792i	0.346-0.586i
0.0305	-0.274+0.295i	2.307+2.282i	-2.535-1.712i	0.505-0.540i

x is grid north, and y is grid east.

Table A.3: Impedance tensor estimates made at BWA1930.

Freq / Hz	Z_{xx}	Z_{xy}	Z_{yx}	Z_{yy}
125	-1.085-0.933i	16.74+15.16i	-16.35-14.99i	-2.727-2.568i
93.8	-1.108-0.659i	16.01+11.78i	-15.34-11.74i	-2.486-1.943i
62.5	-0.962-0.590i	13.93+8.97i	-13.27-9.01i	-2.161-1.373i
46.9	-0.892-0.531i	12.96+7.05i	-12.28-7.21i	-2.041-0.996i
31.2	-0.767-0.448i	12.23+5.11i	-11.55-5.49i	-1.987-0.553i
23.4	-0.674-0.440i	11.81+4.09i	-10.93-4.55i	-2.027-0.390i
15.6	-0.493-0.347i	11.38+3.12i	-10.31-3.69i	-2.123-0.215i
11.7	-0.481-0.494i	11.59+2.75i	-10.54-3.16i	-2.059-0.410i
7.81	-0.280-0.164i	10.75+2.23i	-9.887-2.986i	-1.984+0.028i
5.86	-0.212-0.373i	10.83+2.32i	-9.604-2.735i	-2.063-0.383i
3.91	-0.165-0.155i	10.15+2.08i	-8.665-2.542i	-2.026-0.390i
2.93	-0.276-0.046i	9.758+1.931i	-8.096-2.445i	-1.898-0.389i
1.95	-0.297-0.042i	9.253+1.730i	-7.484-2.127i	-1.741-0.361i
1.46	-0.333-0.047i	9.074+1.699i	-7.086-1.965i	-1.707-0.338i
0.977	-0.269-0.097i	8.704+1.514i	-6.603-1.591i	-1.649-0.306i
0.732	-0.264+0.014i	8.570+1.544i	-6.463-1.669i	-1.676-0.333i
0.488	-0.288+0.050i	8.394+1.771i	-6.180-1.740i	-1.617-0.420i
0.366	-0.306+0.136i	8.149+1.857i	-5.874-1.696i	-1.648-0.563i
0.244	-0.494+0.198i	7.745+2.205i	-5.430-1.841i	-1.486-0.691i
0.183	-0.508+0.198i	7.042+2.540i	-5.088-1.716i	-1.259-0.725i
0.0458	-0.728+0.234i	3.738+3.196i	-3.127-2.140i	0.111-0.989i
0.0305	-0.779+0.053i	2.774+2.634i	-2.419-1.762i	0.075-0.765i

x is grid north, and y is grid east.

Table A.4: Impedance tensor estimates made at BWA2350.

Freq / Hz	Z_{xx}	Z_{xy}	Z_{yx}	Z_{yy}
188	-1.592-0.967i	22.23+15.03i	-20.93-13.98i	-1.556-0.841i
93.8	-1.522-0.497i	18.03+9.47i	-16.95-8.79i	-1.215-0.538i
62.5	-1.467-0.399i	16.73+7.47i	-15.85-6.74i	-1.176-0.414i
46.9	-1.440-0.321i	15.92+6.24i	-15.21-5.58i	-1.147-0.339i
31.2	-1.407-0.251i	15.18+5.06i	-14.69-4.58i	-1.116-0.255i
23.4	-1.388-0.220i	14.57+4.46i	-14.08-4.16i	-1.092-0.265i
15.6	-1.312-0.195i	13.80+3.89i	-13.30-3.78i	-1.079-0.216i
11.7	-1.372-0.284i	13.62+3.47i	-13.45-3.34i	-0.962-0.516i
7.81	-1.205-0.085i	12.50+3.18i	-12.54-3.44i	-0.730+0.033i
5.86	-1.188-0.327i	12.30+3.11i	-12.15-3.28i	-0.793-0.437i
3.91	-1.097-0.189i	11.39+2.81i	-10.88-3.17i	-0.743-0.402i
2.93	-1.134-0.136i	10.81+2.55i	-10.10-3.09i	-0.630-0.316i
1.95	-1.081-0.144i	10.18+2.22i	-9.289-2.746i	-0.469-0.273i
1.46	-1.094-0.187i	9.918+2.124i	-8.816-2.534i	-0.467-0.198i
0.732	-1.008-0.102i	9.259+1.856i	-8.053-2.082i	-0.442-0.171i
0.488	-1.008-0.065i	9.085+2.113i	-7.682-2.164i	-0.459-0.249i
0.366	-1.006-0.002i	8.840+2.270i	-7.435-2.056i	-0.437-0.398i
0.244	-0.922+0.049i	8.315+2.691i	-6.986-2.232i	-0.462-0.534i
0.183	-1.092+0.034i	7.553+2.764i	-6.601-2.354i	-0.258-0.706i
0.122	-1.242-0.048i	7.380+3.639i	-6.041-2.717i	0.298-0.463i
0.0916	-1.012+0.187i	6.149+3.926i	-5.370-2.707i	0.585-0.946i
0.061	-1.407-0.183i	5.072+3.167i	-4.627-2.543i	0.851-1.035i
0.0458	-1.365-0.125i	4.021+3.107i	-4.241-2.568i	0.881-0.744i
0.0305	-1.125-0.127i	2.871+2.750i	-3.114-2.238i	0.959-0.480i

x is grid north, and y is grid east.

Table A.5: Impedance tensor estimates made at BWA2890.

Freq / Hz	Z_{xx}	Z_{xy}	Z_{yx}	Z_{yy}
125	-2.353+0.275i	24.18+14.68i	-23.81-15.14i	0.933-1.784i
93.8	-2.406+0.978i	23.02+10.92i	-22.90-11.53i	1.239-1.705i
62.5	-2.975+1.223i	21.31+8.91i	-21.29-9.00i	1.831-1.740i
46.9	-3.372+1.277i	20.22+7.57i	-20.34-7.55i	2.226-1.624i

Table A.5: Impedance tensor estimates made at BWA2890 (continued).

Freq / Hz	Z_{xx}	Z_{xy}	Z_{yx}	Z_{yy}
31.2	-3.870+1.200i	19.14+6.36i	-19.45-6.25i	2.691-1.372i
23.4	-4.226+0.959i	18.22+5.65i	-18.56-5.66i	3.007-1.195i
15.6	-4.402+0.635i	17.16+4.95i	-17.46-5.03i	3.233-0.871i
11.7	-4.722+0.347i	17.06+4.37i	-17.75-4.56i	3.596-1.124i
7.81	-4.721+0.278i	15.65+4.03i	-16.43-4.41i	3.666-0.099i
5.86	-4.657-0.208i	15.31+3.82i	-15.98-4.36i	3.724-0.494i
3.91	-4.364-0.292i	14.21+3.38i	-14.35-4.11i	3.629-0.315i
2.93	-4.210-0.376i	13.44+3.14i	-13.42-4.03i	3.715-0.132i
1.95	-4.013-0.482i	12.71+2.76i	-12.23-3.53i	3.700-0.012i
1.46	-3.965-0.507i	12.42+2.66i	-11.68-3.32i	3.718+0.101i
0.732	-3.653-0.371i	11.62+2.24i	-10.62-2.77i	3.336+0.411i
0.488	-3.634-0.436i	11.35+2.62i	-10.22-2.77i	3.239+0.340i
0.244	-3.128+0.068i	10.28+3.06i	-9.200-2.949i	2.976+0.279i
0.061	-3.420-0.486i	7.188+3.001i	-6.822-3.170i	2.266+0.915i
0.0458	-3.418-0.943i	5.601+3.070i	-5.707-3.179i	2.653+0.752i
0.0305	-2.652-0.794i	3.882+3.114i	-4.355-2.891i	2.366+0.598i

x is grid north, and y is grid east.

Table A.6: Impedance tensor estimates made at BWA3140.

Freq / Hz	Z_{xx}	Z_{xy}	Z_{yx}	Z_{yy}
125	-2.001-1.128i	14.22+10.25i	-14.52-10.60i	1.968+0.897i
93.8	-2.010-0.795i	13.82+7.66i	-13.92-8.28i	2.027+0.693i
62.5	-1.874-0.724i	12.74+5.55i	-12.61-6.30i	1.934+0.571i
46.9	-1.771-0.676i	12.31+4.27i	-11.94-5.13i	1.865+0.483i
31.2	-1.595-0.609i	12.14+3.13i	-11.45-4.05i	1.798+0.431i
23.4	-1.474-0.559i	11.98+2.67i	-10.99-3.56i	1.733+0.392i
15.6	-1.260-0.443i	11.63+2.39i	-10.38-3.12i	1.623+0.368i
11.7	-1.317-0.524i	11.79+2.25i	-10.44-2.73i	1.693+0.131i
7.81	-1.102-0.208i	10.82+2.20i	-9.793-2.668i	1.666+0.435i
5.86	-1.091-0.409i	10.79+2.29i	-9.515-2.559i	1.587+0.131i
3.91	-0.988-0.201i	9.981+2.156i	-8.643-2.531i	1.490+0.107i
2.93	-1.082-0.139i	9.488+2.047i	-8.095-2.465i	1.495+0.105i
1.95	-1.083-0.136i	8.969+1.851i	-7.345-2.184i	1.489+0.115i

Table A.6: Impedance tensor estimates made at BWA3140 (continued).

Freq / Hz	Z_{xx}	Z_{xy}	Z_{yx}	Z_{yy}
1.46	-1.037-0.194i	8.686+1.772i	-6.908-2.014i	1.516+0.189i
0.732	-0.983-0.080i	8.156+1.574i	-6.252-1.696i	1.355+0.254i
0.488	-0.882-0.053i	7.880+1.790i	-6.067-1.635i	1.326+0.151i
0.366	-0.882-0.049i	7.672+1.929i	-5.591-1.615i	1.180+0.114i
0.183	-1.159-0.193i	7.018+2.139i	-5.128-1.480i	0.994+0.167i
0.122	-1.444-0.846i	6.119+3.054i	-4.281-1.768i	0.889+0.069i
0.061	-0.960+0.127i	3.725+3.080i	-3.399-1.730i	0.408+0.078i
0.0458	-1.190+0.163i	3.612+2.843i	-3.189-1.635i	0.666+0.060i
0.0305	-0.999-0.165i	2.793+2.510i	-2.491-1.702i	1.024+0.036i

x is grid north, and y is grid east.

Table A.7: Impedance tensor estimates made at BWA3700.

Freq / Hz	Z_{xx}	Z_{xy}	Z_{yx}	Z_{yy}
125	0.116+0.034i	12.61+9.50i	-12.63-9.75i	1.536+1.084i
93.8	0.041+0.076i	12.18+7.30i	-12.11-7.51i	1.531+0.876i
62.5	0.042+0.044i	10.95+5.45i	-10.92-5.66i	1.364+0.711i
46.9	0.040+0.016i	10.39+4.21i	-10.34-4.50i	1.275+0.576i
31.2	0.077+0.043i	10.07+2.98i	-9.979-3.405i	1.192+0.477i
23.4	0.089+0.059i	9.929+2.385i	-9.632-2.876i	1.113+0.381i
15.6	0.126+0.128i	9.712+1.948i	-9.237-2.429i	1.027+0.309i
11.7	0.065+0.014i	9.918+1.842i	-9.466-2.085i	1.143+0.010i
7.81	0.098+0.258i	9.180+1.680i	-8.999-2.106i	1.167+0.348i
5.86	0.069+0.040i	9.200+1.872i	-8.828-2.065i	1.119+0.015i
3.91	-0.016+0.204i	8.568+1.764i	-8.037-2.029i	1.029-0.025i
2.93	-0.156+0.218i	8.181+1.675i	-7.518-1.990i	1.108-0.004i
1.95	-0.252+0.169i	7.743+1.500i	-6.944-1.855i	1.149+0.000i
1.46	-0.284+0.100i	7.528+1.439i	-6.593-1.742i	1.171+0.041i
0.732	-0.269+0.114i	7.091+1.341i	-6.038-1.485i	1.110+0.135i
0.488	-0.278+0.121i	6.958+1.472i	-5.761-1.575i	1.024+0.134i
0.366	-0.316+0.170i	6.761+1.562i	-5.560-1.512i	1.029+0.031i
0.244	-0.440+0.211i	6.314+1.889i	-5.201-1.594i	1.032+0.074i
0.183	-0.230+0.377i	5.890+2.201i	-4.375-1.412i	1.161+0.031i
0.122	-0.691+0.401i	5.167+1.858i	-4.229-1.476i	0.567+0.086i

Table A.7: Impedance tensor estimates made at BWA3700 (continued).

Freq / Hz	Z_{xx}	Z_{xy}	Z_{yx}	Z_{yy}
0.0916	-0.981+0.151i	4.558+1.674i	-4.115-1.895i	1.271+0.048i
0.061	-0.791+0.201i	3.429+2.807i	-3.561-1.690i	0.677+0.040i
0.0458	-0.695+0.130i	3.166+2.694i	-3.145-1.736i	0.977+0.319i
0.0305	-0.752+0.025i	2.377+2.070i	-2.468-1.638i	1.204-0.062i

x is grid north, and y is grid east.

Table A.8: Impedance tensor estimates made at BWA4200.

Freq / Hz	Z_{xx}	Z_{xy}	Z_{yx}	Z_{yy}
125	-0.189-0.355i	16.52+9.31i	-15.72-9.63i	1.673+0.919i
93.8	-0.175-0.231i	15.85+7.11i	-14.89-7.51i	1.669+0.732i
62.5	-0.127-0.200i	14.60+5.45i	-13.50-5.92i	1.538+0.600i
46.9	-0.096-0.198i	13.97+4.33i	-12.78-4.84i	1.463+0.505i
31.2	0.009-0.131i	13.57+3.22i	-12.28-3.85i	1.421+0.461i
23.4	0.044-0.088i	13.32+2.73i	-11.77-3.40i	1.317+0.402i
15.6	0.129+0.065i	12.97+2.35i	-11.13-3.01i	1.188+0.388i
11.7	0.070-0.115i	13.17+2.35i	-11.33-2.67i	1.282+0.053i
7.81	0.125+0.296i	12.11+2.18i	-10.66-2.71i	1.289+0.487i
5.86	0.085-0.004i	12.15+2.47i	-10.40-2.62i	1.227+0.063i
3.91	0.013+0.234i	11.28+2.35i	-9.360-2.557i	1.115+0.009i
2.93	-0.205+0.305i	10.78+2.26i	-8.771-2.498i	1.166+0.025i
1.95	-0.329+0.223i	10.15+2.00i	-8.017-2.267i	1.214+0.054i
1.46	-0.374+0.114i	9.893+1.972i	-7.580-2.095i	1.200+0.048i
0.732	-0.387+0.141i	9.252+1.762i	-6.936-1.830i	1.170+0.123i
0.488	-0.394+0.148i	9.002+1.981i	-6.579-1.889i	1.008+0.161i
0.366	-0.373+0.309i	8.716+2.119i	-6.169-1.826i	0.951-0.046i
0.183	-0.654+0.576i	7.737+2.393i	-5.313-1.614i	1.107+0.075i
0.122	-0.941+0.080i	6.548+2.868i	-4.380-1.869i	1.266-0.159i
0.0916	-0.951+0.270i	6.203+3.182i	-4.229-2.266i	1.471-0.040i
0.061	-0.856+0.239i	5.162+3.611i	-3.828-2.099i	0.931-0.014i
0.0458	-1.001+0.235i	4.109+3.379i	-3.456-2.112i	1.112+0.030i
0.0305	-1.022+0.072i	2.932+2.703i	-2.733-1.827i	1.043+0.114i

x is grid north, and y is grid east.

A.1.2 Detailed survey over spring

Table A.9: Impedance tensor estimates made at BSPRW1.

Freq / Hz	Z_{xx}	Z_{xy}	Z_{yx}	Z_{yy}
188	0.306-0.929i	30.08+15.56i	-24.54-13.67i	-1.326-0.167i
125	0.785-0.338i	23.77+13.03i	-19.16-12.13i	-1.541+0.098i
93.8	0.557-0.173i	23.27+10.65i	-18.27-10.02i	-1.421+0.116i
62.5	0.642+0.121i	21.37+8.27i	-16.45-7.85i	-1.373-0.086i
46.9	0.473+0.137i	21.01+7.40i	-15.87-6.69i	-1.416-0.130i
31.2	0.183+0.400i	19.71+5.80i	-14.65-5.53i	-1.273-0.280i
23.4	0.147+0.364i	18.98+5.22i	-14.07-4.84i	-1.135-0.352i
15.6	-0.092+0.362i	18.21+4.66i	-13.04-4.28i	-1.072-0.325i
11.7	0.042+0.181i	17.66+4.64i	-12.88-3.70i	-1.172-0.598i
7.81	-0.088+0.363i	16.53+4.06i	-12.20-3.70i	-0.612-0.051i
5.86	-0.055+0.317i	15.90+4.13i	-11.70-3.45i	-0.647-0.591i
3.91	-0.050+0.409i	14.74+3.68i	-10.93-3.45i	-0.385-0.291i
2.93	-0.249+0.463i	14.05+3.53i	-9.889-3.158i	-0.268-0.596i
1.95	-0.693+0.381i	13.39+3.08i	-8.789-2.628i	-0.238-0.534i
1.46	-0.775+0.107i	12.94+2.88i	-8.481-2.338i	-0.254-0.366i
0.977	-0.620+0.137i	12.17+2.43i	-7.890-2.241i	-0.111-0.234i
0.732	-0.754-0.041i	12.18+2.52i	-7.484-1.765i	-0.056-0.399i
0.488	-0.757+0.101i	11.87+2.83i	-7.099-1.789i	-0.046-0.219i
0.366	-0.786+0.231i	11.68+2.86i	-6.883-1.982i	-0.037-0.303i
0.244	-0.787+0.369i	10.65+3.58i	-6.497-2.231i	0.115-0.699i
0.183	-0.740+0.504i	9.901+3.935i	-6.041-2.049i	0.399-0.719i
0.122	-0.926+0.395i	8.431+4.459i	-5.548-2.003i	0.315-0.473i
0.0916	-0.901+0.354i	7.674+4.634i	-5.385-2.218i	0.413-0.469i
0.061	-1.173+0.115i	6.448+4.796i	-4.645-2.262i	0.838-0.503i
0.0458	-0.685-0.369i	4.496+2.363i	-7.391-3.301i	-0.069+0.267i
0.0305	-1.492+1.749i	8.046+1.465i	-1.53-12.99i	5.297+5.565i
0.0229	0.001+2.117i	9.519+0.105i	-0.233-9.062i	8.409+3.694i
0.0153	-0.054+1.298i	10.24+1.07i	0.265-5.627i	5.923+4.202i
0.0114	7.918+1.939i	13.90+3.22i	1.772-2.473i	4.537+3.520i
0.00763	7.773+3.190i	13.55+5.47i	1.527-1.505i	3.521+2.787i
0.00572	2.834+1.124i	7.488+3.974i	2.183+5.707i	3.251+5.880i
0.00381	1.929+1.399i	5.027+4.240i	1.217+3.766i	1.940+4.140i

Table A.9: Impedance tensor estimates made at BSPRW1 (continued).

Freq / Hz	Z_{xx}	Z_{xy}	Z_{yx}	Z_{yy}
-----------	----------	----------	----------	----------

x is grid north, and y is grid east.

Table A.10: Impedance tensor estimates made at BSPRW2.

Freq / Hz	Z_{xx}	Z_{xy}	Z_{yx}	Z_{yy}
188	-3.128-1.940i	32.60+18.86i	-31.70-17.28i	4.918+1.689i
125	-1.778-1.400i	25.09+16.23i	-25.58-16.19i	3.503+1.578i
93.8	-2.245-1.044i	24.60+13.60i	-24.86-12.67i	3.651+1.127i
62.5	-2.205-0.748i	22.33+10.86i	-23.01-9.87i	3.728+0.525i
46.9	-2.347-0.346i	21.53+9.17i	-22.49-8.46i	3.822+0.214i
31.2	-2.514-0.141i	19.93+7.32i	-21.02-6.99i	3.972+0.105i
23.4	-2.591-0.097i	19.13+6.20i	-20.35-6.09i	4.224-0.015i
15.6	-2.679-0.093i	18.25+5.22i	-19.00-5.25i	4.245-0.032i
11.7	-2.658-0.152i	18.10+4.68i	-19.11-4.70i	4.283-0.112i
7.81	-2.721-0.011i	16.97+4.24i	-18.08-4.47i	4.513+0.233i
5.86	-2.835-0.208i	16.51+4.07i	-17.71-4.42i	4.438+0.038i
3.91	-2.916+0.043i	15.40+3.60i	-15.98-4.30i	4.238+0.381i
2.93	-2.625+0.053i	14.47+3.60i	-15.16-4.23i	4.190+0.423i
1.95	-2.474-0.018i	13.47+2.94i	-13.99-3.73i	4.172+0.483i
1.46	-2.585+0.052i	13.05+2.79i	-13.24-3.42i	3.940+0.393i
0.977	-2.241-0.267i	12.45+2.45i	-12.27-2.80i	3.937+0.396i
0.732	-2.343-0.287i	12.49+2.63i	-11.88-2.69i	3.847+0.561i
0.488	-2.274-0.100i	11.64+2.41i	-11.51-2.64i	3.579+0.415i
0.366	-2.137-0.081i	11.51+2.93i	-11.16-2.89i	3.554+0.426i
0.244	-2.296-0.038i	10.68+3.44i	-10.48-2.93i	3.327+0.382i
0.183	-2.232-0.305i	10.26+3.83i	-9.902-3.181i	3.360+0.469i
0.122	-2.335-0.226i	8.999+4.415i	-9.047-3.311i	3.268+0.630i
0.0916	-2.244-0.138i	8.066+4.751i	-8.507-3.468i	3.212+0.791i
0.061	-2.321-0.388i	6.640+4.550i	-7.794-3.803i	3.014+0.551i
0.0458	-7.227-0.870i	4.612+1.274i	-7.422-1.883i	3.159+0.495i
0.0305	-15.93-16.12i	8.43+11.42i	-9.399-5.848i	-2.100+4.387i
0.0229	-39.98-25.05i	15.03+14.96i	-13.43-2.73i	-11.83+2.48i
0.0153	-30.36-29.79i	11.51+13.29i	-11.15-5.23i	-12.96+0.86i
0.0114	-17.49-22.75i	10.19+13.28i	-9.106-6.450i	-17.09-1.88i

Table A.10: Impedance tensor estimates made at BSPRW2 (continued).

Freq / Hz	Z_{xx}	Z_{xy}	Z_{yx}	Z_{yy}
0.00763	-10.33-20.25i	7.46+11.37i	-4.688-5.131i	-15.21-3.21i
0.00572	-10.10-15.97i	-18.28-64.65i	4.507-1.750i	-27.23-19.52i
0.00381	-5.50-18.23i	3.274-4.433i	3.885-0.609i	-17.76-13.32i

x is grid north, and y is grid east.

Table A.11: Impedance tensor estimates made at BSPR.

Freq / Hz	Z_{xx}	Z_{xy}	Z_{yx}	Z_{yy}
188	7.496+4.267i	33.85+20.96i	-61.37-38.38i	-6.515-4.620i
125	4.769+3.797i	25.22+19.84i	-45.90-39.90i	-4.862-4.248i
93.8	5.534+3.938i	25.64+15.36i	-49.15-27.53i	-5.157-3.076i
62.5	5.437+2.931i	23.27+12.07i	-47.39-19.24i	-4.805-2.647i
46.9	4.918+2.913i	22.59+10.58i	-47.05-16.21i	-4.811-2.382i
31.2	4.006+2.575i	20.35+8.41i	-44.71-12.51i	-4.277-1.791i
23.4	3.420+2.204i	19.23+7.43i	-43.47-11.30i	-3.831-1.759i
15.6	2.854+1.906i	18.12+6.32i	-41.34-9.48i	-3.792-1.553i
11.7	3.062+1.652i	17.52+5.94i	-41.99-10.42i	-3.269-2.085i
7.81	2.264+1.833i	16.11+4.97i	-38.89-9.76i	-3.300-1.134i
5.86	2.067+1.497i	15.41+4.67i	-37.71-10.07i	-2.618-1.501i
3.91	1.951+2.014i	14.27+4.26i	-34.36-9.71i	-2.883-1.507i
2.93	1.622+1.628i	13.57+3.75i	-32.48-9.16i	-2.342-1.392i
1.95	1.460+0.801i	12.48+3.09i	-30.07-8.16i	-1.762-0.996i
1.46	1.261+1.276i	12.28+2.85i	-28.40-8.92i	-1.384-1.043i
0.977	0.651+1.036i	11.83+2.69i	-26.57-7.10i	-1.408-0.840i
0.732	1.019+1.166i	11.49+2.60i	-26.21-6.62i	-1.112-0.594i
0.488	1.262+0.750i	11.01+2.63i	-26.12-5.78i	-1.173-0.436i
0.366	0.649+0.812i	10.67+2.98i	-23.16-6.89i	-1.250-0.524i
0.244	0.445+0.811i	9.906+3.563i	-21.58-6.63i	-0.940-0.917i
0.183	0.918+1.555i	9.402+3.776i	-21.18-8.21i	-0.689-0.939i
0.122	-1.318+1.555i	7.425+4.091i	-14.94-9.91i	0.864-0.428i
0.0916	-0.788+0.314i	7.025+4.452i	-11.27-11.97i	1.711-0.639i
0.061	-2.260+1.517i	5.807+4.541i	-12.72-10.96i	0.242-0.501i
0.0458	-1.492+0.782i	1.972+1.273i	-8.35-10.90i	2.043-3.109i
0.0305	0.472-1.625i	-19.17-1.73i	-11.68-2.91i	9.979-0.933i

Table A.11: Impedance tensor estimates made at BSPR (continued).

Freq / Hz	Z_{xx}	Z_{xy}	Z_{yx}	Z_{yy}
0.0229	8.24-14.79i	-247.9+31.5i	-12.34-0.48i	43.09-4.33i
0.0153	13.23-11.06i	-313.9-7.2i	-13.63-0.04i	69.92+4.28i
0.0114	-63.08+24.72i	1438+458i	216.7-26.4i	-4276-2752i
0.00763	-72.28+16.48i	1792+498i	215.3+0.4i	-4973-2737i
0.00572	-32.36+13.53i	1011+35i	30.95-8.88i	-1076-249i
0.00381	73.35-3.55i	-2166-530i	38.65-1.25i	-1283-397i

x is grid north, and y is grid east.

Table A.12: Impedance tensor estimates made at BSPRE1.

Freq / Hz	Z_{xx}	Z_{xy}	Z_{yx}	Z_{yy}
188	2.966+0.744i	19.72+13.21i	-13.49-8.19i	-2.034-0.903i
125	1.691+0.134i	16.81+13.55i	-12.56-9.39i	-1.184+0.238i
93.8	2.123+0.124i	18.58+11.69i	-15.18-7.91i	-0.569+0.240i
62.5	2.249+0.072i	17.06+9.66i	-15.02-6.02i	-0.294-0.163i
46.9	2.260+0.247i	16.68+8.49i	-15.33-5.13i	-0.195-0.215i
31.2	1.943+0.469i	14.75+6.82i	-14.50-4.25i	0.160-0.272i
23.4	1.729+0.470i	14.01+5.99i	-14.25-3.92i	0.382-0.417i
15.6	1.452+0.530i	13.17+4.88i	-13.19-3.53i	0.302-0.313i
11.7	1.677+0.329i	12.94+4.69i	-13.71-3.53i	0.617-0.797i
7.81	1.326+0.679i	11.63+3.61i	-12.45-3.47i	0.715+0.004i
5.86	1.315+0.460i	11.24+3.52i	-12.13-3.35i	1.006-0.392i
3.91	1.191+0.910i	10.36+2.84i	-10.82-3.24i	0.419+0.063i
2.93	1.083+0.577i	9.768+2.702i	-10.02-2.94i	0.617-0.197i
1.95	0.985+0.214i	8.901+2.209i	-9.134-2.493i	0.956-0.295i
1.46	0.901+0.376i	8.868+2.011i	-8.842-2.480i	0.883-0.268i
0.977	0.695+0.413i	8.613+1.898i	-8.429-2.304i	0.784-0.002i
0.732	0.730+0.212i	8.304+1.835i	-7.813-1.908i	0.819-0.220i
0.488	0.760+0.268i	7.957+1.980i	-7.588-1.493i	0.794-0.060i
0.366	0.675+0.393i	7.691+2.068i	-7.575-1.866i	0.774-0.122i
0.244	0.360+0.542i	7.151+2.407i	-7.162-2.056i	0.765-0.123i
0.183	0.239+0.681i	6.501+2.733i	-5.450-1.696i	0.745+0.075i
0.122	-0.132+0.758i	5.485+2.994i	-4.442-1.636i	0.921+0.203i
0.0916	-0.119+0.671i	5.283+3.079i	-4.737-1.840i	0.945-0.065i

Table A.12: Impedance tensor estimates made at BSPRE1 (continued).

Freq / Hz	Z_{xx}	Z_{xy}	Z_{yx}	Z_{yy}
0.061	-0.012+0.285i	4.158+3.286i	-4.916-2.376i	1.295-0.128i
0.0458	-0.290+0.504i	1.615+0.958i	-3.121-1.136i	1.671-0.002i
0.0305	8.572-0.683i	-7.656+0.353i	-12.30-0.03i	8.903+0.010i
0.0229	13.15-0.19i	-12.22+0.08i	-17.85-0.10i	12.17+0.06i
0.0153	13.22+0.23i	-11.98-0.17i	-17.88-0.50i	12.10+0.35i
0.0114	13.67+0.24i	-12.42-0.28i	-15.74-0.45i	13.02+0.54i
0.00763	14.33+0.58i	-13.16-0.57i	-16.63-0.97i	13.71+0.92i
0.00572	14.68+0.98i	-12.94-0.84i	-16.16-1.50i	13.49+1.25i
0.00381	13.07+1.42i	-11.52-1.22i	-14.32-2.10i	11.95+1.76i

x is grid north, and y is grid east.

Table A.13: Impedance tensor estimates made at BSPRE2.

Freq / Hz	Z_{xx}	Z_{xy}	Z_{yx}	Z_{yy}
188	1.028+0.311i	16.26+8.27i	-14.37-8.81i	-2.298-2.215i
125	0.190-0.528i	13.91+8.84i	-12.23-8.27i	-1.252-0.852i
93.8	-0.200-0.485i	15.34+7.21i	-13.25-7.32i	-0.546-0.432i
62.5	-0.219-0.456i	14.58+5.78i	-12.65-5.81i	-0.230-0.210i
46.9	-0.196-0.526i	14.59+5.12i	-12.62-4.85i	-0.062-0.069i
31.2	-0.089-0.389i	13.69+4.40i	-11.99-3.98i	-0.008-0.073i
23.4	-0.015-0.334i	13.14+3.91i	-11.67-3.53i	0.004-0.153i
15.6	-0.070-0.162i	12.54+3.45i	-10.86-3.18i	0.007-0.127i
11.7	0.128-0.197i	12.28+3.33i	-10.96-2.91i	-0.073-0.265i
7.81	0.011-0.011i	11.42+2.85i	-10.17-2.85i	0.268-0.038i
5.86	0.040+0.015i	11.05+2.73i	-9.789-2.698i	0.175-0.347i
3.91	0.042+0.259i	9.987+2.302i	-8.718-2.499i	0.166-0.191i
2.93	0.069+0.275i	9.508+2.185i	-8.096-2.239i	0.015-0.309i
1.95	0.131+0.152i	8.744+1.889i	-7.185-1.901i	0.151-0.382i
1.46	0.098+0.102i	8.508+1.851i	-6.903-1.873i	0.203-0.283i
0.977	-0.092+0.034i	8.293+1.679i	-6.683-1.644i	0.163-0.084i
0.732	-0.077+0.061i	8.178+1.812i	-6.558-1.525i	0.425-0.221i
0.488	-0.144+0.187i	7.817+1.730i	-6.439-1.465i	0.433+0.027i
0.366	-0.173+0.248i	7.720+1.941i	-6.359-1.729i	0.346-0.110i
0.244	-0.318+0.283i	7.328+2.335i	-5.870-1.817i	0.450-0.342i

Table A.13: Impedance tensor estimates made at BSPRE2 (continued).

Freq / Hz	Z_{xx}	Z_{xy}	Z_{yx}	Z_{yy}
0.183	-0.591+0.333i	6.898+2.571i	-5.377-1.710i	0.403-0.234i
0.122	-0.738+0.388i	5.944+2.857i	-5.095-1.871i	0.530-0.298i
0.0916	-0.419+0.330i	5.437+3.213i	-4.825-1.673i	0.599-0.262i
0.061	-0.598+0.178i	4.327+3.335i	-4.239-2.137i	0.785-0.410i
0.0458	-1.441-0.141i	2.433+1.541i	-3.833-1.753i	1.123-0.103i
0.0305	-0.836+0.495i	-2.684+0.605i	-1.422-1.178i	-0.596+0.428i
0.0229	1.760+0.409i	-3.964-0.062i	6.658-0.532i	-1.634+0.014i
0.0153	1.921+0.283i	-3.959-0.119i	7.334-0.029i	-1.594-0.048i
0.0114	5.433-0.098i	-4.451-0.164i	4.157+0.202i	-0.929+0.000i
0.00763	5.786+0.022i	-4.699-0.255i	4.376+0.464i	-0.979-0.029i
0.00572	1.895-0.057i	-4.707-0.302i	4.682+0.710i	-3.226-0.502i
0.00381	1.724-0.000i	-4.206-0.427i	4.019+1.028i	-2.798-0.652i

x is grid north, and y is grid east.

A.2 Warburton Spring

A.2.1 AMT survey

Table A.14: Impedance tensor estimates made at WZW3.

Freq / Hz	Z_{xx}	Z_{xy}	Z_{yx}	Z_{yy}
8.19e+03	41.37+63.97i	217.3+177.8i	-106.2-135.1i	-13.04-19.79i
6.14e+03	33.24+53.19i	186.8+153.3i	-93.8-116.8i	-10.62-15.45i
4.1e+03	24.07+40.90i	150.8+124.5i	-78.74-95.21i	-7.95-10.68i
3.07e+03	18.89+33.89i	129.5+107.4i	-69.63-82.37i	-6.493-8.057i
2.05e+03	13.09+25.90i	104.4+87.2i	-58.61-67.18i	-4.921-5.199i
1.54e+03	9.84+21.36i	89.55+75.31i	-51.93-58.14i	-4.086-3.649i
1.02e+03	6.21+16.21i	72.01+61.24i	-43.86-47.43i	-3.216-1.982i
768	4.17+13.30i	61.61+52.90i	-38.97-41.04i	-2.782-1.097i
512	1.89+10.02i	49.32+43.06i	-33.11-33.48i	-2.390-0.167i
384	0.596+8.108i	42.00+37.17i	-29.59-28.92i	-2.261+0.372i
256	-0.801+5.463i	33.39+29.71i	-25.64-23.17i	-2.466+1.255i
192	-1.542+3.525i	28.30+24.85i	-23.80-19.80i	-3.203+1.669i

Table A.14: Impedance tensor estimates made at WZW3 (continued).

Freq / Hz	Z_{xx}	Z_{xy}	Z_{yx}	Z_{yy}
128	-2.067+0.552i	22.55+18.34i	-22.26-16.69i	-4.800+1.212i
96	-1.271-0.602i	20.17+15.04i	-20.72-14.69i	-5.165+1.039i
64	0.482-0.402i	18.05+12.65i	-18.22-11.53i	-4.914+1.596i
48	2.261+0.379i	17.43+11.86i	-15.83-9.30i	-3.852+2.242i
32	3.654+0.642i	15.89+10.22i	-13.52-7.39i	-3.088+2.254i
24	4.239+0.702i	14.61+9.11i	-12.40-6.34i	-2.834+2.161i
16	4.440+0.680i	13.31+7.75i	-10.81-5.09i	-3.034+1.944i
12	4.514+0.666i	12.50+6.88i	-9.906-4.399i	-3.245+1.801i
8	4.677+0.694i	11.49+5.88i	-8.970-3.657i	-3.560+1.522i
6	4.765+0.697i	10.83+5.26i	-8.432-3.222i	-3.747+1.336i
4	5.476+0.665i	9.316+4.471i	-8.427-2.687i	-3.291+1.118i
1.5	5.262+0.480i	7.662+2.940i	-7.038-1.684i	-3.639+0.773i

x is grid north, and y is grid east.

Table A.15: Impedance tensor estimates made at WZW2.

Freq / Hz	Z_{xx}	Z_{xy}	Z_{yx}	Z_{yy}
1.54e+03	-27.29+39.88i	57.7+101.7i	-16.29-83.41i	13.90-2.40i
1.02e+03	-13.45+28.97i	53.59+74.51i	-24.25-63.24i	5.969-0.432i
768	-6.59+22.30i	49.32+58.44i	-27.20-51.46i	2.844+1.176i
512	0.41+14.48i	41.90+39.77i	-29.08-38.19i	1.270+3.256i
384	4.32+10.15i	36.11+29.81i	-29.87-31.22i	1.872+3.517i
256	2.185+1.537i	35.30+27.02i	-25.14-20.90i	-2.327-5.367i
192	0.139+0.706i	32.39+21.18i	-22.44-19.49i	-2.891-6.097i
128	-1.284-0.426i	28.32+15.08i	-20.47-15.95i	-2.913-5.486i
96	-1.385-0.603i	26.68+12.12i	-19.31-13.48i	-2.778-4.683i
64	-0.635+0.755i	25.54+10.37i	-17.68-10.24i	-1.745-3.308i
48	-0.752+2.443i	24.04+10.63i	-16.79-7.90i	-0.355-1.768i
32	-1.017+2.727i	21.30+9.30i	-16.22-5.40i	1.591-0.345i
24	-1.048+2.554i	20.10+7.97i	-15.96-4.03i	2.200+0.382i
16	-0.925+2.401i	18.97+6.23i	-15.73-2.64i	2.450+0.953i
12	-0.200+2.265i	17.92+5.42i	-16.19-1.83i	2.857+0.845i
8	-0.409+2.030i	17.73+4.38i	-15.57-0.79i	2.120+0.568i
6	-0.403+1.929i	17.41+3.56i	-15.27-0.21i	1.772+0.465i

Table A.15: Impedance tensor estimates made at WZW2 (continued).

Freq / Hz	Z_{xx}	Z_{xy}	Z_{yx}	Z_{yy}
-----------	----------	----------	----------	----------

x is grid north, and y is grid east.

Table A.16: Impedance tensor estimates made at WZW1.

Freq / Hz	Z_{xx}	Z_{xy}	Z_{yx}	Z_{yy}
4.1e+03	-65.06+90.01i	106.7+206.5i	-7.2-120.2i	7.390-8.267i
3.07e+03	-49.13+71.69i	100.3+173.0i	-16.9-100.8i	4.524-4.455i
2.05e+03	-32.50+50.76i	90.1+133.8i	-25.34-77.95i	2.791-0.316i
1.54e+03	-23.85+38.87i	82.4+110.9i	-28.62-64.58i	2.675+1.794i
1.02e+03	-14.87+25.54i	71.64+84.58i	-30.64-49.13i	3.499+3.728i
768	-10.15+18.07i	64.18+69.47i	-30.83-40.20i	4.546+4.430i
512	-4.978+9.638i	53.99+52.41i	-30.21-29.87i	6.541+4.505i
384	-1.530+4.909i	46.82+43.30i	-29.95-23.94i	8.443+3.561i
256	2.963+1.948i	38.10+33.29i	-29.79-19.52i	10.41+1.69i
192	4.012+0.974i	33.53+26.98i	-27.98-17.66i	10.56+0.95i
128	4.376-0.170i	28.94+19.84i	-25.19-15.13i	9.629+0.230i
96	4.339-0.296i	26.69+16.27i	-23.74-13.26i	8.933+0.265i
64	4.036+0.688i	24.51+13.52i	-22.08-10.80i	7.850+0.650i
48	2.984+1.726i	23.11+12.82i	-20.64-9.39i	7.295+1.044i
32	0.970+2.335i	21.29+11.47i	-18.19-7.56i	6.580+1.564i
24	-1.463+2.248i	21.54+10.44i	-15.38-6.24i	4.658+1.703i
16	-1.704+2.117i	19.36+8.97i	-14.53-4.83i	4.678+1.762i
12	-1.885+2.065i	18.16+7.96i	-13.87-4.08i	4.466+1.736i
8	-1.109+1.994i	15.83+6.80i	-13.93-3.24i	4.957+1.474i
6	-1.144+1.935i	14.89+6.07i	-13.36-2.73i	4.682+1.253i
2	-1.264+1.689i	11.89+3.67i	-11.17-1.29i	3.669+0.521i
1.5	-1.277+1.626i	11.21+3.16i	-10.62-1.00i	3.431+0.364i

x is grid north, and y is grid east.

Table A.17: Impedance tensor estimates made at WZS.

Freq / Hz	Z_{xx}	Z_{xy}	Z_{yx}	Z_{yy}
8.19e+03	-109.6+41.1i	220.7+327.5i	-99.6-261.6i	54.47-49.38i

Table A.17: Impedance tensor estimates made at WZS (continued).

Freq / Hz	Z_{xx}	Z_{xy}	Z_{yx}	Z_{yy}
6.14e+03	-91.05+38.85i	200.2+270.4i	-98.5-214.0i	47.62-44.74i
4.1e+03	-68.55+29.07i	175.2+210.5i	-92.5-166.2i	42.02-33.36i
3.07e+03	-55.81+19.93i	159.3+178.9i	-87.0-142.1i	39.61-23.71i
2.05e+03	-41.96+7.20i	138.3+144.9i	-79.1-116.7i	36.57-10.52i
1.54e+03	-34.33-0.60i	123.9+125.8i	-73.4-102.6i	34.11-2.52i
1.02e+03	-25.62-8.91i	104.2+103.3i	-65.51-86.04i	29.89+5.84i
768	-20.46-12.60i	90.53+89.23i	-60.01-75.51i	26.38+9.32i
512	-14.19-14.78i	71.69+70.84i	-53.02-61.46i	21.00+10.56i
384	-10.18-14.65i	57.88+58.03i	-49.65-52.23i	17.26+8.90i
256	-3.675-7.862i	44.10+43.33i	-43.15-38.04i	15.71+9.50i
192	-1.544-5.112i	40.20+33.52i	-38.34-30.56i	16.41+7.53i
128	-8.329-3.857i	43.14+24.44i	-29.15-22.41i	9.153+4.472i
96	-8.260-3.690i	41.38+20.19i	-27.91-18.98i	9.125+2.829i
64	-8.197-3.765i	38.36+16.37i	-25.90-16.49i	9.147+1.215i
48	-8.130-4.046i	35.51+14.03i	-23.98-14.97i	9.069+0.665i
32	-7.477-4.492i	32.39+10.36i	-22.03-12.58i	8.534+0.039i
24	-6.871-4.386i	30.93+8.55i	-21.12-11.37i	8.305-0.467i
16	-6.124-3.865i	29.11+7.13i	-19.58-9.94i	8.403-0.678i
12	-5.650-3.352i	27.87+6.56i	-18.47-8.88i	8.494-0.483i
8	-5.062-2.648i	26.23+6.03i	-17.05-7.49i	8.563-0.069i
6	-4.829-2.265i	25.00+5.68i	-16.31-6.68i	8.409+0.159i
2	-4.642-1.405i	20.72+4.63i	-14.63-4.78i	7.425+0.596i
1.5	-4.628-1.271i	19.74+4.39i	-14.27-4.44i	7.168+0.642i

x is grid north, and y is grid east.

Table A.18: Impedance tensor estimates made at WZE1.

Freq / Hz	Z_{xx}	Z_{xy}	Z_{yx}	Z_{yy}
8.19e+03	-83.98+45.51i	229.2+202.3i	-77.32-85.23i	-60.37-78.30i
6.14e+03	-67.84+34.67i	205.8+161.2i	-79.28-58.15i	-48.73-55.45i
4.1e+03	-56.21+25.11i	186.0+121.1i	-80.56-38.23i	-20.42-36.14i
3.07e+03	-54.97+20.85i	177.2+102.0i	-84.14-32.68i	0.98-28.20i
2.05e+03	-58.98+15.28i	165.7+86.1i	-91.95-32.34i	25.55-18.45i
1.54e+03	-61.75+9.20i	154.2+82.7i	-96.06-36.90i	35.46-9.06i

Table A.18: Impedance tensor estimates made at WZE1 (continued).

Freq / Hz	Z_{xx}	Z_{xy}	Z_{yx}	Z_{yy}
1.02e+03	-58.37-4.17i	124.4+86.9i	-93.30-49.10i	30.90+9.10i
768	-37.61-30.72i	103.7+69.5i	-72.40-74.46i	24.99+0.11i
512	-18.90-22.56i	76.02+59.60i	-53.25-63.11i	14.41+1.34i
384	-12.51-15.71i	63.38+51.95i	-46.71-52.66i	11.78+1.64i
256	-6.55-10.51i	48.31+40.41i	-42.01-40.30i	9.495+1.625i
192	-2.935-7.111i	40.10+30.74i	-40.88-33.50i	10.36+2.15i
128	-7.557-5.224i	40.59+22.32i	-33.08-25.06i	4.441+0.609i
96	-7.632-4.916i	38.59+18.33i	-31.57-21.20i	4.110-0.561i
64	-7.403-4.663i	35.78+14.70i	-29.23-18.08i	4.231-1.565i
48	-6.678-4.551i	33.77+12.63i	-26.71-16.26i	4.826-1.875i
32	-6.166-4.436i	30.89+9.54i	-24.46-13.57i	4.858-2.210i
24	-5.497-4.209i	29.75+7.98i	-23.13-12.08i	5.211-2.404i
16	-4.612-3.658i	28.31+6.79i	-21.20-10.45i	5.897-2.370i
12	-4.098-3.155i	27.22+6.32i	-19.88-9.30i	6.319-2.090i
8	-3.498-2.362i	25.77+5.91i	-18.23-7.74i	6.801-1.556i
6	-3.323-1.896i	24.69+5.66i	-17.37-6.83i	6.950-1.235i
2	-3.517-1.060i	20.64+4.98i	-15.17-4.97i	6.803-0.361i
1.5	-3.618-0.959i	19.66+4.79i	-14.70-4.67i	6.681-0.216i

x is grid north, and y is grid east.

Table A.19: Impedance tensor estimates made at WZE2.

Freq / Hz	Z_{xx}	Z_{xy}	Z_{yx}	Z_{yy}
8.19e+03	-26.65-16.41i	402.7+216.7i	-122.4+2.6i	6.27+94.13i
6.14e+03	-16.20+0.76i	355.1+225.1i	-122.8-25.8i	-4.25+47.40i
4.1e+03	-12.47+10.61i	287.1+221.6i	-113.1-46.8i	-5.280+4.731i
3.07e+03	-12.60+7.78i	243.7+208.0i	-103.9-49.2i	-2.969-9.577i
2.05e+03	-13.54-2.92i	192.8+179.7i	-91.20-43.04i	-0.93-14.94i
1.54e+03	-14.67-11.55i	163.6+157.3i	-82.52-36.09i	-1.06-13.03i
1.02e+03	-17.32-21.60i	130.3+127.3i	-70.58-26.85i	-3.000-7.647i
768	-20.03-26.24i	111.0+108.5i	-62.53-22.02i	-5.375-3.924i
512	-23.82-29.87i	88.54+85.07i	-51.60-19.16i	-9.880-1.370i
384	-20.64-36.53i	79.68+63.77i	-38.99-25.66i	-9.304-8.509i
256	-18.42-23.47i	68.45+53.90i	-25.68-17.36i	-10.57-3.85i

Table A.19: Impedance tensor estimates made at WZE2 (continued).

Freq / Hz	Z_{xx}	Z_{xy}	Z_{yx}	Z_{yy}
192	-18.14-16.83i	62.52+44.86i	-19.81-15.43i	-9.958-5.202i
128	-17.71-11.78i	54.39+33.19i	-17.03-11.45i	-7.104-4.410i
96	-16.85-10.27i	51.18+25.83i	-16.56-9.95i	-5.833-3.952i
64	-15.59-9.09i	47.58+19.71i	-16.59-9.55i	-4.524-3.248i
48	-14.18-8.84i	44.07+16.71i	-15.52-9.56i	-4.105-2.833i
32	-12.27-8.08i	39.71+11.83i	-14.52-7.91i	-3.792-2.930i
24	-10.96-7.50i	38.03+9.17i	-14.62-6.77i	-3.118-2.852i
16	-9.028-6.634i	36.19+7.08i	-14.75-5.82i	-2.198-2.359i
12	-7.763-5.816i	34.97+6.28i	-14.68-5.21i	-1.710-1.886i
8	-6.322-4.584i	33.21+5.64i	-14.62-4.48i	-1.088-1.283i
6	-5.506-3.918i	31.81+5.35i	-14.77-4.10i	-0.569-0.912i
2	-3.265-2.292i	26.91+4.21i	-15.56-3.08i	0.456-0.166i
1.5	-2.846-1.993i	25.81+3.92i	-15.68-2.88i	0.536-0.087i

x is grid north, and y is grid east.

A.2.2 MT survey

Table A.20: Impedance tensor estimates made at WW2.

Freq / Hz	Z_{xx}	Z_{xy}	Z_{yx}	Z_{yy}
125	7.324+6.314i	20.84+15.83i	-22.54-15.47i	-7.026-4.800i
93.8	7.845+4.573i	21.04+12.05i	-21.65-11.28i	-7.422-3.880i
62.5	6.971+3.378i	18.93+8.90i	-19.76-8.21i	-6.768-2.678i
46.9	6.729+2.641i	18.38+7.18i	-19.30-6.60i	-6.567-2.005i
31.2	6.553+1.920i	17.57+5.41i	-18.62-5.10i	-6.553-1.476i
23.4	6.522+1.465i	17.29+4.43i	-18.30-4.33i	-6.529-1.128i
15.6	6.568+1.270i	16.97+3.73i	-17.89-3.71i	-6.588-0.987i
11.7	6.519+1.262i	16.71+3.57i	-17.51-3.67i	-6.525-1.023i
7.81	6.286+1.310i	16.05+3.43i	-16.86-3.60i	-6.400-1.095i
5.86	6.046+1.390i	15.49+3.38i	-16.24-3.75i	-6.110-1.310i
3.91	5.555+1.533i	14.47+3.32i	-15.24-3.85i	-5.821-1.512i
2.93	5.212+1.497i	13.87+3.25i	-14.34-3.79i	-5.352-1.630i
1.95	4.659+1.339i	12.92+3.02i	-13.03-3.61i	-4.701-1.616i

Table A.20: Impedance tensor estimates made at WW2 (continued).

Freq / Hz	Z_{xx}	Z_{xy}	Z_{yx}	Z_{yy}
1.46	4.369+1.170i	12.35+2.82i	-12.35-3.26i	-4.289-1.434i
0.977	4.386+0.998i	11.93+2.51i	-11.61-2.96i	-3.989-1.141i
0.732	4.147+1.102i	11.51+2.61i	-11.23-2.79i	-3.854-1.139i
0.488	3.854+1.158i	10.73+2.71i	-10.39-2.83i	-3.562-1.124i
0.366	3.676+1.237i	10.28+2.88i	-10.03-2.91i	-3.503-1.353i
0.244	3.286+1.581i	9.566+3.335i	-9.444-3.078i	-3.106-1.492i
0.183	2.868+1.748i	9.017+3.676i	-8.814-3.328i	-2.598-1.639i

x is grid north, and y is grid east.

Table A.21: Impedance tensor estimates made at WW1.

Freq / Hz	Z_{xx}	Z_{xy}	Z_{yx}	Z_{yy}
375	-3.389-2.904i	17.12+19.73i	-13.29-15.46i	2.695+4.511i
250	-0.641+0.284i	23.12+19.03i	-18.25-15.81i	1.953+2.011i
188	-0.090+0.756i	19.48+15.59i	-15.56-13.49i	1.484+1.307i
125	1.078+0.799i	16.72+14.56i	-13.83-12.06i	0.865+0.748i
93.8	0.811+0.617i	15.88+10.63i	-12.97-8.84i	0.890+0.511i
62.5	0.755+0.276i	14.49+7.59i	-11.86-6.30i	0.797+0.602i
46.9	0.822+0.084i	14.25+6.01i	-11.69-5.01i	0.672+0.699i
31.2	0.955-0.062i	13.63+4.49i	-11.19-3.82i	0.411+0.771i
23.4	1.054-0.094i	13.36+3.76i	-10.95-3.24i	0.192+0.728i
15.6	1.084+0.032i	12.93+3.09i	-10.47-2.83i	-0.001+0.642i
11.7	1.300-0.053i	12.78+2.95i	-10.44-2.50i	-0.246+0.401i
7.81	1.182+0.287i	11.88+2.64i	-9.836-2.483i	-0.077+0.404i
5.86	1.216+0.163i	11.56+2.75i	-9.537-2.386i	-0.281+0.045i
3.91	1.059+0.246i	10.67+2.52i	-8.579-2.277i	-0.283-0.081i
2.93	0.904+0.358i	10.30+2.36i	-8.156-2.281i	-0.196-0.071i
1.95	0.740+0.445i	9.647+2.011i	-7.508-2.124i	-0.109-0.017i
1.46	0.683+0.384i	9.399+1.962i	-7.204-2.015i	-0.073-0.031i
0.977	0.645+0.330i	9.047+1.844i	-6.787-1.801i	-0.081-0.033i
0.732	0.581+0.284i	8.865+1.835i	-6.541-1.710i	-0.097-0.026i
0.488	0.564+0.314i	8.510+2.029i	-6.181-1.719i	-0.151-0.124i
0.366	0.535+0.332i	8.194+2.067i	-5.892-1.724i	-0.163-0.211i
0.244	0.412+0.407i	7.633+2.399i	-5.417-1.768i	-0.089-0.397i

Table A.21: Impedance tensor estimates made at WW1 (continued).

Freq / Hz	Z_{xx}	Z_{xy}	Z_{yx}	Z_{yy}
0.183	0.267+0.384i	7.054+2.665i	-5.023-1.854i	0.085-0.440i
0.122	0.066+0.611i	5.918+2.826i	-4.489-1.865i	0.187-0.485i
0.0916	-0.073+0.594i	5.402+2.912i	-4.156-1.964i	0.521-0.522i

x is grid north, and y is grid east.

Table A.22: Impedance tensor estimates made at WWB.

Freq / Hz	Z_{xx}	Z_{xy}	Z_{yx}	Z_{yy}
375	-10.12-11.51i	11.64+12.62i	-20.25-23.04i	0.626-1.707i
250	-12.08-10.95i	13.12+11.51i	-22.92-21.80i	1.298-0.158i
188	-10.48-8.68i	11.33+9.15i	-19.50-16.61i	1.466+0.380i
125	-8.913-7.701i	9.485+7.942i	-17.08-14.73i	1.339+0.942i
93.8	-8.983-5.916i	9.421+6.010i	-17.03-11.01i	1.558+1.059i
62.5	-8.324-4.570i	8.709+4.624i	-15.92-8.17i	1.276+1.024i
46.9	-8.237-3.830i	8.535+3.846i	-15.73-6.89i	1.141+1.057i
31.2	-7.551-3.084i	7.849+3.098i	-14.80-5.69i	0.815+0.957i
23.4	-7.191-2.682i	7.458+2.689i	-14.18-5.06i	0.647+0.828i
15.6	-6.657-2.269i	7.004+2.307i	-13.26-4.44i	0.480+0.655i
11.7	-6.421-2.008i	6.683+2.028i	-12.89-3.94i	0.301+0.389i
7.81	-6.034-1.775i	6.269+1.812i	-12.02-3.74i	0.535+0.406i
5.86	-5.739-1.564i	5.936+1.495i	-11.43-3.47i	0.285+0.048i
3.91	-5.230-1.347i	5.419+1.179i	-10.34-3.15i	0.255-0.144i
2.93	-5.010-1.242i	5.179+1.048i	-9.790-3.113i	0.389-0.068i
1.95	-4.536-1.208i	4.809+1.144i	-8.844-2.776i	0.572+0.037i
1.46	-4.484-1.179i	4.674+1.078i	-8.460-2.587i	0.711-0.011i
0.977	-4.176-1.172i	4.325+1.063i	-7.905-2.271i	0.615+0.016i
0.732	-3.882-1.124i	4.184+1.172i	-7.582-2.127i	0.512-0.006i
0.488	-3.735-1.113i	3.947+1.014i	-7.075-2.089i	0.360-0.079i
0.366	-3.530-1.069i	3.604+0.959i	-6.624-1.957i	0.266-0.231i
0.244	-3.150-0.904i	3.183+1.107i	-6.035-1.997i	0.190-0.334i
0.183	-2.905-0.842i	3.199+1.246i	-5.795-2.073i	0.164-0.175i
0.122	-2.852-0.892i	2.746+1.258i	-5.010-2.132i	0.192-0.272i
0.0916	-2.838-1.122i	2.736+1.216i	-4.818-2.127i	0.490-0.462i
0.061	-2.652-1.116i	2.101+1.036i	-4.023-2.282i	0.745-0.272i

Table A.22: Impedance tensor estimates made at WWB (continued).

Freq / Hz	Z_{xx}	Z_{xy}	Z_{yx}	Z_{yy}
-----------	----------	----------	----------	----------

x is grid north, and y is grid east.

Table A.23: Impedance tensor estimates made at WWA.

Freq / Hz	Z_{xx}	Z_{xy}	Z_{yx}	Z_{yy}
188	-0.034+0.409i	25.34+21.61i	-23.95-21.36i	1.814+0.267i
93.8	-0.353-0.069i	21.94+13.57i	-21.21-14.24i	1.942+1.011i
62.5	-0.313-0.129i	20.50+10.29i	-19.69-10.83i	1.737+0.917i
46.9	-0.333-0.186i	20.17+8.77i	-19.30-9.29i	1.661+0.906i
31.2	-0.247-0.191i	18.86+7.30i	-17.87-7.70i	1.411+0.797i
23.4	-0.238-0.117i	17.99+6.45i	-16.97-6.80i	1.322+0.692i
15.6	-0.333+0.040i	16.87+5.48i	-15.67-5.82i	1.177+0.592i
11.7	-0.162-0.096i	16.24+5.08i	-15.19-5.10i	1.008+0.325i
7.81	-0.238+0.240i	14.78+4.26i	-14.10-4.68i	1.261+0.491i
5.86	-0.204+0.054i	14.31+4.11i	-13.46-4.27i	0.961+0.070i
3.91	-0.254+0.040i	12.90+3.63i	-12.21-3.76i	1.016+0.017i
2.93	-0.100+0.068i	12.30+3.76i	-11.50-3.34i	1.011+0.046i
1.95	-0.449+0.105i	11.46+2.84i	-10.23-3.31i	0.952+0.380i
1.46	-0.496+0.006i	11.14+2.66i	-9.946-2.936i	1.059+0.187i
0.977	-0.510+0.075i	10.72+2.22i	-9.317-2.720i	1.037+0.122i
0.732	-0.459+0.061i	10.33+2.38i	-8.927-2.552i	1.014+0.118i
0.488	-0.396+0.147i	9.956+2.403i	-8.357-2.496i	0.764+0.008i
0.366	-0.300+0.301i	9.346+2.457i	-7.998-2.302i	0.820-0.141i
0.244	-0.240+0.261i	8.551+2.830i	-7.233-2.396i	0.492-0.378i
0.183	-0.393+0.311i	7.830+3.140i	-6.823-2.519i	0.374-0.296i
0.122	-0.527+0.425i	6.865+3.725i	-6.129-2.549i	0.543-0.265i
0.0916	-0.789+0.358i	6.318+3.558i	-5.821-2.544i	0.821-0.362i
0.061	-1.077+0.229i	4.922+3.764i	-4.815-2.537i	1.156+0.108i

x is grid north, and y is grid east.

Table A.24: Impedance tensor estimates made at WS.

Freq / Hz	Z_{xx}	Z_{xy}	Z_{yx}	Z_{yy}
188	-2.052-1.807i	38.27+26.85i	-30.58-19.79i	-3.452-2.934i
93.8	-3.394-0.836i	33.30+18.15i	-27.62-13.81i	-1.011-2.550i
62.5	-3.647-0.586i	30.81+14.45i	-25.66-11.17i	-0.280-2.106i
46.9	-3.808-0.491i	29.89+12.71i	-24.95-9.95i	0.084-1.855i
31.2	-3.761-0.492i	27.47+10.96i	-22.97-8.80i	0.509-1.478i
23.4	-3.713-0.466i	25.89+9.82i	-21.64-8.01i	0.740-1.296i
15.6	-3.731-0.389i	23.97+8.47i	-19.90-7.07i	1.058-0.987i
11.7	-3.526-0.515i	22.77+7.70i	-19.11-6.37i	1.114-0.930i
7.81	-3.583-0.339i	20.90+6.58i	-17.67-5.80i	1.594-0.501i
5.86	-3.433-0.556i	19.97+6.07i	-16.82-5.36i	1.419-0.712i
3.91	-3.378-0.590i	18.43+5.26i	-15.16-4.98i	1.558-0.564i
2.93	-3.301-0.544i	17.57+4.82i	-14.19-4.76i	1.691-0.413i
1.95	-3.134-0.442i	16.46+4.03i	-12.92-4.24i	1.784-0.103i
1.46	-3.035-0.525i	16.00+3.78i	-12.33-3.90i	1.857-0.049i
0.977	-2.796-0.519i	15.30+3.49i	-11.52-3.44i	1.720+0.054i
0.732	-2.678-0.527i	14.90+3.45i	-11.01-3.27i	1.592+0.074i
0.488	-2.555-0.401i	14.29+3.62i	-10.37-3.14i	1.500+0.019i
0.366	-2.531-0.342i	13.66+3.74i	-9.891-3.036i	1.483-0.076i
0.244	-2.290-0.283i	12.62+4.13i	-8.873-3.157i	1.542-0.251i
0.183	-2.478-0.257i	11.60+4.31i	-8.288-3.248i	1.786-0.372i
0.122	-2.451-0.230i	9.881+4.753i	-6.947-3.199i	2.008-0.035i
0.0916	-2.599-0.235i	8.609+5.095i	-6.717-3.020i	2.077+0.102i
0.061	-2.328-0.220i	7.011+5.307i	-5.121-2.978i	1.912+0.685i

x is grid north, and y is grid east.

Table A.25: Impedance tensor estimates made at WE0.

Freq / Hz	Z_{xx}	Z_{xy}	Z_{yx}	Z_{yy}
125	2.890+0.916i	19.20+12.28i	-17.71-12.95i	0.864+1.919i
93.8	2.508+0.509i	18.46+9.23i	-16.74-10.03i	0.943+1.525i
62.5	2.551+0.184i	17.21+7.02i	-15.33-7.61i	0.678+1.189i
46.9	2.715+0.062i	16.98+5.96i	-15.02-6.45i	0.563+1.028i
31.2	2.810+0.080i	16.04+5.05i	-14.02-5.35i	0.355+0.777i

Table A.25: Impedance tensor estimates made at WE0 (continued).

Freq / Hz	Z_{xx}	Z_{xy}	Z_{yx}	Z_{yy}
23.4	2.811+0.224i	15.38+4.56i	-13.38-4.79i	0.311+0.592i
15.6	2.649+0.434i	14.46+3.94i	-12.34-4.21i	0.224+0.463i
11.7	2.756+0.327i	14.08+3.76i	-12.13-3.72i	0.183+0.151i
7.81	2.513+0.711i	12.74+3.15i	-11.15-3.52i	0.398+0.347i
5.86	2.460+0.521i	12.44+3.17i	-10.65-3.24i	0.211-0.044i
3.91	2.283+0.605i	11.31+2.82i	-9.485-2.949i	0.050-0.062i
2.93	2.054+0.726i	10.97+2.55i	-9.063-2.882i	0.160+0.019i
1.95	1.699+0.665i	10.36+2.18i	-8.175-2.546i	0.213+0.120i
1.46	1.683+0.535i	10.04+2.08i	-7.877-2.428i	0.341+0.094i
0.977	1.605+0.490i	9.653+1.938i	-7.382-2.169i	0.271+0.083i
0.732	1.569+0.479i	9.447+1.934i	-7.106-2.031i	0.190+0.054i
0.488	1.535+0.535i	9.121+2.116i	-6.757-2.004i	0.104-0.041i
0.366	1.463+0.589i	8.746+2.258i	-6.417-1.979i	0.134-0.167i
0.244	1.300+0.816i	8.086+2.541i	-5.903-2.066i	0.071-0.283i
0.183	1.038+0.909i	7.624+2.790i	-5.550-2.124i	0.301-0.399i
0.122	0.753+1.017i	6.757+3.291i	-5.014-2.275i	0.461-0.459i
0.0916	0.307+0.898i	6.072+3.467i	-4.613-2.297i	0.593-0.380i
0.061	-0.140+0.949i	4.634+3.336i	-3.818-2.303i	0.993-0.214i

x is grid north, and y is grid east.

Table A.26: Impedance tensor estimates made at WE1.

Freq / Hz	Z_{xx}	Z_{xy}	Z_{yx}	Z_{yy}
125	-4.740-3.117i	20.29+14.02i	-23.50-15.33i	1.257+1.752i
93.8	-6.417-4.187i	22.53+13.19i	-23.46-13.33i	4.788+3.819i
62.5	-6.737-3.754i	22.24+10.54i	-22.31-10.72i	6.484+4.191i
46.9	-6.719-3.716i	22.40+9.37i	-21.73-9.08i	6.454+3.880i
31.2	-6.262-2.991i	21.38+7.49i	-20.78-7.50i	6.542+3.428i
23.4	-5.995-2.662i	20.90+6.66i	-20.21-6.60i	6.600+3.046i
15.6	-5.710-1.969i	20.09+5.54i	-19.03-5.66i	6.046+2.542i
11.7	-5.237-1.742i	19.34+4.99i	-18.63-5.06i	5.738+2.243i
7.81	-5.105-1.243i	18.38+4.17i	-17.86-4.87i	5.962+2.085i
5.86	-4.606-0.921i	17.22+3.89i	-16.97-4.47i	5.219+1.695i
3.91	-4.360-0.157i	14.84+2.42i	-15.30-4.64i	4.906+2.322i

Table A.26: Impedance tensor estimates made at WE1 (continued).

Freq / Hz	Z_{xx}	Z_{xy}	Z_{yx}	Z_{yy}
2.93	-3.815-0.576i	13.96+2.47i	-14.43-4.15i	4.815+1.211i
1.95	-2.799-1.182i	12.21+2.43i	-12.69-3.42i	4.340+0.385i
1.46	-2.664-1.006i	12.05+2.23i	-11.70-3.09i	3.575+0.141i
0.977	-2.059-1.018i	11.11+2.19i	-10.41-2.61i	2.500-0.063i
0.732	-2.031-0.800i	10.86+2.16i	-9.871-2.356i	2.244-0.083i
0.488	-1.189-0.418i	9.280+2.023i	-8.746-2.299i	1.541-0.123i
0.366	-1.193-0.718i	8.705+2.426i	-7.798-2.191i	1.214-0.417i
0.244	-2.167-0.167i	9.250+2.824i	-8.316-2.493i	1.790-0.153i
0.183	-2.473+0.148i	9.128+2.886i	-7.995-2.362i	2.021-0.088i
0.122	-1.696+0.676i	7.252+3.225i	-4.728-1.828i	0.994+0.231i
0.0916	-1.361+0.577i	6.240+2.788i	-3.512-1.339i	0.830-0.010i
0.061	-0.902+0.507i	4.293+3.263i	-2.888-1.515i	0.422-0.048i

x is grid north, and y is grid east.

Table A.27: Impedance tensor estimates made at WE2.

Freq / Hz	Z_{xx}	Z_{xy}	Z_{yx}	Z_{yy}
125	0.367+0.696i	15.48+11.92i	-15.93-12.08i	1.166+0.455i
93.8	0.432+0.401i	13.86+9.17i	-14.29-9.27i	0.965+0.533i
62.5	0.396+0.179i	12.31+6.70i	-12.69-6.79i	0.822+0.509i
46.9	0.418+0.007i	11.96+5.37i	-12.34-5.47i	0.757+0.545i
31.2	0.530-0.146i	11.24+4.01i	-11.58-4.13i	0.581+0.555i
23.4	0.598-0.212i	10.91+3.34i	-11.24-3.47i	0.445+0.532i
15.6	0.726-0.118i	10.46+2.67i	-10.76-2.88i	0.317+0.486i
11.7	0.893-0.238i	10.47+2.35i	-10.87-2.57i	0.113+0.343i
7.81	0.927+0.067i	9.795+2.100i	-10.19-2.46i	0.093+0.428i
5.86	0.947-0.018i	9.649+2.041i	-9.930-2.445i	0.022+0.114i
3.91	0.858+0.147i	8.940+1.906i	-9.027-2.363i	0.019+0.065i
2.93	0.820+0.209i	8.688+1.811i	-8.600-2.400i	0.034+0.067i
1.95	0.684+0.231i	8.113+1.524i	-7.901-2.162i	0.092+0.010i
1.46	0.612+0.178i	8.019+1.522i	-7.569-2.076i	0.095+0.061i
0.977	0.570+0.200i	7.733+1.439i	-7.128-1.854i	0.038+0.040i
0.732	0.554+0.218i	7.523+1.486i	-6.871-1.764i	-0.026+0.067i
0.488	0.521+0.281i	7.274+1.623i	-6.489-1.776i	-0.071+0.023i

Table A.27: Impedance tensor estimates made at WE2 (continued).

Freq / Hz	Z_{xx}	Z_{xy}	Z_{yx}	Z_{yy}
0.366	0.458+0.361i	6.973+1.669i	-6.201-1.717i	-0.077-0.088i
0.244	0.379+0.428i	6.546+1.949i	-5.580-1.820i	-0.004-0.202i
0.183	0.165+0.519i	6.005+2.132i	-5.160-1.832i	0.042-0.246i
0.122	0.096+0.573i	5.141+2.256i	-4.430-1.814i	0.152-0.184i
0.0916	-0.099+0.582i	4.452+2.190i	-4.000-1.911i	0.095-0.295i

x is grid north, and y is grid east.

A.3 Area surrounding Beresford and Warburton Springs

A.3.1 Line C

Table A.28: Impedance tensor estimates made at BWR1.

Freq / Hz	Z_{xx}	Z_{xy}	Z_{yx}	Z_{yy}
125	0.716+0.399i	15.95+15.62i	-15.97-15.58i	-2.247-1.950i
93.8	0.341+0.039i	15.91+12.96i	-15.88-12.97i	-1.382-0.782i
62.5	0.236-0.094i	14.33+9.60i	-14.56-9.76i	-0.723-0.340i
46.9	0.209-0.114i	14.11+7.78i	-14.22-7.94i	-0.684-0.105i
31.2	0.270-0.089i	13.23+5.89i	-13.38-5.97i	-0.666-0.026i
23.4	0.279-0.062i	12.91+4.90i	-13.03-4.93i	-0.583-0.055i
15.6	0.281+0.051i	12.18+4.00i	-12.30-4.02i	-0.626+0.021i
11.7	0.360-0.030i	12.32+3.61i	-12.48-3.44i	-0.846-0.249i
7.81	0.180+0.153i	11.26+3.20i	-11.74-3.21i	-0.205-0.044i
5.86	0.269+0.077i	10.99+3.07i	-11.53-3.05i	-0.495-0.410i
3.91	0.237+0.219i	9.998+2.825i	-10.32-2.82i	-0.635-0.366i
2.93	0.062+0.313i	9.530+2.525i	-9.696-2.774i	-0.489-0.190i
1.95	-0.018+0.315i	8.831+2.166i	-8.973-2.503i	-0.394-0.065i
1.46	-0.062+0.216i	8.620+1.977i	-8.660-2.382i	-0.111-0.142i
0.732	-0.100+0.130i	8.044+1.845i	-7.917-2.119i	-0.249-0.162i
0.488	0.010+0.151i	7.600+1.811i	-7.407-1.931i	-0.147-0.274i
0.366	-0.183+0.223i	7.415+1.938i	-7.174-1.981i	-0.353-0.163i
0.244	-0.187+0.325i	6.799+2.232i	-6.704-2.237i	-0.070-0.349i
0.183	-0.250+0.452i	6.361+2.497i	-5.958-2.210i	-0.151-0.424i

Table A.28: Impedance tensor estimates made at BWR1 (continued).

Freq / Hz	Z_{xx}	Z_{xy}	Z_{yx}	Z_{yy}
0.122	-0.392+0.441i	5.353+2.498i	-4.763-2.088i	0.136-0.184i

x is grid north, and y is grid east.

Table A.29: Impedance tensor estimates made at BWC1000.

Freq / Hz	Z_{xx}	Z_{xy}	Z_{yx}	Z_{yy}
188	-0.673-1.408i	14.40+17.79i	-17.82-20.13i	-1.732-1.918i
93.8	-1.083-0.607i	15.19+10.63i	-17.54-11.11i	-1.256-1.138i
62.5	-0.976-0.388i	12.85+8.15i	-15.39-8.95i	-1.058-0.909i
46.9	-0.980-0.272i	12.47+6.26i	-14.79-7.05i	-0.991-0.724i
31.2	-0.982-0.150i	12.04+4.84i	-14.22-5.54i	-0.951-0.571i
23.4	-0.992-0.095i	11.74+4.03i	-13.81-4.65i	-0.913-0.480i
15.6	-1.013-0.029i	11.31+3.46i	-13.27-4.04i	-0.828-0.359i
11.7	-1.079-0.070i	11.20+2.99i	-13.33-3.37i	-0.841-0.566i
7.81	-1.050+0.031i	10.41+2.76i	-12.64-3.25i	-0.588-0.142i
5.86	-1.066-0.098i	10.20+2.60i	-12.40-3.07i	-0.660-0.472i
3.91	-1.021-0.045i	9.450+2.396i	-11.37-3.05i	-0.536-0.467i
2.93	-1.016-0.023i	8.884+2.224i	-10.60-2.94i	-0.385-0.472i
1.95	-1.040-0.031i	8.351+1.944i	-9.751-2.647i	-0.229-0.365i
1.46	-1.024-0.045i	8.111+1.788i	-9.229-2.478i	-0.178-0.237i
0.977	-1.016-0.124i	7.823+1.625i	-8.688-2.344i	-0.168-0.118i
0.732	-1.031-0.129i	7.607+1.581i	-8.287-2.196i	-0.132-0.091i
0.488	-0.965-0.035i	7.295+1.679i	-7.949-2.142i	-0.226-0.200i
0.366	-0.886+0.052i	7.095+1.786i	-7.583-2.144i	-0.295-0.331i
0.244	-0.861+0.082i	6.585+2.051i	-7.076-2.200i	-0.102-0.415i
0.183	-0.970+0.017i	6.325+2.221i	-6.318-2.360i	-0.048-0.450i
0.122	-0.951+0.206i	5.302+2.402i	-5.825-2.437i	0.369-0.436i
0.0916	-1.084+0.107i	5.019+2.571i	-5.509-2.594i	0.700-0.857i
0.061	-1.212-0.058i	3.440+2.612i	-4.525-2.453i	0.861-0.493i
0.0458	-1.166-0.121i	3.304+2.599i	-4.281-2.625i	0.834-0.557i
0.0305	-1.059-0.173i	2.561+2.271i	-3.400-2.355i	1.013-0.440i
0.0229	-0.977-0.184i	2.040+1.704i	-2.588-1.791i	1.310-0.229i

x is grid north, and y is grid east.

Table A.30: Impedance tensor estimates made at BWC1500.

Freq / Hz	Z_{xx}	Z_{xy}	Z_{yx}	Z_{yy}
188	-0.422-1.830i	15.84+20.78i	-15.47-19.71i	-1.319-0.089i
93.8	-0.694-0.761i	16.05+10.46i	-15.86-10.36i	-0.945-0.288i
62.5	-0.515-0.752i	14.13+8.37i	-13.72-8.27i	-0.995-0.213i
46.9	-0.466-0.547i	13.48+6.18i	-13.11-6.24i	-0.910-0.155i
31.2	-0.300-0.490i	12.82+5.05i	-12.39-5.16i	-1.035-0.052i
23.4	-0.238-0.338i	12.45+4.00i	-11.98-4.18i	-1.034-0.086i
15.6	-0.246-0.138i	11.96+3.40i	-11.39-3.67i	-0.912+0.042i
11.7	-0.212-0.223i	12.11+2.97i	-11.61-3.16i	-0.966-0.229i
7.81	-0.348-0.043i	11.16+2.70i	-10.83-2.90i	-0.644+0.287i
5.86	-0.422-0.333i	11.19+2.79i	-10.95-2.86i	-0.548-0.108i
3.91	-1.477-0.587i	10.99+2.66i	-11.29-2.98i	0.359-0.096i
1.95	-4.305-2.149i	12.45+3.19i	-13.70-4.46i	3.669+1.040i

x is grid north, and y is grid east.

Table A.31: Impedance tensor estimates made at BWC2000.

Freq / Hz	Z_{xx}	Z_{xy}	Z_{yx}	Z_{yy}
188	1.538+1.373i	16.71+18.14i	-16.72-17.81i	-1.146-0.699i
62.5	0.998+0.888i	13.59+8.72i	-13.52-8.55i	-0.429-0.564i
46.9	0.928+0.644i	12.88+6.55i	-12.87-6.55i	-0.386-0.397i
31.2	0.880+0.440i	12.34+5.11i	-12.22-5.08i	-0.361-0.246i
23.4	0.870+0.348i	11.96+4.17i	-11.84-4.25i	-0.377-0.156i
15.6	0.881+0.314i	11.53+3.52i	-11.32-3.64i	-0.371-0.045i
11.7	0.831+0.140i	11.55+3.02i	-11.25-3.09i	-0.401-0.175i
7.81	0.874+0.300i	10.65+2.77i	-10.68-2.88i	-0.316+0.077i
5.86	0.870+0.120i	10.55+2.71i	-10.45-2.69i	-0.383-0.162i
3.91	0.787+0.254i	9.723+2.517i	-9.576-2.678i	-0.397-0.221i
2.93	0.645+0.265i	9.106+2.302i	-8.993-2.616i	-0.318-0.215i
1.95	0.508+0.217i	8.538+2.031i	-8.241-2.310i	-0.252-0.176i
1.46	0.396+0.104i	8.249+1.797i	-7.841-2.284i	-0.173-0.034i
0.977	0.317+0.137i	7.948+1.668i	-7.376-2.038i	-0.197-0.062i
0.732	0.435+0.007i	7.713+1.729i	-7.191-2.023i	-0.269-0.110i
0.488	0.537+0.190i	7.431+1.690i	-6.621-1.675i	-0.360-0.308i

Table A.31: Impedance tensor estimates made at BWC2000 (continued).

Freq / Hz	Z_{xx}	Z_{xy}	Z_{yx}	Z_{yy}
0.366	0.177+0.037i	7.221+1.638i	-6.677-1.881i	-0.249-0.237i
0.244	-0.136+0.243i	6.787+1.914i	-5.643-2.115i	-0.355-0.160i
0.061	-0.360+0.270i	3.449+2.770i	-3.678-2.138i	0.657-0.578i
0.0458	-0.369+0.355i	3.260+2.792i	-3.513-2.218i	0.664-0.540i
0.0305	-0.441+0.249i	2.480+2.406i	-2.787-2.021i	0.800-0.404i

x is grid north, and y is grid east.

Table A.32: Impedance tensor estimates made at BWC2500.

Freq / Hz	Z_{xx}	Z_{xy}	Z_{yx}	Z_{yy}
188	-0.240-0.883i	19.44+21.77i	-21.10-21.26i	-1.945-1.224i
93.8	-0.475-0.581i	17.75+13.25i	-18.76-13.32i	-1.457-0.754i
62.5	-0.331-0.510i	15.34+10.31i	-16.37-10.21i	-1.363-0.633i
46.9	-0.303-0.398i	14.50+7.99i	-15.45-7.94i	-1.299-0.442i
31.2	-0.231-0.355i	13.68+6.31i	-14.70-6.15i	-1.309-0.281i
23.4	-0.176-0.269i	13.10+5.22i	-14.29-5.06i	-1.284-0.249i
15.6	-0.155-0.108i	12.44+4.42i	-13.70-4.33i	-1.203-0.071i
11.7	-0.092-0.211i	12.37+3.96i	-13.91-3.71i	-1.278-0.323i
7.81	-0.189-0.019i	11.33+3.61i	-13.03-3.46i	-1.019+0.135i
5.86	0.035-0.202i	10.96+3.42i	-12.93-3.38i	-1.068-0.255i
3.91	0.125-0.084i	9.818+2.935i	-11.86-3.37i	-0.976-0.282i
2.93	-0.036-0.077i	9.262+2.730i	-10.67-3.03i	-0.970-0.431i
1.95	0.031+0.076i	8.606+2.093i	-10.38-3.11i	-0.737+0.002i
1.46	-0.009-0.014i	8.357+1.998i	-9.479-2.602i	-0.749-0.206i
0.732	-0.069+0.026i	7.940+1.744i	-8.661-2.252i	-0.842-0.189i
0.488	-0.126+0.090i	7.725+1.853i	-8.378-2.549i	-0.846-0.233i
0.366	0.029+0.063i	7.380+2.033i	-7.905-2.238i	-0.834-0.513i
0.244	-0.011+0.185i	6.981+2.258i	-7.043-2.568i	-1.289-0.634i
0.183	-0.226+0.361i	6.715+2.919i	-6.842-2.872i	-0.955-0.990i
0.122	-0.258+0.379i	5.743+2.745i	-5.953-2.696i	-0.482-0.954i
0.0916	-0.362+0.323i	5.389+2.885i	-5.579-2.761i	0.020-1.122i
0.061	-0.557+0.278i	4.249+2.983i	-4.728-2.810i	0.481-1.116i
0.0458	-0.651+0.224i	3.557+2.864i	-4.374-2.803i	0.572-0.980i
0.0305	-0.619+0.151i	2.600+2.304i	-3.282-2.529i	0.782-0.785i

Table A.32: Impedance tensor estimates made at BWC2500 (continued).

Freq / Hz	Z_{xx}	Z_{xy}	Z_{yx}	Z_{yy}
-----------	----------	----------	----------	----------

x is grid north, and y is grid east.

Table A.33: Impedance tensor estimates made at BWC3000.

Freq / Hz	Z_{xx}	Z_{xy}	Z_{yx}	Z_{yy}
188	-1.752-2.897i	21.93+29.22i	-24.36-31.18i	-2.500-2.561i
93.8	-2.422-1.819i	20.53+17.66i	-23.24-19.21i	-1.712-1.658i
62.5	-2.121-1.329i	17.83+13.27i	-20.31-14.50i	-1.460-1.399i
46.9	-2.071-1.018i	17.03+10.34i	-19.27-11.35i	-1.339-1.048i
31.2	-2.036-0.799i	16.20+7.88i	-18.26-8.74i	-1.266-0.747i
23.4	-1.981-0.647i	15.62+6.47i	-17.69-7.22i	-1.203-0.629i
15.6	-1.903-0.458i	14.97+5.39i	-16.86-6.07i	-1.051-0.337i
11.7	-1.906-0.495i	14.85+4.70i	-17.03-5.18i	-1.107-0.573i
7.81	-1.913-0.285i	13.79+4.39i	-15.90-4.70i	-0.775+0.018i
5.86	-1.722-0.527i	13.31+4.17i	-15.74-4.52i	-0.828-0.385i
3.91	-1.464-0.466i	11.93+3.69i	-14.41-4.35i	-0.696-0.344i
2.93	-1.546-0.354i	11.22+3.32i	-12.95-3.87i	-0.670-0.524i
1.95	-1.435-0.296i	10.41+2.72i	-12.46-3.84i	-0.446-0.077i
1.46	-1.381-0.442i	10.12+2.49i	-11.40-3.23i	-0.520-0.318i
0.732	-1.333-0.252i	9.553+2.101i	-10.36-2.78i	-0.621-0.246i
0.488	-1.418-0.253i	9.334+2.199i	-10.03-3.05i	-0.611-0.262i
0.366	-1.450+0.058i	9.047+2.243i	-9.398-2.866i	-0.792-0.370i
0.183	-1.585+0.158i	7.771+2.509i	-8.440-3.328i	-0.357-0.746i
0.122	-1.617-0.083i	6.286+3.150i	-7.357-2.922i	-0.134-0.865i
0.0916	-1.477-0.047i	6.032+3.429i	-6.817-3.072i	0.129-0.739i
0.061	-1.690-0.087i	4.631+3.416i	-6.002-3.180i	0.500-0.840i
0.0458	-1.509-0.139i	4.316+3.379i	-5.309-3.316i	0.866-0.990i
0.0305	-1.350-0.216i	2.945+2.657i	-4.035-2.913i	0.930-0.593i

x is grid north, and y is grid east.

Table A.34: Impedance tensor estimates made at BWC3580.

Freq / Hz	Z_{xx}	Z_{xy}	Z_{yx}	Z_{yy}
188	-0.128-0.713i	19.97+23.02i	-22.02-22.19i	-0.448+0.256i
93.8	-0.347-0.462i	18.28+14.05i	-19.08-14.12i	-0.224+0.113i
62.5	-0.236-0.355i	15.64+10.86i	-16.38-11.03i	-0.270-0.061i
46.9	-0.250-0.221i	14.76+8.30i	-15.28-8.61i	-0.206-0.052i
31.2	-0.275-0.135i	13.96+6.37i	-14.29-6.77i	-0.197-0.046i
23.4	-0.282-0.046i	13.45+5.14i	-13.79-5.53i	-0.138-0.092i
15.6	-0.330+0.089i	12.93+4.27i	-13.06-4.65i	-0.066+0.084i
11.7	-0.331-0.046i	12.97+3.77i	-13.31-4.04i	-0.043-0.190i
7.81	-0.466+0.126i	12.05+3.50i	-12.36-3.59i	0.120+0.297i
5.86	-0.287-0.120i	11.70+3.42i	-12.27-3.51i	0.093-0.047i
3.91	-0.197-0.062i	10.54+3.05i	-11.24-3.35i	0.116-0.014i
2.93	-0.347-0.031i	9.902+2.764i	-10.12-2.96i	0.081-0.217i
1.95	-0.299+0.062i	9.182+2.196i	-9.714-2.984i	0.135+0.162i
1.46	-0.344+0.007i	8.942+1.993i	-8.943-2.495i	0.155-0.073i
0.732	-0.344-0.039i	8.534+1.757i	-8.131-2.149i	-0.000-0.060i
0.488	-0.391+0.077i	8.310+1.845i	-7.771-2.476i	0.052-0.088i
0.366	-0.344+0.142i	8.167+1.875i	-7.127-2.183i	-0.150-0.183i
0.183	-0.491+0.230i	6.643+2.586i	-6.422-2.350i	-0.308-0.782i
0.122	-0.726+0.432i	5.804+2.903i	-5.397-2.337i	0.342-0.760i
0.0916	-0.799+0.326i	5.433+3.179i	-5.190-2.504i	0.635-0.748i
0.061	-0.979+0.271i	4.296+3.178i	-4.401-2.505i	1.167-0.643i
0.0458	-0.916+0.186i	3.810+3.049i	-4.068-2.604i	0.950-0.654i
0.0305	-0.918+0.115i	2.713+2.496i	-3.045-2.273i	1.042-0.434i

x is grid north, and y is grid east.

Table A.35: Impedance tensor estimates made at BWC4050.

Freq / Hz	Z_{xx}	Z_{xy}	Z_{yx}	Z_{yy}
188	-0.476-1.005i	18.57+22.21i	-20.80-21.27i	1.001+1.436i
93.8	-0.874-0.593i	16.91+13.80i	-17.44-13.79i	1.068+0.831i
62.5	-0.754-0.488i	14.19+10.72i	-14.63-10.73i	0.907+0.531i
46.9	-0.747-0.360i	13.27+8.18i	-13.53-8.30i	0.925+0.428i
31.2	-0.728-0.292i	12.43+6.20i	-12.59-6.37i	0.885+0.361i

Table A.35: Impedance tensor estimates made at BWC4050 (continued).

Freq / Hz	Z_{xx}	Z_{xy}	Z_{yx}	Z_{yy}
23.4	-0.712-0.211i	11.94+4.92i	-12.16-5.10i	0.885+0.282i
15.6	-0.713-0.091i	11.47+3.95i	-11.59-4.16i	0.890+0.400i
11.7	-0.684-0.204i	11.53+3.41i	-11.85-3.56i	0.899+0.140i
7.81	-0.752-0.079i	10.79+3.08i	-11.11-3.12i	0.961+0.570i
5.86	-0.566-0.297i	10.54+2.96i	-11.03-3.02i	0.915+0.245i
3.91	-0.426-0.200i	9.592+2.631i	-10.23-2.95i	0.817+0.227i
2.93	-0.509-0.130i	9.081+2.431i	-9.318-2.598i	0.745+0.005i
1.95	-0.350-0.037i	8.396+1.949i	-9.027-2.651i	0.704+0.269i
1.46	-0.460-0.129i	8.180+1.825i	-8.220-2.192i	0.730+0.035i
0.732	-0.437-0.062i	7.812+1.580i	-7.484-1.919i	0.628+0.151i
0.488	-0.376-0.046i	7.671+1.760i	-7.238-2.140i	0.474+0.049i
0.122	-0.464+0.254i	5.760+2.618i	-5.260-2.356i	0.710-0.642i
0.0916	-0.632+0.260i	5.527+2.744i	-4.901-2.238i	1.210+0.071i
0.061	-0.725+0.128i	4.436+2.838i	-4.377-2.430i	0.691-0.832i
0.0458	-0.846+0.105i	3.742+2.752i	-3.930-2.477i	1.238-0.544i
0.0305	-0.775+0.048i	2.650+2.379i	-3.199-2.129i	1.086-0.413i

x is grid north, and y is grid east.

Table A.36: Impedance tensor estimates made at BWC4700.

Freq / Hz	Z_{xx}	Z_{xy}	Z_{yx}	Z_{yy}
188	0.266+0.117i	15.73+19.59i	-17.33-19.52i	0.858+1.019i
93.8	0.060+0.044i	14.19+12.51i	-14.48-12.92i	0.822+0.687i
62.5	0.085+0.013i	11.62+9.77i	-11.82-10.08i	0.642+0.458i
46.9	0.037+0.034i	10.71+7.48i	-10.78-7.79i	0.626+0.376i
31.2	0.009+0.011i	9.865+5.582i	-9.858-5.866i	0.567+0.328i
23.4	-0.001+0.018i	9.427+4.351i	-9.489-4.631i	0.562+0.263i
15.6	-0.014+0.048i	9.041+3.335i	-9.018-3.653i	0.560+0.350i
11.7	0.026-0.068i	9.125+2.787i	-9.232-3.075i	0.563+0.149i
7.81	-0.027-0.011i	8.592+2.375i	-8.666-2.595i	0.572+0.473i
5.86	0.149-0.181i	8.485+2.240i	-8.626-2.451i	0.522+0.247i
3.91	0.264-0.127i	7.840+2.013i	-8.092-2.348i	0.434+0.222i
2.93	0.157-0.063i	7.427+1.848i	-7.269-2.081i	0.332+0.111i
1.95	0.239-0.011i	6.936+1.502i	-7.042-2.105i	0.311+0.223i

Table A.36: Impedance tensor estimates made at BWC4700 (continued).

Freq / Hz	Z_{xx}	Z_{xy}	Z_{yx}	Z_{yy}
1.46	0.167-0.044i	6.731+1.373i	-6.448-1.753i	0.259+0.088i
0.732	0.131+0.048i	6.511+1.229i	-5.853-1.563i	0.210+0.067i
0.488	0.065+0.089i	6.405+1.363i	-5.678-1.723i	0.265+0.022i
0.366	-0.002+0.110i	6.267+1.382i	-5.108-1.321i	0.100-0.059i
0.244	-0.159+0.203i	5.785+1.368i	-4.524-1.324i	-0.212-0.178i
0.183	0.071+0.197i	5.061+1.881i	-4.722-1.612i	0.235-0.309i
0.122	-0.180+0.374i	4.782+2.197i	-4.124-1.726i	0.117-0.472i
0.0916	-0.258+0.335i	4.452+2.346i	-3.869-1.768i	0.520-0.465i
0.061	-0.392+0.254i	3.532+2.403i	-3.415-1.781i	0.597-0.386i
0.0458	-0.442+0.284i	3.130+2.425i	-3.107-1.817i	0.664-0.409i
0.0305	-0.455+0.164i	2.177+1.976i	-2.325-1.658i	0.685-0.323i

x is grid north, and y is grid east.

Table A.37: Impedance tensor estimates made at BWC5150.

Freq / Hz	Z_{xx}	Z_{xy}	Z_{yx}	Z_{yy}
188	-1.347-2.330i	17.30+19.89i	-17.25-18.89i	-2.786-2.206i
93.8	-1.534-1.577i	14.73+13.09i	-15.04-12.68i	-2.090-1.492i
62.5	-1.151-1.233i	11.88+10.37i	-12.24-10.03i	-1.762-1.330i
46.9	-1.087-0.892i	10.84+7.96i	-11.07-7.78i	-1.571-1.022i
31.2	-1.035-0.659i	9.870+5.949i	-10.05-5.88i	-1.408-0.751i
23.4	-1.003-0.502i	9.395+4.610i	-9.642-4.635i	-1.299-0.598i
15.6	-1.000-0.352i	8.942+3.483i	-9.160-3.650i	-1.214-0.321i
11.7	-0.976-0.401i	9.048+2.893i	-9.390-3.044i	-1.235-0.401i
7.81	-0.994-0.260i	8.638+2.411i	-8.790-2.546i	-1.172+0.013i
5.86	-0.824-0.406i	8.540+2.236i	-8.812-2.403i	-1.210-0.175i
3.91	-0.624-0.417i	7.877+1.931i	-8.228-2.167i	-1.147-0.199i
2.93	-0.618-0.262i	7.522+1.775i	-7.470-1.998i	-1.195-0.254i
1.95	-0.423-0.169i	6.977+1.348i	-7.277-2.121i	-1.105+0.066i
1.46	-0.488-0.299i	6.852+1.381i	-6.750-1.678i	-1.065-0.256i
0.732	-0.536-0.125i	6.649+1.150i	-6.146-1.591i	-1.173-0.285i
0.488	-0.617-0.102i	6.682+1.250i	-5.643-1.731i	-1.271-0.212i
0.122	-0.594+0.061i	4.913+2.220i	-4.615-1.708i	-1.179-1.033i
0.0916	-0.682+0.174i	4.602+2.431i	-4.040-1.953i	-0.766-0.851i

Table A.37: Impedance tensor estimates made at BWC5150 (continued).

Freq / Hz	Z_{xx}	Z_{xy}	Z_{yx}	Z_{yy}
0.061	-0.741+0.050i	3.671+2.330i	-3.428-1.860i	0.221-0.644i
0.0458	-0.790+0.089i	3.187+2.406i	-3.104-1.927i	0.401-0.679i
0.0305	-0.742-0.002i	2.240+2.005i	-2.490-1.759i	0.333-0.463i

x is grid north, and y is grid east.

A.4 The Bubbler Spring complex

A.4.1 Line A

Table A.38: Impedance tensor estimates made at WKA5750.

Freq / Hz	Z_{xx}	Z_{xy}	Z_{yx}	Z_{yy}
375	2.331-2.011i	36.36+36.09i	-32.47-28.47i	5.112+5.590i
250	0.341-3.652i	37.94+29.06i	-36.00-22.53i	5.088+4.013i
188	0.529-0.083i	31.87+22.80i	-29.76-19.33i	4.802+3.475i
125	0.885+0.260i	29.22+17.88i	-26.83-15.55i	4.140+2.665i
93.8	0.567+0.106i	27.28+14.72i	-25.47-12.77i	3.967+2.314i
62.5	0.387+0.091i	24.95+11.38i	-23.37-10.26i	3.629+1.894i
46.9	0.388-0.090i	24.56+9.59i	-22.62-8.49i	3.480+1.653i
31.2	0.334-0.143i	23.01+7.93i	-21.00-6.70i	3.321+1.305i
23.4	0.417-0.154i	22.11+7.27i	-20.40-5.94i	3.119+1.425i
15.6	0.592-0.239i	20.10+6.71i	-18.69-5.32i	2.645+1.545i
11.7	0.684-0.716i	20.62+6.74i	-19.21-4.87i	2.326+0.829i
7.81	0.969-0.254i	17.94+6.19i	-18.50-4.86i	2.659+1.709i
5.86	1.327-0.438i	17.17+6.41i	-18.10-4.82i	2.277+0.977i
3.91	1.962+0.685i	14.94+5.37i	-16.19-4.99i	1.544+1.004i
2.93	0.974+0.121i	13.94+5.34i	-15.08-4.69i	1.520+0.745i
1.95	1.388+0.468i	12.49+4.18i	-13.44-4.15i	1.352+0.464i
1.46	1.644-0.159i	11.76+3.91i	-12.82-4.32i	1.345+0.390i
0.977	0.721+0.864i	11.46+3.61i	-11.83-3.16i	1.350+0.298i
0.732	1.093+0.640i	10.90+2.84i	-11.38-3.13i	1.228+0.196i
0.488	1.289+0.740i	10.34+3.11i	-10.88-3.38i	1.184-0.118i
0.366	0.751+0.591i	9.960+2.930i	-10.83-3.29i	1.198-0.133i

Table A.38: Impedance tensor estimates made at WKA5750 (continued).

Freq / Hz	Z_{xx}	Z_{xy}	Z_{yx}	Z_{yy}
0.244	-0.122+0.387i	9.354+3.126i	-9.994-3.230i	1.212-0.402i

x is grid north, and y is grid east.

Table A.39: Impedance tensor estimates made at WKA5625.

Freq / Hz	Z_{xx}	Z_{xy}	Z_{yx}	Z_{yy}
375	-3.490-4.850i	38.48+35.78i	-32.25-28.03i	-2.665-3.031i
250	-4.929-3.512i	39.71+27.85i	-33.48-20.72i	-1.898-2.877i
188	-3.163-2.523i	32.71+23.07i	-28.73-18.15i	-1.504-1.713i
125	-3.311-2.076i	30.99+18.50i	-25.81-14.24i	-1.333-1.070i
93.8	-3.041-1.559i	28.93+15.30i	-24.56-11.88i	-1.034-0.894i
62.5	-2.923-1.261i	26.63+12.09i	-22.52-9.50i	-0.917-0.570i
46.9	-2.857-1.109i	26.14+10.17i	-21.90-7.80i	-0.975-0.384i
31.2	-2.708-1.021i	24.37+8.55i	-20.54-6.17i	-0.970-0.345i
23.4	-2.532-0.944i	23.45+7.84i	-19.88-5.68i	-1.013+0.077i
15.6	-2.169-0.985i	21.42+7.25i	-18.26-5.03i	-1.165+0.219i
11.7	-2.075-1.349i	21.40+7.20i	-18.76-4.76i	-1.306-0.461i
7.81	-1.816-0.990i	19.16+6.89i	-17.78-4.84i	-0.976+0.430i
5.86	-1.404-1.122i	18.22+6.88i	-17.31-4.88i	-1.039-0.246i
3.91	-0.954-0.439i	15.96+5.98i	-15.49-4.82i	-1.155-0.147i
2.93	-0.836-0.435i	14.74+5.62i	-14.49-4.72i	-0.971-0.302i
1.95	-0.575-0.368i	13.13+4.42i	-13.14-4.29i	-0.773-0.312i
1.46	-0.892-0.293i	12.63+4.51i	-12.31-4.00i	-0.886-0.231i
0.977	-0.761-0.232i	11.77+3.41i	-11.51-2.88i	-0.713-0.150i
0.732	-0.677+0.080i	11.35+3.05i	-10.99-3.10i	-0.849-0.309i
0.488	-0.504+0.373i	10.88+3.20i	-10.20-3.23i	-0.733-0.474i
0.366	-0.685+0.219i	10.39+3.09i	-9.791-3.355i	-0.742-0.592i
0.244	-0.309+0.944i	9.681+3.534i	-9.310-3.226i	-0.548-0.887i
0.183	-1.200+0.591i	9.143+3.695i	-9.198-3.793i	-0.088-1.105i
0.122	-0.254+0.776i	7.622+4.046i	-7.661-4.086i	0.149-1.230i
0.061	-2.911+0.323i	6.561+4.324i	-6.575-3.534i	0.739-0.954i

x is grid north, and y is grid east.

Table A.40: Impedance tensor estimates made at WKA5475.

Freq / Hz	Z_{xx}	Z_{xy}	Z_{yx}	Z_{yy}
375	-0.223+0.164i	31.91+32.27i	-34.08-32.08i	-3.606-5.706i
250	-0.931-0.027i	34.42+24.07i	-36.60-24.09i	-4.508-4.197i
188	-1.562+0.319i	30.77+19.63i	-31.70-20.17i	-3.740-3.282i
125	-2.008+0.473i	28.93+15.42i	-29.30-15.25i	-3.252-2.770i
93.8	-1.911+0.277i	26.99+12.99i	-27.73-12.96i	-2.984-1.986i
62.5	-2.022+0.019i	24.75+10.54i	-25.71-10.27i	-2.661-1.371i
46.9	-2.012-0.062i	24.25+8.87i	-25.24-8.47i	-2.684-1.061i
31.2	-1.796-0.373i	22.49+7.65i	-23.51-7.11i	-2.715-0.566i
23.4	-1.759-0.399i	21.55+7.11i	-22.98-6.37i	-2.597-0.446i
15.6	-1.578-0.477i	19.92+6.59i	-21.69-5.75i	-2.287-0.185i
11.7	-1.430-0.862i	19.99+6.45i	-21.94-5.35i	-2.937-0.961i
7.81	-1.234-0.697i	17.49+6.29i	-20.69-5.43i	-1.679-0.033i
5.86	-0.838-0.811i	16.79+6.20i	-20.18-5.42i	-2.135-0.842i
3.91	-0.274-0.373i	14.53+5.43i	-18.15-5.60i	-2.114-0.539i
2.93	-0.306-0.323i	13.53+5.03i	-16.54-5.35i	-1.950-0.742i
1.95	-0.259-0.235i	11.98+4.20i	-14.54-4.56i	-1.537-0.855i
1.46	-0.608-0.152i	11.47+3.87i	-14.37-4.82i	-1.672-0.484i
0.977	-0.375-0.163i	10.75+3.22i	-12.96-3.78i	-1.426-0.386i
0.732	-0.437+0.164i	10.59+2.87i	-12.26-3.35i	-1.534-0.692i
0.488	-0.405+0.376i	10.14+2.96i	-11.82-3.65i	-1.468-0.903i
0.366	-0.469+0.378i	9.869+3.015i	-11.27-3.71i	-1.416-0.877i
0.244	-0.788+0.422i	9.183+3.177i	-11.04-3.71i	-1.309-1.372i
0.122	-1.329-0.152i	7.444+3.158i	-9.241-3.902i	-0.881-1.887i

x is grid north, and y is grid east.

Table A.41: Impedance tensor estimates made at WKA5360.

Freq / Hz	Z_{xx}	Z_{xy}	Z_{yx}	Z_{yy}
375	1.452-0.562i	36.69+35.73i	-37.06-31.91i	1.128+0.307i
250	1.061-1.057i	37.52+26.84i	-39.31-23.78i	1.025+0.399i
188	0.354-0.276i	34.16+21.88i	-33.98-19.95i	0.999+0.420i
125	0.095+0.056i	32.13+17.06i	-31.45-15.14i	0.976+0.023i
93.8	0.213+0.095i	29.98+14.44i	-29.88-12.97i	0.960+0.361i

Table A.41: Impedance tensor estimates made at WKA5360 (continued).

Freq / Hz	Z_{xx}	Z_{xy}	Z_{yx}	Z_{yy}
62.5	0.074-0.007i	27.39+11.73i	-27.76-10.39i	0.932+0.474i
46.9	0.073-0.086i	26.84+9.86i	-27.25-8.62i	0.815+0.494i
31.2	0.192-0.259i	24.90+8.44i	-25.44-7.35i	0.475+0.691i
23.4	0.218-0.238i	23.91+7.78i	-24.89-6.65i	0.540+0.673i
15.6	0.331-0.244i	22.07+7.20i	-23.47-6.12i	0.586+0.823i
11.7	0.497-0.636i	22.28+7.10i	-23.71-5.82i	-0.002-0.058i
7.81	0.590-0.362i	19.46+6.84i	-22.31-5.99i	0.946+0.962i
5.86	0.937-0.480i	18.69+6.84i	-21.66-6.11i	0.406+0.123i
3.91	1.337+0.077i	16.32+6.00i	-19.27-6.13i	0.081+0.198i
2.93	1.291+0.054i	15.06+5.57i	-17.54-5.86i	0.070-0.003i
1.95	1.171+0.061i	13.54+4.72i	-15.38-4.96i	0.296-0.257i
1.46	0.719+0.264i	13.00+4.35i	-15.25-5.24i	0.085+0.124i
0.977	0.880+0.148i	12.11+3.56i	-13.75-4.03i	0.241+0.059i
0.732	0.692+0.396i	11.91+3.29i	-13.02-3.40i	0.022-0.285i
0.488	0.656+0.764i	11.36+3.35i	-12.49-3.83i	0.029-0.525i
0.366	0.539+0.644i	11.07+3.30i	-11.95-3.90i	0.011-0.456i
0.244	0.455+0.915i	10.29+3.79i	-11.64-3.68i	0.079-0.919i

x is grid north, and y is grid east.

Table A.42: Impedance tensor estimates made at WKA5250.

Freq / Hz	Z_{xx}	Z_{xy}	Z_{yx}	Z_{yy}
375	2.678+4.304i	7.407+8.802i	-7.755-9.082i	-5.307-4.916i
250	4.178+4.667i	13.41+9.94i	-16.38-11.50i	-8.482-5.401i
188	2.608+2.774i	19.32+13.86i	-20.88-14.13i	-6.658-4.426i
125	-1.246+0.112i	26.16+15.66i	-26.84-14.85i	-2.682-2.395i
93.8	-2.878-0.905i	29.46+15.13i	-28.43-13.57i	-0.977-0.718i
62.5	-3.203-0.986i	28.51+12.42i	-27.68-10.92i	-0.359-0.168i
46.9	-3.189-0.975i	28.11+10.85i	-27.42-9.29i	-0.355-0.064i
31.2	-2.991-1.073i	26.22+9.43i	-25.95-7.94i	-0.450+0.065i
23.4	-2.865-1.086i	25.27+8.56i	-25.23-7.09i	-0.481+0.145i
15.6	-2.621-1.019i	23.77+7.75i	-24.29-6.29i	-0.399+0.092i
11.7	-2.370-1.283i	23.31+7.23i	-24.04-5.84i	-0.882-0.064i
7.81	-2.221-0.913i	20.99+7.20i	-22.62-6.06i	0.013+0.080i

Table A.42: Impedance tensor estimates made at WKA5250 (continued).

Freq / Hz	Z_{xx}	Z_{xy}	Z_{yx}	Z_{yy}
5.86	-1.681-1.083i	19.88+6.93i	-21.34-6.05i	-0.547-0.301i
3.91	-0.940-0.731i	16.81+6.09i	-18.02-5.83i	-0.698-0.453i
2.93	-0.742-0.688i	15.42+5.60i	-16.73-5.66i	-0.488-0.382i
1.95	-0.718-0.494i	13.74+4.66i	-14.54-4.94i	-0.271-0.418i
1.46	-0.758-0.307i	13.14+4.19i	-14.02-4.70i	-0.439-0.214i
0.977	-0.788-0.196i	12.41+3.42i	-12.52-3.44i	-0.422-0.228i
0.732	-0.698-0.055i	12.20+3.23i	-12.72-3.83i	-0.563-0.396i
0.488	-0.661+0.355i	11.76+3.14i	-12.12-3.63i	-0.502-0.680i
0.366	-0.908+0.502i	11.43+3.36i	-11.24-3.48i	-0.422-0.567i
0.244	-1.138+0.690i	10.56+3.62i	-9.419-3.369i	-0.252-0.364i
0.183	-1.176+0.611i	10.17+3.87i	-8.768-3.359i	0.036-0.392i
0.122	-1.643+0.613i	8.792+4.363i	-8.098-4.057i	0.703-0.946i
0.0916	-1.951+0.460i	8.010+4.585i	-8.053-4.369i	0.963-1.105i
0.061	-2.268+0.244i	6.883+4.647i	-7.198-4.830i	1.526-0.976i

x is grid north, and y is grid east.

Table A.43: Impedance tensor estimates made at WKA5125.

Freq / Hz	Z_{xx}	Z_{xy}	Z_{yx}	Z_{yy}
375	2.814+3.847i	6.930+7.640i	-8.349-8.093i	-6.396-4.730i
250	4.717+4.311i	12.54+8.71i	-16.29-9.92i	-10.05-5.23i
188	3.454+2.639i	18.00+12.07i	-20.81-12.15i	-8.940-5.014i
125	0.434+0.427i	23.66+13.51i	-26.05-12.57i	-5.860-3.608i
93.8	-0.936-0.423i	26.61+12.98i	-27.45-11.63i	-4.623-2.000i
62.5	-1.179-0.540i	25.68+10.68i	-26.65-9.47i	-3.903-1.345i
46.9	-1.197-0.564i	25.38+9.32i	-26.41-8.09i	-3.888-1.111i
31.2	-1.087-0.631i	23.80+8.13i	-25.07-7.04i	-3.767-0.931i
23.4	-0.991-0.642i	22.97+7.36i	-24.44-6.36i	-3.651-0.797i
15.6	-0.870-0.579i	21.70+6.69i	-23.55-5.78i	-3.364-0.823i
11.7	-0.681-0.835i	21.35+6.27i	-23.32-5.40i	-3.792-0.899i
7.81	-0.672-0.474i	19.24+6.33i	-21.91-5.80i	-2.584-0.772i
5.86	-0.302-0.656i	18.31+6.19i	-20.66-5.88i	-3.000-1.113i
3.91	0.216-0.448i	15.53+5.58i	-17.46-5.62i	-2.680-1.107i
2.93	0.366-0.312i	14.27+5.03i	-16.23-5.49i	-2.373-1.062i

Table A.43: Impedance tensor estimates made at WKA5125 (continued).

Freq / Hz	Z_{xx}	Z_{xy}	Z_{yx}	Z_{yy}
1.95	0.258-0.234i	12.76+4.26i	-14.01-4.73i	-1.990-0.945i
1.46	0.239-0.016i	12.20+3.79i	-13.51-4.62i	-2.077-0.722i
0.977	0.042+0.007i	11.48+3.12i	-12.04-3.34i	-1.947-0.687i
0.732	0.168+0.164i	11.26+3.01i	-12.22-3.75i	-2.102-0.767i
0.488	0.138+0.526i	10.92+2.95i	-11.65-3.61i	-1.908-1.030i
0.366	-0.137+0.644i	10.58+3.11i	-10.69-3.47i	-1.826-0.920i
0.244	-0.523+0.763i	9.812+3.386i	-8.949-3.391i	-1.539-0.766i
0.183	-0.628+0.694i	9.375+3.570i	-8.201-3.241i	-1.312-0.766i
0.122	-1.019+0.812i	8.053+4.051i	-7.576-3.965i	-0.435-1.447i
0.0916	-1.275+0.656i	7.344+4.244i	-7.519-4.316i	-0.027-1.617i
0.061	-1.647+0.516i	6.265+4.337i	-6.673-4.701i	0.602-1.538i

x is grid north, and y is grid east.

Table A.44: Impedance tensor estimates made at WKA5050.

Freq / Hz	Z_{xx}	Z_{xy}	Z_{yx}	Z_{yy}
375	1.988+2.930i	5.961+6.519i	-7.590-7.789i	-6.220-4.935i
250	2.975+3.345i	10.88+7.34i	-14.88-9.54i	-9.450-5.592i
188	1.371+1.647i	15.56+10.43i	-19.05-11.52i	-8.635-5.328i
125	-2.116-0.402i	21.40+11.92i	-23.81-11.52i	-5.702-4.013i
93.8	-3.513-1.254i	24.21+11.63i	-25.14-10.48i	-4.731-2.457i
62.5	-3.699-1.229i	23.55+9.57i	-24.61-8.46i	-4.082-1.703i
46.9	-3.679-1.139i	23.22+8.33i	-24.49-7.19i	-4.039-1.451i
31.2	-3.454-1.137i	21.80+7.26i	-23.37-6.29i	-3.881-1.185i
23.4	-3.329-1.104i	21.08+6.59i	-22.80-5.72i	-3.755-1.050i
15.6	-3.135-1.005i	19.98+5.99i	-22.04-5.26i	-3.429-1.013i
11.7	-2.972-1.214i	19.63+5.58i	-21.83-4.97i	-3.792-1.093i
7.81	-2.809-0.962i	17.85+5.73i	-20.50-5.37i	-2.604-0.893i
5.86	-2.295-1.166i	16.92+5.54i	-19.36-5.44i	-2.936-1.200i
3.91	-1.511-0.880i	14.45+4.94i	-16.27-5.27i	-2.685-1.138i
2.93	-1.358-0.773i	13.18+4.65i	-15.15-5.13i	-2.339-1.103i
1.95	-1.198-0.703i	11.84+3.91i	-13.02-4.48i	-1.905-0.932i
1.46	-1.187-0.485i	11.33+3.46i	-12.55-4.32i	-2.013-0.743i
0.977	-1.189-0.281i	10.61+2.80i	-11.14-3.15i	-1.992-0.665i

Table A.44: Impedance tensor estimates made at WKA5050 (continued).

Freq / Hz	Z_{xx}	Z_{xy}	Z_{yx}	Z_{yy}
0.732	-1.045-0.193i	10.39+2.71i	-11.33-3.53i	-2.038-0.732i
0.488	-1.040+0.158i	10.11+2.63i	-10.82-3.37i	-1.884-1.022i
0.366	-1.203+0.253i	9.797+2.852i	-9.943-3.236i	-1.850-0.928i
0.244	-1.355+0.460i	9.091+3.088i	-8.304-3.159i	-1.533-0.763i
0.183	-1.283+0.462i	8.729+3.349i	-7.744-3.035i	-1.301-0.827i
0.122	-1.685+0.361i	7.542+3.657i	-7.015-3.691i	-0.452-1.360i
0.0916	-1.991+0.211i	6.898+3.888i	-6.943-4.004i	-0.150-1.546i
0.061	-2.234+0.004i	5.983+3.947i	-6.133-4.379i	0.503-1.437i

x is grid north, and y is grid east.

Table A.45: Impedance tensor estimates made at WKA4930.

Freq / Hz	Z_{xx}	Z_{xy}	Z_{yx}	Z_{yy}
265	1.208-0.004i	35.13+34.69i	-37.59-27.29i	-0.877-2.004i
187	0.818+0.276i	32.14+25.27i	-32.69-20.98i	-0.799-0.870i
132	-0.091+0.553i	30.95+20.07i	-30.61-15.95i	-0.846-0.721i
93.1	0.536+0.235i	28.28+15.63i	-29.46-12.42i	-0.540-0.417i
65.7	0.615+0.129i	26.26+12.57i	-28.13-9.92i	-0.568-0.315i
46.4	0.639+0.019i	25.60+9.93i	-27.75-7.74i	-0.676-0.247i
32.7	0.695-0.064i	24.21+8.41i	-26.61-6.67i	-0.745-0.161i
23.1	0.607+0.016i	23.13+7.29i	-26.05-6.14i	-0.471-0.278i
16.3	0.658+0.046i	22.02+6.65i	-24.76-6.08i	-0.354+0.025i
11.5	0.807-0.339i	22.01+6.48i	-25.09-5.98i	-0.688-0.763i
8.12	0.734-0.091i	19.84+6.30i	-23.68-6.43i	0.378+0.414i
5.73	1.126-0.302i	18.91+6.38i	-22.63-6.72i	0.047-0.298i
4.04	1.304+0.147i	17.03+5.86i	-19.98-6.70i	-0.270-0.097i
2.85	1.042-0.008i	15.48+5.56i	-17.87-6.30i	-0.006-0.251i
2.01	1.301+0.337i	14.20+4.61i	-15.56-5.43i	-0.054-0.429i
1.42	1.121+0.240i	13.34+4.05i	-15.00-5.56i	-0.052-0.224i
1	1.135+0.472i	12.63+3.70i	-13.73-4.06i	0.027-0.424i
0.708	0.727+0.384i	12.14+3.25i	-12.93-4.08i	-0.035-0.342i

x is grid north, and y is grid east.

Table A.46: Impedance tensor estimates made at WKA4645.

Freq / Hz	Z_{xx}	Z_{xy}	Z_{yx}	Z_{yy}
375	1.359+1.285i	30.93+38.57i	-31.79-31.01i	-2.308-4.242i
250	2.070+1.324i	35.43+29.50i	-35.92-23.28i	-1.849-3.957i
188	1.453+1.356i	30.88+23.72i	-30.43-20.02i	-1.831-2.245i
125	0.574+1.555i	29.56+17.69i	-28.32-14.83i	-1.657-1.845i
93.8	0.912+1.149i	27.30+14.46i	-27.25-11.96i	-1.261-1.455i
62.5	0.702+0.890i	25.21+10.99i	-25.72-9.21i	-1.090-1.114i
46.9	0.618+0.728i	24.86+9.02i	-25.48-7.56i	-0.974-0.960i
31.2	0.442+0.520i	23.38+7.34i	-24.18-6.37i	-0.895-0.826i
23.4	0.292+0.467i	22.77+6.46i	-23.80-5.85i	-0.661-0.840i
15.6	0.223+0.343i	21.75+5.77i	-22.65-5.62i	-0.266-0.491i
11.7	0.354-0.094i	22.16+5.65i	-22.93-5.52i	-0.723-1.013i
7.81	0.217+0.018i	19.82+5.71i	-21.46-5.99i	0.743+0.092i
5.86	0.538-0.272i	19.39+5.92i	-20.56-6.22i	0.157-0.514i
3.91	0.858+0.050i	17.17+5.52i	-17.91-6.22i	-0.140-0.160i
2.93	0.753+0.075i	15.99+5.21i	-16.19-5.84i	-0.029-0.262i
1.95	0.731+0.306i	14.53+4.47i	-14.35-5.13i	0.010-0.191i
1.46	0.535+0.130i	13.80+4.09i	-13.70-5.10i	-0.008-0.181i
0.977	0.732+0.428i	13.03+3.56i	-12.41-3.83i	0.053-0.270i
0.732	0.349+0.421i	12.72+3.12i	-11.79-3.64i	0.077-0.192i
0.488	0.311+0.706i	12.16+3.30i	-11.32-3.41i	-0.065-0.337i
0.366	0.313+0.599i	11.63+3.40i	-10.79-3.58i	0.048-0.402i
0.244	-0.093+0.726i	10.84+3.69i	-9.856-3.745i	0.162-0.907i

x is grid north, and y is grid east.

A.4.2 Line C

Table A.47: Impedance tensor estimates made at WKC2350.

Freq / Hz	Z_{xx}	Z_{xy}	Z_{yx}	Z_{yy}
375	-1.715-1.994i	31.51+41.19i	-30.67-38.28i	-0.961-5.642i
250	-1.025-1.872i	34.80+31.30i	-34.91-29.83i	-1.965-4.386i
188	-1.176-1.141i	30.62+23.81i	-29.93-23.47i	-1.764-2.699i
125	-1.889-0.553i	29.45+18.03i	-27.52-17.63i	-1.832-1.829i

Table A.47: Impedance tensor estimates made at WKC2350 (continued).

Freq / Hz	Z_{xx}	Z_{xy}	Z_{yx}	Z_{yy}
93.8	-1.092-0.612i	27.13+14.93i	-26.47-14.09i	-1.601-1.174i
62.5	-0.845-0.607i	24.95+11.75i	-24.86-10.45i	-1.635-0.710i
46.9	-0.756-0.606i	24.54+10.11i	-24.66-8.34i	-1.770-0.411i
31.2	-0.528-0.524i	22.63+8.77i	-23.52-6.58i	-2.006-0.149i
23.4	-0.588-0.336i	21.57+8.17i	-23.28-5.88i	-1.893-0.219i
15.6	-0.467-0.184i	19.64+7.52i	-22.12-5.52i	-1.873-0.026i
11.7	-0.330-0.558i	19.65+7.47i	-22.55-5.22i	-2.416-0.806i
7.81	-0.473-0.173i	16.64+6.81i	-21.34-5.64i	-1.100+0.124i
5.86	-0.183-0.365i	15.97+6.66i	-20.72-5.78i	-1.464-0.800i
3.91	0.144+0.058i	13.77+5.51i	-18.35-5.93i	-1.543-0.478i
2.93	-0.037-0.045i	12.73+4.98i	-16.72-5.56i	-1.198-0.667i
1.95	0.013+0.145i	11.57+4.03i	-14.62-4.95i	-1.075-0.762i
1.46	-0.175-0.046i	11.09+3.64i	-14.01-4.98i	-0.974-0.656i
0.977	0.065-0.010i	10.48+3.05i	-12.88-3.74i	-0.785-0.602i
0.732	-0.135+0.039i	10.24+2.62i	-12.27-3.59i	-0.633-0.556i
0.488	-0.289+0.369i	9.804+2.702i	-11.69-3.51i	-0.976-0.687i
0.366	-0.306+0.385i	9.365+2.831i	-11.09-3.72i	-0.741-0.672i

x is grid north, and y is grid east.

Table A.48: Impedance tensor estimates made at WKC2200.

Freq / Hz	Z_{xx}	Z_{xy}	Z_{yx}	Z_{yy}
375	1.147+0.536i	35.19+37.47i	-34.27-34.32i	-2.952-4.008i
250	2.295+0.207i	36.21+28.13i	-36.66-25.91i	-3.390-3.107i
188	1.838+0.610i	32.07+21.58i	-32.22-20.92i	-2.872-1.950i
125	0.972+1.123i	30.89+16.08i	-29.58-15.72i	-2.751-1.474i
93.8	1.508+0.690i	28.43+13.79i	-28.45-12.97i	-2.436-1.111i
62.5	1.467+0.426i	26.19+11.18i	-26.57-10.00i	-2.307-0.850i
46.9	1.458+0.305i	25.78+9.72i	-26.26-8.12i	-2.349-0.659i
31.2	1.457+0.231i	23.74+8.66i	-24.89-6.62i	-2.382-0.463i
23.4	1.300+0.362i	22.58+8.23i	-24.52-6.06i	-2.118-0.543i
15.6	1.223+0.409i	20.53+7.64i	-23.13-5.73i	-1.936-0.262i
11.7	1.419-0.006i	20.52+7.70i	-23.61-5.46i	-2.446-1.100i
7.81	1.160+0.323i	17.27+6.97i	-22.26-5.87i	-1.057+0.016i

Table A.48: Impedance tensor estimates made at WKC2200 (continued).

Freq / Hz	Z_{xx}	Z_{xy}	Z_{yx}	Z_{yy}
5.86	1.442+0.149i	16.64+6.85i	-21.63-6.08i	-1.493-0.853i
3.91	1.491+0.639i	14.43+5.61i	-19.11-6.11i	-1.463-0.548i
2.93	1.176+0.384i	13.33+5.28i	-17.50-5.76i	-1.204-0.779i
1.95	1.210+0.513i	11.96+4.22i	-15.30-4.96i	-0.956-0.837i
1.46	1.035+0.328i	11.48+3.78i	-14.76-5.18i	-0.899-0.587i
0.977	0.940+0.294i	10.89+3.22i	-13.40-3.74i	-0.695-0.676i
0.732	0.804+0.408i	10.60+2.78i	-12.90-3.76i	-0.604-0.548i
0.488	0.691+0.643i	10.20+2.91i	-12.30-3.64i	-1.042-0.701i
0.366	0.591+0.742i	9.785+3.005i	-11.67-3.88i	-0.743-0.656i
0.244	0.433+0.742i	9.398+3.339i	-10.81-4.11i	-0.453-1.391i

x is grid north, and y is grid east.

Table A.49: Impedance tensor estimates made at WKC2100.

Freq / Hz	Z_{xx}	Z_{xy}	Z_{yx}	Z_{yy}
375	1.140-0.825i	32.54+36.36i	-39.66-36.65i	-5.743-6.976i
250	0.653-1.040i	35.60+26.46i	-41.56-26.42i	-6.859-4.620i
188	0.175-0.285i	31.25+21.81i	-36.61-22.38i	-6.166-4.013i
125	0.022-0.135i	29.43+16.40i	-34.04-16.56i	-5.663-3.202i
93.8	0.141-0.010i	28.00+13.77i	-32.77-13.95i	-5.490-2.542i
62.5	0.042+0.058i	25.89+11.14i	-30.70-11.06i	-5.037-2.003i
46.9	0.043+0.084i	25.46+9.55i	-30.31-9.03i	-5.006-1.722i
31.2	0.086+0.011i	23.50+8.45i	-28.63-7.63i	-4.747-1.318i
23.4	-0.007+0.103i	22.46+8.07i	-28.08-6.95i	-4.505-1.275i
15.6	-0.007+0.145i	20.23+7.55i	-26.63-6.56i	-4.035-1.022i
11.7	-0.014-0.295i	20.35+7.55i	-26.97-6.22i	-4.393-1.989i
7.81	-0.020-0.040i	17.25+6.92i	-25.44-6.67i	-2.850-0.734i
5.86	0.227-0.240i	16.52+6.79i	-24.73-6.74i	-3.107-1.692i
3.91	0.516+0.200i	14.25+5.65i	-22.02-6.84i	-2.842-1.346i
2.93	0.366+0.094i	13.19+5.18i	-20.11-6.61i	-2.525-1.296i
1.95	0.340+0.066i	11.90+4.20i	-17.76-5.72i	-2.004-1.254i
1.46	0.072+0.105i	11.45+3.84i	-17.21-5.88i	-2.114-0.816i
0.977	0.234+0.106i	10.72+3.09i	-15.73-4.76i	-1.786-0.645i
0.732	0.012+0.317i	10.53+2.88i	-14.95-4.10i	-1.857-0.913i

Table A.49: Impedance tensor estimates made at WKC2100 (continued).

Freq / Hz	Z_{xx}	Z_{xy}	Z_{yx}	Z_{yy}
0.488	0.066+0.494i	10.06+2.88i	-14.20-4.36i	-1.845-1.085i
0.366	-0.051+0.532i	9.819+2.855i	-13.58-4.38i	-1.742-1.199i
0.244	-0.319+0.789i	9.131+3.239i	-12.92-4.70i	-1.434-1.622i
0.183	-0.960+1.398i	8.088+3.337i	-10.86-4.06i	-0.661-1.377i
0.122	-1.005+0.450i	7.370+3.641i	-10.82-5.40i	-0.599-1.953i

x is grid north, and y is grid east.

Table A.50: Impedance tensor estimates made at WKC1850.

Freq / Hz	Z_{xx}	Z_{xy}	Z_{yx}	Z_{yy}
375	2.922+1.266i	38.72+36.00i	-34.74-34.14i	-1.076-1.136i
250	1.933+1.736i	39.12+26.68i	-35.63-24.06i	-0.313-1.869i
188	1.896+1.866i	35.01+20.59i	-31.25-20.12i	0.062-0.708i
125	1.314+1.946i	33.31+14.88i	-28.45-15.24i	0.147-0.475i
93.8	1.245+1.479i	31.23+13.35i	-27.31-12.84i	0.494-0.381i
62.5	0.871+1.036i	28.87+11.08i	-25.23-10.22i	0.601-0.209i
46.9	0.808+0.805i	28.45+9.49i	-24.71-8.43i	0.584-0.096i
31.2	0.729+0.570i	26.19+8.65i	-23.22-6.65i	0.471-0.062i
23.4	0.682+0.455i	25.19+8.20i	-22.46-6.28i	0.505+0.331i
15.6	0.616+0.244i	22.86+7.84i	-20.95-5.67i	0.407+0.518i
11.7	0.758-0.201i	22.78+7.86i	-21.43-5.42i	0.083-0.319i
7.81	0.660+0.092i	20.14+7.53i	-20.23-5.46i	0.802+1.002i
5.86	1.001-0.175i	19.05+7.41i	-19.64-5.63i	0.507+0.200i
3.91	1.372+0.143i	16.22+6.18i	-17.73-5.63i	0.348+0.458i
2.93	1.341+0.296i	15.01+5.63i	-16.17-5.50i	0.147+0.020i
1.95	1.133+0.172i	13.48+4.58i	-14.44-4.79i	0.356-0.109i
1.46	0.715+0.331i	13.31+4.52i	-13.82-4.68i	0.293+0.013i
0.977	0.787+0.196i	12.37+3.47i	-12.38-3.39i	0.347-0.089i
0.732	0.837+0.507i	11.92+3.14i	-12.01-3.31i	0.269-0.279i
0.488	0.738+0.651i	11.63+3.26i	-11.38-3.65i	0.301-0.243i
0.366	0.574+0.712i	11.21+3.31i	-10.92-3.60i	0.260-0.390i
0.244	0.383+0.739i	10.64+3.72i	-9.945-3.605i	0.329-0.583i
0.183	0.100+0.500i	9.964+3.826i	-10.19-3.59i	0.387-1.039i

Table A.50: Impedance tensor estimates made at WKC1850 (continued).

Freq / Hz	Z_{xx}	Z_{xy}	Z_{yx}	Z_{yy}
-----------	----------	----------	----------	----------

x is grid north, and y is grid east.

Table A.51: Impedance tensor estimates made at WKC1330.

Freq / Hz	Z_{xx}	Z_{xy}	Z_{yx}	Z_{yy}
375	0.154-1.242i	29.16+32.93i	-33.04-30.03i	-6.881-6.954i
250	-0.517-1.908i	31.09+26.04i	-33.00-23.59i	-7.417-5.338i
188	-0.928-1.085i	25.64+20.86i	-27.10-20.61i	-6.179-4.132i
125	-0.977-0.959i	22.92+16.73i	-23.97-16.44i	-5.405-3.242i
93.8	-0.687-0.915i	20.85+12.97i	-21.55-13.70i	-5.156-2.153i
62.5	-0.473-1.003i	18.94+9.47i	-19.11-10.50i	-4.964-1.228i
46.9	-0.318-1.047i	18.69+7.39i	-18.48-8.53i	-5.107-0.701i
31.2	0.072-1.086i	17.77+5.51i	-16.90-6.59i	-5.333-0.201i
23.4	0.273-1.054i	17.54+4.72i	-16.41-5.56i	-5.416-0.035i
15.6	0.605-0.943i	16.90+4.17i	-15.54-4.46i	-5.440+0.072i
11.7	0.866-1.205i	17.53+4.09i	-15.84-3.82i	-6.116-0.556i
7.81	1.158-0.810i	15.79+4.37i	-15.24-3.59i	-5.176-0.251i
5.86	1.543-0.803i	15.48+4.63i	-15.13-3.51i	-5.531-1.001i
3.91	1.971-0.247i	13.61+4.40i	-14.00-3.70i	-5.120-1.092i
2.93	1.822-0.080i	12.66+4.30i	-12.99-3.57i	-4.766-1.327i
1.95	1.757+0.039i	11.22+3.75i	-11.60-3.09i	-4.114-1.324i
1.46	1.378+0.322i	10.76+3.56i	-11.37-3.45i	-4.095-1.052i
0.977	1.404+0.160i	9.942+2.893i	-10.38-2.66i	-3.777-0.951i
0.732	1.170+0.433i	9.751+2.765i	-9.784-2.394i	-3.814-1.122i
0.488	1.193+0.701i	9.322+2.781i	-9.461-2.882i	-3.590-1.378i
0.366	1.077+0.743i	9.028+2.748i	-9.018-2.990i	-3.532-1.400i
0.244	0.766+0.899i	8.435+3.141i	-8.476-2.896i	-3.300-1.814i
0.183	0.241+0.966i	7.855+2.994i	-7.743-2.929i	-2.093-1.771i
0.122	0.485+0.397i	7.250+3.304i	-7.096-2.801i	-2.061-2.011i
0.061	-0.819+0.868i	5.228+3.441i	-5.360-3.466i	-0.906-1.699i

x is grid north, and y is grid east.

Table A.52: Impedance tensor estimates made at WKC1100.

Freq / Hz	Z_{xx}	Z_{xy}	Z_{yx}	Z_{yy}
375	-2.240-2.460i	32.17+35.30i	-29.48-27.01i	-3.758-4.245i
250	-1.737-2.062i	32.52+29.40i	-29.88-23.14i	-3.681-3.723i
188	-1.677-1.436i	26.57+23.20i	-23.79-19.94i	-2.954-2.523i
125	-2.237-1.334i	22.92+19.21i	-20.05-16.59i	-2.458-1.890i
93.8	-1.453-1.023i	20.04+14.88i	-17.69-13.64i	-2.090-1.231i
62.5	-1.265-0.984i	17.60+10.63i	-15.19-10.31i	-1.955-0.693i
46.9	-1.175-1.003i	17.16+8.25i	-14.42-8.34i	-1.997-0.353i
31.2	-0.868-1.067i	16.18+5.79i	-13.00-6.17i	-2.172+0.012i
23.4	-0.754-1.075i	16.02+4.59i	-12.50-5.09i	-2.146+0.172i
15.6	-0.343-1.042i	15.77+3.67i	-11.69-3.86i	-2.401+0.403i
11.7	-0.070-1.350i	16.52+3.47i	-12.02-3.21i	-2.818+0.001i
7.81	0.231-1.013i	15.21+3.76i	-11.69-2.84i	-2.360+0.341i
5.86	0.631-1.095i	15.19+4.12i	-11.64-2.66i	-2.662-0.225i
3.91	1.159-0.464i	13.36+3.96i	-10.74-2.67i	-2.633-0.317i
2.93	0.966-0.353i	12.44+4.02i	-10.08-2.63i	-2.446-0.494i
1.95	1.014+0.061i	11.18+3.59i	-9.014-2.480i	-2.318-0.547i
1.46	0.969-0.010i	10.58+3.32i	-8.897-2.661i	-2.102-0.579i
0.977	0.841-0.138i	9.848+3.060i	-8.068-1.925i	-1.975-0.659i
0.732	0.554+0.344i	9.765+2.496i	-7.509-1.995i	-2.103-0.545i
0.488	0.628+0.380i	9.382+2.559i	-7.404-2.054i	-2.121-0.739i

x is grid north, and y is grid east.

A.5 Freeling Springs

A.5.1 Line S1

Table A.53: Impedance tensor estimates made at FW2.

Freq / Hz	Z_{xx}	Z_{xy}	Z_{yx}	Z_{yy}
93.8	36.30+37.98i	260.8+137.4i	-194.8-204.1i	-169.0-68.8i
62.5	27.24+23.63i	232.2+123.2i	-155.6-166.9i	-149.8-64.5i
46.9	23.90+16.58i	218.7+116.0i	-136.1-145.9i	-140.9-62.2i
31.2	23.05+5.56i	189.0+107.2i	-107.1-112.3i	-122.9-59.7i

Table A.53: Impedance tensor estimates made at FW2 (continued).

Freq / Hz	Z_{xx}	Z_{xy}	Z_{yx}	Z_{yy}
23.4	25.93-0.55i	169.7+100.3i	-93.48-91.62i	-111.3-56.5i
15.6	32.83-7.45i	141.6+89.5i	-80.75-65.37i	-94.35-51.05i
11.7	35.53-10.78i	130.8+81.9i	-75.63-52.37i	-87.57-46.34i
7.81	43.07-5.16i	107.6+67.5i	-69.90-40.45i	-75.17-37.76i
5.86	43.06-4.68i	100.4+59.2i	-64.81-32.94i	-72.00-32.58i
3.91	41.45+6.93i	85.65+41.25i	-58.93-33.22i	-65.13-20.10i
2.93	43.30+7.01i	78.81+37.55i	-58.83-28.53i	-60.28-20.39i
1.95	42.20+7.15i	70.21+30.71i	-54.54-23.54i	-54.71-18.17i
1.46	39.22+5.10i	66.07+30.27i	-50.11-19.29i	-51.78-19.64i
0.977	36.96+4.77i	60.81+27.37i	-45.59-16.47i	-48.15-18.54i
0.732	35.06+5.19i	57.83+26.23i	-42.42-15.25i	-46.05-18.37i
0.488	32.00+5.12i	53.05+26.52i	-36.63-13.22i	-42.97-19.61i
0.366	31.63+7.33i	48.46+24.06i	-35.15-13.77i	-39.67-18.28i
0.244	28.30+7.27i	40.52+24.51i	-30.16-12.83i	-33.07-18.89i
0.183	26.13+10.84i	36.97+23.92i	-28.11-15.27i	-30.28-18.20i
0.122	13.24+9.38i	30.87+16.78i	-14.60-11.73i	-26.63-11.78i
0.0916	9.41+11.45i	24.11+11.77i	-10.44-12.37i	-22.27-8.65i

x is grid north, and y is grid east.

Table A.54: Impedance tensor estimates made at FW1.

Freq / Hz	Z_{xx}	Z_{xy}	Z_{yx}	Z_{yy}
125	36.00+0.82i	103.6+19.3i	-117.1-29.9i	-39.05+10.53i
93.8	34.22-0.54i	89.14+26.56i	-100.0-31.6i	-39.86+3.09i
62.5	32.94+1.28i	75.09+30.61i	-83.92-31.78i	-37.42-4.85i
46.9	32.50+1.77i	68.21+33.27i	-77.07-30.04i	-35.19-9.28i
31.2	30.96+3.16i	53.19+33.65i	-66.22-26.32i	-27.81-13.67i
23.4	31.15+2.02i	47.46+33.00i	-61.82-22.31i	-24.03-14.97i
15.6	29.43+4.33i	34.66+27.39i	-56.19-18.59i	-16.81-12.72i
11.7	28.89+3.44i	29.99+23.98i	-53.28-15.23i	-14.10-11.31i
7.81	26.22+3.75i	24.25+17.51i	-49.30-11.43i	-11.55-7.62i
5.86	24.95+3.17i	21.98+14.11i	-47.23-9.03i	-10.26-5.90i
3.91	23.57+1.56i	20.17+10.30i	-45.22-5.32i	-9.704-4.303i
2.93	23.72+0.09i	19.64+8.69i	-45.57-3.12i	-9.407-3.792i

Table A.54: Impedance tensor estimates made at FW1 (continued).

Freq / Hz	Z_{xx}	Z_{xy}	Z_{yx}	Z_{yy}
1.95	24.66-1.43i	19.11+7.65i	-46.72-0.42i	-9.318-3.795i
1.46	26.08-2.08i	18.82+7.72i	-48.94+0.45i	-9.255-4.135i
0.977	28.47-1.02i	17.02+8.79i	-51.66-1.59i	-7.568-5.353i
0.732	29.62+0.70i	15.07+9.06i	-53.01-4.43i	-5.891-5.654i
0.488	29.24+4.49i	11.51+9.22i	-50.80-10.85i	-2.502-5.606i
0.366	27.38+7.41i	8.794+8.782i	-47.67-14.63i	-1.426-4.603i

x is grid north, and y is grid east.

Table A.55: Impedance tensor estimates made at FS.

Freq / Hz	Z_{xx}	Z_{xy}	Z_{yx}	Z_{yy}
93.8	12.78-7.67i	61.77+18.40i	-124.6-42.5i	-14.87+4.09i
62.5	13.95-5.72i	55.64+18.01i	-110.7-41.9i	-16.25+2.47i
46.9	15.33-4.86i	54.75+17.77i	-106.8-40.3i	-17.08+0.53i
31.2	15.99-2.76i	48.64+18.56i	-93.75-38.66i	-16.79-4.33i
23.4	16.60-1.09i	45.21+19.43i	-86.77-38.29i	-15.20-6.71i
15.6	16.26+1.08i	39.04+19.52i	-74.26-35.26i	-11.59-11.69i
11.7	16.98+2.47i	37.01+20.10i	-72.93-34.60i	-9.99-13.77i
7.81	14.23+4.99i	29.15+18.09i	-60.82-31.04i	-2.05-11.65i
5.86	12.90+5.93i	25.57+16.89i	-56.84-29.21i	0.91-11.97i
3.91	8.747+6.769i	20.32+13.85i	-46.87-21.77i	2.911-5.176i
2.93	7.079+5.624i	18.27+12.20i	-42.56-19.70i	6.088-3.504i
1.95	4.998+3.815i	14.20+9.61i	-37.14-16.20i	8.620-2.444i
1.46	4.791+2.903i	12.48+8.21i	-35.44-15.93i	7.625-3.252i
0.977	4.088+2.425i	10.51+7.39i	-32.46-14.59i	8.185-2.759i
0.732	3.755+1.913i	9.095+6.383i	-30.67-14.11i	8.303-2.229i
0.488	3.268+1.716i	6.960+5.619i	-27.81-13.56i	9.039-1.620i
0.366	2.773+1.672i	5.631+4.765i	-24.81-12.97i	8.807-1.591i
0.244	2.620+1.388i	4.981+4.364i	-22.37-11.81i	10.34+0.93i

x is grid north, and y is grid east.

Table A.56: Impedance tensor estimates made at FE1.

Freq / Hz	Z_{xx}	Z_{xy}	Z_{yx}	Z_{yy}
375	-0.138-3.344i	27.36+19.06i	-51.88-35.39i	1.957+2.816i
250	-2.780-2.045i	26.06+11.04i	-45.04-32.57i	2.290+1.377i
188	-5.045-3.149i	26.84+6.59i	-42.78-30.72i	3.048+1.009i
125	-4.566-5.148i	27.52+1.26i	-41.20-31.42i	3.012+0.951i
93.8	-3.314-8.089i	29.73+2.99i	-39.97-27.21i	2.722+0.893i
62.5	0.319-9.363i	29.03+3.70i	-35.30-22.62i	2.414+0.773i
46.9	2.74-10.03i	29.62+3.55i	-33.38-20.17i	2.331+0.654i
31.2	6.218-9.370i	28.30+4.75i	-29.17-17.48i	2.092+0.422i
23.4	8.464-8.140i	27.77+5.76i	-26.66-15.68i	2.115+0.375i
15.6	11.78-5.92i	25.21+6.84i	-22.60-13.22i	1.856+0.057i
11.7	13.69-4.55i	24.86+7.67i	-21.69-11.80i	1.941-0.051i
7.81	13.74+0.22i	21.27+8.04i	-18.75-9.90i	2.132-0.083i
5.86	13.40+2.86i	19.42+8.17i	-17.69-8.68i	2.110-0.104i
3.91	8.462+8.124i	16.71+8.06i	-15.29-6.05i	2.196+0.477i
2.93	6.957+6.129i	15.66+7.39i	-14.25-5.90i	2.406+0.384i
1.95	5.036+4.880i	13.85+6.76i	-12.73-5.19i	2.348+0.285i
1.46	4.532+3.929i	12.77+6.25i	-12.04-5.17i	2.145+0.197i
0.977	3.835+2.847i	11.16+5.87i	-10.99-4.65i	2.109+0.099i
0.732	3.002+2.285i	10.05+5.56i	-10.32-4.55i	2.078+0.093i
0.488	3.086+2.048i	8.378+5.018i	-9.555-4.536i	2.039+0.058i
0.366	2.558+1.442i	7.192+4.607i	-8.652-4.192i	2.074+0.223i
0.244	2.772+1.846i	6.098+4.416i	-7.400-4.199i	1.984+0.231i
0.183	1.900+2.163i	5.388+4.229i	-6.779-4.029i	1.882+0.516i
0.122	1.533+2.917i	3.847+3.898i	-4.877-3.289i	1.412+0.942i

x is grid north, and y is grid east.

Table A.57: Impedance tensor estimates made at FE2.

Freq / Hz	Z_{xx}	Z_{xy}	Z_{yx}	Z_{yy}
375	-0.219-0.667i	20.30+27.98i	-26.36-28.00i	-2.297-0.902i
250	-1.219-0.799i	19.44+23.07i	-25.61-24.21i	-1.567-0.673i
188	-1.396-0.468i	17.98+16.82i	-22.90-19.71i	-1.298-0.403i
125	-2.327-1.286i	17.71+10.41i	-20.87-17.75i	-0.494+0.208i

Table A.57: Impedance tensor estimates made at FE2 (continued).

Freq / Hz	Z_{xx}	Z_{xy}	Z_{yx}	Z_{yy}
93.8	-2.431-2.019i	19.37+6.52i	-19.25-14.25i	-0.403+0.078i
62.5	-1.626-2.951i	20.90+3.70i	-16.99-11.42i	-0.195-0.137i
46.9	-0.829-3.410i	22.27+2.64i	-16.13-10.05i	-0.114-0.220i
31.2	0.541-3.544i	22.68+2.73i	-14.14-8.51i	-0.008-0.327i
23.4	1.530-3.315i	22.89+3.16i	-12.97-7.57i	0.121-0.332i
15.6	2.920-2.722i	21.80+4.15i	-11.11-6.33i	0.109-0.569i
11.7	3.760-2.346i	21.96+4.74i	-10.77-5.68i	0.197-0.706i
7.81	4.149-0.471i	19.52+5.63i	-9.319-4.745i	0.551-0.680i
5.86	4.245+0.550i	18.22+6.06i	-8.925-4.230i	0.630-0.743i
3.91	2.680+2.783i	16.27+6.33i	-7.704-3.167i	0.813-0.093i
2.93	2.028+2.044i	15.31+6.06i	-7.103-3.027i	1.086-0.112i
1.95	1.236+1.622i	13.65+5.80i	-6.245-2.550i	1.252-0.152i
1.46	1.108+1.251i	12.68+5.40i	-5.784-2.542i	1.082-0.295i
0.977	0.870+0.954i	11.32+5.36i	-5.273-2.173i	1.276-0.443i
0.732	0.612+0.682i	10.08+5.09i	-5.008-2.082i	1.221-0.312i
0.488	0.646+0.515i	8.765+4.766i	-4.504-2.095i	1.572-0.379i
0.366	0.373+0.453i	7.660+4.500i	-4.032-1.916i	1.529-0.152i
0.244	0.498+0.391i	6.368+4.329i	-3.776-1.857i	1.761-0.113i
0.183	0.391+0.431i	5.791+4.054i	-3.306-1.981i	1.427+0.139i
0.122	0.306+0.452i	4.718+3.527i	-2.518-1.654i	1.202+0.827i
0.0916	0.124+0.270i	3.960+2.846i	-1.552-1.132i	1.178+1.292i
0.061	0.297+0.401i	2.910+2.537i	-1.746-1.608i	0.934+1.623i

x is grid north, and y is grid east.

Table A.58: Impedance tensor estimates made at FE3.

Freq / Hz	Z_{xx}	Z_{xy}	Z_{yx}	Z_{yy}
125	2.555-0.237i	13.45+12.49i	-16.16-15.70i	-2.185+0.009i
93.8	2.315-1.012i	14.09+10.14i	-17.88-13.56i	-0.543+0.930i
62.5	1.884-2.237i	14.12+6.18i	-16.27-10.88i	0.061-0.001i
46.9	1.252-2.519i	16.91+4.42i	-14.60-9.91i	-1.532-0.816i
31.2	2.889-3.809i	16.41+2.55i	-12.84-7.76i	-0.990-0.516i
23.4	2.908-3.381i	17.91+2.49i	-11.17-6.96i	-1.562-1.002i
15.6	4.159-2.312i	18.27+3.38i	-9.779-5.770i	-1.624-1.192i

Table A.58: Impedance tensor estimates made at FE3 (continued).

Freq / Hz	Z_{xx}	Z_{xy}	Z_{yx}	Z_{yy}
11.7	4.567-2.665i	20.32+3.86i	-9.468-4.940i	-1.738-1.303i
7.81	5.486-0.459i	19.02+4.42i	-8.441-4.226i	-1.471-1.042i
5.86	5.262-0.095i	18.54+4.78i	-7.949-3.634i	-1.258-1.121i
3.91	4.292+1.393i	16.02+4.59i	-6.728-3.048i	-1.068-0.809i
2.93	3.662+1.851i	14.88+4.70i	-6.174-2.808i	-0.980-0.598i
1.95	2.733+1.847i	13.41+4.44i	-5.511-2.427i	-0.841-0.541i
1.46	2.425+1.669i	12.74+4.74i	-5.285-2.320i	-0.700-0.551i
0.977	1.789+1.495i	11.56+4.63i	-4.746-2.157i	-0.645-0.568i
0.732	1.707+1.350i	10.61+4.72i	-4.429-2.051i	-0.544-0.653i
0.488	1.519+1.188i	8.968+4.598i	-3.999-1.851i	-0.242-0.725i
0.366	1.357+1.411i	7.825+4.165i	-3.661-1.857i	-0.031-0.580i
0.244	1.074+1.056i	6.520+3.613i	-3.102-1.726i	0.003-0.356i
0.183	0.821+1.039i	5.855+3.753i	-2.806-1.647i	0.204-0.153i
0.122	0.324+0.728i	4.681+3.228i	-2.294-1.590i	0.326+0.111i
0.0916	-0.081+0.318i	4.110+2.932i	-2.011-1.466i	0.452+0.115i
0.061	0.250+0.626i	3.775+3.243i	-1.643-1.447i	0.359+0.119i

x is grid north, and y is grid east.

A.5.2 Line N1

Table A.59: Impedance tensor estimates made at FN1.

Freq / Hz	Z_{xx}	Z_{xy}	Z_{yx}	Z_{yy}
375	-19.25+10.82i	205.2+30.1i	-78.56-39.79i	45.20+7.22i
250	-45.49+13.11i	241.0+34.4i	-96.55-43.60i	58.85+7.12i
188	-65.47+5.44i	260.6+46.8i	-89.22-41.87i	65.21+11.09i
125	-77.96-8.66i	283.0+65.3i	-81.45-49.93i	71.88+21.57i
93.8	-83.34-13.99i	298.7+68.9i	-76.28-45.19i	76.67+25.89i
62.5	-80.37-22.63i	291.5+78.8i	-65.56-42.34i	72.41+29.49i
46.9	-75.30-26.84i	283.0+85.7i	-58.57-39.91i	67.28+30.05i
31.2	-66.15-31.06i	258.8+95.6i	-48.14-35.40i	58.77+30.08i
23.4	-58.80-32.30i	240.2+100.0i	-41.85-31.53i	53.26+28.72i
15.6	-48.80-31.87i	212.2+103.2i	-34.97-26.12i	47.06+26.28i

Table A.59: Impedance tensor estimates made at FN1 (continued).

Freq / Hz	Z_{xx}	Z_{xy}	Z_{yx}	Z_{yy}
11.7	-41.89-30.29i	191.4+103.5i	-32.42-22.73i	44.16+25.25i
7.81	-34.76-26.39i	164.2+99.6i	-31.52-19.73i	50.10+27.17i

x is grid north, and y is grid east.

Table A.60: Impedance tensor estimates made at FN2.

Freq / Hz	Z_{xx}	Z_{xy}	Z_{yx}	Z_{yy}
375	-7.843-5.745i	55.66+17.58i	-17.83-5.95i	13.73-4.30i
250	-6.671+0.499i	68.07+10.98i	-42.01-13.47i	12.25-10.21i
188	-11.86-2.31i	74.89+7.04i	-42.37-17.70i	16.27-11.09i
125	-11.07+6.99i	84.87+9.27i	-67.29-30.69i	2.320-4.463i
93.8	-13.91+5.76i	88.13+11.31i	-63.89-33.88i	2.949-2.830i
62.5	-14.47+1.33i	86.47+14.16i	-53.92-32.47i	3.239-1.470i
46.9	-14.03-1.42i	86.14+15.97i	-48.79-30.84i	3.014-0.840i
31.2	-11.85-4.45i	80.87+19.84i	-39.69-27.16i	3.066-0.586i
23.4	-9.859-5.718i	76.77+22.04i	-34.22-24.35i	3.019-0.650i
15.6	-7.543-6.426i	70.44+24.43i	-27.93-19.49i	3.355-0.776i
11.7	-4.647-6.558i	65.93+25.36i	-26.09-16.96i	3.039-0.742i
7.81	-2.307-4.444i	56.49+26.24i	-22.24-13.33i	3.630+0.205i
5.86	-1.110-3.409i	50.28+25.48i	-21.04-11.37i	3.598+0.151i
3.91	-1.675-1.058i	40.46+21.91i	-18.56-8.98i	3.394+1.714i
2.93	-1.750-0.342i	36.24+20.20i	-17.78-8.02i	2.719+1.432i
1.95	-2.413-0.301i	31.56+17.46i	-16.17-6.97i	1.811+1.416i
1.46	-2.511-1.081i	29.01+16.25i	-15.28-6.42i	1.874+1.049i
0.977	-1.850-1.917i	24.67+14.68i	-13.60-5.70i	1.520+0.405i
0.732	-1.235-2.378i	22.11+14.04i	-12.72-5.14i	1.706+0.108i
0.488	-0.444-1.987i	17.08+11.53i	-10.80-4.64i	1.437-0.107i
0.366	0.223-2.457i	14.82+11.33i	-8.904-3.838i	1.831-0.886i
0.244	1.240-0.525i	11.90+9.99i	-8.316-3.967i	0.340-0.625i
0.183	0.478+0.516i	10.17+7.92i	-6.998-4.227i	-0.116+0.846i
0.122	-0.306+0.720i	5.405+4.472i	-4.565-3.161i	0.235+1.594i
0.0916	-0.207+0.500i	4.295+3.306i	-3.516-2.464i	0.288+1.118i

x is grid north, and y is grid east.

Table A.61: Impedance tensor estimates made at FN3.

Freq / Hz	Z_{xx}	Z_{xy}	Z_{yx}	Z_{yy}
375	0.066-0.130i	12.07+9.01i	-19.42-11.86i	1.030-4.774i
250	0.746+0.794i	17.23+5.41i	-24.25-11.19i	2.753-3.238i
188	-0.032+1.557i	19.49+4.14i	-25.19-11.42i	3.005-1.617i
125	-0.877+2.854i	21.54+1.15i	-25.60-10.45i	3.325-2.388i
93.8	-2.872+3.397i	25.04-0.85i	-25.21-10.01i	4.770-3.355i
62.5	-4.718+2.374i	27.98-1.22i	-23.34-9.73i	6.677-3.666i
46.9	-5.340+1.495i	29.63-0.76i	-22.31-9.65i	7.701-3.540i
31.2	-5.391+0.155i	30.11+0.91i	-19.48-9.39i	8.966-2.788i
23.4	-5.131-0.601i	30.05+1.96i	-17.51-8.95i	9.598-2.223i
15.6	-4.683-1.266i	29.55+3.26i	-14.94-7.76i	10.27-1.39i
11.7	-3.894-1.835i	29.17+3.88i	-13.84-7.12i	10.43-0.86i
7.81	-2.837-1.395i	27.47+5.46i	-11.85-5.75i	10.48+0.45i
5.86	-2.304-1.376i	26.03+6.21i	-11.10-5.04i	10.14+1.06i
3.91	-2.271-0.269i	22.70+6.58i	-9.969-3.801i	9.079+2.067i
2.93	-2.210+0.034i	21.09+6.87i	-9.518-3.379i	8.276+2.332i
1.95	-2.650+0.103i	19.22+6.72i	-8.965-2.954i	7.469+2.501i
1.46	-2.783-0.522i	18.06+6.72i	-8.552-3.030i	7.141+2.426i
0.977	-2.693-1.075i	16.17+6.59i	-7.772-2.938i	6.349+2.244i
0.732	-2.315-1.479i	14.86+6.64i	-7.199-2.796i	5.866+2.170i
0.488	-1.520-1.469i	12.45+6.32i	-5.996-2.761i	5.048+2.075i
0.366	-1.368-1.994i	11.19+6.43i	-5.116-2.582i	4.776+1.795i
0.244	-0.611-0.866i	9.634+5.832i	-4.565-2.370i	3.662+1.855i
0.183	-0.655-0.433i	8.421+5.177i	-3.906-2.264i	2.900+2.274i
0.122	-1.085-0.048i	4.551+3.720i	-2.624-1.729i	1.824+2.298i
0.0916	-0.747-0.078i	3.786+2.903i	-1.944-1.481i	1.553+1.887i
0.061	-0.633+0.071i	3.715+3.421i	-2.121-1.676i	1.682+1.775i

x is grid north, and y is grid east.

Appendix B

Self-potential

B.1 Data tables

All potential measurements shown in these tables are averages of two field measurements at each location:

$$SP = \frac{SP_{\text{fwd}} - SP_{\text{rev}}}{2} \quad (\text{B.1})$$

The forward measurement (SP_{fwd}) is made with the positive lead of the voltmeter attached to the roving electrode, and the negative voltmeter lead attached to the base electrode via a reel of insulated wire. The leads are then reversed for the reverse measurement (SP_{rev}). Figure B.1 shows that the uncertainty due to voltmeter polarity is ± 2 mV.

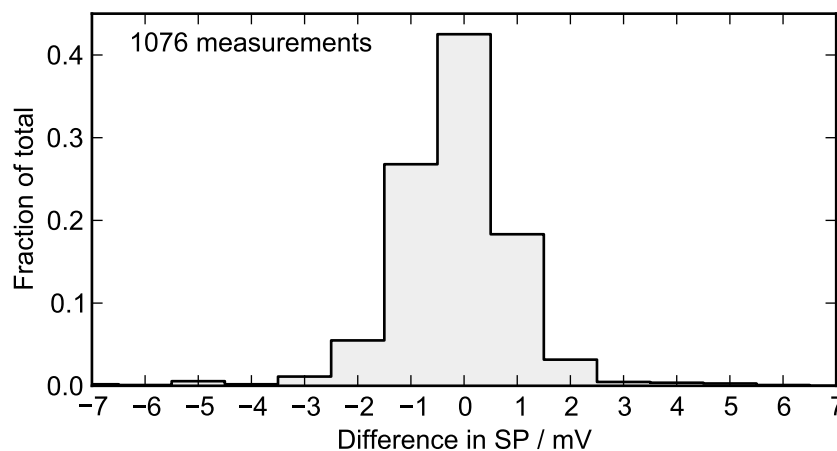


Figure B.1: Uncertainty in field potential measurements due to voltmeter polarity.

The resistance is measured in the same way as the potential. Note that the resistance shown in the following tables is an approximation only, as the observed resistance tends to drift when the multimeter leads are applied between electrodes.

Further corrections applied to the data are noted in each section below.

Note that all the SP data are available for download at <http://dx.doi.org/10.6084/m9.figshare.715294>.

B.1.1 Beresford Spring

The base electrode is at a location with easting 662132 and northing 6762489 in UTM zone 53J.

B.1.1.1 Daily corrections

A number of corrections were estimated and applied to the data collected on this survey in an attempt to correct for the existence of potentials between individual electrodes (electrode potentials ΔV_E). These occur due solely to small differences in the composition of copper sulfate solutions, and differences in the conditions of the copper electrodes or porous bases. The potentials can also change with temperature and the level of exposure to ultraviolet light (e.g. sunlight). They are measured by placing both electrodes in a bath of saturated copper sulfate solution and measuring the potential difference with the leads in the same orientation as described above for normal measurements (the electrode mentioned first has the positive lead applied).

The situation can be described with a simple equation,

$$\Delta V_{\text{Roving-Base}} = \text{SP} + \Delta V_{E(\text{Roving-Base})} \quad (\text{B.2})$$

where $\Delta V_{\text{Roving-Base}}$ is each measurement made along the line, SP is the true self-potential existing in the ground, and $\Delta V_{E(\text{Roving-Base})}$ is the electrode potential between the two measuring electrodes. The latter quantity can be measured at the beginning and the end of each day, and then a linear interpolation can be used to correct each measured value of $\Delta V_{\text{Roving-Base}}$ for the true SP. On this survey, however, an additional measurement was made to further constrain possible changes throughout the day in the value of $\Delta V_{E(\text{Roving-Base})}$, by using a third reference electrode. This reference electrode was carried to-

gether with the roving electrode in a bath of saturated copper sulfate solution all day. Equation B.2 then becomes:

$$\Delta V_{\text{Roving-Base}} = \text{SP} + \Delta V_{E(\text{Roving-Ref})} + \Delta V_{E(\text{Ref-Base})} \quad (\text{B.3})$$

Numerous measurements of $\Delta V_{E(\text{Roving-Ref})}$ were made within the copper sulfate bath throughout the day, together with measurements of $\Delta V_{E(\text{Ref-Base})}$ in the morning and evening, and each value of $\Delta V_{\text{Roving-Base}}$ was then corrected for the true SP according to B.3.

After the above drift corrections were made, there were still significant differences between the potentials measured at different times of the day at the same location (the Beresford Spring vent). This was accounted for by adding an arbitrary value to each dataset such that the potential at the spring vent was always 60 mV.

Both corrections described above are shown in Figures B.2 through B.6. Note that electrode potential measurements were not taken on 22 April, so no corrections of this type were performed for datasets taken that day.

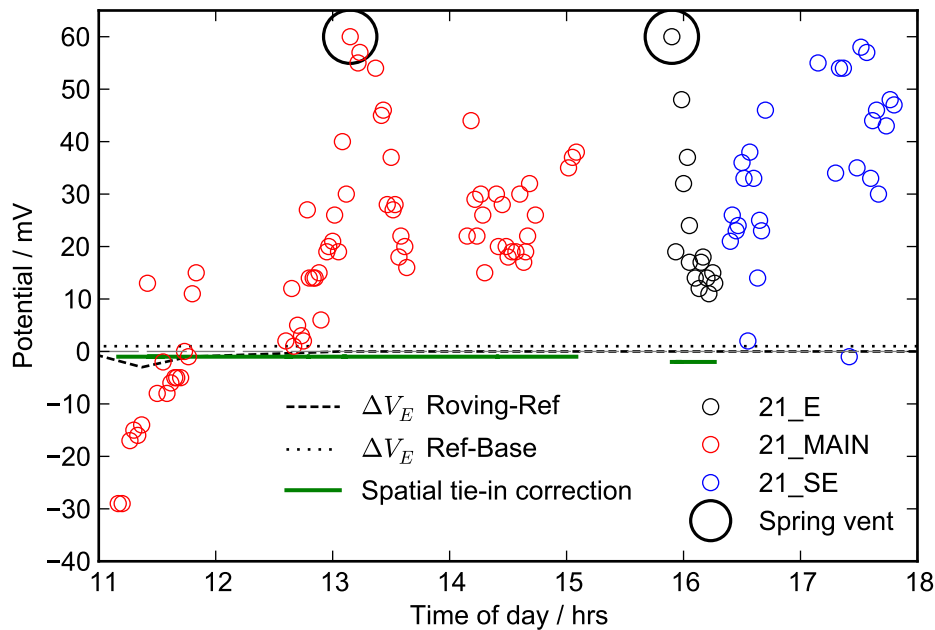


Figure B.2: Corrections applied to potential data from 21 April 2012. See Section B.1.1.1 for details.

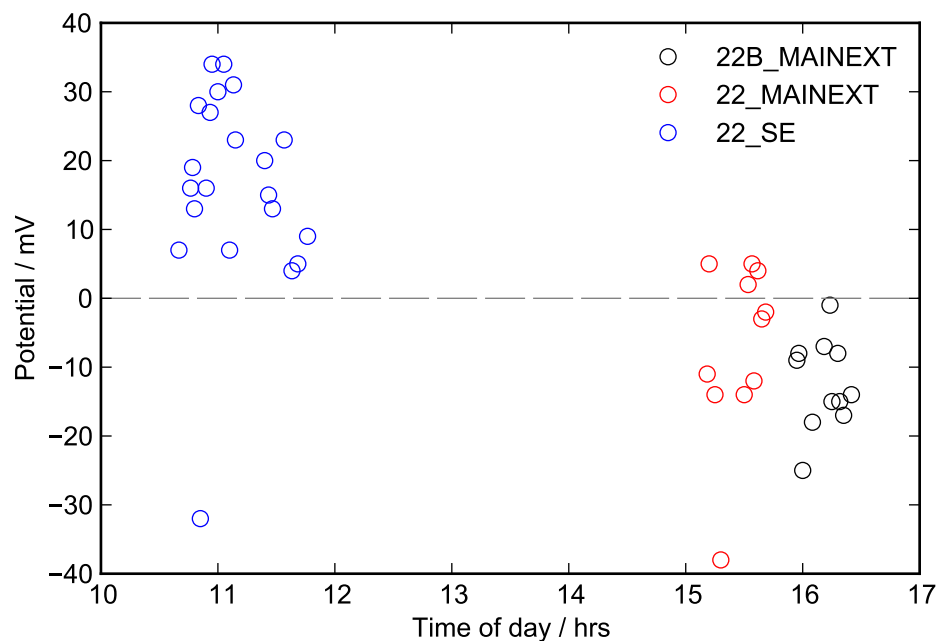


Figure B.3: No corrections were applied to potential data from 22 April 2012.

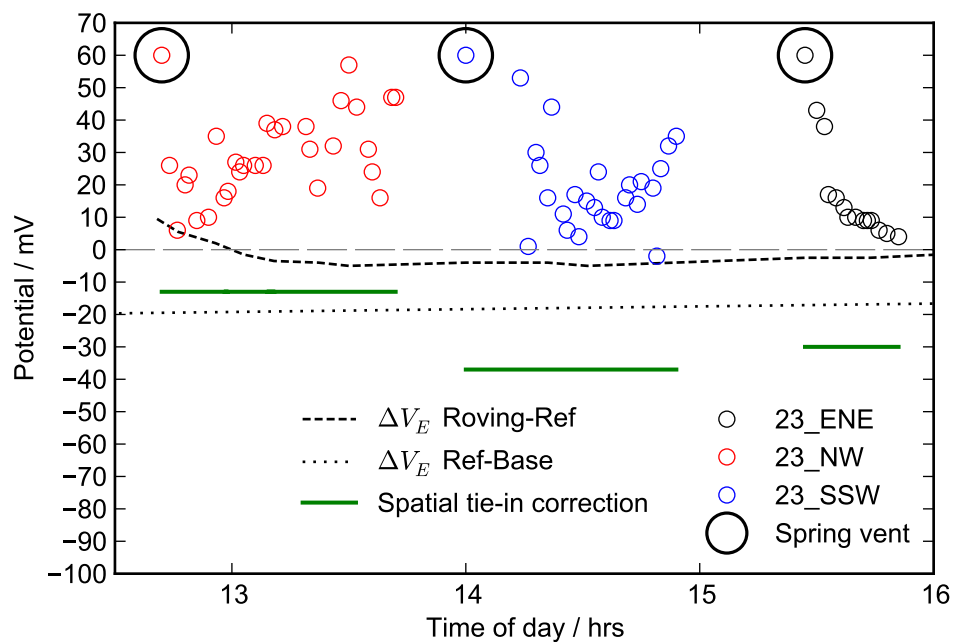


Figure B.4: Corrections applied to potential data from 23 April 2012. See Section B.1.1.1 for details.

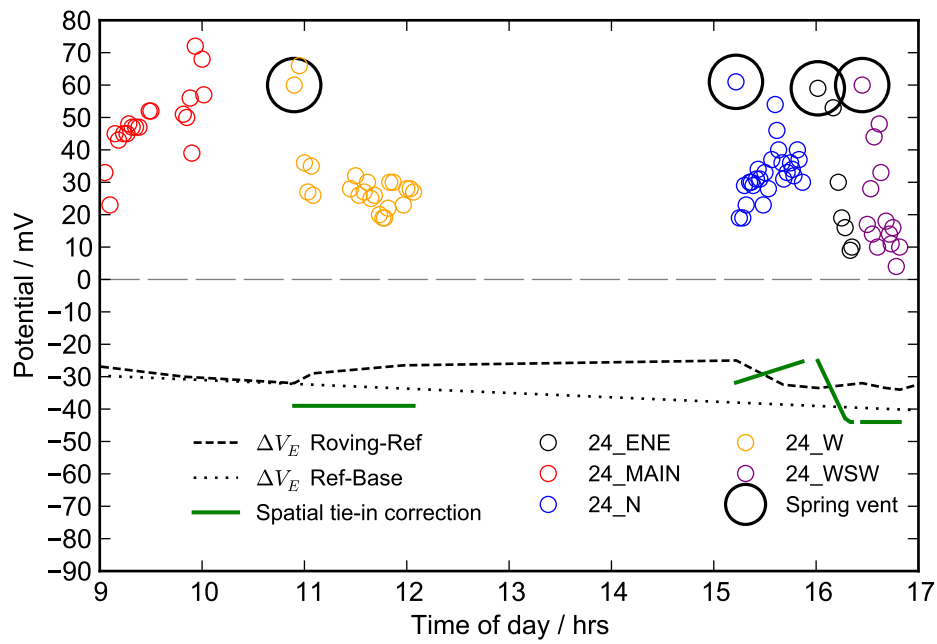


Figure B.5: Corrections applied to potential data from 24 April 2012. See Section B.1.1.1 for details.

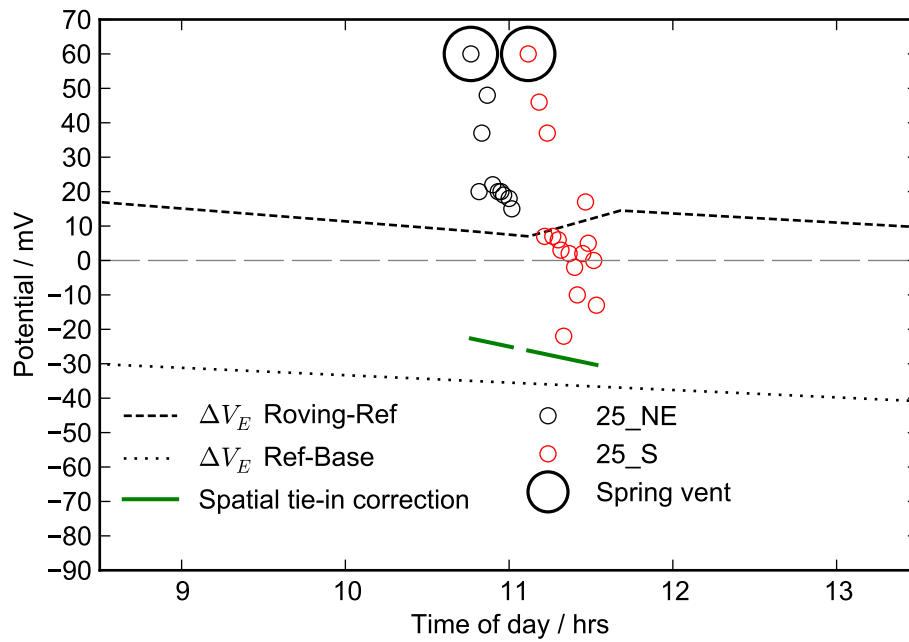


Figure B.6: Corrections applied to potential data from 25 April 2012. See Section B.1.1.1 for details.

Per-line spatial corrections

Overlapping sets of potential data were collected along Line MAIN and Line SE. An arbitrary value was added to potential values from one of the overlapping datasets along each line in order that potentials measured at the same location were similar. These corrections are shown in Figure B.7 and Figure B.8.

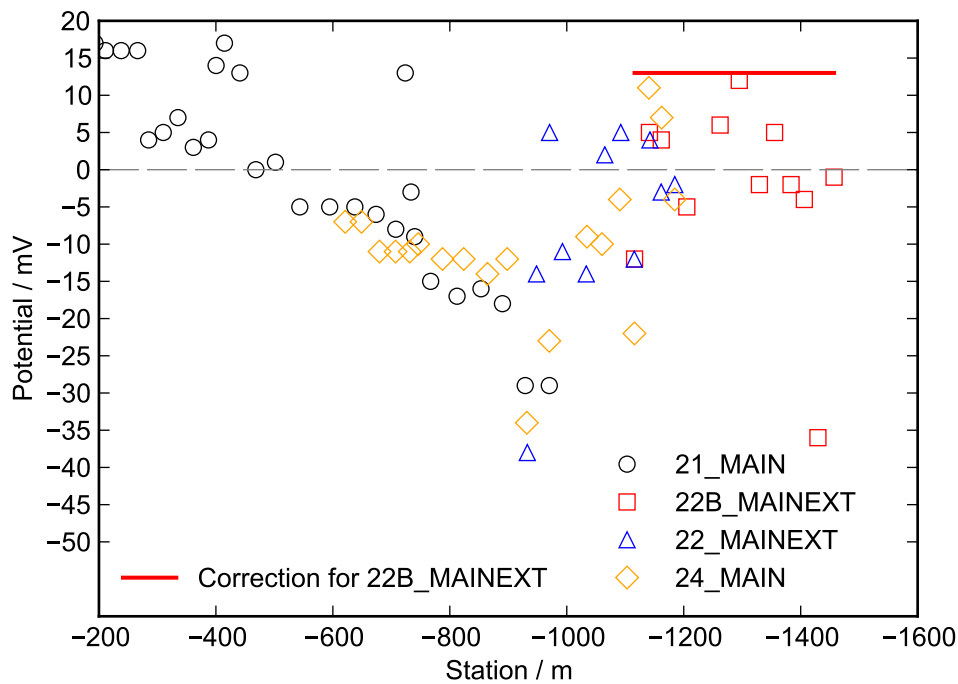


Figure B.7: Spatial corrections for potentials measured along Line MAIN. Corrections are drawn as lines, and the corrected potentials are plotted as symbols.

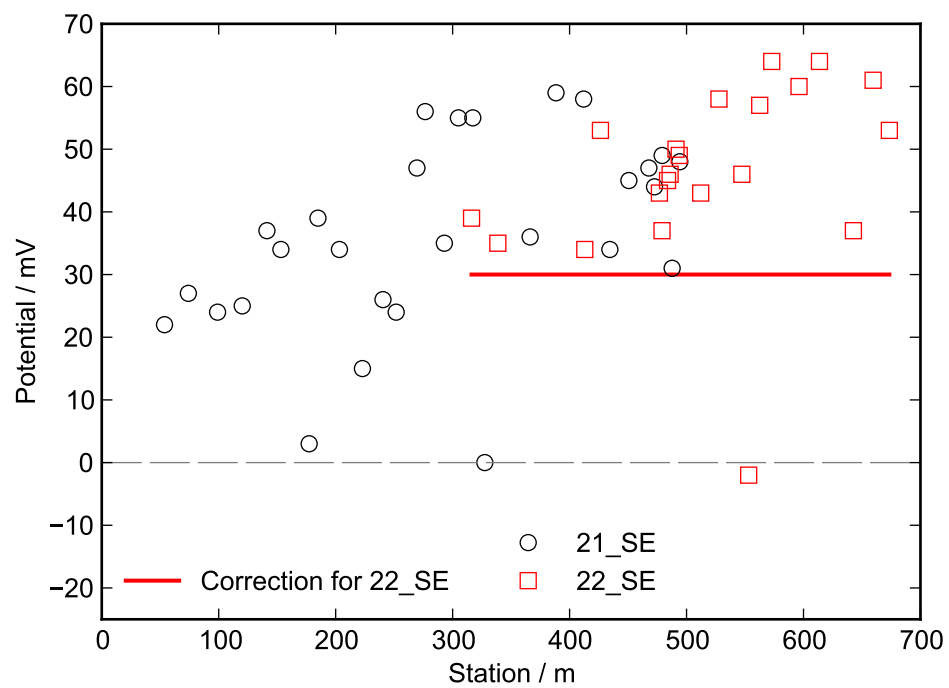


Figure B.8: Spatial corrections for potentials measured along Line SE. Corrections are drawn as lines, and the corrected potentials are plotted as symbols.

B.1.1.2 Data

Table B.1: Self-potential data along Line 21_E.

Date	Time	Easting / m	Northing / m	Station/m	Resistance/k Ω	SP/mV
2012-04-21	15:54	661646	6761600	0	54	60.0
2012-04-21	15:58	661657	6761601	11	9.0	48.0
2012-04-21	15:56	661664	6761600	18	1.5	19.0
2012-04-21	16:00	661671	6761590	27	60	32.0
2012-04-21	16:02	661677	6761586	34	130	37.0
2012-04-21	16:03	661686	6761583	43	1.3	24.0
2012-04-21	16:03	661707	6761578	65	1.2	17.0
2012-04-21	16:06	661735	6761573	93	1.2	14.0
2012-04-21	16:07	661757	6761572	114	1.1	12.0
2012-04-21	16:08	661784	6761572	141	1.3	17.0
2012-04-21	16:10	661811	6761575	167	1.3	18.0
2012-04-21	16:11	661838	6761574	194	1.2	14.0
2012-04-21	16:12	661865	6761573	221	1.1	11.0
2012-04-21	16:15	661893	6761571	249	1.1	15.0
2012-04-21	16:15	661918	6761573	273	1.1	13.0

The local date and time is used (UTC+9.5). Map coordinates are UTM 53J (EPSG:28353).

Table B.2: Self-potential data along Line 21_MAIN.

Date	Time	Easting / m	Northing / m	Station/m	Resistance/k Ω	SP/mV
2012-04-21	11:09	662111	6762451	-970	20	-29.0
2012-04-21	11:11	662091	6762415	-929	20	-29.0
2012-04-21	11:16	662072	6762381	-890	17	-18.0
2012-04-21	11:18	662054	6762349	-853	20	-16.0
2012-04-21	11:20	662031	6762315	-812	16	-17.0
2012-04-21	11:22	662010	6762275	-767	16	-15.0
2012-04-21	11:30	661997	6762251	-740	15	-9.0
2012-04-21	11:33	661993	6762246	-734	15	-3.0
2012-04-21	11:24	661989	6762237	-724	20	13.0
2012-04-21	11:35	661979	6762224	-708	14	-8.0
2012-04-21	11:37	661960	6762196	-674	14	-6.0
2012-04-21	11:39	661941	6762165	-638	14	-5.0
2012-04-21	11:39	661919	6762128	-595	14	-5.0
2012-04-21	11:41	661891	6762085	-543	14	-5.0
2012-04-21	11:43	661872	6762048	-502	14	1.0
2012-04-21	11:48	661842	6761995	-441	14	13.0
2012-04-21	11:50	661829	6761972	-415	110	17.0
2012-04-21	12:39	661823	6761959	-400	11	14.0
2012-04-21	12:35	661816	6761948	-387	10.0	4.0

Table B.2: Self-potential data along Line 21_MAIN (continued).

Date	Time	Easting / m	Northing / m	Station/m	Resistance/k Ω	SP/mV
2012-04-21	12:39	661806	6761924	−361	8.2	3.0
2012-04-21	12:41	661795	6761900	−335	8.2	7.0
2012-04-21	12:43	661783	6761878	−310	7.8	5.0
2012-04-21	12:45	661771	6761856	−285	7.5	4.0
2012-04-21	12:48	661763	6761839	−266	93	16.0
2012-04-21	12:46	661757	6761828	−254	16	29.0
2012-04-21	12:50	661750	6761814	−238	8.2	16.0
2012-04-21	12:50	661738	6761790	−211	8.0	16.0
2012-04-21	12:52	661728	6761775	−193	8.0	17.0
2012-04-21	12:54	661717	6761753	−169	9.6	8.0
2012-04-21	12:56	661711	6761738	−153	8.1	21.0
2012-04-21	12:58	661697	6761713	−124	7.9	22.0
2012-04-21	13:00	661683	6761688	−95	7.8	23.0
2012-04-21	13:01	661666	6761659	−62	8.4	28.0
2012-04-21	13:03	661666	6761659	−62	15	21.0
2012-04-21	13:07	661648	6761624	−22	8.3	32.0
2012-04-21	13:05	661641	6761614	−10	14	42.0
2012-04-21	13:09	661637	6761605	−1	57	62.0
2012-04-21	13:13	661636	6761601	4	10	57.0
2012-04-21	13:13	661633	6761594	11	55	59.0
2012-04-21	13:22	661623	6761582	27	9.6	56.0
2012-04-21	13:24	661613	6761563	48	8.8	47.0
2012-04-21	13:26	661604	6761544	69	72	48.0
2012-04-21	13:28	661599	6761523	90	6.9	30.0
2012-04-21	13:30	661589	6761511	105	61	39.0
2012-04-21	13:31	661573	6761488	133	7.4	29.0
2012-04-21	13:31	661555	6761466	161	7.5	30.0
2012-04-21	13:33	661539	6761440	192	5.7	20.0
2012-04-21	13:35	661527	6761423	212	6.4	24.0
2012-04-21	13:37	661512	6761401	239	6.0	22.0
2012-04-21	13:37	661496	6761379	266	6.0	18.0
2012-04-21	14:09	661478	6761354	297	28	24.0
2012-04-21	14:11	661462	6761331	325	18	46.0
2012-04-21	14:13	661454	6761319	339	5.7	31.0
2012-04-21	14:13	661447	6761309	351	2.9	24.0
2012-04-21	14:16	661438	6761297	366	8.6	32.0
2012-04-21	14:16	661425	6761279	389	3.0	28.0
2012-04-21	14:18	661409	6761256	417	2.3	17.0
2012-04-21	14:24	661394	6761241	437	2.2	22.0
2012-04-21	14:24	661389	6761234	446	2.4	32.0
2012-04-21	14:26	661382	6761221	461	2.2	30.0
2012-04-21	14:28	661370	6761204	481	2.1	22.0
2012-04-21	14:30	661354	6761182	509	2.0	20.0
2012-04-21	14:31	661343	6761167	527	2.0	21.0
2012-04-21	14:33	661322	6761141	561	2.1	21.0
2012-04-21	14:35	661299	6761110	599	15	32.0
2012-04-21	14:37	661282	6761084	630	2.0	19.0
2012-04-21	14:39	661268	6761066	653	2.1	21.0

Table B.2: Self-potential data along Line 21_MAIN (continued).

Date	Time	Easting / m	Northing / m	Station/m	Resistance/k Ω	SP/mV
2012-04-21	14:39	661255	6761046	677	2.5	24.0
2012-04-21	14:41	661241	6761026	701	60	34.0
2012-04-21	14:43	661226	6761007	725	6.5	28.0
2012-04-21	15:01	661213	6760989	748	11	37.0
2012-04-21	15:03	661198	6760968	773	9.5	39.0
2012-04-21	15:05	661164	6760920	832	62	40.0

The local date and time is used (UTC+9.5). Map coordinates are UTM 53J (EPSG:28353).

Table B.3: Self-potential data along Line 21_SE.

Date	Time	Easting / m	Northing / m	Station/m	Resistance/k Ω	SP/mV
2012-04-21	16:22	661694	6761576	54	1.1	22.0
2012-04-21	16:25	661707	6761558	74	3.0	27.0
2012-04-21	16:26	661724	6761539	99	1.4	24.0
2012-04-21	16:26	661739	6761524	120	18	25.0
2012-04-21	16:30	661754	6761509	141	15	37.0
2012-04-21	16:30	661762	6761500	153	18	34.0
2012-04-21	16:33	661781	6761485	177	12	3.0
2012-04-21	16:33	661784	6761477	185	21	39.0
2012-04-21	16:36	661797	6761464	203	73	34.0
2012-04-21	16:37	661809	6761448	223	7.0	15.0
2012-04-21	16:37	661819	6761433	240	2.5	26.0
2012-04-21	16:40	661824	6761422	252	60	24.0
2012-04-21	16:41	661832	6761405	269	81	47.0
2012-04-21	17:07	661837	6761400	277	68	56.0
2012-04-21	17:18	661846	6761386	293	126	35.0
2012-04-21	17:18	661854	6761377	305	110	55.0
2012-04-21	17:22	661858	6761364	317	78	55.0
2012-04-21	17:29	661871	6761311	366	68	36.0
2012-04-21	17:30	661880	6761290	388	60	59.0
2012-04-21	17:33	661890	6761268	412	57	58.0
2012-04-21	17:36	661902	6761249	434	12	34.0
2012-04-21	17:37	661909	6761234	451	7.3	45.0
2012-04-21	17:37	661916	6761218	468	1.9	47.0
2012-04-21	17:44	661910	6761208	473	1.5	44.0
2012-04-21	17:45	661902	6761195	479	6.7	49.0
2012-04-21	17:40	661925	6761200	488	96	31.0
2012-04-21	17:48	661900	6761176	494	6.9	48.0

The local date and time is used (UTC+9.5). Map coordinates are UTM 53J (EPSG:28353).

Table B.4: Self-potential data along Line 22_MAINEXT.

Date	Time	Easting / m	Northing / m	Station/m	Resistance/k Ω	SP/mV
2012-04-22	15:41	662209	6762642	−1185	14	−2.0
2012-04-22	15:39	662199	6762621	−1161	3.3	−3.0
2012-04-22	15:37	662190	6762604	−1142	4.0	4.0
2012-04-22	15:35	662178	6762580	−1115	1.3	−12.0
2012-04-22	15:33	662170	6762558	−1092	18	5.0
2012-04-22	15:31	662157	6762534	−1065	11	2.0
2012-04-22	15:30	662144	6762505	−1033	9.5	−14.0
2012-04-22	15:11	662123	6762470	−993	40	−11.0
2012-04-22	15:11	662112	6762451	−971	35	5.0
2012-04-22	15:15	662102	6762431	−948	5.2	−14.0
2012-04-22	15:18	662093	6762418	−933	25	−38.0

The local date and time is used (UTC+9.5). Map coordinates are UTM 53J (EPSG:28353).

Table B.5: Self-potential data along Line 22_SE.

Date	Time	Easting / m	Northing / m	Station/m	Resistance/k Ω	SP/mV
2012-04-22	11:46	661856	6761375	316	63	39.0
2012-04-22	11:41	661855	6761344	339	40	35.0
2012-04-22	11:37	661871	6761263	413	42	34.0
2012-04-22	11:33	661894	6761263	426	3.5	53.0
2012-04-22	11:28	661908	6761211	477	2.0	43.0
2012-04-22	10:39	661909	6761209	479	2.2	37.0
2012-04-22	11:26	661901	6761198	484	6.0	45.0
2012-04-22	10:46	661902	6761196	486	3.4	46.0
2012-04-22	11:24	661889	6761182	491	9.0	50.0
2012-04-22	10:46	661891	6761180	494	3.5	49.0
2012-04-22	10:48	661900	6761164	512	2.8	43.0
2012-04-22	10:50	661912	6761153	528	16	58.0
2012-04-22	10:54	661925	6761138	547	13	46.0
2012-04-22	10:50	661928	6761133	553	30	−2.0
2012-04-22	10:56	661933	6761125	563	25	57.0
2012-04-22	10:56	661938	6761116	573	75	64.0
2012-04-22	11:00	661950	6761096	596	38	60.0
2012-04-22	11:03	661959	6761081	614	17	64.0
2012-04-22	11:05	661977	6761058	643	40	37.0
2012-04-22	11:07	661988	6761045	660	13	61.0
2012-04-22	11:09	661995	6761033	673	21	53.0

The local date and time is used (UTC+9.5). Map coordinates are UTM 53J (EPSG:28353).

Table B.6: Self-potential data along Line 22B_MAINEXT.

Date	Time	Easting / m	Northing / m	Station/m	Resistance/k Ω	SP/mV
2012-04-22	16:25	662302	6762901	−1457	6.0	−1.0
2012-04-22	16:22	662296	6762873	−1429	18	−36.0
2012-04-22	16:21	662288	6762851	−1406	5.1	−4.0
2012-04-22	16:18	662281	6762829	−1384	4.0	−2.0
2012-04-22	16:18	662270	6762803	−1355	5.5	5.0
2012-04-22	16:15	662258	6762780	−1329	3.5	−2.0
2012-04-22	16:14	662243	6762749	−1295	15	12.0
2012-04-22	16:11	662237	6762715	−1262	12	6.0
2012-04-22	16:03	662219	6762660	−1205	13	−5.0
2012-04-22	15:56	662201	6762620	−1162	14	4.0
2012-04-22	15:58	662190	6762603	−1141	70	5.0
2012-04-22	16:00	662179	6762580	−1116	3.0	−12.0

The local date and time is used (UTC+9.5). Map coordinates are UTM 53J (EPSG:28353).

Table B.7: Self-potential data along Line 23_ENE.

Date	Time	Easting / m	Northing / m	Station/m	Resistance/k Ω	SP/mV
2012-04-23	15:26	661638	6761604	4	600	60.0
2012-04-23	15:30	661661	6761608	27	5.5	43.0
2012-04-23	15:31	661676	6761618	44	1.2	38.0
2012-04-23	15:33	661702	6761626	72	0.90	17.0
2012-04-23	15:35	661721	6761642	95	1.00	16.0
2012-04-23	15:37	661741	6761657	120	0.90	13.0
2012-04-23	15:37	661763	6761674	147	0.90	10.0
2012-04-23	15:39	661783	6761685	170	0.90	10.0
2012-04-23	15:41	661803	6761700	195	0.90	9.0
2012-04-23	15:43	661823	6761711	218	0.90	9.0
2012-04-23	15:43	661850	6761719	245	0.90	9.0
2012-04-23	15:46	661871	6761728	268	0.80	6.0
2012-04-23	15:48	661894	6761737	293	0.80	5.0
2012-04-23	15:50	661907	6761742	306	0.80	4.0

The local date and time is used (UTC+9.5). Map coordinates are UTM 53J (EPSG:28353).

Table B.8: Self-potential data along Line 23_NW.

Date	Time	Easting / m	Northing / m	Station/m	Resistance/k Ω	SP/mV
2012-04-23	12:41	661637	6761604	4	6.3	60.0

Table B.8: Self-potential data along Line 23_NW (continued).

Date	Time	Easting / m	Northing / m	Station/m	Resistance/k Ω	SP/mV
2012-04-23	12:43	661628	6761614	15	14	26.0
2012-04-23	12:46	661607	6761631	41	1.5	6.0
2012-04-23	12:48	661592	6761642	59	1.4	20.0
2012-04-23	12:48	661581	6761653	75	12	23.0
2012-04-23	12:50	661574	6761666	89	2.0	9.0
2012-04-23	12:54	661558	6761681	111	2.4	10.0
2012-04-23	12:56	661545	6761699	133	30	35.0
2012-04-23	12:58	661539	6761707	143	1.00	18.0
2012-04-23	12:58	661532	6761716	154	1.00	16.0
2012-04-23	13:01	661518	6761734	177	1.7	27.0
2012-04-23	13:01	661506	6761748	196	1.1	24.0
2012-04-23	13:03	661492	6761764	217	1.2	26.0
2012-04-23	13:05	661476	6761783	242	2.2	26.0
2012-04-23	13:07	661455	6761805	272	1.9	26.0
2012-04-23	13:11	661442	6761821	293	1.3	37.0
2012-04-23	13:09	661432	6761832	308	1.2	39.0
2012-04-23	13:13	661415	6761845	329	1.2	38.0
2012-04-23	13:18	661400	6761857	348	9.8	38.0
2012-04-23	13:20	661383	6761871	369	1.5	31.0
2012-04-23	13:22	661350	6761887	404	75	19.0
2012-04-23	13:26	661332	6761892	420	1.3	32.0
2012-04-23	13:28	661309	6761893	438	16	46.0
2012-04-23	13:30	661284	6761889	454	12	57.0
2012-04-23	13:31	661259	6761891	475	8.0	44.0
2012-04-23	13:35	661235	6761895	496	55	31.0
2012-04-23	13:35	661208	6761896	519	17	24.0
2012-04-23	13:37	661178	6761899	546	16	16.0
2012-04-23	13:41	661154	6761899	566	10.0	47.0
2012-04-23	13:41	661129	6761903	589	16	47.0

The local date and time is used (UTC+9.5). Map coordinates are UTM 53J (EPSG:28353).

Table B.9: Self-potential data along Line 23_SSW.

Date	Time	Easting / m	Northing / m	Station/m	Resistance/k Ω	SP/mV
2012-04-23	14:00	661637	6761605	4	650	60.0
2012-04-23	14:13	661634	6761589	12	580	53.0
2012-04-23	14:16	661636	6761562	39	13	1.0
2012-04-23	14:18	661637	6761535	66	6.5	30.0
2012-04-23	14:18	661637	6761508	93	1.5	26.0
2012-04-23	14:20	661619	6761485	117	1.8	16.0
2012-04-23	14:22	661615	6761466	136	545	44.0
2012-04-23	14:24	661610	6761447	156	1.3	11.0
2012-04-23	14:26	661605	6761424	180	2.2	6.0

Table B.9: Self-potential data along Line 23_SSW (continued).

Date	Time	Easting / m	Northing / m	Station/m	Resistance/k Ω	SP/mV
2012-04-23	14:28	661600	6761401	203	8.7	17.0
2012-04-23	14:28	661590	6761378	227	2.3	4.0
2012-04-23	14:31	661582	6761354	253	1.7	15.0
2012-04-23	14:33	661575	6761331	277	1.2	13.0
2012-04-23	14:33	661573	6761309	299	15	24.0
2012-04-23	14:35	661561	6761288	322	12	10.0
2012-04-23	14:37	661549	6761264	348	1.3	9.0
2012-04-23	14:37	661535	6761250	365	7.5	9.0
2012-04-23	14:41	661532	6761250	366	1.2	16.0
2012-04-23	14:41	661527	6761210	406	1.1	20.0
2012-04-23	14:43	661522	6761189	427	2.2	14.0
2012-04-23	14:45	661518	6761168	449	1.3	21.0
2012-04-23	14:48	661514	6761144	473	1.00	19.0
2012-04-23	14:48	661509	6761124	493	1.1	−2.0
2012-04-23	14:50	661510	6761102	514	1.1	25.0
2012-04-23	14:52	661509	6761084	532	1.2	32.0
2012-04-23	14:54	661506	6761070	546	1.3	35.0

The local date and time is used (UTC+9.5). Map coordinates are UTM 53J (EPSG:28353).

Table B.10: Self-potential data along Line 24_ENE.

Date	Time	Easting / m	Northing / m	Station/m	Resistance/k Ω	SP/mV
2012-04-24	16:00	661637	6761599	1	0.70	59.0
2012-04-24	16:10	661650	6761609	17	0.30	53.0
2012-04-24	16:12	661686	6761623	56	9.6	30.0
2012-04-24	16:15	661698	6761627	68	0.20	19.0
2012-04-24	16:17	661716	6761635	88	0.30	16.0
2012-04-24	16:19	661736	6761644	110	0.20	9.0
2012-04-24	16:21	661736	6761644	110	0.20	10.0

The local date and time is used (UTC+9.5). Map coordinates are UTM 53J (EPSG:28353).

Table B.11: Self-potential data along Line 24_MAIN.

Date	Time	Easting / m	Northing / m	Station/m	Resistance/k Ω	SP/mV
2012-04-24	10:01	662207	6762643	−1185	8.0	−4.0
2012-04-24	10:00	662197	6762623	−1162	3.4	7.0
2012-04-24	09:56	662188	6762603	−1140	4.5	11.0

Table B.11: Self-potential data along Line 24_MAIN (continued).

Date	Time	Easting / m	Northing / m	Station/m	Resistance/k Ω	SP/mV
2012-04-24	09:54	662175	6762582	−1116	1.8	−22.0
2012-04-24	09:52	662163	6762560	−1091	1.6	−4.0
2012-04-24	09:50	662149	6762533	−1060	0.80	−10.0
2012-04-24	09:48	662141	6762508	−1035	2.0	−9.0
2012-04-24	09:03	662111	6762451	−970	2.9	−23.0
2012-04-24	09:05	662093	6762417	−932	9.8	−34.0
2012-04-24	09:09	662076	6762388	−898	1.1	−12.0
2012-04-24	09:11	662059	6762359	−864	1.2	−14.0
2012-04-24	09:13	662040	6762323	−824	0.40	−12.0
2012-04-24	09:16	662021	6762292	−787	0.30	−12.0
2012-04-24	09:16	662002	6762255	−746	0.30	−10.0
2012-04-24	09:18	661994	6762243	−731	0.50	−11.0
2012-04-24	09:20	661980	6762223	−707	0.30	−11.0
2012-04-24	09:22	661965	6762200	−680	0.30	−11.0
2012-04-24	09:28	661950	6762173	−649	0.30	−7.0
2012-04-24	09:30	661934	6762150	−621	0.30	−7.0

The local date and time is used (UTC+9.5). Map coordinates are UTM 53J (EPSG:28353).

Table B.12: Self-potential data along Line 24_N.

Date	Time	Easting / m	Northing / m	Station/m	Resistance/k Ω	SP/mV
2012-04-24	15:13	661637	6761599	3	0.70	61.0
2012-04-24	15:15	661632	6761613	12	5.3	19.0
2012-04-24	15:16	661633	6761631	30	0.40	19.0
2012-04-24	15:18	661634	6761648	47	1.3	29.0
2012-04-24	15:18	661638	6761669	68	4.6	23.0
2012-04-24	15:20	661642	6761695	94	1.2	30.0
2012-04-24	15:22	661648	6761719	119	3.4	30.0
2012-04-24	15:33	661645	6761730	129	3.7	37.0
2012-04-24	15:22	661655	6761739	139	2.7	29.0
2012-04-24	15:35	661635	6761743	142	6.3	54.0
2012-04-24	15:37	661627	6761755	154	2.0	46.0
2012-04-24	15:24	661670	6761753	156	1.5	31.0
2012-04-24	15:37	661623	6761765	164	0.30	40.0
2012-04-24	15:26	661690	6761758	166	2.2	34.0
2012-04-24	15:28	661717	6761748	168	9.4	23.0
2012-04-24	15:26	661706	6761758	172	0.70	31.0
2012-04-24	15:31	661720	6761752	173	10	28.0
2012-04-24	15:39	661620	6761785	185	0.40	36.0
2012-04-24	15:30	661739	6761755	186	5.0	33.0
2012-04-24	15:41	661616	6761808	208	0.40	31.0
2012-04-24	15:43	661611	6761832	232	0.30	33.0
2012-04-24	15:45	661607	6761854	255	0.40	36.0

Table B.12: Self-potential data along Line 24_N (continued).

Date	Time	Easting / m	Northing / m	Station/m	Resistance/k Ω	SP/mV
2012-04-24	15:46	661602	6761879	280	0.80	34.0
2012-04-24	15:46	661596	6761907	308	1.00	32.0
2012-04-24	15:48	661593	6761931	333	0.80	40.0
2012-04-24	15:50	661588	6761954	356	0.40	37.0
2012-04-24	15:52	661585	6761971	373	0.40	30.0

The local date and time is used (UTC+9.5). Map coordinates are UTM 53J (EPSG:28353).

Table B.13: Self-potential data along Line 24_W.

Date	Time	Easting / m	Northing / m	Station/m	Resistance/k Ω	SP/mV
2012-04-24	10:54	661637	6761603	3	0.80	60.0
2012-04-24	10:56	661628	6761601	7	0.70	66.0
2012-04-24	11:00	661613	6761595	23	0.70	36.0
2012-04-24	11:01	661582	6761597	53	1.3	27.0
2012-04-24	11:03	661564	6761600	71	1.9	35.0
2012-04-24	11:05	661539	6761599	96	1.3	26.0
2012-04-24	11:26	661513	6761593	122	340	28.0
2012-04-24	11:30	661493	6761588	143	180	32.0
2012-04-24	11:31	661469	6761583	167	220	26.0
2012-04-24	11:35	661443	6761579	193	46	27.0
2012-04-24	11:37	661410	6761574	227	64	30.0
2012-04-24	11:39	661384	6761570	253	26	25.0
2012-04-24	11:41	661360	6761573	276	1.5	26.0
2012-04-24	11:43	661327	6761572	309	0.70	20.0
2012-04-24	11:46	661301	6761570	335	0.60	19.0
2012-04-24	11:46	661274	6761563	363	4.6	19.0
2012-04-24	11:48	661243	6761557	394	0.60	22.0
2012-04-24	11:50	661211	6761550	427	25	30.0
2012-04-24	11:52	661179	6761545	459	6.0	30.0
2012-04-24	11:58	661150	6761540	489	2.0	23.0
2012-04-24	12:00	661122	6761533	517	4.0	28.0
2012-04-24	12:01	661096	6761534	543	10	28.0
2012-04-24	12:03	661061	6761524	579	14	27.0

The local date and time is used (UTC+9.5). Map coordinates are UTM 53J (EPSG:28353).

Table B.14: Self-potential data along Line 24_WSW.

Date	Time	Easting / m	Northing / m	Station/m	Resistance/k Ω	SP/mV
2012-04-24	16:26	661640	6761602	3	0.60	60.0
2012-04-24	16:30	661613	6761592	28	14	17.0
2012-04-24	16:32	661592	6761585	50	3.7	28.0
2012-04-24	16:33	661570	6761580	72	2.0	14.0
2012-04-24	16:33	661553	6761575	90	30	44.0
2012-04-24	16:36	661544	6761570	100	0.50	10.0
2012-04-24	16:37	661536	6761568	108	150	33.0
2012-04-24	16:37	661530	6761565	115	35	48.0
2012-04-24	16:41	661516	6761558	130	1.4	18.0
2012-04-24	16:42	661501	6761552	147	1.00	14.0
2012-04-24	16:44	661480	6761547	168	1.2	11.0
2012-04-24	16:45	661458	6761538	192	0.80	16.0
2012-04-24	16:47	661438	6761531	213	0.20	4.0
2012-04-24	16:48	661409	6761523	243	0.80	10.0

The local date and time is used (UTC+9.5). Map coordinates are UTM 53J (EPSG:28353).

Table B.15: Self-potential data along Line 25_NE.

Date	Time	Easting / m	Northing / m	Station/m	Resistance/k Ω	SP/mV
2012-04-25	10:46	661638	6761602	2	1.2	60.0
2012-04-25	10:48	661649	6761614	15	0.80	20.0
2012-04-25	10:50	661665	6761629	37	0.90	37.0
2012-04-25	10:52	661673	6761636	47	1.1	48.0
2012-04-25	10:54	661689	6761649	68	0.70	22.0
2012-04-25	10:56	661702	6761658	84	0.70	20.0
2012-04-25	10:56	661718	6761668	102	0.70	20.0
2012-04-25	10:58	661736	6761680	124	0.70	19.0
2012-04-25	11:00	661750	6761700	148	0.70	18.0
2012-04-25	11:01	661766	6761722	174	0.60	15.0

The local date and time is used (UTC+9.5). Map coordinates are UTM 53J (EPSG:28353).

Table B.16: Self-potential data along Line 25_S.

Date	Time	Easting / m	Northing / m	Station/m	Resistance/k Ω	SP/mV
2012-04-25	11:07	661641	6761606	4	1.2	60.0
2012-04-25	11:11	661650	6761590	18	1.2	46.0
2012-04-25	11:13	661662	6761577	36	7.4	7.0

Table B.16: Self-potential data along Line 25_S (continued).

Date	Time	Easting / m	Northing / m	Station/m	Resistance/k Ω	SP/mV
2012-04-25	11:13	661671	6761565	51	1.00	37.0
2012-04-25	11:16	661680	6761555	65	0.60	7.0
2012-04-25	11:18	661680	6761547	71	0.50	6.0
2012-04-25	11:18	661680	6761547	71	0.50	3.0
2012-04-25	11:20	661681	6761531	85	21	−22.0
2012-04-25	11:22	661679	6761509	103	12	2.0
2012-04-25	11:24	661681	6761488	124	7.3	−2.0
2012-04-25	11:24	661682	6761467	144	0.60	−10.0
2012-04-25	11:26	661679	6761447	162	12	2.0
2012-04-25	11:28	661676	6761423	185	14	17.0
2012-04-25	11:28	661673	6761398	209	1.7	5.0
2012-04-25	11:31	661669	6761351	255	17	−13.0

The local date and time is used (UTC+9.5). Map coordinates are UTM 53J (EPSG:28353).

B.1.2 Warburton Spring

No corrections were made to SP data collected at Warburton Spring. The data are shown in Table B.17.

Table B.17: Self-potential data.

Date	Time	Easting / m	Northing / m	Station/m	Resistance/k Ω	SP/mV
2012-11-18	14:46	661854	6759952	−14	1.4	10.5
2012-11-18	11:10	661863	6759963	0	1.04	7.0
2012-11-18	11:12	661874	6759975	16	1.3	9.0
2012-11-18	11:14	661888	6759987	35	1.15	10.5
2012-11-18	11:16	661901	6760001	54	1.17	14.5
2012-11-18	11:17	661913	6760015	72	1.26	19.0
2012-11-18	14:41	661929	6760030	94	1.55	17.5
2012-11-18	11:21	661932	6760031	97	1.27	14.5
2012-11-18	11:22	661945	6760047	117	1.32	23.0
2012-11-18	11:23	661960	6760061	138	1.45	31.0
2012-11-18	11:25	661976	6760079	162	1.45	29.0
2012-11-18	11:27	661991	6760091	181	1.6	23.5
2012-11-18	11:29	662005	6760105	201	1.68	21.0
2012-11-18	14:38	662020	6760119	221	2.07	18.0
2012-11-18	11:30	662020	6760120	222	1.7	20.0
2012-11-18	11:32	662033	6760134	241	1.5	27.0
2012-11-18	11:33	662048	6760149	262	1.5	31.0
2012-11-18	11:35	662063	6760136	264	1.6	37.0
2012-11-18	11:36	662076	6760177	302	1.6	33.0

Table B.17: Self-potential data from Warburton Spring (continued).

Date	Time	Easting / m	Northing / m	Station/m	Resistance/k Ω	SP/mV
2012-11-18	14:34	662092	6760189	322	1.58	29.0
2012-11-18	11:37	662091	6760191	322	1.75	36.5
2012-11-18	11:39	662106	6760205	343	1.6	34.0
2012-11-18	11:42	662134	6760233	383	1.2	21.0
2012-11-18	11:44	662147	6760248	402	1.2	20.0
2012-11-18	11:45	662162	6760262	423	1.84	26.0
2012-11-18	14:30	662178	6760274	443	1.666	25.0
2012-11-18	11:47	662177	6760276	443	2.7	26.0
2012-11-18	11:51	662189	6760291	462	1.99	32.0
2012-11-18	11:54	662204	6760305	483	1.95	46.0
2012-11-18	11:56	662218	6760319	503	1.5	39.5
2012-11-18	11:58	662231	6760322	514	1.6	41.5
2012-11-18	12:01	662246	6760346	542	1.62	41.0
2012-11-18	12:04	662261	6760359	561	5.5	50.5
2012-11-18	12:06	662273	6760374	581	6.28	60.5
2012-11-18	12:11	662288	6760387	600	6.5	63.5
2012-11-18	12:13	662300	6760402	619	6.45	62.5
2012-11-18	14:22	662314	6760417	640	1.7	48.5
2012-11-18	12:14	662315	6760419	642	5.4	51.0
2012-11-18	14:19	662329	6760432	661	6.44	61.0
2012-11-18	12:17	662328	6760433	661	6.27	60.5
2012-11-18	12:27	662341	6760448	681	6.0	59.0
2012-11-18	12:29	662355	6760465	703	5.7	56.5
2012-11-18	12:32	662371	6760480	725	5.64	53.5
2012-11-18	12:34	662389	6760495	748	5.5	47.5
2012-11-18	12:37	662401	6760506	764	1.72	29.0
2012-11-18	12:39	662417	6760519	785	1.4	51.5
2012-11-18	12:43	662430	6760535	805	1.7	25.5
2012-11-18	12:46	662448	6760547	827	12.0	19.0
2012-11-18	12:48	662463	6760562	848	1.16	13.0
2012-11-18	12:51	662477	6760576	868	2.6	17.5
2012-11-18	12:53	662494	6760589	889	14.0	15.5
2012-11-18	12:55	662511	6760604	911	2.15	15.5
2012-11-18	12:57	662526	6760617	931	2.27	13.0
2012-11-18	12:59	662541	6760629	950	2.27	8.0
2012-11-18	13:03	662554	6760642	969	1.73	4.0
2012-11-18	13:07	662569	6760656	989	1.97	3.0
2012-11-18	13:09	662584	6760669	1009	2.12	6.0
2012-11-18	13:11	662602	6760685	1033	4.2	15.0
2012-11-18	13:13	662617	6760701	1055	2.79	15.0
2012-11-18	13:14	662636	6760716	1079	2.3	12.5
2012-11-18	13:16	662654	6760730	1102	3.0	11.5
2012-11-18	13:19	662671	6760748	1127	2.4	12.0
2012-11-18	13:25	662688	6760762	1148	2.9	15.0
2012-11-18	13:27	662707	6760776	1172	6.2	17.0
2012-11-18	13:29	662722	6760793	1194	1.4	17.0
2012-11-18	11:40	662119	6760219	1282	1.6	25.0

Table B.17: Self-potential data from Warburton Spring (continued).

Date	Time	Easting / m	Northing / m	Station/m	Resistance/k Ω	SP/mV
The local date and time is used (UTC+10.5). Map coordinates are UTM 53J (EPSG:28353).						

B.1.3 The Bubbler spring complex

The simple averaging referred to in Section B.1 above was performed for data collected at the Bubbler, and some sections of data along Line A and Line B were subject to further spatial corrections described below.

B.1.3.1 Spatial corrections for Lines A and B

Self-potential data were collected over four days, and there are sections on Line A and Line B where datasets collected on different days overlap for several hundred metres. For each of these lines, a single correction potential was added to each data point in one of the overlapping datasets, such that the overlapping potentials (measured at the same locations) from the two datasets were similar. For Line A the overlapping section was between stations 5551 and 5620, and data to the north of station 5540 had a correction of -7 applied (Figure B.9). For Line C the overlapping section was between stations 1020 and 1350, and data to the north-west of station 1000 had a correction of $+41$ mV applied (Figure B.10).

B.1.3.2 Data

All the SP data are shown below in Tables B.18 through B.20, which are sorted by station number.

Table B.18: Self-potential data along Line A.

Date	Time	Easting / m	Northing / m	Station/m	Resistance/k Ω	SP/mV
2011-07-27	17:12	680988	6739948	4801	0.63	6.0
2011-07-27	17:19	680985	6739972	4825	0.30	18.0
2011-07-27	17:25	680982	6739997	4849	0.66	15.0
2011-07-27	17:30	680978	6740022	4875	0.67	27.0
2011-07-27	17:33	680973	6740047	4900	0.58	23.5
2011-07-27	17:34	680969	6740073	4926	0.28	15.5

Table B.18: Self-potential data along Line A (continued).

Date	Time	Easting / m	Northing / m	Station/m	Resistance/k Ω	SP/mV
2011-07-27	17:38	680965	6740097	4951	0.61	34.0
2011-07-27	17:42	680960	6740122	4976	0.42	7.0
2011-07-27	17:51	680955	6740147	5002	0.57	31.5
2011-07-27	17:54	680952	6740171	5026	0.66	28.0
2011-07-27	17:56	680948	6740195	5051	0.32	26.5
2011-07-27	17:58	680944	6740219	5075	0.29	19.5
2011-07-27	18:01	680939	6740244	5100	0.30	18.0
2011-07-27	18:04	680937	6740269	5126	0.85	20.5
2011-07-27	18:10	680938	6740287	5143	0.36	15.5
2011-07-27	18:12	680928	6740321	5178	0.36	19.0
2011-07-27	18:15	680924	6740343	5201	2.1	39.0
2011-07-27	18:17	680920	6740366	5224	0.69	31.5
2011-07-27	18:18	680913	6740393	5252	0.21	30.0
2011-07-27	18:20	680907	6740417	5277	0.58	29.5
2011-07-27	18:21	680904	6740442	5301	0.72	20.5
2011-07-27	18:25	680902	6740467	5326	1.6	25.0
2011-07-27	18:27	680897	6740491	5351	0.41	14.0
2011-07-27	18:29	680895	6740515	5375	0.33	22.5
2011-07-27	18:30	680890	6740539	5400	0.32	22.0
2011-07-27	18:32	680888	6740565	5425	0.35	16.0
2011-07-27	18:34	680881	6740588	5450	0.43	13.0
2011-07-27	18:36	680876	6740613	5475	0.29	5.5
2011-07-27	18:43	680874	6740636	5498	0.25	-3.5
2011-07-27	18:51	680871	6740662	5524	0.22	-1.5
2011-07-27	19:00	680870	6740689	5551	0.23	-9.5
2011-07-31	13:03	680866	6740685	5551	0.32	-11.5
2011-07-27	19:03	680866	6740711	5573	0.30	-15.5
2011-07-31	13:06	680864	6740709	5573	0.38	-14.0
2011-07-27	19:09	680864	6740723	5585	0.26	-3.5
2011-07-31	13:11	680864	6740718	5585	0.38	2.0
2011-07-27	19:06	680860	6740733	5596	0.39	15.0
2011-07-31	13:09	680859	6740736	5596	0.60	17.0
2011-07-27	19:13	680858	6740757	5620	0.30	15.0
2011-07-31	13:15	680853	6740759	5620	0.56	14.5
2011-07-31	13:18	680852	6740783	5646	0.67	23.5
2011-07-31	13:21	680848	6740809	5673	0.69	31.0
2011-07-31	13:24	680842	6740834	5698	1.5	30.0
2011-07-31	13:27	680841	6740857	5721	1.1	27.5
2011-07-31	13:31	680832	6740890	5756	0.77	34.0
2011-07-31	13:45	680820	6740896	5763	0.68	25.5
2011-07-31	13:36	680823	6740907	5774	0.33	-1.5
2011-07-31	13:46	680827	6740940	5805	0.29	-10.0
2011-07-31	13:49	680825	6740955	5820	0.30	-8.0

The local date and time is used (UTC+9.5). Map coordinates are UTM 53J (EPSG:28353).

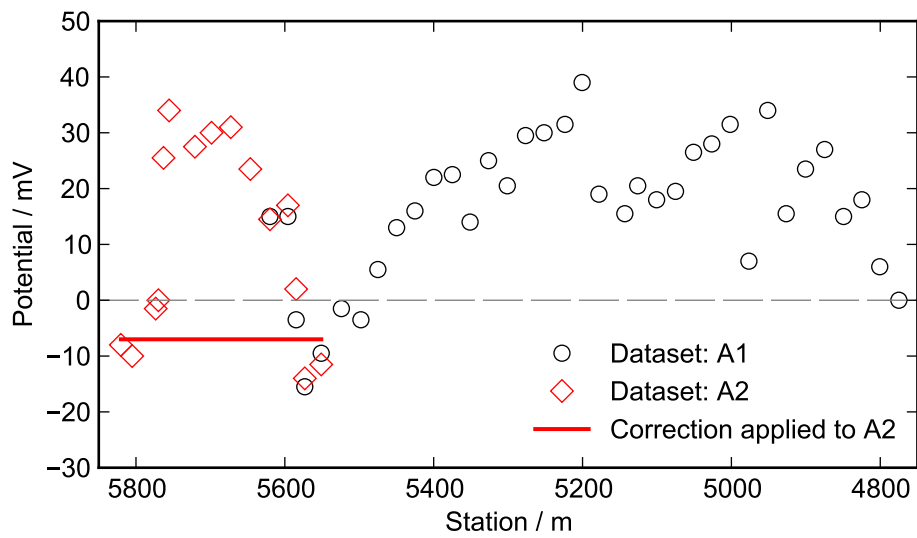


Figure B.9: Spatial corrections for potentials measured along Line A. Corrections are drawn as lines, and the corrected potentials are plotted as symbols.

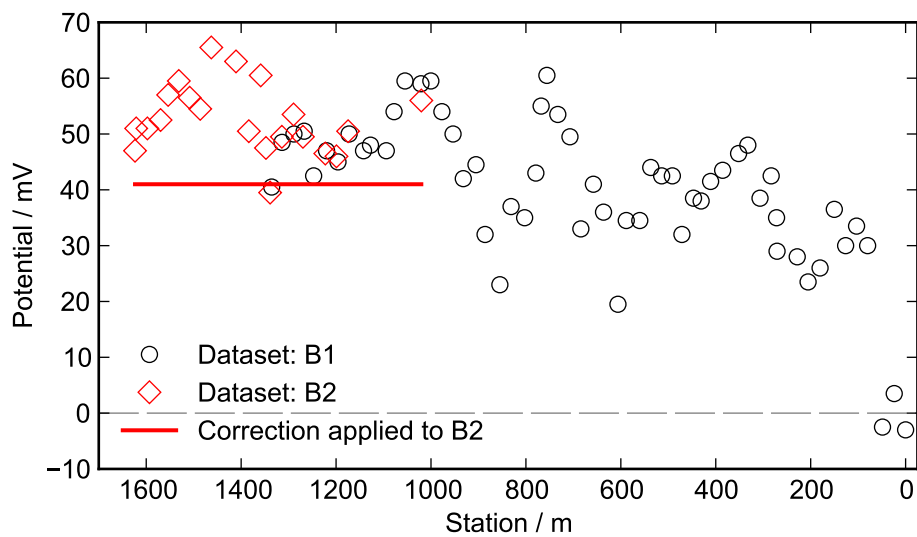


Figure B.10: Spatial corrections for potentials measured along Line B. Corrections are drawn as lines, and the corrected potentials are plotted as symbols.

Table B.19: Self-potential data along Line B.

Date	Time	Easting / m	Northing / m	Station/m	Resistance/k Ω	SP/mV
2011-07-28	13:07	681242	6740138	0	0.34	−3.0
2011-07-28	13:13	681225	6740155	24	0.33	3.5
2011-07-28	13:17	681205	6740170	49	0.31	−2.5
2011-07-28	13:49	681183	6740192	80	0.61	30.0
2011-07-28	13:53	681164	6740206	103	0.63	33.5
2011-07-28	13:57	681149	6740224	126	0.69	30.0
2011-07-28	14:00	681132	6740240	150	0.67	36.5
2011-07-28	14:07	681109	6740260	180	0.60	26.0
2011-07-28	14:10	681091	6740278	205	0.56	23.5
2011-07-28	14:22	681078	6740296	228	0.56	28.0
2011-07-28	14:26	681041	6740319	271	0.60	29.0
2011-07-28	14:34	681043	6740323	272	0.67	35.0
2011-07-28	14:30	681037	6740334	283	0.73	42.5
2011-07-28	14:56	681015	6740344	307	0.16	38.5
2011-07-28	15:01	680998	6740364	332	0.85	48.0
2011-07-28	15:05	680980	6740373	352	0.82	46.5
2011-07-28	15:08	680956	6740397	385	0.76	43.5
2011-07-28	15:18	680938	6740414	411	0.76	41.5
2011-07-28	15:33	680929	6740434	431	0.68	38.0
2011-07-28	15:37	680914	6740441	447	0.69	38.5
2011-07-28	15:44	680894	6740456	471	1.5	32.0
2011-07-28	16:02	680880	6740470	491	1.8	42.5
2011-07-28	16:08	680864	6740486	514	0.72	42.5
2011-07-28	16:13	680849	6740503	537	0.47	44.0
2011-07-28	16:16	680831	6740518	560	0.62	34.5
2011-07-28	16:18	680810	6740538	589	0.60	34.5
2011-07-28	16:21	680797	6740550	606	0.35	19.5
2011-07-28	16:24	680775	6740571	636	0.88	36.0
2011-07-28	16:26	680760	6740586	658	0.67	41.0
2011-07-28	16:29	680738	6740601	684	0.62	33.0
2011-07-28	16:31	680723	6740618	707	0.82	49.5
2011-07-28	16:33	680706	6740637	733	0.86	53.5
2011-07-28	16:37	680689	6740653	756	0.94	60.5
2011-07-28	16:41	680681	6740662	768	0.98	55.0
2011-07-28	16:39	680671	6740668	779	0.73	43.0
2011-07-28	16:44	680654	6740684	803	0.64	35.0
2011-07-28	16:48	680634	6740704	831	0.64	37.0
2011-07-28	16:51	680617	6740722	855	0.34	23.0
2011-07-28	16:53	680593	6740742	886	0.60	32.0
2011-07-28	16:58	680580	6740755	905	0.77	44.5
2011-07-28	17:01	680560	6740772	932	0.74	42.0
2011-07-28	17:03	680546	6740790	954	0.86	50.0
2011-07-28	17:06	680530	6740807	977	0.31	54.0
2011-07-28	17:09	680508	6740817	1000	0.95	59.5
2011-07-31	17:24	680494	6740832	1020	0.39	56.0
2011-07-28	17:11	680495	6740834	1021	0.94	59.0
2011-07-28	17:13	680475	6740862	1055	0.95	59.5

Table B.19: Self-potential data along Line B (continued).

Date	Time	Easting / m	Northing / m	Station/m	Resistance/k Ω	SP/mV
2011-07-28	17:16	680453	6740872	1078	0.89	54.0
2011-07-28	17:18	680444	6740887	1094	0.81	47.0
2011-07-28	17:22	680419	6740908	1127	0.81	48.0
2011-07-28	17:26	680410	6740920	1142	0.80	47.0
2011-07-28	17:28	680385	6740938	1173	0.85	50.0
2011-07-31	17:15	680384	6740940	1175	0.31	50.5
2011-07-28	17:31	680367	6740953	1196	0.80	45.0
2011-07-31	17:13	680364	6740955	1199	0.34	46.0
2011-07-28	17:34	680349	6740969	1220	0.78	47.0
2011-07-31	17:09	680348	6740972	1223	0.32	46.5
2011-07-28	17:36	680328	6740986	1247	0.74	42.5
2011-07-28	17:41	680315	6741002	1267	0.83	50.5
2011-07-31	16:07	680313	6741004	1270	0.29	49.5
2011-07-28	17:47	680297	6741014	1289	0.82	50.0
2011-07-31	16:08	680298	6741016	1290	0.30	53.5
2011-07-28	17:49	680281	6741033	1314	0.87	48.5
2011-07-31	16:11	680279	6741032	1314	0.33	49.5
2011-07-28	17:57	680265	6741048	1336	0.79	40.5
2011-07-31	16:13	680261	6741049	1339	0.48	39.5
2011-07-31	16:17	680256	6741056	1348	0.39	47.5
2011-07-31	16:15	680247	6741064	1359	1.1	60.5
2011-07-31	16:20	680226	6741077	1384	0.35	50.5
2011-07-31	16:23	680206	6741096	1411	0.55	63.0
2011-07-31	16:28	680172	6741135	1463	0.34	65.5
2011-07-31	16:31	680155	6741151	1486	0.29	54.5
2011-07-31	16:34	680143	6741171	1508	0.32	56.5
2011-07-31	16:36	680127	6741188	1531	0.34	59.5
2011-07-31	16:39	680114	6741206	1554	0.31	57.0
2011-07-31	16:42	680106	6741221	1570	0.32	52.5
2011-07-31	16:46	680089	6741244	1598	0.31	51.0
2011-07-31	16:49	680076	6741264	1621	0.31	51.0
2011-07-31	16:51	680075	6741266	1624	0.31	47.0

The local date and time is used (UTC+9.5). Map coordinates are UTM 53J (EPSG:28353).

Table B.20: Self-potential data along Line C.

Date	Time	Easting / m	Northing / m	Station/m	Resistance/k Ω	SP/mV
2011-07-29	12:16	681303	6740963	1173	0.69	−5.5
2011-07-29	12:20	681284	6740952	1195	0.81	−2.0
2011-07-29	12:25	681277	6740946	1204	0.61	−11.5
2011-07-29	12:23	681266	6740938	1218	0.63	−19.0
2011-07-29	12:28	681243	6740928	1242	0.61	−17.0
2011-07-29	12:31	681223	6740920	1264	0.64	−15.0

Table B.20: Self-potential data along Line C (continued).

Date	Time	Easting / m	Northing / m	Station/m	Resistance/k Ω	SP/mV
2011-07-29	12:38	681216	6740914	1273	0.80	2.0
2011-07-29	12:41	681209	6740911	1280	1.8	3.5
2011-07-29	12:43	681208	6740908	1283	2.5	15.5
2011-07-29	12:35	681204	6740906	1287	2.3	14.0
2011-07-29	12:49	681185	6740898	1307	0.59	−12.5
2011-07-29	12:52	681164	6740886	1331	1.5	6.5
2011-07-29	12:57	681144	6740875	1355	0.65	4.0
2011-07-29	13:00	681124	6740861	1378	0.57	8.0
2011-07-29	13:02	681106	6740850	1400	0.70	9.5
2011-07-29	13:05	681087	6740841	1421	0.78	17.5
2011-07-29	13:15	681086	6740841	1422	0.73	13.0
2011-07-29	13:12	681081	6740836	1428	0.61	2.5
2011-07-29	13:12	681070	6740833	1440	0.68	−1.0
2011-07-29	13:21	681049	6740822	1463	0.61	5.5
2011-07-29	13:37	681006	6740798	1512	0.69	9.5
2011-07-29	13:43	680989	6740792	1530	0.76	16.5
2011-07-29	13:45	680968	6740784	1553	1.2	13.5
2011-07-29	13:48	680947	6740765	1580	0.65	6.5
2011-07-29	13:52	680920	6740754	1609	0.66	5.0
2011-07-29	13:57	680917	6740753	1612	0.77	16.5
2011-07-29	13:55	680898	6740741	1634	0.76	19.5
2011-07-29	14:00	680877	6740730	1658	0.74	18.5
2011-07-29	14:07	680865	6740729	1670	0.76	18.5
2011-07-29	14:09	680855	6740723	1681	0.61	7.5
2011-07-29	14:04	680854	6740719	1684	0.56	−2.0
2011-07-29	14:17	680845	6740713	1695	0.52	−6.5
2011-07-29	14:12	680834	6740707	1708	0.51	−10.5
2011-07-29	14:35	680813	6740710	1724	0.51	−1.0
2011-07-29	14:22	680810	6740691	1736	0.62	12.0
2011-07-29	14:40	680785	6740676	1765	0.65	13.0
2011-07-29	14:45	680768	6740666	1785	0.62	12.5
2011-07-29	14:51	680762	6740658	1794	0.69	19.0
2011-07-29	14:50	680755	6740658	1800	0.76	25.0
2011-07-29	14:47	680747	6740653	1809	0.83	25.5
2011-07-29	14:58	680736	6740642	1824	1.0	30.5
2011-07-29	15:00	680729	6740635	1834	0.89	37.5
2011-07-29	14:55	680721	6740631	1843	0.97	42.5
2011-07-29	15:04	680706	6740618	1862	1.2	38.0
2011-07-29	15:10	680686	6740599	1889	0.93	45.5
2011-07-29	15:15	680664	6740584	1916	0.94	41.5
2011-07-29	15:18	680643	6740575	1938	0.86	36.5
2011-07-29	15:22	680619	6740562	1966	0.68	22.5
2011-07-29	15:53	680595	6740551	1992	0.79	32.0
2011-07-29	15:58	680571	6740538	2019	0.86	37.5
2011-07-29	16:01	680552	6740526	2042	0.84	35.5
2011-07-29	16:04	680529	6740512	2069	0.83	39.0
2011-07-29	16:13	680504	6740500	2096	0.91	45.0
2011-07-29	16:18	680481	6740491	2121	0.84	39.0

Table B.21: Static corrections applied to SP data from the Bubbler spring complex.

Line	Stations		Correction / mV
A	5551	5820	-7
B	1020	1624	41

Table B.20: Self-potential data along Line C (continued).

Date	Time	Easting / m	Northing / m	Station/m	Resistance/k Ω	SP/mV
2011-07-29	16:21	680448	6740500	2145	0.85	40.0
2011-07-29	16:23	680427	6740478	2174	0.84	39.0
2011-07-29	16:26	680400	6740466	2204	0.84	37.5
2011-07-29	16:28	680376	6740455	2230	0.84	38.5
2011-07-29	16:31	680350	6740445	2258	0.83	36.0
2011-07-29	16:33	680323	6740434	2287	0.90	43.5
2011-07-29	16:50	680300	6740423	2312	0.95	45.0
2011-07-29	16:54	680280	6740413	2334	1.0	51.0
2011-07-29	17:02	680254	6740397	2364	1.5	56.5
2011-07-29	17:02	680234	6740389	2386	1.3	51.0
2011-07-29	17:07	680213	6740381	2409	0.45	46.0
2011-07-29	18:05	680172	6740376	2446	0.87	42.0
2011-07-29	18:08	680156	6740380	2459	6.6	38.0
2011-07-29	18:10	680126	6740382	2486	6.7	38.0
2011-07-29	18:13	680109	6740387	2498	2.4	27.5
2011-07-29	18:20	680079	6740391	2523	1.1	24.5
2011-07-29	18:22	680049	6740389	2552	0.63	22.0
2011-07-29	18:25	680027	6740394	2569	0.62	22.5
2011-07-29	18:27	680004	6740400	2589	0.55	13.0
2011-07-29	18:29	679977	6740405	2611	0.44	12.5
2011-07-29	18:33	679951	6740410	2633	0.43	5.5

The local date and time is used (UTC+9.5). Map coordinates are UTM 53J (EPSG:28353).

B.1.4 Freeling Springs

Self-potential data collected at Freeling Springs are shown in Tables B.22 through B.25, which are sorted by station number. No corrections were applied to the data other than the simple averaging referred to in Section B.1 above. Repeat measurements are shown in the table.

Table B.22: Self-potential data along Line N1.

Date	Time	Easting / m	Northing / m	Station/m	Resistance/k Ω	SP/mV
2012-11-24	9:53	588775	6894356	875	4000	28.0
2012-11-24	9:50	588792	6894359	892	6300	7.0
2012-11-24	9:47	588810	6894361	910	3000	−2.5
2012-11-24	9:45	588831	6894366	932	7500	24.5
2012-11-24	9:42	588845	6894371	946	7000	57.0
2012-11-24	9:40	588861	6894372	962	2.6	2.0
2012-11-24	9:39	588873	6894375	975	1.5	14.5
2012-11-24	9:38	588889	6894378	991	40	5.0
2012-11-24	9:30	588916	6894384	1019	1.8	21.0
2012-11-24	7:19	588917	6894385	1020	2.4	23.5
2012-11-24	7:24	588917	6894385	1020	2.4	25.0
2012-11-24	7:29	588917	6894385	1020	2.7	25.5
2012-11-24	7:35	588917	6894385	1020	3.0	23.15
2012-11-24	7:38	588917	6894385	1020	2.8	26.0
2012-11-24	9:31	588936	6894387	1039	73	2.5
2012-11-24	7:44	588936	6894390	1040	970	−23.5
2012-11-24	9:34	588958	6894393	1062	5500	−31.0
2012-11-24	7:46	588959	6894393	1063	130	−59.0
2012-11-24	9:25	588978	6894395	1082	1.6	18.0
2012-11-24	7:49	588978	6894396	1082	2.0	18.5
2012-11-24	7:50	588989	6894398	1093	21	−4.0
2012-11-24	7:52	589001	6894402	1106	2000	13.5
2012-11-24	7:53	589001	6894402	1106	10 000	5.0
2012-11-24	7:55	589021	6894407	1126	200	35.0
2012-11-24	9:22	589022	6894405	1127	900	38.0
2012-11-24	7:57	589041	6894410	1146	1800	51.0
2012-11-24	7:59	589060	6894413	1166	10 000	29.5
2012-11-24	8:00	589080	6894416	1186	168	45.0
2012-11-24	9:19	589097	6894421	1203	725	69.0
2012-11-24	8:02	589100	6894421	1206	1000	74.5
2012-11-24	8:03	589118	6894426	1225	1000	101.5
2012-11-24	8:04	589135	6894430	1242	700	69.5
2012-11-24	8:06	589157	6894434	1265	3500	70.0
2012-11-24	8:07	589175	6894437	1283	5000	107.0
2012-11-24	9:16	589194	6894436	1301	9000	60.0
2012-11-24	8:09	589196	6894440	1304	5600	58.0
2012-11-24	8:10	589213	6894445	1322	1500	51.5
2012-11-24	8:11	589233	6894445	1341	600	55.0
2012-11-24	8:13	589249	6894449	1358	2200	18.5
2012-11-24	8:14	589268	6894452	1377	700	42.5
2012-11-24	8:15	589284	6894455	1393	8000	24.0
2012-11-24	9:01	589287	6894455	1396	2300	35.5
2012-11-24	8:17	589303	6894460	1413	79	−12.5
2012-11-24	8:25	589323	6894463	1433	7000	14.0
2012-11-24	8:27	589343	6894468	1454	130	−16.5
2012-11-24	8:29	589365	6894473	1476	27	−20.5
2012-11-24	8:56	589381	6894477	1493	1700	−5.0

Table B.22: Self-potential data along Line N1 (continued).

Date	Time	Easting / m	Northing / m	Station/m	Resistance/k Ω	SP/mV
2012-11-24	8:31	589382	6894478	1494	10 000	21.5
2012-11-24	8:57	589382	6894478	1494	16 000	14.0
2012-11-24	8:54	589399	6894480	1511	18	-35.0
2012-11-24	8:33	589399	6894481	1511	30	-34.0
2012-11-24	8:34	589419	6894486	1532	53	-38.0
2012-11-24	8:35	589438	6894489	1551	43	-13.5
2012-11-24	8:37	589460	6894495	1574	60	-39.5
2012-11-24	8:52	589462	6894494	1576	21	-42.0
2012-11-24	8:38	589481	6894499	1595	100	-14.5
2012-11-24	8:40	589501	6894502	1615	280	-30.0
2012-11-24	8:42	589520	6894507	1635	58	-49.0
2012-11-24	8:43	589534	6894510	1649	12	-48.0
2012-11-24	8:45	589553	6894515	1669	22	-51.0

The local date and time is used (UTC+10.5). Map coordinates are UTM 53J (EPSG:28353).

Table B.23: Self-potential data along Line N2.

Date	Time	Easting / m	Northing / m	Station/m	Resistance/k Ω	SP/mV
2012-11-24	19:01	588902	6894378	1005	600	15.0
2012-11-24	19:04	588907	6894381	1011	7.7	-2.5
2012-11-24	19:05	588912	6894382	1016	560	14.5
2012-11-24	19:06	588917	6894384	1021	1.6	15.5
2012-11-24	19:07	588921	6894384	1025	3.2	5.0
2012-11-24	19:08	588927	6894385	1031	140	-1.5
2012-11-24	19:09	588932	6894386	1036	17	12.5
2012-11-24	19:10	588937	6894388	1041	4000	-20.0
2012-11-24	19:11	588941	6894389	1046	1600	-15.0
2012-11-24	19:12	588947	6894389	1051	35 000	-15.5

The local date and time is used (UTC+10.5). Map coordinates are UTM 53J (EPSG:28353).

Table B.24: Self-potential data along Line N3.

Date	Time	Easting / m	Northing / m	Station/m	Resistance/k Ω	SP/mV
2012-11-24	19:25	588928	6894358	-27	28	-2.0
2012-11-24	19:23	588927	6894364	-21	8.0	1.0
2012-11-24	19:22	588924	6894370	-14	1.5	10.5
2012-11-24	19:20	588924	6894374	-10	1.9	6.5

Table B.24: Self-potential data along Line N3 (continued).

Date	Time	Easting / m	Northing / m	Station/m	Resistance/k Ω	SP/mV
2012-11-24	19:19	588924	6894379	−6	1.7	4.5
2012-11-24	19:32	588920	6894388	4	1.7	8.0
2012-11-24	19:33	588916	6894392	9	120	−3.5
2012-11-24	19:34	588915	6894398	15	1.6	8.0
2012-11-24	19:35	588912	6894402	20	1.5	4.0
2012-11-24	19:37	588908	6894406	26	1.4	2.0
2012-11-24	19:38	588904	6894409	30	70	8.0
2012-11-24	19:39	588897	6894414	38	170	−2.0
2012-11-24	19:40	588893	6894416	43	1800	25.0
2012-11-24	19:45	588889	6894419	47	1.9	13.5
2012-11-24	19:46	588884	6894424	54	1.8	22.0
2012-11-24	19:48	588880	6894428	60	1.9	27.5
2012-11-24	19:50	588873	6894433	69	1.8	12.5
2012-11-24	19:51	588871	6894436	72	90	47.5
2012-11-24	19:52	588865	6894440	79	8.0	23.5
2012-11-24	19:53	588861	6894443	84	530	18.0
2012-11-24	19:54	588859	6894446	88	45	2.5
2012-11-24	19:54	588856	6894450	93	2200	−21.5
2012-11-24	19:56	588851	6894451	97	1800	20.5
2012-11-24	19:58	588844	6894463	110	1.1	1.5
2012-11-24	19:58	588844	6894463	110	20	0.5

The local date and time is used (UTC+10.5). Map coordinates are UTM 53J (EPSG:28353).

Table B.25: Self-potential data along Line S1.

Date	Time	Easting / m	Northing / m	Station/m	Resistance/k Ω	SP/mV
2012-11-22	13:38	588780	6893818	738	2500	75.0
2012-11-22	13:35	588800	6893822	758	9000	64.5
2012-11-22	13:33	588825	6893824	784	1300	55.5
2012-11-22	13:31	588843	6893825	802	2500	55.0
2012-11-22	14:03	588846	6893828	805	2000	73.0
2012-11-22	14:05	588854	6893828	813	720	77.0
2012-11-22	13:28	588862	6893828	821	3200	125.0
2012-11-22	14:07	588863	6893829	822	12 000	108.5
2012-11-22	13:25	588884	6893830	843	4500	90.5
2012-11-22	13:20	588901	6893832	860	70	53.0
2012-11-22	13:18	588921	6893833	880	570	28.0
2012-11-22	13:15	588940	6893836	899	17 000	31.0
2012-11-22	13:14	588960	6893835	919	1750	96.5
2012-11-22	13:11	588979	6893840	938	800	92.5
2012-11-22	12:59	589002	6893837	961	4000	83.0
2012-11-22	12:57	589021	6893837	980	7500	46.5
2012-11-22	12:54	589041	6893838	1000	700	82.5

Table B.25: Self-potential data along Line S1 (continued).

Date	Time	Easting / m	Northing / m	Station/m	Resistance/k Ω	SP/mV
2012-11-22	14:15	589042	6893838	1001	650	77.0
2012-11-22	14:18	589053	6893837	1012	650	77.5
2012-11-22	12:52	589064	6893838	1023	6.5	53.0
2012-11-22	14:21	589064	6893839	1023	6.7	57.5
2012-11-22	14:25	589081	6893842	1040	6.2	44.0
2012-11-22	12:50	589081	6893843	1040	5.6	44.0
2012-11-22	14:27	589094	6893842	1053	1860	84.5
2012-11-22	12:48	589101	6893843	1060	1400	80.5
2012-11-22	14:29	589103	6893845	1062	1360	83.5
2012-11-22	12:46	589120	6893850	1080	2000	52.5
2012-11-22	12:43	589139	6893848	1099	270	71.5
2012-11-22	12:40	589160	6893851	1120	870	71.0
2012-11-22	12:38	589179	6893853	1139	6.0	21.0
2012-11-22	15:04	589182	6893854	1142	110	41.0
2012-11-22	15:06	589182	6893854	1142	100	38.0
2012-11-22	12:35	589199	6893856	1159	21 000	35.0
2012-11-22	12:33	589219	6893860	1179	14 000	49.0
2012-11-22	12:31	589236	6893860	1196	8000	47.5
2012-11-22	12:26	589253	6893863	1213	950	61.5
2012-11-22	12:25	589273	6893862	1233	93	49.0
2012-11-22	15:09	589276	6893860	1236	560	54.5
2012-11-22	12:24	589292	6893862	1252	10.0	18.5
2012-11-22	12:22	589311	6893862	1271	16	17.0
2012-11-22	12:19	589331	6893863	1291	2.8	16.5
2012-11-22	15:13	589332	6893861	1292	12	19.5

The local date and time is used (UTC+10.5). Map coordinates are UTM 53J (EPSG:28353).

References

- Abdelrahman, E.-S. M., El-Araby, H. M., Hassaneen, A.-R. G., and Hafez, M. A. (2003). New methods for shape and depth determinations from SP data. *Geophysics*, 68:1202–1210.
- Adelsberger, K. A. and Smith, J. R. (2010). Paleolandscape and paleoenvironmental interpretation of spring-deposited sediments in Dakhleh Oasis, Western Desert of Egypt. *Catena*, 83:7–22.
- Ah Chee, D. (1995). *Indigenous people's connection with kwatye (water) in the Great Artesian Basin*. Department of Environment and Natural Resources, South Australia.
- Aizawa, K., Uyeshima, M., and Nogami, K. (2008). Zeta potential estimation of volcanic rocks on 11 island arc-type volcanoes in Japan: implication for the generation of local self-potential anomalies. *Journal of Geophysical Research*, 113(B2):1–9.
- Al-Saigh, N. H., Mohammed, Z. S., and Dahham, M. S. (1994). Detection of water leakage from dams by self-potential method. *Engineering Geology*, 37:115–121.
- Alaia, R., Patella, D., and Mauriello, P. (2009). Imaging multipole self-potential sources by 3D probability tomography. *Progress in Electromagnetics Research B*, 14:311–339.
- Aldam, R. and Kuang, K. (1988). An investigation of structures controlling discharge of spring waters in the south western Great Artesian Basin. Report Book 88/4, Department of Mines and Energy, South Australia.
- Alexander, E. M., Sansome, A., and Cotton, T. B. (2006). Lithostratigraphy and environments of deposition. In T. B. Cotton, M. F. Scardigno, and J. E. Hibburt, editors, *The petroleum geology of South Australia, Vol. 2: Eromanga*

- Basin*, chapter 5. Department of Primary Industries and Resources, South Australia, 2nd edition.
- Anderson, E. I. and Bakker, M. (2008). Groundwater flow through anisotropic fault zones in multiaquifer systems. *Water Resources Research*, 44(11):1–11.
- Apaydin, A. (2010). Relation of tectonic structure to groundwater flow in the Beypazari region, NW Anatolia, Turkey. *Hydrogeology Journal*, 18:1343–1356.
- Auken, E., Pellerin, L., Christensen, N. B., and Sorensen, K. (2006). A survey of current trends in near-surface electrical and electromagnetic methods. *Geophysics*, 71(5):G249–G260.
- Bahr, K. (1988). Interpretation of the magnetotelluric impedance tensor: regional induction and local telluric distortion. *Journal of Geophysics*, 62:119–127.
- Ball, L. B., Ge, S., Caine, J. S., Revil, A., and Jardani, A. (2010). Constraining fault-zone hydrogeology through integrated hydrological and geoelectrical analysis. *Hydrogeology Journal*, 18(5):1057–1067.
- Barus, C. (1882). On the electrical activity of ore bodies. In *Geology of the Comstock Lode and the Washoe District*, chapter 10, pages 309–367. United States Geological Survey.
- Bense, V. and Person, M. (2006). Faults as conduit-barrier systems to fluid flow in siliciclastic sedimentary aquifers. *Water Resources Research*, 42(5):W05421, pp. 1–18.
- Bense, V. F. and Balen, R. V. (2004). The effect of fault relay and clay smearing on groundwater flow patterns in the Lower Rhine Embayment. *Basin Research*, 16:397–411.
- Berdichevsky, M. M. N. and Dmitriev, V. I. (2008). *Models and Methods of Magnetotellurics*. Springer.
- Birch, F. S. (1993). Testing Fournier's Method for Finding Water Table from Self-Potential. *Ground Water*, 31(1):50–56.
- Bodmer, R., Ward, S., and Morrison, H. (1968). On induced electrical polarization and groundwater. *Geophysics*, 33:805–821.
- Boleve, A., Revil, A., Janod, F., Mattiuzzo, J., and Jardani, A. (2007). Forward modeling and validation of a new formulation to compute self-potential sig-

- nals associated with ground water flow. *Hydrology and Earth System Science*, 11:1661–1671.
- Booker, J. R. (2013). The magnetotelluric phase tensor: a critical review. *Surveys in Geophysics*, pages 1–34.
- Burbank, J. E. (1905). Earth-currents and a proposed method for their investigation. *Terrestrial Magnetism and Atmospheric Electricity*, 10(1):23–49.
- Burr, S. (1986). Discussion on: "The electrochemical mechanics of sulfide self-potentials" by M. Sato and H. M. Mooney. *Geophysics*, 51(1):194–196.
- Byrdina, S., Revil, A., and Pant, S. (2009). Dipolar self-potential anomaly associated with carbon dioxide and radon flux at Syabru-Bensi hot springs in central Nepal. *Journal of Geophysical Research*, 114:1–14.
- Caldwell, T. G., Bibby, H. M., and Brown, C. (2004). The magnetotelluric phase tensor. *Geophysical Journal International*, 158(2):457–469.
- Cartwright, J. (2011). Diagenetically induced shear failure of fine-grained sediments and the development of polygonal fault systems. *Marine and Petroleum Geology*, 28:1593–1610.
- Cartwright, J. A. (1994). Episodic basin-wide hydrofracturing of overpressured Early Cenozoic mudrock sequences in the North Sea Basin. *Marine and Petroleum Geology*, 11:587–607.
- Chave, A. D. and Jones, A. G., editors (2012). *The Magnetotelluric Method: Theory and Practice*. Cambridge University Press.
- Chave, A. D. and Thomson, D. J. (2004). Bounded influence magnetotelluric response function estimation. *Geophysical Journal International*, 157(3):988–1006.
- Cobb, M. (1975). Sampling and measurement of mound springs, Great Artesian Basin, South Australia: progress report no. 2, for Marree, Curdimurka, and Billa Kalina sheets. Report Book 75/90, Department of Mines, South Australia.
- Constable, S. C., Parker, R. L., and Constable, C. G. (1987). Occam's inversion: a practical algorithm for generating smooth models from EM sounding data. *Geophysics*, 52:289–300.
- Corry, C. (1985). Spontaneous polarization associated with porphyry sulfide mineralization. *Geophysics*, 50(6):1020–1034.

- Corry, C. E., DeMouilly, G. T., and Gerety, M. T. (1983). *Field procedure manual for self-potential surveys*. Zonge Engineering and Research Organization.
- Crombie, M. K., Arvidson, R. E., Sturchio, N. C., Alf, Z. E., and Zeid, K. A. (1997). Age and isotopic constraints on Pleistocene pluvial episodes in the Western Desert, Egypt. *Palaeogeography, Palaeoclimatology, Palaeoecology*, 130:337–355.
- Dailey, M. K. M. (2011). Hydrogeophysical evidence for ground water mixing at Freeling Spring Group, South Australia. Master's thesis, Oklahoma State University.
- Danielsen, J. E., Auken, E., Jørgensen, F., Søndergaard, V., and Sørensen, K. I. (2003). The application of the transient electromagnetic method in hydrogeophysical surveys. *Journal of Applied Geophysics*, 53:181–198.
- de Groot-Hedlin, C. and Constable, S. (1990). Occam's inversion to generate smooth, two-dimensional models from magnetotelluric data. *Geophysics*, 55(12):1613–1624.
- de Groot-Hedlin, C. and Constable, S. (2004). Inversion of magnetotelluric data for 2D structure with sharp resistivity contrasts. *Geophysics*, 69(1):78–86.
- de Witte, L. (1948). A new method of interpretation of self-potential field data. *Geophysics*, 13(4):600–608.
- Dekker, D. L. and Hastie, L. (1980). Magnetotelluric impedances of an anisotropic layered earth model. *Geophysical Journal of the Royal Astronomical Society*, 61:11–20.
- Department of Environment, Water and Natural Resources, South Australia (2013). Groundwater Data: <https://www.waterconnect.sa.gov.au/Systems/GD>. Accessed 13 October 2013.
- Egholm, D. L., Clausen, O. R., Sandiford, M., Kristensen, M. B., and Korstgard, J. A. (2008). The mechanics of clay smearing along faults. *Geology*, 36:787–790.
- Ernstson, K. and Scherer, H. U. (1986). Self-potential variations with time and their relation to hydrogeologic and meteorological parameters. *Geophysics*, 51:1967–1977.

- Fischer, G. and Masero, W. (1994). Rotational properties of the magnetotelluric impedance tensor: the example of the Araguinha impact crater, Brazil. *Geophysical Journal International*, 119:548–560.
- Fitterman, D. V. (1978). Electrokinetic and magnetic anomalies associated with dilatant regions in a layered earth. *Journal of Geophysical Research*, 83(8):5923–5928.
- Flis, M. F., Newman, G. A., and Hohmann, G. W. (1989). Induced-polarization effects in time-domain electromagnetic measurements. *Geophysics*, 54(4):514–523.
- Florek, S. M. (1987). The archaeological variability of mound spring sites at Lake Eyre South, South Australia: work in progress. *Australian Archaeology*, 24:27–31.
- Forbes, B. G. (1988). Pre-Mesozoic geology of the Curdimurka region. Technical report, Department of Mines and Energy, South Australia, Report Book 88/51.
- Ford, T. and Pedley, H. (1996). A review of tufa and travertine deposits of the world. *Earth-Science Reviews*, 41(3):117–175.
- Fox, R. W. (1830). On the electromagnetic properties of metalliferous veins in the mines of Cornwall. *Philosophical Transactions of the Royal Society of London*, 120:399–414.
- Gamble, T., Goubau, W., and Clarke, J. (1979). Magnetotellurics with a remote reference. *Geophysics*, 44:53–68.
- Garcia, X. and Jones, A. G. (2002a). Atmospheric sources for audio-magnetotelluric (AMT) sounding. *Geophysics*, 67:448–458.
- Garcia, X. and Jones, A. G. (2002b). Decomposition of three-dimensional electromagnetic data. In P. E. Wannamaker and M. S. Zhdanov, editors, *Three-Dimensional Electromagnetics*, volume 35 of *Methods in Geochemistry and Geophysics*, chapter 13, pages 235–250. Elsevier.
- Gibert, D. and Pessel, M. (2001). Identification of sources of potential fields with the continuous wavelet transform: Application to self-potential profiles. *Geophysical Research Letters*, 28:1863–1866.
- Green, G. and Berens, V. (2013). Relationship between aquifer pressure changes and spring discharge rates. In A. J. Love, P. Shand, L. Crossey,

- G. A. Harrington, and P. Rousseau-Gueutin, editors, *Allocating Water and Maintaining Springs in the Great Artesian Basin, Volume III: Groundwater Discharge of the Western Great Artesian Basin*, chapter 7, pages 101–114. National Water Commission, Australia.
- Groom, R. and Bahr, K. (1992). Corrections for near surface effects: decomposition of the magnetotelluric impedance tensor and scaling corrections for regional resistivities: a tutorial. *Surveys in Geophysics*, 13:341–379.
- Groom, R. W. and Bailey, R. C. (1989). Decomposition of Magnetotelluric Impedance Tensors in the Presence of Local Three-Dimensional Galvanic Distortion. *Journal of Geophysical Research*, 94:1913–1925.
- Habermehl, M. A. (1980). The Great Artesian Basin, Australia. *BMR Journal of Australian Geology and Geophysics*, 5:9–38.
- Habermehl, M. A. (2006). The Great Artesian Basin, Australia. In S. Foster and D. P. Loucks, editors, *Non-renewable groundwater resources: a guidebook on socially-sustainable management for water-policy makers*. UNESCO International Hydrological Programme.
- Habermehl, M. A. (2011). Hydrogeology of the Great Artesian Basin - Boundaries of the Hydrogeological Units. Geoscience Australia, Catalogue No. 72665, <http://tinyurl.com/ga-gab-72665>.
- Halihan, T., Love, A. J., Keppel, M. N., and Berens, V. (2013). Analysis of subsurface mound spring connectivity in shale of the western margin of the Great Artesian Basin, South Australia. *Hydrogeology Journal*, 21:1605–1617.
- Hamilton, S. and Hattori, K. (2008). Spontaneous potential and redox responses over a forest ring. *Geophysics*, 73(3):B67–B75.
- Hammann, M., Maurer, H. R., Green, A. G., and Horstmeyer, H. (1997). Self-potential image reconstruction: capabilities and limitations. *Journal of Environmental and Engineering Geophysics*, 2(1):21–35.
- Hancock, P., Chalmers, R., Altunel, E., and Çakir, Z. (1999). Travitronics: using travertines in active fault studies. *Journal of Structural Geology*, 21(8-9):903–916.
- Harrington, G. A., Smerdon, B. D., Gardner, P. W., Taylor, A. R., and Hendry, J. (2013). Diffuse discharge. In A. J. Love, P. Shand, L. Crossey, G. A.

- Harrington, and P. Rousseau-Gueutin, editors, *Allocating Water and Maintaining Springs in the Great Artesian Basin, Volume III: Groundwater Discharge of the Western Great Artesian Basin*, chapter 8, pages 115–132. National Water Commission, Australia.
- Harris, C. (1992). Mound springs: South Australian conservation initiatives. *The Rangeland Journal*, 14(2):157–173.
- Heise, W., Caldwell, T., Bibby, H., and Brown, C. (2006). Anisotropy and phase splits in magnetotellurics. *Physics of the Earth and Planetary Interiors*, 158(2-4):107–121.
- Herman, J. S. and Lorah, M. M. (1988). Calcite precipitation rates in the field: measurement and prediction for a travertine-depositing stream. *Geochimica et Cosmochimica Acta*, 52(10):2347–2355.
- Hohmann, G. W. and Newman, G. A. (1990). Transient electromagnetic responses of surficial, polarizable patches. *Geophysics*, 55(8):1098–1100.
- Ishido, T. and Pritchett, J. W. (1999). Numerical simulation of electrokinetic potentials associated with subsurface fluid flow. *Journal of Geophysical Research*, 104(B7):15247–15259.
- Jackson, M. D. (2010). Multiphase electrokinetic coupling: insights into the impact of fluid and charge distribution at the pore scale from a bundle of capillary tubes model. *Journal of Geophysical Research*, 115(B7):1–17.
- Jardani, A., Dupont, J. P., and Revil, A. (2006a). Self-potential signals associated with preferential groundwater flow pathways in sinkholes. *Journal of Geophysical Research*, 111(B9):1–13.
- Jardani, A., Revil, A., Bolève, A., and Dupont, J. P. (2008). Three-dimensional inversion of self-potential data used to constrain the pattern of groundwater flow in geothermal fields. *Journal of Geophysical Research*, 113(B9):1–22.
- Jardani, A., Revil, A., and Dupont, J. P. (2006b). Self-potential tomography applied to the determination of cavities. *Geophysical Research Letters*, 33(13):3–6.
- Jensen-Schmidt, B., Alexander, E. M., and Cotton, T. B. (2006). Structural and tectonic setting. In T. B. Cotton, M. F. Scardigno, and J. E. Hibburt, editors, *The petroleum geology of South Australia, Vol. 2: Eromanga Basin*, chapter 4. Department of Primary Industries and Resources, South Australia, 2nd edition.

- Jiracek, G. R. (1990). Near-surface and topographic distortions in electromagnetic induction. *Surveys in Geophysics*, 11:163–203.
- Jones, B. and Renaut, R. W. (2010). Calcareous spring deposits in continental settings. In A. Alonso-Zarza and L. Tanner, editors, *Carbonates in Continental Settings: Facies, Environments, and Processes*, volume 61 of *Developments in Sedimentology*, pages 177 – 224. Elsevier.
- Jones, F. W. and Price, A. T. (1970). The perturbations of alternating geomagnetic fields by conductivity anomalies. *Geophysical Journal International*, 20(3):317–334.
- Jouniaux, L., Maineult, A., Naudet, V., Pessel, M., and Sailhac, P. (2009). Review of self-potential methods in hydrogeophysics. *Comptes Rendus Geoscience*, 341:928–936.
- Jouniaux, L., Maineult, A., Naudet, V., Pessel, M., and Sailhac, P. (2010). Reply to the comment by A. Revil on “Review of self-potential methods in hydrogeophysics” by L. Jouniaux et al. *Comptes Rendus Geoscience*, 342:810–813.
- Karlstrom, K. E., Keppel, M. N., Crossey, L., Love, A. J., and Boreham, C. (2013). Structural and tectonic history. In M. Keppel, K. E. Karlstrom, A. J. Love, S. Priestley, D. Wohling, and S. D. Ritter, editors, *Allocating Water and Maintaining Springs in the Great Artesian Basin, Volume I: Hydrogeological Framework of the Western Great Artesian Basin*, chapter 4, pages 44–65. National Water Commission, Australia.
- Kaufman, A. A. (1988). Reduction of the geological noise in magnetotelluric soundings. *Geoexploration*, 25:145–161.
- Keller, G. and Frischknecht, F. (1966). *Electrical methods in geophysical prospecting*. Pergamon Press.
- Keppel, M., Karlstrom, K. E., Love, A. J., Priestley, S., Wohling, D., and Ritter, S. D., editors (2013a). *Allocating Water and Maintaining Springs in the Great Artesian Basin, Volume I: Hydrogeological Framework of the Western Great Artesian Basin*. National Water Commission, Australia.
- Keppel, M., Post, V. E. A., Love, A. J., Clarke, J. D. A., and Werner, A. D. (2012). Influences on the carbonate hydrochemistry of mound spring environments, Lake Eyre South region, South Australia. *Chemical Geology*, 296-297:50–65.

- Keppel, M., Wohling, D., Fulton, S., Sampson, L., Karlstrom, K. E., Nelson, G., Ransley, T., and Love, A. J. (2013b). Summary of hydrogeology and hydrostratigraphy. In M. Keppel, K. E. Karlstrom, A. J. Love, S. Priestley, D. Wohling, and S. D. Ritter, editors, *Allocating Water and Maintaining Springs in the Great Artesian Basin, Volume I: Hydrogeological Framework of the Western Great Artesian Basin*, chapter 3, pages 22–43. National Water Commission, Australia.
- Keppel, M. N. (2012). The geology and hydrochemistry of calcareous mound spring wetland environments in the Lake Eyre South region, Great Artesian Basin, South Australia. Ph.D. thesis, School of the Environment.
- Keppel, M. N., Clarke, J. D., Halihan, T., Love, A. J., and Werner, A. D. (2011). Mound springs in the arid Lake Eyre South region of South Australia: a new depositional tufa model and its controls. *Sedimentary Geology*, 240:55–70.
- Keppel, M. N., Halihan, T., Love, A. J., Post, V., Werner, A., and Clarke, J. (2013c). Formation and evolution of mound springs. In A. J. Love, P. Shand, L. Crossey, G. A. Harrington, and P. Rousseau-Gueutin, editors, *Allocating Water and Maintaining Springs in the Great Artesian Basin, Volume III: Groundwater Discharge of the Western Great Artesian Basin*, chapter 3, pages 35–60. National Water Commission, Australia.
- Kosmulski, M. and Dahlsten, P. (2006). High ionic strength electrokinetics of clay minerals. *Colloids and Surfaces A: Physicochemical and Engineering Aspects*, 291:212–218.
- Krieg, G., Rogers, P., Callen, R., and Freeman, P. (1991). *Explanatory Notes for the Curdimurka 1:250 000 geological map*. Geological Survey, South Australia.
- Lewis, M. M., White, D., and Gotch, T., editors (2013). *Allocating Water and Maintaining Springs in the Great Artesian Basin, Volume IV: Spatial Survey and Remote Sensing of Artesian Springs of the Western Great Artesian Basin*. National Water Commission, Australia.
- Linares, R., Rosell, J., Roque, C., and Gutierrez, F. (2010). Origin and evolution of tufa mounds related to artesian karstic springs in Isona area (Pyrenees, NE Spain). *Geodinamica Acta*, 23:129–150.
- Love, A. J., Wohling, D., Fulton, S., Rousseau-Gueutin, P., and Ritter, S. D., editors (2013). *Allocating Water and Maintaining Springs in the Great Artesian*

- Basin, Volume II: Groundwater Recharge, Hydrodynamics and Hydrochemistry of the Western Great Artesian Basin*. National Water Commission, Australia.
- MacInnes, S. (2010). *STEMINV: Smooth model TEM Inversion*. Zonge Engineering, Tucson, AZ.
- Magee, J. W., Miller, G. H., Spooner, N. A., and Questiaux, D. (2004). Continuous 150 k.y. monsoon record from Lake Eyre, Australia: insolation-forcing implications and unexpected Holocene failure. *Geology*, 32:885–888.
- Martí, A. (2013). The role of electrical anisotropy in magnetotelluric responses: From modelling and dimensionality analysis to inversion and interpretation. *Surveys in Geophysics*, pages 1–40. DOI 10.1007/s10712-013-9233-3.
- Martí, A., Queralt, P., and Ledo, J. (2009). WALDIM: A code for the dimensionality analysis of magnetotelluric data using the rotational invariants of the magnetotelluric tensor. *Computers & Geosciences*, 35:2295–2303.
- Martí, A., Queralt, P., Ledo, J., and Farquharson, C. (2010). Dimensionality imprint of electrical anisotropy in magnetotelluric responses. *Physics of the Earth and Planetary Interiors*, 182:139–151.
- McNeill, J. (1980). *Applications of transient electromagnetic techniques*. Geonics Technical Note TN-7.
- Miles, C., White, M., and Scholz, G., editors (2012). *Assessment of the impacts of future climate and groundwater development on Great Artesian Basin springs / A technical report to the Australian Government from the CSIRO Great Artesian Basin Water Resource Assessment*. CSIRO Water for a Healthy Country Flagship, Australia.
- Minsley, B. J., Sogade, J., and Morgan, F. D. (2007). Three-dimensional self-potential inversion for subsurface DNAPL contaminant detection at the Savannah River Site, South Carolina. *Water Resources Research*, 43:1–13.
- Morgan, F. (1989). Fundamentals of streaming potentials in geophysics: laboratory methods. In *Detection of Subsurface Flow Phenomena*, volume 27 of *Lecture Notes in Earth Sciences*, pages 133–144. Springer Verlag.
- Morgan, R. (1980). *Eustacy in the Australian Early and Middle Cretaceous*. Geological Survey of New South Wales Bulletin 27.
- Morton, S. R., Doherty, M. D., and Barker, R. D. (1995). *Natural heritage values*

- of the Lake Eyre Basin in South Australia: World Heritage Assessment*. CSIRO Division of Wildlife and Ecology, Canberra.
- Mudd, G. (2000). Mound springs of the Great Artesian Basin in South Australia: a case study from Olympic Dam. *Environmental Geology*, 39:463–476.
- Nabighian, M. N. and Macnae, J. C. (1991). Time domain electromagnetic prospecting methods. In M. N. Nabighian, editor, *Electromagnetic Methods in Applied Geophysics*, volume 2, pages 427–489. Society of Exploration Geophysicists, Tulsa, OK, USA.
- Nelson, S. T., Karlsson, H. R., Paces, J. B., Tingey, D. G., Ward, S., and Peters, M. T. (2001). Paleohydrologic record of spring deposits in and around Pleistocene pluvial Lake Tecopa, southeastern California. *GSA Bulletin*, 113:659–670.
- Nobes, D. C. (1996). Troubled waters: Environmental applications of electrical and electromagnetic methods. *Surveys in Geophysics*, 17:393–454.
- Nourbehecht, B. (1963). Irreversible thermodynamic effects in inhomogeneous media and their applications in certain geoelectric problems. Ph.D. thesis, Massachusetts Institute of Technology.
- Ogilvy, A. A., Ayed, M. A., and Bogoslovsky, V. A. (1969). Geophysical studies of water leakages from reservoirs. *Geophysical Prospecting*, 17:36–62.
- Özkul, M., Gökgöz, A., and Horvatinčić, N. (2010). Depositional properties and geochemistry of Holocene perched springline tufa deposits and associated spring waters: a case study from the Denizli Province, Western Turkey. *Geological Society, London, Special Publications*, 336:245–262.
- Parker, R. L. (1983). The magnetotelluric inverse problem. *Geophysical Surveys*, 6:5–25.
- Patella, D. (1997). Introduction to ground surface self-potential tomography. *Geophysical Prospecting*, 45:653–681.
- Paul, M. K. (1965). Self-potential anomalies caused by inclined sheets of infinite horizontal extension. *Geophysics*, 30:418–423.
- Pek, J. and Santos, F. (2002). Magnetotelluric impedances and parametric sensitivities for 1-D anisotropic layered media. *Computers & Geosciences*, 28:939–950.

- Pellerin, L. (2002). Applications of electrical and electromagnetic methods for environmental and geotechnical investigations. *Surveys in Geophysics*, 23:101–132.
- Pentecost, A. (2005). *Travertine*. Springer.
- Petiau, G. (2000). Second Generation of Lead-lead Chloride Electrodes for Geophysical Applications. *Pure Applied Geophysics*, 157:357–382.
- Ponder, W. (1986). Mound springs of the Great Artesian Basin. In P. De Dekker and W. D. Williams, editors, *Limnology in Australia*, pages 403–420. CSIRO, Australia.
- Pous, J., Heise, W., Schnegg, P.-A., Munoz, G., Marti, J., and Soriano, C. (2002). Magnetotelluric study of the Las Canades caldera (Tenerife, Canary Islands): structural and hydrogeological implications. *Earth and Planetary Science Letters*, 204:249–263.
- Preiss, W. (2000). The Adelaide Geosyncline of South Australia and its significance in Neoproterozoic continental reconstruction. *Precambrian Research*, 100:21–63.
- Preiss, W. V. (1987). *The Adelaide Geosyncline: Late Proterozoic stratigraphy, sedimentation, palaeontology and tectonics*. Department of Mines and Energy, South Australia, Bulletin 53.
- Prescott, J. R. and Habermehl, M. A. (2008). Luminescence dating of spring mound deposits in the southwestern Great Artesian Basin, northern South Australia. *Australian Journal of Earth Sciences*, 55(2):167–181.
- Price, A. T. (1973). The theory of geomagnetic induction. *Physics of the Earth and Planetary Interiors*, 7(3):227–233.
- Priestley, S., Karlstrom, K. E., Love, A. J., Crossey, L., Polyak, V., and Asmerom, Y. (2013). Palaeo-discharge inferred from U-series dating of spring travertine deposits. In A. J. Love, P. Shand, L. Crossey, G. A. Harrington, and P. Rousseau-Gueutin, editors, *Allocating Water and Maintaining Springs in the Great Artesian Basin, Volume III: Groundwater Discharge of the Western Great Artesian Basin*, chapter 5, pages 67–80. National Water Commission, Australia.
- Radke, B. (2009). *Hydrothermal and Geothermal Prospectivity of Sedimentary*

Basins in Central Australia; Warburton, Cooper, Perdirka, Galilee, Simpson and Eromanga Basins. Geoscience Australia Record 2009/25.

Ransley, T. R., Radke, B. M., and Kellett, J. R. (2012a). Jurassic–Cretaceous geology. In T. R. Ransley and B. D. Smerdon, editors, *Hydrostratigraphy, hydrogeology and system conceptualisation of the Great Artesian Basin / A technical report to the Australian Government from the CSIRO Great Artesian Basin Water Resource Assessment*, chapter 2, pages 15–54. CSIRO Water for a Healthy Country Flagship, Australia.

Ransley, T. R., Radke, B. M., Kellett, J. R., Carey, H., Bell, J. G., and O'Brien, P. E. (2012b). Hydrogeology of the Great Artesian Basin. In T. R. Ransley and B. D. Smerdon, editors, *Hydrostratigraphy, hydrogeology and system conceptualisation of the Great Artesian Basin / A technical report to the Australian Government from the CSIRO Great Artesian Basin Water Resource Assessment*, chapter 5, pages 77–122. CSIRO Water for a Healthy Country Flagship, Australia.

Ransley, T. R., Radke, B. M., and O'Brien, P. E. (2012c). Stratigraphy of the Great Artesian Basin. In T. R. Ransley and B. D. Smerdon, editors, *Hydrostratigraphy, hydrogeology and system conceptualisation of the Great Artesian Basin / A technical report to the Australian Government from the CSIRO Great Artesian Basin Water Resource Assessment*, chapter 4, pages 71–76. CSIRO Water for a Healthy Country Flagship, Australia.

Ransley, T. R. and Smerdon, B. D., editors (2012). *Hydrostratigraphy, hydrogeology and system conceptualisation of the Great Artesian Basin / A technical report to the Australian Government from the CSIRO Great Artesian Basin Water Resource Assessment*. CSIRO Water for a Healthy Country Flagship, Australia.

Revil, A. (2003a). Principles of electrography applied to self-potential electrokinetic sources and hydrogeological applications. *Water Resources Research*, 39(5):1–15.

Revil, A. (2003b). The volcano-electric effect. *Journal of Geophysical Research*, 108(B5):1987–1989.

Revil, A., Cathles, L. M. I., Losh, S., and Nunn, J. A. (1998). Electrical conductivity in shaly sands with geophysical applications. *Journal of Geophysical Research*, 103(B10):23,925–23,936.

Revil, A., Jardani, J., and Dupont, J. P. (2008). Reply to comment by D.

- Gibert and P. Sailhac on "Self-potential signals associated with preferential groundwater flow pathways in sinkholes". *Journal of Geophysical Research*, 113:2007–2009.
- Revil, A., Karaoulis, M., Johnson, T., and Kemna, A. (2012). Review: Some low-frequency electrical methods for subsurface characterization and monitoring in hydrogeology. *Hydrogeology Journal*, 20:617–658.
- Revil, A. and Leroy, P. (2001). Hydroelectric coupling in a clayey material. *Geophysical Research Letters*, 28:1643–1646.
- Revil, A., Mendonca, C. A., Atekwana, E. A., Kulesa, B., Hubbard, S. S., and Bohlen, K. (2010). Understanding biogeobatteries: Where geophysics meets microbiology. *Journal of Geophysical Research*, 115(G00G02):1–22.
- Revil, A., Pezard, P. A., and Glover, P. W. J. (1999). Streaming potential in porous media 1. Theory of the zeta potential. *Journal of geophysical research*, 104(B9):20,021–20,031.
- Roberts, C. and Mitchell, C. (1987). Spring mounds in southern Tunisia. *Geological Society, London, Special Publications*, 35(1):321–334.
- Rodi, W. and Mackie, R. (2001). Nonlinear conjugate gradients algorithm for 2-D magnetotelluric inversion. *Geophysics*, 66:174–187.
- Rogers, P. A. and Freeman, P. J. (1996a). *Explanatory Notes for the Warrina 1:250 000 geological map*. Geological Survey, South Australia.
- Rogers, P. A. and Freeman, P. J. (1996b). WARRINA map sheet. In *South Australia. Geological Survey. Geological Atlas 1 : 250 000 Series, sheet SH 53-3*.
- Rubin, Y. and Hubbard, S. S. (2005). *Hydrogeophysics*. Springer.
- Rust, W. M. (1938). A historical review of electrical prospecting methods. *Geophysics*, 3:1–6.
- Sailhac, P. and Marquis, G. (2001). Analytic potential for the forward and inverse modeling of SP anomalies caused by subsurface fluid flow. *Geophysical Research Letters*, 28:1851.
- Sanders, D., Wertl, W., and Rott, E. (2011). Spring-associated limestones of the Eastern Alps: overview of facies, deposystems, minerals, and biota. *Facies*, 57:395–416.

- Sato, M. and Mooney, H. M. (1960). The electrochemical mechanism of sulfide self-potentials. *Geophysics*, 25:226–249.
- Schiavone, D. and Quarto, R. (1984). Self-potential prospecting in the study of water movements. *Geoexploration*, 22:47–58.
- Scholl, D. W. (1960). Pleistocene algal pinnacles at Searles lake, California. *Journal of Sedimentary Research*, 30:414–431.
- Scholl, D. W. and Taft, W. H. (1964). Algae, contributors to the formation of calcareous tufa, Mono Lake, California. *Journal of Sedimentary Petrology*, 34:309–319.
- Sill, W. R. (1983). Self-potential modeling from primary flows. *Geophysics*, 48(1):76.
- Simpson, F. and Bahr, K. (2005). *Practical magnetotellurics*. Cambridge University Press.
- Slater, L. D. and Lesmes, D. (2002). IP interpretation in environmental investigations. *Geophysics*, 67:77–88.
- Smith, D. A. (1980). Sealing and Nonsealing Faults in Louisiana Gulf Coast Salt Basin. *AAPG Bulletin*, 64:145–172.
- Smith, J. T. and Booker, J. R. (1988). Magnetotelluric inversion for minimum structure. *Geophysics*, 53(12):1565–1576.
- Smith, R. S. and West, G. F. (1988). An explanation of abnormal TEM responses: coincident-loop negatives, and the loop effect. *Exploration Geophysics*, 19:435–446.
- Spies, B. R. (1989). Depth of investigation in electromagnetic sounding methods. *Geophysics*, 54(7):872–888.
- Sternberg, B. K. (2010). The variability of naturally occurring magnetic field levels: 10 Hz to 8 kHz. *Geophysics*, 75:F187–F197.
- Stoll, J., Bigalke, J., and Grabner, E. (1995). Electrochemical modelling of self-potential anomalies. *Surveys in Geophysics*, 16:107–120.
- Stratton, J. A. (1941). *Electromagnetic theory*. McGraw-Hill Book Co., New York.
- Sumner, J. S. (1984). *Principles of induced polarization for geophysical exploration*. Elsevier Science.

- Swift, C. M. (1962). A Magnetotelluric Investigation of an Electrical Conductivity Anomaly in the Southwestern United States. Ph.D. thesis, Princeton University.
- Torres-Verdin, C. and Bostick, F. X. (1992). Principles of spatial surface electric field filtering in magnetotellurics: Electromagnetic array profiling (EMAP). *Geophysics*, 57(4):603–622.
- Unsworth, M., Soyer, W., Tuncer, V., Wagner, A., and Barnes, D. (2007). Hydrogeologic assessment of the Amchitka Island nuclear test site (Alaska) with magnetotellurics. *Geophysics*, 72(3):B47–B57.
- Vacquier, V., Holmes, C. R., Kintzinger, P. R., and Lavergne, M. (1957). Prospecting for ground water by induced electrical polarization. *Geophysics*, 22:660–687.
- Watterson, J., Walsh, J., Nicol, A., Nell, P., and Bretan, P. (2000). Geometry and origin of a polygonal fault system. *Journal of the Geological Society*, 157:151–162.
- Weidelt, P. (1972). The Inverse Problem of Geomagnetic Induction. *Zeitschrift fur Geophysik*, 38:257–289.
- Weidelt, P. (1982). Response characteristics of coincident loop transient electromagnetic systems. *Geophysics*, 47:1325–1330.
- Weidelt, P. (1999). 3-D conductivity models: implications of electrical anisotropy. In M. Oristaglio and B. R. Spies, editors, *Three-dimensional electromagnetics*, volume 7 of *Geophysical Development Series*, chapter 8, pages 119–137. Society of Exploration Geophysicists.
- White, D. C. and Lewis, M. M. (2011). A new approach to monitoring spatial distribution and dynamics of wetlands and associated flows of Australian Great Artesian Basin springs using QuickBird satellite imagery. *Journal of Hydrology*, 408:140–152.
- Williams, A. F. and Holmes, J. W. (1978). A novel method of estimating the discharge of water from mound springs of the Great Artesian Basin, central Australia. *Journal of Hydrology*, 38:263–272.
- Williams, K. H., Hubbard, S. S., and Banfield, J. F. (2007). Galvanic interpretation of self-potential signals associated with microbial sulfate-reduction. *Journal of Geophysical Research*, 112(G3):1–8.

- Zlotnicki, J. and Nishida, Y. (2003). Review on morphological insights of self-potential anomalies on volcanoes. *Surveys in Geophysics*, 24:291–338.